Experimental Behaviour of Inelastic Mass–Asymmetric Multi–Storey Buildings under Seismic Loading

Eric Andrew Nichol

Submitted for the degree of Doctor of Philosophy

UNIVERSITY COLLEGE LONDON
DEPARTMENT OF CIVIL & ENVIRONMENTAL ENGINEERING
GOWER STREET, LONDON, WC1E 6BT, UK

ABSTRACT

Buildings with non coincident centres of mass and stiffness respond in both translation and rotation during seismic ground excitations. This translational and rotational interaction (torsional coupling) can lead to excessive forces in some structural members. This could possibly lead to structural failure if the building is not properly designed to accommodate this response interaction. Previous elastic analytical studies have determined the structural parameters that govern the degree of torsional coupling. However, the parameters found influencing torsional coupling during inelastic response in previous analytical studies have been found to be both more numerous and contradictory than those associated with the elastic response.

This study concentrates on the inelastic behaviour of a series of four storey models representing idealized buildings. These building models have been developed from a previous experimental study on the elastic behaviour of torsional coupling. In this inelastic study, hinge units have been designed and used to simulate the yielding of the column or beam members in the experimental model, while maintaining ease of repeatability between tests. The yielding moment in these hinge units can be adjusted to alter the effective strength of the columns or beams in the model. This, along with the ability to vary the floor mass distribution, column sizes (diameter and length), and stiffness distribution

allows for a degree of control on the structural parameters deemed important in previous inelastic analytical studies.

Results are presented which illustrate the effects that the various structural configurations have on the different measures of inelastic building response, and its vulnerability to damage. These include changes in the building frequencies, member displacement ductilities and vulnerability, hysteretic energy dissipation, and peak structural responses. The study presents a comprehensive investigation of the column–yielding building models. Additionally, select key cases of the column yielding configurations are compared to both the beam–yielding models, and a computational model.

ACKNOWLEGEMENTS

This thesis is based on a research programme funded by the UK Science Engineering Research Council (Grant GR/F/60632), whose support is gratefully acknowledged. The findings and recommendations in this study are those of the author and not necessarily those of the grant sponsor.

ALL MISSING PAGES ARE BLANK

IN

ORIGINAL

TABLE OF CONTENTS

LIST OF FIGURES

Hinge Unit Performance 165

ANALYTICAL STUDY 185

Design and Performance of Model Floor-Column Joints for Simulation of Inelastic Structural Response under Earthquake Loading 313

LIST OF TABLES

CHAPTER 1

INTRODUCTION

Inelastic yielding of structural elements in buildings subjected to severe earthquakes can result in the formation of collapse mechanisms, leading to failure and possibly loss of life. Buildings which have asymmetric distributions of mass, stiffness, and/or strength can be especially vulnerable due to increased ductility and displacement demands caused by lateral-torsional response interaction (torsional coupling). If the locations of yielding can be deliberately controlled, then the damping and energy absorbing capacity of plastic yield can usually be arranged to protect the durability and general stability of the building. However, yielding is accompanied by changes in the dynamic behaviour of the structure,

such as changes in the fundamental structural frequency and stiffness distribution. Yielding is particularly critical when torsional coupling is involved, as the initiation of plastic hinges is progressive beginning usually with the outer elements of a structure, leading to increased eccentricity (of stiffness and/or strength) and therefore larger torsional response. Simplified provisions for torsional coupling in current building codes linearise the potential non-linear seismic behaviour of buildings. In lieu of this approach, most building codes also allow a full non-linear analysis if the simplified approach leads to excessive demand to capacity ratios.

This project formed the second-stage[1] of a research programme involving small-scale parametric model testing of torsional coupling effects in multi-storey buildings under seismic loading. The tests were carried out using the SERC (now EPSRC) 6-axis earthquake simulator facility at Bristol University. The principal objectives of this study are in the development and non-linear capabilities of an experimental model, its hinging mechanisms, and its dynamic characteristics. The performance of the hinge units, which were developed for this study, will indicate their applicability for further experimental research on fully code-compatible building models. The main aim of this study is towards examining and understanding the experimental behaviour of the building model and the performance of its hinge units. The intent is to highlight the general inelastic response characteristics of the model built to various configurations, and to compare with an analytical model counterpart. The hinge units are a valuable tool in experimental research, enabling numerous non-destructive inelastic tests to be performed in a relatively short period of time. This pro-

1. The first stage of this research programme involved the elastic response of multi-storey small-scale parametric models. This research was performed by M.R. Maheri, A.M. Chandler, and R.H. Bassett (SERC grant # GR/E83641).

vides cost savings in both labour and materials, since a non-destructive test allows the reuse of structural components. This study will also show the high degree of repeatability between the experiments, as a result of utilizing the hinge units for modelling elastic behaviour. The following points emphasise the scope of this research project:

- Develop and calibrate a simulated hinge joint model for experimental dynamic response studies of multi-storey buildings.

- Quantify the performance of the experimental hinge unit devices.

- Assess the performance of the hinge units with regards to future experimental and commercial applications.

- Characterise the combinations of mass and strength eccentricity that give rise to significant inelastic lateral-torsional coupling in the building models.

- Highlight combinations of mass and strength eccentricities that counter-balance the adverse affects of torsional coupling.

- Identify changes in the dynamic amplification of torsional response due to asymmetric yielding, and how this compares to the elastic modal coupling identified in earlier studies.

- Identify and quantify changes to building frequencies and dynamic earthquake response, caused by plastic yield.

- Quantify the energy absorbing capabilities of the hinge units, and their influence on the model's response.

- Develop an analytical model that accurately predicts the response of the various experimental models.

- Determine the required design forces, and assess existing analytical and codified design procedures with regards to the analytical model.

The thesis is presented in eight chapters, with four appendices further detailing some of the results. This *Introduction* (Chapter 1) clarifies the aims of this study, and details the order in which the material is presented. The next Chapter on the *Background* identifies and discusses previous analytical and experimental research relevant to this study. Due to the scarcity of experimental parametric studies in the field of torsional coupling, mainly the results from previous analytical studies on torsional coupling are presented. The emphasis of the previous work selected for review is in the behaviour of structures undergoing non-linear torsional coupling; not in the strengths and weaknesses of current building code design guidelines, a review of which is not considered directly relevant to this study.

The experimental model is presented in Chapters 3 and 4 of this study. In Chapter 3, the *Experimental Model* is discussed in terms of the model characteristics in a series of parametrically controlled structural configurations. This includes descriptions of the overall building model geometry, column configurations, and mass distribution. Details are also presented in this chapter on the shake table tests performed on three distinct types of

building configuration: single-storey, multi-storey beam-yielding (inelastic behaviour simulated to occur in beam elements located in the model floors), and multi-storey column-yielding (inelastic behaviour concentrated in the columns at floor level). The dynamic characteristics of these three model configurations are also presented. This includes their elastic frequencies, mode shapes, and damping characteristics. The details of the shake table instrumentation and calibration of the hinge units are also discussed.

Chapter 4, *Hinge Unit Design*, focuses on the hinge units and their physical characteristics. This includes their design, assembly, capability, and placement within the various building models. The influence that the hinge units have on the model characteristics (as discussed in Chapter 3) is also presented.

Chapter 5, entitled *Experimental Shaking Table Studies*, presents in detail the methodology of the shaking table experiments, as well as the model displacement results from the shake table motions. Results are presented for each of the three model configurations (single-storey, multi-storey beam-yield, and multi-storey column-yield set-ups), each with various possible model configurations (mass and strength eccentricity), and various levels of table forcing intensity. The results presented in this chapter emphasise the displacements recorded during the shaking table tests. Results for all experiments are given in a summarised form (i.e. peak responses and displacement ratios). Key shake table tests are also presented quantitatively (i.e. displacement traces and time dependent frequency response).

The *Hinge Unit Performance* is presented in Chapter 6. This chapter describes the response characteristics of the individual hinge units—both experimentally and analyti-

cally. Results are presented for the displacement ductility and absorbed energy, as a result of introducing the hinge units. As in the previous chapter, results are presented in this chapter quantitatively for all model configurations and forcing intensities, and qualitatively for key shake table tests. This chapter also details some of the possible academic and commercial applications, as well as some of the drawbacks of the hinge units in their existing form.

The methodology and results found from the *Analytical Study* are presented in Chapter 7. This contains a comparison between the experimental results, and results obtained through finite element methods. Since a code evaluation based on the experimental model did not form part of the original intent of this study, the analytical model modifies some of the shortcomings of the experimental model—in terms of code compatibility with the 1994 edition of the Uniform Building Code, which is regarded as typical with respect to codified torsional provisions.

The *Conclusion* of both the experimental and analytical research is presented finally in Chapter 8. This section summarises the findings of this study, as well as the correlation and discrepancies found between previous research and this study.

The appendices to this thesis present in more detail some of the original work performed for reference in the main chapters. Appendix A details the current design philosophy, in regard to "irregular" buildings, of the 1994 edition of the Uniform Building Code. Some discussion is also presented in this appendix on the potential application of the experimental model to the evaluation of codified design guidelines. The modifications required on

the experimental model in order to permit a code-compatible study are treated in Appendix C. Appendix D presents the analytically determined response of a structure based directly on a codified experimental model, which arises from the modifications outlined and discussed in Appendix C. Appendix E tabulates and describes the different variables used throughout this study. A list of references used in this study are presented in Appendix F. Finally, Appendix G contains two publications that have arisen to date as a result of this research programme. These include, first, a paper which highlights the effects of mass and stiffness eccentricity on floor displacements determined through both experimental and analytical methods. The second paper discusses the initial performance of the experimental hinge units on a single-storey model.

In summary, this experimental research programme provides a valuable source of data to complement analytical studies in the field of torsional coupling. The performance of the hinge unit devices will benefit future inelastic, experimental research programmes by providing a cost effective means of modelling semi–idealised elastic–perfectly plastic behaviour.

CHAPTER 2

BACKGROUND

2.1 OVERVIEW

Structures in which the centres of mass are offset from their centre of stiffness respond in both translation and rotation when subjected to pure translational ground (base) motions. This "torsional coupling" of the response of asymmetric structures has been an area of study over the past few decades. Initially, analytical studies into the elastic response of this class of structure formed the main body of research. As a result, the elastic response in asymmetric structures is well understood. However, current seismic design criteria allow

inelastic structural behaviour. This applies particularly during MPE (maximum probable event) and MCE (maximum credible event) motions, where an elastic response may not economically feasible. As a result, the more recent research into the response of asymmetric structures has involved some degree of inelastic behaviour.

The elastic response of torsionally coupled buildings has been extensively studied. Their response characteristics, particularly in single storey structures, is understood. As one would expect, as the distance between the centres of mass and stiffness increases, so does the torsional response. Researchers also found that the ratio of uncoupled rotation to translation frequencies is also an important parameter [KAN, 1977; TSICNIAS, 1981]. When this frequency ratio $\left(\Omega = \frac{\omega_\Theta}{\omega_y}\right)$ is close to unity, some of the energy of the translational (lateral) response is shifted to the rotational response. As a result, torsional motions are amplified, and translations are reduced. Structures with Ω less than 0.6 do not suffer greatly from torsional coupling, but are sensitive to torsional vibrations. Likewise, when Ω is greater than about 1.6, a structure will respond primarily in translation, with negligible adverse affects from torsional coupling. Researchers also found that the uncoupled lateral frequency also affects the torsional amplification [RADY, 1988]. They found that torsional amplification increased for decreasing lateral frequency (ω_y) when $\Omega<1$. Conversely, torsional amplification decreased for increasing lateral frequency when $\Omega>1$.

The inelastic response of torsionally coupled buildings has many more variables affecting their behaviour. In addition to the elastic parameters mentioned above are the distribution, capacity, and post-elastic behaviour of each of the structural elements. Additionally, the phasing of the ground motion can also lead to varying results. This has led to various ine-

lastic models which have resulted in varying conclusions. Researchers [CHANDLER, 1991] have addressed these discrepancies introduced by contradictory structural configurations and response parameters.

Single storey "shear wall" type models have been used for the majority of the analytical research in the inelastic asymmetric response. Typical plan views of two such systems are shown in Figure 2.1. The "shear wall" type models all assume that the individual shear wall elements provide stiffness along their major axis only. Furthermore, their stiffness behaviour is normally elastic-perfectly plastic.[1]

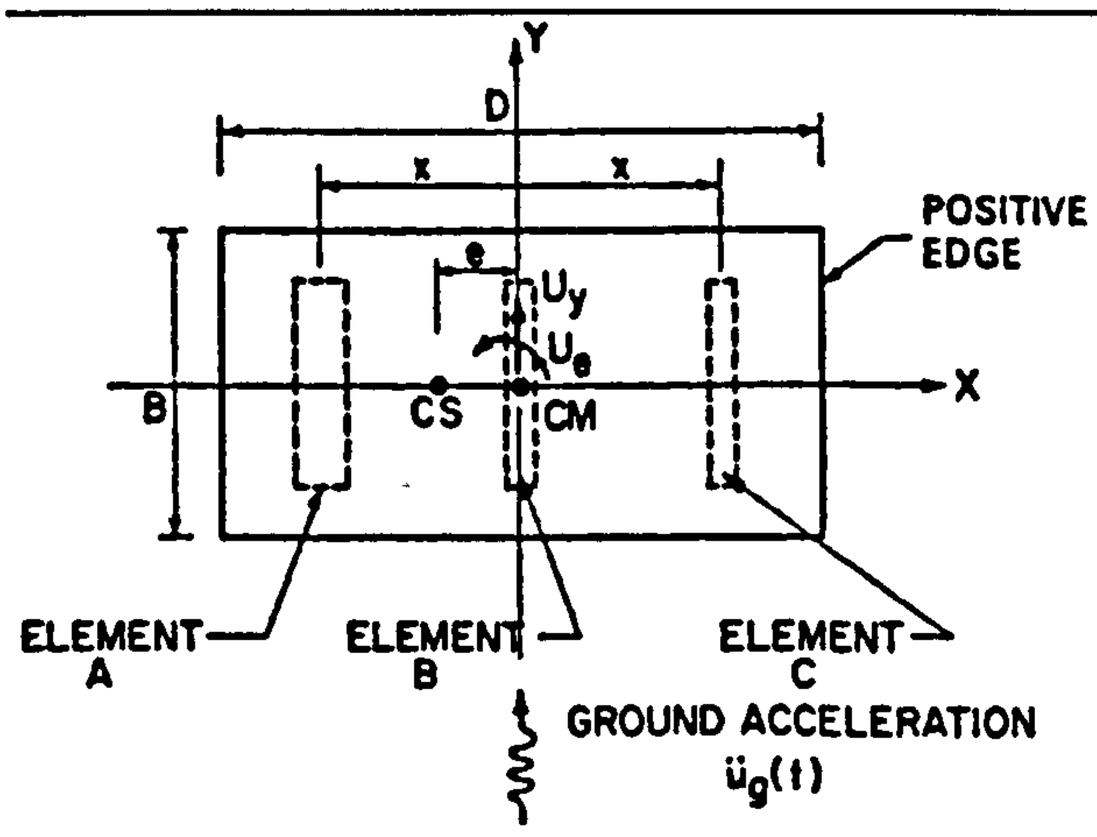

"Shear Wall" model from TSO, 1985.

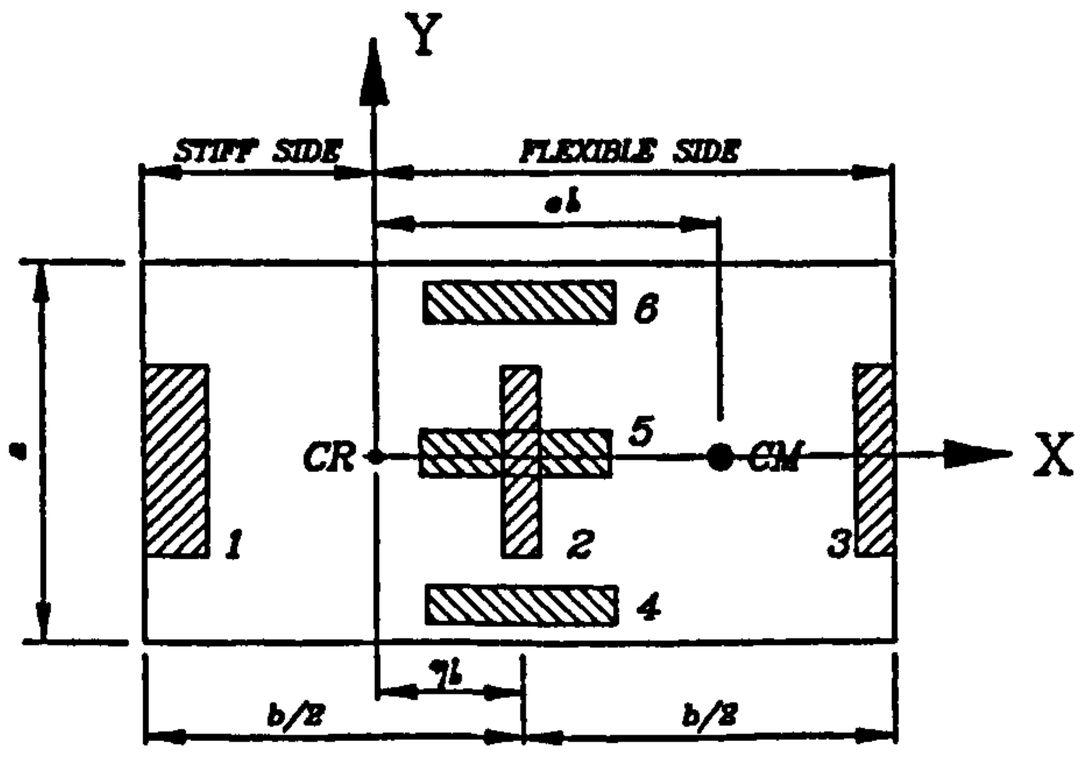

"Shear Wall" model from WONG, 1995.

Figure 2.1: Comparison of the two typical types of "Shear Wall" models used in previous analytical studies.

An extensive parametric study [GOEL, 1990] on a series of single storey "shear wall" models assessed the influence of elastic eccentricity type (mass or stiffness), number of resisting elements, their orientation, strength eccentricity, and member overstrength on the inelastic response. Goel found that for the type "shear wall" models studied, stiffness asymmetric (centre of stiffness offset from coincident geometric and mass centres) models

1. Some model studies assume a small value of post-elastic stiffness (hardening) of 1% to 5% of the elastic stiffness. This is normally required for numerical stability of the various software packages used to analyse the building models.

behaved differently from mass asymmetric (centre of mass offset from coincident geometric and stiffness centres) models. Goel also found that lateral-torsional deformations decreased with systems that have small strength eccentricities.

For the response of multi-storey buildings, the number of parameters increase even further from those of the single-storey models. A number of research papers have discussed mechanisms for extrapolating results from single-storey analyses to multi-storey buildings. One main difference with multi-storey buildings is in the calculation of the centre of stiffness (or rigidity for multi-storey buildings). Humar [1984] adopted the definition that the centre of rigidity is the location at which a load may be applied, and the floor in consideration does not rotate. Humar found that for the ten-storey models studied, this location does not reside on a vertical axis, even though the building model did not have vertical irregularities. Other researchers [CHEUNG, 1986] investigated the difficulties in determining the centre of rigidity. Their definition, which is a function of both stiffness and lateral load distribution, is the set of locations on each floor where the distribution of seismic shear can be positioned resulting in no building floor rotation. In another approach, Sternik [1993] discussed methods to decouple the equilibrium equations of multi-storey buildings, allowing the translational and rotational floor motions to be separated. Other researchers [GOEL, 1993] offer design methods in which the centres of rigidity need not be calculated. In this method, seismic shears are placed at the centre of mass of each floor without the need to specifically compute the eccentricity of each floor. However, this method also requires several iterations with a frame analysis computer program. As can be seen from all of the above, the coupled inelastic response of multi-storey buildings can become quite complicated and parameter driven.

2.2 BUILDING CODE COMPARISONS

In addition to the theoretical studies into the behaviour of elastic and inelastic torsional coupling, a significant amount of research has involved the effectiveness of various building code provisions with regards to lateral-torsional response coupling. Building codes assist the design engineer or architect in establishing both the design criteria and corresponding design loadings for the structure. They also present guidelines for distributing the seismic shear along both the horizontal and vertical axes of the building. This is normally accomplished by applying two sets of equivalent static loadings at specified distances from the floor's centre of mass, resulting in a design eccentricity that can be used during static analysis to account for dynamic effects from torsional-coupling. Appendix A (starting on page 229) offers a complete description of this method for the 1994 Uniform Building Code (UBC94). The various code based studies have compared these equivalent static loading procedures for different building codes, for a variety of model types and configurations.

As with the theoretical behavioural studies on torsionally-coupled buildings, the inelastic response of code compatible building models have resulted in varying conclusions, dependant upon the analysis model and building code used for the study. Appendix C and D in this study present a Uniform Building Code (UBC) code compatible strength distribution for an analytical model that is based on the experimental model. This study does not attempt to offer recommendations for UBC94 by the inclusion of a code compatible model. This is included to present the inelastic response of an analytical model that is similar to the experimental model, but with a more appropriate strength distribution.

2.3 EXPERIMENTAL RESEARCH

This research study was initiated to experimentally determine the inelastic response of a class of four-storey building models, and to assess the performance of the hinge units developed to model the member plasticity. Prior to the start of this study, there had been limited experimental research on the effects of torsional coupling of buildings. The first of these [AYRE, 1943] studied the effects of simple harmonic motions on single-storey asymmetric building models. These test were elastic, and only acknowledged the existence of lateral-torsional interaction. Full-scale elastic tests on multi-storey steel buildings [FOUTCH, 1978] also measured the presence of torsional-coupling. In another experimental study, researchers [BOURAHLA and BLAKEBOROUGH, 1994] studied the performance of knee braced frames in a series of building models. The building models studied were both symmetric and asymmetric, with eccentricities existing for the centres of mass, stiffness, or strength. The emphasis of the study was mainly on the elastic model response, with limited inelastic tests.

Lacking in previous experimental studies was the ability to parametrically investigate torsional coupling, especially in multi-storey buildings. Using a four-storey rigid floor model, researchers (M.R. Maheri, A. M. Chandler, and R.H. Bassett) were able to experimentally study the effect of torsional coupling. Their research parametrically studied the influence of mass distribution, and the ratio of uncoupled rotational to translational frequency, Ω. Their research generally agreed with previous analytical research. However, for a strongly coupled structure (Ω=1.2) they concluded that theory (modal analysis) underestimates the significance of the fundamental torsional mode of vibration during lat-

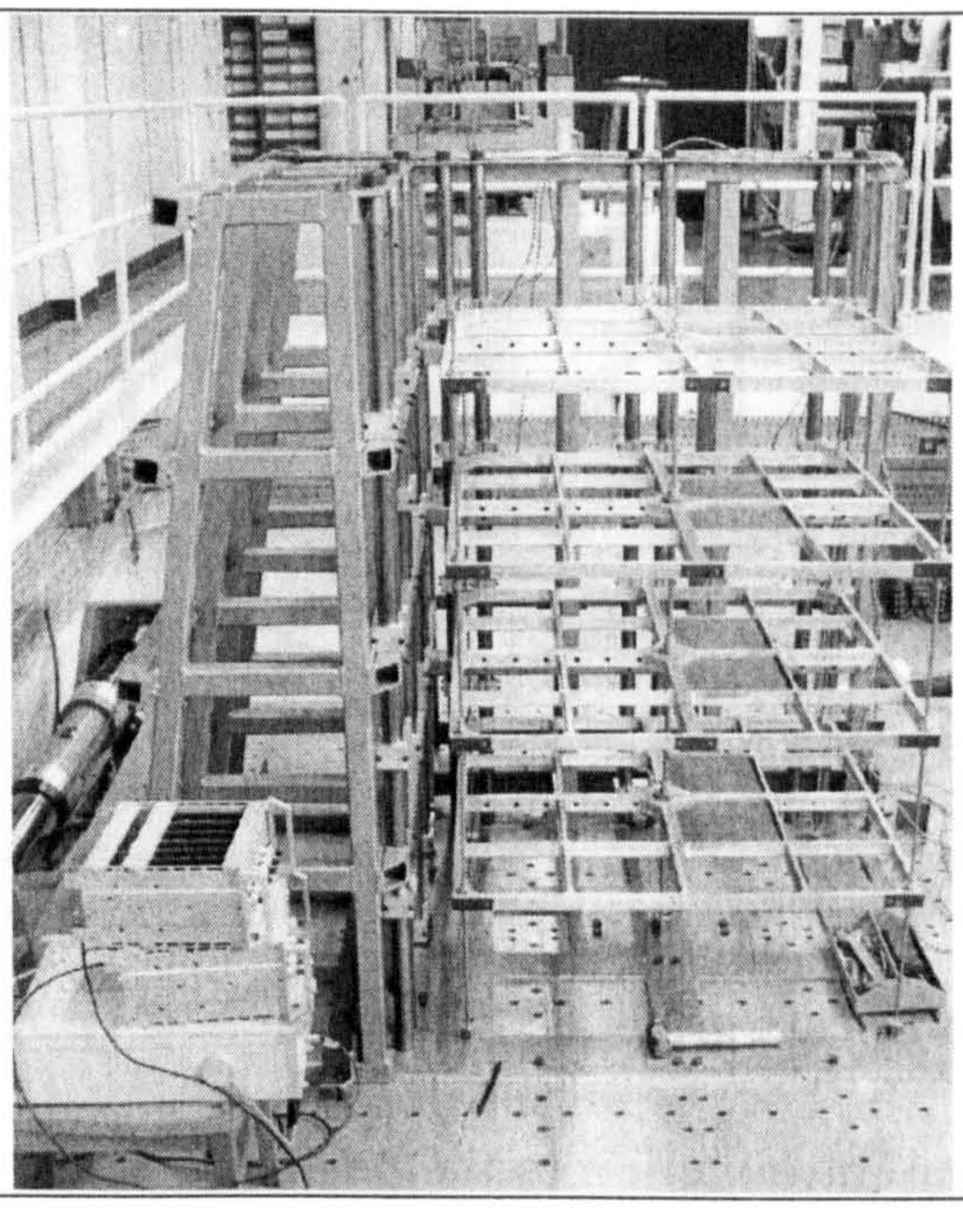

Figure 2.2: Elastic four-storey model test from Maheri, Chandler, and Bassett.

eral-torsional interaction. Theory also overestimates the contribution of the first lateral mode. This can result in large inaccuracies on the side of the building which is commonly assumed to benefit from torsional-coupling (the side furthest from the centre of mass in the case of their experimental model).

This research program is the second stage to the experimental model presented by Maheri, Chandler and Bassett. The elastic model used in their study was modified for this study by incorporating hinge units to simulate yielding at the floor-column connections. Through these modifications, changes in building frequency and dynamic earthquake response due to plastic yield could be identified, as well as the energy-absorbing capability of the building, and the benefits to asymmetric structures.

This study concentrates on the dynamic behaviour (both elastic and inelastic) of the four-storey building models. However, prior to testing these modified multi-storey experimental models, a series of single-storey models (Figure 2.3) were tested on a shake table.

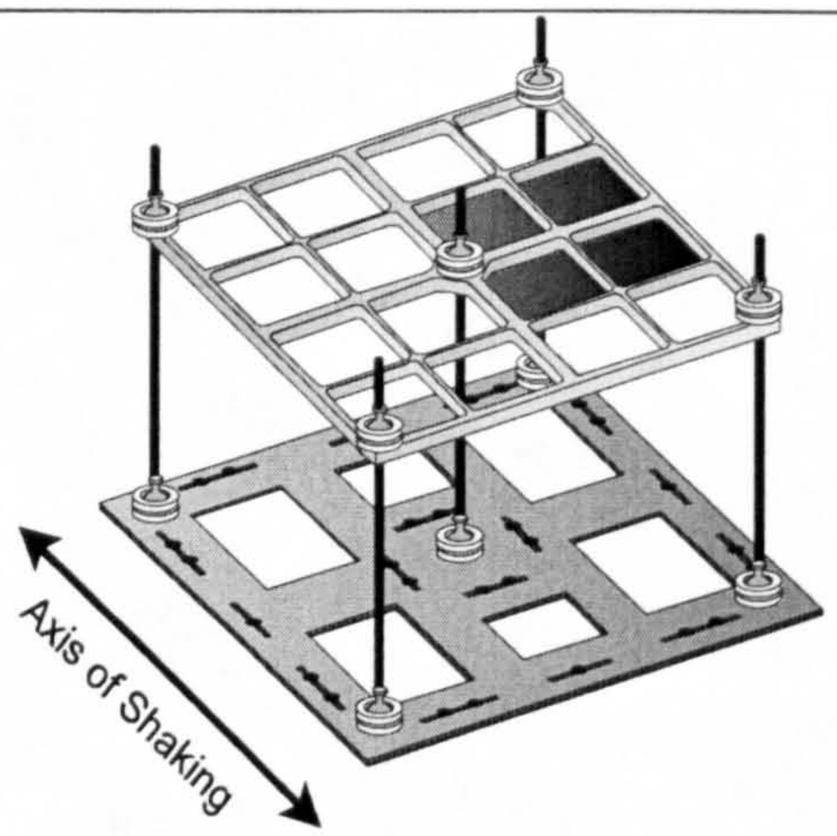

Figure 2.3: Sketch of single-storey experimental model used during preliminary tests.

These single-storey experiments provided the researchers (E.A. Nichol, A.M. Chandler, and R.H. Bassett) with an introduction to the performance of both the hinge units and shake table facility. The results and finding of these tests were published [NICHOL, 1991], and have also been reproduced after the appendices of this study (starting on page 313).

The building model presented in this study is based on a moment resisting frame (MRF) system, and not the "shear wall" type models that have encompassed the majority of previous analytical research. The main difference between a "shear wall" model and a MRF is in the added inelastic parameter of yield location in a MRF system. In this model, plastic yield may occur in either the beams or columns of the building frame. Both result in a structural softening upon yield, but to a different degree. The experimental model is comprised of a relatively rigid floor in comparison to its flexible columns. Recent research [Ju, 1999] has shown that rigid floor frame models are as accurate as flexible floor models when simulating the response of actual frame buildings. This may not be the case for "shear wall" models.

CHAPTER 3

EXPERIMENTAL MODEL

The building models used in this study were designed to approximate theoretical behaviour of multi-storey, moment-resisting frame buildings under seismic loading. Modelling the behaviour of actual concrete or steel-frame buildings, at either full or reduced scale, is beyond the scope of this research. Instead, the experimental model is intentionally idealised, and has been designed to behave in a manner similar to computational or analytical models which have idealised properties. The study also presents an analytical model verified by comparison with some of the results from the experimental models—this is presented in Chapter 7. Modelling the dynamic earthquake response behaviour

experimentally allows the results of this research to be compared with previous elastic and inelastic analytical studies. Although analogies can be made with the performance of actual buildings, the experimental models are not scaled or designed to be fully representative of prototypical structures. The experimental model was designed to exhibit perfect plasticity with non–degrading hysteresis loops, and plastic deformations concentrated at the beam–column connections. This is similar to the post–elastic behaviour specified in previous analytical studies. In actual buildings, the inelastic behaviour is normally far from perfect. Other building elements such as walls, infill panels, and secondary structural systems can significantly affect response frequencies, elastic damping, and the inelastic response—all of which have not been considered in this study. Notwithstanding these discrepancies, the experimental model provides a valuable insight for improving understanding of the inelastic coupled lateral and torsional response of actual framed structures.

3.1 EXPERIMENTAL MODEL DESCRIPTION

This experimental and analytical study is based primarily on the response of a series of four–storey, mass asymmetric building models, which allow yielding at the beam–column connections. Some results are also presented for a single–storey model, with yielding allowed at both top and bottom column ends. The experimental building model is a modified version of an elastic four–storey model developed and used in a prior SERC research grant (G/E/83641, 1986-89), the results of which have been reported in a series of papers [Chandler, et al., 1988(b); Bassett, et al., 1990; Maheri, et al., 1991]. The modified mode in this study permits inelastic behaviour during testing without permanent damage to the

model. The alterations made to the original elastic model consist of attaching mechanical hinge units to the floors of the model at the column connections (see Figures 3.4 and 3.5, starting on page 53). In most circumstances, hinge units were also mounted on the shake table surface at the column bases. The hinge units, developed specifically for this study, simulate nearly perfect plasticity in the beam–column connections of the structure, and are discussed in the following Chapter.

This chapter details the general arrangement of the various building models. This includes the structural layout and configuration of the test models. The determination of the dynamic characteristics, such as the frequencies, mode shapes, and elastic (viscous) damping are also presented. An overview of the non-linear response arising as a result of introducing the hinge units is covered in the following two chapters.

Three basic model configurations have been studied experimentally. The first of these is a single–storey model, which allows yielding at both the column base and the beam–column connection of the floor. This model configuration was primarily intended to test:

- The behaviour of the hinge units.
- The effectiveness of the table forcing motions.
- The quality of the data acquisition methods.

An overview of results from this model has been presented in a paper by the grant researchers [Nichol, et al., 1991], which has been reproduced in Appendix G. The remaining two inelastic model configurations form the basis of the majority of this study. These two configurations differ in the location of concentrated yielding during inelastic

behaviour—either in the floor beams or columns of the model. The beam yielding configuration simulates buildings where the columns remain elastic, and damage is concentrated in the floor beams. The column yielding configuration simulates yielding in the columns, concentrated at the centre line of each floor. Figure 3.1 shows the two configurations, and the region in which beam or column yielding is simulated.

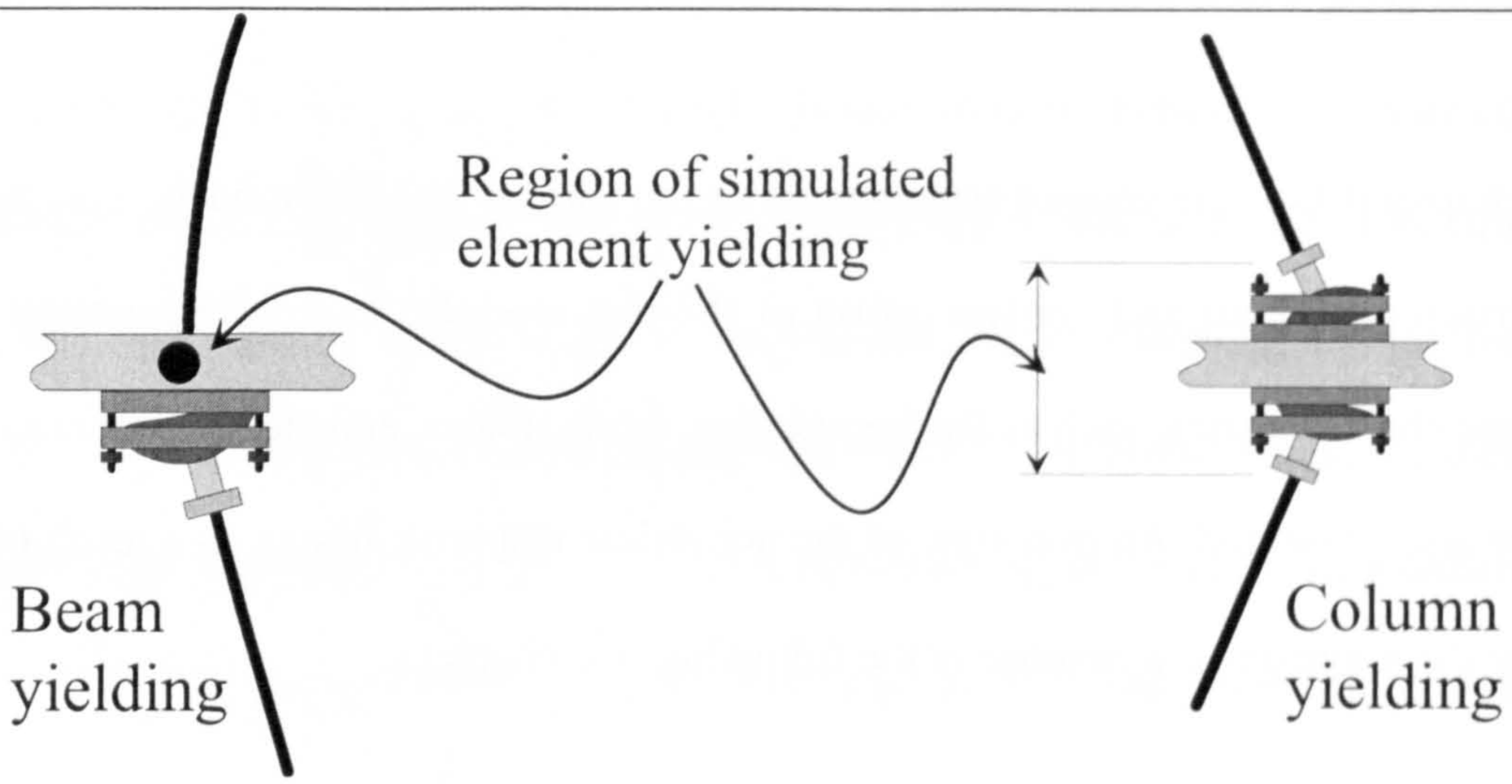

Figure 3.1: Zones of simulated yielding for the column and beam yielding configuration.

3.1.1 Floor and Mass Configurations

Each floor of the experimental model is constructed of four rigid, square, aluminium sub–panels, each panel measuring 0.5 m on a side. These are bolted together to produce a single square floor, measuring 1.0 m on a side, as shown in Figure 3.2. The benefit of the sub–panel construction is for planned future research, in that various geometric floor configurations can be achieved. This will allow the effects of geometric asymmetry on the seismic response to be studied. This study, however, is limited to buildings with geometric symmetry arising from the 1.0 m square floor sections.

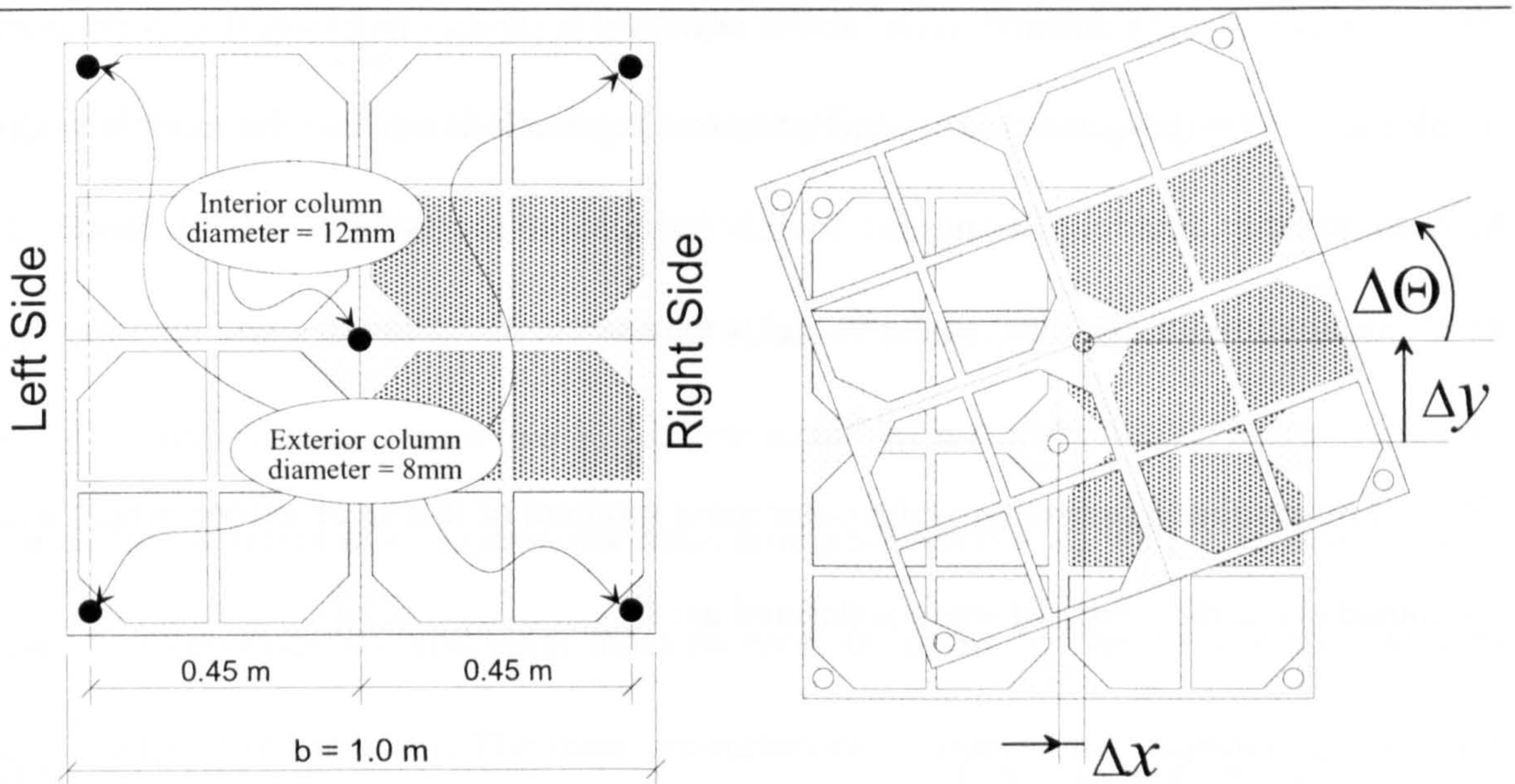

a) Column arrangement for column configuration 3. The axis orientation is identical to that shown in b).

b) Definition of coordinate system used throughout the study.

Figure 3.2: Column arrangement and coordinate system definitions.

There are three mass-related parameters which influence the response of a structure. These parameters are defined for individual floors. Equation (3.1) defines the total mass for a particular floor in terms of its discrete sections, m_i:

$$M = \sum_i m_i \tag{3.1}$$

The discrete sections pertain to the floor's aluminium sub–panels, the individual hinge units, and each of the lead plates used to achieve different mass distributions. The mass eccentricity for a particular floor is defined by equation (3.2). In this equation, M is the total floor mass and x_i is the distance from the centre of storey stiffness to the centre of mass for element m_i:

$$e_m = \frac{\sum_i m_i x_i}{M} \tag{3.2}$$

The mass eccentricity defined in the above equation is directional, in that x_i is measured along the X–axis (perpendicular to the table forcing motions). All of the models studied have no mass eccentricity along the Y–axis (parallel to the table motions). Hence, the mass distribution for all floors in the model is symmetric about the X–axis.

The last mass related parameter is the polar mass moment of inertia of a floor, which when computed about the centre of mass is defined as:

$$J_{\Theta m} = \sum_i m_i (x_i - e_m)^2 \tag{3.3}$$

The above parameters completely describe the mass distribution of a particular floor, for both the elastic and inelastic ranges of response. The floors of the models were assembled to represent a range of these parameters by distributing a series of lead plates in any of 16 possible locations (see Figure 3.3). Each of these locations can safely accommodate up to four, 5mm thick lead plates, each having a mass of 1.8kg. In this study, the total number of lead plates per floor has been held constant at eight. This results in over 15,000 possible combinations of the above three mass parameters. The simplest eight of these configura-

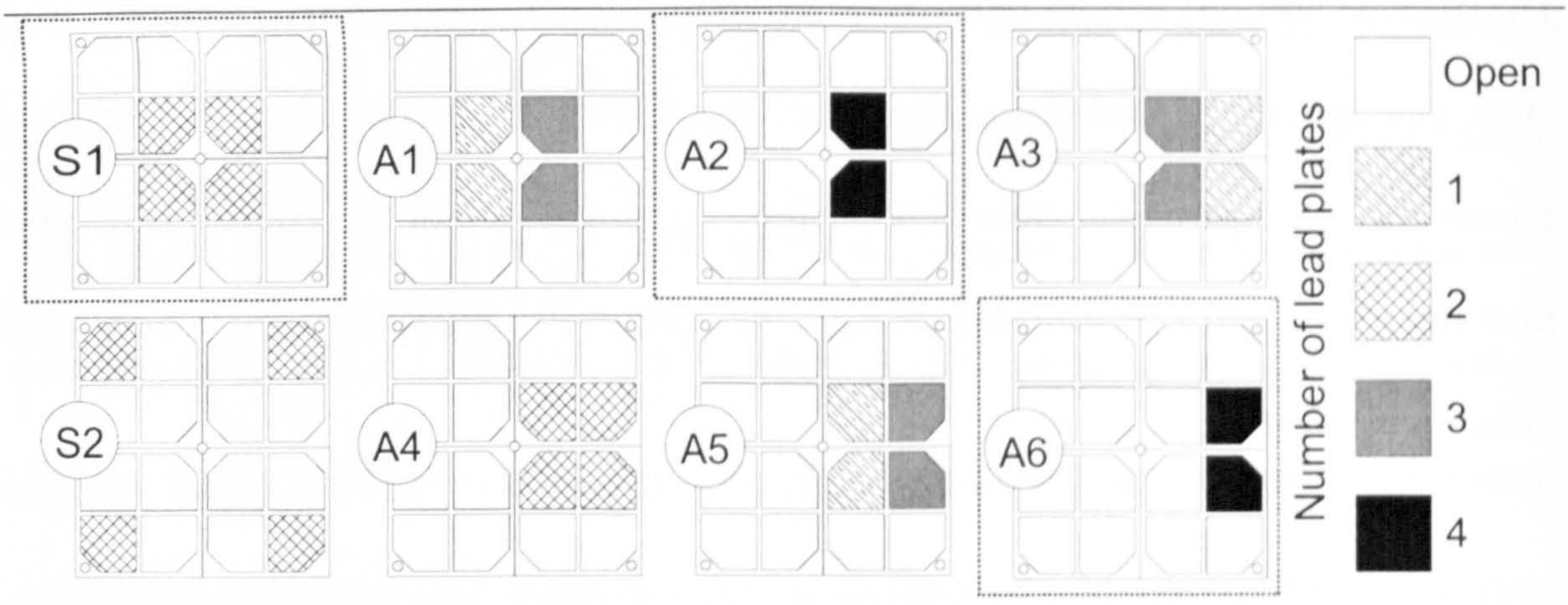

Figure 3.3: Possible planer floor mass distributions for a typical model floor. The three selected mass configurations are indicated by the dashed outlines.

tions are shown in Figure 3.3. In order to simplify the parameter range, only three of the eight mass configurations shown have been studied—these are outlined as S1, A2, and A6. These three configurations were selected due to the emphasis on these mass configurations in the previous elastic experimental study. Throughout this study, the prefix 'S' in the mass configuration refers to a *symmetric* arrangement of the lead plates (i.e. $e_m = 0$). The prefix 'A' refers to an *asymmetric* mass configuration (i.e. $e_m \neq 0$). The values of floor mass, mass eccentricity, and polar mass moment of inertia for the three mass configurations are listed in Table 3.1. The mass properties of a floor are also affected by the placement of the hinge units, as each hinge unit adds a mass of 2kg to the total floor mass. Table 3.1 indicates the mass properties as a function of the number of hinge units at each column–floor connection. As will be explained in more detail in the following chapter, *beam yielding* is achieved by adding a single hinge unit to the floor–column connection at each column location. This results in a total of five hinge units per floor (Figure 3.4 on page 53), which when used with continuous columns simulate yielding in the floors at the column locations. *Column yielding* is achieved by placing two hinge units (one on the top of the floor, and one on the bottom of the floor, as in Figure 3.5 on page 55) at each column location for a total of ten hinge units per floor. Short column segments, only one storey in height, are connected between the hinge units to simulate yielding in the region between the top and bottom hinge units on a floor. The fourth floor of the column yield configuration has only five hinge units, since the top floor has no column group above it. As a result, the fourth floor in the column yield test has different mass properties than those of the first three floors. Table 3.1 also lists the configuration with no added hinges, as evaluated in the previous elastic study.

Table 3.1: Mass properties of the experimental models.

	Mass Configuration	Total Floor Mass		
		27.1 kg no added hinge units	37.1 kg 5 hinge units per floor	47.1 kg 10 hinge units per floor
mass eccentricity e_m	S1	0.0 mm	0.0 mm	0.0 mm
	A2	65.3	47.7	37.6
	A6	195.8	143.0	112.7
polar mass moment of inertia $J_{\Theta m}$	S1	2.72 kg·m^2	5.96 kg·m^2	9.20 kg·m^2
	A2	2.59	5.84	9.09
	A6	3.45	6.79	10.13
mass radius of gyration r_m	S1	317 mm	401 mm	442 mm
	A2	309	397	439
	A6	357	428	464

Mass configuration S1 is symmetric, in that the centre of mass for a typical floor coincides with the centres of stiffness for the column groups of both the storey above and below the floor. The centre of stiffness is the location of resultant stiffness due to the group of columns above and below the floor in consideration. Throughout this study, the initial elastic centre of stiffness coincides with the geometric centre for each floor. Configurations A2 and A6 represent mass distributions with increasing mass eccentricity, e_m. However, the mass eccentricity is not a good descriptive measure by itself, since it does not take into consideration the relative dimensions of the building floor plan. It is from this reasoning that the mass eccentricity is commonly normalised by the building dimension parallel to the eccentricity (dimension b in Figure 3.2a), or the mass radius of gyration, r_m.

$$e'_m = \frac{e_m}{b} \tag{3.4}$$

$$e_m^* = \frac{e_m}{r_m} = \frac{e_m}{\sqrt{\frac{J_{\Theta m}}{M}}} \tag{3.5}$$

The values from equations (3.4) and (3.5) are listed in Table 3.2 for a building dimension (b) of 1m, and the values of r_m from Table 3.1.

Table 3.2: Normalised mass eccentricity of the experimental models.

Yielding Configuration	Mass Configuration	Mass eccentricity normalised by building dimension, b e'_m		Mass eccentricity normalised by mass radius of gyration, r_m e_m^*	
		Floors 1-3	Floor 4	Floors 1-3	Floor 4
Beam Yield	S1	0.0		0.0	
	A2	0.0477		0.120	
	A6	0.143		0.334	
Column Yield	S1	0.0	0.0	0.0	0.0
	A2	0.0376	0.0477	0.086	0.120
	A6	0.113	0.143	0.243	0.334

The mass eccentricity normalised by the mass radius of gyration, e_m^*, provides a better description of the degree of mass asymmetry. The mass radius of gyration, r_m, is a function of the mass moment of inertia, $J_{\Theta m}$, and the total floor slab mass, M, as shown in equation (3.5) above. These are both important parameters, since $J_{\Theta m}$ measures the resistance of the floor mass to torsional acceleration, due to inertia, and M quantifies the expected forces on the floor, assuming a constant translational spectral acceleration. For example, if the lead plates in mass configuration A6 (Figure 3.3) remained on the same side, but were moved to the panel positions in the upper right and lower right corners of the floor, the mass eccentricity would remain unchanged. However, the torsional response

of the mass configuration would be smaller than that of configuration A6, due to $J_{\Theta m}$ increasing. Normalising the mass eccentricity by the building dimension, b, (resulting in e'_m) would not reflect these differences. On the other hand, values of e'_m are more tangible to an engineer since they can be reported as a percentage of the plan dimension. Building codes specify mass eccentricity in terms of the plan dimension and not the mass radius of gyration. If the building is not 'regular', then dynamic analysis, which considers $J_{\Theta m}$, is normally performed (Appendix B).

3.1.2 Column Configurations

In each storey, a total of five column elements can be used—one at each of the four corners, and one at the floor centre (see Figure 3.2). Four different column diameters, ranging from 6mm to 12mm can be placed at any of these column locations, allowing possible variations in the storey stiffness distribution. The storey heights are constant for each yielding configuration. The first floor of the beam yielding configuration is 360mm. The upper stories of this configuration are 315mm in height. This larger ground storey height counteracts the shorter effective column length as a result of the two hinge units in this storey. The column yielding configuration, with the two hinge units in each storey, has a constant storey height of 314mm throughout. Table 3.3 lists some of the possible column configurations maintaining stiffness symmetry (centre of stiffness coincides with the floor centre of geometry). All of these configurations have been studied in terms of their elastic response in the earlier research grant supported study. For reasons given below, only column configuration 3, which has 8mm diameter exterior columns and a 12mm diameter central column, has been considered in this study. This configuration results in the ratio of

fundamental uncoupled torsional to translational frequencies ($\Omega = \frac{\omega_\theta}{\omega_y}$) being close to unity. As stated in Chapter 2, previous analytical studies have found that when Ω is near unity, elastic torsional coupling can have its most pronounced affects. Concentrating on this column configuration ensures that modal torsional coupling is a factor, at least during elastic portions of the response. Studying more than a single column configuration would not only compound the number of parameters involved in the experiments, but would also limit the range of these parameters since testing time on the shake table was limited. The solid brass columns in the building model are of a circular cross–section, and have been strain–hardened to extend their range of elastic stress ($\sigma_y = 400\text{MPa}$). This results in a yielding moment for the small (8mm diameter) and large (12mm diameter) brass columns of 20.1N·m and 67.9N·m, respectively. The Modulus of Elasticity for the brass columns is taken as $100\times10^9\text{N/m}^2$.

Table 3.3: Column diameter and uncoupled torsional / lateral frequency ratio for the various configurations.

		Column Configuration				
	Column Location	1	2	3	4	5
Column Diameters	Exterior (corners)	6mm	6mm	8mm	8mm	10mm
	Interior (centre)	12mm	10mm	12mm	10mm	—
$\Omega^\dagger$	Single-Storey	0.71	0.93	1.05	1.25	1.59
	Beam Yield	0.71	0.92	1.05	1.25	1.58
	Column Yield	0.66	0.86	1.09	1.16	1.46

†Based on the uncalibrated analytical frequencies.

Values of Ω for column configuration 3 are listed in Table 3.4 for both the experimental frequencies (from spectral analysis) and analytical frequencies (from eigenvalue analysis). Two sets of analytical values are indicated, differing in the column lengths used in the calculations. The calibrated analytical results have had their column lengths adjusted to match the experimental frequencies with the least error, thus considering the clamping development lengths in the hinge units (see Chapter 4). The uncalibrated analytical values are based upon the direct measurement of the column length between column collets in the hinge units. In all hinge configurations, the experimental value of Ω is greater than the uncalibrated analytical estimates. This is a result of the columns not achieving perfect fixity at the column collets, and this is discussed further in Chapter 5.

Table 3.4: Uncoupled torsional to translational frequency ratios, Ω

Model	Experimental	Analytical†	
		Uncalibrated	Calibrated
Single–storey	1.20	1.05	N/A
Beam yield	1.18	1.04	1.11
Column yield	1.19	1.09	1.18

†The analytical values are based on the undamped frequencies.

3.2 YIELDING CONFIGURATIONS

3.2.1 Single–storey model

The single–storey models were primarily used as proving tests for the multi-storey inelastic models, and their hinge units. The table accelerations for dynamic testing of these models are based on a spectrum compatible acceleration, as defined by Eurocode–8

[Commission of the European Communities, 1993], and a short duration impulse load. Unlike the multi-storey studies, two column configurations were studied during the single–storey tests. These were column configurations 3 and 5. The results from this study are presented in Appendix G (page 313).

3.2.2 Beam yielding configuration (4–storey model)

The beam yielding models have continuous columns through all four floors of the structure. At each column location, hinge units are rigidly affixed to the floor, with the orientation shown in Figure 3.4b. The weight of each floor is supported by the clamping collets of the five hinges. For simplicity, and due to lack of additional information, the distribution of floor weight to each column was assumed proportional to the column cross–sec-

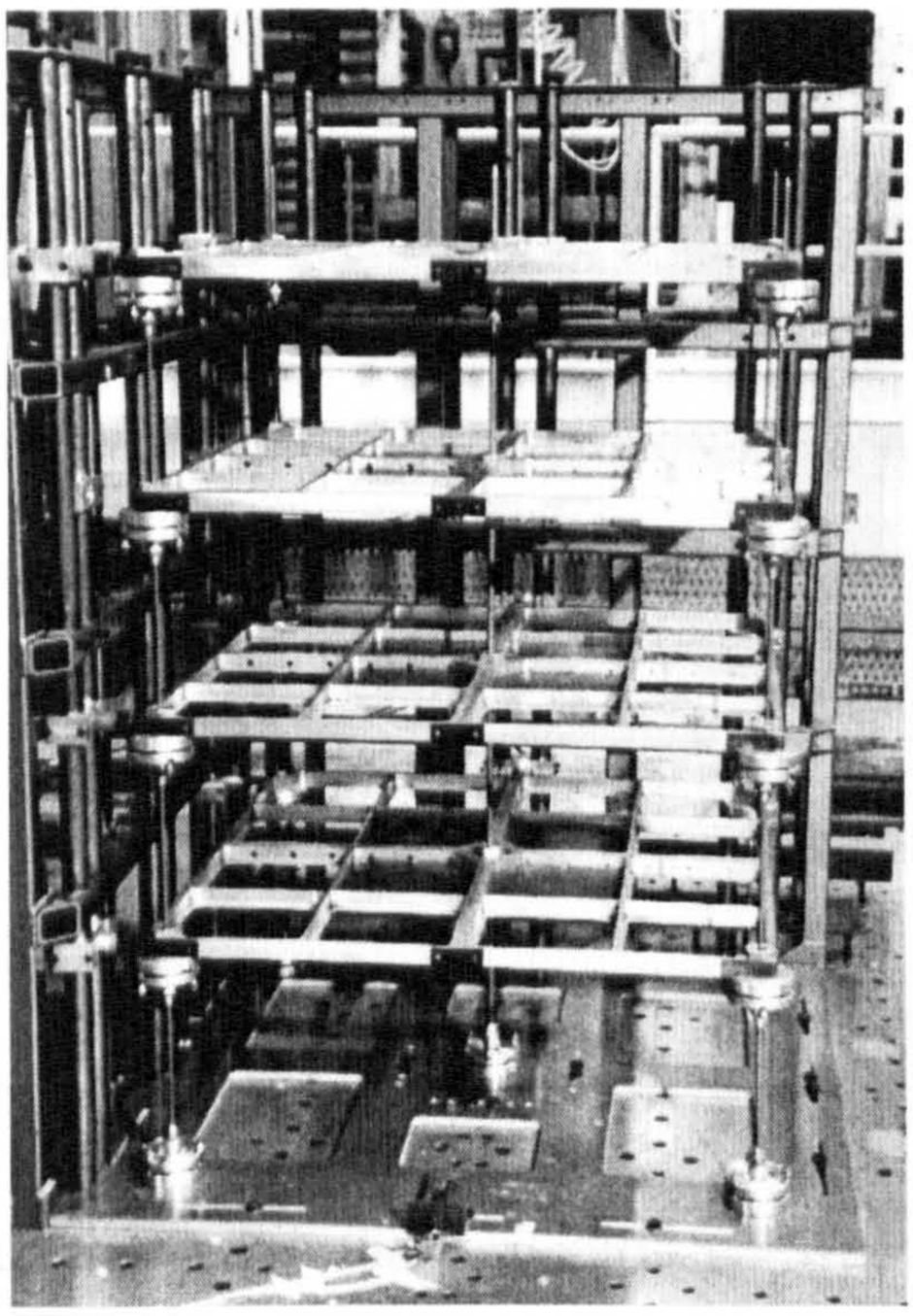

a. Beam yield model set-up with mass configuration S1.

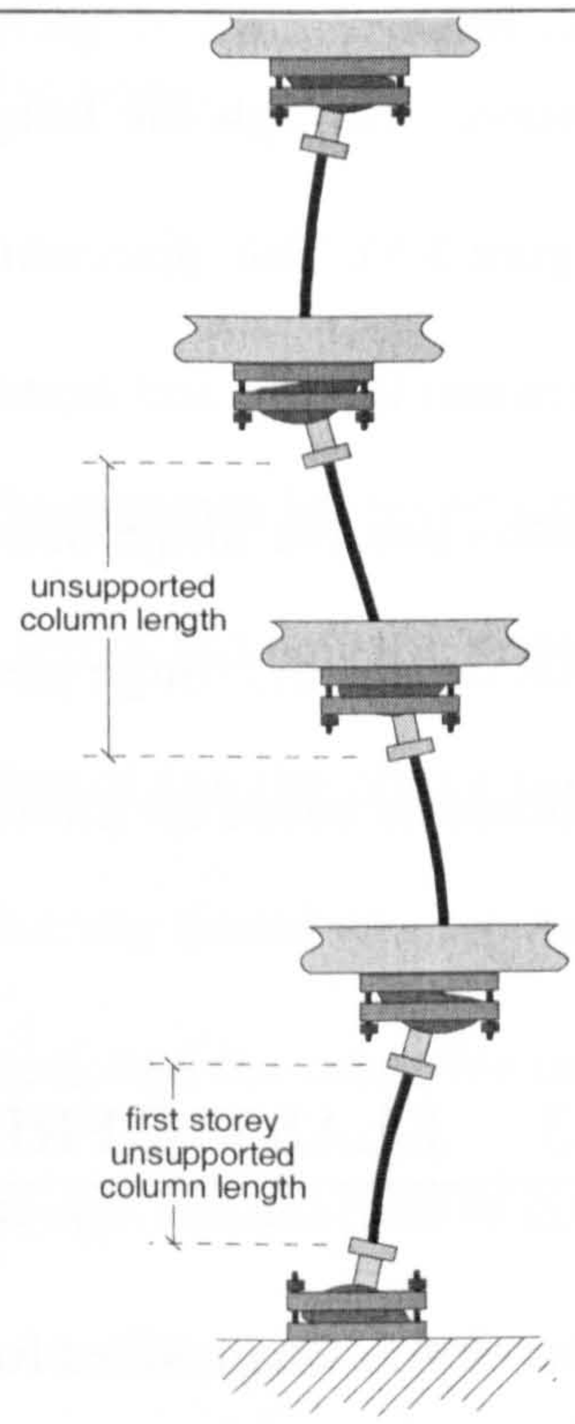

b. Hinge layout for beam yielding configuration.

Figure 3.4: Beam yielding column and hinge configuration.

tional area (i.e. the central and an exterior column support 36% and 16%, respectively). The floor weight supported by a hinge unit adds to the yielding moment in the hinge. This additional moment was the same for each floor in the model, since the continuous columns assured that the five hinges on each floor supported only the weight of that floor. Hinge units were also placed on the shake table at the base of the columns. The configuration of the hinges is such that the moment in each column transferred from the floor connection is limited to the yielding moment, M_y, of the hinge unit. Since the curvature of the columns remain continuous, the effect on the response is similar to plastic hinges forming in the aluminium floor panel at the column location.

3.2.3 Column yielding configuration (4–storey model)

Unlike the beam yielding models, the columns in the column yielding models are not continuous through the height of the model, but have been cut at each floor level (see Figure 3.5). This discontinuity in column curvature simulates plastic yield in the columns between the top and bottom hinge collets at each floor. The lack of continuous columns means that the hinge units must support the weight of their floor, and all stories above. This causes the hinge yielding moments to increase on lower floors, since the yielding moment is based on friction in the hinge units.

3.3 ELASTIC FREQUENCIES

The elastic frequencies for the above two model configurations (beam yield and column yield) were determined both experimentally and analytically. The analytical model assumes a lumped mass computational model.

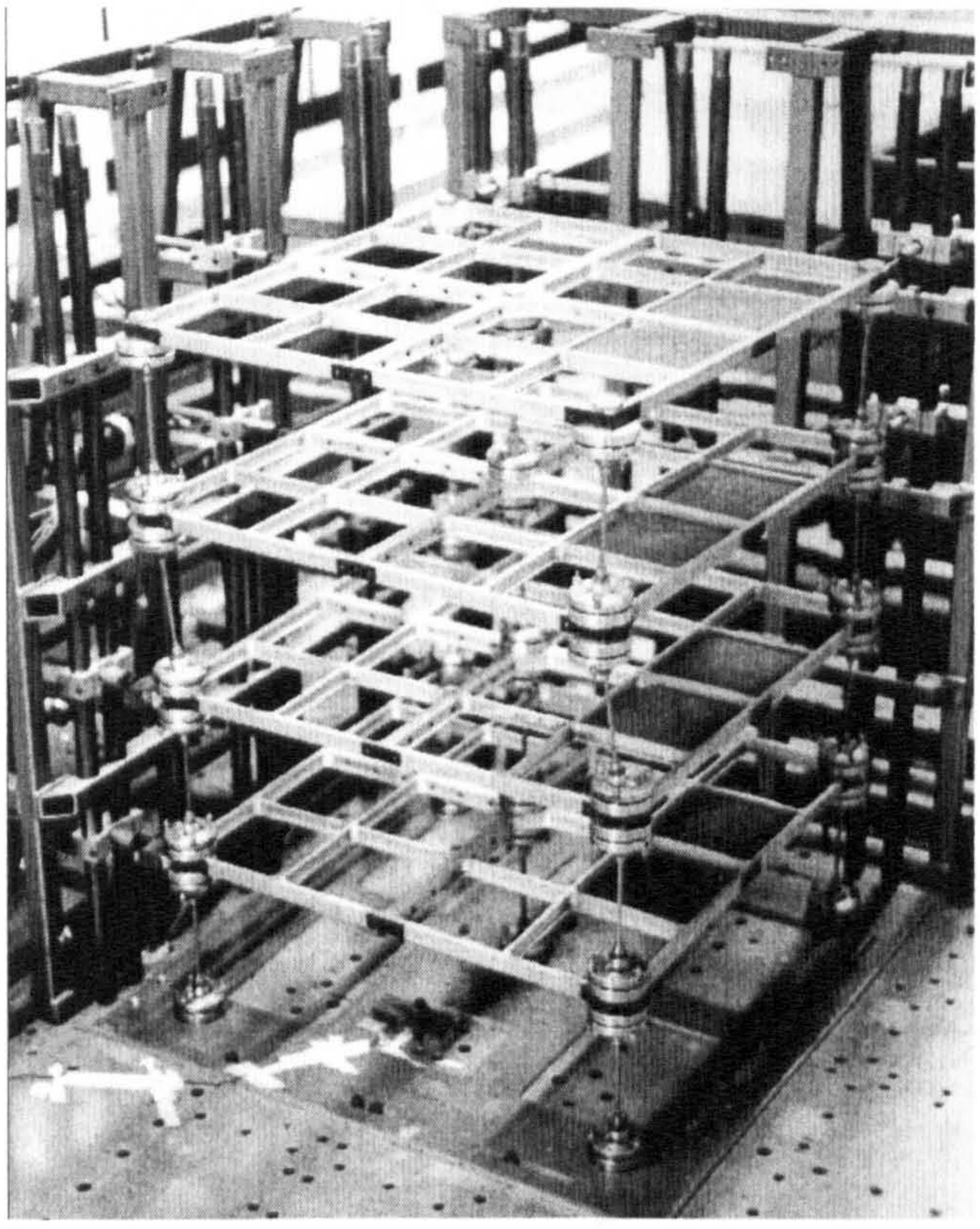

a) Column yielding set-up with mass configuration A6.

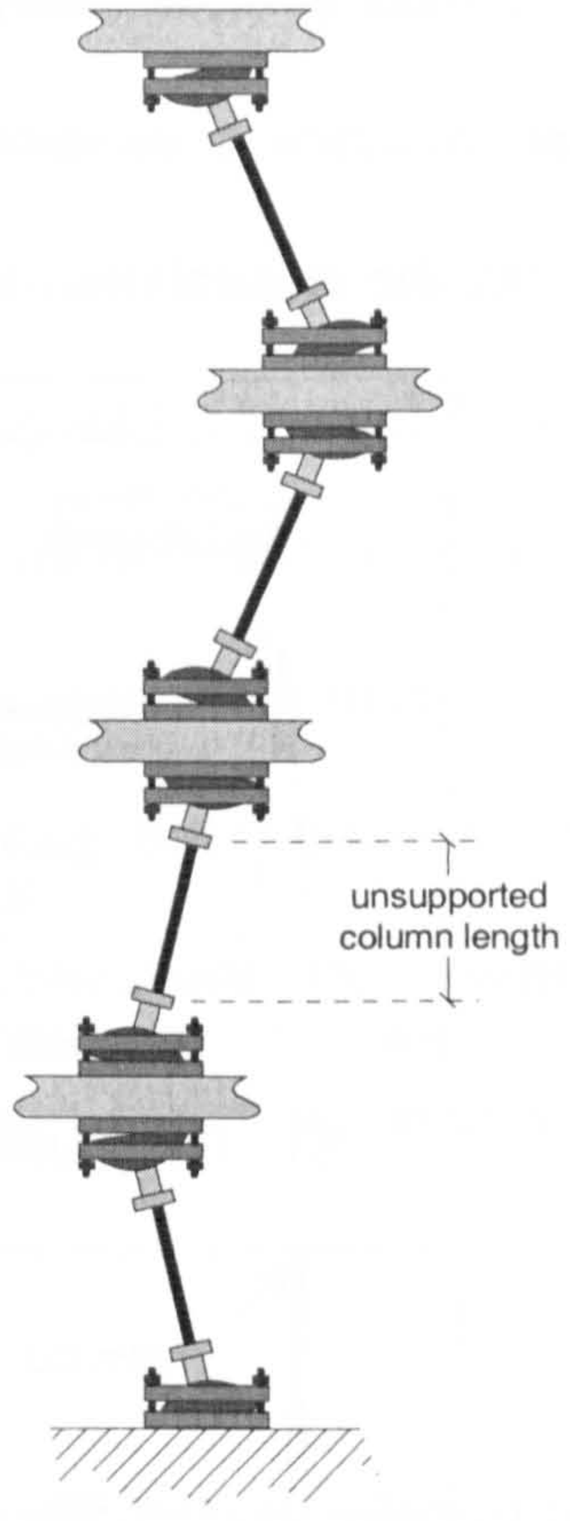

b) Hinge layout for column yielding model.

Figure 3.5: Column yielding hinge configuration.

3.3.1 Experimental evaluation of frequencies

The experimental method of determining the building model frequencies involved using an *Advantest*® FFT spectral analyser. This analyser (shown on top of the actuator control panel in Figure 5.2 on page 118) generated an excitation signal for the shake table motions. The model displacement response resulting from this forcing signal was recorded on two of the acquisition channels—one for recording translation, and the other for rotation. These acquired displacements are then fed back through the spectral analyser to compute the average power spectra of the displacement response. The power spectrum indicates the energy content distribution over various frequencies. However, since the forcing is not stationary, the power spectrum indicates the average power content distribu-

tion. Some of these power spectra plots, as generated by the spectral analyser for the two input directions, are shown in Figure 3.6 for the column yielding model. In an effort to reduce the spectral noise and obtain statistically reliable results, this process was repeated

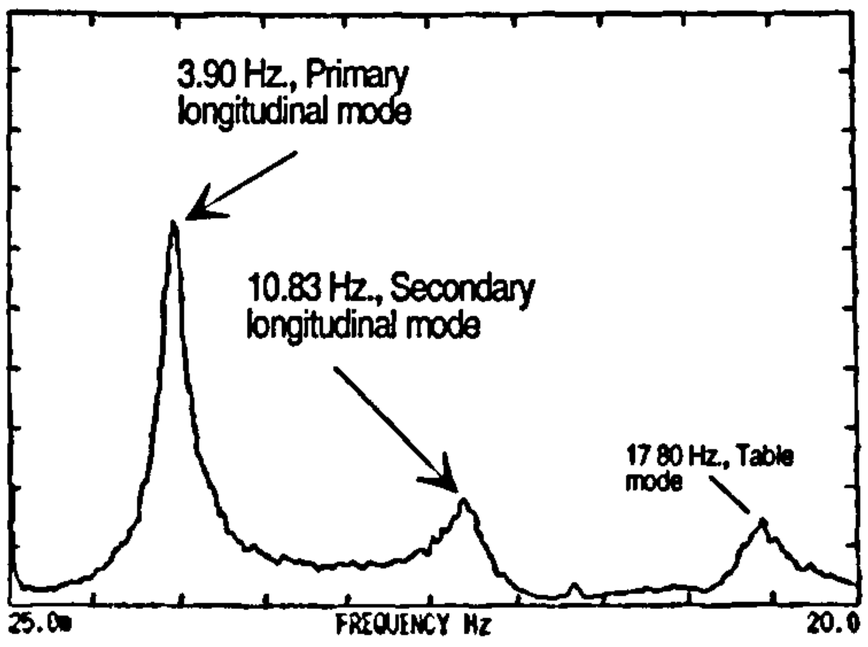

S1 - Longitudinal Forcing

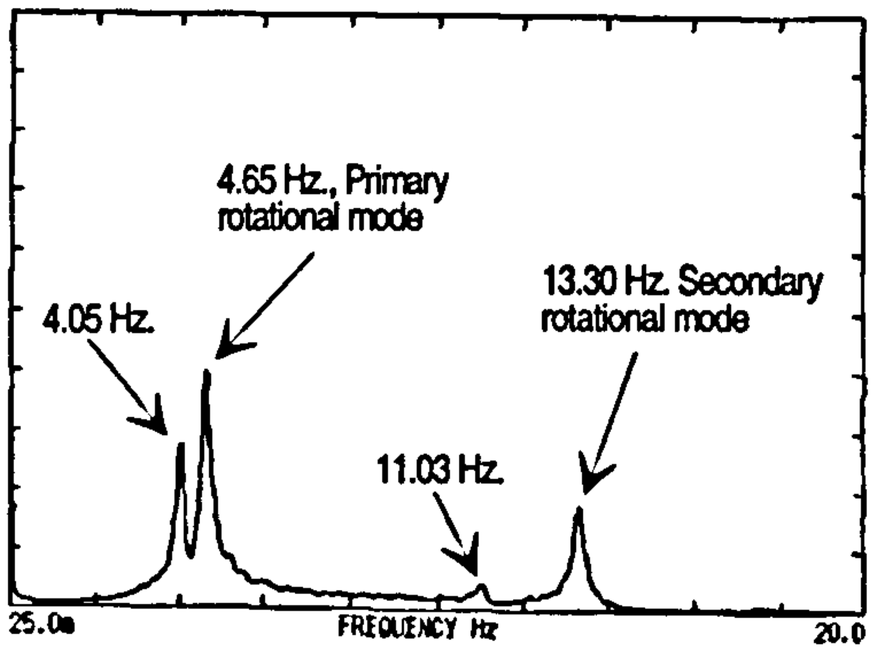

S1 - Yaw Forcing

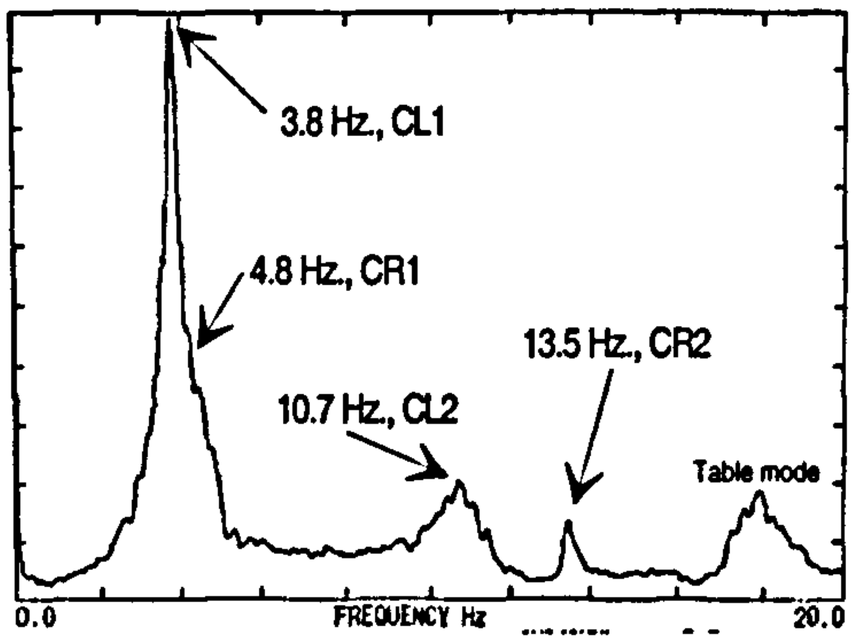

A2 - Longitudinal Forcing

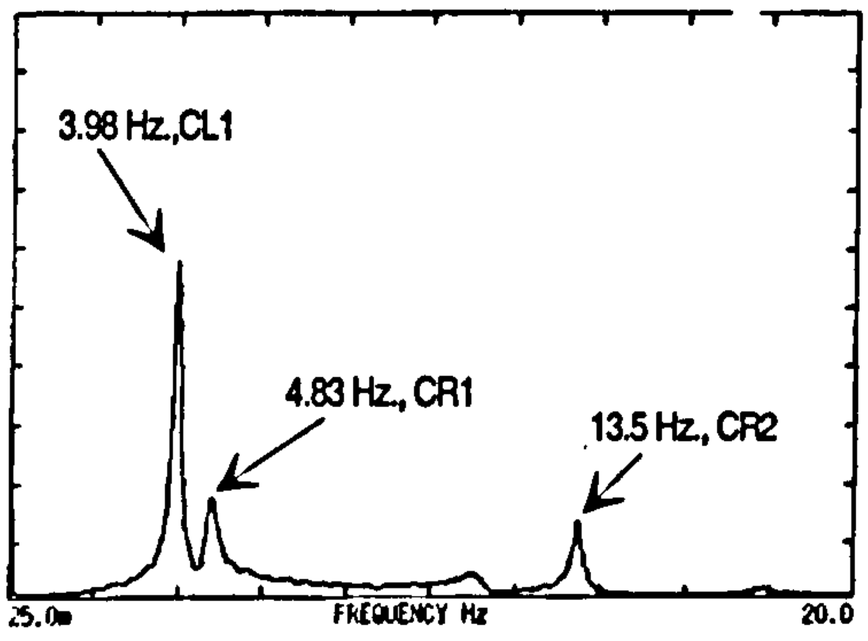

A2 - Yaw Forcing

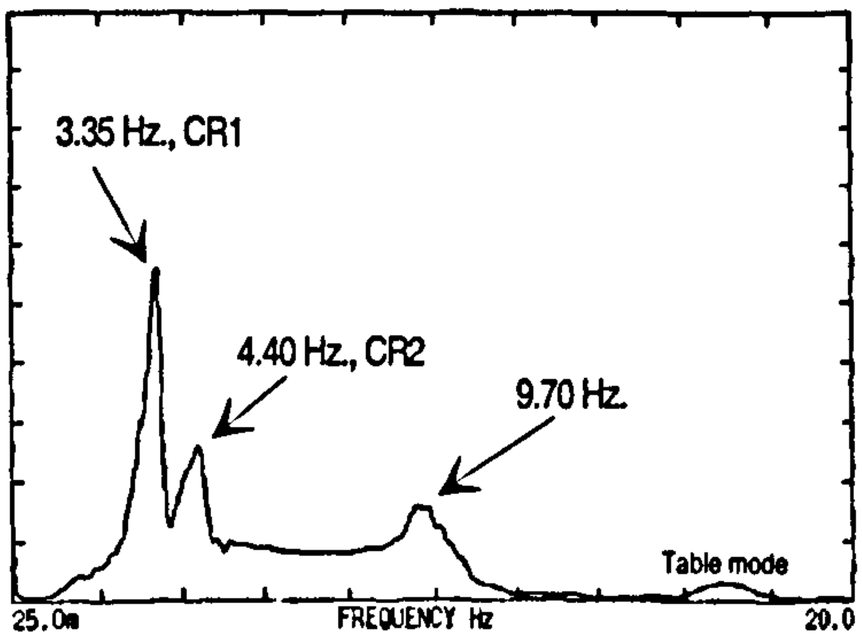

A6 - Longitudinal Forcing

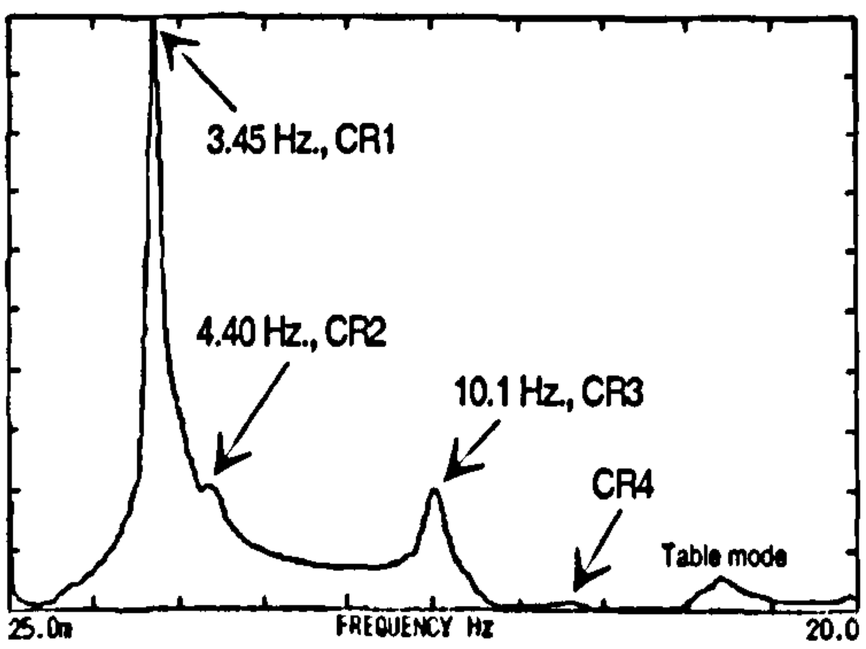

A6 - Yaw Forcing

Figure 3.6: Response power spectra for the column yielding configuration. CL*n* and CR*n* denote the n^{th} dominant coupled longitudinal and rotational modes, respectively. The vertical scales shown are not identical

over several runs (typically between four and eight, depending on the quality of response correlation) then averaged to obtain a single representative power spectrum. To achieve the best response, each structural configuration was excited separately along two axes—*longitudinal* translation (along the Y–axis), and *yaw* rotation (about the vertical Z–axis). The longitudinal forcing normally provided a better correlation for the translational dominated frequencies. Conversely, yaw excitation normally resulted in better estimates of the rotational dominated frequencies. This is to be expected, as forcing in the direction of the dominant modal response has the most influence on that particular mode. This results in higher modal displacements for the same forcing intensity, thus a higher signal to noise ratio.

The selected table forcing gain used in measuring the frequencies was selected low enough to suggest elastic behaviour of the model, whilst maintaining a reasonably high signal to noise ratio of the response. However, the high stiffness in comparison to the low yielding moment of the central column may have resulted in some inelastic behaviour, especially at resonant forcing frequencies.

The excitation signals chosen were a sine–sweep (simple sine wave of monotonically increasing frequency from 0.5 to 20 Hz) and a finite length random signal (banded white noise), also between 0.5 to 20 Hz. The random excitation signal usually resulted in much more distinct frequency peaks, but at the cost of a lower correlation between testing runs. This is to be expected, since theoretically the random signal is exciting all modes (within its banded white noise) in any given envelope of time. The sine–sweep, on the other hand, is only exciting the model at a single frequency at any given time. This tended to give a

higher response (or energy in terms of the power spectra) at the modal frequencies for the same forcing gain. This could have resulted in some hinge yielding at the base of the central column, which would generally result in a higher measured damping, due to the frictional-type hinge yielding (i.e. Coulomb damping). Hence, the wider and less distinct power spectra peaks, as compared to the randomly forced power spectra.

3.3.2 Analytical evaluation of frequencies

The global lumped mass matrix for all eight degrees of freedom of the four–storey models can be defined in terms of the floor mass for floor i (M_i), its mass eccentricity (e_{mi}), and its polar mass moment of inertia ($J_{\Theta si}$) about the centre of stiffness:

$$\underset{\sim}{M} = \begin{bmatrix} M_1 & M_1 e_{m1} & 0 & 0 & 0 & 0 & 0 & 0 \\ M_1 e_{m1} & M_1 J_{\Theta s1} & 0 & 0 & 0 & 0 & 0 & 0 \\ 0 & 0 & M_2 & M_2 e_{m2} & 0 & 0 & 0 & 0 \\ 0 & 0 & M_2 e_{m2} & M_2 J_{\Theta s2} & 0 & 0 & 0 & 0 \\ 0 & 0 & 0 & 0 & M_3 & M_3 e_{m3} & 0 & 0 \\ 0 & 0 & 0 & 0 & M_3 e_{m3} & M_3 J_{\Theta s3} & 0 & 0 \\ 0 & 0 & 0 & 0 & 0 & 0 & M_4 & M_4 e_{m4} \\ 0 & 0 & 0 & 0 & 0 & 0 & M_4 e_{m4} & M_4 J_{\Theta s4} \end{bmatrix} \tag{3.6}$$

The polar moment of inertia about the centre of stiffness (J_{Θ_s}) is required rather than that about the centre of mass ($J_{\Theta m}$), since both the mass and stiffness matrices are formulated about the centre of stiffness. Transforming the polar mass from the centre of mass (from Equation (3.3)) to the centre of stiffness for floor i results in:

$$J_{\Theta si} = J_{\Theta mi} + M_i e_{mi}^2 = M_i\left(e_{mi}^2 + r_{mi}^2\right) \tag{3.7}$$

The global stiffness matrix for the four–storey models can be defined as:

$$\underset{\sim}{K} = \begin{bmatrix} K_{y1}+K_{y2} & 0 & -K_{y2} & 0 & 0 & 0 & 0 & 0 \\ 0 & K_{\Theta 1}+K_{\Theta 2} & 0 & -K_{\Theta 2} & 0 & 0 & 0 & 0 \\ -K_{y2} & 0 & K_{y2}+K_{y3} & 0 & -K_{y3} & 0 & 0 & 0 \\ 0 & -K_{\Theta 2} & 0 & K_{\Theta 2}+K_{\Theta 3} & 0 & -K_{\Theta 3} & 0 & 0 \\ 0 & 0 & -K_{y3} & 0 & K_{y3}+K_{y4} & 0 & -K_{y4} & 0 \\ 0 & 0 & 0 & -K_{\Theta 3} & 0 & K_{\Theta 3}+K_{\Theta 4} & 0 & -K_{\Theta 4} \\ 0 & 0 & 0 & 0 & -K_{y4} & 0 & K_{y4} & 0 \\ 0 & 0 & 0 & 0 & 0 & -K_{\Theta 4} & 0 & K_{\Theta 4} \end{bmatrix} \tag{3.8}$$

where, K_{yi} and $K_{\Theta i}$ are the translational and rotational stiffness of storey i, respectively, and can be defined as:

$$K_{yi} = \sum_{j} (k_{yi})_j \tag{3.9}$$

and

$$K_{\Theta i} = \sum_{j} (k_{yi})_j (d_i)_j^2 \tag{3.10}$$

where, $(k_{yi})_j$ is the translational stiffness along the y–axis for column j in storey i, and $(d_i)_j$ is the distance of column j from the stiffness centre of storey i.

Performing an eigenvalue analysis from the above mass and stiffness matrices results in the natural undamped frequencies, ω, of the building model:

$$\left| \underset{\sim}{K} - \omega^2 \underset{\sim}{M} \right| = 0 \tag{3.11}$$

3.3.3 Column Yield Configuration

Table 3.5 lists the results from equation (3.11) for the first four frequencies in each mass configuration for the column yield models. The experimental frequencies correspond to those at the averaged power spectra peaks, as generated by the spectral analyser in

Table 3.5: Modal frequencies of the multi–storey column yielding configuration.

		Mode	Mass S1	Mass A2	Mass A6
Experimental	Frequencies	1	3.90Hz.	3.80Hz.	3.35Hz.
		2	4.65	4.83	4.40
		3	10.83	10.70	10.33
		4	13.30	13.50	N/A
Analytical (Uncalibrated)	Frequencies	1	4.28Hz.	4.21Hz.	3.73Hz.
		2	4.66	4.77	5.12
		3	12.20	12.00	10.67
		4	13.31	13.60	14.57
	Frequency Error	1	9.8%	10.9%	6.7%
		2	-0.9	-0.6	16.3
		3	13.0	12.3	4.6
		4	0.0	0.9	N/A
Analytical (Calibrated)	Frequencies	1	3.98 Hz.	3.94 Hz.	3.67 Hz.
		2	4.70	4.79	4.87
		3	11.36	11.24	10.49
		4	13.39	13.64	13.88
	Frequency Error	1	2.1%	3.7%	4.9%
		2	0.0	-0.2	10.7
		3	5.2	5.1	2.9
		4	0.7	1.0	N/A

Figure 3.6. The fundamental frequency of the SERC shake table with the attached measurement frames is around 16.8 Hertz in rotation and 17.8 Hertz in longitudinal translation. These frequencies, also indicated in Figure 3.6, are just above the fourth mode of the building model, thus creating difficulty in determining the higher experimental frequencies.

The uncalibrated and calibrated frequencies correspond to the analytical frequencies resulting from the directly measured and calibrated inter–storey column length (as defined earlier), respectively. Discussions on the differences between the calibrated and uncalibrated frequencies are given below. The frequency error listed for these two cases are based on the damped experimental frequencies.

Mass eccentricity affects the frequencies of the column yield models in two distinct ways, as can be seen in Figure 3.7, and in the results presented in Table 3.5. The frequencies of the initially uncoupled translational modes decrease as they become coupled with a rotational degree of freedom. The greater the mass eccentricity, the greater the frequency decrease. The reverse is also true for the frequencies of initially uncoupled rotational modes, where the modal frequencies increase, albeit at a slower rate, as they become coupled with translation. It is important to mention that Figure 3.7 is based on a theoretical, parametric study of only the mass eccentricity in the column yield model. The mass radius of gyration ($\sqrt{\frac{J_{\Theta m}}{M}}$) is held constant, which is not the case in with the experimental models.

Although not shown in the figure, the beam yield configuration displays a similar relationship between the elastic frequencies and mass eccentricity.

3.3.4 Beam Yield Configuration

The main differences, elastically, between the beam and column yield configurations are in the shorter height of the first storey, taller second through fourth storeys, and the lighter floor weights in the beam yield models. The reduction in weight of the bottom three floors is due to the use of five fewer hinge units, four of which are located at the corners. This

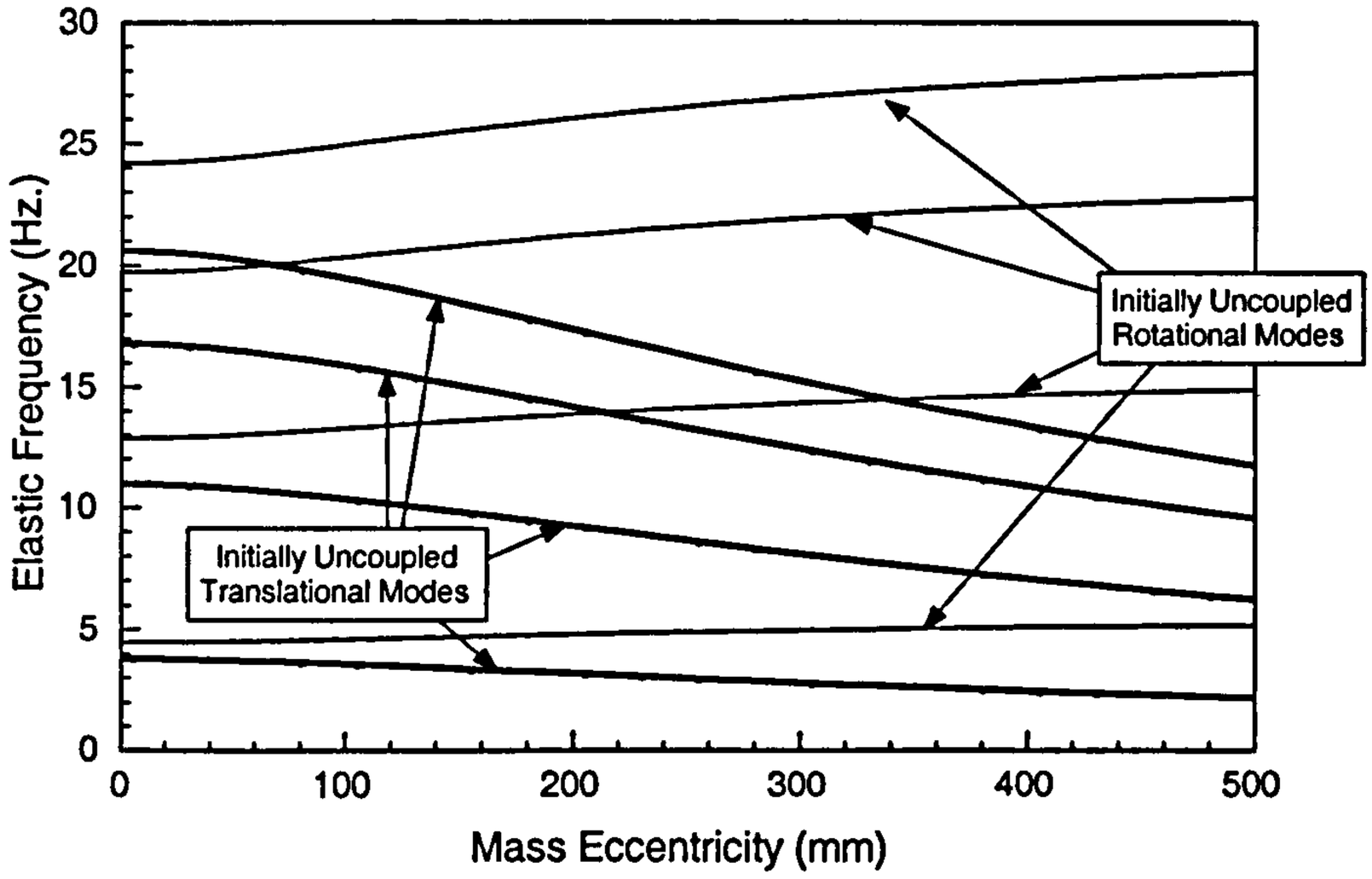

Figure 3.7: Effect of mass eccentricity on the eight modal frequencies of the column yielding models.

significantly affects the polar mass ($J_{\Theta m}$), causing a reduction of about 35% (see Table 3.1 on page 48). This reduction in polar mass tends to increase the rotational dominated frequencies more than the corresponding translational dominated frequencies, since most floor masses are reduced by only 20%. However, the effects of the reduced masses are counteracted by the reduction in both lateral and torsional stiffness due to the significant increase in storey height for the top three storeys. Table 3.6 tabulates both the experimental and analytical frequencies for the beam yield configuration. Comparing the frequencies for the two yielding configurations, it's shown that those of the beam yield configuration are much lower (by almost 50%) than those of the column yield configuration.

It is also evident in Table 3.6 that the uncalibrated column lengths result in a fairly poor estimate of the experimental frequencies, with errors up to 35%. The uncalibrated column lengths are measured directly by the distance between the point at which the hinges clamp onto the columns (indicated by the *unsupported column length* dimension in Figures 3.4

Table 3.6: Modal frequencies of the multi–storey beam yielding configuration.

		Mode	Mass S1	Mass A2	Mass A6
Experimental	Frequencies	1	1.98Hz.	1.90Hz.	1.70Hz.
		2	2.35	2.44	2.51
		3	6.21	6.00	5.55
		4	7.20	7.33	7.49
Analytical (Uncalibrated)	Frequencies	1	1.49Hz.	1.48Hz.	1.28Hz.
		2	2.01	2.04	2.19
		3	4.23	4.20	3.63
		4	5.68	5.77	5.36
	Frequency Error	1	3.0%	22.1%	24.7%
		2	14.5	16.4	12.7
		3	31.9	30.0	34.6
		4	21.1	21.3	28.4
Analytical (Calibrated)	Frequencies	1	1.97Hz.	1.96Hz.	1.70Hz.
		2	2.57	2.62	2.82
		3	5.63	5.59	4.83
		4	7.33	7.45	7.19
	Frequency Error	1	0.0%	3.2%	0.0%
		2	9.5	7.4	12.4
		3	9.3	6.8	13.0
		4	1.8	1.6	4.0

and 3.5). The calibrated column lengths are described in the following Chapter, and are based on matching frequencies between the analytical and experimental models. All of the uncalibrated frequencies underestimate those obtained from the experiments. This is the reverse of the uncalibrated column yield configuration frequencies, which tended to over-estimate their corresponding experimental frequencies.

3.4 MODE SHAPES

The mode shapes of both yielding configurations were determined analytically. During the previous experimental study on the building models without hinge units, the deflected mode shapes were also measured experimentally. However, time restraints on the availability of the SERC shake table prohibited such tests.

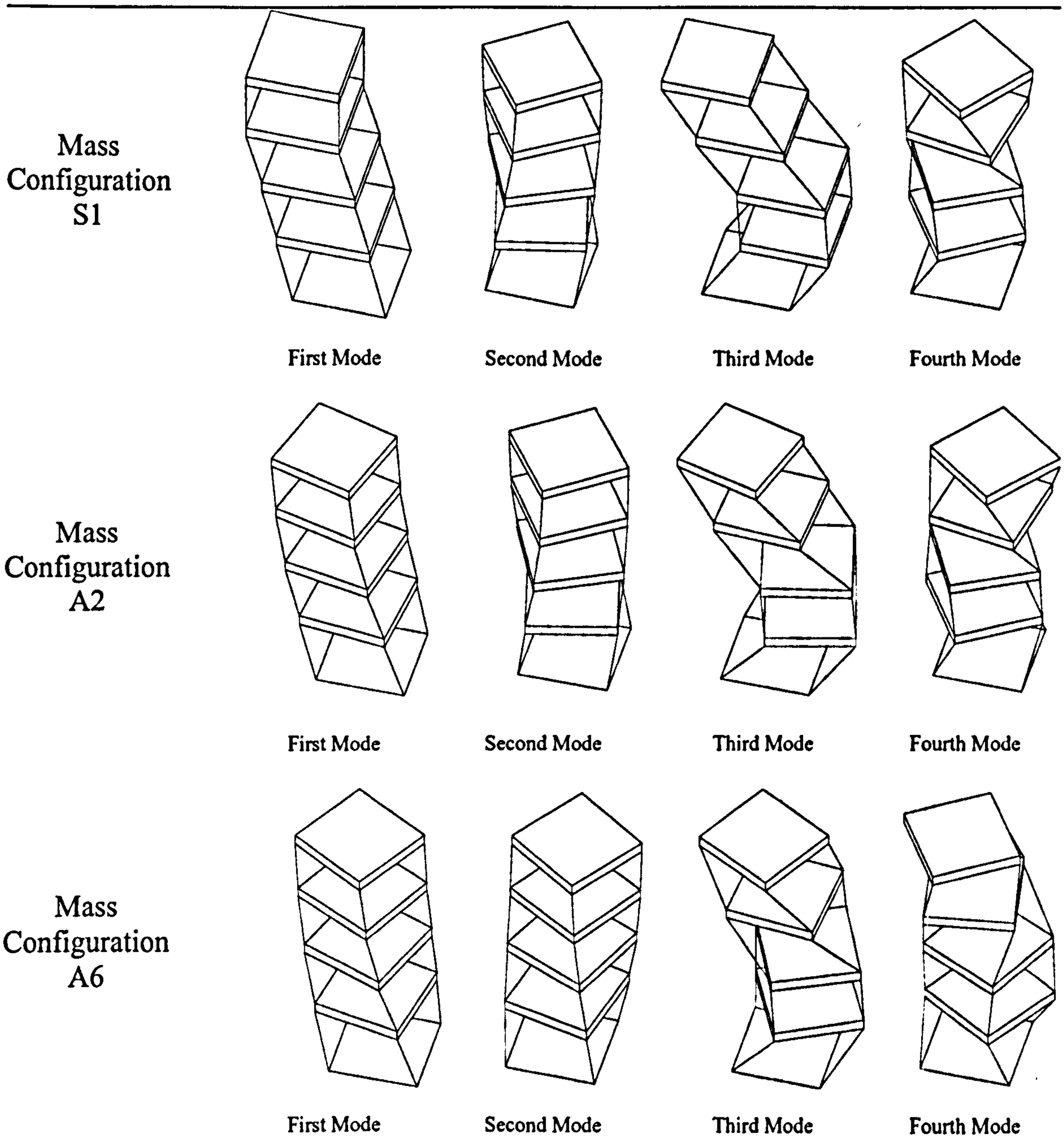

Figure 3.8: Deflected mode shapes for the column yield model configuration.

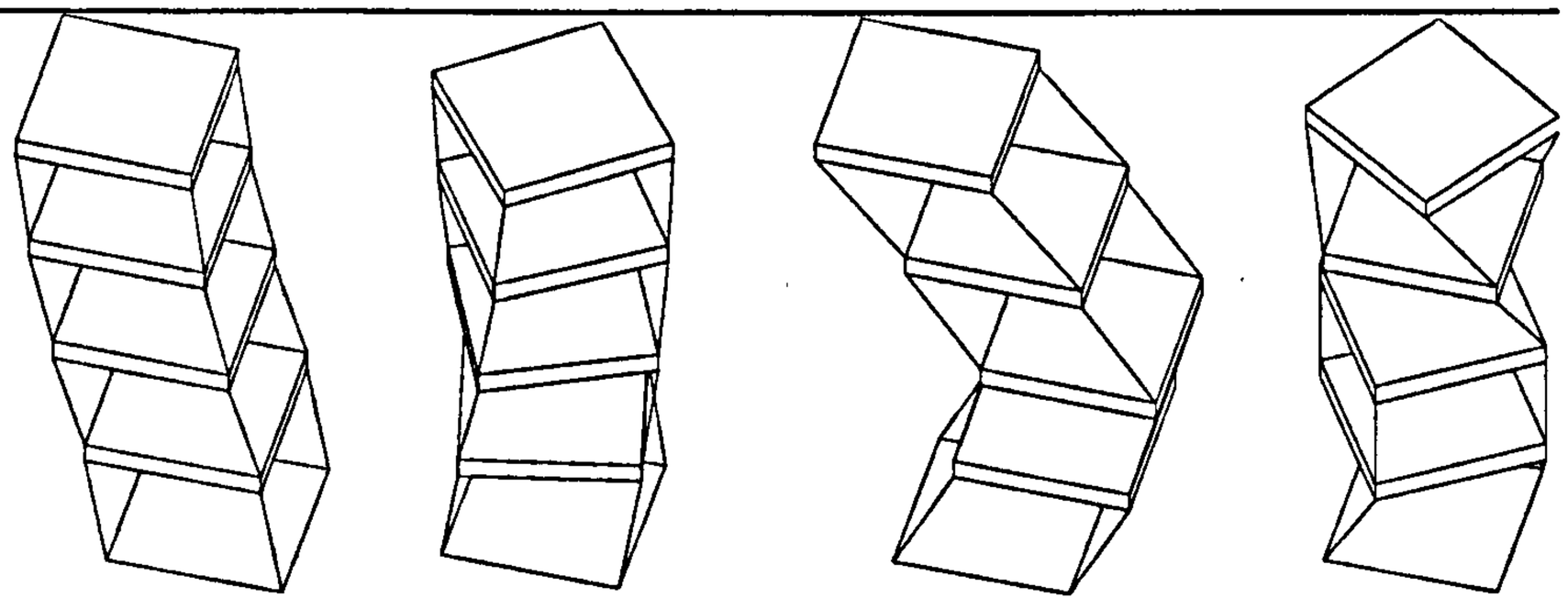

Figure 3.9: Deflected mode shapes for the beam yield model configuration.

The deflection mode shapes from the (elastic) column yield configurations are shown in Figure 3.8, and those for the beam yield configuration are shown in Figure 3.9. The side of the mass eccentricity in these Figures is that closest to the viewpoint (out of the page). Although these Figures provides a familiar perspective into the modal displacement shapes, it's difficult to visualize the relationship between the translation and rotation

modal components. This relationship is better observed in Figure 3.10, where the rotational modal component is plotted as a function of the translational modal component. The four labelled lines indicate the first four mode shapes. In each label, the first number indicates the mode number; the second value indicates the floor number. The diagonal lines in each plot indicate the regions of a particular modal displacement component. The left and right triangles indicate translation modal dominance. The top and bottom regions indicate rotation modal dominance. For example, symmetric mass (S1) modes for both column configurations are uncoupled. This is indicated in Figure 3.10 by the horizontal (translational component) lines for the first and third modes, and the vertical (rotational component) lines for the second and fourth modes. The fact that these modal lines are perfectly horizontal or vertical indicate that they are uncoupled. Eigenvectors which reside near the boundaries of these regions (such as the first and third modes in both the column yield and beam yield configurations for mass distribution A6) are highly coupled, and do not show a dominant directional response.

As the mass eccentricity of the model floors increases, the translational modes (first and third) increase their rotational component. This can be seen in Figure 3.10 where the first and third modes 'shift' in a counter–clockwise direction in the *Rotation–Translation* modal value plane. With mass configuration A6, this shifting is enough to make the first and third modes rotational dominant, albeit highly coupled. The second and third frequencies are pure rotational modes in the symmetric mass model. These two modes also shift counter–clockwise to become more translational as the mass eccentricity increases. However, this shifting towards translational dominance is not as prominent as with the first and third modes, which shift from pure rotation in case S1 to slightly translational dominant in

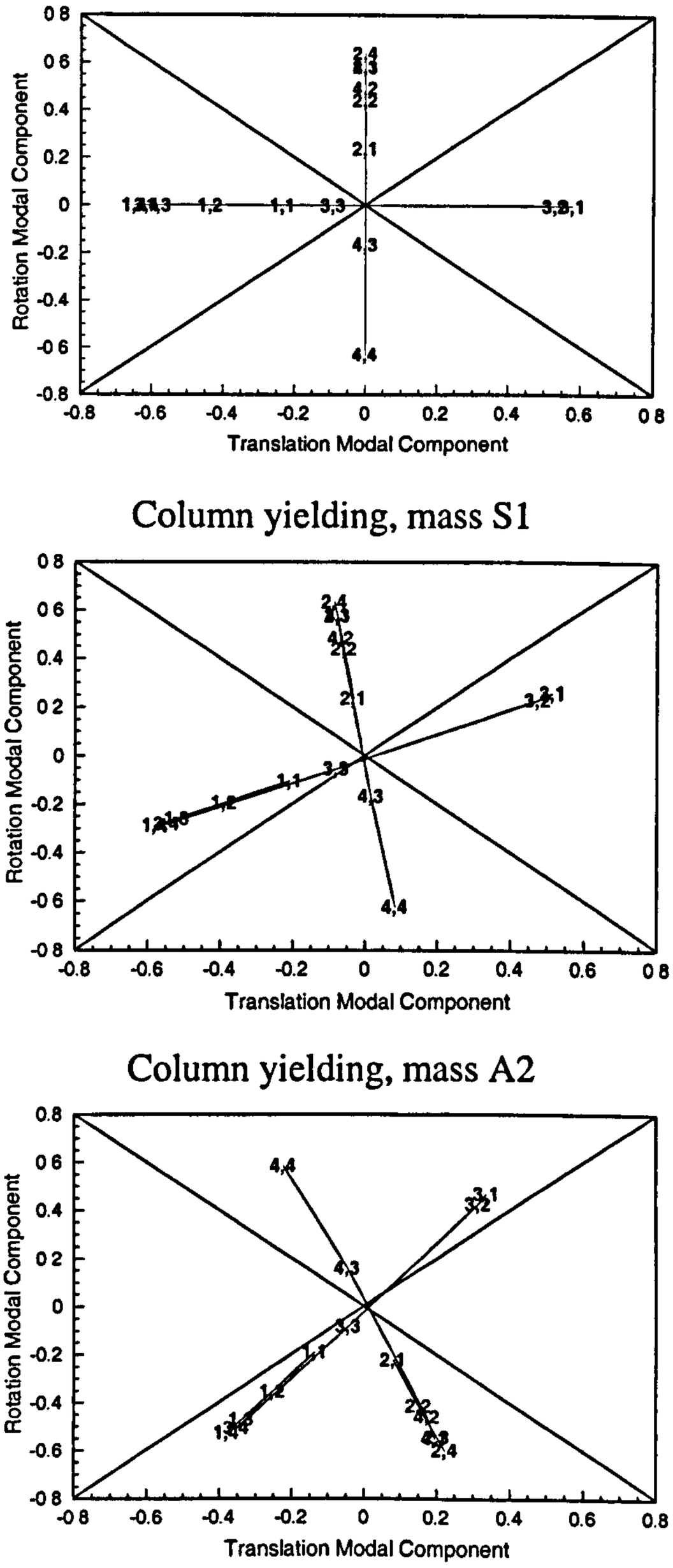

Figure 3.10: Graphical depiction of the degree of modal coupling. The centres of the top and bottom triangles represent areas of rotational dominance. The centres of the left and right triangles are areas of translational dominance. The two numbers on the data lines (**x,y**) indicate the mode number (**x**), and floor number (**y**).

case A6. This is most evident in the column yield case with mass configuration A6, where all of the first four modes are generally rotational dominant. This shifting can also be

related back to Figure 3.7, where the initially uncoupled translational modes are influenced more, in terms of a change in frequency, by the increasing mass eccentricity than the initially uncoupled rotational modes.

3.5 ELASTIC DAMPING

Damping ratios were determined through free vibration decay of both the column and beam yield model configurations. The method of half–power bandwidth was also utilized to estimate elastic damping for the various column yield models. This method was not available for the beam yield configuration, due to a lack of harmonically forced response data. The damping for most of the first four modes of the various symmetric and mass–asymmetric column yield configurations has been measured. The beam yield configurations have their elastic damping measured for only the first two modes, as difficulty was experienced during the experiments which measured the higher modes. This was alleviated during the later column yield tests, when better instrumentation and knowledge of the shake table utilisation was available.

The displacement responses used for the damping calculations were acquired from the fourth (top) floor. Two different instrument configurations were utilized, based on the type of model studied: beam yield or column yield.

3.5.1 Beam yield configuration damping instrumentation

The proximity probe (non–contacting) displacement transducers used for the beam yielding models have a very limited range. This created problems when placed on the fourth

floor, where displacements were the highest. As a result, two instrument channels were utilized—one to measure pure translation, and the other to record the pure rotation. This arrangement, depicted in Figure 3.11, alleviated some of the displacement range problem by dividing the response into two components. Either of these channels were utilized in the damping calculations, depending upon which channel provided highest signal to noise ratio.

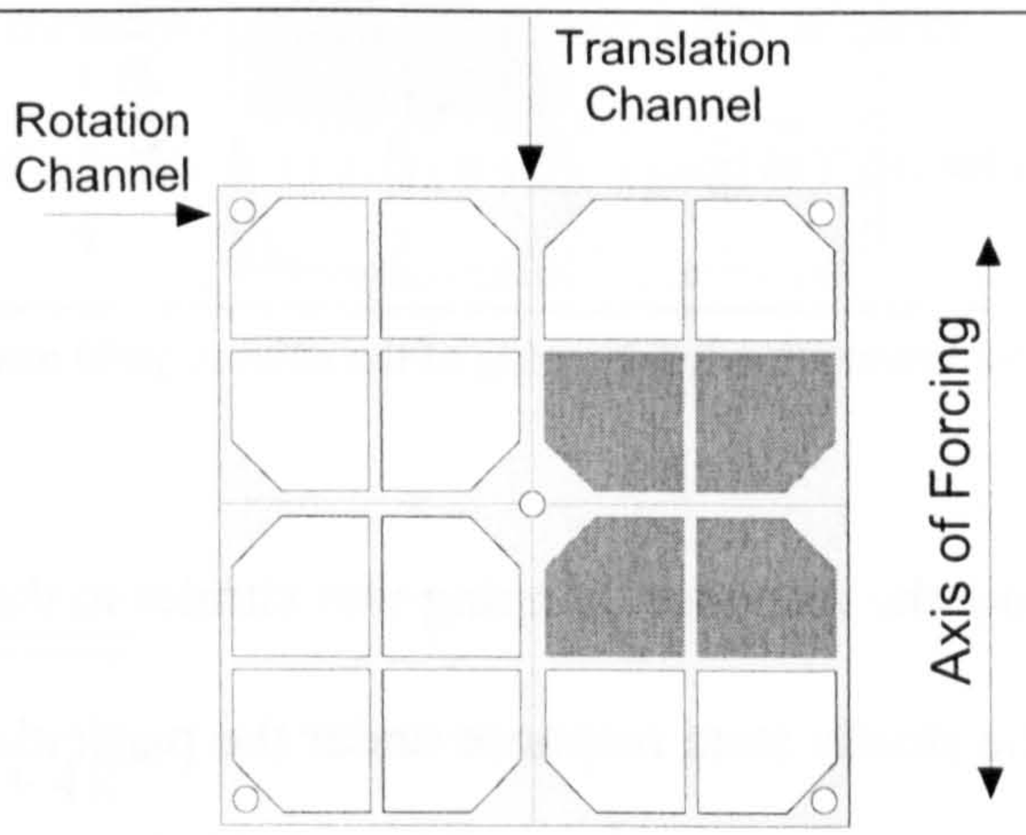

Figure 3.11: Fourth floor instrumentation for damping of the beam yield tests.

During a typical test, the building model was brought to a steady state response under a harmonic forcing at the frequency of the mode for which the damping was being calculated. The response acquisition was then started, and the forcing gain swiftly reduced to zero, so that the free vibration response decay could be measured with a minimum effect from stopping the vibration of the shake table.

3.5.2 Column yield configuration damping instrumentation

The stroke transducers that were available during the column yield tests provided a much larger displacement range. From this, only a single transducer was required to measure the

coupled translational and rotational response. This was placed at the fourth floor corner on the right side of the model, as in Figure 3.12.

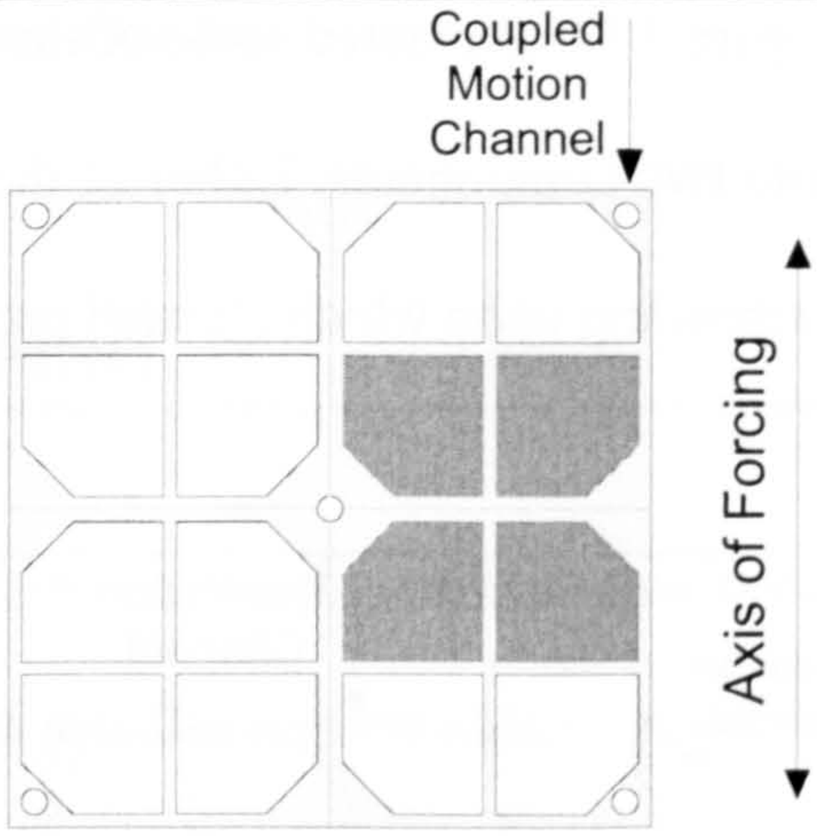

Figure 3.12: Fourth floor instrumentation for damping of the column yield tests.

The method of measuring the response damping was similar to that of the beam yield configuration. However, the steady state response under the particular harmonic loading was also recorded for a duration between 15 and 20 seconds. This allowed the half–power bandwidth damping calculations to also be performed.

3.5.3 Free vibration decay

This method entails measuring the peak displacement at successive cycles in the displacement response time–history to compute the elastic viscous damping ratio, ξ. This assumes that the decay due to damping of the free vibration peak displacement response of the measured channel can be written as:

$$y(t) = Ce^{-\xi\omega t} \tag{3.12}$$

where C is a constant determined from the modal displacement and velocity when the shake table (forcing) was turned off. From equation (3.12), two methods of determining

the damping are available. One method, *logarithmic decrement*, involves solving for ξ directly from the peak periodic displacement at two different times during the response. The other method, *exponential fit*, involves finding C and ξ through a least squares fit of the cyclic displacement of the peaks. Both methods are presented below.

3.5.3.1 Logarithmic Decrement

Computing the displacement, $y(t)$, from equation (3.12) at successive time intervals equal to the damped period of vibration (i.e. $y_1=y(t)$, $y_2=y(t+T_d)$), where is T_d is the damped period, results in:

$$\xi = \frac{\ln\left(\frac{y_1}{y_2}\right)}{\sqrt{\ln\left(\frac{y_1}{y_2}\right)^2 + 4\pi^2}} \tag{3.13}$$

A disadvantage in this method for the current study is that the damping ratios become increasingly difficult to measure in the higher modes of vibration. This can be attributed to the sensitivity of equation (3.13) to the peak cyclic displacements, y_1 and y_2. Also, in most higher modes, a 'beating' peak response was recorded, which can be attributed to modal interaction. This was possibly introduced during the transition from forced to free vibrations, or possibly by the forcing frequency not being exactly coincident with the modal frequency.

In order to obtain a better damping estimate, the damping ratios were determined at successive cycles for the entire length of recorded decay. This typically resulted in 20 to 50 cycles, depending on the modal frequency. The jagged lines in Figure 3.13 represent the

relationship between damping and decay cycle for the beam yield configurations. The damping ratios for both the beam yield and column yield (not shown for brevity) models typically became unrealistic near the end of their response. Although this could partially be attributed to other modes with lower damping, it is mainly due to the lower signal to noise ratio associated with the lower displacements. To remove these unrealistic values from the statistical average, outliers were discarded until 75% of the data remained. The mean and standard deviation for the retained values calculated for the beam yield configuration are shown in Figure 3.13.

3.5.3.2 Exponential Fit

This method fits an exponential curve, equation (3.12), through the same initial set of values used in the method above. The advantage of this method is that the fitting process tends to reduce the errors without having to discarded the outliers. These curves are shown in Figure 3.14 for the same model configurations shown in Figure 3.13. The vertical axis in Figure 3.14 represents the peak cyclic displacements. The solid line in the Figure represents the fitted damping curve.

Tables 3.7 and 3.8 summarise the damping ratios calculated by both the logarithmic decrement and exponential fit methods. The mean damping from these two methods are similar, with damping ratios generally being highest in the second (rotational dominant) mode for the column yield models. The beam yield models have higher damping in the first mode, than in the second. The column yield models generally have a higher elastic damping.

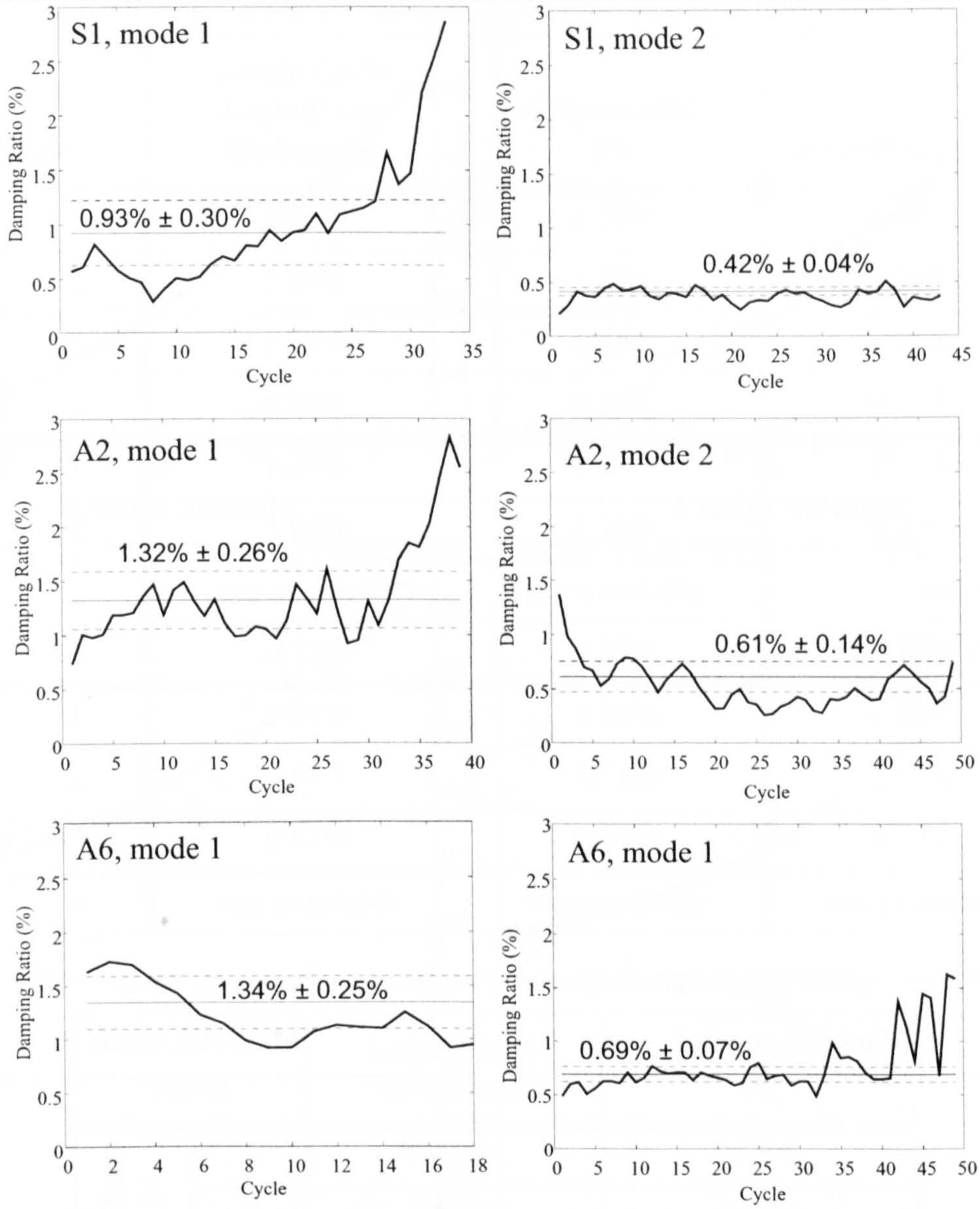

Figure 3.13: Logarithmic decrement damping ratios for the first two modes of beam yield configuration.

The overall level of elastic damping computed for the two multi–storey models is very low. The previous research study on the elastic models without hinge units, measured even lower damping ratios of around 0.5%. This is very low when compared to actual 4–storey buildings, which typically are assumed to have around 3% to 5% elastic damping. However, the higher value of 5% is associated with R/C buildings. Taller multi–storey, steel moment resisting frame buildings have damping ratios of around 3%, which are increased by subsequent addition of secondary structural and architectural elements.

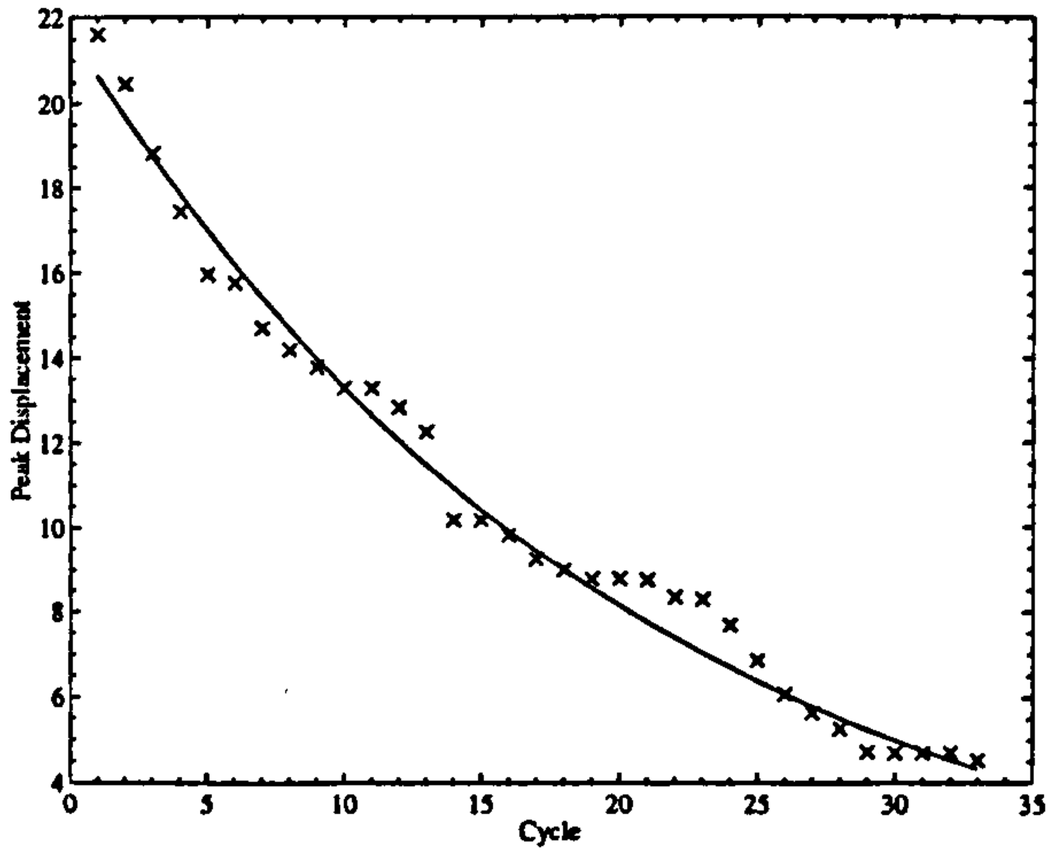

Mass S1, mode 1

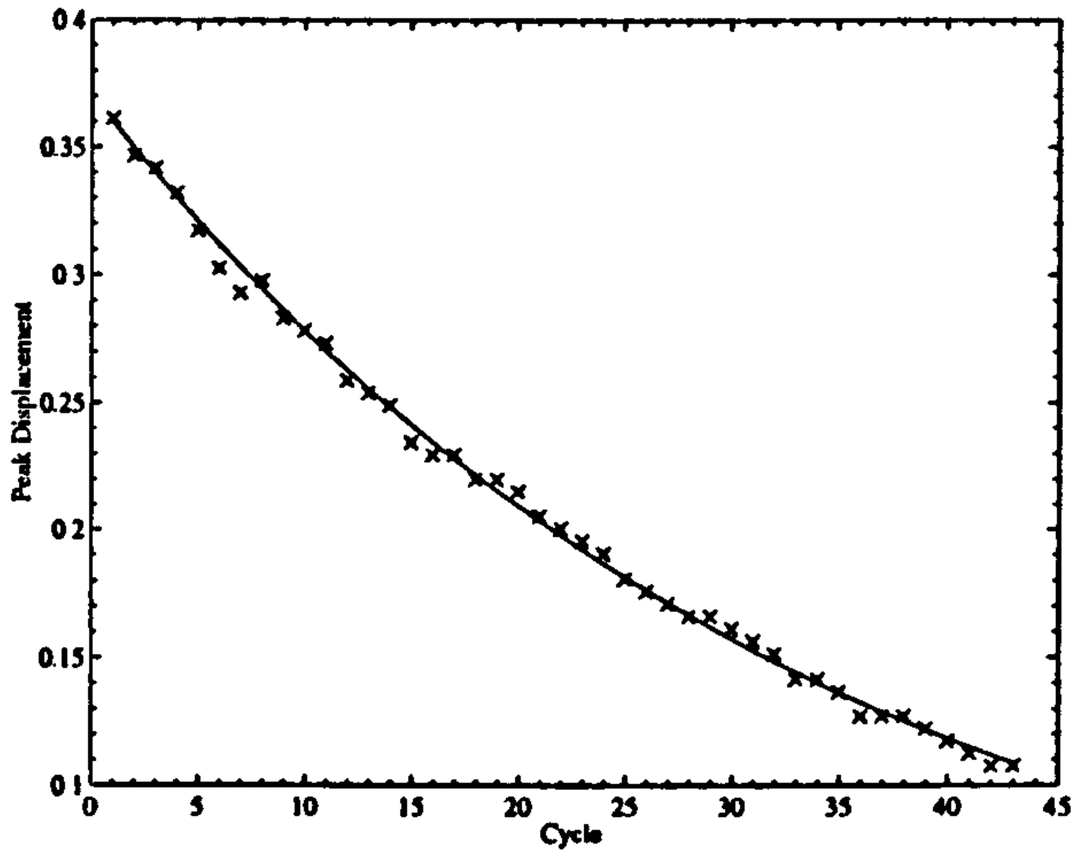

Mass S1, mode 2

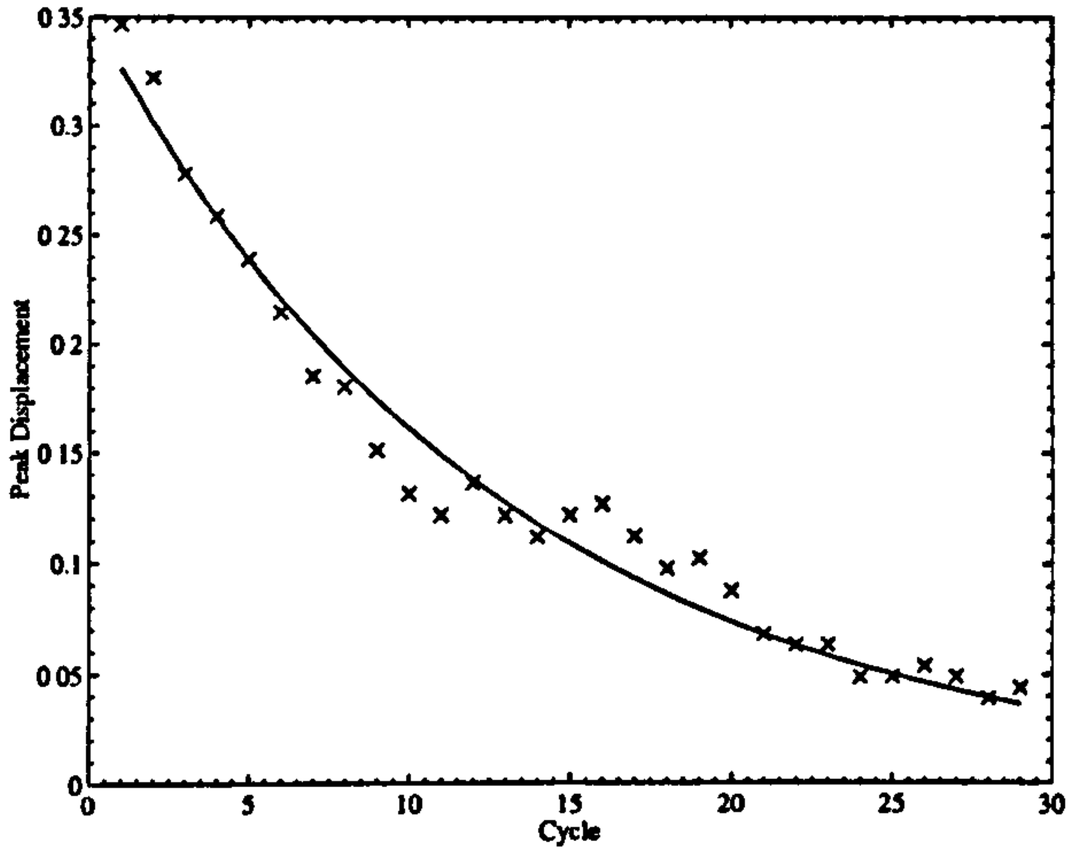

Mass A2, mode 1

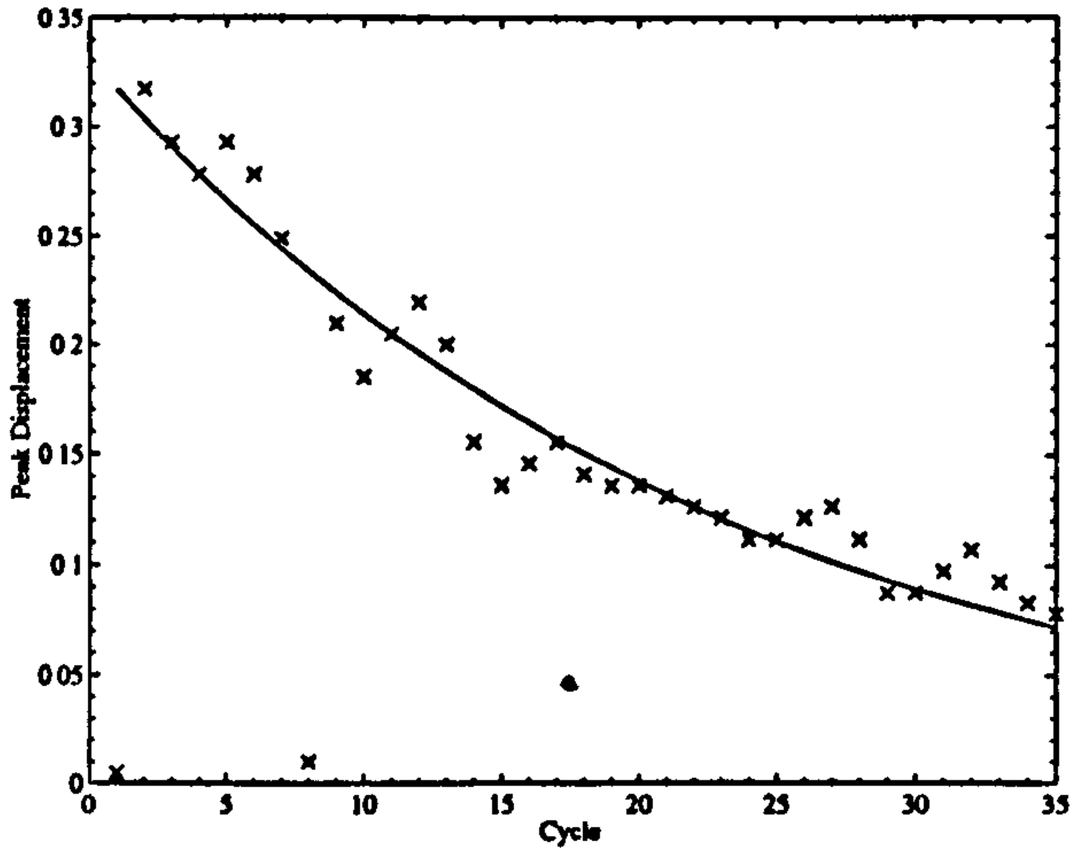

Mass A2, mode 2

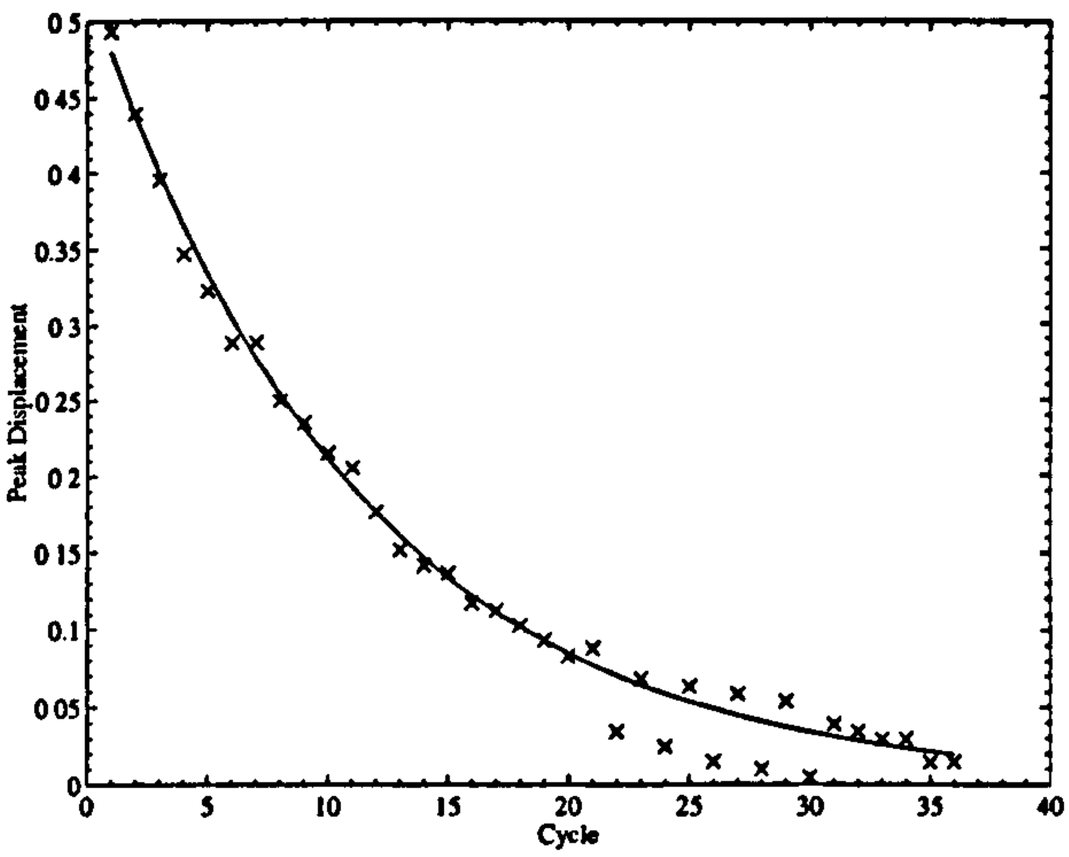

Mass A6, mode 1

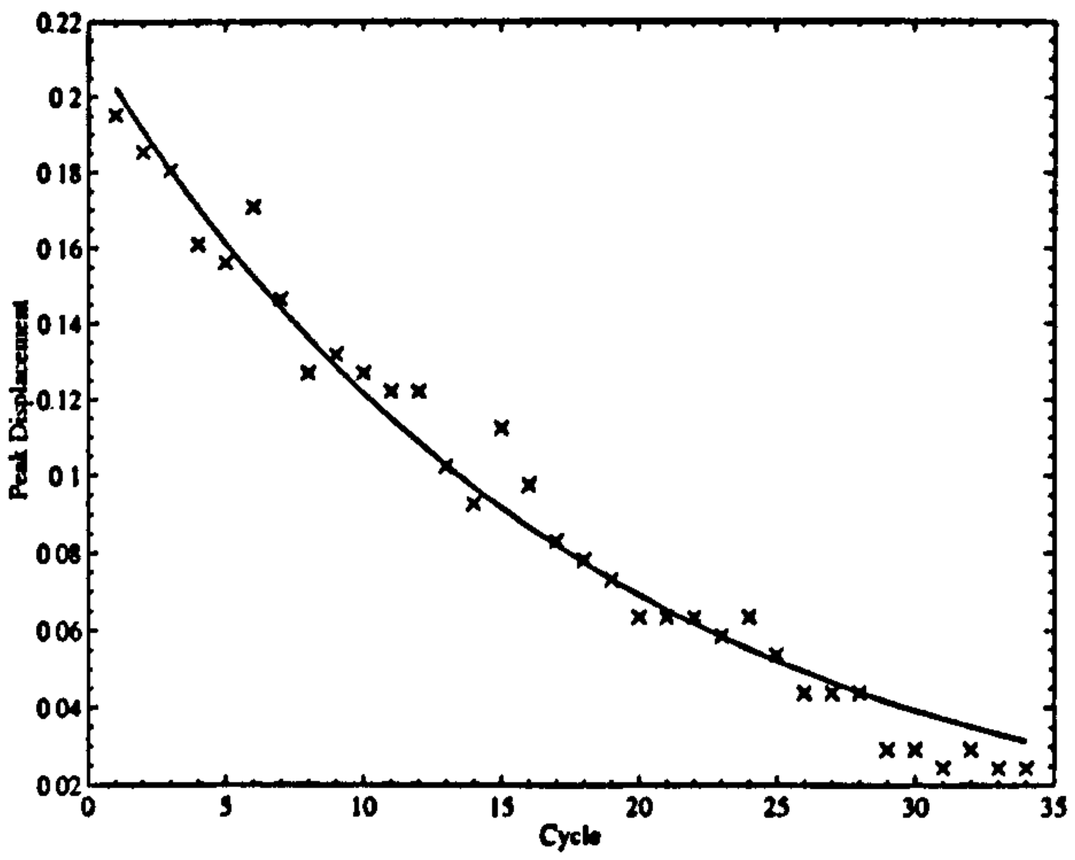

Mass A6, mode 2

Figure 3.14: Exponential fitted damping ratios for the first two modes of beam yield configuration.

Table 3.7: Column yield configuration mean elastic damping ratios.

Mode		Single Cycle Logarithmic Decrement	Exponential Fit	Half–Bandwidth
Mass S1	1	1.26%	1.20%	1.59%
	2	2.07%	1.82%	0.70%
	3	1.74%	1.73%	0.29%
	4	0.53%	0.50%	0.27%
Mass A2	1	1.21%	1.20%	1.32%
	2	1.84%	1.54%	0.69%
	3	*not available*	*not available*	*not available*
	4	0.53%	0.55%	0.36%
Mass A6	1	1.31%	1.28%	1.87%
	2	1.59%	1.51%	0.87%
	3	0.61%	0.55%	0.33%
	4	*not available*	*not available*	*not available*

Table 3.8: Beam yield configuration mean elastic damping ratios.

Mode		Logarithmic Decrement	Exponential Fit
Mass S1	1	0.93%	0.78%
	2	0.42%	0.45%
Mass A2	1	1.32%	1.24%
	2	0.61%	0.69%
Mass A6	1	1.34%	1.45%
	2	0.69%	0.90%

3.5.4 Half–power (bandwidth) method

For an ordinary structure without high damping, the width of the frequency power spectrum about a particular modal frequency response peak can be used to calculate the level

of damping for that particular mode. This is illustrated in Figure 3.15, and is discussed in many dynamics textbooks [PAZ, 1991].

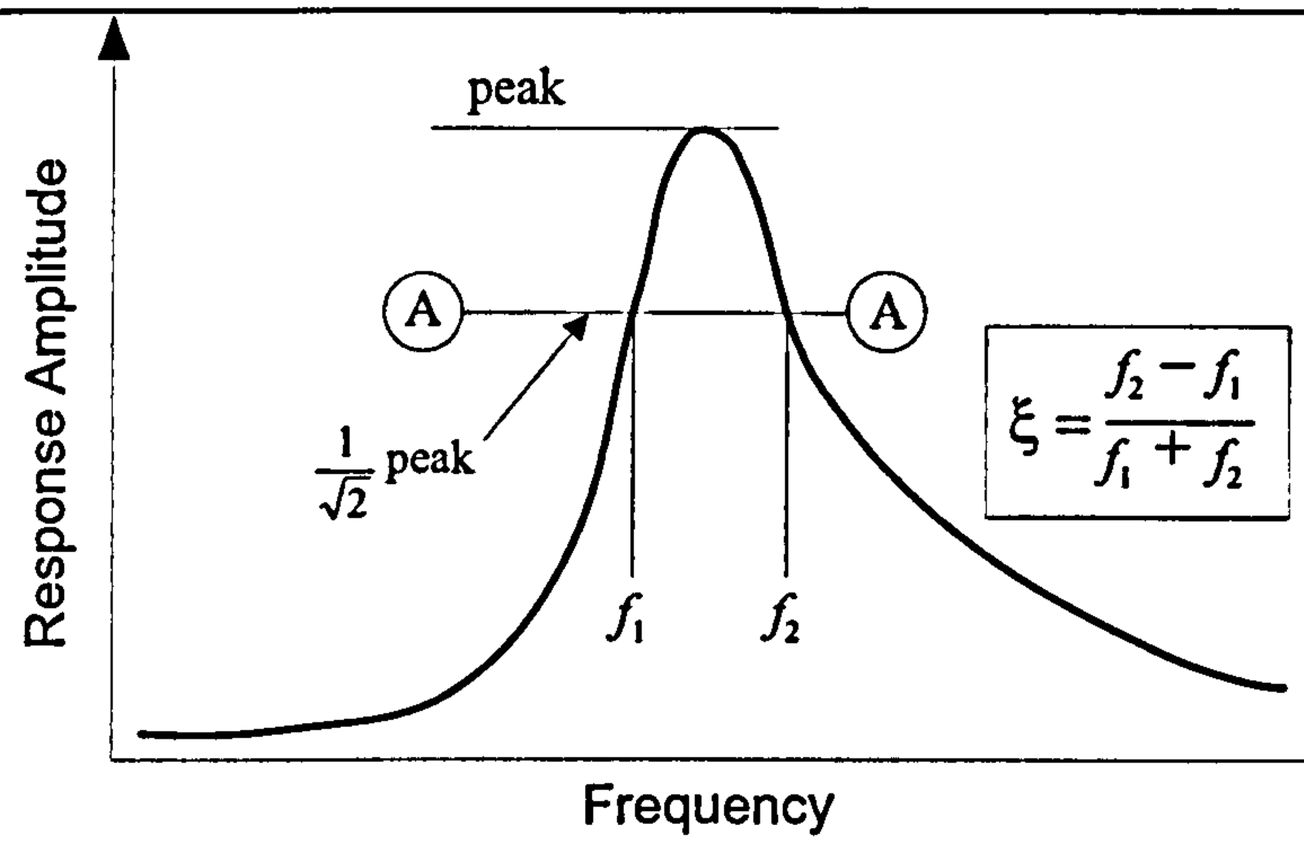

Figure 3.15: Definition of half–power bandwidth method.

During the column yield tests, the models were also vibrated elastically at steady state with a series of simple harmonic motions at the modal frequency. Each test duration was between 10 and 15 seconds, and acquired at a sampling rate of 128Hz. This method has the advantage in that the damping for a particular vibratory mode can be isolated in the response of multiple modes. This reduces some of the 'beating' effects associated with using the logarithmic decay on higher modes, and also alleviates some of the statistical reduction required to obtain a reasonable damping ratio.

The level of damping computed for the models is small ($\xi < 1.5\%$). As a result, the resonance peaks are fairly narrow. The number of points in the response time–history used to calculate the frequency power spectra is, on average, between 1500 and 2000. This results in a frequency increment, δf, of around 0.075Hz. Since a damping of 1.5% results in a bandwidth at section A–A (Figure 3.15) of 0.15Hz. for a central frequency of 5Hz., numerical accuracy can become a problem in the damping calculation (i.e. only 1 to 2 fre-

quency points represent the entire amplitude peak). As a result, polynomials are used to estimate and smooth the peak amplitude. These are shown in Figures 3.16 through 3.18 for

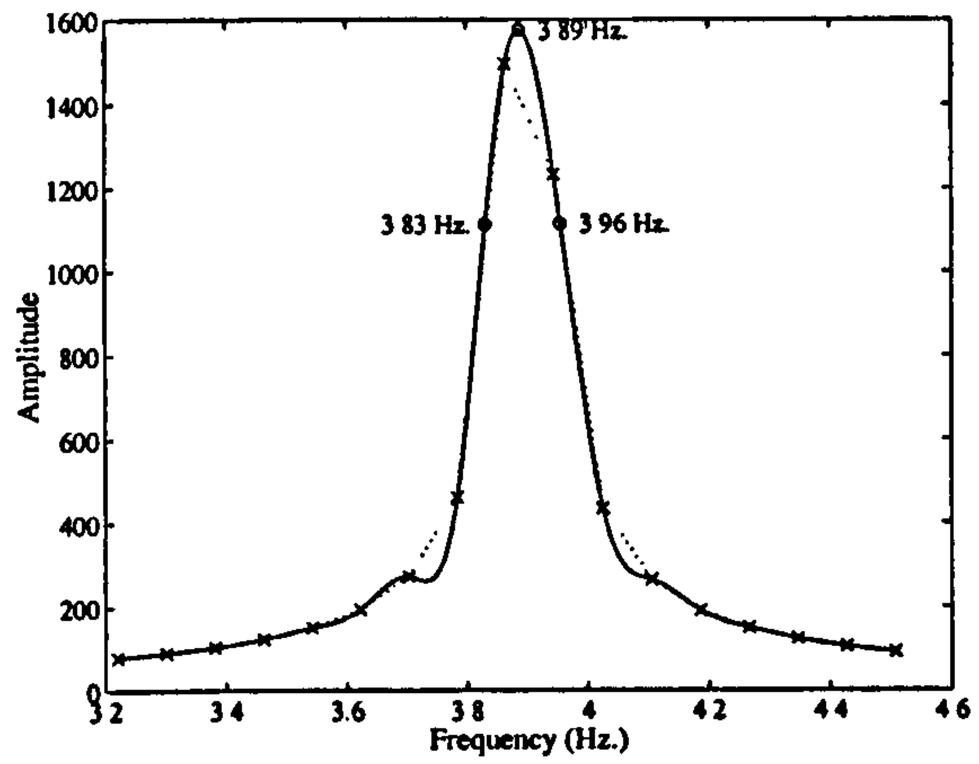

Mode 1: ξ=1.59% @ 3.89Hz.

forcing frequency = 3.90Hz.

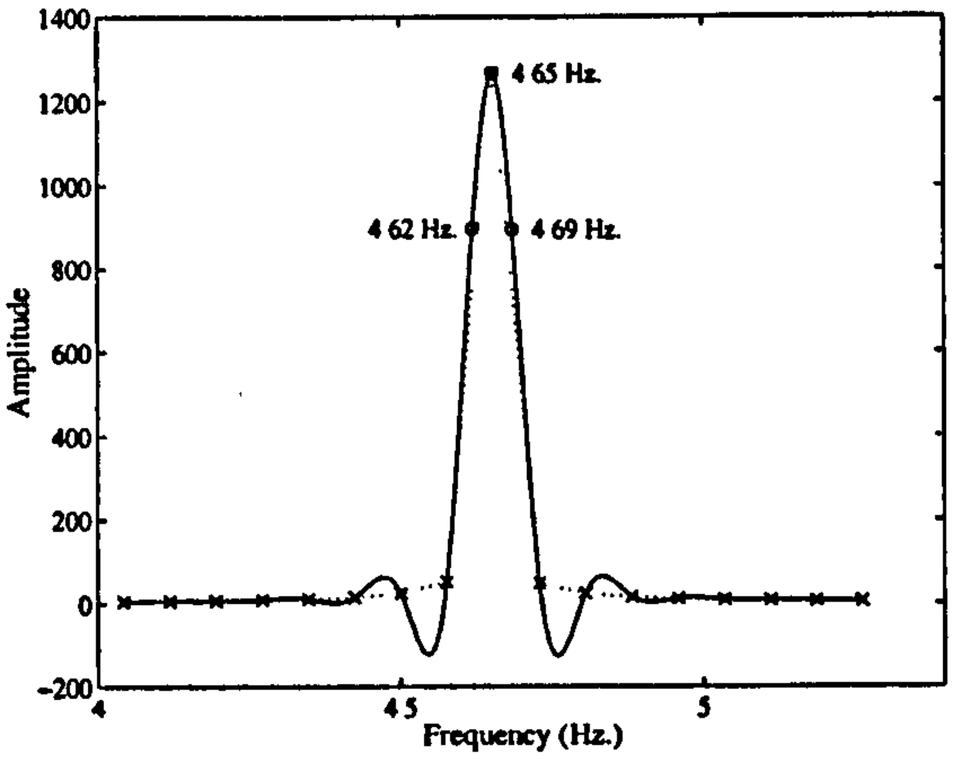

Mode 2: ξ=0.70% @ 4.65Hz.

forcing frequency = 4.65Hz.

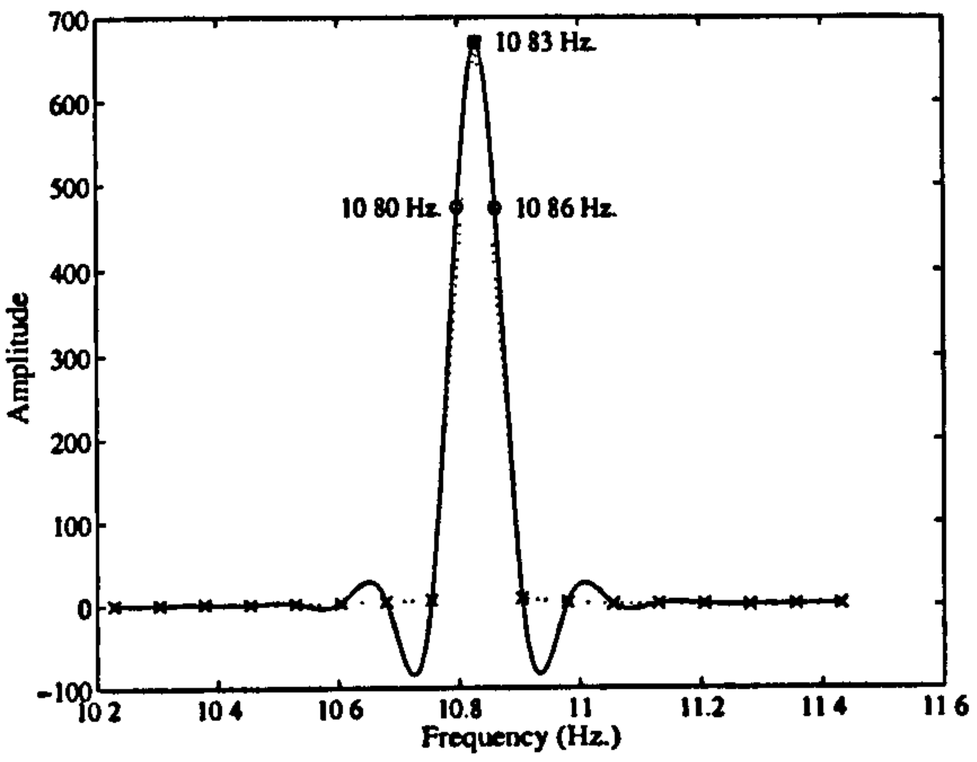

Mode 3: ξ=0.29% @ 10.83Hz.

forcing frequency = 10.83Hz.

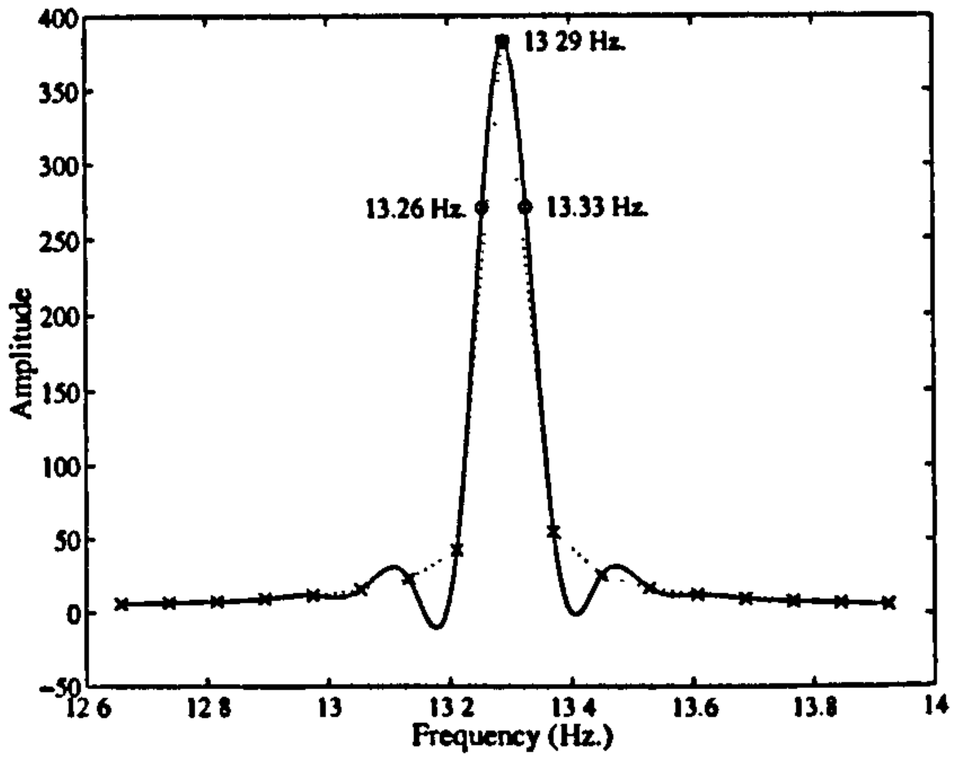

Mode 4: ξ=0.27% @ 13.29Hz.

forcing frequency = 13.30Hz.

Figure 3.16: Half–power bandwidth curves for the column yield models with mass configuration S1.

the three structural mass configurations. The values in these Figures indicate the peak and half–bandwidth frequencies. The amplitude response points in these Figures are interpolated with a high order polynomial. The polynomial is mainly used in determining the peak amplitude, and its usefulness is most evident in the first modes of mass configurations S1 and A6. The quality of the fitted polynomial is important only above the $\frac{1}{\sqrt{2}}$ peak, and the effect of the 'over-fit' below the $\frac{1}{\sqrt{2}}$ peak is negligible. The damping values still

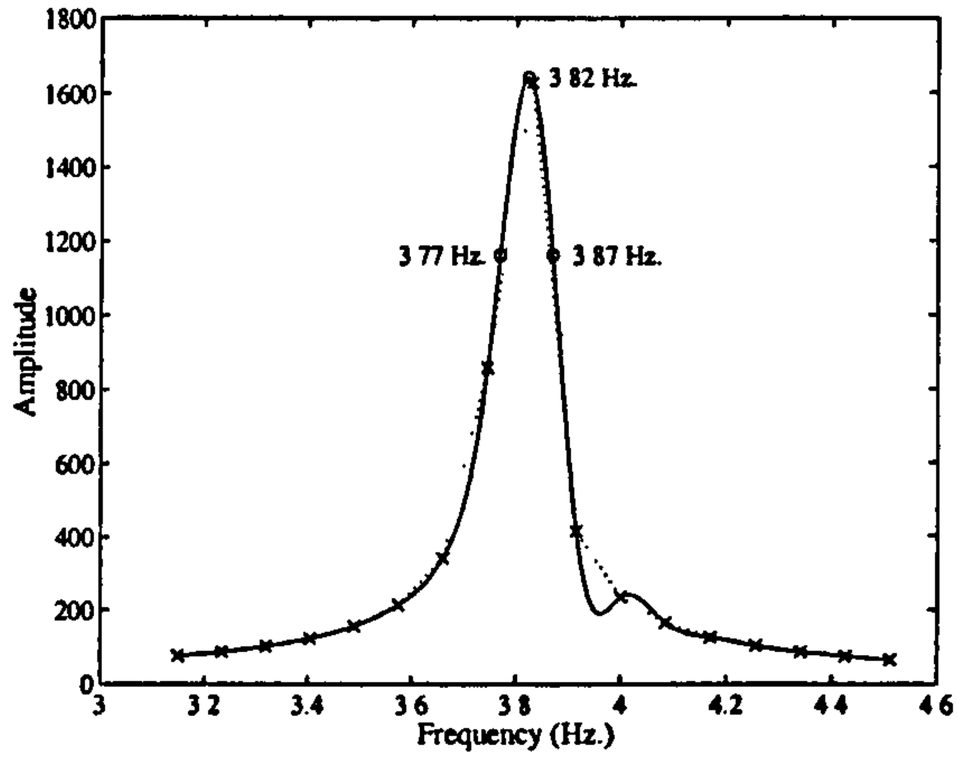

Mode 1: ξ=1.32% @ 3.82Hz.

forcing frequency = 3.80Hz.

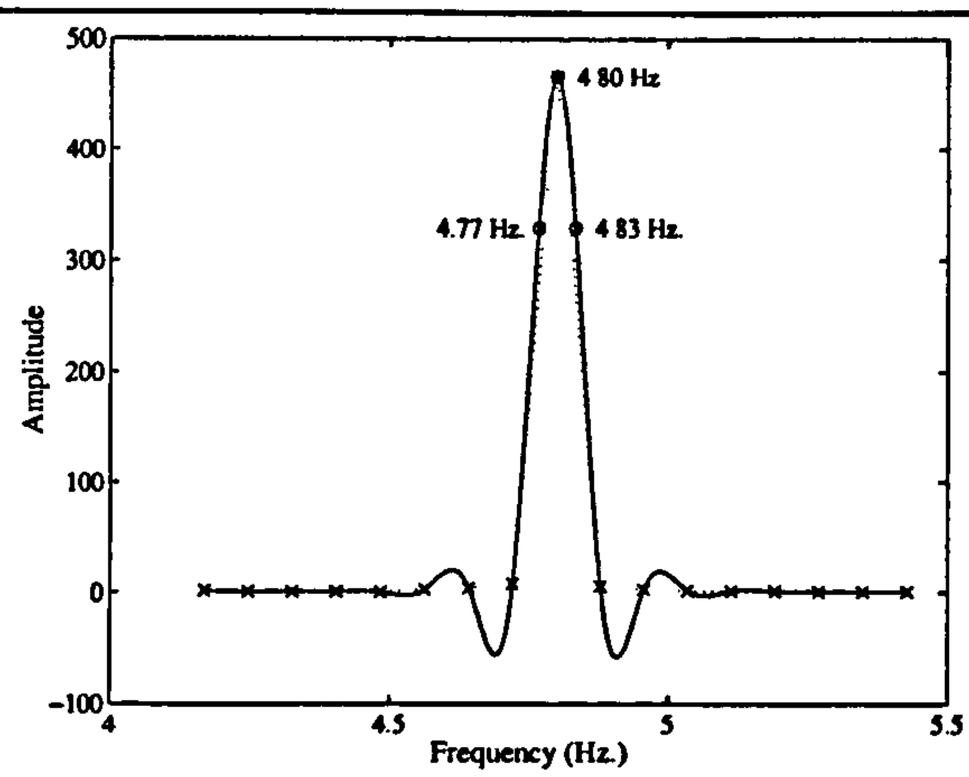

Mode 2: ξ=0.69% @ 4.80Hz.

forcing frequency = 4.80Hz.

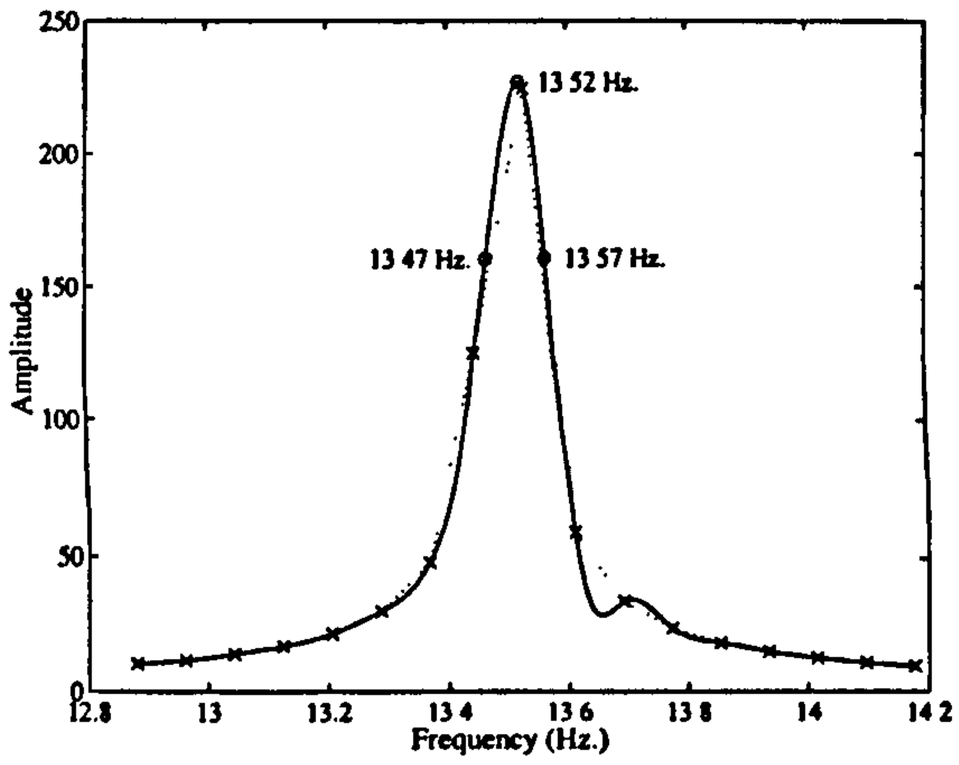

Mode 4: ξ=0.36% @ 13.52Hz.

forcing frequency = 13.50Hz.

Figure 3.17: Half–power bandwidth curves for the column yield models with mass configuration A2.

underestimate those obtained through free–vibration, as indicated in Table 3.7. The damping ratios from each mass configuration decrease with increasing modal frequency.

The accuracy of this method could have been improved during the experimental process if the duration of acquisition was increased to better describe the frequency response peaks.

Rewriting the half–power damping equation if terms of the damping ratio (ξ), the frequency of the mode in consideration (f_ξ), and the number of points (η) desired between the half–power frequencies (f_1 and f_2):

$$\xi = \frac{f_2 - f_1}{f_2 + f_1} = \frac{\eta \delta f}{2 f_\xi} \tag{3.14}$$

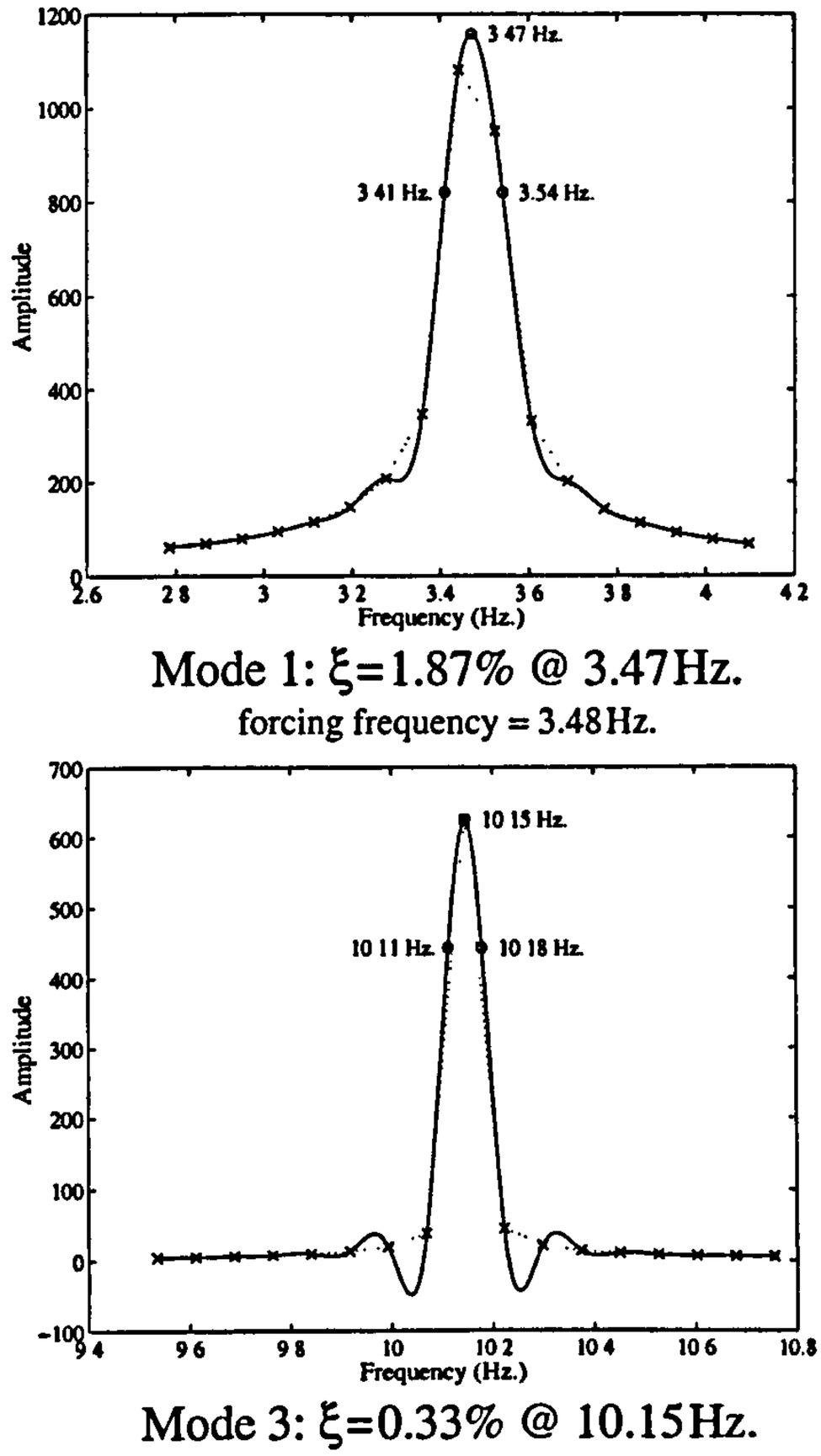

Mode 1: ξ=1.87% @ 3.47Hz.
forcing frequency = 3.48Hz.

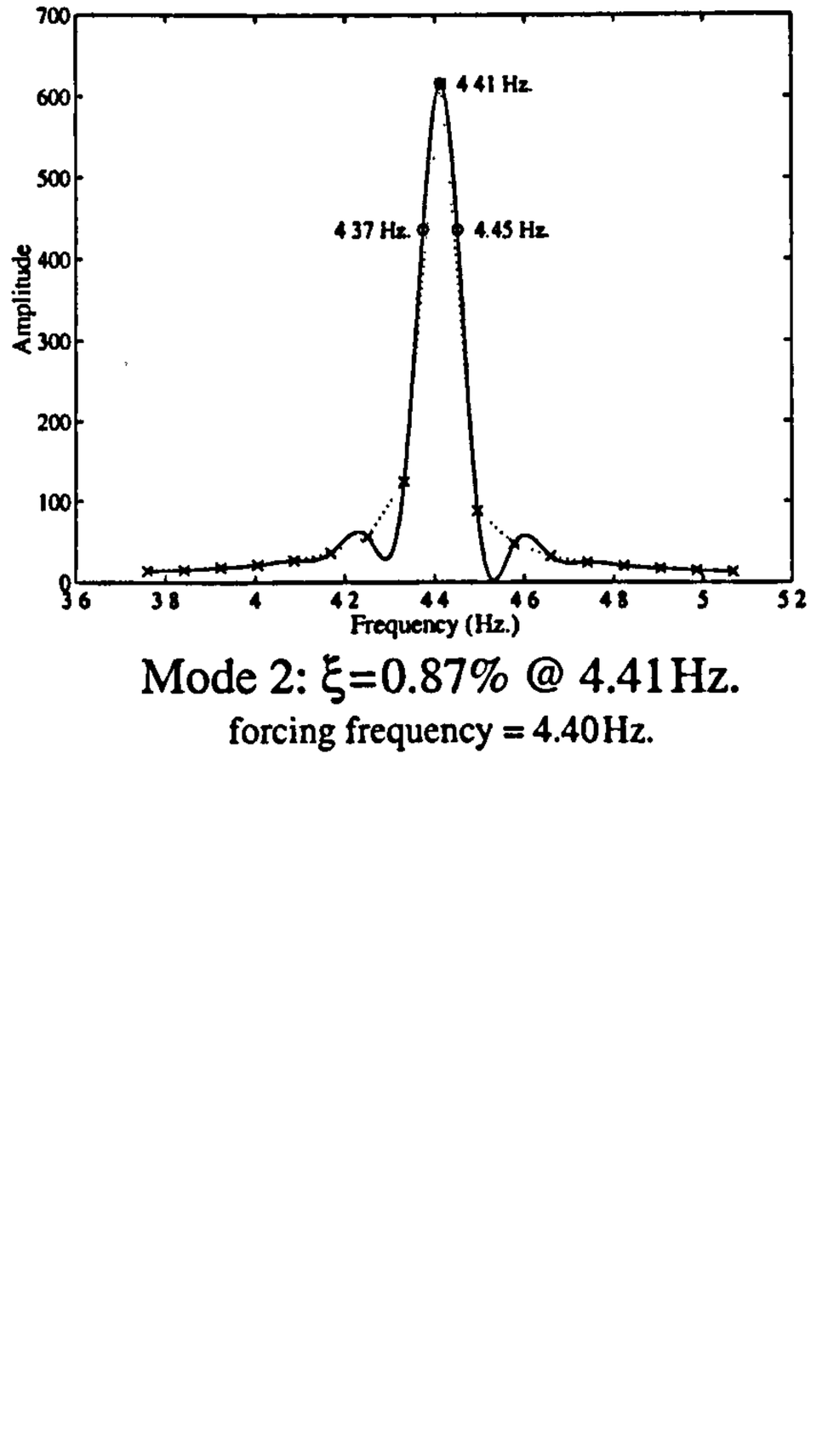

Mode 2: ξ=0.87% @ 4.41Hz.
forcing frequency = 4.40Hz.

Mode 3: ξ=0.33% @ 10.15Hz.
forcing frequency = 10.15Hz.

Figure 3.18: Half–power bandwidth curves for the column yield models with mass configuration A6.

The frequency increment (δf) is simply related to the sampling duration (D in seconds) by:

$$\delta f = \frac{1}{2D} \tag{3.15}$$

Additionally, the sampling rate should be at least twice the forcing frequency (in Hertz) to avoid the Nyquist[1] frequency cutoff. Combining the above two equations into a more suitable form yields the suggested sampling duration in seconds:

1. The Nyquist frequency is theoretically the highest recordable response frequency. It is equal to one–half the sampling frequency (i.e. 64 Hertz, as the data acquisition frequency is 128 Hertz in all tests of this study).

$$D = \frac{\eta}{4\xi f_\xi} \tag{3.16}$$

In the above equation, estimates for ξ and f_ξ for can be used, and a value of 3 to 5 for η should give sufficient accuracy to describe the frequency response peak at the desired frequency, f.

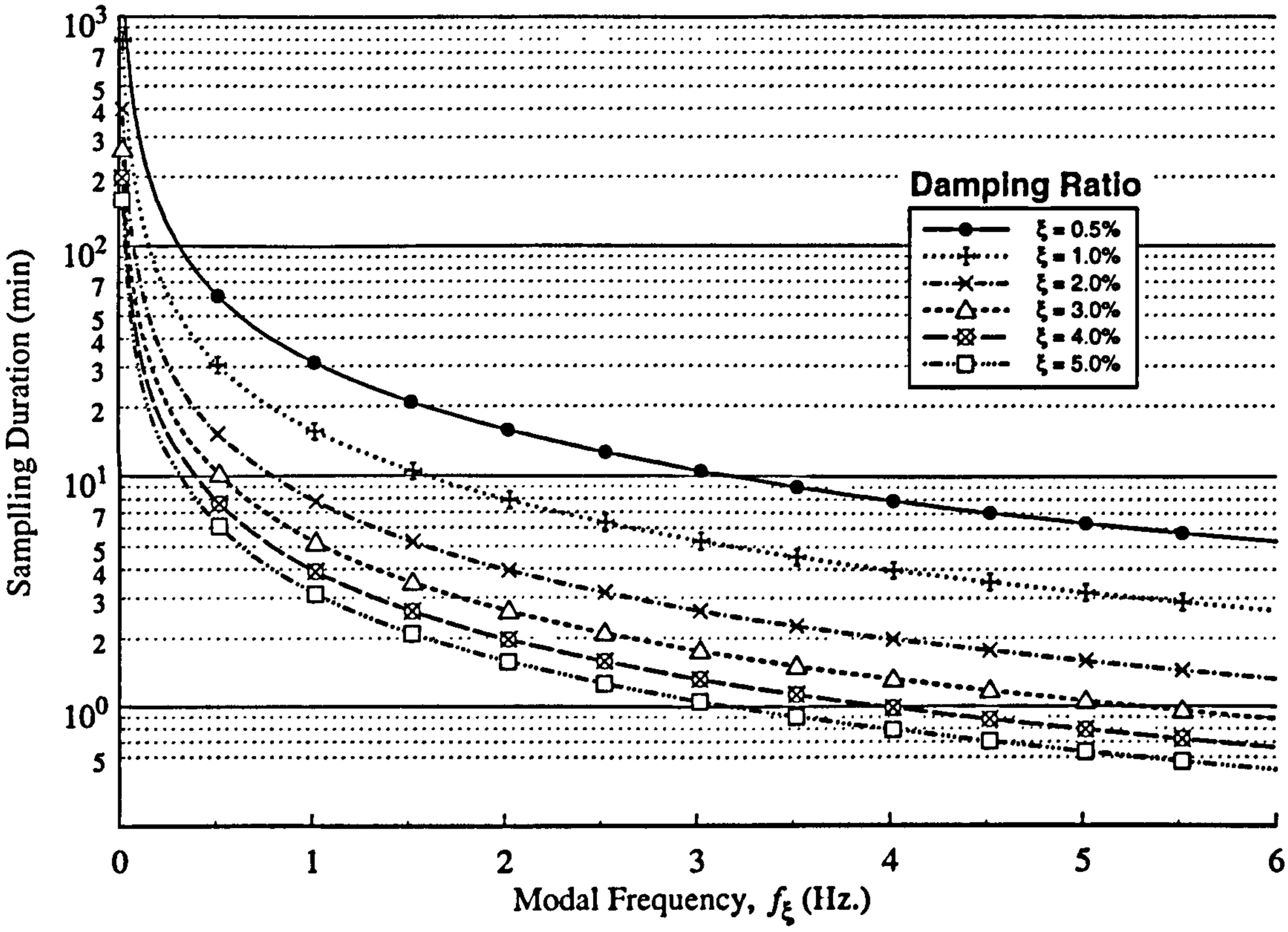

Figure 3.19: Suggested sampling duration in terms of mode frequency and damping

Figure 3.19 shows the simple relationship between D, ξ, and f_ξ. From this relationship, it's shown that the suggested sampling duration should be between 1 to 2 minutes for the fundamental frequencies of the models studied.

CHAPTER 4

HINGE UNIT DESIGN

This chapter describes the hinge unit devices, which allow inelastic behaviour in the experimental model. The effect of the hinge units on both the dynamic characteristics (as presented in the previous chapter) and model geometry are defined. The first section of this chapter describes the physical dimensions and assembly of the hinge units. These units are unique, in that their component design allows the yielding moment to be adjusted by both the type of interchangeable friction pad material, and the normal force applied to this material. This is described in the second section of the chapter. The third section details the effect of the hinge units on the column length for each model configuration.

The final section of this chapter presents a static loading analysis to assess the performance of the hinge units for a typical floor in the model.

4.1 HINGE UNIT DESIGN

The hinge units have the ability to introduce repeatable, non-destructive inelastic behaviour into the experimental model subjected to seismic base excitation. Although designed for this research programme, their usefulness can extend beyond the scope of this study.

4.1.1 Construction and manufacture

The hinge units were designed (by Dr. R.H. Bassett of University College London) as a method of extending the previously elastic experimental model into the non-linear range, where the effects of inelastic torsional coupling can be studied. Figure 4.1 shows an exploded cross–sectional view of a typical hinge unit. The hinge units operate by squeezing together two clamping collars to provide a normal force on the hinge bell. The clamping collars exert the normal force on the two friction plates—one on the top and one on the bottom of the highly polished hinge bell surface. The friction plates are inlaid with a friction pad material, which as a result of the normal force controls the maximum shear along the surface of the hinge bell before slippage occurs.

This is depicted in Figure 4.2, where the shear force along the top and bottom surface of the polished hinge bell is indicated as V_{top} and V_{bottom}, respectively:

$$\begin{aligned} V_{top} &= \mu N_{top}, \text{ and} \\ V_{bottom} &= \mu N_{bottom} \end{aligned} \tag{4.1}$$

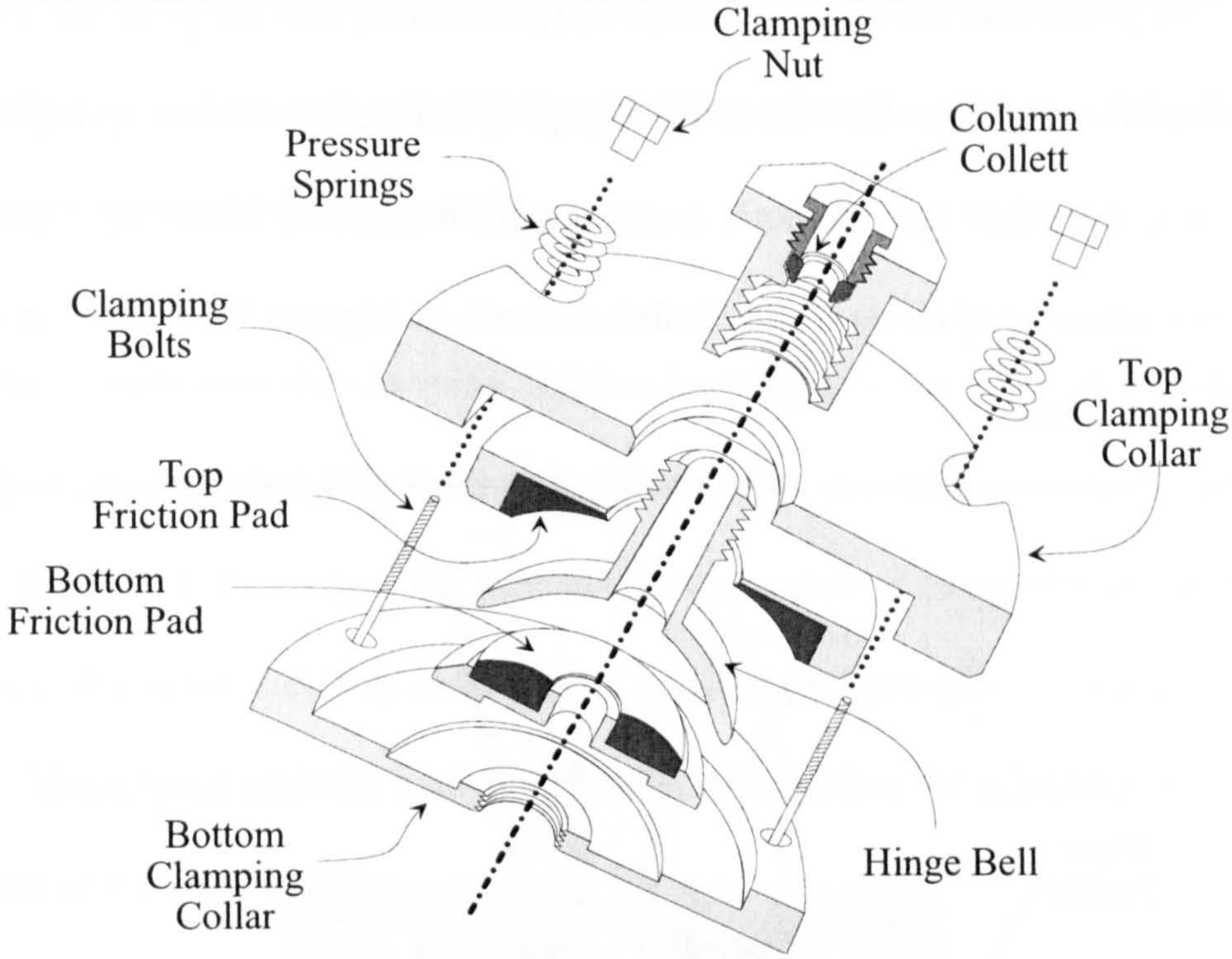

Figure 4.1: Exploded cross-sectional view of a typical hinge unit.

where N_{top} and N_{bottom} are the average applied forces normal to the top and bottom surfaces of the hinge bell, respectively. As discussed in Section 4.2.2, μ in the above equation is the dynamic (kinetic) coefficient of friction.

The moment which generates the slipping shear force (onset of hinge rotation) on the top and bottom hinge bell surfaces is the yielding moment of the hinge unit, M_y:

$$M_y = V_{top}45\text{mm} + V_{bottom}40\text{mm} \tag{4.2}$$

The two dimensions in the above equation represent the distances from the two hinge bell surfaces to the centre of hinge rotation (see Figure 4.2).

With the exception of the friction pads, clamping bolts, and spring washers, the hinge units are constructed of solid brass. This was a requirement, as some of the measuring transducers (proximity probes) are sensitive to the magnetic properties of ferrous materi-

als. The clamping bolts are constructed of stainless steel, and the pressure springs are manufactured from spring steel. Both the clamping bolts and pressure springs are small enough not to influence the magnetic displacement transducer recordings. The friction pads were constructed of either PTFE, Stainless Steel, or Lignum Vitae, and are discussed in Section 4.1.2 below.

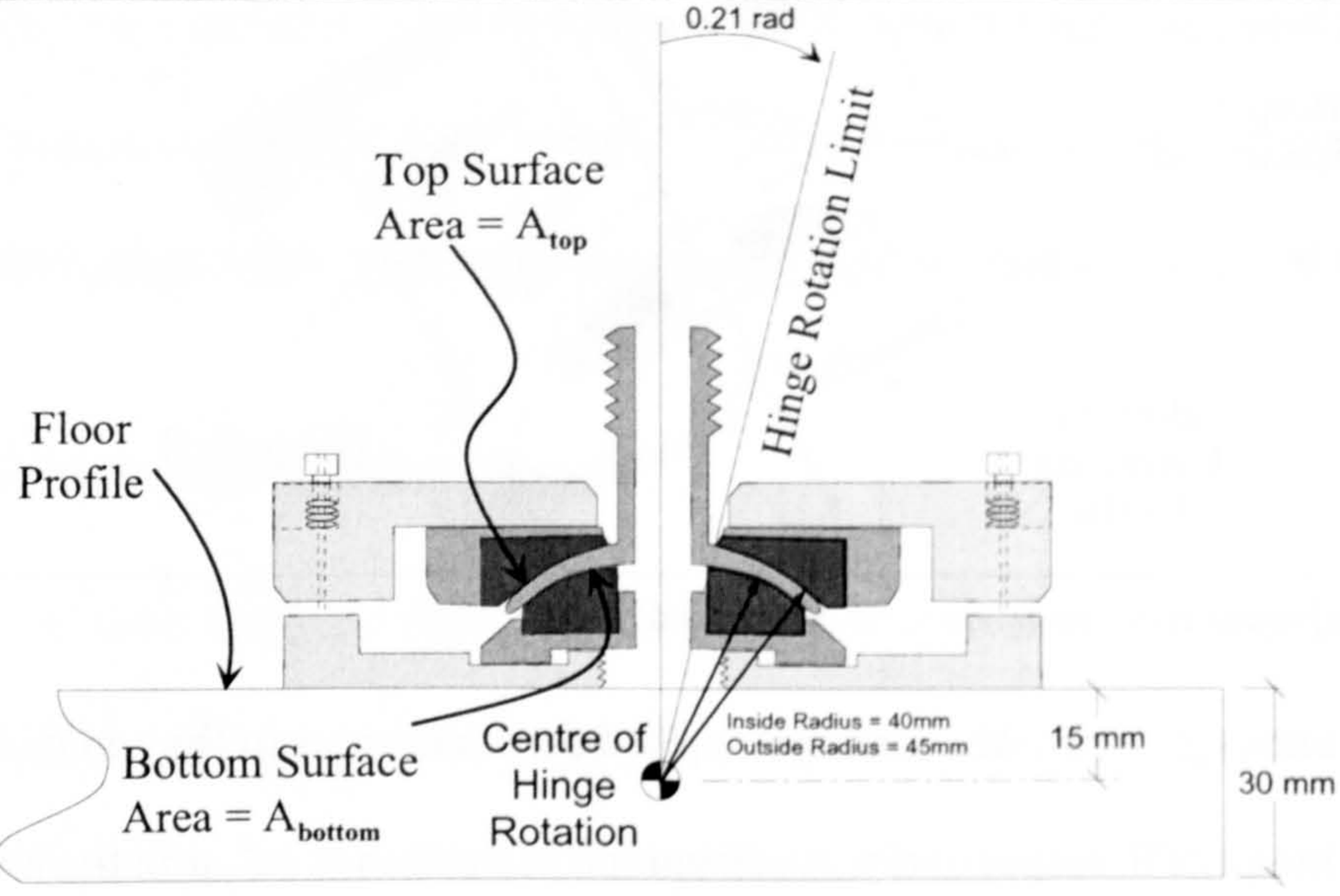

Figure 4.2: Illustrated cross-sectional view of the hinge unit, as attached to the model floor. Note the location of the centre of rotation, and the hinge rotational limit.

The columns of the model are attached to the hinge units by a column adaptor, specific to each column diameter. The column adaptor screws onto the neck of the hinge bell (Figure 4.1), and acts as a nipple for the column collet, which is the connection point (point of fixity) for the column. The neck of the hinge bell can accommodate column diameters up to 20mm.

The hinge units were manufactured using a computer–aided system, at Cambridge University. The CADD/CAM system utilised during the manufacturing process assures a high level of consistency between the individual hinge units. Therefore, with a high degree of

confidence, calibrations made on a single hinge unit are representative of all of the hinge units constructed. The beam yield tests required a total of 25 hinge units. The column yield tests utilized 40 of the hinge units.

The centre of rotation of the clamping bell has been designed to coincide with the centre-line of the floor elevation (15mm into the floor from the bottom of the hinge unit), as shown in Figure 4.2. From this, the location for the centre of hinge rotation during yielding for both the beam yielding and column yielding configurations coincide. This is in keeping with previous inelastic analytical research which has not accounted for the spatial dimensions of the plastic hinges.

The hinge units have a physical rotation limitation of about 0.21 radians (Figure 4.2). This did not prove to be a hindrance, as hinge rotations near this limit resulted in floor displacements well beyond the recording capabilities of the instrumentation. This physical limit on the hinge rotation has the added benefit of protecting the experimental model from total collapse, and safeguards the instrumentation from damage.

4.1.2 Friction pad material

Three different material types are available for use as friction pads in the hinge units:

- PTFE—Polytetrafluoroethylene, a material commonly used for bridge bearing pads when low friction coefficients are required. PTFE is also known by its brand names: Teflon (Dupont), Algoflon (Ausimont), and Fluon (ICI).
- Lignum Vitae—A very hard wood, historically used for brake pads.
- Stainless Steel.

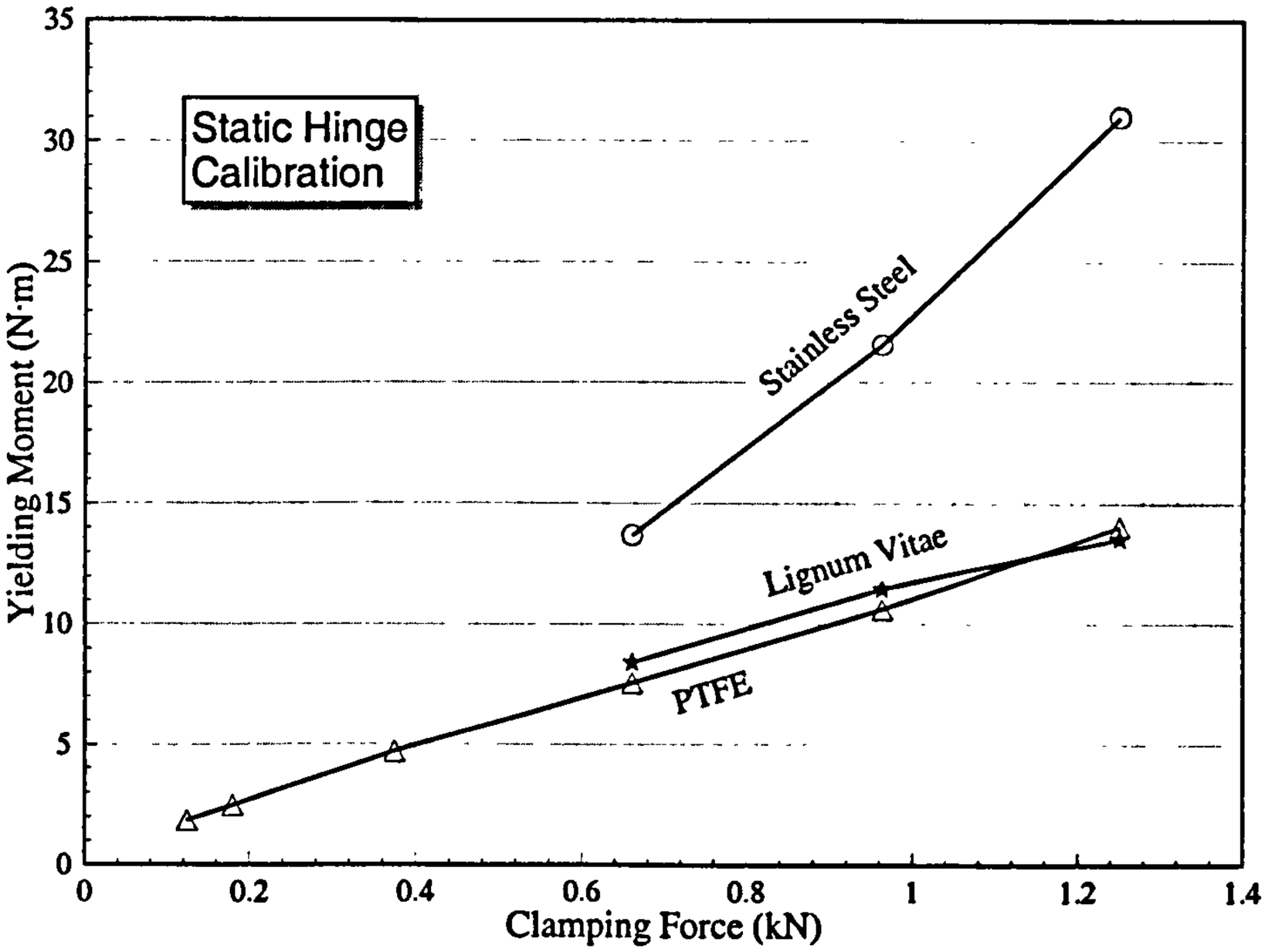

Figure 4.3: Static moment calibration for all three friction pad materials.

Figure 4.3 shows the relationship between the plastic moment (M_y), and the clamping force in the hinge unit. This relationship was created using the static hinge calibration method (described below in Section 4.2.1) for all three friction pad materials. From these tests, the PTFE material was found to be the most reliable. Lignum Vitae, although having a similar moment to clamping force relationship, had a higher standard deviation of the calibration results. As Lignum Vitae is a natural product, its material properties are not as consistent between hinge units as PTFE or stainless steel. The friction pads made out of stainless steel performed quite well. However, the resulting yielding moments they produced were thought to be too high for the column configurations—especially the exterior columns. As a result of initial static yielding moment tests (described below in Section 4.2.1), it was determined that PTFE would be the most appropriate of these three materials. Selecting a pad material with a low standard deviation of the yielding moment pro-

vided better estimates of extrapolated responses such as displacement ductility and hysteretic energy (Chapter 6). From this reasoning, PTFE was selected as the sole friction pad material used throughout the studies.

4.2 CALIBRATED YIELDING MOMENTS

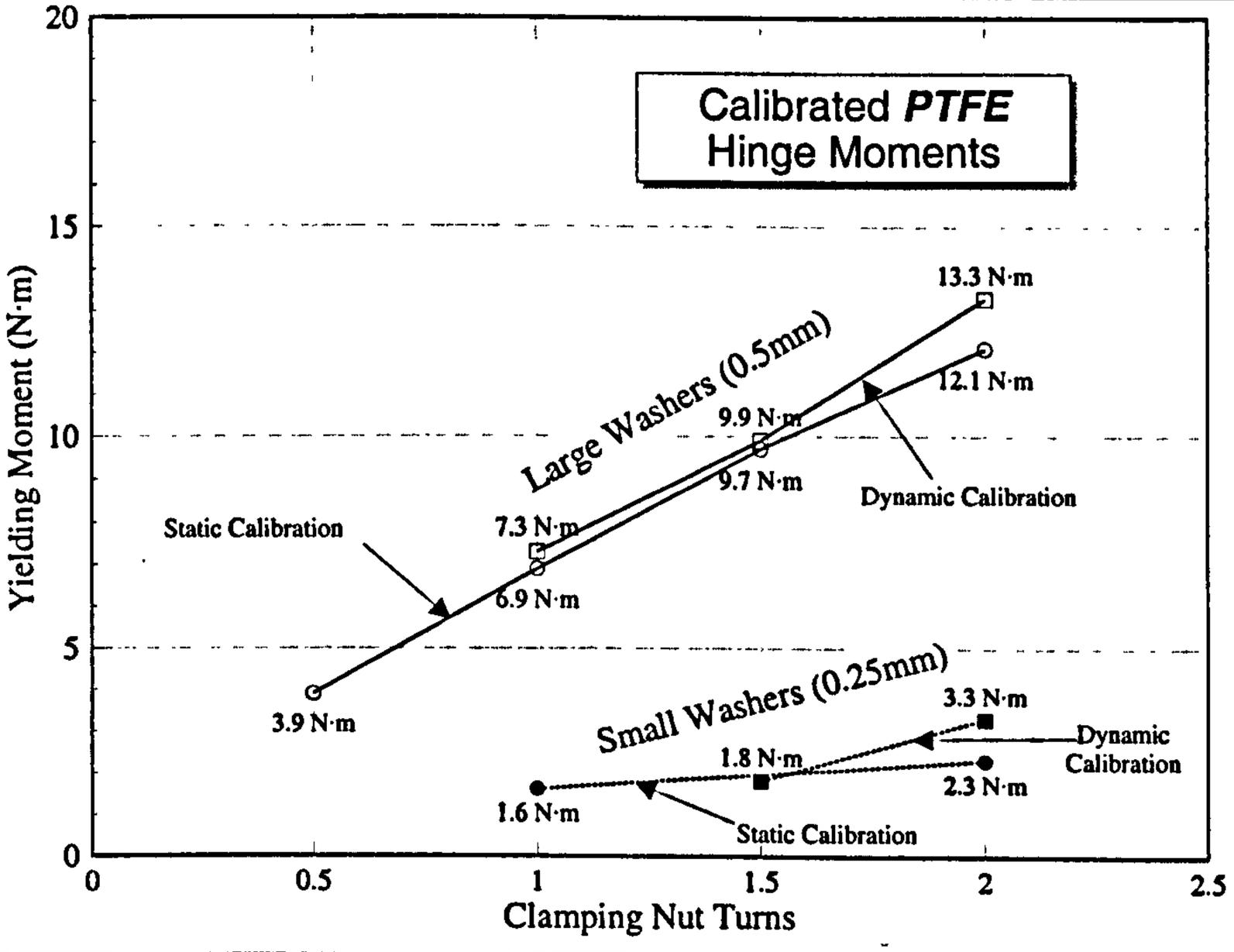

Figure 4.4: Hinge yielding moment calibration for PTFE bearing pads.

The magnitude of the clamping force, and hence yielding moment, is controlled by the bolts along the perimeter of the clamping collars. The hinges were designed with six clamping bolts—three large bolts for coarse adjustments, and three small bolts for fine tuning of the clamping force between the top and bottom clamping collars. The larger diameter clamping bolts have a thread pitch of 1mm, whereas the smaller diameter (fine tuning) bolts have a 0.5mm thread pitch. As a result of the preliminary static moment calibration tests, it was determined that the smaller diameter adjustment bolts were not

Table 4.1: Hinge configuration and individual column strengths for the **column** yield configuration.

Floor		Left Side			Centre			Right Side			Strength Eccen.
		Nut Turns	M_y (N–m)	F_y (N)	Nut Turns	M_y (N–m)	F_y (N)	Nut Turns	M_y (N–m)	F_y (N)	e_s (mm)
Hinge CA	4	2s	3.3	26.2	2s	3.3	35.1	2s	3.3	26.2	0.0
	3	2s	3.3	26.2	2s	3.3	35.1	2s	3.3	26.2	0.0
	2	2	13.3	105.6	2	13.3	141.5	2	13.3	105.6	0.0
	1	2	13.3	105.6	2	13.3	141.5	2	13.3	105.6	0.0
Hinge CB	4	*locked*	20.1	159.6	*locked*	67.9	722.3	*locked*	20.1	159.6	0.0
	3	*locked*	20.1	159.6	*locked*	67.9	722.3	*locked*	20.1	159.6	0.0
	2	2	13.3	105.6	2	13.3	141.5	2	13.3	105.6	0.0
	1	2	13.3	105.6	2	13.3	141.5	2	13.3	105.6	0.0
Hinge CC	4	*locked*	20.1	159.6	*locked*	67.9	722.3	*locked*	20.1	159.6	0.0
	3	*locked*	20.1	159.6	*locked*	67.9	722.3	*locked*	20.1	159.6	0.0
	2	1.5	9.9	78.6	2	13.3	141.5	2	13.3	105.6	63.6
	1	1.5	9.9	78.6	2	13.3	141.5	2	13.3	105.6	63.6
Hinge CD	4	*locked*	20.1	159.6	*locked*	67.9	722.3	*locked*	20.1	159.6	0.0
	3	*locked*	20.1	159.6	*locked*	67.9	722.3	*locked*	20.1	159.6	0.0
	2	1.5	9.9	78.6	1.5	9.9	78.6	2	13.3	105.6	67.9
	1	1.5	9.9	78.6	1.5	9.9	78.6	2	13.3	105.6	67.9

1. The suffix 's' denotes small (0.25mm) thickness washers.
2. Hinges with *locked* clamping nuts are essentially elastic. The values of M_y and F_y relate to that of the brass columns

required, and complicated the testing procedure. Adequate control of the PTFE friction pads was available through the coarse adjustment bolts[1].

1. This was not the case with the stainless steel friction pads, which have a higher coefficient of friction compared to the PTFE pads. The tighter thread pitch on the smaller diameter bolts in a hinge unit with stainless steel friction pads allow a greater control of the hinge yielding moment.

As a means of regulating the clamping force, a series of eight spring washers are placed on each clamping bolt shaft, and arranged into four pairs with the concave side of each washer in a pair juxtaposed with the other. This arrangement reduces the sensitivity of the washers, by a factor of eight, to the displacement of the clamping nut. The displacement to spring–load relationship of the individual washers have been calibrated by the manufacturer, and are shown in relationship to the number of turns of the clamping nut in Figure 4.5 for both the large (0.50mm) and small (0.25mm) washer thicknesses. The

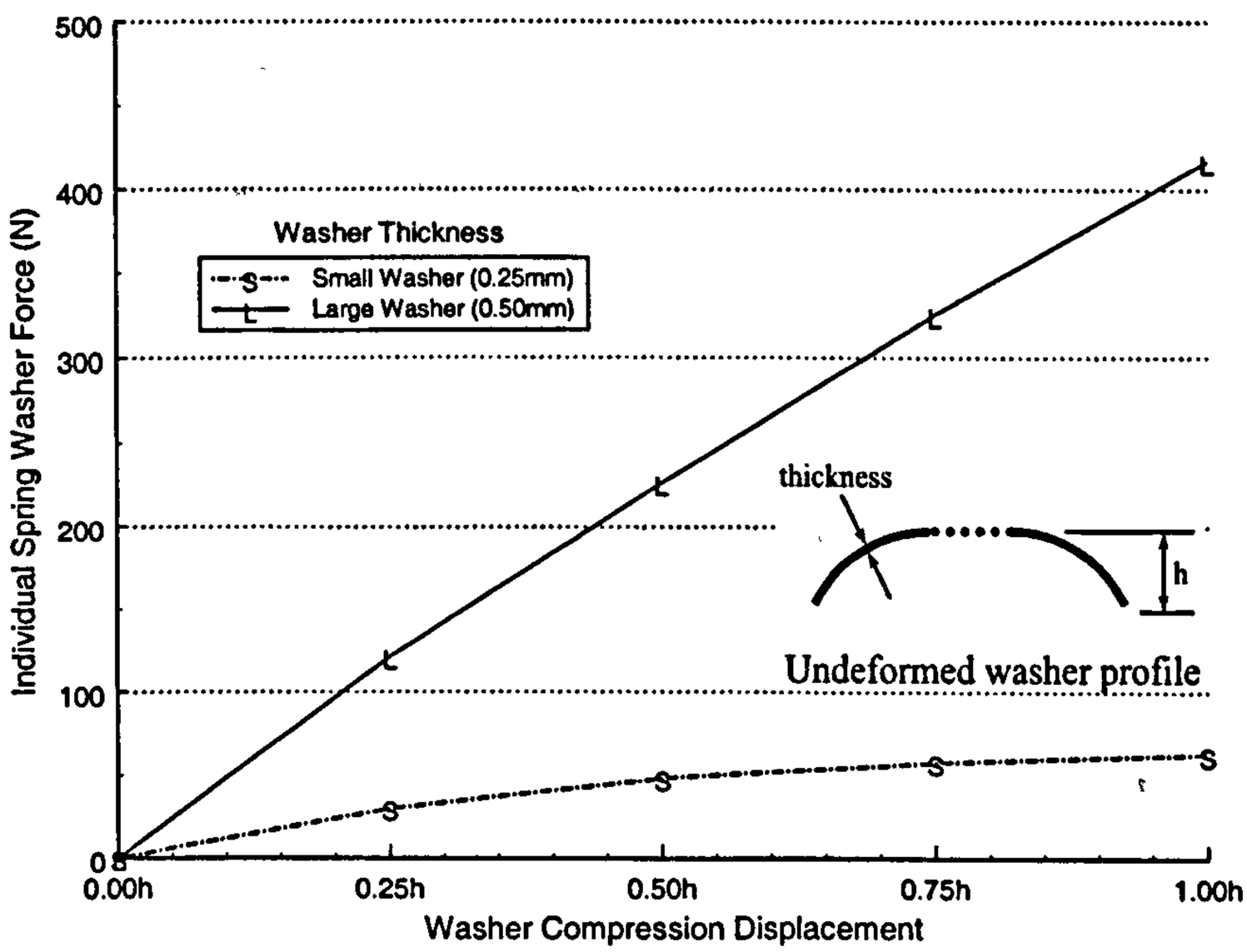

Figure 4.5: Spring washer specifications, as provided by the manufacturer. The undeformed washer height, h, is 0.30mm for the small washers, and 0.25mm for the large thickness washers.

dimension, *h*, in Figure 4.5 is the undeformed profile height of an individual spring washer. This dimension is 0.30mm for the smaller washers, and 0.25mm for the larger thickness washers. The method for regulating the clamping force in each bolt, although very simplistic, proved quite adequate. During adjustments of the hinge units, spacer blocks were inserted between the floors to remove the self-weight of the floors from the

hinge units. The clamping force was completely removed from each clamping bolt in the hinge unit. The clamping nuts were then screwed down just until contact with the spring washer is made. After initial contact has been made for all clamping nuts in a hinge unit, the nuts are tightened to the required number of turns to achieve the proper hinge yielding moment. Each nut is rotated in ½ turn increments, progressing in an orbital fashion around the hinge unit, until all of the nuts are tightened. Tables 4.1 and 4.2 show the hinge configurations for the column yield and beam yield set–ups, respectively. The hinge configurations for both model set-ups are based on a convenient distribution of clamping nut turns, in ½ turn increments. Clamping nut turns beyond 2 revolutions were at the limit of the spring washers, and as a result, tended to lock the hinge, and produce unpredictable yielding moments. The yielding moment, M_y, and strength, F_y, are for a single hinge location. Therefore, actual strength values for the entire left or right bents are twice the values of those listed, since each exterior bent has two hinge locations.

4.2.1 Static calibration

Preliminary static moment calibration tests were performed on the hinge units for all friction pad material types. This helped determine the friction pad material best suited for the shake table studies. The column clamping bell has been machine milled to the same inside and outside radius as the bottom and top friction pads, respectively. From this, the clamping force has the same proportionality to the surface shear force on the bell, over its entire range of motion. Hence, the assumption is made for the static calibration tests of perfectly–plastic behaviour in the hinge unit once yielding. This assumption was proved appropriate through the dynamic calibration tests (Section 4.2.2).

Table 4.2: Hinge configuration and individual column strengths for the **beam** yield configuration.

Floor		Left Side			Centre			Right Side			Strength Eccen. e_s (mm)
		Nut Turns	M_p (N–m)	F_y (N)	Nut Turns	M_p (N–m)	F_y (N)	Nut Turns	M_p (N–m)	F_y (N)	
Hinge BA	4	2	13.3	80.6	2	13.3	80.6	2	13.3	80.6	0.0
	3	2	13.3	80.6	2	13.3	80.6	2	13.3	80.6	0.0
	2	2	13.3	80.6	2	13.3	80.6	2	13.3	80.6	0.0
	1	2	13.3	122.0	2	13.3	95.0	2	13.3	122.0	0.0
Hinge BB	4	1	6.9	41.8	1	6.9	41.8	1	6.9	41.8	0.0
	3	1	6.9	41.8	1	6.9	41.8	1	6.9	41.8	0.0
	2	1½	9.9	60.0	1½	9.9	60.0	1½	9.9	60.0	0.0
	1	2	13.3	122.0	2	13.3	95.0	2	13.3	122.0	0.0
Hinge BC	4	1	6.9	41.8	2	13.3	80.6	2	13.3	80.6	92.5
	3	1	6.9	41.8	2	13.3	80.6	2	13.3	80.6	92.5
	2	1	6.9	41.8	2	13.3	80.6	2	13.3	80.6	92.5
	1	1	6.9	63.3	2	13.3	95.0	2	13.3	122.0	116.7

The static tests involved increasing the moment in a typical hinge unit, in increments of about 0.02N·m, until the hinge becomes plastic. The testing rig used for these tests is depicted in Figure 4.6 where the increment in loading mass (δM) is 100g, and the static moment arm is 0.2 metres. Figure 4.6 shows the average plastic moment (from 10 tests) for each turn–of–the–nut clamping level. This is a standard box–whisker plot, where the centre notch indicates the average value. The box corners mark the 10th and 90th percentile; the whiskers denote the 5th and 95th percentile.

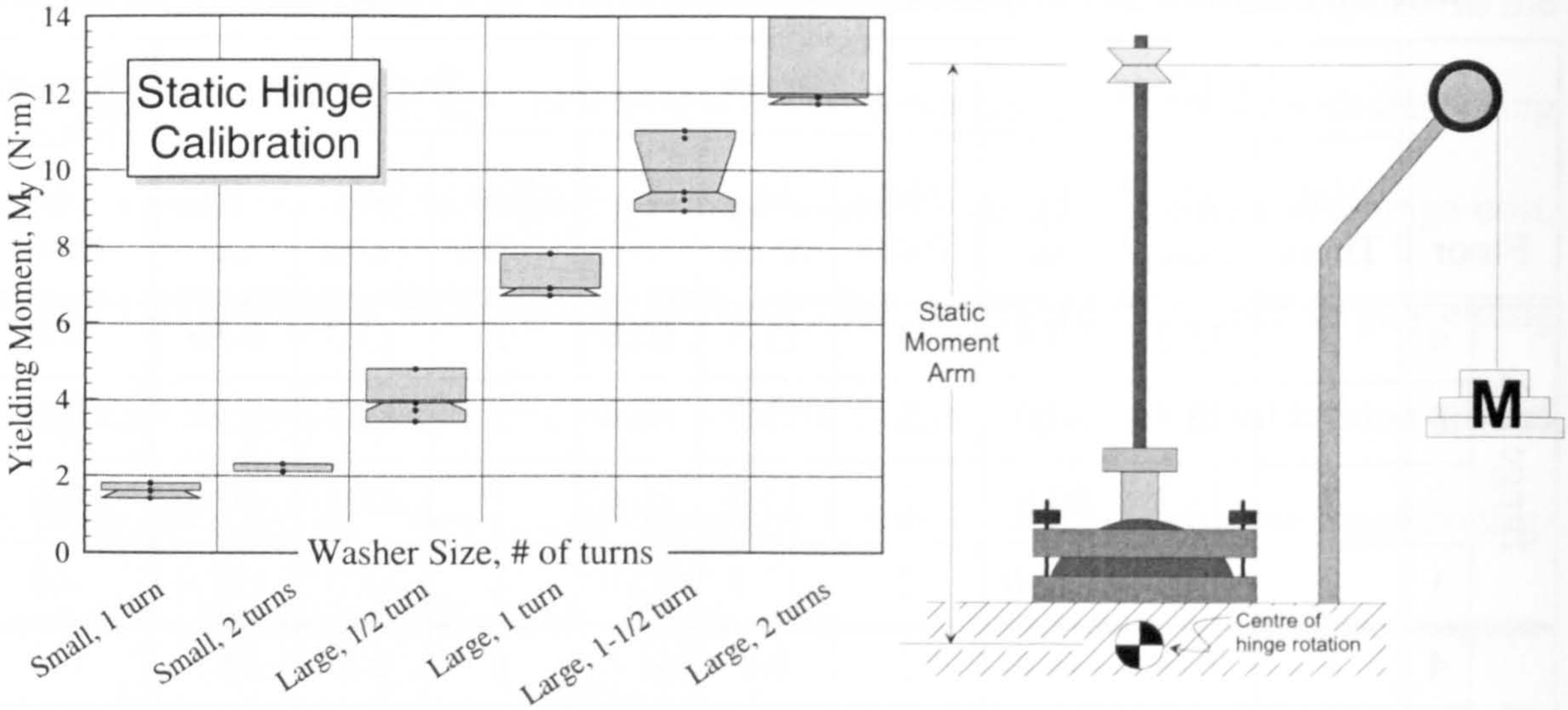

Figure 4.6: Statically calibrated hinge yielding moments, and testing apparatus.

4.2.2 Dynamic calibration

Figure 4.7 shows the statistical results from the dynamic hinge calibrations in the form of a box–whisker plot. The dynamic tests were performed by acquiring the strain time–history off of two strain gauges positioned parallel to the direction of bending stress. These gauges are placed on the two major bending axes, and near the clamping collet of the hinge unit, as in Figure 4.7.

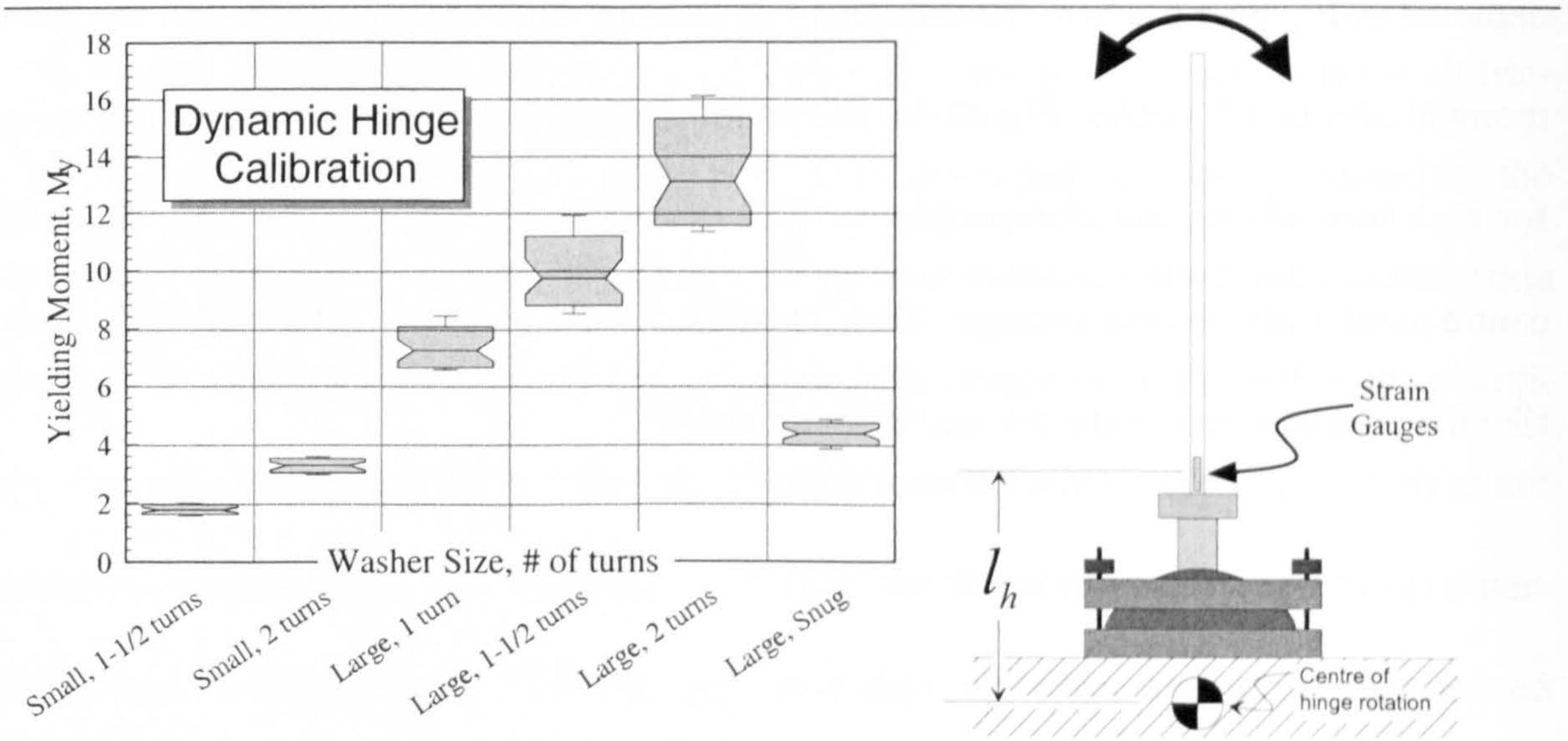

Figure 4.7: Dynamically calibrated hinge moments, and dynamic method of testing.

The bending moment magnitude at the location of the strain gauges, M_{gauge}, is calculated by the following equation:

$$M_{gauge} = \frac{\sigma I}{c} = \frac{EI\sqrt{\varepsilon_1^2 + \varepsilon_2^2}}{c} \tag{4.3}$$

where c is the column radius, and ε_1 and ε_2 are the extreme fibre strain at the two orthogonal strain gauges.

The measured bending moment magnitude, M_{gauge}, is that at the strain gauges, and not at the centre of hinge rotation. This results in an underestimate of the true moment in the hinge unit. The moment at the centre of hinge rotation, M_{hinge}, can be calculated by adding the moment error, M_{error}, to the measured moment, M_{gauge}:

$$M_{hinge} = M_{gauge} + M_{error} \tag{4.4}$$

The term M_{error} is the error in measuring the moment above the clamping collet, and not at the centre of rotation:

$$M_{error} = Fl_h \tag{4.5}$$

where F is the horizontal shear force at the gauges, and l_h is the distance between the strain gauges and the centre of hinge rotation.

Since the dynamic calibration was performed by applying a horizontal force at the top of the cantilever column (as in Figure 4.7), the correction for the corrected moment at the centre of rotation can be calculated as:

$$M_{hinge} = M_{gauge}\left(1 + \frac{l_h}{l_f}\right) \tag{4.6}$$

where l_f is the distance from the top of the cantilever column (application of horizontal force) to the strain gauges. This equation increases the measured moment at the strain gauges by about 5% to obtain the dynamically calibrated hinge moment at the centre of hinge rotation.

The acquired orthogonal strain time–histories can be transformed into a polar time–history plot, as in Figure 4.8 for a typical hinge unit. In the polar plot, the magnitude is the hinge moment and the angle is the planar hinge rotation angle. For purposes of analysis, hinge moments considered to be elastic were removed from the statistics. The 'elastic' threshold

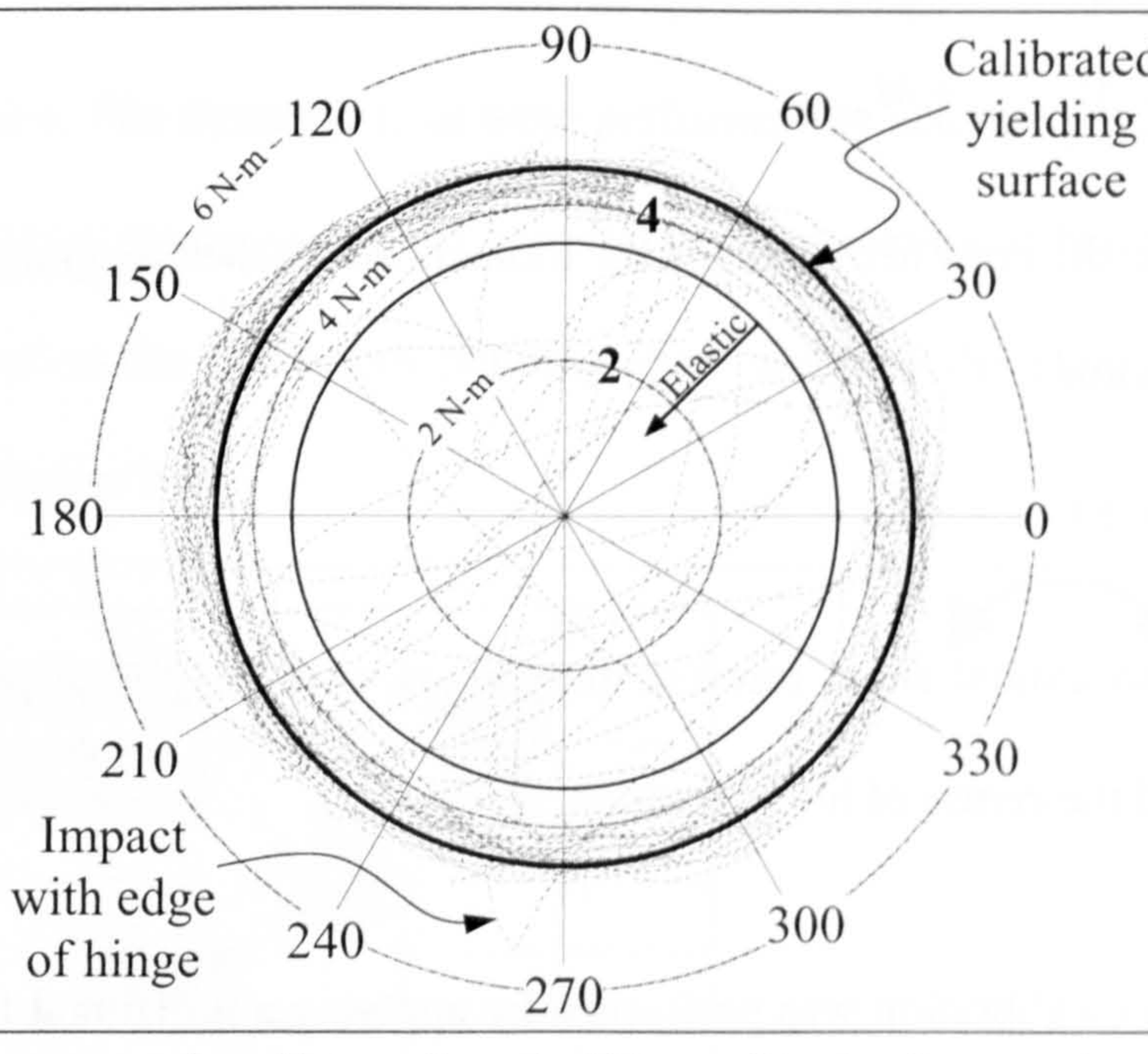

Figure 4.8: Bending moment time–history of a typical hinge calibration (large washer with snug fit).

is indicated by the bottom bin of the histograms in Figure 4.9, and is based on a visual inspection of the moment magnitude time–histories.

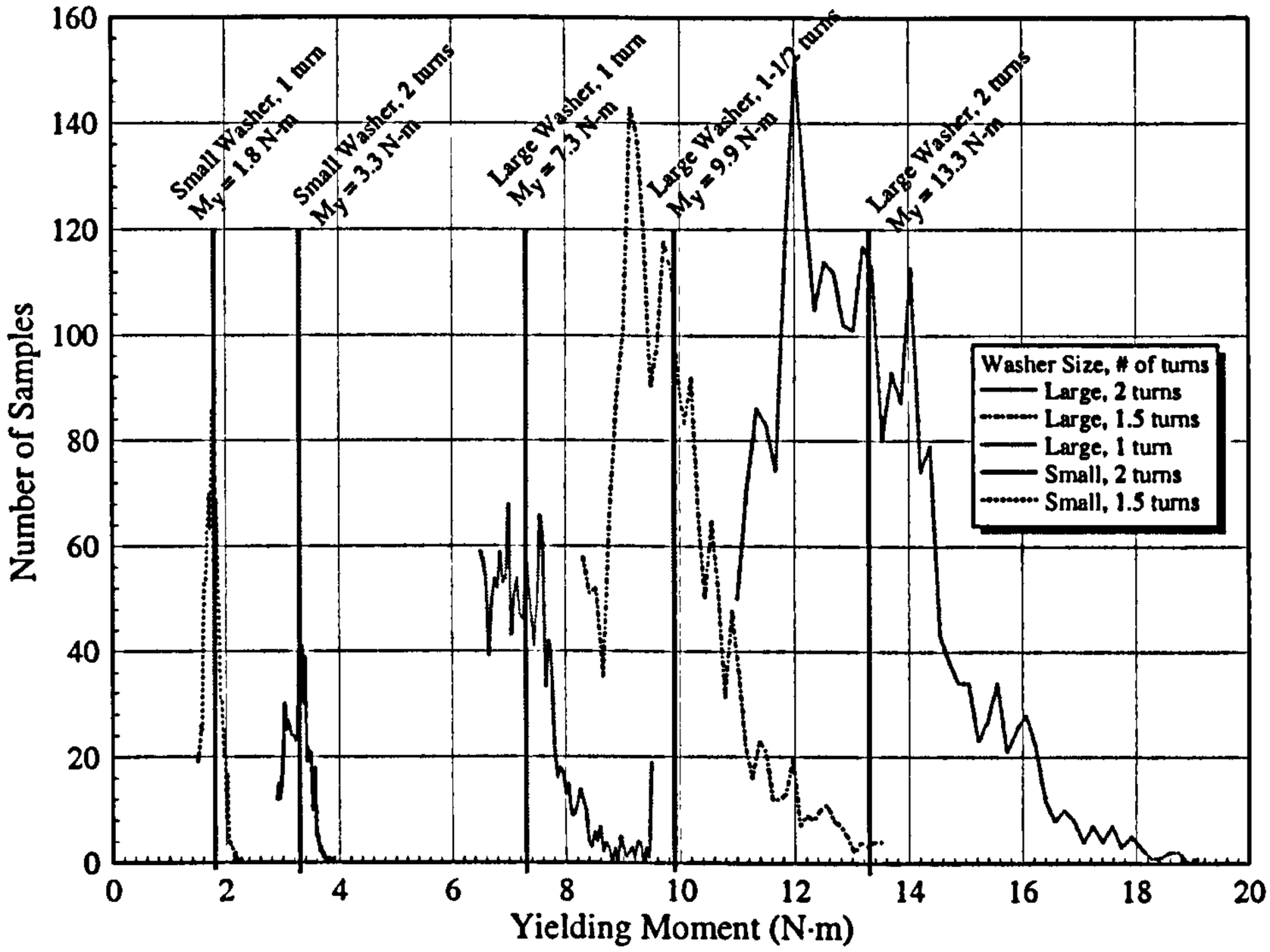

Figure 4.9: Yielding moment histogram depicting the statistical error in the dynamic calibrations.

4.2.3 Comparison of calibration test methods

Table 4.3 shows the average yielding moment (PTFE) from both the static and dynamic hinge unit calibrations for the various clamping configurations used in this study. The

Table 4.3: Calibrated hinge yielding moments, PTFE

Spring Washer Size	Number of Clamping Nut Turns	Static Calibration (N-m)	Dynamic Calibration (N-m)	Percent Difference
Small Washers (0.25mm)	1 turn	1.6	N/A	—
	1-½ turns	N/A	1.8	—
	2 turns	2.3	3.3	35.7%
Large Washers (0.50mm)	½ turn	3.9	N/A	—
	1 turn	6.9	7.3	5.6%
	1-½ turns	9.7	9.9	2.0%
	2 turns	12.1	13.3	9.4%

dynamic calibrations were performed on all clamping nut configurations used in the experimental test. The static calibrations, as the initial hinge calibrations, contain clamping nut configurations not used during the experiments, thus missing from the dynamic calibrations. For all of the acquired moment calibrations, the static calibrations resulted in lower yielding moments. This could possibly be a result of the slight impact force in placing the masses onto the calibration rig, or the creep effect inherent in the static calibration procedure.

4.2.4 Hinge orientation

The difference between the beam and column yielding hinge configurations are a result of the curvature discontinuity in the columns at the hinge locations. The column curvatures in the beam yielding configuration are continuous, with limited maximum curvature at the beam–column connections. The curvature of the columns in the column yielding configuration, on the other hand, are discontinuous at the floor–column joints. This is what distinguishes between the two types of inelastic behaviour. At the onset of yielding, the beam yielding configuration will redistribute the joint resisting moment to the other elastic joints in the column. This action also distributes damage over a wider vertical distance in the structure, thus potentially permitting a greater energy absorption capacity. Also, structures designed to yield in the beams do not face the risk of structural collapse (as long as rupture does not occur). However, the greater distribution of damage can also lead to a greater cost of repair, or even an unusable structure. Column yielding on the other hand tends to concentrate damage in a single storey due to its potential soft storey effect. To ensure structural safety, a soft storey must be designed to survive the expected cyclic load-

ing through means of high ductility and energy absorption capacity. This adds considerably to the cost of the design.

It was found that through repeat testing, the hinge yielding moments degraded slightly between tests. This is thought to be caused by the clamping nut loosening due to the cyclic compressing and decompressing of the spring washers during the tests. This is a result of the curved friction pad surfaces which create small pitching and rolling motions in the top clamping collar.

The large spring washers (0.5mm thick) were used in the first and second storeys where larger shear forces occur. The smaller washers (0.25mm thick) were used in the third and fourth storeys, but were normally locked to ensure no yielding in the top two storeys. It was found the third and fourth stories were the weakest in terms of design (Appendix B) if the small washers were used at their maximum regulated moment (approximately 3N-m). The quantity of available large spring washers was not sufficient to accommodate all forty hinges in the column yield configuration.

Adjusting the distribution of yielding moments across the floor plan allowed some variation in the strength eccentricity, e_s. This is the distance between the centre of elastic stiffness and the resultant force when all members are yielding. This parameter is similar to the mass eccentricity in equation (3.2), but is based on the column (or hinge) yield strength:

$$e_{s_x} = \frac{\sum_i f_{y_i} x_i}{\sum_i f_{y_i}} \tag{4.7}$$

where, f_{y_i} is the yield strength of column i, and is located a distance x_i along the x–axis from the centre of stiffness. Equation (4.7) is defined for a particular floor, and is based on the column group above and below the floor in consideration. All of the building models in this study have no strength eccentricity along the axis parallel to the forcing direction (i.e. $e_s = 0.0$). For simplicity, e_{s_x} is referred to as e_s throughout this study. The last column in Tables 4.1 (page 88) and 4.2 (page 91) shows the strength eccentricity, e_s, for all floors of the hinge configurations for the column and beam yielding models.

4.3 EFFECTIVE COLUMN LENGTHS

The hinge units clamp onto the columns at a position approximately 85mm along the column from its centre of rotation, as indicated by the dimension, l_h, in Figure 4.7. For the most part, this does not affect the column length between the floors of the beam yield models. The reduction in column length by the distance l_h from the hinge at the bottom of the column is offset by the same increase of column length, l_h, by the hinge at the top of the column (see Figure 3.5 on page 55). This results in a measured unsupported column length equal to the inter–storey height, approximately 400mm. The exception to this is the ground storey, where the hinges on the shake table reduce the effective column lengths to approximately 200mm. This is unlike actual buildings which generally have taller and softer first stories. The ground storey height could not be physically increased due to limi-

tations of the measurement frames, and its restrictions on the positioning of displacement transducers. The column yielding configuration has equal column lengths in all four stories due to the dual hinges at each beam–column joint.

The inter-storey column lengths in the model are important parameters for the calculations of both the analytical and assumed experimental responses. The inter-storey heights are easily measured. However, their effective column lengths cannot be measured directly. This is due to uncertainties in the column length required to achieve complete fixity from the collets in the hinge units.

The method on which the determination of the effective column length is based relies on elastic frequency matching between an analytical lumped mass model and the experimental model for the symmetric mass configuration (S1), during which all model hinges are fully locked. The analytical frequencies are determined through eigenvalue analysis on a range of column lengths. The torsional resistance of the central column is accounted for in determining the elastic frequencies (a Poisson ratio of 0.3 is assumed). Only the first two frequencies of the analytical model are considered, as the higher modes have been shown to be negligible in the elastic response of this class of model [CHANDLER, et al., 1990]. Additionally, the higher frequencies are more difficult to determine experimentally, and are affected more by small changes of column length. The effective column lengths are considered as those which result in the smallest differences between the first two experimental and computed analytical frequencies.

To simplify the analysis, the axial forces in the columns are neglected, and the resulting stiffness is used to estimate both the analytical undamped elastic frequencies (sections 3.3.3 and 3.3.4) and assumed column end moments (Section 6.1 on page 167). The mass of the structure is that of the combined floor and hinge unit masses on each floor (column masses are negligible), while the modulus of elasticity for the columns is taken as 1.0×10^8 kN/m^2, as reported in a previous publication [CHANDLER, et al., 1988(b)].

This method of frequency matching is advantageous, in that any constant error in the values of the modulus of elasticity of the columns are accounted for in the resulting effective column length. However, the frequencies determined by the analytical model are the undamped frequencies, whereas the experimental frequencies are damped. This does not contribute significantly to the error, since the ratio of viscous damping for the experimental model, as discussed in Section 3.5, is very low.

4.3.1 Column Yield Tests

All four floors of the column yielding hinge arrangement are equally spaced, and the hinge units are placed on both the top and bottom of each column segment. From this, it is valid to assume that the exterior column lengths for all four floors are similar. The central column, due to its larger diameter and different collet size does not necessarily have an effective length equal to that of the exterior columns. This is considered in the frequency matching by specifying the internal column length as a ratio of the exterior column lengths. In determining the range of possible frequencies, the exterior column lengths were varied between 170mm and 250mm in increments of 2mm. In addition, the effective

length of a typical centre column was varied between 80% and 140% of the length of an exterior column.

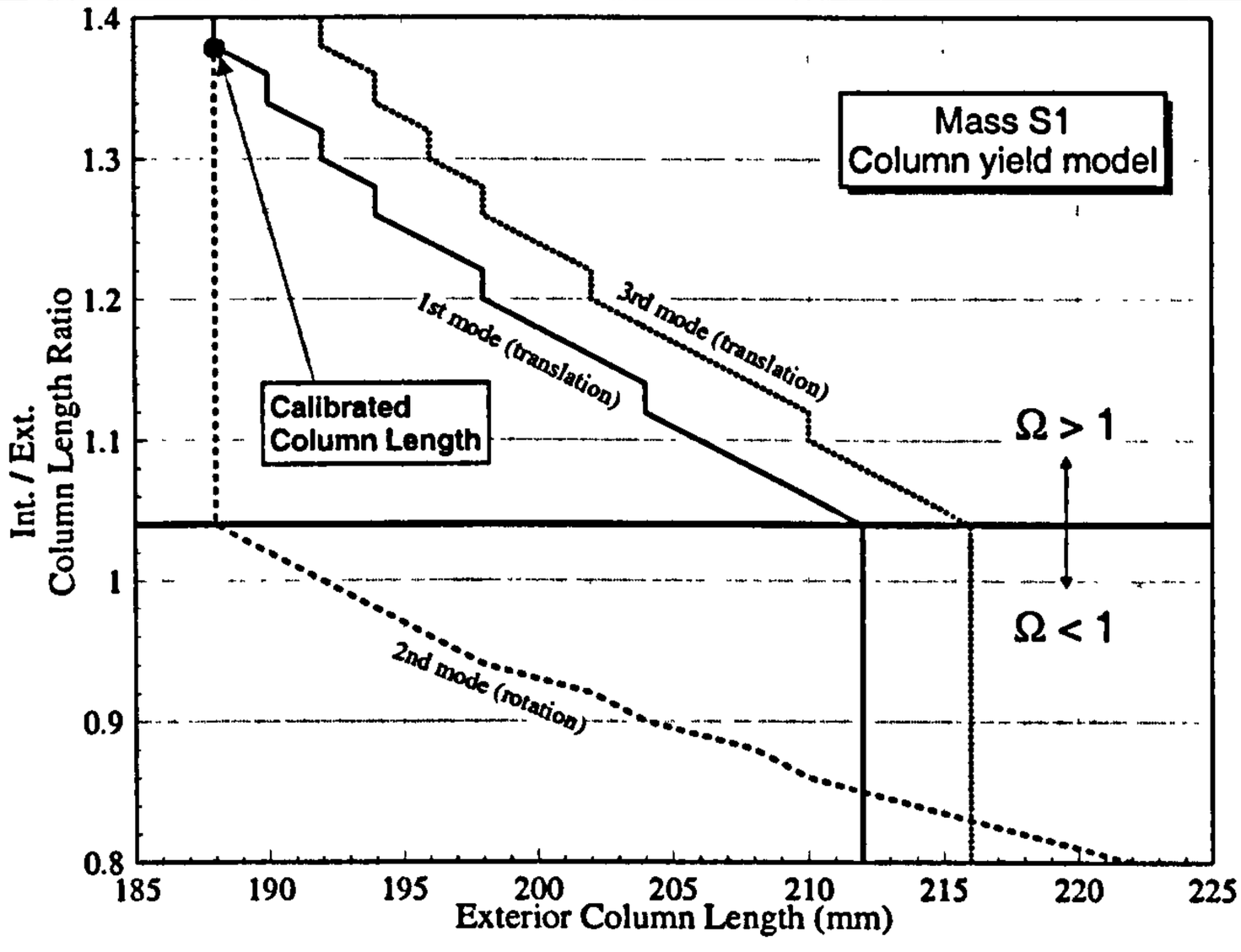

Figure 4.10: Minimum frequency error determination for the first three modes of the symmetric mass configurations, S1

The results of the eigenvalue analysis for the aforementioned parameter range and the three mass configurations are shown in Figure 4.10. This Figure shows the frequency error for the first and second modes in the symmetric mass model (the third mode is also shown for reference). The contours on the horizontal base plane indicate the lowest frequency errors. As the interior to exterior column length ratio (R_{col}) decreases, the translational frequencies increase due to the increased central column stiffness. However, the rotational frequencies are unaffected by R_{col} since the torsional stiffness provided by the central column is negligible, and its geometric location coincides with the centre of elastic stiffness. This is evident in the second mode in Figure 4.10, where values of R_{col} less than about 1.04 result in a torsional frequency less than the translational frequency ($\Omega < 1.0$). In this range, the modal frequency is essentially independent of R_{col}, as is indicated by the verti-

cal lines for the first and third modes. From the experimental frequencies, it was determined that the fundamental mode was in translation. Therefore, it can be assumed that R_{col} is greater than or equal to 1.04 for all four floors in the column yielding model configurations. From the frequency error for the second mode, R_{col} should be at least 1.04 so that $\Omega > 1.0$. In this parameter range, the lowest error occurs when the exterior column length is about 188mm. This is acceptable, since the physically measured distance between the hinge collets is also 188mm. Combining this effective length with the criteria that $R_{col} \geq 1.04$, Figure 4.10 suggests that $R_{col} \cong 1.38$. This value indicates that the interior column length is about a third greater than the exterior column lengths. This value of R_{col} is suspiciously high, and would suggest possible yielding of the central column during the experimental frequency tests. This was indeed a problem during the inelastic tests, in that the plastic moment of the central column was low in comparison with its stiffness. However, the frequency tests employed locked hinges which alleviates this problem. Also, if the central column was yielding during the damping tests, it would be expected that R_{col} has a value much greater than that reported. The high calibrated value of R_{col} is due to a reduced translational stiffness. This is most likely due to a lack of fixity in the centre column clamping collet. Table 4.4 lists the resulting effective column lengths.

Table 4.4: Calibrated and uncalibrated column lengths for the **column** yield configurations

	Column Lengths (mm)	
Column Location	Uncalibrated	Calibrated
Interior (centre)	190	252
Exterior (corners)	188	188

4.3.2 Beam Yield Tests

As a result of the hinge design, it is easier to regulate the clamping force in the hinge units when they were mounted on the bottom of each floor. This is due to the weight of each floor being supported directly by the concave portion of the hinge bell. If the hinges were placed on the top of the floors, the floors would essentially be supported by the pressure springs, and regulation of the yielding moments would be difficult. Unfortunately, mounting the hinges on the bottom of the floors means a smaller effective column length in the ground storey, since hinge units also had to be mounted on top of the shake table surface to simulate yielding in the column foundations. The floors could not be repositioned vertically, since the absolute floor elevations were limited by transducer placement in the adjacent instrumentation frames. In calibrating the column lengths, three parameters were considered. These were the interior and exterior column lengths in the first storey, and the column lengths in the second through fourth storeys. The upper floors have identical column lengths for the interior and exterior columns, since the columns are continuous (Figure 3.4b on page 53). Only the symmetric mass configuration is considered. The calibration method used to determine the column lengths in the beam yield model is similar to that used in the column yield model. The correlation between the frequency error and column lengths is also similar to Figure 4.10, and is not shown for brevity. In determining the frequency error, the first three modes were considered to have equal importance, and the combination of column lengths resulting in the minimum frequency error are listed in Table 4.5. There is a significant difference in the uncalibrated to calibrated column lengths, especially in the upper floors.

Table 4.5: Calibrated and uncalibrated column lengths for the **beam** yield configurations

	Interior Column Lengths (mm)		Exterior Column Lengths (mm)	
	Uncalibrated	Calibrated	Uncalibrated	Calibrated
Ground Storey	217	280	227	218
Other Storeys	407	330	407	330

4.4 STATIC LOADING ANALYSIS

This section describes the response until failure[1] of a series of single-storey models under a monotonically increasing horizontal load applied at the centre of mass. The structural configuration of the single-storey models are identical to the first storey of the column yielding, four-storey models. This is appropriate, since the first floor is the most critical in most of the column yielding hinge configurations. The models associated with hinge configuration CA have not been included since these have a similar horizontal strength and stiffness distribution to those of hinge configuration CB, but with the lowest strength in the third storey.

The results have been obtained analytically assuming that the floor acts as a rigid diaphragm, and that the two sets of exterior columns on either side of the model behave as single resisting units, as shown in Figure 4.11. This is in keeping with the methodology of previous simplified analytical studies on torsional coupling. The stiffness of the columns perpendicular to the translational floor displacement, Δ, have been not been considered. Hence, the additional torsional stiffness resulting from the corner placement of the col-

1. In this section, "failure" denotes the inability of the structural system to resist an additional increment of applied loading (i.e. zero stiffness).

umns (about 40%) is ignored. This assumption both overestimates the torsional displacement, Θ, during the mass asymmetric cases, and underestimates the overall torsional strength. However, the static model with uniaxial forcing only considers half of the planar loading. The inclusion of transverse loading, as experienced in actual earthquakes, would significantly reduce the aforementioned errors.

The effects of dynamic torsional coupling are not considered, as they are beyond the scope of this Section. These effects have been studied thoroughly by previous researchers for single-storey models, as described in Chapter 2. Instead, the emphasis in this Section is to reveal the general static relationship between mass eccentricity, strength eccentricity, and overall storey strength.

The total applied horizontal shear force on the floor, F, is varied from zero to a total failure load of 800N. The column stiffness is assumed elastic–perfectly plastic, as indicated in Section 4.2.2.

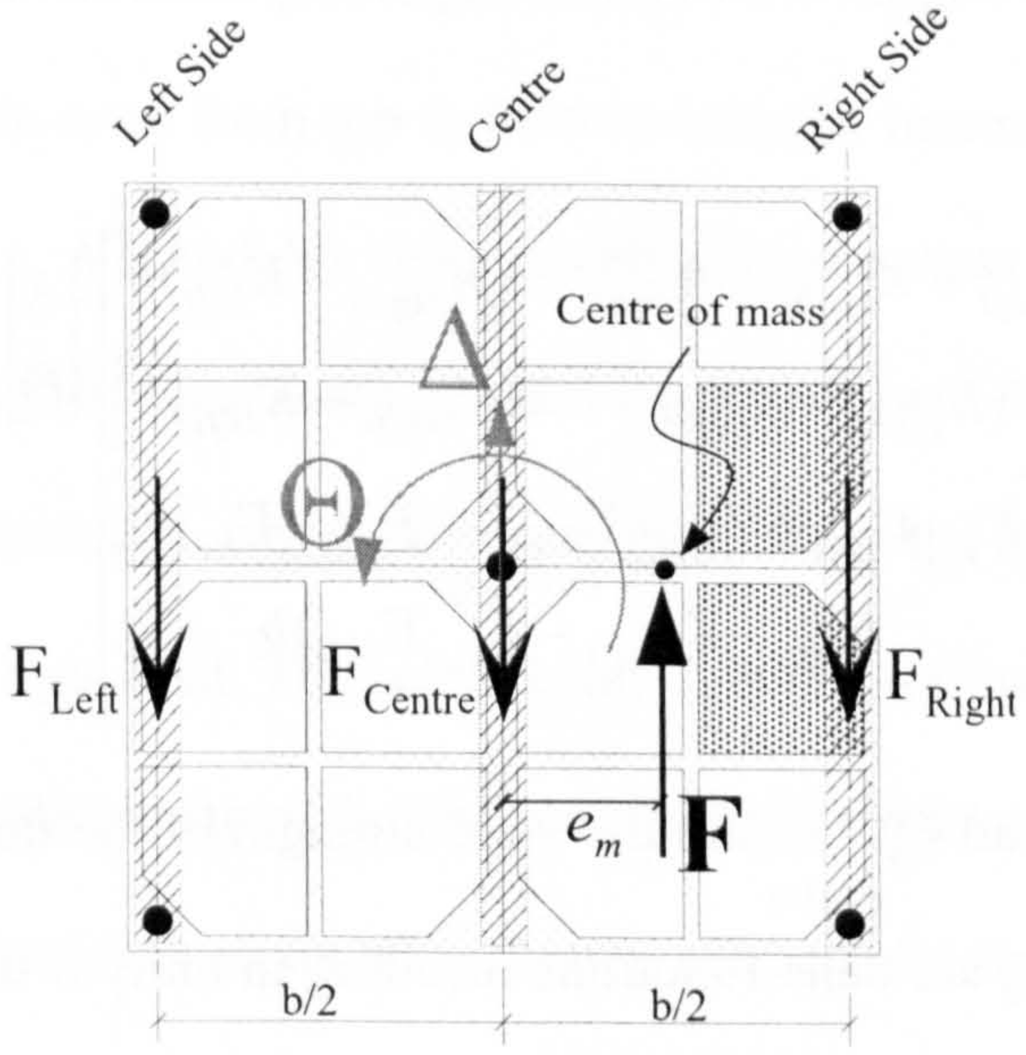

Figure 4.11: Representation of the single-storey analytical model under uniaxial loading.

The translational and rotational displacements (Δ and Θ, respectively) are the floor displacements at the centre of geometry. Summing the forces along the longitudinal axis results in the following equation:

$$\begin{aligned} F &= F_{left} + F_{right} + F_{centre} \\ &= K_{left}(\Delta - b\Theta) + K_{right}(\Delta + b\Theta) + K_{centre}\Delta \end{aligned} \tag{4.8}$$

where F_{left}, F_{right}, and F_{centre} are the internal forces in the left, right, and centre bents, respectively. K_{left}, K_{right}, and K_{centre} are the corresponding bent stiffnesses. Similarly, summing the moments about the centre of geometry results in:

$$\begin{aligned} M = Fe_m &= (F_{right} - F_{left})b \\ &= \{K_{right}(\Delta + b\Theta) - K_{left}(\Delta - b\Theta)\}b \end{aligned} \tag{4.9}$$

where e_m is the mass eccentricity, and b is the distance between the centre of geometry and the external bents. The values of e_m were taken as those of the column yield configuration models. Specifically, e_m is equal to 0mm, 38mm, and 113mm for mass configurations S1, A2, and A6, respectively. Combining these two equations into matrix form, and taking into account the elastic–perfectly plastic force-displacement relationship of left, right, and centre bents:

$$\begin{bmatrix} F \\ Fe_m \end{bmatrix} = \begin{bmatrix} K_{left} + K_{right} + K_{centre} & (K_{right} - K_{left})b \\ (K_{right} - K_{left})b & (K_{right} + K_{left})b^2 \end{bmatrix} \begin{bmatrix} \Delta \\ \Theta \end{bmatrix} + \begin{bmatrix} F_{y_{left}}\Gamma_{left} + F_{y_{right}}\Gamma_{right} + F_{y_{centre}}\Gamma_{centre} \\ (F_{y_{right}}\Gamma_{right} - F_{y_{left}}\Gamma_{left})b \end{bmatrix} \tag{4.10}$$

where $F_{y_{right}}$, $F_{y_{left}}$, and $F_{y_{centre}}$ are the yield strength of the three bents. The variables Γ_{left}, Γ_{right}, and Γ_{centre} are delta functions resulting in unity if the bent is yielding; zero otherwise. Solving the above equation in terms of Δ and Θ results in:

$$\begin{bmatrix}\Delta\\ \Theta\end{bmatrix} = \begin{bmatrix}\frac{K_{left}+K_{right}}{\Psi} & \frac{K_{left}-K_{right}}{\Psi b}\\ \frac{K_{left}-K_{right}}{\Psi b} & \frac{K_{left}+K_{right}+K_{centre}}{\Psi b^2}\end{bmatrix}\begin{bmatrix}F-F_{y_{left}}\Gamma_{left}-F_{y_{right}}\Gamma_{right}-F_{y_{centre}}\Gamma_{centre}\\ Fe_m-F_{y_{right}}\Gamma_{right}b+F_{y_{left}}\Gamma_{left}b\end{bmatrix} \quad (4.11)$$

where for ease of readability, $\Psi = 4K_{left}K_{right} + K_{left}K_{centre} + K_{right}K_{centre}$

When any two of the three column bents become inelastic, Ψ is zero, and equation (4.11) becomes singular. In order to calculate the internal bent forces up until the onset of failure, the new floor displacement, Δ, is calculated by assuming no additional floor rotation when two of the three bents have yielded. Without this condition, failure would occur after the first exterior bent yields, since the transverse stiffness of the individual columns are neglected, and the centre bent yields before either of the exterior bents. However, this stipulation only leads to errors in the rotational displacement after the onset of yielding in the first exterior bent.

The results from the above equations are depicted in Figure 4.12. The column of plots from left to right indicate increasing strength eccentricity (hinge configurations B, C, and D, respectively), and the rows from top to bottom indicate increasing mass eccentricity (mass configurations S1, A2, and A6, respectively). As the mass eccentricity increases, the proportion of the applied shear force resisted by the left bent decreases. This is due to the additional torsional moment, which decreases the shear in the left bent at the cost of an increase in shear in the right bent. The centre bent, C, is always the first to yield due to its high stiffness and low relative strength. The plots in Figure 4.12 can be divided into four sections along the *Applied Force* axis, as indicated by the solid fine vertical lines in each plot. In the first section, all of the column bents are elastic. The second section has a single

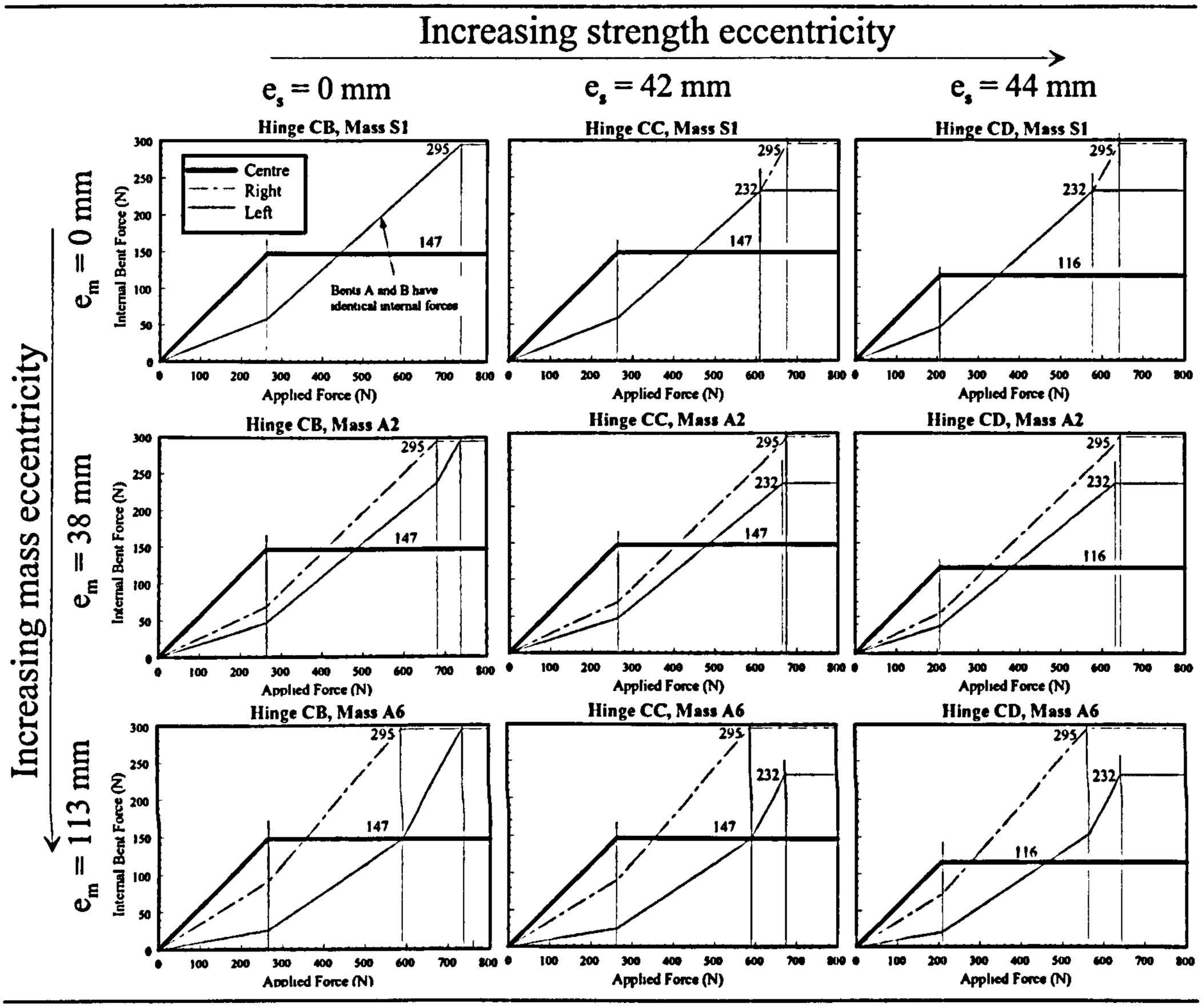

Figure 4.12: Internal bent force as a function of the applied static horizontal storey shear. The results are based upon a single–storey model.

bent yielding (the centre bent), while the two exterior bents remain elastic. In the third section, one of the two exterior bents become inelastic, and in the fourth section all bents are yielding, resulting in a failure of the analytical model. The slope of the internal bent force lines in each section indicate the contribution, in terms of percentage, of that bent in resisting any additional applied horizontal shear force to the model. Hence, the sum of the slopes of all three lines in the first three sections of each plot is equal to unity. In the fourth section, the sum of the slopes does not equal unity, hence the model floor is accelerating and has thus failed. Table 4.6 quantifies the slopes of the first two sections of the plots in Figure 4.12. Since the various hinge configurations affect only the column strength (not

Table 4.6: Bent contribution towards resisting any additional applied horizontal shear force.

Mass Configuration	Elastic			One column bent yielding		
	Left Bent	Centre Bent	Right Bent	Left Bent	Centre Bent	Right Bent
S1	22.1%	55.8%	22.1%	50.0%	*yielding*	50.0%
A2	18.0%	55.8%	26.2%	45.8%	*yielding*	54.2%
A6	9.6%	55.8%	34.6%	37.5%	*yielding*	62.5%

stiffness), the slope values are only a function of the mass eccentricity. The third (two columns yielding) and fourth (failure) sections are not tabulated since the results are trivial. As indicated in the table, the centre bent develops over half of the resisting force while the model remains elastic, regardless of the mass configuration. The slope of the lines for the centre bent are identical, regardless of the mass or strength eccentricity. This is a result of the location of the centre column coinciding with the elastic centre of stiffness of the model floor (i.e. stiffness eccentricity is zero). Since this bent is the first to yield, it is not affected by the strength eccentricity. However, its yield strength is reduced as part of the set–up requirements for hinge configuration CD.

As the mass eccentricity increases, the proportion of applied force resisted by the right bent is higher then that for the left bent. This is due to the addition of a torsional moment resulting from the mass eccentricity, e_m, which is beneficial to the left bent. As a result of the symmetric arrangement of the columns, the magnitude of the force increase applied to the right bent in the symmetric mass case (S1) is identical to the magnitude of force decrease in the left bent. For the low mass eccentricity case, A2, this is about 18% (i.e. the force in the left bent decreases by 18%, while that in the right bent increases by 18%). This value increases to over 56% for the high mass eccentricity, A6, case. The increase

from 18% to 56%, is due to the mass eccentricity increase (from 38mm in case A2 to 113mm in case A6).

The influence of the strength eccentricity is revealed primarily in shifting the lines separating the yielding regions. In Figure 4.12, comparing the first column (hinge configuration CB) to the second (hinge configuration CC), the yield strength of the left bent is reduced. For the symmetric (S1) and low mass eccentricity (A2) cases, this has the effect of allowing the left bent to yield before the right bent. In the high mass eccentricity (A6) case, the right bent is still the first of the exterior bents to yield, due to the reduction of forces in the left bent from the higher torsional moment. The difference between hinge configuration CC and hinge configuration CD (plot columns 2 and 3) is due to the reduction in the strength of the centre bent. This simply has the effect of shifting the three delineating lines of the four sections to the right. The amount by which these lines are shifted are identical, and equal to the reduction of yield strength in the centre bent.

Figure 4.13 shows the relationship between displacement and applied loading for the nine structural configurations indicated in Figure 4.12. Each plot contains the results of all three mass eccentricities, for a particular hinge configuration. The left vertical axis in Figure 4.13 corresponds to the solid lines, and denotes longitudinal translation (Y). The right axis, in conjunction with the dotted lines, indicates rotation about the vertical axis at the centre of geometry (Θ). No rotation for the symmetric mass (S1) case is apparent due to the stipulation that no additional floor rotation occurs when two bents have yielded. The failure demarkation line indicates the applied force at which the third bent yields, and the structure consequently "fails".

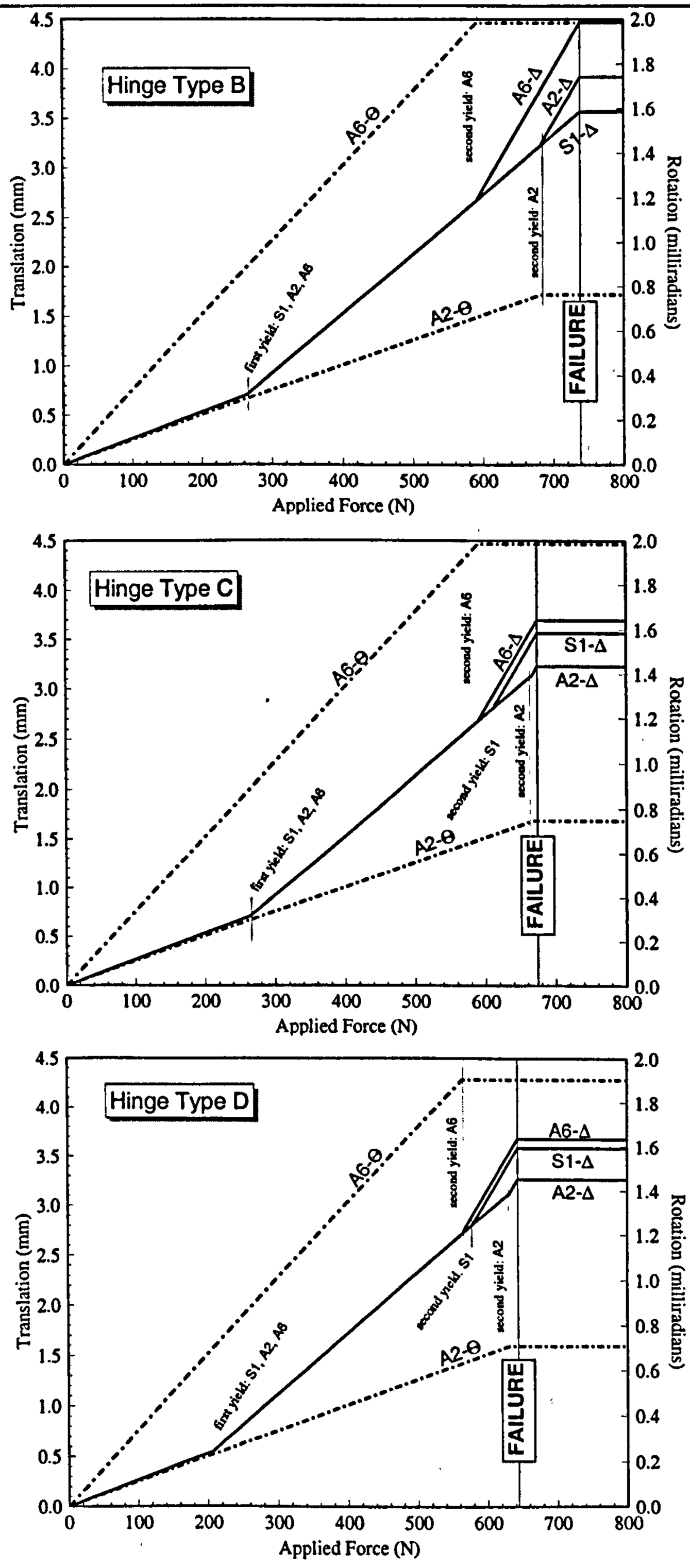

Figure 4.13: Displacement (translation and rotation) as a function of the applied horizontal shear force.

As can be seen in Figure 4.13, the translational displacements are identical for a particular hinge configuration up until the first exterior bent yields. The slope of the displacement versus loading lines are identical in each of the four regions (delineated by a change in slope and vertical tick marks) for a particular hinge configuration, since column stiffnesses are constant. The centre bent yielding has no influence on the rate of rotational displacement, since its location is coincident with the centre of stiffness. The centre of stiffness moves from the centre of geometry only when the first exterior bent yields. Once the first exterior bent yields, the change in rotational displacement becomes zero, as stipulated for solution stability. For hinge configurations CC and CD, it can be seen that mass configuration A2 benefits the most, in terms of reduced translational displacements. This is a result of the strength eccentricity for these two hinge configurations being nearly equivalent to the mass eccentricity of mass configuration A2. Table 4.7 quantifies the net

Table 4.7: Net mass eccentricity ($e_m - e_s$) when all column bents have yielded.

Hinge Configuration	Net Mass Eccentricity upon Failure		
	Mass S1	Mass A2	Mass A6
CB	0mm	38mm	113mm
CC	–42	–4	71
CD	–44	–6	69

mass eccentricity, which is the difference between the mass and strength eccentricity, between the various mass and hinge configurations. The larger the net mass eccentricity, the lower the applied force at which the first exterior bent yields. Also, a smaller net mass eccentricity reduces the difference in load between the yielding of the two exterior bents. Clearly, mass configuration A2 is nearly symmetric for hinge configurations CC and CD,

whereas configurations S1 and A6 are asymmetric in the negative and positive directions, respectively. This accounts for the reduced translational displacement at failure for case A2.

CHAPTER 5

EXPERIMENTAL SHAKING TABLE STUDIES

This chapter identifies observed trends in the displacement response measurements from the experimental shaking table tests. A description of the forcing motions used in this study, as well as the methods of acquiring the floor displacements of the model floors, are also presented. Results are summarized for all of the experimental tests, in terms of peak response. This lends itself to a discussion of displacement trends as a function of hinge configuration, degree of mass asymmetry, and forcing intensity. The time-history and

response frequencies[1] from key experiments are also presented in detail. These involve configurations and forcing intensities which result in representative displacement behaviour. The emphasis of this chapter is on the floor displacement responses measured directly from the shake table tests. Results of displacement ductility and energy absorption, as a result of the hinge units, are presented in the following chapter, *Hinge Unit Performance.*

5.1 TESTING PROCEDURE

The experimental model was tested on the EPSRC (formally SERC) 6–axis shake table facility located at Bristol University's Earthquake Engineering Research Laboratory (BEELAB). The model configurations were systematically tested by a single acceleration time-history record. The intensity of this acceleration time-history was increased between successive tests of each model configuration, resulting in model behaviour ranging from elastic to highly inelastic, with permanent plastic deformations up to 1.4% of the model height. The direction of forcing is uniaxial, and along the axis perpendicular to the direction of mass eccentricity (see Figure 5.1). The response of the model to the forcing is measured by displacement transducers mounted on rigid instrumentation frames on two sides adjacent to the building model.

Figure 5.1 illustrates the general testing layout of the model on the shake table. The geometric and initial stiffness centres for all four floors of the model coincide with the centre

1. *Response frequencies*, as opposed to natural frequencies, refer to the frequency domain displacement responses of the building models to the applied table forcing motions.

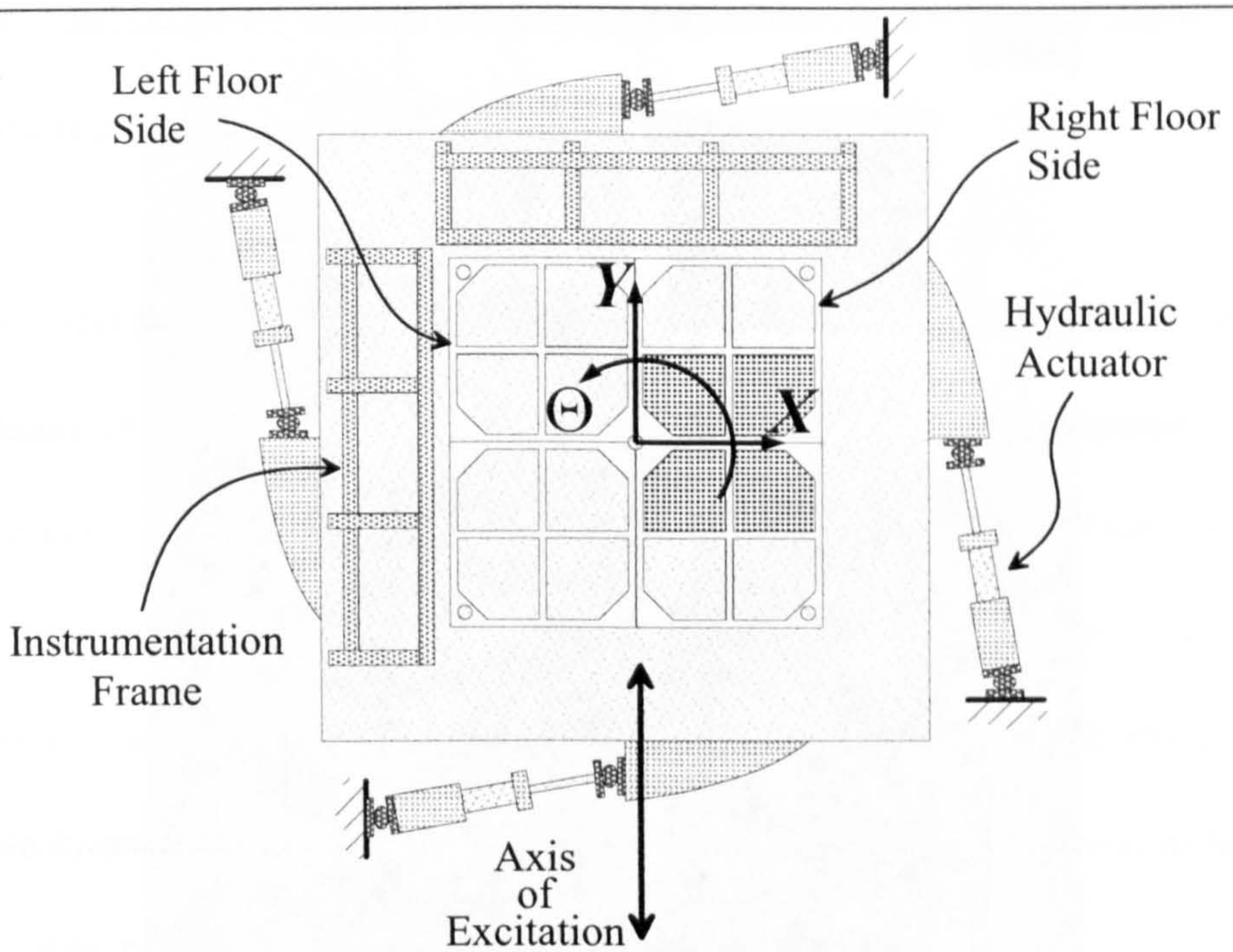

Figure 5.1: Planar view of the EPSRC shake table with the mounted instrumentation frames and model floors.

of the shake table. The shake table has a total of eight hydraulic actuators. One actuator is located on each side of the table. These four actuators control the rotation about the vertical axis and the two axes of horizontal motion. The remaining four actuators are positioned at each corner on the underside of the table, and provide vertical, roll and pitch motions. Although this results in 6 possible table degrees of freedom, only the longitudinal translation direction (Y–axis) was utilized, as indicated in Figure 5.1. The payload capacity of the shake table is well above that of the model and its associated measurement frames, hence no special levelling or reverse loading of the shake table was required prior to testing.

5.1.1 Response Measurements

Each floor in the model is capable of three significant displacement directions. These are considered as the transverse (X), longitudinal (Y), and rotational (Θ) degrees of freedom.

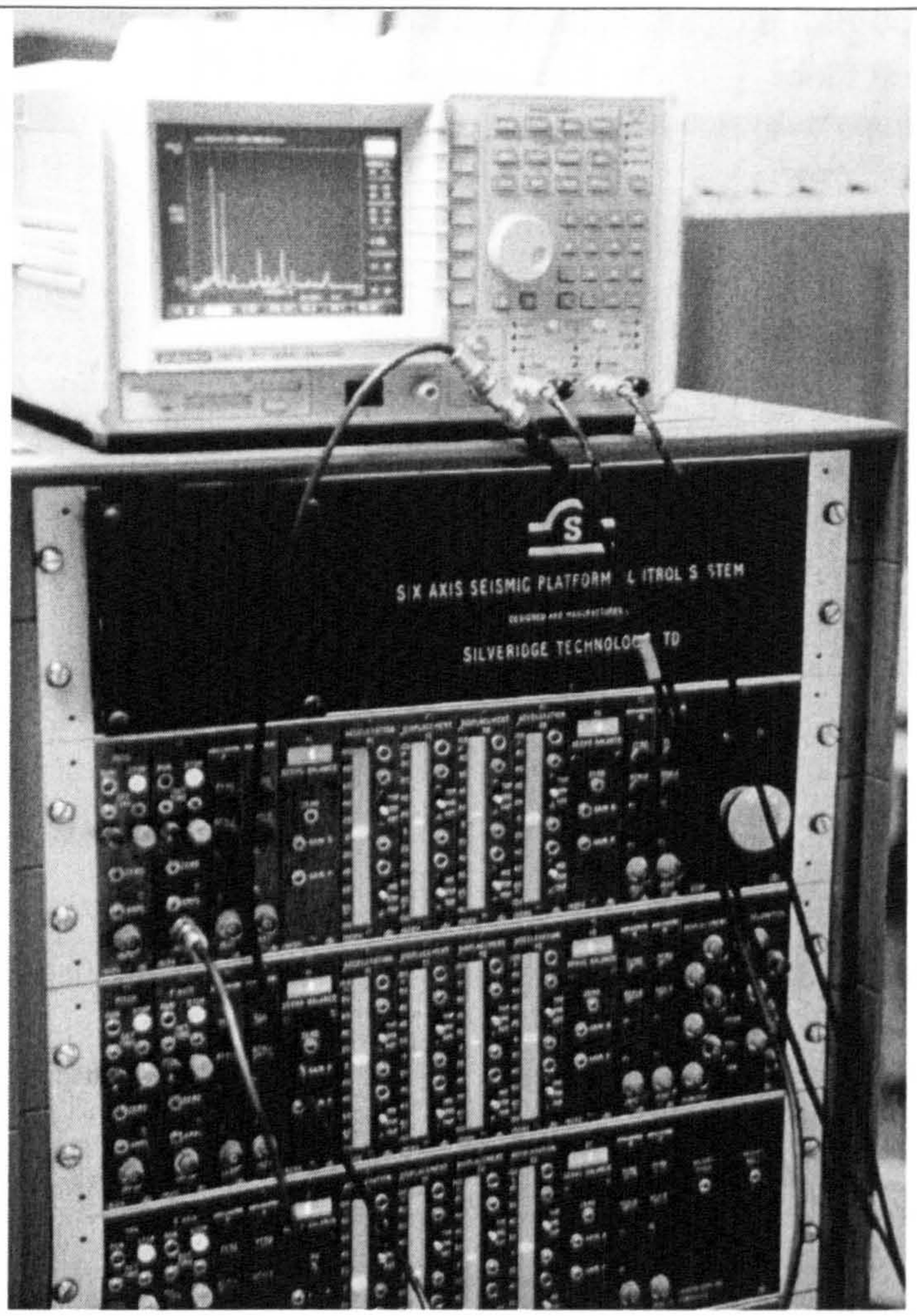

Figure 5.2: Shake table actuator control panel and FFT spectral analyser.

These directions have been defined in Chapter 3, and are also shown in Figure 5.1. The origin of the co-ordinates are taken from the centre of geometry of each floor. The geometric centre does not change in time (as is the case with the centre of stiffness when hinges yield), or between tests (as with the centre of mass for the three different mass configurations). The model is mounted on the shake table such that the mass eccentricity is along the X–axis (perpendicular to the forcing axis). From this, the primary responses of the model are along the longitudinal (Y) and rotational (Θ) degrees of freedom. Since the transverse degree of freedom is not coupled with rotation, theory dictates that these trans-

verse displacements are negligible. This is also observed, as transverse displacements are negligible during most tests.

The experimental time–history response of the floors are measured by displacement transducers mounted on the instrumentation frames (see Figure 5.1). The response output from these transducers is a voltage time-history which is correlated to a displacement response. The calibrations were performed by statically displacing the structure in increments of known displacement, and recording the corresponding output voltage from each transducer. These known displacement values were then fitted with a function in terms of the acquired voltage readings.

A large number of experimental tests had to be performed to encompass the range of parameters studied. This necessitated minimal setup time between shake tests, whilst maintaining reasonable accuracy of the recorded displacements. One of the easiest ways to accomplish this is through enforcing a linear relationship between the transducer voltage and model displacements. The contacting displacement transducers display a linear voltage–displacement relationship throughout their entire range. However, the proximity probes can become highly non-linear towards the limit of their displacement range. This is discussed in more detail in Section 5.1.1.1 below.

5.1.1.1 Non–contacting Proximity Probes

Proximity probes were used to instrument the first, second, and fourth floors in the beam yielding model configurations (see Figure 5.3). They were also used on the bottom two floors in the column yield models. These probes measure displacement by the change in

magnetic flux measured off a metallic surface. The advantage of this measurement method is that these probes do not come in contact with the experimental model, and thus do not influence its dynamic response. Unfortunately, these probes are restricted to a relatively small displacement range, limiting their use on the upper storeys where greater total floor displacements occur.

Two different models of proximity probes were used—a low range probe accurate within ±7mm and a larger probe with a displacement range of ±15mm. The smaller probes are used to measure the first floor displacements in the beam yielding models. The second and fourth floors of these building models have displacements recorded by the larger proximity probes. The third floor displacements in the beam yield models could not be recorded due to insufficient instrumentation. Unfortunately, the larger displacements associated with the fourth floor pushed the limit of the large displacement probes, resulting in some signal clipping (see Section 5.1.3).

The larger displacements associated with column yielding models were felt to be beyond the range of the smaller probes. As a result, the larger displacement capacity proximity probes were used to measure the floor displacements on only the first two floors of the column yielding models.

5.1.1.2 Contacting Stroke Transducers

The stroke displacement transducers were used on the third and fourth floors of the column yield model configuration. These devices measure the response displacement through variable electrical capacitance caused by the stroke shaft displacements. The transducers

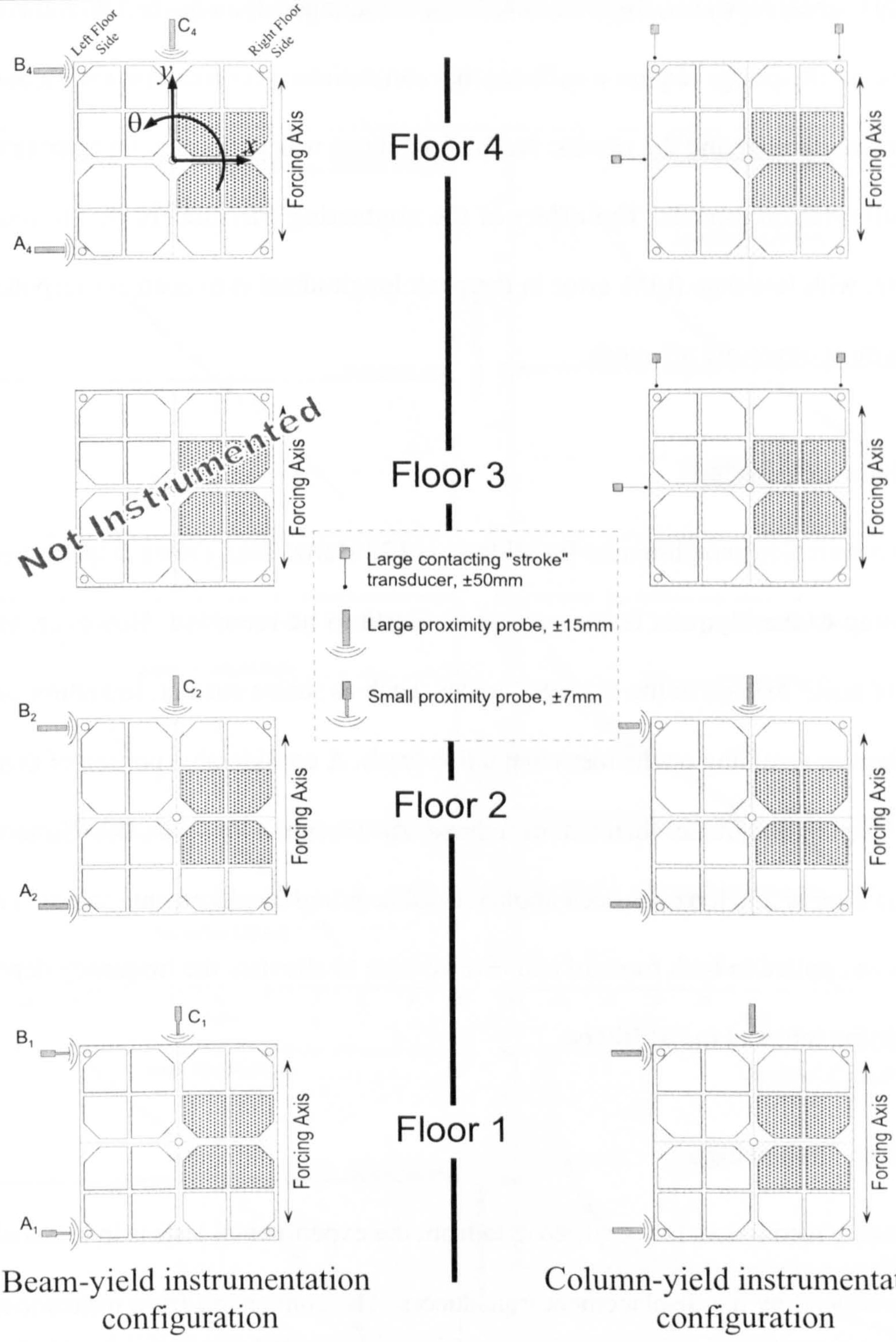

Figure 5.3: Displacement recording instrumentations for the two 4-storey model configurations studied.

have a total range of 100mm, thus easily accommodating the large displacements associated with the top two floors. The calibrated displacement–voltage curves for these transducers are essentially linear, thus alleviating much of the error associated with the

proximity probes. However, these transducers are continuously in contact with the model. The stroke shaft springs require a stiffness that can maintain contact with the model without significantly affecting the results. An analytical test was performed on a series of column configuration models. The effect of the contacting transducers was found to be negligible, with less than 0.1 % error in the peak longitudinal displacement response (the direction most adversely affected).

5.1.2 Data Acquisition

The data acquisition sampling rate for all tests is 128 Hertz. This allows displacement frequencies up to the Nyquist frequency of 64 Hertz to be recorded. However, various sources of noise existed in the recorded traces, such as mains current, induction current, and inadequate shielding on the instrumentation leads. A considerable portion of this noise is in the frequencies greater than that of interest. As a result, a low-pass IIR (Butterworth, 3rd order) filter at 25 Hertz has been applied to all acquired displacement records. This filter has been applied in both forward and reverse time to alleviate the frequency dependent phase shifting inherent in IIR filters.

5.1.3 Data Processing

As previously mentioned, the acquired data from the experimental tests is in terms of voltage, as produced by the displacement transducers. The conversion from instrument voltage to floor displacement is based on experimental calibration curves of each displacement transducer (Figures 5.4 and 5.5). For each instrument configuration (see Figure 5.3), known static displacements on the floors at the transducer locations were imposed, and the corresponding transducer voltage tabulated. These calibration curves, for

all transducers, are shown in Figures 5.4 and 5.5, for the proximity probes and contacting transducers, respectively.

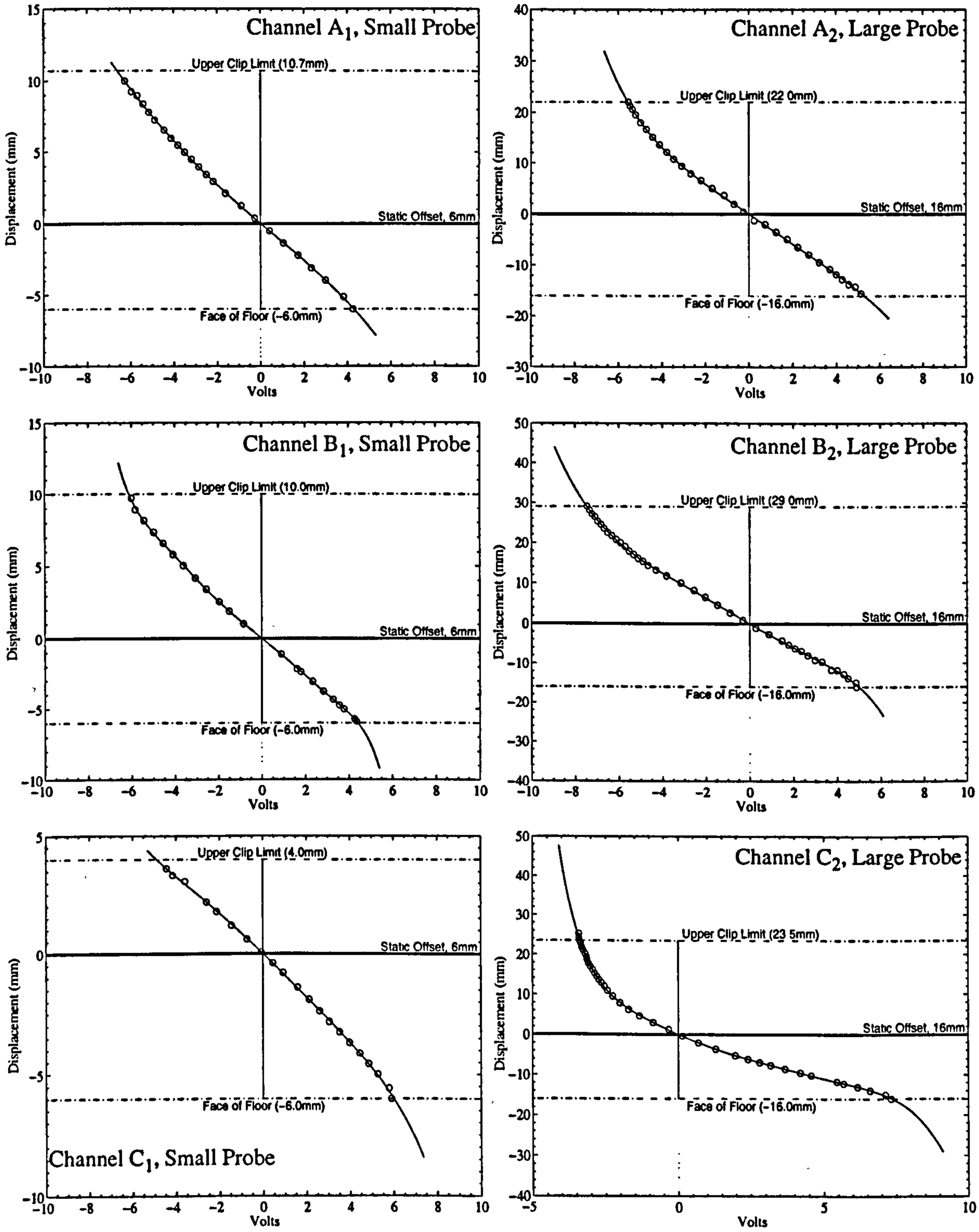

Figure 5.4: Proximity probe voltage–displacement instrumentation calibration curves for the first two floors of the beam yield configuration.

The proximity probe calibration curves do not exhibit a linear voltage–displacement relationship over their full range of usage. As can be seen in Figure 5.4, the calibration curves for the probes are fairly linear between their *static offset* and *face of floor* lines. The static offset is defined as the initial distance between the face of the probe, and its corresponding metallic measuring plate on the side of the floor. The face of floor is the displacement at which the probe comes into contact with the side of floor. The static offset was selected for each transducer type, such that its location is near the centre of the expected experimental displacement range. The calibration curves for the proximity probes become non-linear between the static offset and the *upper clip limit.* The upper clip limit is the limit at which the calibrated displacements (acquired voltage) is beyond the range of, or too sensitive to, the transducer voltage. Displacements were calculated in these clipped regions by a least squares fit of a fourth order polynomial through the valid displacements on both sides of the clipped region. The number of fitted displacement points on either side of the clipped region is equal to the number of displacement points clipped[1]. The order of the polynomial, and the number of valid displacement points to be used for the least squares fit were determined through trial and error.

A typical calibration curve for a contacting transducer is shown in Figure 5.5. The voltage–displacement relationship for these transducers are linear, throughout their required range. These transducers performed quite well, and did not require any clipping adjustments to the recorded signal.

1. If only a single data displacement point is clipped, a second order polynomial was used, fitting two points on either side of the clipped point.

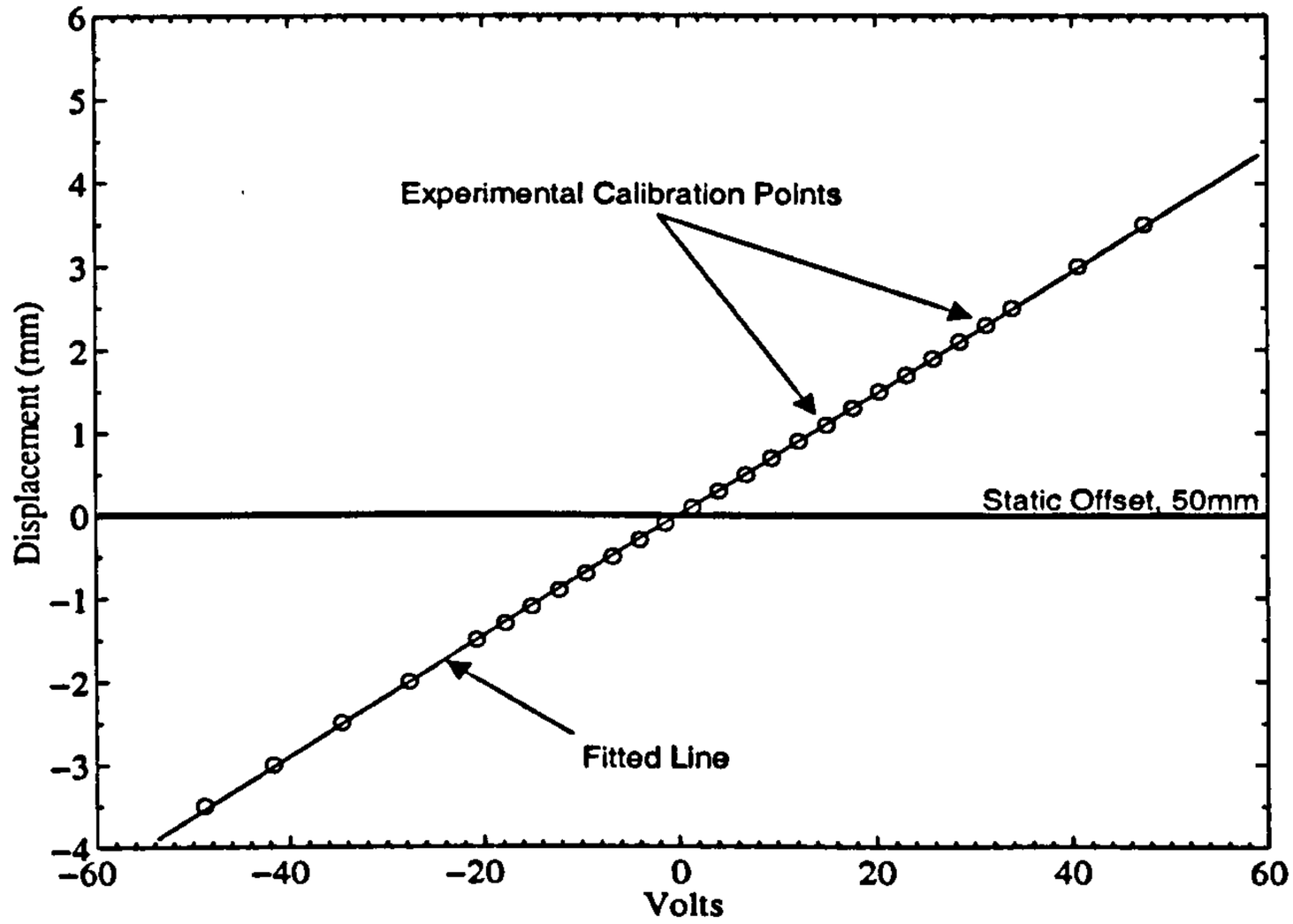

Figure 5.5: Typical contacting transducer calibration curve.

5.2 SHAKE TABLE FORCING TIME-HISTORIES

Throughout this study, only a single forcing time history has been used in reporting the results from the multi-storey testing. Experimental shake table studies normally rely on more than a single forcing time-history to gain a better statistical knowledge of the dynamic response. Even time-histories with similar response spectra can result in varying non-linear displacements, as a result of the different phasing of the frequencies contained in the acceleration record. However, increasing the number of table forcing time-histories would reduce the parameter ranges (forcing intensity, mass eccentricity, and hinge configuration) of the models studied, as access time to the shake table facilities was limited.

As described in Chapter 2, the number of parameters involved in a non-linear study is increased significantly over its elastic model counterpart. As a result, non-linear analysis based on distinct multiple time-histories can become quite expensive. Concentrating on a

single time history allowed emphasis to be placed on the non-linear parameters of the model. This is the current philosophy in the United States with the California Department of Transportation (CALTRANS), where the non-linear seismic retrofit analysis of the largest, most important bridges in the State are based on a single seismic event.

The single time-history used in this study has been artificially generated, and is based on an acceleration response spectrum as defined by the design response spectrum of the 1994 Uniform Building Code for stiff to firm soil.

The shape of the chosen response spectrum is defined as:

$$\frac{S_a}{A_g} = \frac{1.25}{\sqrt[3]{T^2}} \leq 2.75 \tag{5.1}$$

where $\frac{S_a}{A_g}$ is the normalized spectral shape, and T is the response period (in seconds). This shape is then scaled by a forcing intensity (peak ground acceleration, A_g) throughout the study to achieve a specific spectral acceleration, S_a.

5.2.1 Generation of Spectrum Compatible Accelerations

The acceleration response spectra can be converted into pseudo-velocity response spectra (S'_v), by dividing the spectral acceleration (S_a) by the frequency (ω):

$$S'_v = \frac{S_a}{\omega} \tag{5.2}$$

This is required, since the shake table actuators require forcing velocity values as an input signal rather than acceleration. The actuators inherently differentiate the input signal, thus creating the desired acceleration record for the shake table response.

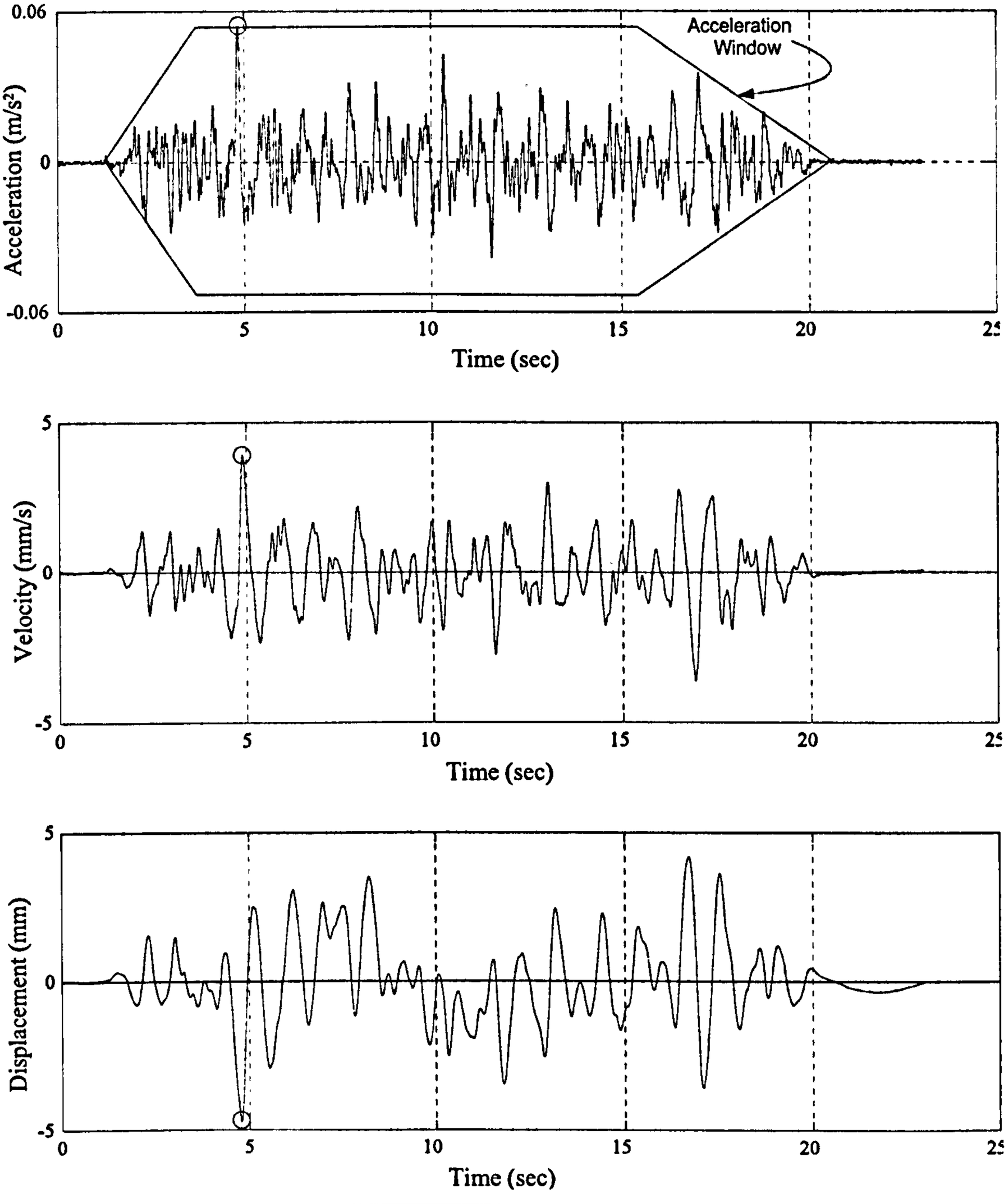

Figure 5.6: Recorded accelerations from the shake table. All three figures are the corrected values (case C3BDG1)

With the spectral pseudo-velocity determined, a velocity time–history can be convoluted from the spectral shape. This is based on a random phase seed, and a windowed acceleration to account for the non–stationarity inherent in real earthquake time–histories. The window is a three second ramp from zero to unity at the beginning of the time history. The end of the earthquake is windowed with a linear transition going from unity to zero in the

final five seconds of the record. This procedure is performed by *EQSIM*, a Bristol University based computer program that is based on CalTech's *SimQuake* computer program [VANMARKE, 1976]. Figure 5.6 shows the resulting time-history (for a peak ground acceleration of 0.6%*g*). Superimposed on the acceleration trace is the windowing envelope used during the fitting process.

In generating the code compatible time-history, the computer program (*EQSIM*) had difficulty matching both the target spectral level and the peak acceleration (A_g) at which that spectrum is defined. As a result, the generated acceleration time-history contains a 'spike' (shown just before 5 seconds in Figure 5.6) to meet the required peak ground acceleration.

Another problem encountered during the matching procedure is that the shake table acts as a filter, and cannot duplicate the response of the input signal accurately. This is due to frequency and energy flux limitations in the actuators, reaction mass characteristics, and other table characteristics. As a result, an iterative process is performed by the following steps to bring the table acceleration response spectra close to the specified UBC target spectra:

1. Generate an initial, spectrum compatible, velocity time-history from the computer program *EQSIM*.

2. Send the velocity time–history signal through the shake table, and record its acceleration time-history response.

3. Compare the target (code-compatible) velocity spectrum of the signal fed into the table to the pseudo-velocity spectrum (equation (5.2)) of the

acquired output acceleration.

4. If the two velocity spectra do not compare satisfactorily, velocities (energies) must be increased or decreased in the input signal at the mismatched frequencies, creating a new velocity spectrum.

5. Using the same phasing (random seed) of the frequencies in the initial time-history, modify the velocity time-history based on the new velocity spectrum.

6. Repeat steps 2 through 5, until an acceptable velocity spectrum is obtained.

Although the above steps are normally based on trial and error, there is a general rule in adjusting the input signal. Since the response spectrum of a single sine-wave affects the response of frequencies higher than the resonant frequency more than those below that frequency, adjustments in the input signal were made initially in the lower frequencies. As the iteration procedure continues, and the output acceleration response spectra begins to match the required design spectra in the lower frequencies, then adjustments in the higher frequencies can also be made.

5.3 RECORD CHARACTERISTICS

5.3.1 Ratio of peak acceleration to peak velocity

The A/V ratio of earthquake recordings can be classified as high (A/V > $1.2\frac{g}{m/s}$), low (A/V < $0.8\frac{g}{m/s}$), or intermediate when the ratio is between these two bounds [Associate Committee on the National Building Code, 1990]. This ratio is generally related to the epi-

central distance of an earthquake to the recording site, since acceleration tends to attenuate faster than velocity. Local site conditions also play a factor in this ratio.

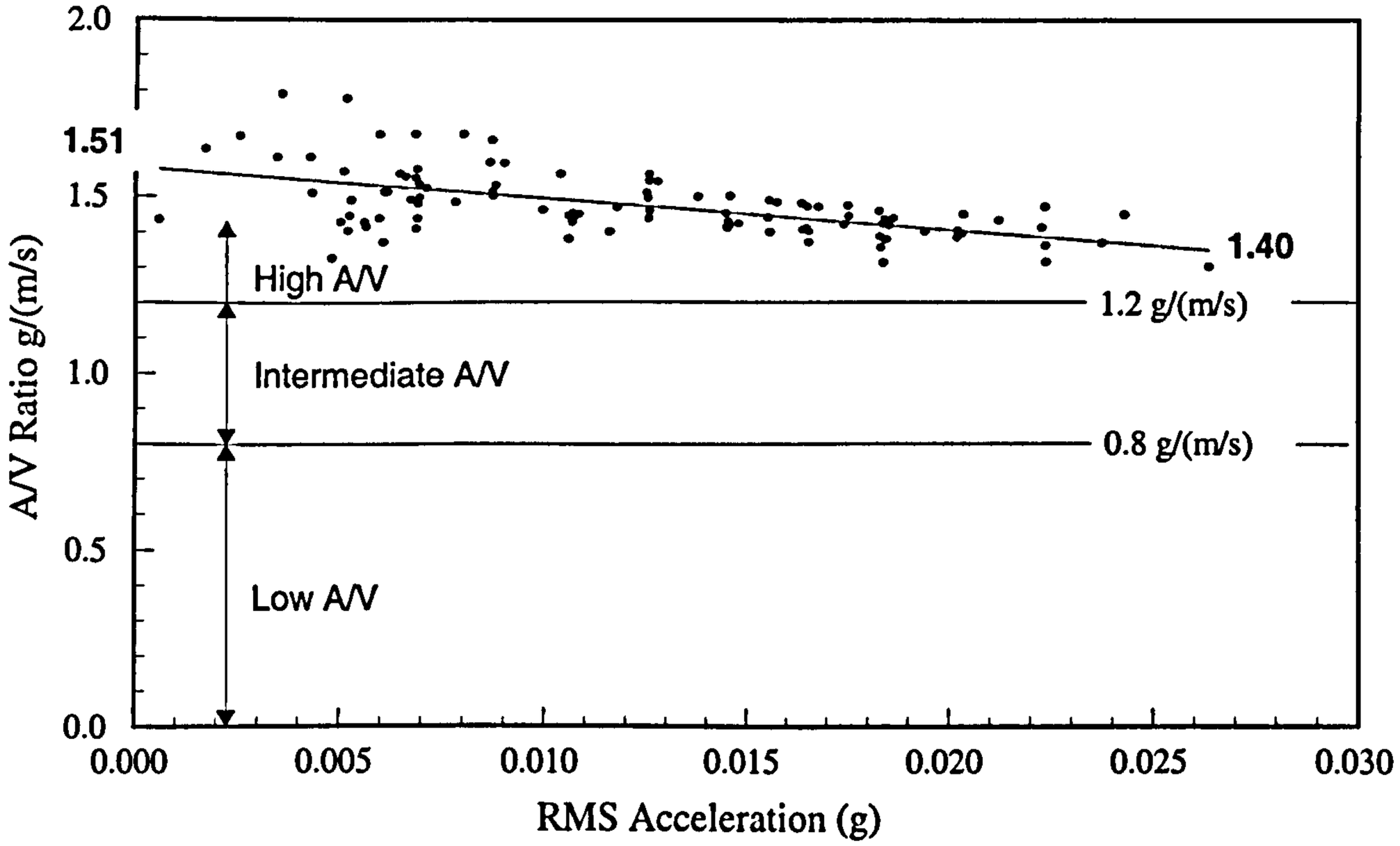

Figure 5.7: The ratio A/V vs. forcing intensity.

As can be see from Figure 5.7, the average value[1] of A/V for the generated input record decreases slightly with an increase in forcing intensity (RMS acceleration, defined below in Section 5.6.3). This trend can be attributed to the shake table actuators. The significant frequencies of an acceleration trace are always greater than that for the velocity trace, since the prior is the derivative of the later. At the higher forcing gains, the actuators handle the lower frequencies better than the higher ones. This in turn can reduce the peak acceleration, thus resulting in the negative slope of the best-fit or trend line in Figure 5.7. The overall average A/V ratio, for all RMSA values, is $1.47 \frac{g}{m/s}$. Although this is classified as high, it is well below the mean A/V ratio for actual earthquake recordings with A/V

1. The sample set consists of only those values between the $\mu \pm \sigma$ lines in Figure 5.11 (page 135).

ratios also classified as high [Chandler, 1990(b)]. Therefore, it represents a good model of a near-field earthquake on harder soil.

5.3.2 Base Acceleration Spectograms

Time dependent frequency spectra (spectograms) are an effective means of visualising the non-stationary response of a particular degree of freedom. In this method, the acquired time history is split into overlapping segments (each of 128 samples, or 1 second of data acquisition). Each overlapping segment is windowed using a Hanning window over the entire 128 point sample length. The windowing function removes adverse effects that result from a segmented time-history (i.e. Gibbs phenomena). The Fourier Transforms for each time segment are then assembled to create a contour plot of the Fourier amplitude at a particular frequency versus time. This is a common technique used in the field of speech analysis, and is particularly well suited for inelastic time series analysis. Spectograms are

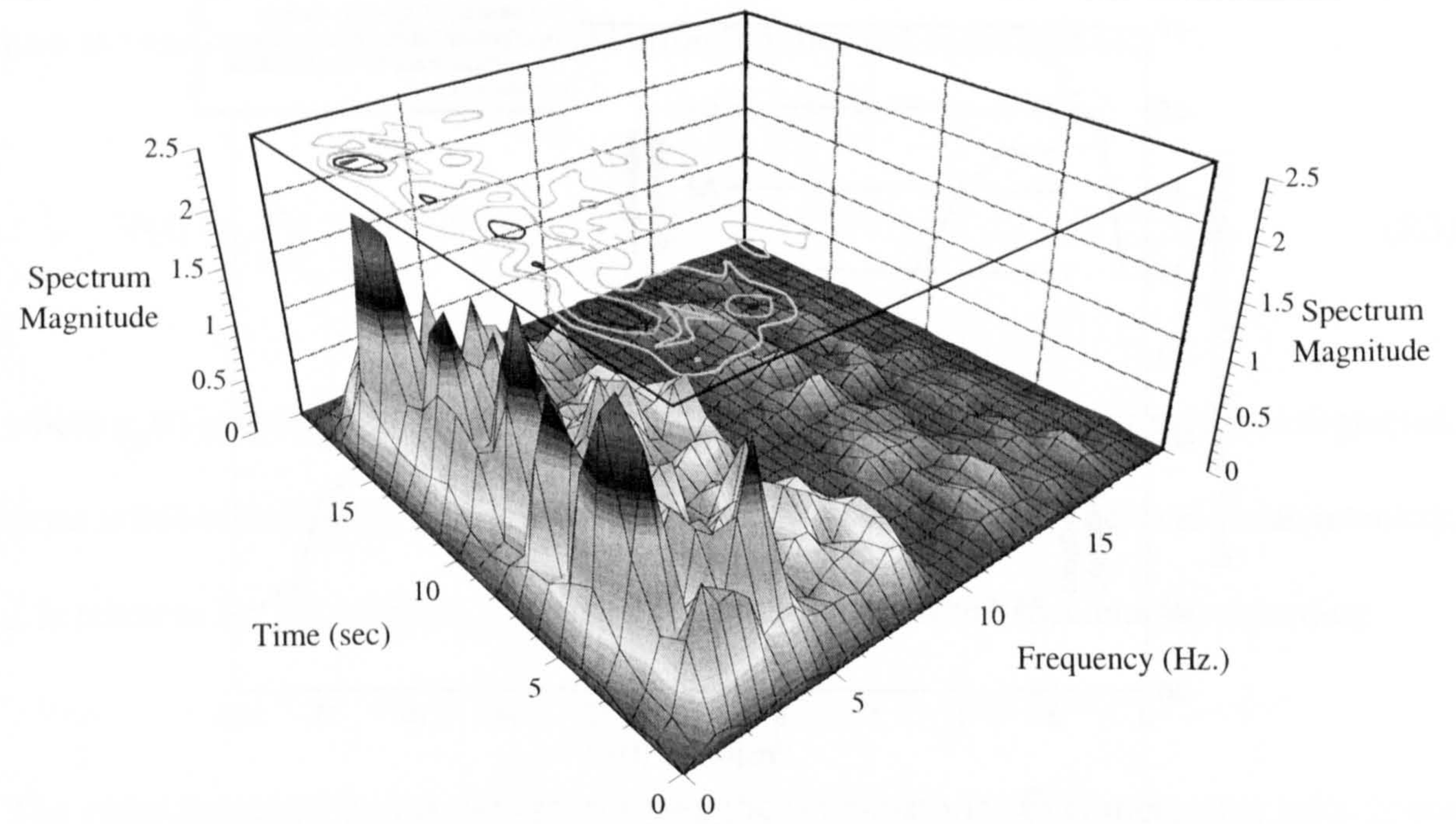

Figure 5.8: Acceleration spectogram for a typical input forcing.

a means of describing the non-stationary frequency content of a signal. Figure 5.8 shows the acceleration spectogram for a typical forcing signal used to drive the shaking table. In theory, the spectograms contours should be similar in placement, varying only in the magnitude of the contour lines for the different records of varying intensity. From this Figure, most of the forcing below 5 Hertz occurs between 5 and 11 seconds into the record, and a short impulse around 16 seconds into the data acquisition.

5.3.3 Power Spectral Densities

The power spectrum is an average quantity which indicates the energy content that is distributed over various frequencies. Since the signal is non-stationary, the method of segmented averaging is used to give a better estimate of the power spectra. Figure 5.9 shows the power spectral density estimate of a typical table acceleration record. This Figure rein-

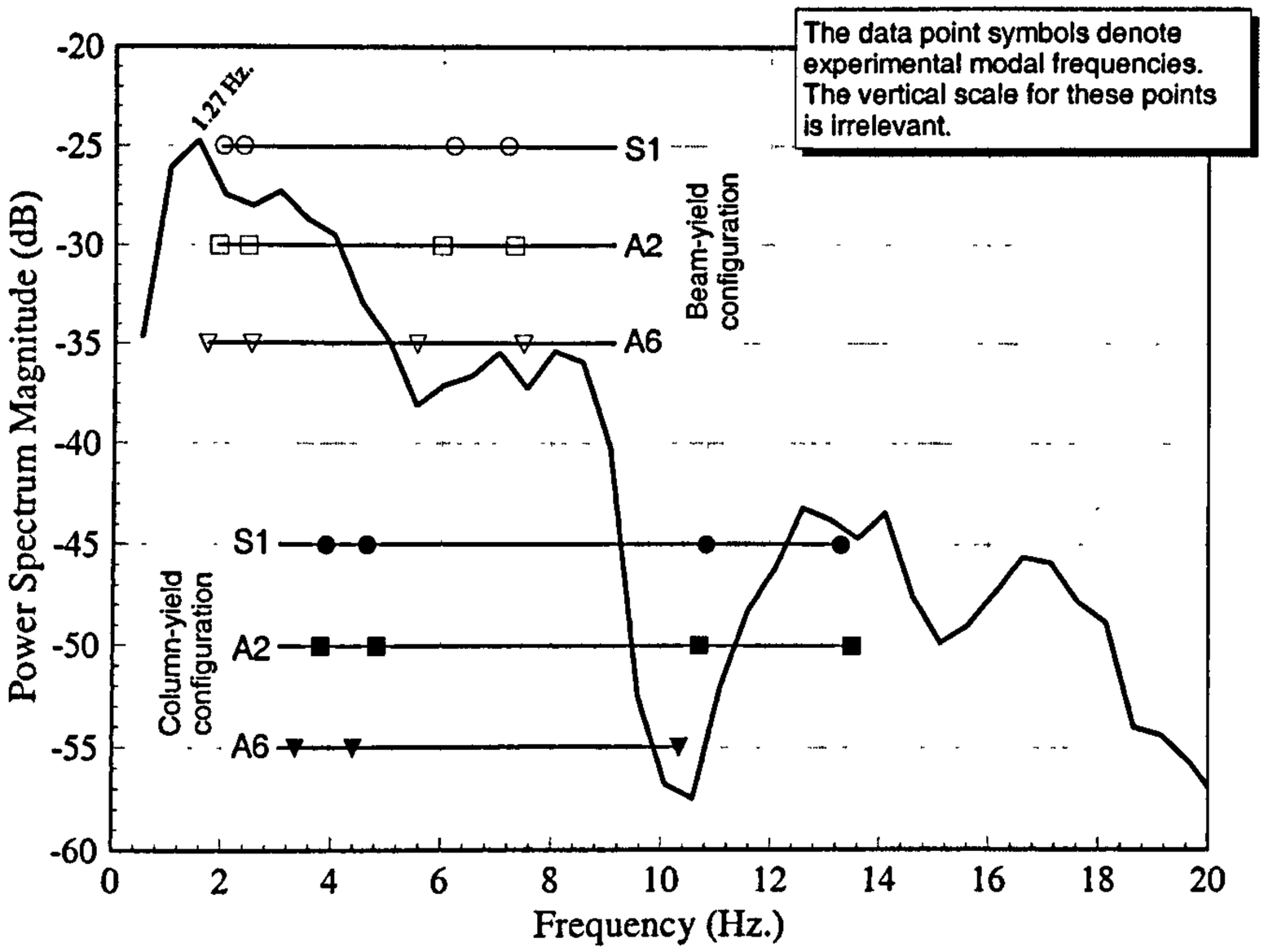

Figure 5.9: Power spectral density estimate of a typical acceleration trace, superimposed with the experimental model modal frequencies.

forces the spectogram shown in Figure 5.8, in that most of the input energy is below 5 Hertz. Also shown as symbols in this Figure are modal frequencies for both the beam and column yielding model configurations. These points have no vertical scale, and are defined only in terms of frequency. The beam yielding model configurations have lower modal frequencies than the column yielding models. As a result, each mode in the beam yielding models is excited more than its corresponding column yielding model, for the same forcing intensity.

5.4 SIGNIFICANT DURATION

The significant duration of the shake table accelerations are independent of the level of excitation applied. The signification duration is defined as the time period between 5% (I_5) and 95% (I_{95}) of the total Arias intensity. The Arias intensity, $I(t)$, is a description of how the earthquake energy is released through time, and is defined as:

$$I(t) = \frac{\pi}{2g}\int_0^t a_g(t)^2 dt \tag{5.3}$$

where $a_g(t)$ is the ground acceleration at time, t. The factor of $\frac{\pi}{2g}$ is sometimes neglected, since it has no influence in determining the significant duration. The total Arias intensity, I, is taken as $I(t_{end})$, where t_{end} denotes the ending time of the acceleration recording.

The Arias intensity is also used in aligning the time-histories in comparative tests. Since the triggering of the data acquisition system is left entirely to the operator's discretion, a

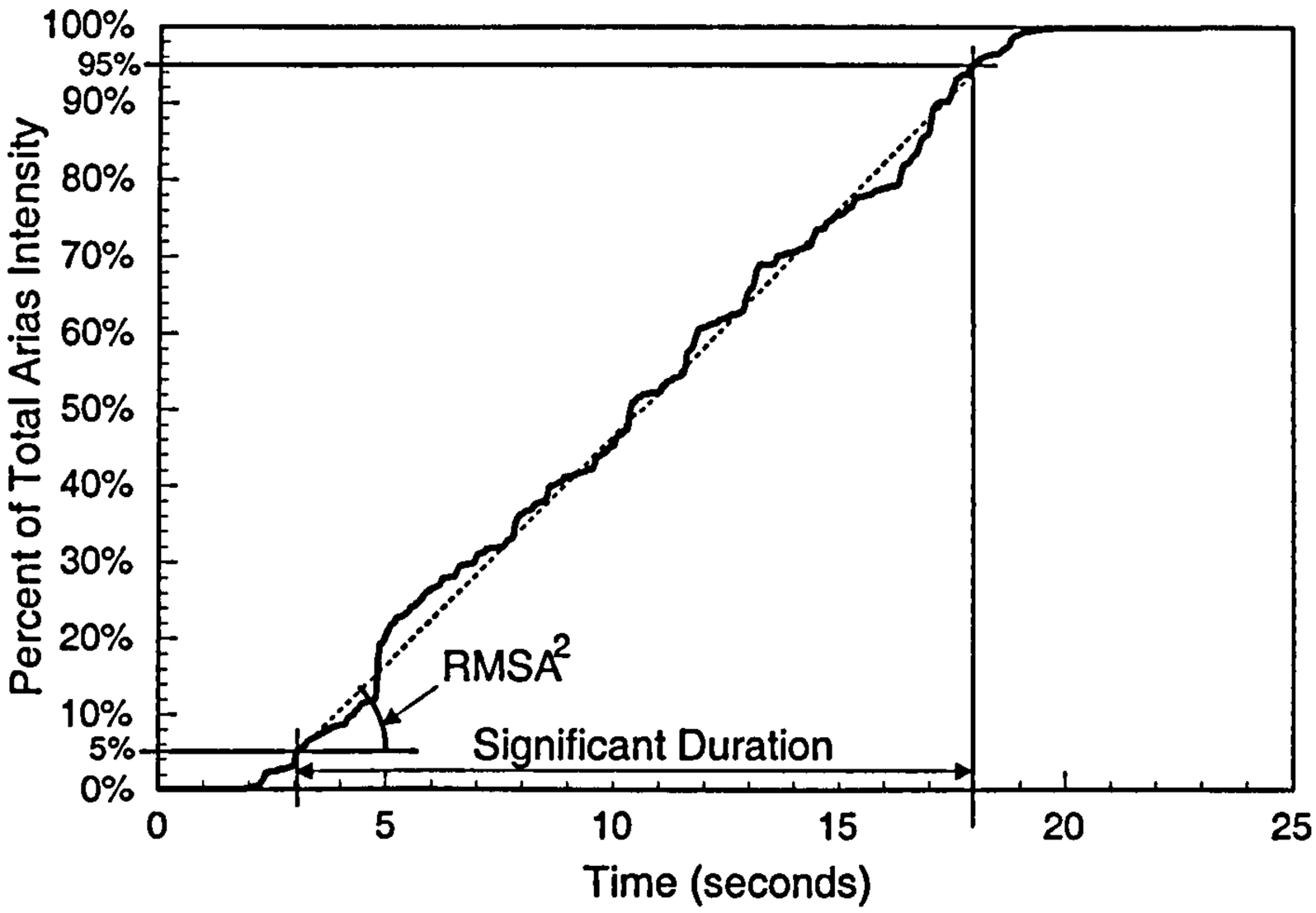

Figure 5.10: Relationship between Arias Intensity, Significant Duration, and Root Mean Squared Acceleration for a typical acceleration time-history.

relative reference time is not directly available. This was overcome by using t_5, which is the time at which I_5 is obtained, as the reference time.

Figure 5.11 shows the relative independence of the significant duration versus the level of excitation for the column yield test forcings. From this Figure, it is obvious that the lower levels of excitation are less consistent. In general, a uniform or "white" noise introduced into the acceleration recording will lengthen the significant duration. The lower signal to noise ratio in the acquired table acceleration at the low forcing intensities shows this effect, thus increasing their significant duration. The middle line in Figure 5.11 depicts the mean significant duration (14.9 seconds), and is based on the "best" 80% of the values. This was accomplished through an iterative procedure, discarding the furthest data point from the ±standard deviation, then re-computing until 20% of the data has been discarded. The other solid lines above and below the mean represent the mean plus and minus one standard deviation, respectively. The length of the significant duration translates to typi-

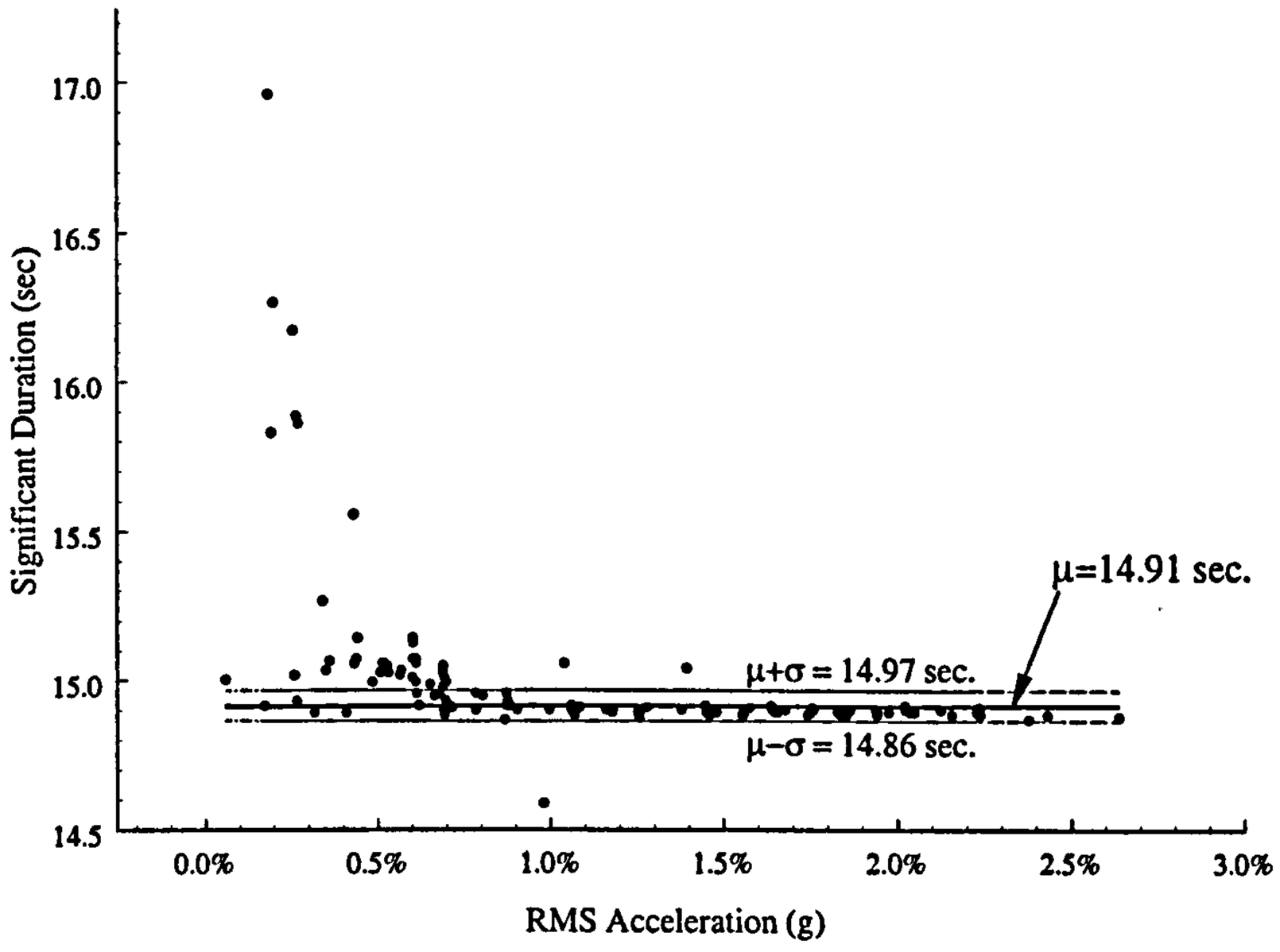

Figure 5.11: Significant duration versus RMS acceleration for all column yield tests.

cally 30 first mode cycles of the beam yielding configuration, and 50 first mode cycles for the column yield configurations.

5.5 RESPONSE SPECTRA

The response spectra for the recorded table accelerations are calculated by the spectrum generation capabilities in MSC/NASTRAN. This is based on the response of a simple oscillator:

$$\frac{d^2}{dt^2}x(t) + 2\omega\xi\frac{d}{dt}x(t) + \omega^2 x(t) = a_g(t) \tag{5.4}$$

where, $a_g(t)$ is the recorded table acceleration, ω is the natural undamped frequency, and ξ is ratio of elastic viscous damping. The acceleration response spectra was computed for three levels of damping (0%, 1%, and 5%) as shown in Figure 5.12. Superimposed on the

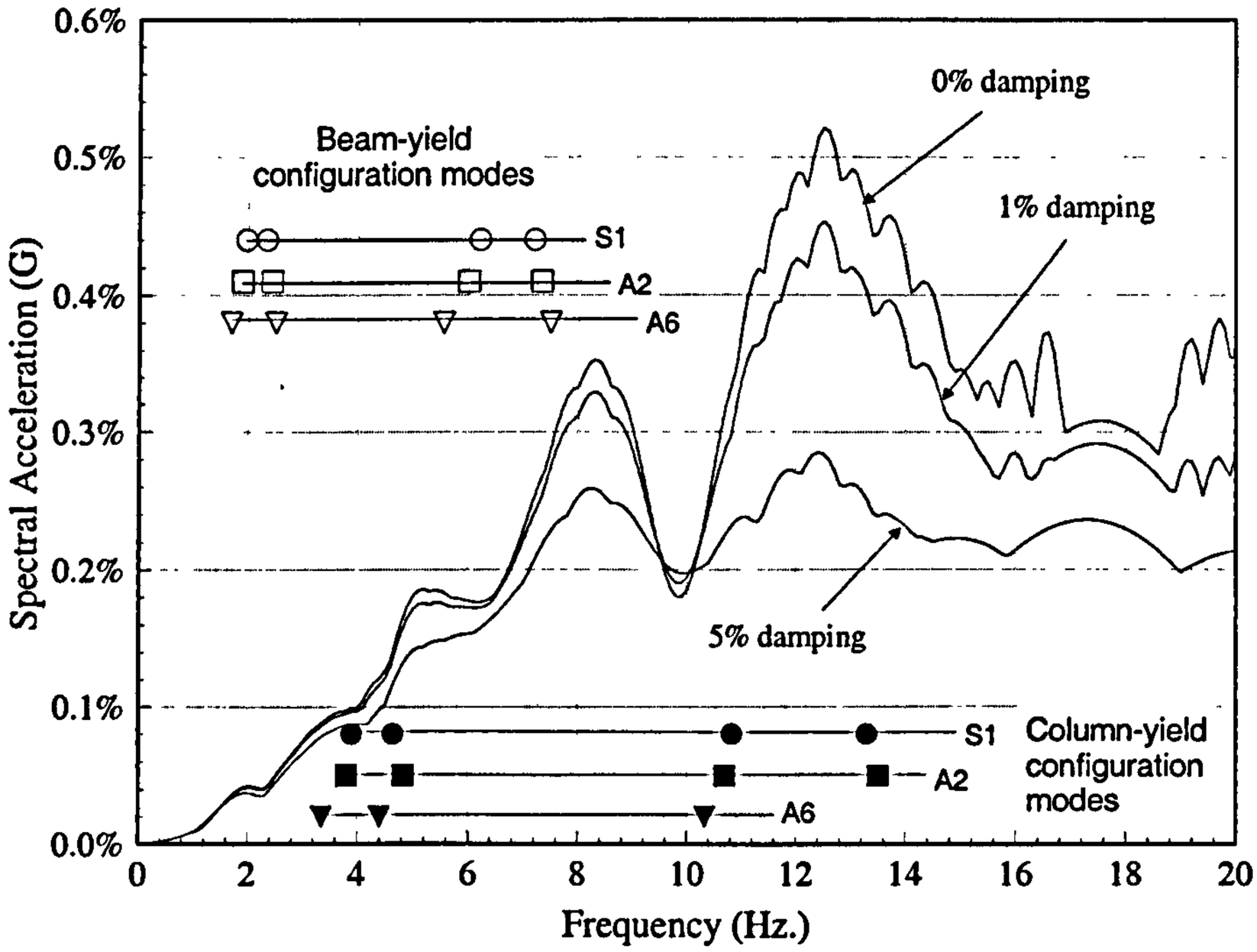

Figure 5.12: Acceleration response spectra. The first four modes of the three mass configurations for both column and beam yielding are shown separately for clarity, indicating only their frequency.

Figure are the modal frequencies of both the column yielding configuration models. As can be seen, the yielding characteristics of the hinge units will reduce the apparent seismic loads upon yielding—especially for the first two modes.

5.6 FORCING INTENSITY INDICATORS

One of the variables in the experimental tests was the intensity of the applied base accelerations. This was the main control in the level of inelastic behaviour during the test. As a result, it is desirable to have a single value to indicate this level of forcing in a comparative manner. These indicators are described below.

5.6.1 Table Gain (volts)

The table voltage gain was the direct means of controlling the force scaling during the operation of the shake table. These values were entered directly by the operator into a program which controls the motion of the shake table. As a result, there are no means of validating these numbers in terms of the recorded output traces. For this reason, the gain is not deemed a reliable forcing indicator.

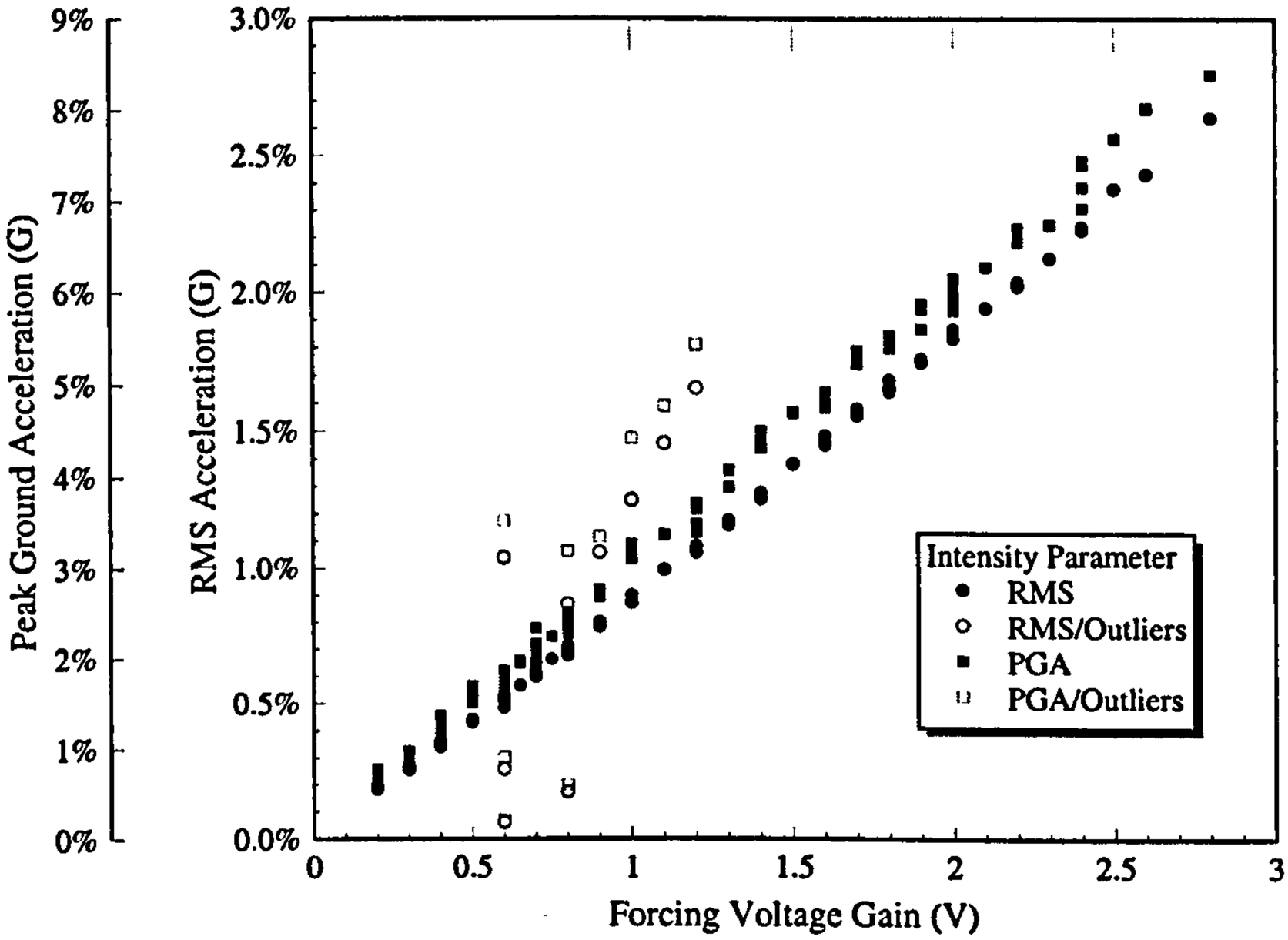

Figure 5.13: Peak ground acceleration and RMS acceleration versus voltage gain for the column yielding tests.

5.6.2 Peak Ground Acceleration (PGA)

The peak ground acceleration is simply the absolute maximum recorded acceleration during a particular test. This proved to be a very unreliable intensity estimate, as the acceleration peak spike occurring just before 5 seconds (see Figure 5.6) did not vary linearly with the input gain. The variance of the PGA in terms of the input table gain was also great, as

can be seen from the spread of the filled square (■) data points for a particular voltage gain in Figure 5.13. This is probably due to the difficulty the actuators have in matching the large acceleration spikes.

5.6.3 Root Mean Squared Acceleration (RMSA)

The root mean squared acceleration (RMSA) is found to be a more consistent intensity measure of the recorded table accelerations. This value is less sensitive to the possible error in matching the single peak acceleration spike. The RMSA is a measure of the average intensity, much like that of the voltage gain. As with the PGA values, there are a few tests below a gain of 1.25 volts that seem to have unreasonable RMSA values. These outliers (indicated by hollow circles, ○) can be attributed to either faulty acceleration recordings, operator error in entering the voltage gain, or shake table malfunction. In any case, the tests corresponding to the RMSA outlier values in Figure 5.13 were discarded from the results, and have not been presented in this study.

5.7 PEAK SIDE DISPLACEMENT RATIO

The upper graph in Figures 5.14 through 5.16 shows the peak displacement of both the right and left sides of the top (fourth) floor of the column yielding models. The lower graph in these Figures show the ratio of the peak right side displacement normalized by the peak left side displacement, both in terms of the RMSA. The indicated peak values are the absolute maximum side displacements. The top floor peak displacements from the symmetric mass configuration are shown in Figure 5.14, where it can be observed that the displacement ratio for hinge configurations CB, CC and CD are all around unity (±10%).

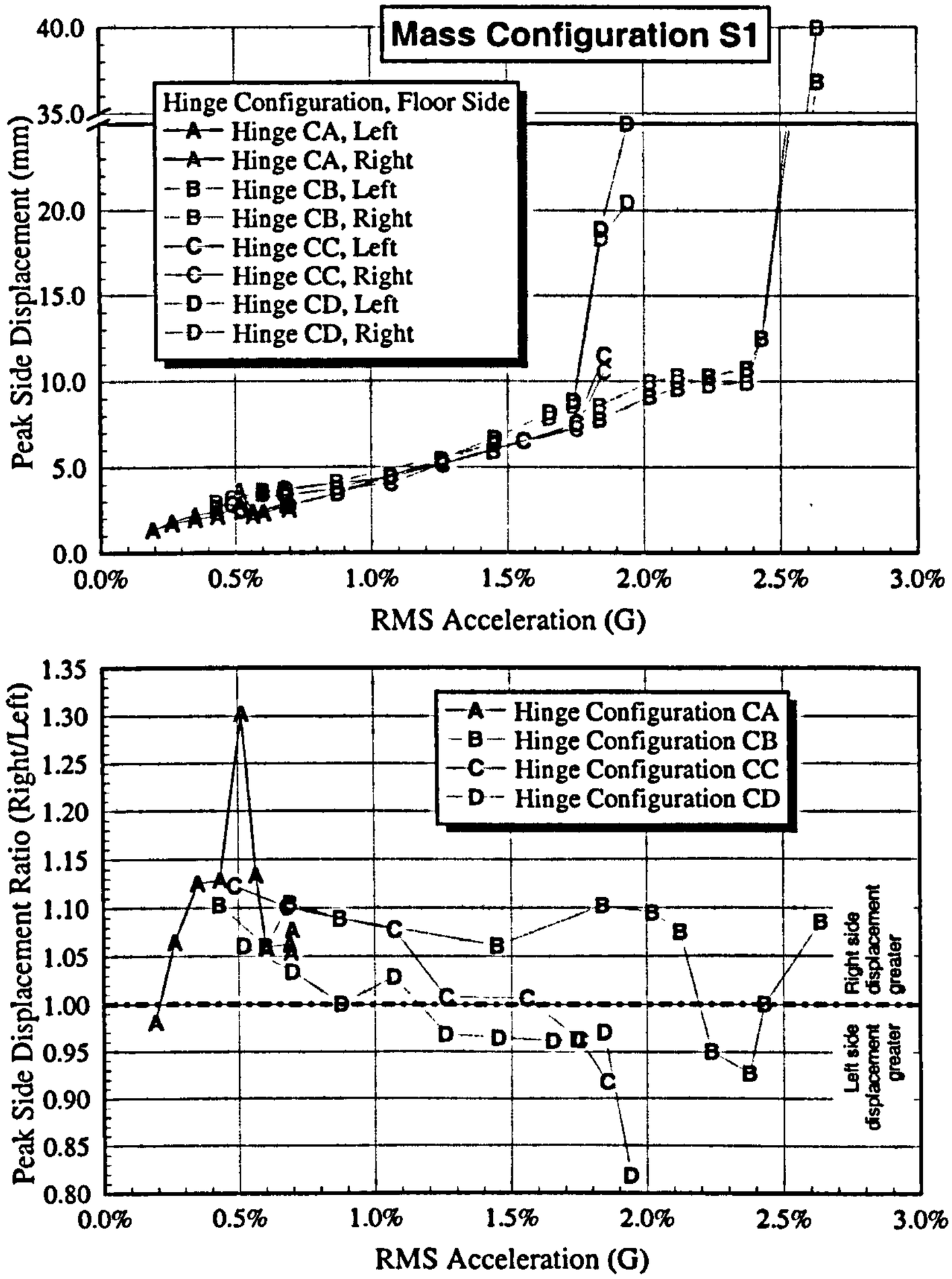

Figure 5.14: Fourth floor peak side displacements for the symmetric mass configuration (S1) of the column yielding models.

For reference, Table 5.1 summarizes the hinge configuration strength eccentricities previously shown in Chapter 4 in Table 4.1 (page 88) and Table 4.2 (page 91). Both hinge configurations CC and CD have a strength eccentricity, with the centre of strength residing closer to the right side of the floor. At low RMSA levels, these two hinge configurations are within the experimental accuracy of the peak side displacement ratio of hinge configuration CB (strength symmetry). This is to be expected, since at low RMSA levels, either

Table 5.1: Strength eccentricity summary for both 4-storey model configurations.

Beam yield configuration			Column yield configuration		
Hinge configuration	Strength Eccentricity (mm)		Hinge Configuration	Strength Eccentricity (mm)	
BA	0.0	all floors	CA	0.0	all floors
BB	0.0	all floors	CB	0.0	all floors
BC	92.5 116.7	floors 2-4 floor 1	CC	0.0 63.6	floors 3-4 floors 1-2
			CD	0.0 63.6	floors 3-4 floors 1-2

the entire structure is elastic, or only the centre column is yielding (as discussed in Section 4.4), thus all three hinge configurations are essentially identical. As the RMSA is increased to a moderate level, both the centre column and left exterior columns in the strength asymmetric hinge configurations experience inelastic deformations. In this region of forcing, the peak displacement ratio decreases slightly for configurations CC and CD (i.e. the peak displacement of the left side becomes larger with respect to the right side). This is due to the shifting of the centre of strength towards the right side of the floors, as hinge yielding is occurring in the column joints at the left side of the floor.

Hinge configuration CB, which is strength symmetric, does not exhibit this trend. The response of hinge configuration CA is a special case, and is discussed in greater detail below.

The low mass eccentricity case, A2, is shown in Figure 5.15. The peak displacement ratio for the two sides in this case vary between 1.5 for a generally elastic response, and

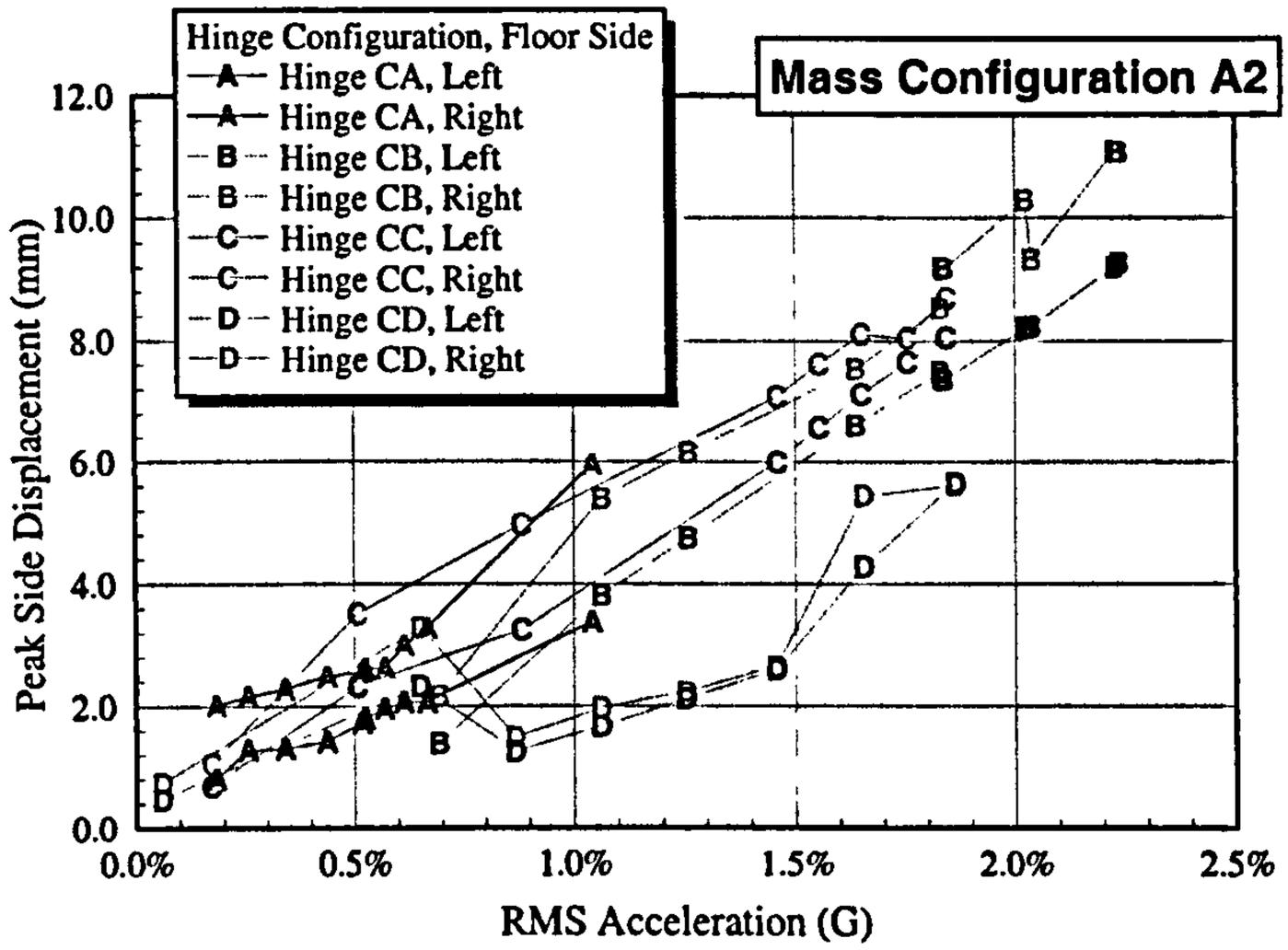

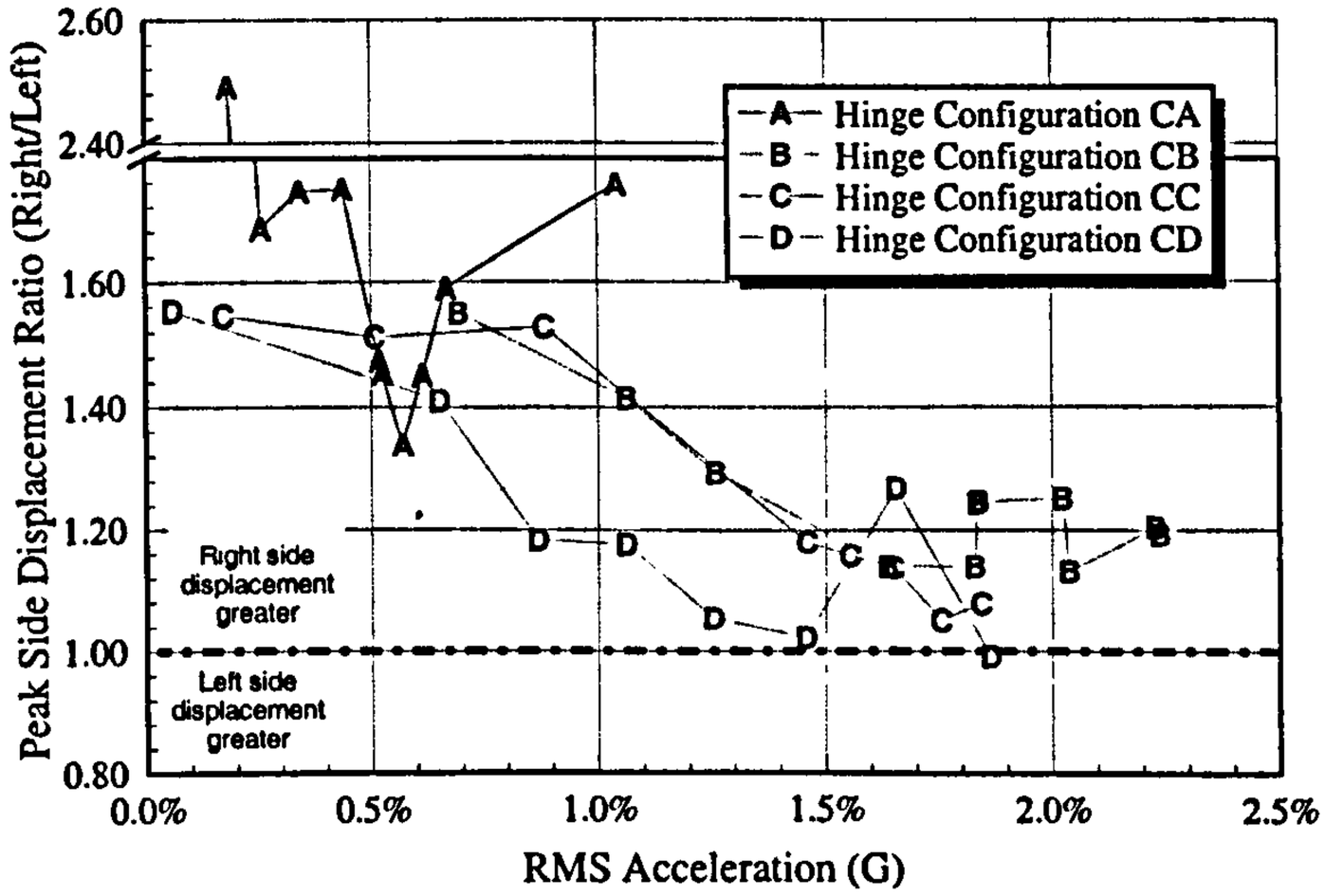

Figure 5.15: Fourth floor peak side displacements for mass configuration A2 of the column yielding models.

decreases towards unity as the forcing level increases (ignoring hinge configuration CA). This suggests that as the level of inelasticity increases, the structure responds primarily in the direction of loading. This was the conclusion of an early study [Kan, Chopra, 1981] on the non-linear torsional coupling of a simple, one-element model. The strength asymmetric hinge configurations CC and CD have peak displacement ratios that are generally less than hinge configuration CB. This is beneficial, in that it suggests a more uniform damage

distribution among the exterior columns upon failure. The displacement ratio for hinge configuration CD is generally lower than that for the other hinge configurations due to its reduced storey strength.

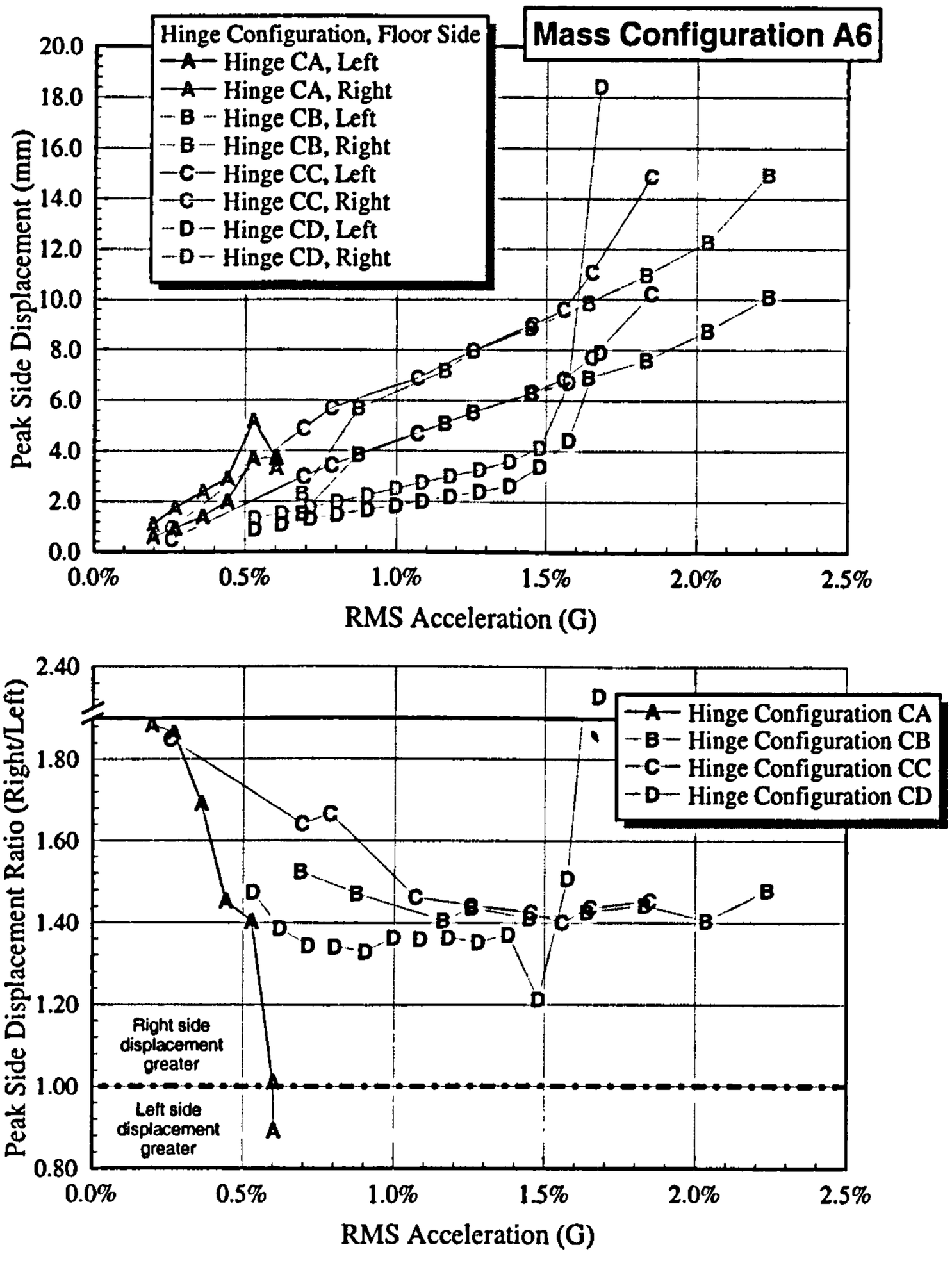

Figure 5.16: Fourth floor peak side displacements for mass configuration A6 of the column yielding models.

The peak side displacements for mass configuration A6 are shown in Figure 5.16. For this mass configuration, the peak side displacement ratio again tends to decrease as the forcing intensity (RMSA) is increased. At an RMSA above 1.0%g, the right side peak displace-

ment tends to be about 40% greater than the left side peak displacement. Hinge configuration CD, with its reduced strength in the first two storeys, exhibits greater peak displacement above an RMSA of 1.4%g (see top graph in Figure 5.16).

Hinge configuration CA (strength symmetric) is different from the other column yield hinge configurations, in that its vertical strength distribution is such that yielding occurs on the third and fourth floors of the model. From this, the input forcing on the yielding floor has been amplified and filtered by the first two stories. Additionally, the yielding floors are subjected to the coupled torsional acceleration inherent in mass eccentric configurations of the first two elastic stories. This can be observed in Figures 5.14 through 5.16 where the 'maximum possible' input RMSA on the hinge configuration CA models is less than half that for the other hinge configurations. Input RMSA beyond the 'maximum possible' were deemed to be excessive, and would potentially cause damage to the experimental equipment.

Figure 5.17 indicates the time at which the fourth floor peak side displacements of hinge configurations CB, CC, and CD occur. In this figure, the peak displacement time is plotted against the RMS acceleration. The peak displacement time is referenced for the average start of record, t_0:

$$t = t_s - t_0 = t - (t_5 - \bar{t_5}) \tag{5.5}$$

where, t_s is the time from start of data acquisition, t_5 is the time at 5% of Arias intensity for the particular record, and $\bar{t_5}$ is the average t_5 for all records studied (2.92s). As is shown in this Figure, both peak side displacements occur just before 5 seconds into the

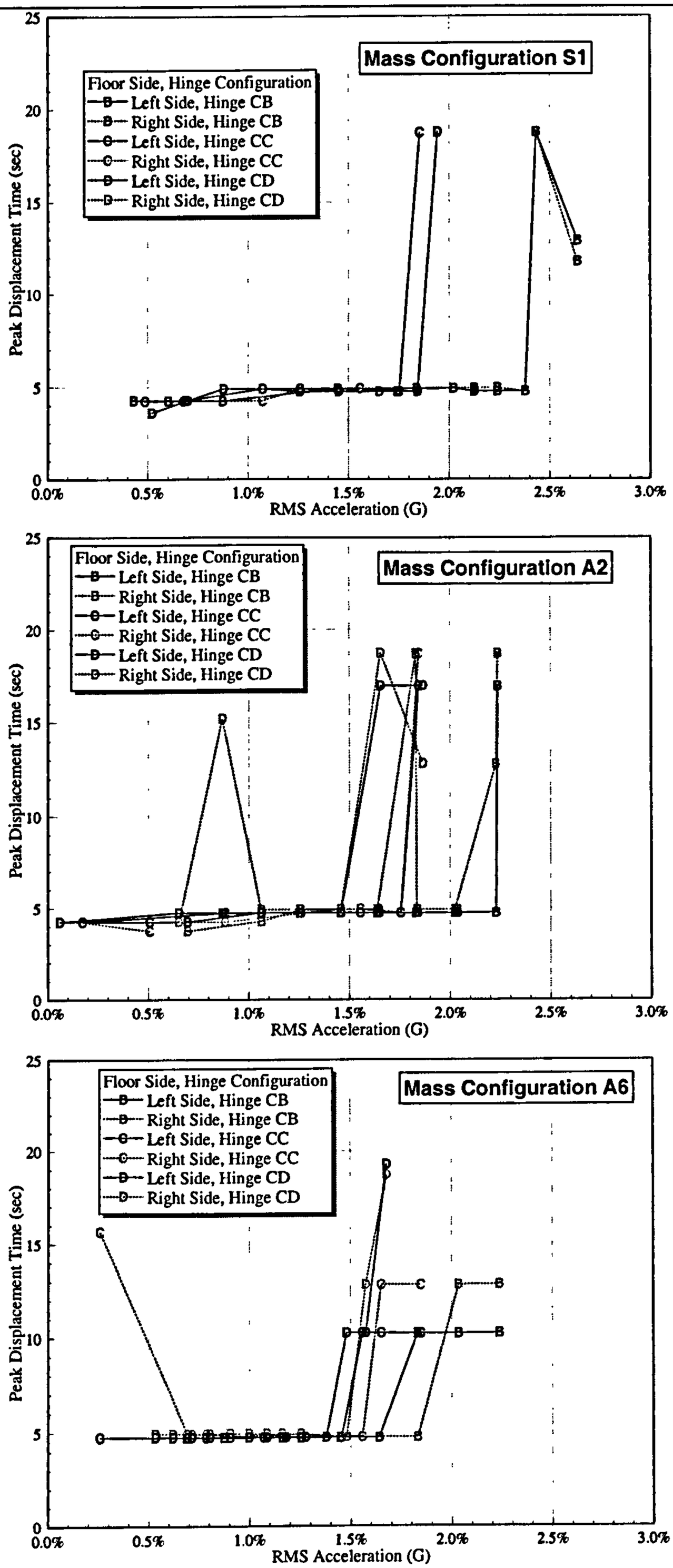

Figure 5.17: Time of peak fourth-floor total displacement for the column yield yielding models.

forcing motion—the location of peak acceleration (see Figure 5.6). At larger forcing intensities, the time of peak displacement is less consistent, as a result of the varying model stiffness from hinges yielding.

Figure 5.18 is similar to Figures 5.14 through 5.16, except results are presented separately for each hinge configuration. This figure clearly show the influence of the mass eccentricity on the peak side displacements for a particular hinge configuration.

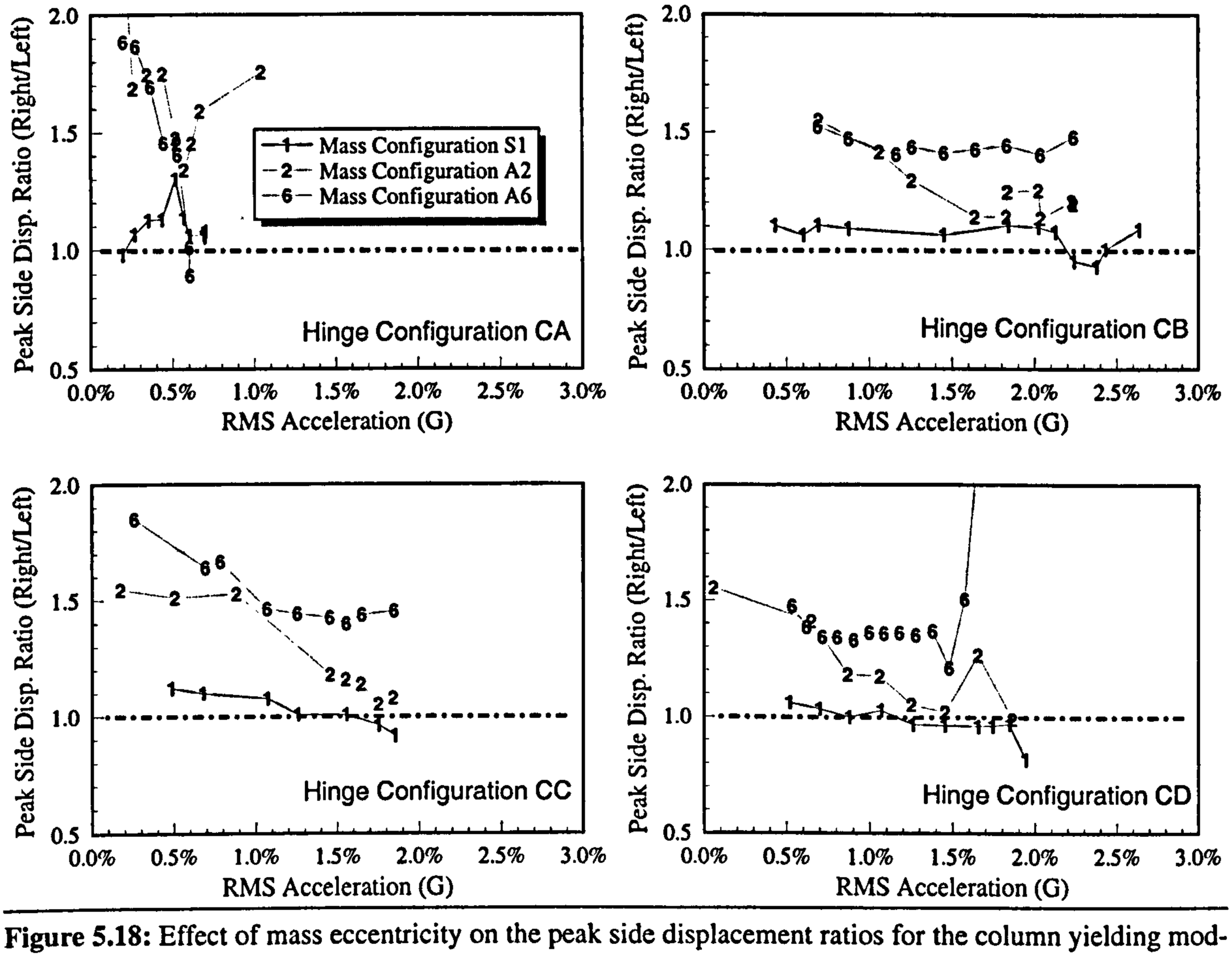

Figure 5.18: Effect of mass eccentricity on the peak side displacement ratios for the column yielding models.

5.8 TIME HISTORY RESPONSE

5.8.1 Floor Displacements

Figure 5.19 shows the time–history traces of the inter–floor (storey) displacements for a highly inelastic test of a column yielding configuration. The traces in the left column are

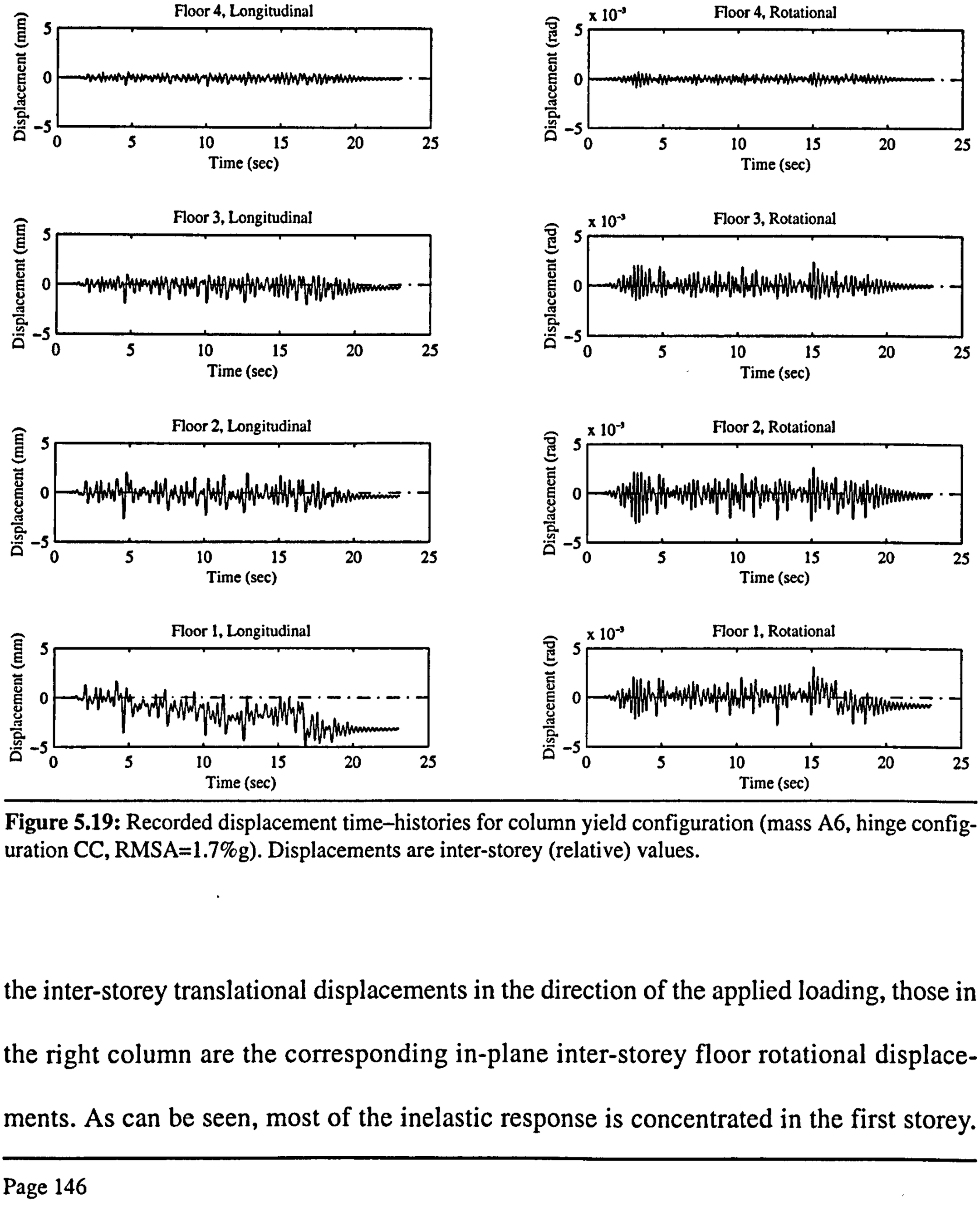

Figure 5.19: Recorded displacement time–histories for column yield configuration (mass A6, hinge configuration CC, RMSA=1.7%g). Displacements are inter-storey (relative) values.

the inter-storey translational displacements in the direction of the applied loading, those in the right column are the corresponding in-plane inter-storey floor rotational displacements. As can be seen, most of the inelastic response is concentrated in the first storey.

The first three stories all experienced some permanent plastic deformation, with the corresponding deformation magnitude decreasing in the upper stories. This is due to both the higher design strengths of the upper floors (Appendix B), and the reduction of applied seismic forces (lower acceleration) in the upper floors as a result of the lower stories yielding. As a result, the yield deformations are mainly concentrated in the first storey.

5.8.2 Side Displacements

The interaction between translation and rotation displacements can be easily visualized in terms of the floor side displacements. In Figures 5.20 through 5.23, the inter–storey longitudinal displacement of the right side is plotted along the vertical axis against the inter-storey longitudinal displacement of the left side (plotted on the horizontal axis). Traces along the positive slope diagonal (solid line) are pure translation, where 'fatter' traces along this diagonal have a greater rotational component in the response. The negative slope diagonal (dashed line) indicates pure rotation. This is shown in Figure 5.20 for all four floors in the same test as shown in Figure 5.19. As in most of the column yielding tests, the inter-storey displacement response diminishes in the upper stories. It is difficult to determine the time-dependent effects from these plots, but they do show the overall parametric effects on the coupled displacement.

Figure 5.21 shows the response from the symmetric mass configuration (S1), at increasing force intensities. The response is mainly along the longitudinal axis, as expected. This is especially true for the symmetric strength configuration (hinge CB), where even at 2% RMSA, the extreme tips of the displacement trace have little to no rotational component. This is not true when strength eccentricity is introduced (shown by hinge configuration

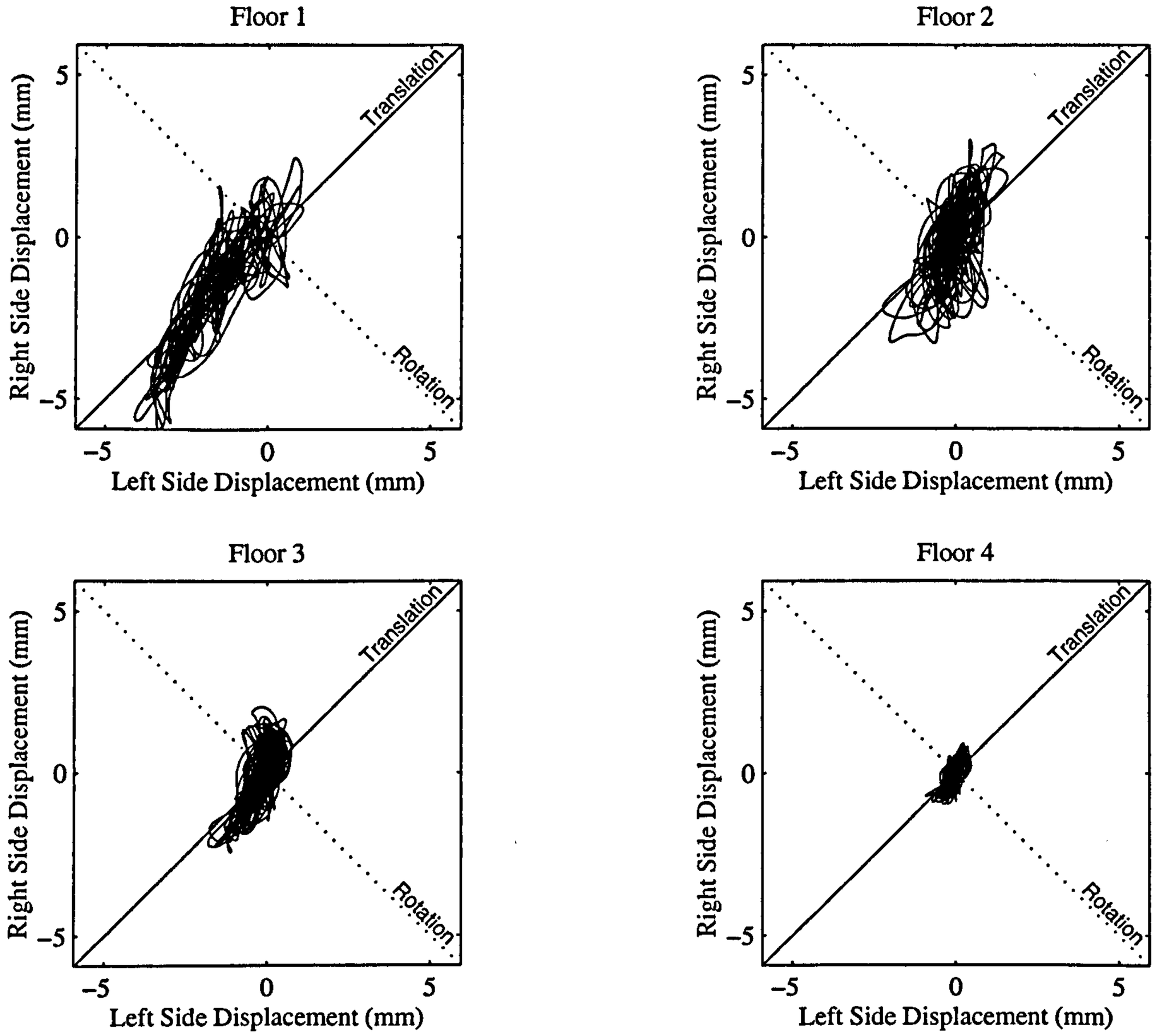

Figure 5.20: Side displacement traces for column yield model (mass A6, hinge configuration CC, RMSA=1.7%g).

CD). With this configuration, the response is still basically in translation, but plastic offset is in both rotation and translation (see traces with 1.5%, 1.7%, and 1.9% RMSA).

Figures 5.22 and 5.23 show in a similar manner the effects of mass eccentricity (at two levels) on the side displacement plots. Mass configuration A2 is shown in Figure 5.22 with four levels of forcing intensity. All four displacement traces with the symmetric strength distribution (hinge CB) are fairly complicated as a result of the coupled response. As the level of forcing is increased, the orientation of the traces is more along the pure

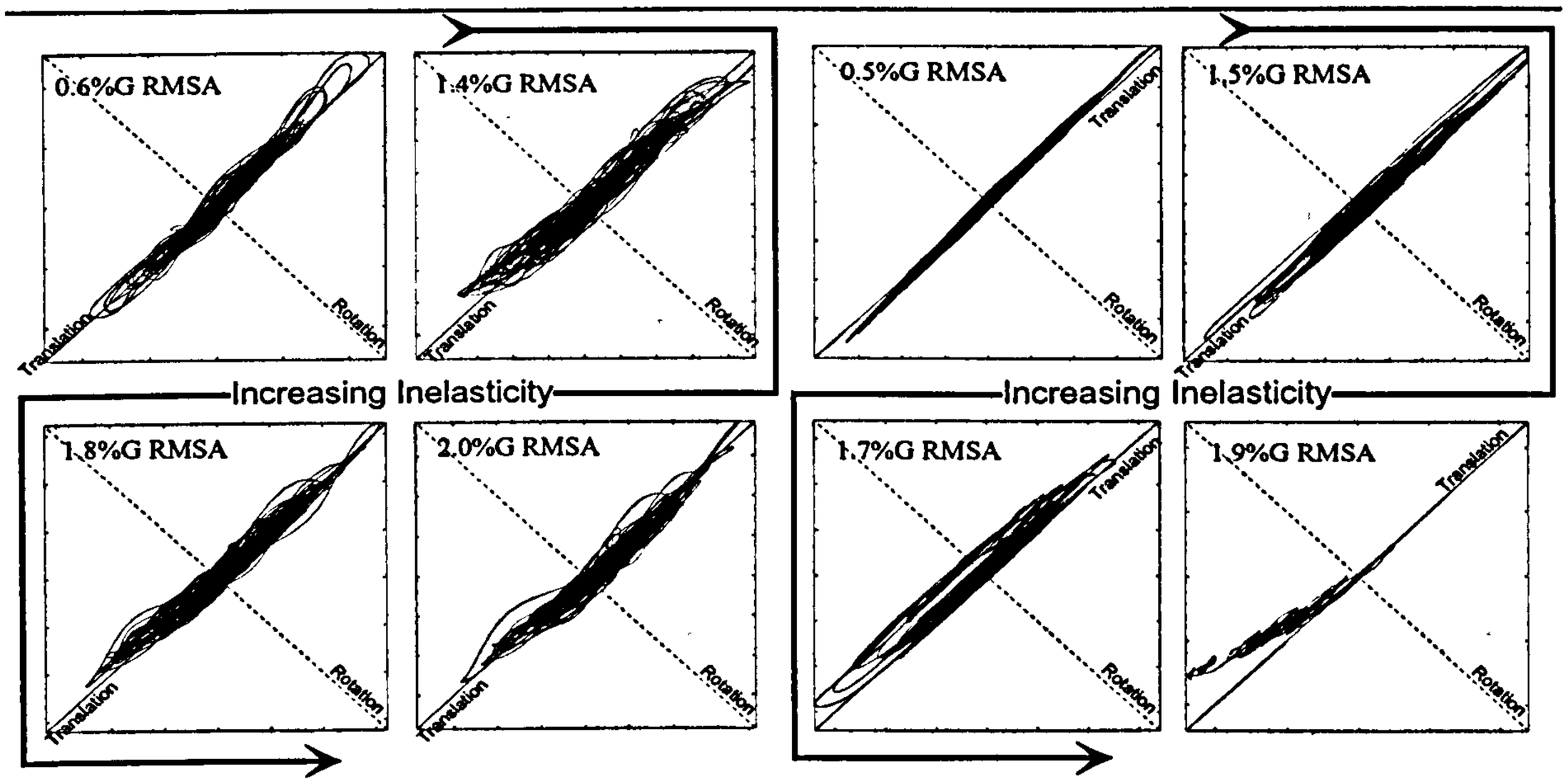

Figure 5.21: First floor side displacement traces (the right side is vertical axis, the left side is horizontal axis) for column yield configuration with symmetric mass distribution, S1. Percentage values indicate RMS acceleration. The definition of e_n is presented in equation (5.6) on page 150

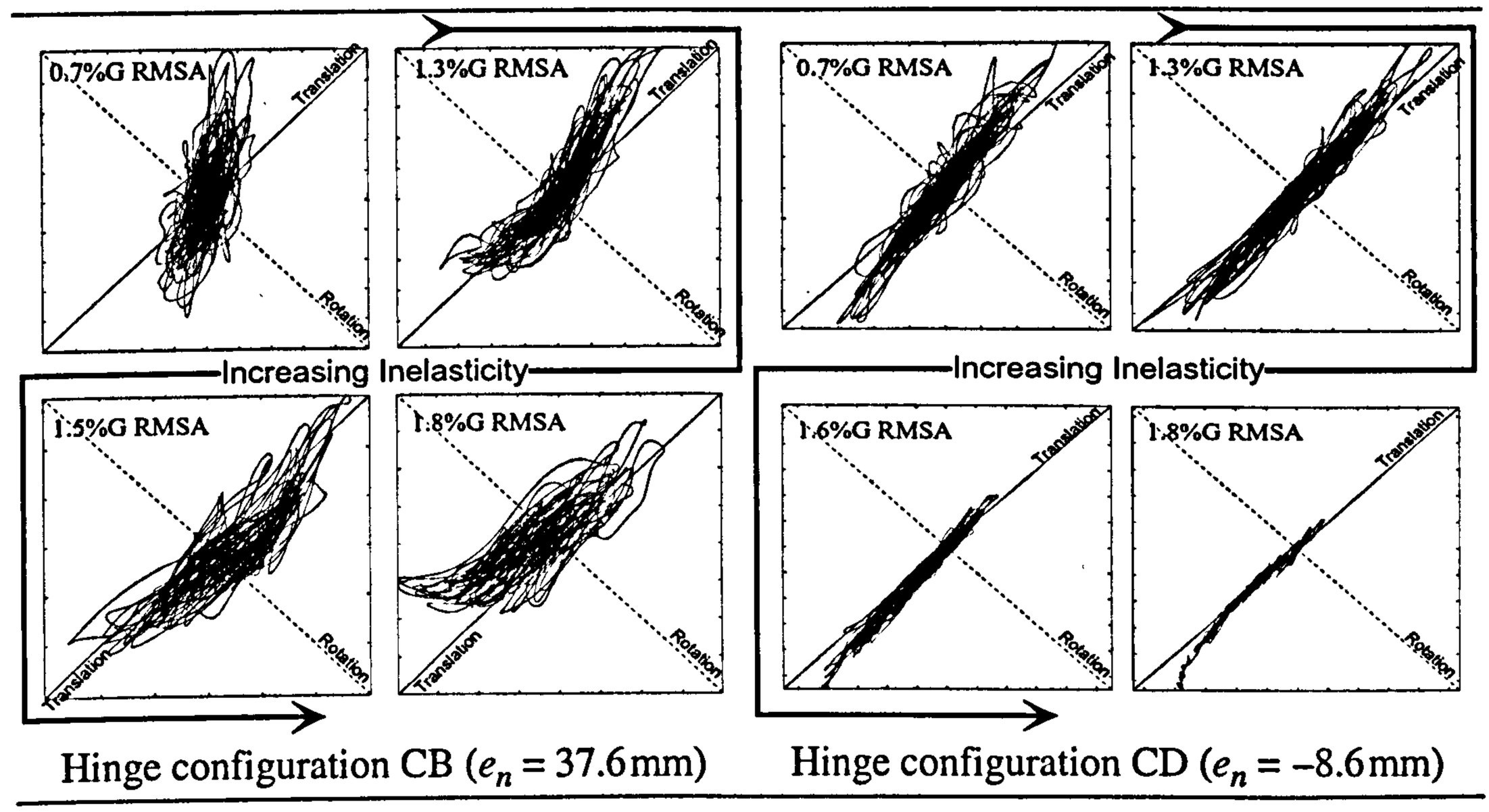

Figure 5.22: First floor side displacement traces for mass configuration A2.

translation axis. This is especially obvious when comparing the 0.7% and 1.5% RMSA traces of the symmetric strength distribution (hinge CB). The traces for 1.8% RMSA (hinge CB) are somewhat wider about the pure translation axis, indicating some plastic offset in rotation. However, the general direction of the traces are parallel to the pure

translation axis. The traces in Figure 5.22 for the strength eccentric case (hinge CD) are much more translational dominated than those of hinge configuration CB. This is a result of the strength eccentricity (46.2mm) being similar to the mass eccentricity (37.6mm). This difference (e_m-e_s) is termed the net eccentricity, e_n:

$$e_n = e_m - e_s \tag{5.6}$$

The net eccentricity is the effective mass eccentricity present when all storey members (above and below the floor in question) are yielding. This parameter is only valid for perfectly plastic systems. The larger the value of e_n, the larger the torsional acceleration of a floor when no resisting storey stiffness is present. This can be observed by the displacement trace "hooking" at the extreme displacements (hinge CB, 1.8% RMSA). Since the net eccentricity is fairly small (e_n=–8.6mm) in hinge configuration CD, the torsional acceleration upon yielding is small resulting in a generally longitudinal response. It is important to note when comparing the response of the two hinge configurations, that hinge configuration CD has an overall reduction in total storey strength. Therefore, a 0.7% RMSA for hinge configuration CD induces a greater inelastic response then that for hinge configuration CB. Table 5.2 quantitatively summarizes the response increase of hinge

Table 5.2: Peak first floor responses for mass configuration A2 (Hinge Configurations CB & CD).

Hinge Configuration	Peak Translation (*Y*-axis) (millimetres)			Peak Rotation (Θ-axis) (milliradians)		
	1.3% g[a]	1.8% g	Increase	1.3% g	1.8% g	Increase
CB	1.82	3.35	84%	4.90	7.25	48%
CD	2.13	5.63	164%	5.20	9.97	92%
Increase	17%	68%		6%	38%	

a. Forcing intensity is in terms of root mean squared acceleration

configuration CD over CB, for an associated increase in forcing intensity. As seen from this table, a 38% increase in forcing intensity (RMSA) results in a 164% translation response increase for hinge configuration CD, and only a 84% increase for hinge configuration CB. Similarly, the peak rotations for hinge configuration CD are increased by 92%, compared to only 48% for hinge configuration CB.

Figure 5.23 shows the first floor side displacements of selected column yielding models with mass configuration A6. Unlike mass configuration A2, mass configuration A6 (e_m=112.7mm) has a significant rotational component, even in the highly inelastic response. This is due to both the higher net eccentricity, and the fact that the first two

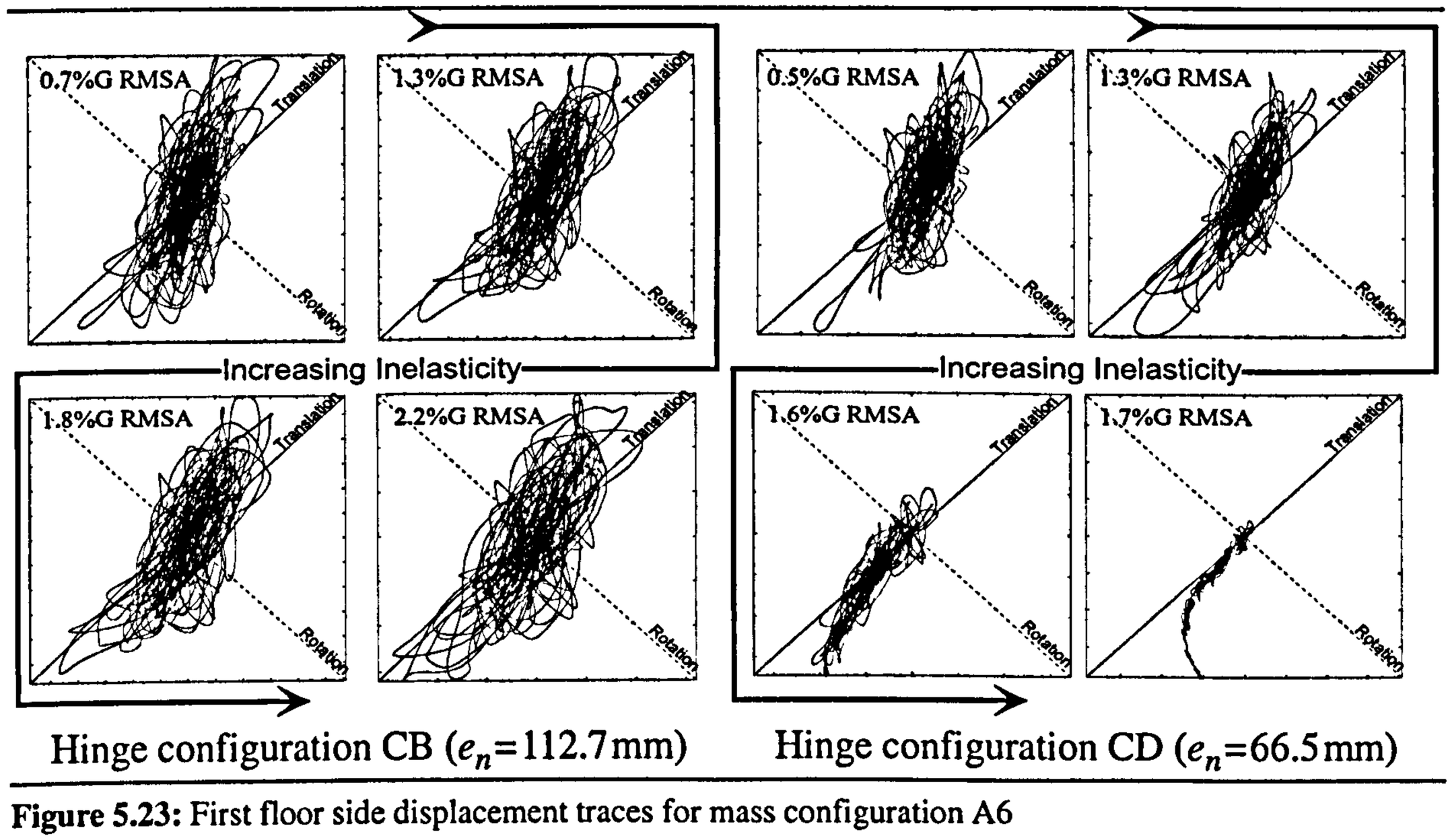

Figure 5.23: First floor side displacement traces for mass configuration A6

modes for mass A6 are rotational dominated. However, the extreme displacements are still aligned along the pure translation axis. Likewise, the larger net eccentricity for hinge configuration CD (e_n=66.5mm) in Figure 5.23 results in a greater torsional response when

compared to hinge configuration CD with mass configuration A2 (e_n=-8.6mm in Figure 5.22). A comparison between hinge configuration CB and CD shows a higher degree of inelastic behaviour at similar forcing intensities due to the overall strength reduction in hinge configuration CD required to achieve the strength eccentricity in the experimental model.

5.9 FREQUENCY RESPONSE

5.9.1 Power Spectral Densities (PSD)

As indicated earlier, the power spectral density (PSD) is an average quantity indicating response energy content for a particular degree of freedom over various frequencies for the applied loading. As the recorded displacements are non–stationary, they are modified with a sliding Hanning windowing function[1]. The length of the sliding window is 2 seconds to form a series of periodograms. These periodograms are then averaged to form the power spectra presented in Figures 5.24 through 5.26. This section pertains only to the lowest forcing level (elastic) recordings, therefore attention is not paid to the various hinge configurations. The frequency response of the inelastic recordings are covered below in Section 5.9.2.

Figure 5.24 shows the PSD for each degree of freedom in a symmetric mass model, S1. The vertical scale is in decibels ($10 \cdot \log_{10}$). The first two modes in the translational degree of freedom are clearly shown at 4± Hz. and 11± Hz. The energy peak at 18± Hz. is a spuri-

1. Windowing is required to reduce the effects of Gibbs phenomenon on the 2 second segmented records.

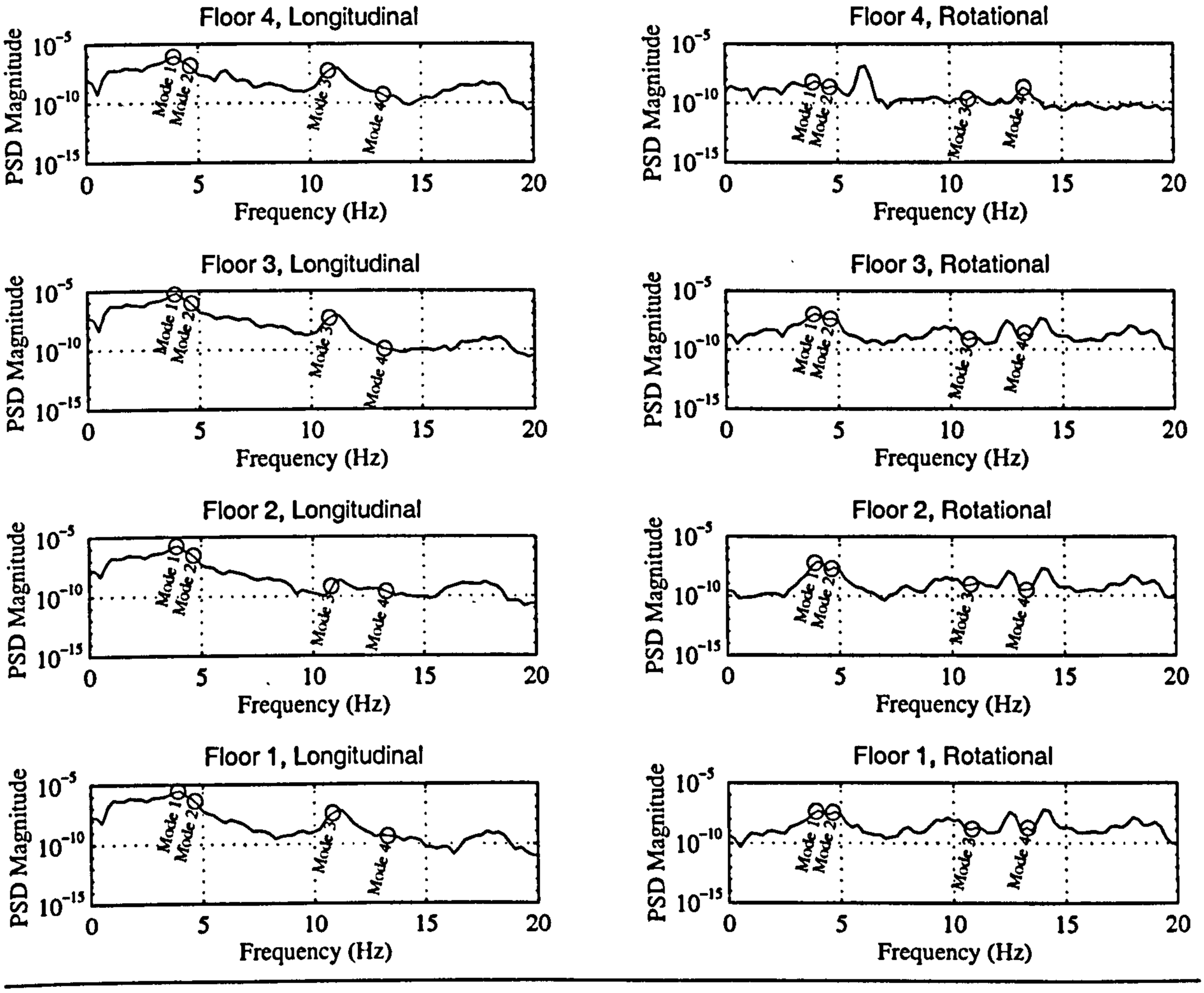

Figure 5.24: Power spectral densities for the symmetric mass configuration, S1 (low level forcing).

ous mode of the shake table and its reaction mass. The energy difference between the first two translational modes (first and third mode, respectively) is greatest in the second and third floors (over a 20dB difference). This difference is reduced in the fourth and first floors to around 10dB. This is to be expected, as a result of the third mode shape which has its highest displacements on the first and fourth floors (see Figure 3.8 on page 64). The rotation PSD is fairly inconsistent above 8 Hertz. The magnitude for the bottom three floors in rotation is generally between –80 and –90dB, leading to the conclusion that anything in this range and below can be considered as noise. These figures cannot be compared directly, due to the different units (translation in metres and rotation in radians) of

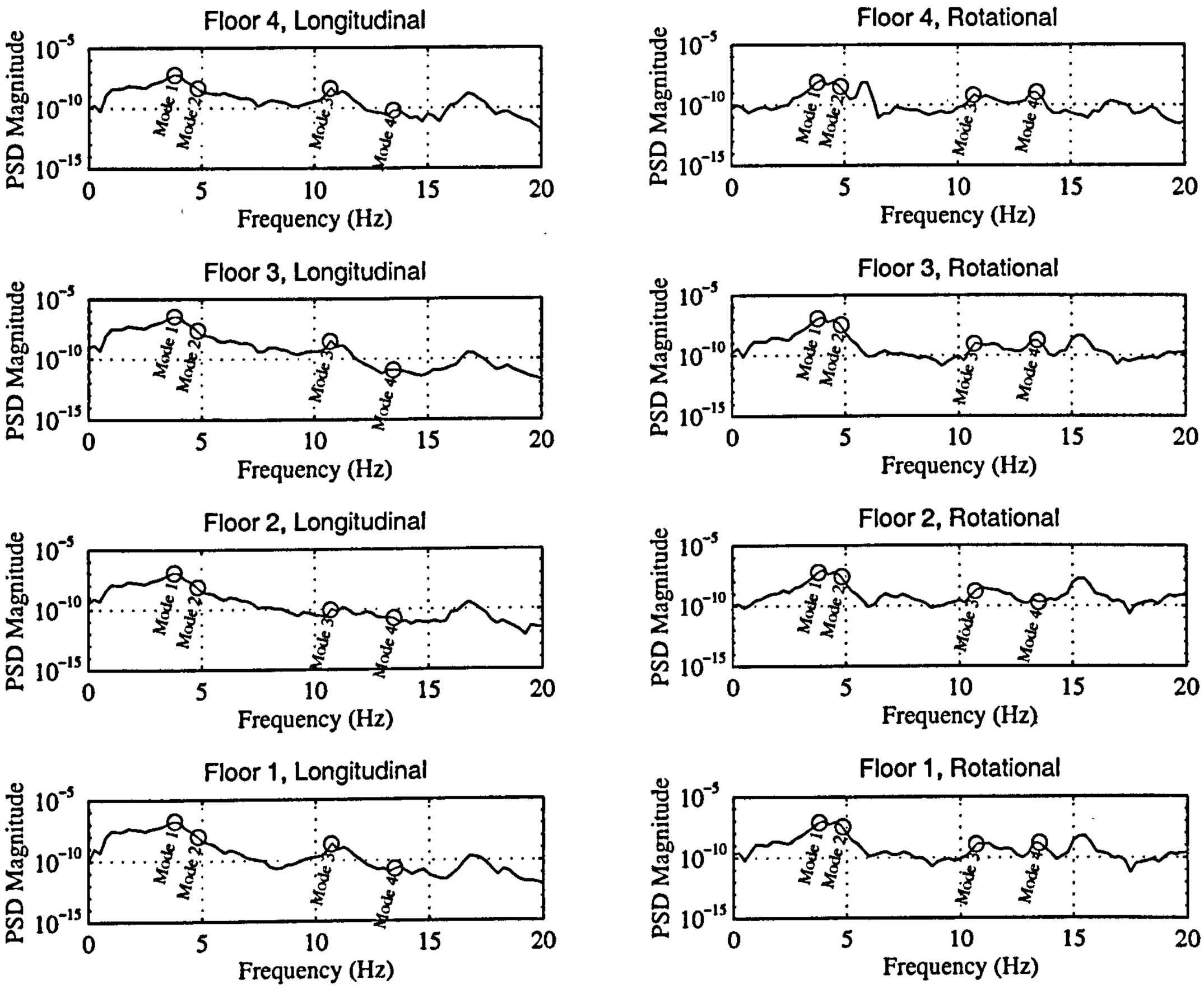

Figure 5.25: Power spectral densities for the low mass eccentricity configuration, A2 (low level forcing).

the two sets of time-histories, and possible variations in forcing intensities for the three mass configurations. Torsional energy might be introduced by a slight misalignment in the model, or from torsional forcing input due to the heavy asymmetrically placed instrumentation frames. Both of these could generate a coupled response. Also, a "pseudo–torsion" can be introduced as a result of the instrumentation arrangement and calibration. The proximity probes will record a slight rotation due to their corner placement (i.e. more magnetic mass at the face perpendicular to the probe measurement face due to the corner plate). As this edge moves transversely in front of the probe, it has the effect of that corner moving closer to the probe. The contacting transducers will also record rotation if not

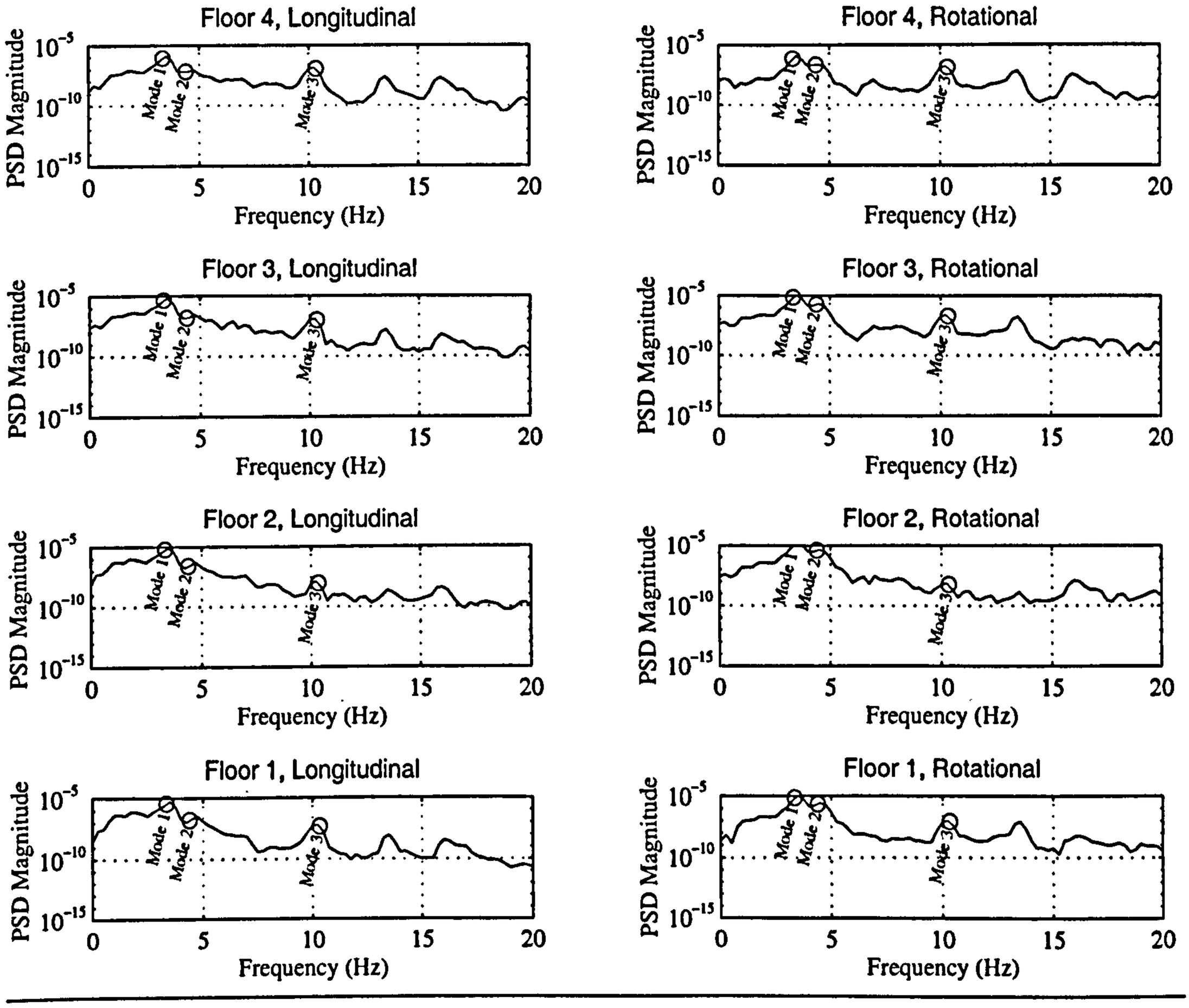

Figure 5.26: Power spectral densities for the high mass eccentricity configuration, A6 (low level forcing).

properly calibrated, since two gauges are responsible for recording both translation and rotation in the top two stories. In both cases, this "imaginary" rotation will have the same frequency as that for the translation.

The PSD's for mass configurations A2 and A6 are shown in Figures 5.25 and 5.26, respectively. The energy content for the first translation dominated mode in Figure 5.25 is slightly greater than that of the first rotation dominated mode. The reverse is true in Figure 5.26 for the higher mass eccentricity case model.

These three figures indicate essentially that over the duration of the applied base acceleration, the response of the symmetric mass model is basically in its fundamental translational mode. The two mass asymmetric models respond primarily in the first two modes, with a higher rotational response in the higher mass eccentricity.

5.9.2 Time-Dependent Frequency Response

As described in Section 5.3.2, spectograms plot the Fourier amplitude at a particular frequency and time. This is a common technique used in the field of speech analysis, and is particularly well suited for inelastic time series analysis. Fourier amplitude ridges parallel to the time axis indicate modal response frequencies. In the case where the frequency is zero, with contour lines running parallel to the time axis, plastic deformation occurs within that region. The contour lines for the longitudinal motions are scaled identically in all floors, in order to identify the largest motions. The same is also true for the rotational motions.

The following spectograms depict all eight degrees of freedom for selected tests for the column yielding models. As with the section on side displacements, emphasis is placed on hinge configurations CB (strength symmetric) and CD (strength asymmetric).

The spectograms for a symmetric mass and strength model are shown in Figure 5.27. This test is “elastic”, and its PSD is also shown in Figure 5.24. The longitudinal response is just below 4 Hertz, with its highest magnitude around 3 seconds into the recording. This corresponds to the impulse of 4 Hertz at 2 seconds into the acceleration forcing, as indicated in the spectogram of the input base motion in Figure 5.8 on page 131. As indicated by the

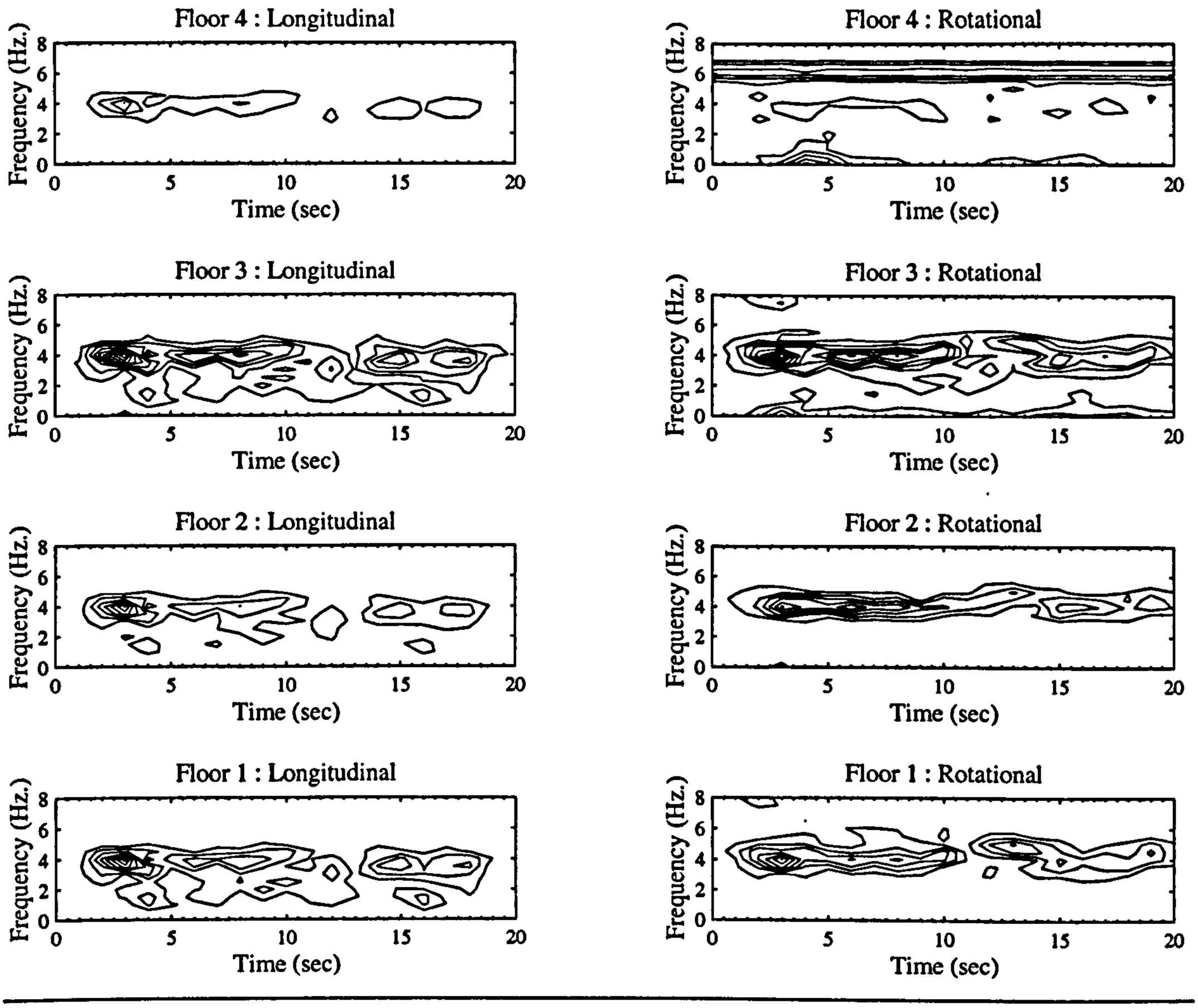

Figure 5.27: Spectogram of low level forcing on a symmetric mass and strength model. (C3SCB1)

PSD, most of the longitudinal response is concentrated in the first and especially third floors. The highest rotational response for this model is also in the third floor, and is probably a result of model and/or instrumentation irregularities, as indicated earlier. The fourth floor rotational record includes a continuous frequency at 6 Hertz. This is probably a result of interference noise in either the acquisition board, or the channel's instrumentation lead. The third and fourth floors possibly indicate some plasticity, occurring first at 3 seconds in the third floor, then at 4 seconds in the fourth floor. Again, these zero frequency contours are so small, that they might also be attributed to noise.

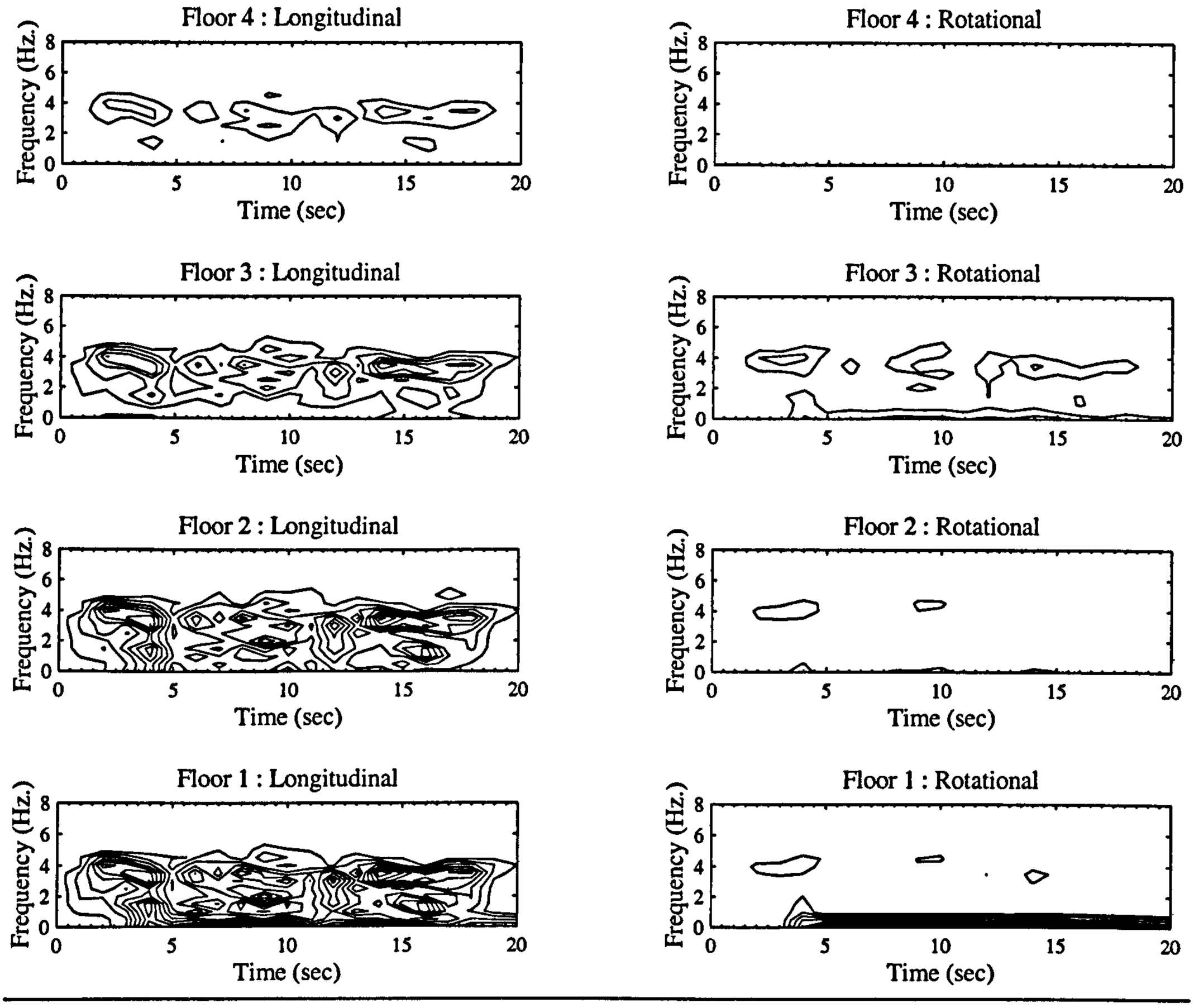

Figure 5.28: High level forcing (2%g RMSA) spectogram for mass and strength symmetry.

Figure 5.28 shows the spectogram for a highly inelastic symmetric mass and strength configuration (first floor side displacements shown in Figure 5.21 at 2% RMSA). Spectograms indicate a plastic offset by a zero frequency contour. Most of the longitudinal inelastic response occurs between 5 and 10 seconds, and again between 12 and 16 seconds. In these two regions, much of the longitudinal response is reduced in the upper three stories. Almost all of the rotational displacement is concentrated in the first floor. Most of this displacement is plastic, and occurs around 5 seconds, when the first floor also yields in the longitudinal direction. The rotational time–history for the first floor is shown in the lower plot in Figure 5.29. The peak rotation of 8×10^{-4} radians in this Figure corresponds

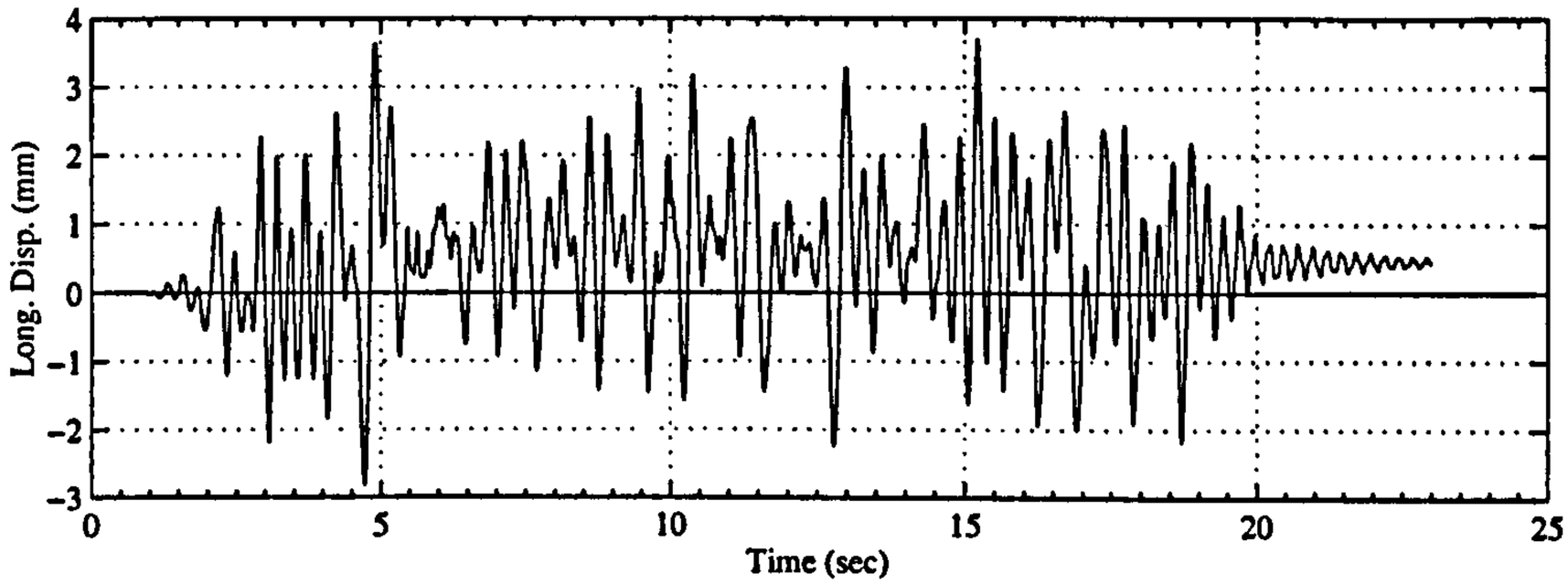

Figure 5.29: Floor 1 time–histories of translation and rotation for the model in Figure 5.28

to a side displacement of just over 0.3 mm—fairly insignificant. Since the rotational yielding only occurs during translational yielding, this can be attributed to accidental eccentricity in the model.

Figure 5.30 shows the longitudinal and rotational displacement traces of the first floor of a mass configuration S1 model with strength asymmetry (RMSA is 1.8%). The strength asymmetry results in obvious floor rotations at the onset of yielding. The two full–cycle pulses at 5 and 13 seconds in the longitudinal displacement result in two half–cycle rotational pulses. Although these rotational spikes are quite obvious in the time–history, their magnitude is equivalent to that for the strength symmetric case in Figure 5.29. Similar comparisons can be made for the other forcing intensities in the symmetric models. In

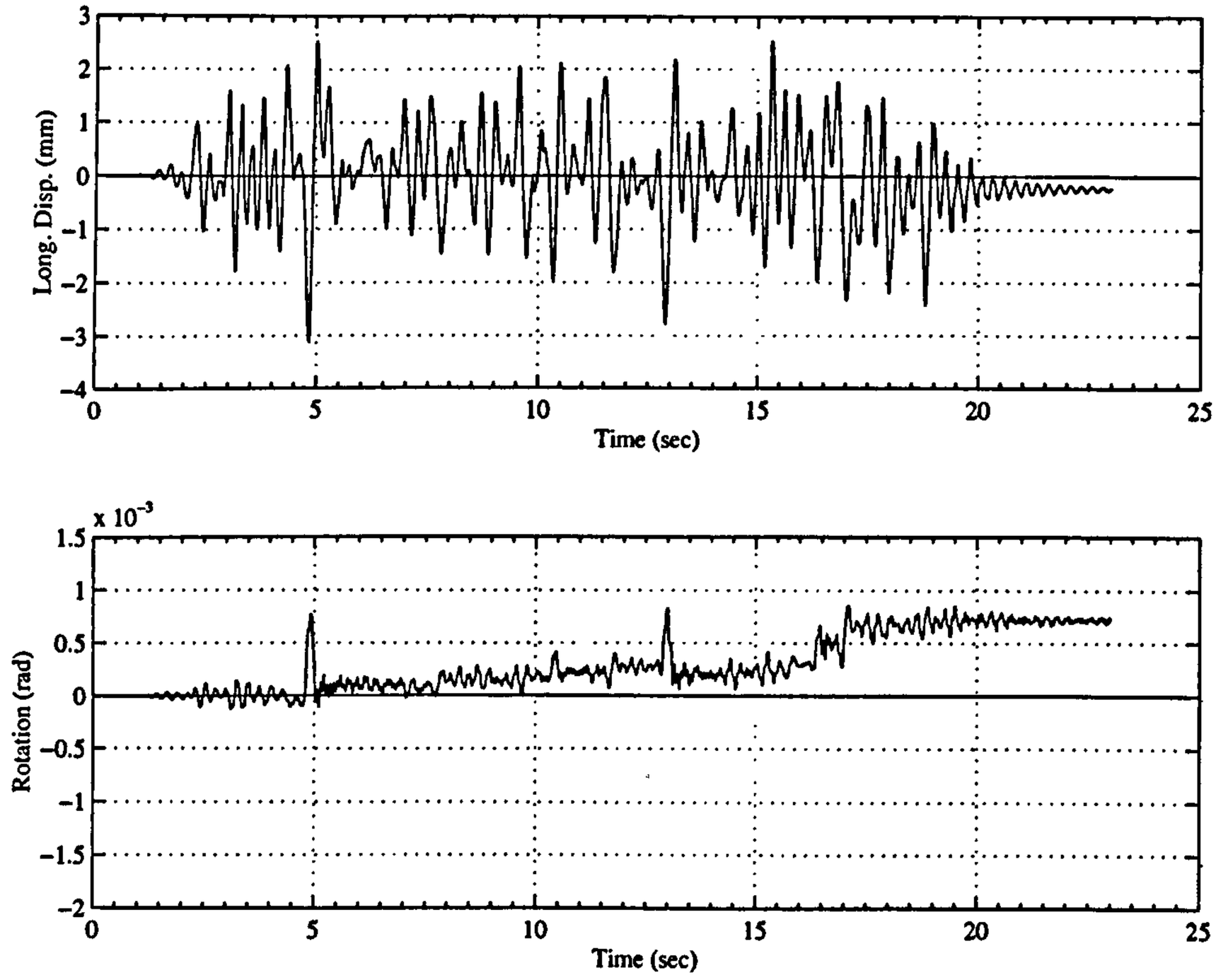

Figure 5.30: Floor 1 time-histories for mass configuration S1 with hinge configuration CD (RMSA = 1.8%g).

other words, strength eccentricity does not play a significant role in the overall inelastic behaviour of symmetric structures.

Spectograms for mass configuration A6 with strength symmetry are shown in Figure 5.31. From this elastic test (floor PSDs are also shown in Figure 5.26), the influence of mass eccentricity on rotation is seen clearly in the first three floors, where Fourier amplitudes are significant. Increasing the input forcing to 2.2%g RMSA results in the spectograms shown in Figure 5.32. As is seen by the number (hence magnitude) of contour lines, most of the response deformation occurs in the first two floors. The four time–histories associated with these two floors are shown in Figure 5.33. Although both floors become inelastic, the greatest deformations occur in the first floor. From Figure 5.32, floor 1 yields in rotation between approximately 12 and 17 seconds. Between these regions in Figure 5.33

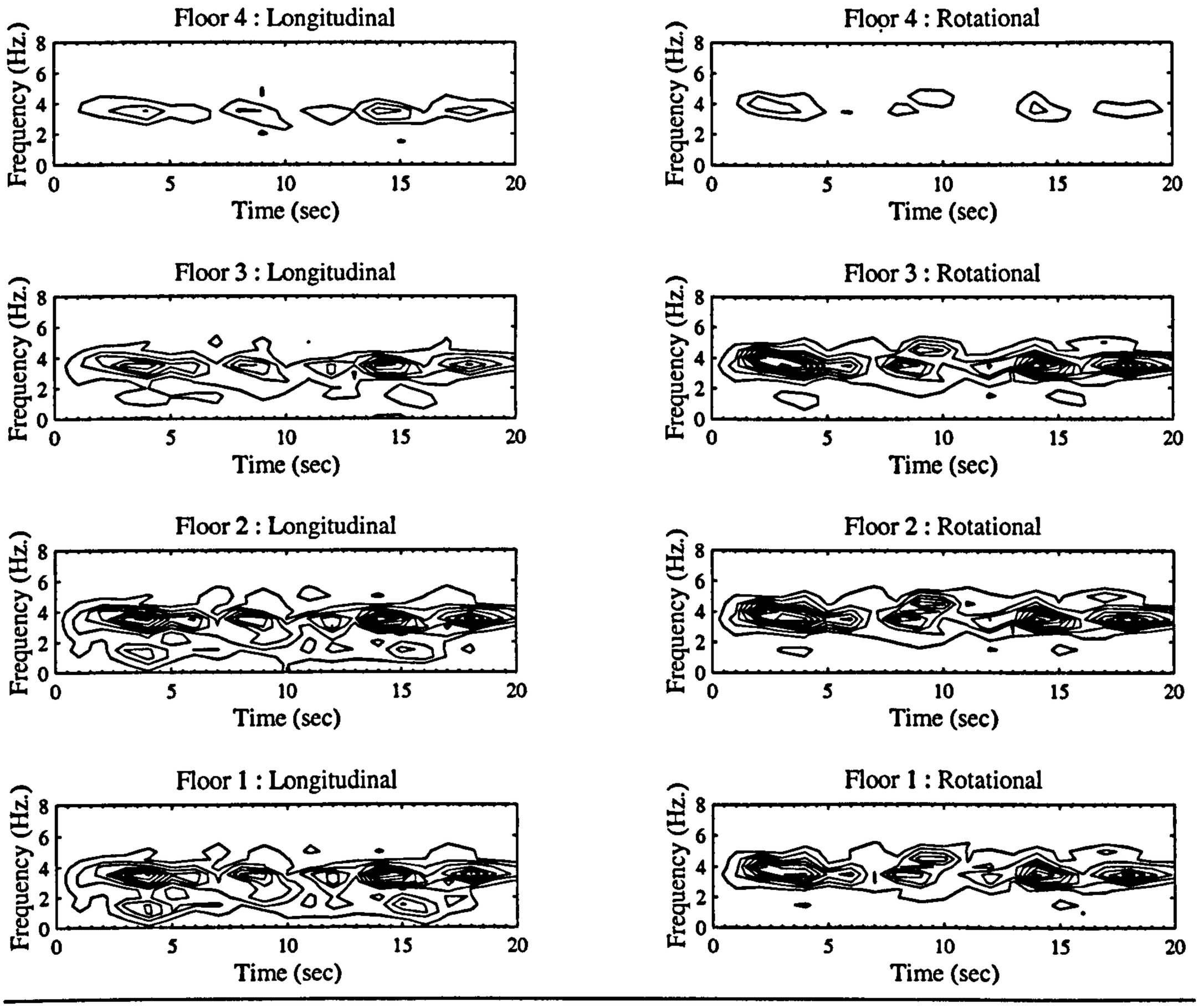

Figure 5.31: Spectogram of mass configuration A6 with strength symmetry (low level forcing).

the rotational amplitude oscillations are reduced, although the mean plastic displacement is still large. This was common in all tests, where associated with longitudinal yielding is reduced torsional vibrations (although plastic deformations may be large).

As observed previously, positioning the centre of strength closer to the centre of mass has the effect of reducing the plastic torsional deformations. This is most obvious with mass configuration A2 and hinge configuration CD (e_n=–8.6mm). The first floor displacement traces are shown in Figure 5.34, for both the symmetric and asymmetric strength distributions. The post elastic behaviour is different between these two hinge configurations due largely to their non-linear parameters. The two model responses are for the most part sim-

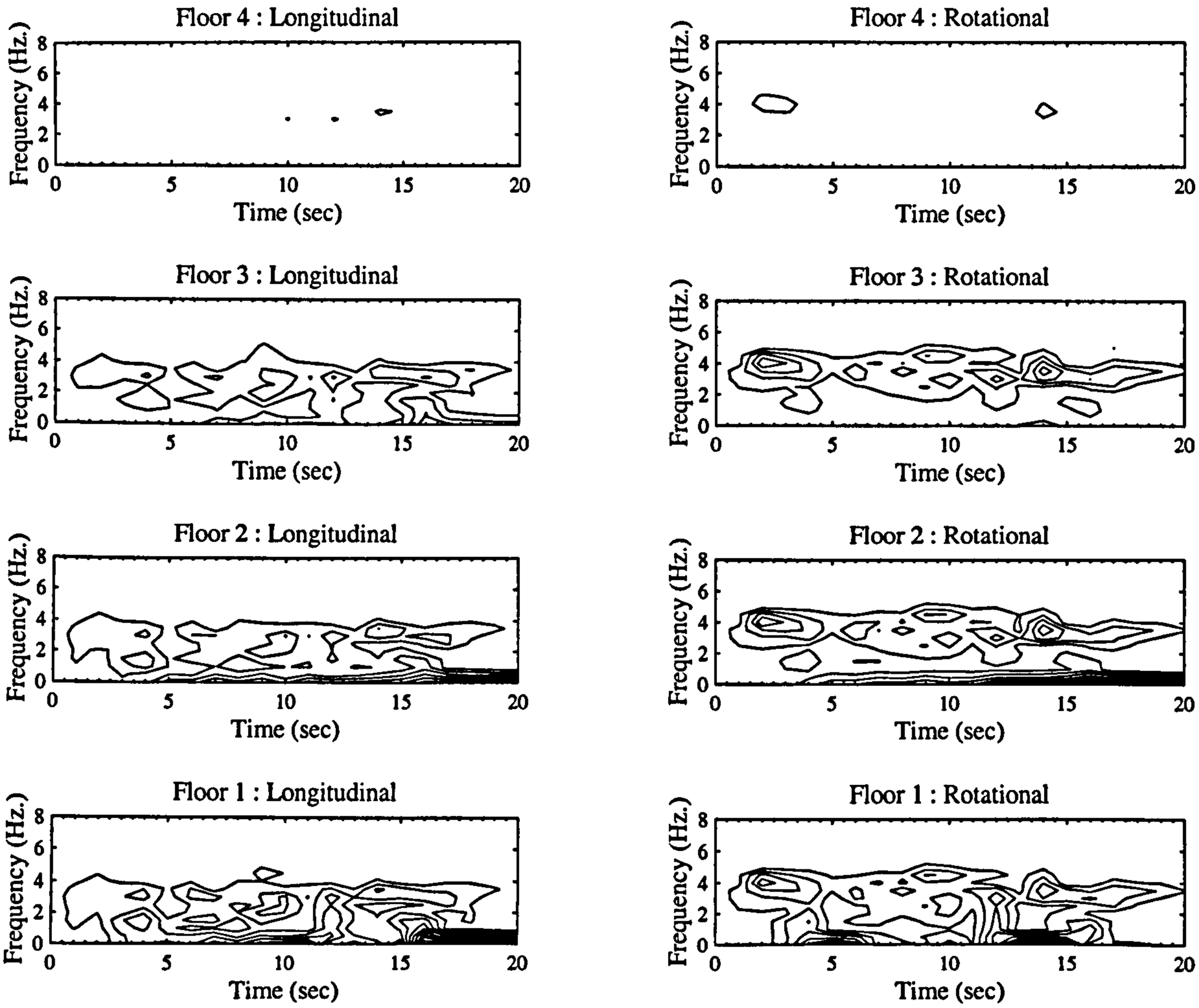

Figure 5.32: Mass configuration A6 with strength symmetry (high level forcing, 2.2%g RMSA).

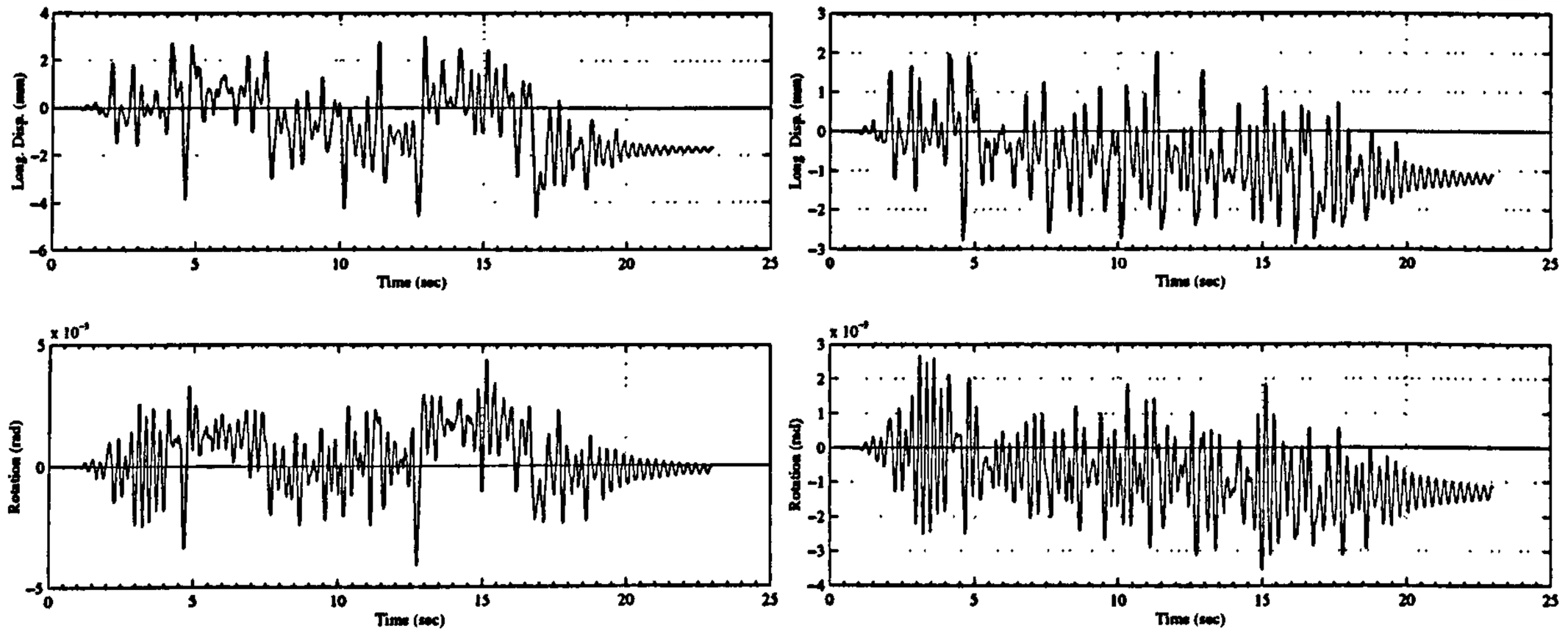

Figure 5.33: Time–history from the first two floors of model shown in Figure 5.32.

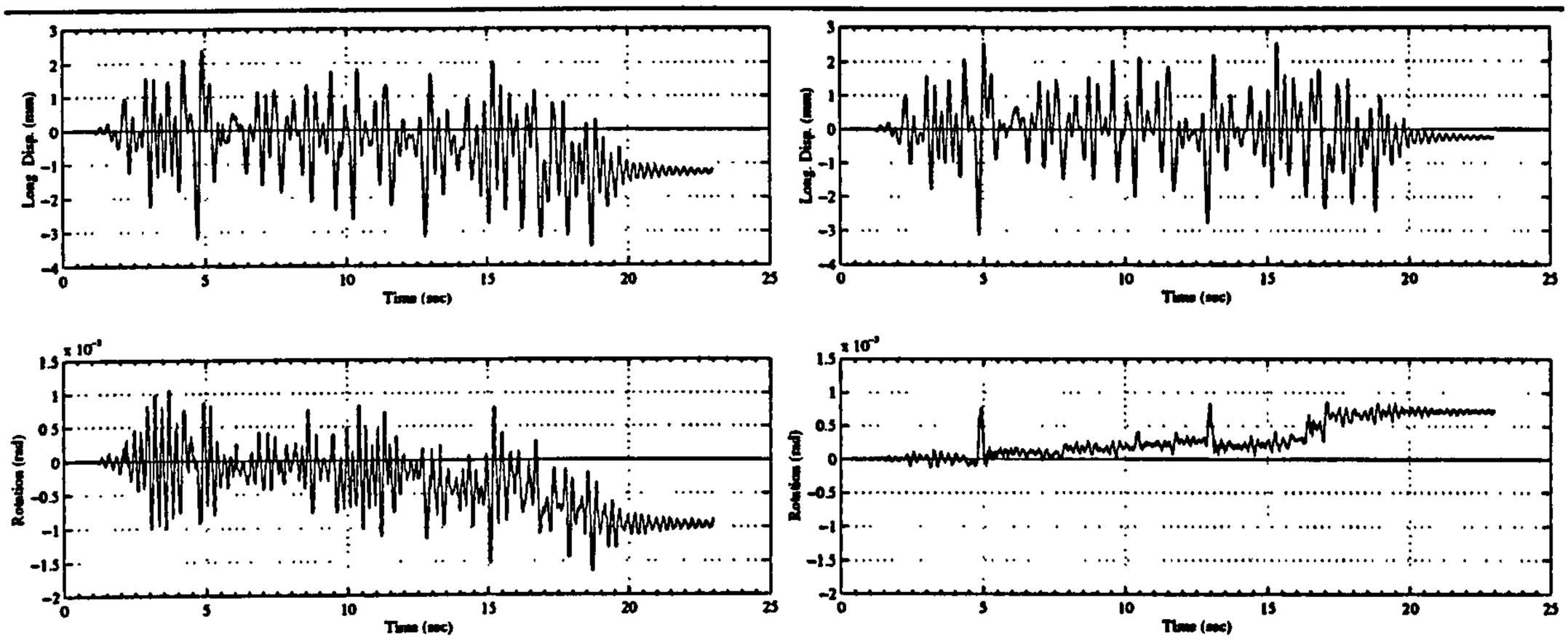

Hinge Configuration CB Hinge Configuration CD

Figure 5.34: First floor displacements for hinge configuration CB and CD at similar forcing levels with mass configuration A2.

ilar for the first 5 seconds. In absolute terms, the forcing for hinge configuration CB is larger, as the total yield strength is greater for the first floor. In observing Figure 5.34, it is obvious the floor rotation corresponding to a given floor translational displacement is greater for hinge configuration CB than for hinge configuration CD.

CHAPTER 6

HINGE UNIT PERFORMANCE

This Chapter presents results from the experimental tests relating to the behaviour and performance of the hinge unit devices. These include the effects of the hinge units on the energy absorption potential of the building models, the influence on the displacement ductility demand of the columns as a result of the hinges, and the general yielding characteristics of the models from the forcing motions.

Unlike the previous Chapter, where results of floor displacement values are recorded directly from the shake table experiments, the values of response in this Chapter are dependent on the properties and calibrations of the experimental model. These include the yielding moment of the hinges, and the length, position, and properties of the individual columns. As a result, the quality of the presented values are dependent on the accuracy of these assumptions and calibrations.

Unfortunately, instrumentation was not available to measure column moments in, or near the hinge units. Placing two strain gauges on the columns at locations near the hinge units (in a configuration similar to that used in the dynamic hinge calibration) to measure the orthogonal bending stresses in a column could have provided a valuable insight into the actual moments in the hinge units. Another benefit from this procedure would be from knowing the residual moment locked into the hinge units between tests. This would reduce the importance placed on maintaining a known hinge clamping force. However, the number of data acquisition channels required increases immensely. At least 2 (4 for the column yield configurations) additional data channels would be required for each column–floor connection being monitored, raising the number of channels for a fully instrumented floor from 3 to 23. Even recording the bending moments at a few key column locations would still be beneficial in authenticating the accuracy of the turn–of–the–nut method used to gauge the hinge moments.

The column yielding models resulted in better accuracy for estimating column forces than the beam yielding models. This is due to the more accurate and complete instrumentation

available with the column yielding model. As a result, only the hinge performance from the column yielding models are presented in this Chapter.

6.1 ESTIMATED COLUMN FORCES

The results presented in this Chapter are an extrapolated response, since their values are not measured directly by the experimental instrumentation. Rather, the hinge rotations and column end moments at the floor are predicted from the experimental floor displacements.

6.1.1 Column Displacements

The individual inter-storey column displacements are based on the acquired displacements of the "rigid" floors. All three degrees of freedom for each floor (X, Y, and Θ) are used in calculating the individual column displacements. The translational displacement of the individual columns along both the X-axis (δ_x) and Y-axis (δ_y) of floor i are:

$$\left[\delta_x\right]_i = \begin{bmatrix} (\delta_1)_x \\ \vdots \\ (\delta_5)_x \end{bmatrix}_i = \begin{bmatrix} 1 \\ 1 \\ 1 \\ 1 \\ 1 \end{bmatrix} X_i + \begin{bmatrix} -r \\ -r \\ r \\ r \\ 0 \end{bmatrix} \Theta_i \quad \text{and}$$

$$\left[\delta_y\right]_i = \begin{bmatrix} (\delta_1)_y \\ \vdots \\ (\delta_5)_y \end{bmatrix}_i = \begin{bmatrix} 1 \\ 1 \\ 1 \\ 1 \\ 1 \end{bmatrix} Y_i + \begin{bmatrix} r \\ -r \\ -r \\ r \\ 0 \end{bmatrix} \Theta_i \qquad (6.1)$$

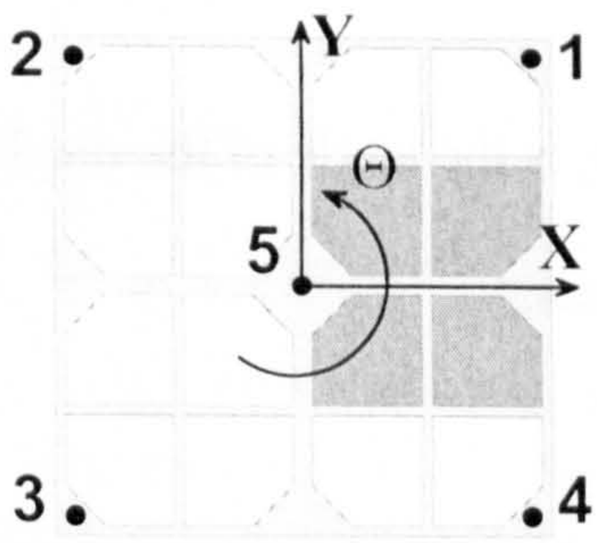

The recorded translational floor motion along the X-axis (X_i) is negligible during most experiments. In the above equation, each of the 5 columns in a floor are represented by a

row in the displacement vector, δ. The column numbers ($\delta_1 \ldots \delta_5$) are identified by the diagram adjacent to equation (6.1). The parameter, *r*, is the distance between the geometric centre of the floor, and the column in consideration, measured along one of the two principle axes (*X* or *Y*). Since the model floors are square, *r* has the same value along both axes, and is taken as 450mm.

The inter-storey column displacements are used to predict the current state of the hinge units (i.e. slipping or non-slipping). The yielding surface of the hinges, as shown by the dynamic hinge calibration (Figure 4.7 on page 92), is circular. As such, the magnitude of a column's displacement for storey *i* (between floors *i* and *i*-1), Δ_i, is used to determine the state of the hinge units for that column:

$$\Delta_i = |\delta_i| = \sqrt{([\delta_x]_i - [\delta_x]_{i-1})^2 + ([\delta_y]_i - [\delta_y]_{i-1})^2} \tag{6.2}$$

The direction of the displacement magnitude is calculated by:

$$\phi_i = \text{atan}\left(\frac{[\delta_y]_i - [\delta_y]_{i-1}}{[\delta_x]_i - [\delta_x]_{i-1}}\right) \tag{6.3}$$

where, ϕ_i is the angle of the displacement magnitude for storey *i*, with respect to the positive X-axis.

Figure 6.1 shows the inter-storey displacement traces for the first storey exterior columns of two typical models. These plots are presented in polar coordinates (ϕ, Δ). In this Chapter, the peak column displacements and forces used to determine displacement ductility and absorbed hysteretic energy are in terms of polar coordinates.

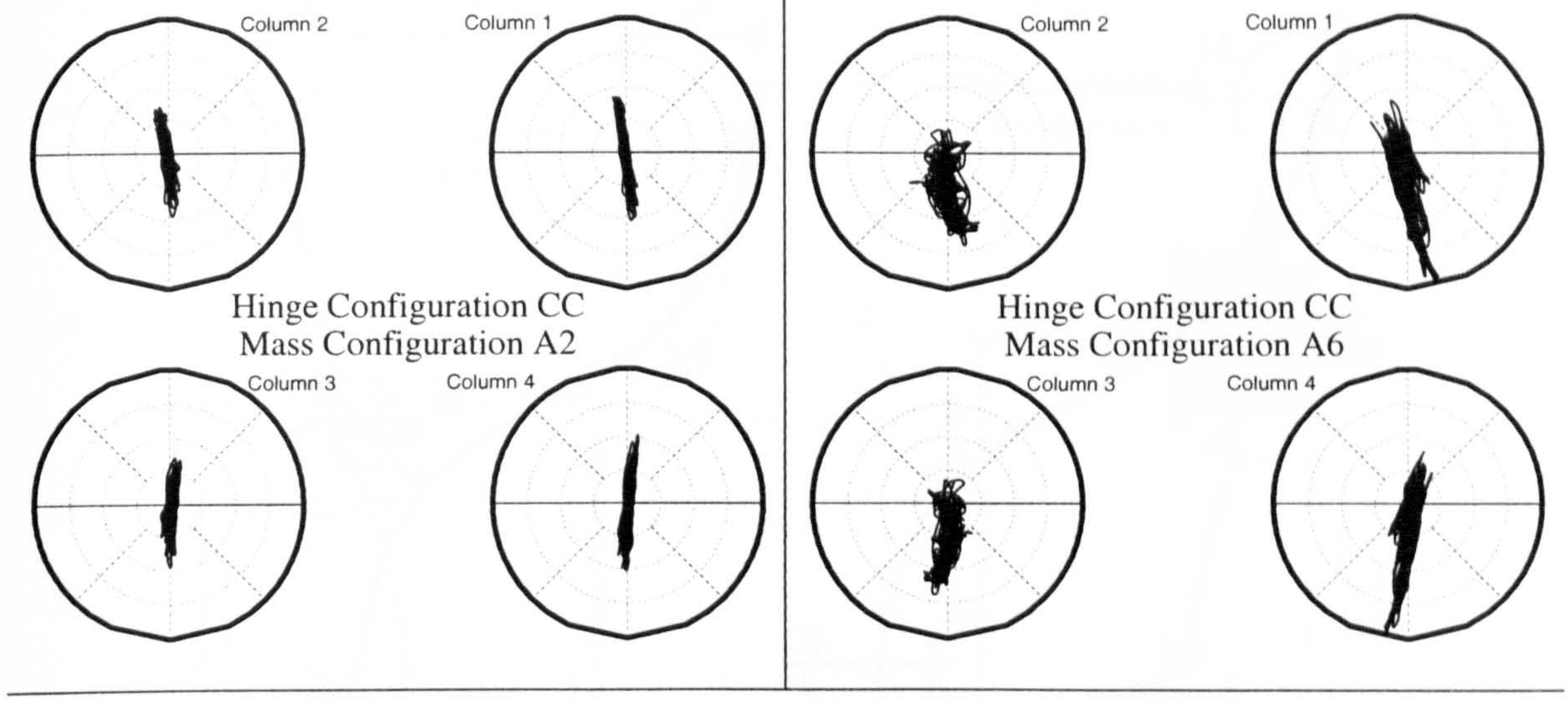

Figure 6.1: First storey displacement traces at the exterior columns.

6.1.2 Estimated Column Forces

Estimating the column forces from the displacement magnitude of each column is not a direct relationship. Rather, the inter-storey displacement magnitude for each column is separated into its *elastic* (Δ_e), and *plastic* (Δ_p) component:

$$\Delta = \Delta_e + \Delta_p \tag{6.4}$$

6.1.2.1 Elastic Displacement

The displacement to force relationship for the elastic displacement component is taken as that of a Euler beam:

$$\begin{bmatrix} V \\ M_t \\ M_b \end{bmatrix} = \frac{EI}{L^3} \begin{bmatrix} 12 & 6L & 6L \\ 6L & 4L^2 & 2L^2 \\ 6L & 2L^2 & 4L^2 \end{bmatrix} \begin{bmatrix} \Delta_e \\ \Theta_t \\ \Theta_b \end{bmatrix} \tag{6.5}$$

The above relationship does not consider second order effects, such as P–Δ, or geometric stiffness. The top and bottom elastic rotations of the column ends are defined as Θ_t and Θ_b, respectively. The left side of Equation (6.5) represents the horizontal column shear

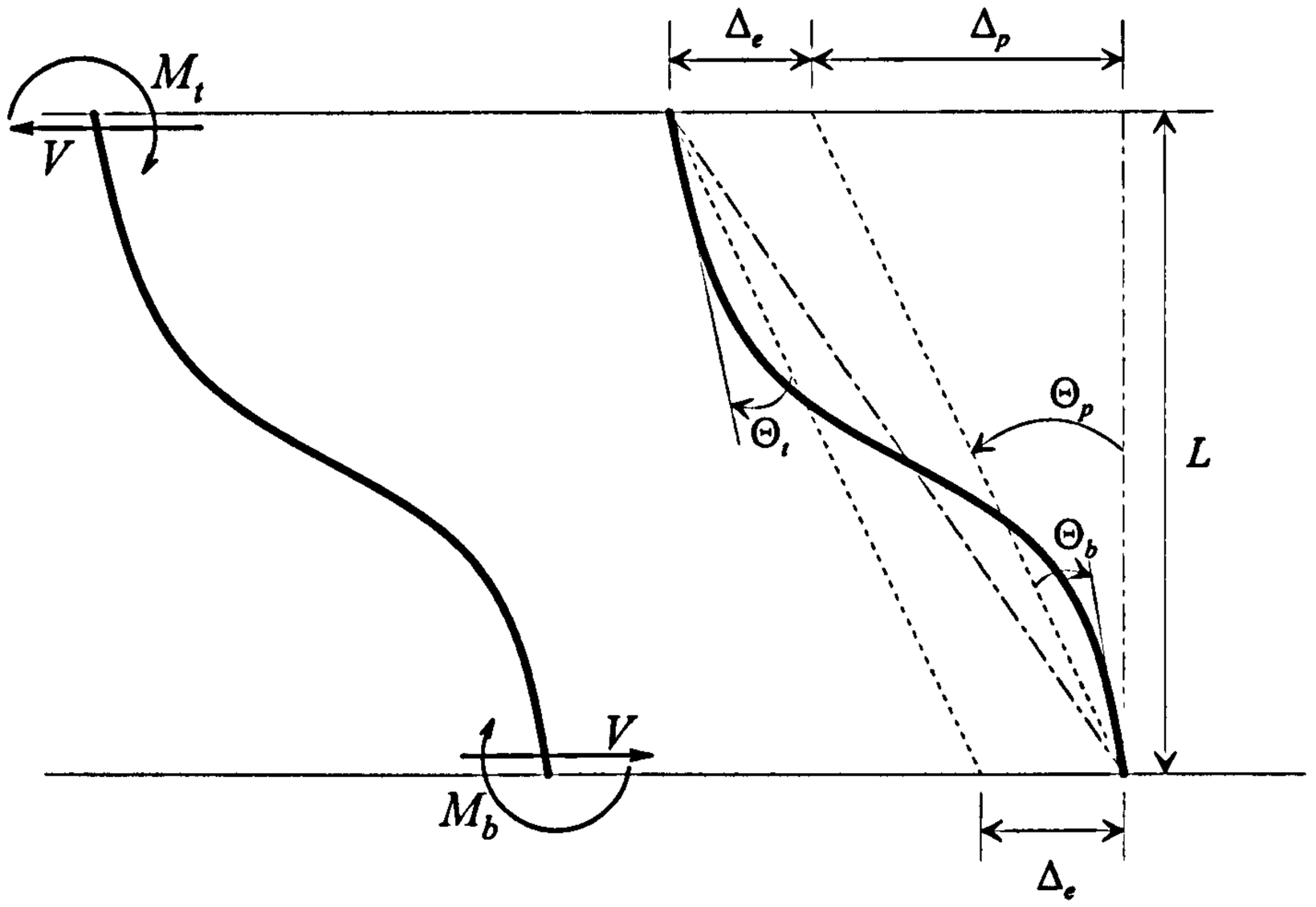

Figure 6.2: Force and displacement definitions for a typical column.

force, V, and the bending moments at the top ($M_t < M_{pt}$) and bottom ($M_b < M_{pb}$) of the column. The Young's modulus of the column is represented by E, and L defines the distance between the centres of rotation of the hinges at each end of the column (i.e. distance between floor centrelines).

6.1.2.2 Plastic Displacement

The effective column lengths based on either the interior (12mm diameter) or exterior (8mm diameter) column vary during a strong response. As seen in Figure 6.3, the effective column length measurements are different during the elastic and plastic states of the hinge units. The column yielding model has an effective elastic column length that is much less than its effective length while yielding. This is a result of the point of fixity being near the clamping collets while elastic, and the centre of hinge rotation coinciding with the floor centreline while plastic. This is accounted for in equation (6.5) by having $L = L_p$, and the moment of inertia for the column varies between that of the column, and that of the hinge

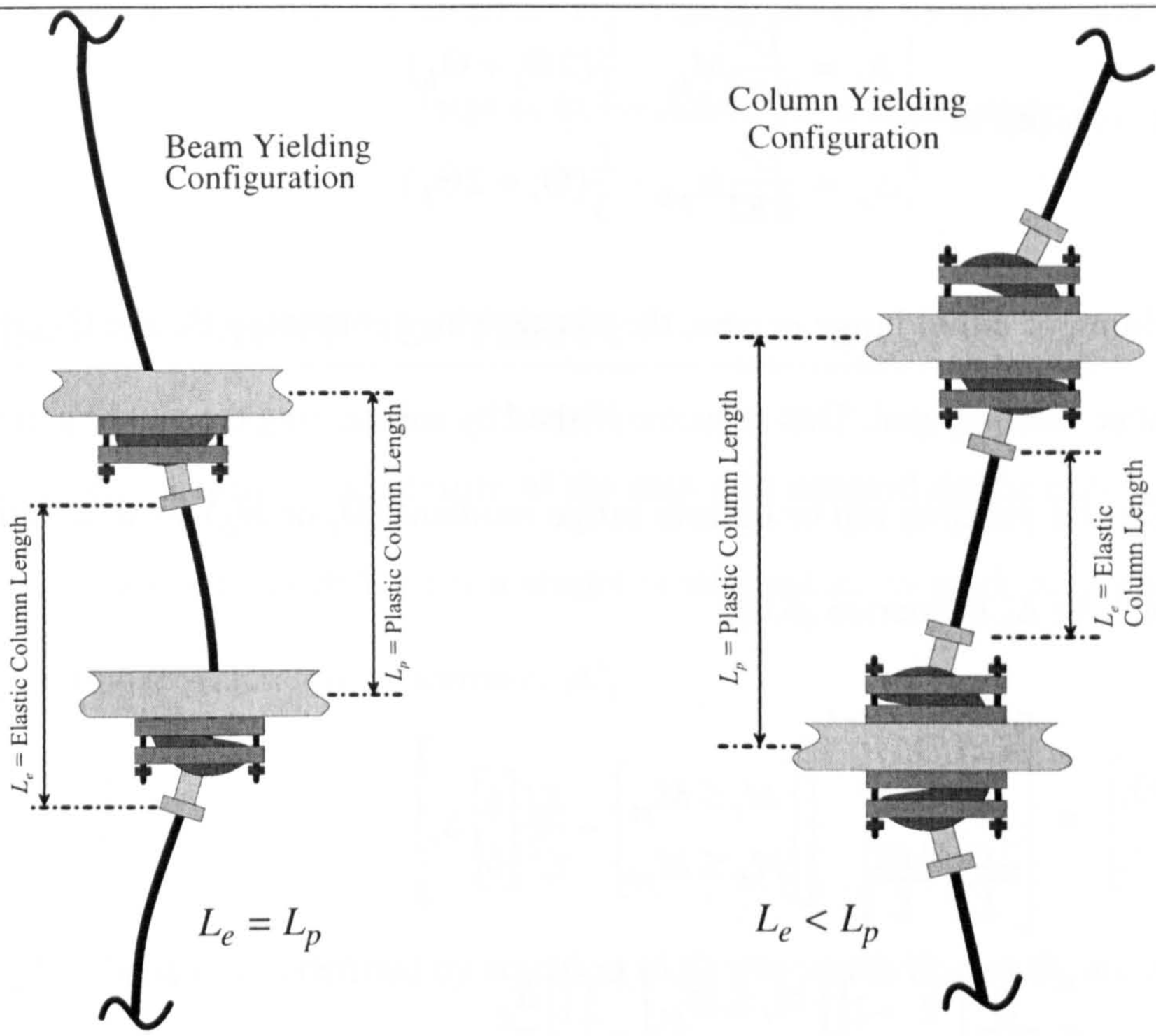

Figure 6.3: Comparison of inter-storey column lengths during elastic (L_e) and inelastic (L_p) behaviour.

bell. Of course, equation (6.5) becomes more complicated, but it can still be condensed back down to a 3×3 matrix. For brevity, all of the equations in this Section are presented in terms of a uniform I.

The column displacements (Δ_e, Θ_t, and Θ_b) are all zero at the beginning of the shake table test. At the onset of yielding (friction slip) of one of the hinge units, the column end moments (M_t or M_b) are limited to their calibrated yielding moment (M_{pt} or M_{pb}, respectively). The column displacement at which yielding first occurs (Δ_y) is the smaller of the two displacements at which the top hinge yields (Δ_t), or the bottom hinge yields (Δ_b) in the storey:

$$\Delta_y \text{ is lesser of } \begin{cases} \Delta_t = \dfrac{L^2}{6EI} M_{pt} - \dfrac{L}{3}(2\Theta_t + \Theta_b) \\ \Delta_b = \dfrac{L^2}{6EI} M_{pb} - \dfrac{L}{3}(\Theta_t + 2\Theta_b) \end{cases} \tag{6.6}$$

Once yielding of either hinge occurs, the elastic hinge rotations (Θ_t and Θ_b) in Equation (6.5) must be re-computed. This is accomplished by substituting the yielding moment (M_{pt} or M_{pb}) for the yielding top or bottom hinge moment (M_t or M_b), as determined by the smaller of Δ_t or Δ_b (Equation (6.6))

$$\begin{aligned} \begin{bmatrix} \Theta_t \\ \Theta_b \end{bmatrix} &= \begin{bmatrix} \dfrac{4EI}{L} & \dfrac{2EI}{L} \\ \dfrac{2EI}{L} & \dfrac{4EI}{L} \end{bmatrix}^{-1} \left[\begin{bmatrix} M_t \le M_{yt} \\ M_b \le M_{yb} \end{bmatrix} - \frac{EI}{L^2} \begin{bmatrix} 6 \\ 6 \end{bmatrix} \Delta_e \right] \\ &= \frac{L}{6EI} \begin{bmatrix} 2 & -1 \\ -1 & 2 \end{bmatrix} \begin{bmatrix} M_t \le M_{pt} \\ M_b \le M_{pb} \end{bmatrix} - \begin{bmatrix} 1 \\ 1 \end{bmatrix} \frac{\Delta_e}{L} \end{aligned} \tag{6.7}$$

This equation is essentially that of a cantilever column, with an applied moment (M_p) at the free end. The corresponding end rotations (Θ_t or Θ_b) are then used for subsequent calculations.

Once both hinges yield simultaneously, a local mechanism is formed, which results in a permanent deformation in the inter-storey column displacement (Δ_p). This plastic deformation can be computed by the following:

$$\Delta_p = \Delta - \frac{L^2}{12EI}(M_{pt} + M_{pb}) \tag{6.8}$$

From the total plastic displacement, Δ_p, the total plastic rotation, Θ_p, can be calculated:

$$\Theta_p \approx \frac{\Delta_p}{L} \tag{6.9}$$

Although the above equations are based on small angle theory, the plastic displacements recorded in this study were not too large as to invalidate these assumptions.

6.2 DISPLACEMENT DUCTILITY

The displacement ductility is a measure of the response demand on the columns. In this study, the displacement ductility for a storey is defined as its peak displacement, Δ, divided by its initial yielding displacement, Δ'_y :

$$\mu_\Delta = \frac{\Delta}{\Delta'_y} \tag{6.10}$$

where, Δ'_y for the storey is defined by equation (6.6) when both Θ_t and Θ_b are zero.

Figure 6.4 shows the peak displacement ductility of the first floor exterior columns for various mass and hinge configurations of the column yielding model. For the symmetric strength distribution (hinge configuration CB), an increase in mass eccentricity adversely affects the side closest to the centre of mass (right side frame). Conversely, for symmetric mass eccentricity (S1), increasing the strength eccentricity increases the displacement ductility demand on the left side frame. As a better visualization of the ductility demand difference for the two sides, Figure 6.5 shows the demand ratio of the right side normalized by that of the left side. In other words, a peak displacement ductility demand ratio greater than unity indicates that the right side of the building model is more vulnerable then the left side. As shown for all mass configurations in Figure 6.5, increasing the strength eccentricity reduces the vulnerability of the right side frame. Conversely, increasing the mass eccentricity increases the vulnerability of the right side frame.

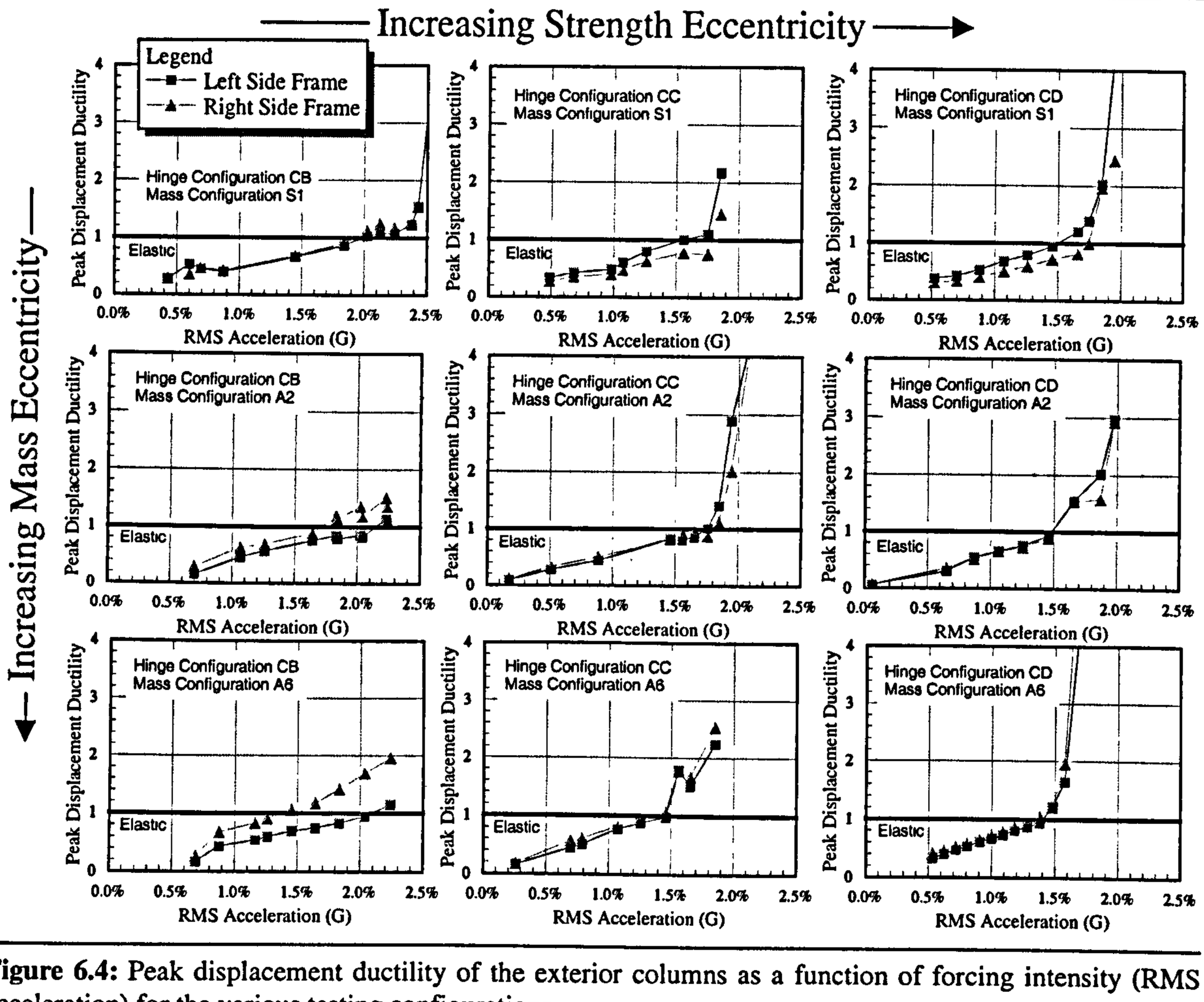

Figure 6.4: Peak displacement ductility of the exterior columns as a function of forcing intensity (RMS acceleration) for the various testing configurations.

6.3 COLUMN YIELDING FORCE INTENSITY

This section identifies the shake table forcing intensity at which the left, right, and centre columns start to yield. This is also the forcing intensity at which the peak ductility lines in Figure 6.4 cross the line indicating a displacement ductility of unity.

The centre column, due to its strength deficiency, starts to yield at a forcing intensity of about 1/5 of that of the most vulnerable exterior column. This is shown in Figure 6.6 for the three main column yielding hinge configurations. The centre column does not remain elastic above an RMSA of 0.4% g. Referring back to Figure 6.4, it is now evident that the

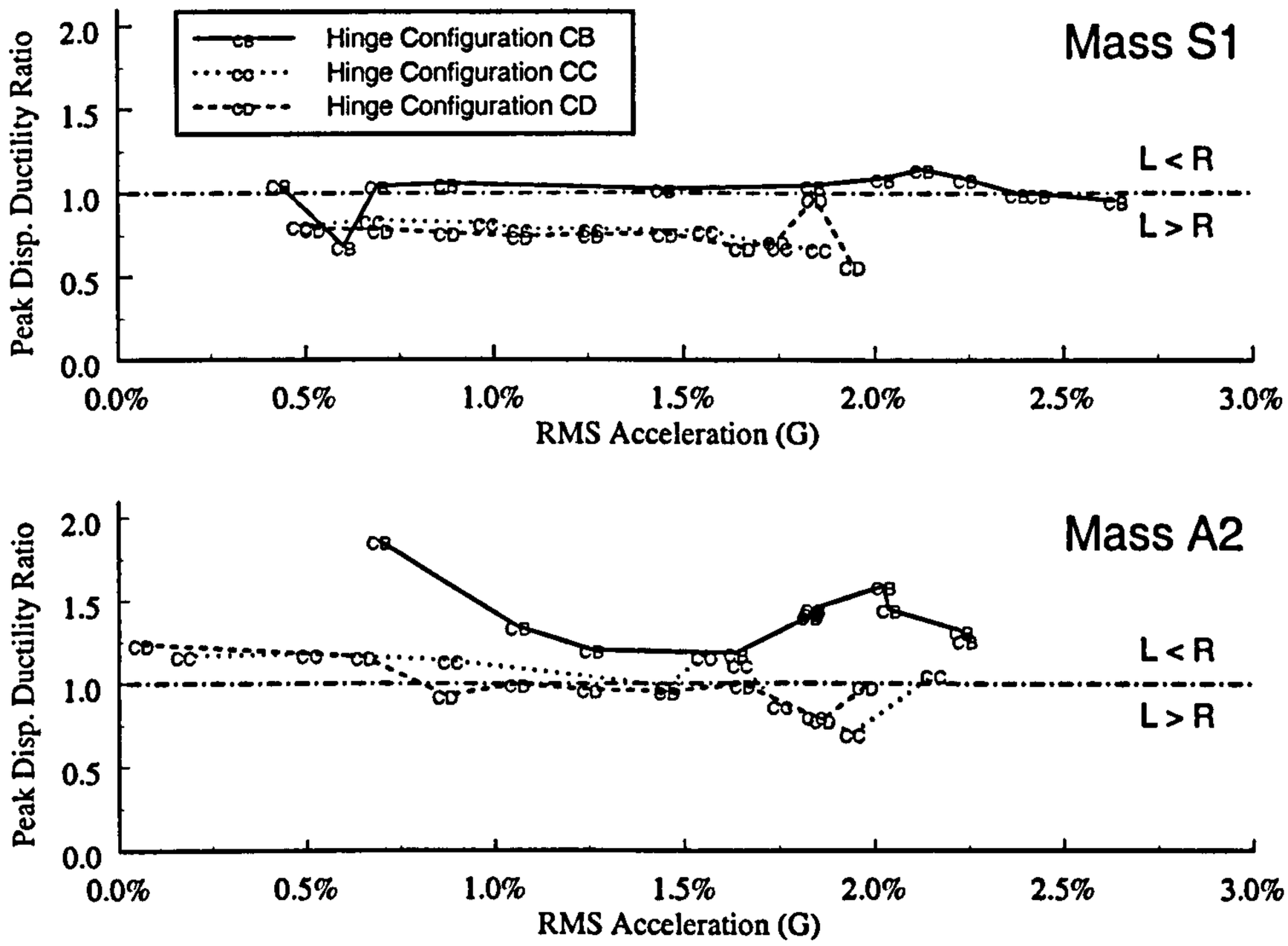

Figure 6.5: Exterior bent ductility difference for the column yielding models.

centre column experiences plastic behaviour at even the lowest tested shaking intensities for all but three model configurations. Lower shaking intensities were not feasible, as this would have resulted in a very low signal to noise ratio of the recorded table acceleration and floor displacements. In these situations, the RMSA values were interpolated between $\mu_\Delta=0$ at RMSA=0 and the lowest μ_Δ with a realistic RMSA. In hindsight, the yielding moment magnitude of the centre column should have been increased by changing the friction pad material from PTFE (M_p=13.3N·m) to Stainless Steel ($M_p\cong$31N·m). PTFE was

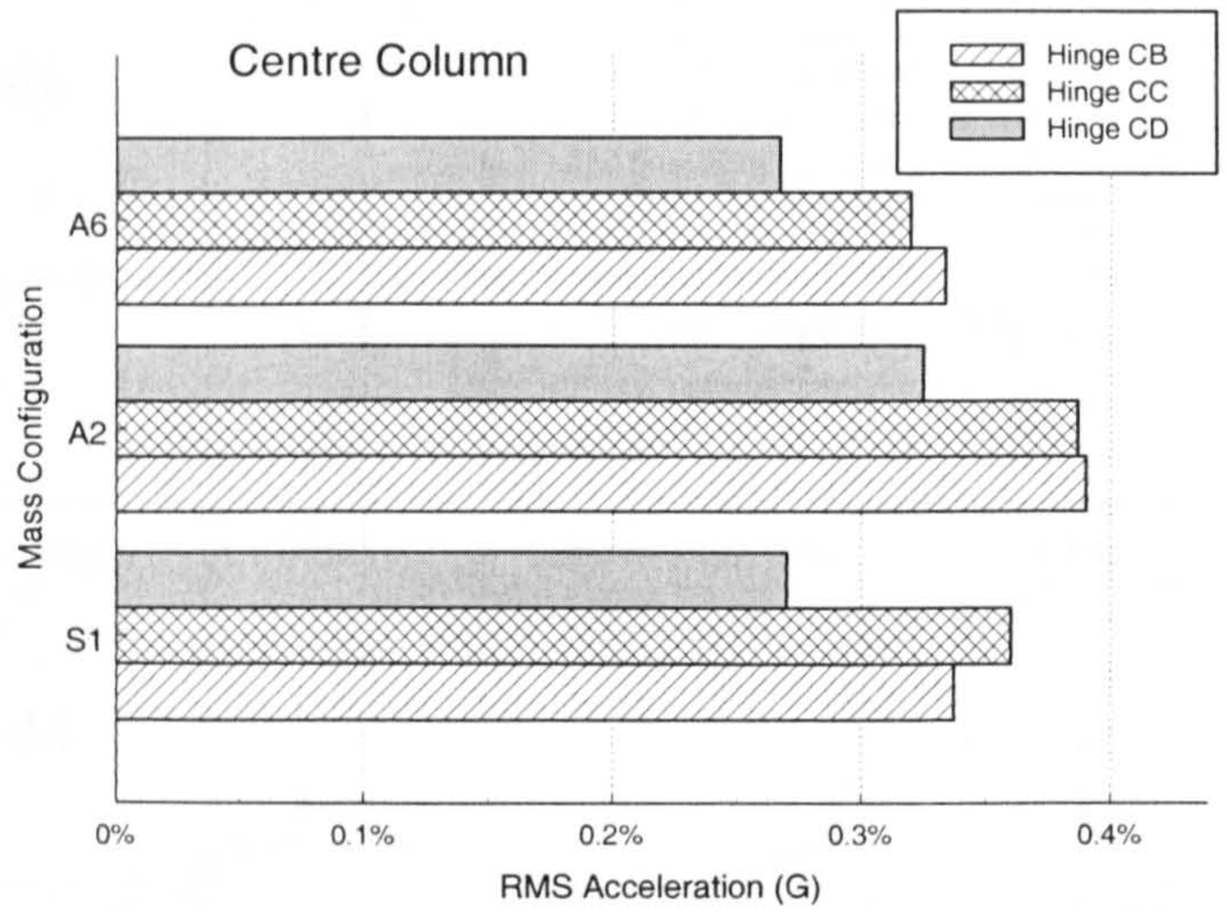

Figure 6.6: RMSA at which yielding first occurs in the centre column.

used because of its low plastic moment variance, and for consistency with the other hinge units in the model. The yielding of the centre column wasn't evident until the acquired displacements were transformed into forces by equation (6.5). Appendix C (Section C.5 on page 264) presents modifications to the experimental/analytical model for a UBC94 code compatible strength distribution. Appendix D presents the results from these modifications on an analytical model.

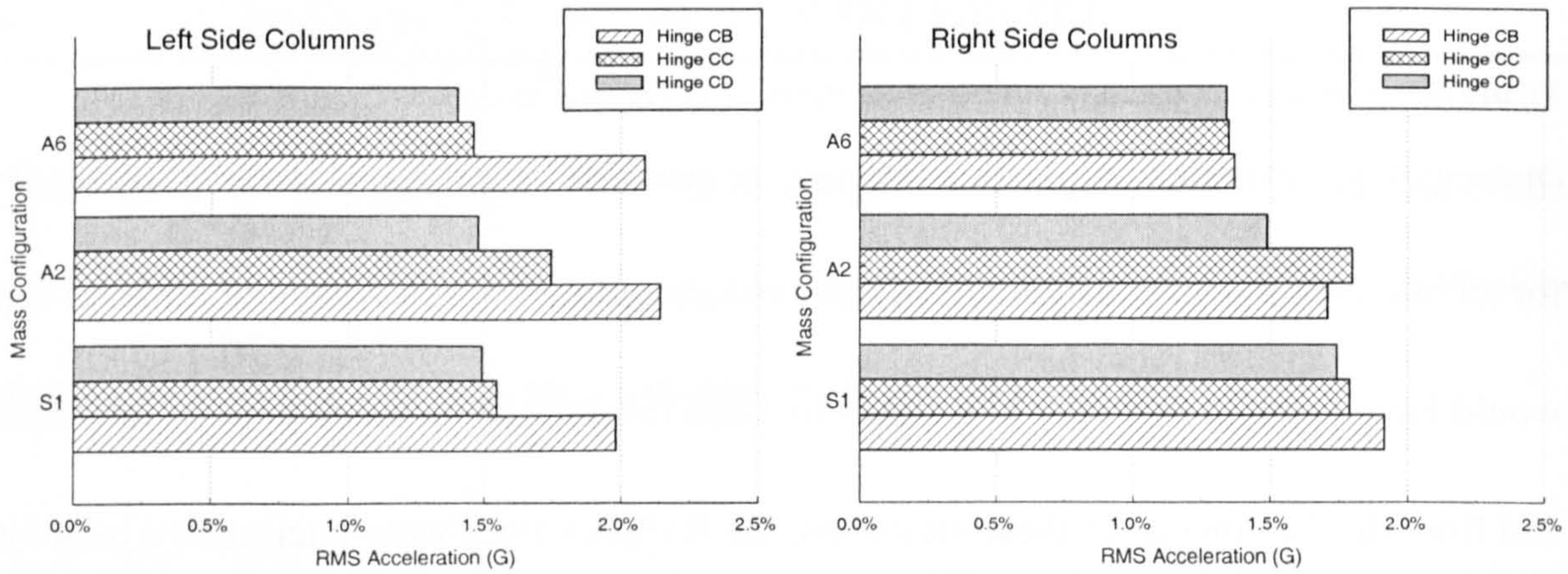

Figure 6.7: RMSA at which yielding first occurs in the two exterior bents of the column yielding models.

Figure 6.7 indicates the RMSA of the table base acceleration which causes the yielding of an exterior bent in one of the specified hinge configurations. The yielding RMSA values indicated are estimated by linear interpolation on the displacement ductility between successive elastic ($\mu_\Delta<1$) and inelastic ($\mu_\Delta\geq1$) bent responses. From Chapter 4 (Table 4.1 on page 88), hinge configurations CC and CD reduce the yielding strength of the left side columns by 25% from that of hinge configuration CB. The effect of this strength reduction is easily observed by the average yielding RMSA reduction of about 25% from that of hinge configuration CB. This same type of reduction is observed in Figure 6.6, as the centre columns strength is also reduced in hinge configuration CD. Since the centre column yields at a lower yielding RMSA, both sides must mobilize a larger resisting force with hinge configuration CD at the same RMSA. As a result, the yielding RMSA for hinge configuration CD is the lowest for all three hinge configurations. Concentrating on the right side of the structure, it is shown that this side becomes more vulnerable as the mass eccentricity increases. However, the vulnerability decreases when the mass eccentricity and strength eccentricity are similar (mass A2, hinge CC). This is also the true for the left column of the same configuration, which has the same level of vulnerability as the right column (i.e. both sides yield as approximately 1.7%g RMSA). The left side of the model does not have a strong correlation between vulnerability and mass eccentricity. The yielding RMSA difference between the exterior bents for the symmetric mass (S1) and symmetric strength (hinge CB) case should be zero. The value shown of almost 4% suggests the error inherent in both the experimental model, and its calibration.

Figure 6.8 shows the difference between the yielding RMSA of the right side and that of the left side. For all of the three hinge configurations shown, the right side becomes more

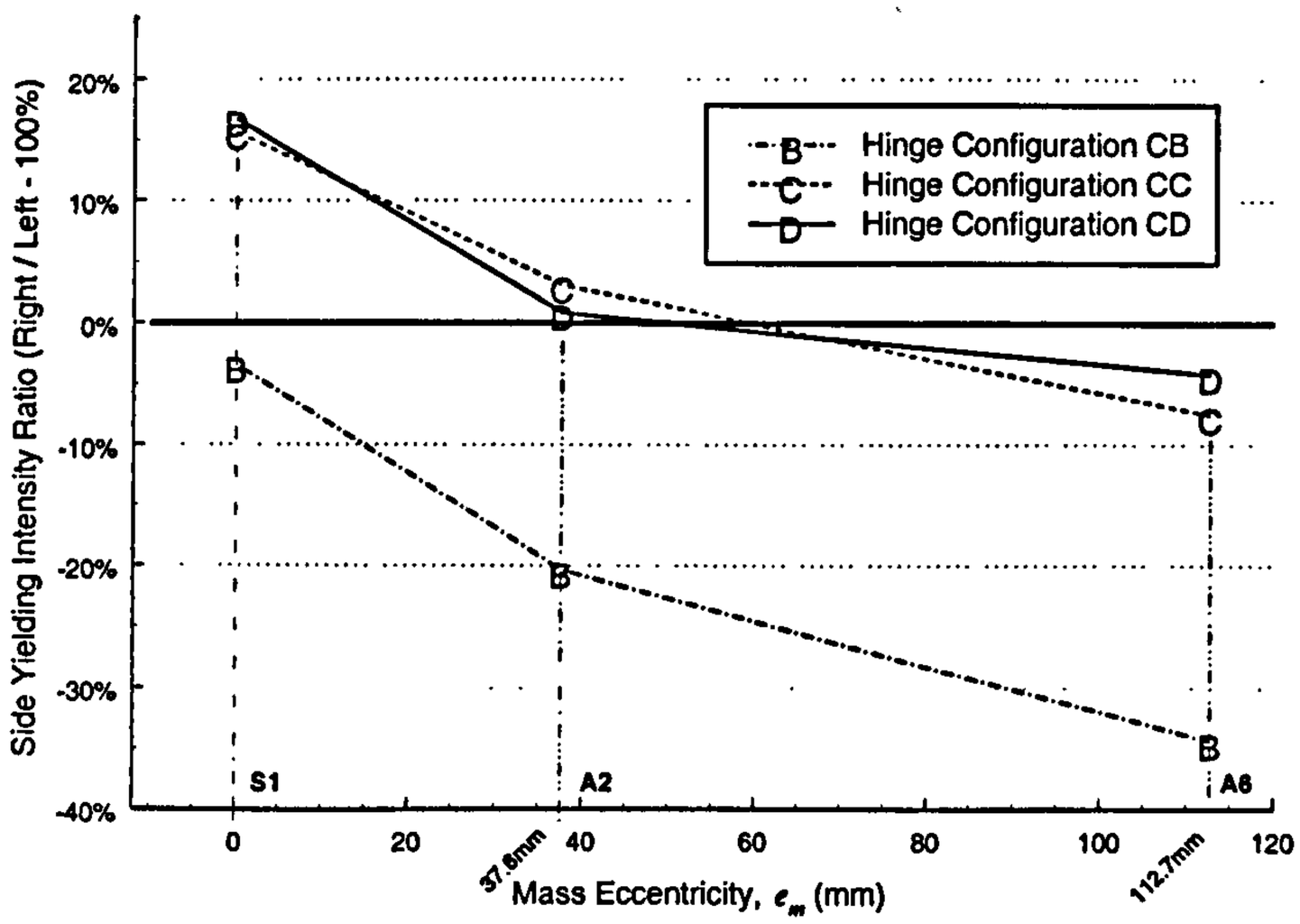

Figure 6.8: Yielding RMSA difference between the right and left sides of the models.

vulnerable with respect to the left side as the mass eccentricity increases (the centre of mass moves closer to the right side). Ideally, when the two sides have the same level of vulnerability (0% difference), the result is a more economical design.[1]

6.4 HINGE ENERGY ABSORPTION

The moment based absorbed hysteretic energy is defined as the net area enclosed by the moment verses curvature graph of a plastic hinge in a column. Since the experimental models in this study are non-destructive, no part of the column length or plastic hinge unit experiences true yielding. Therefore, with zero plastic curvature, there is zero absorbed hysteretic energy. However, the hinge units do absorb energy through friction, which from the design of the hinge units is very similar to hysteretic damping.

1. This is for design economy based on strength, which may or may not satisfy code serviceability (stiffness) requirements.

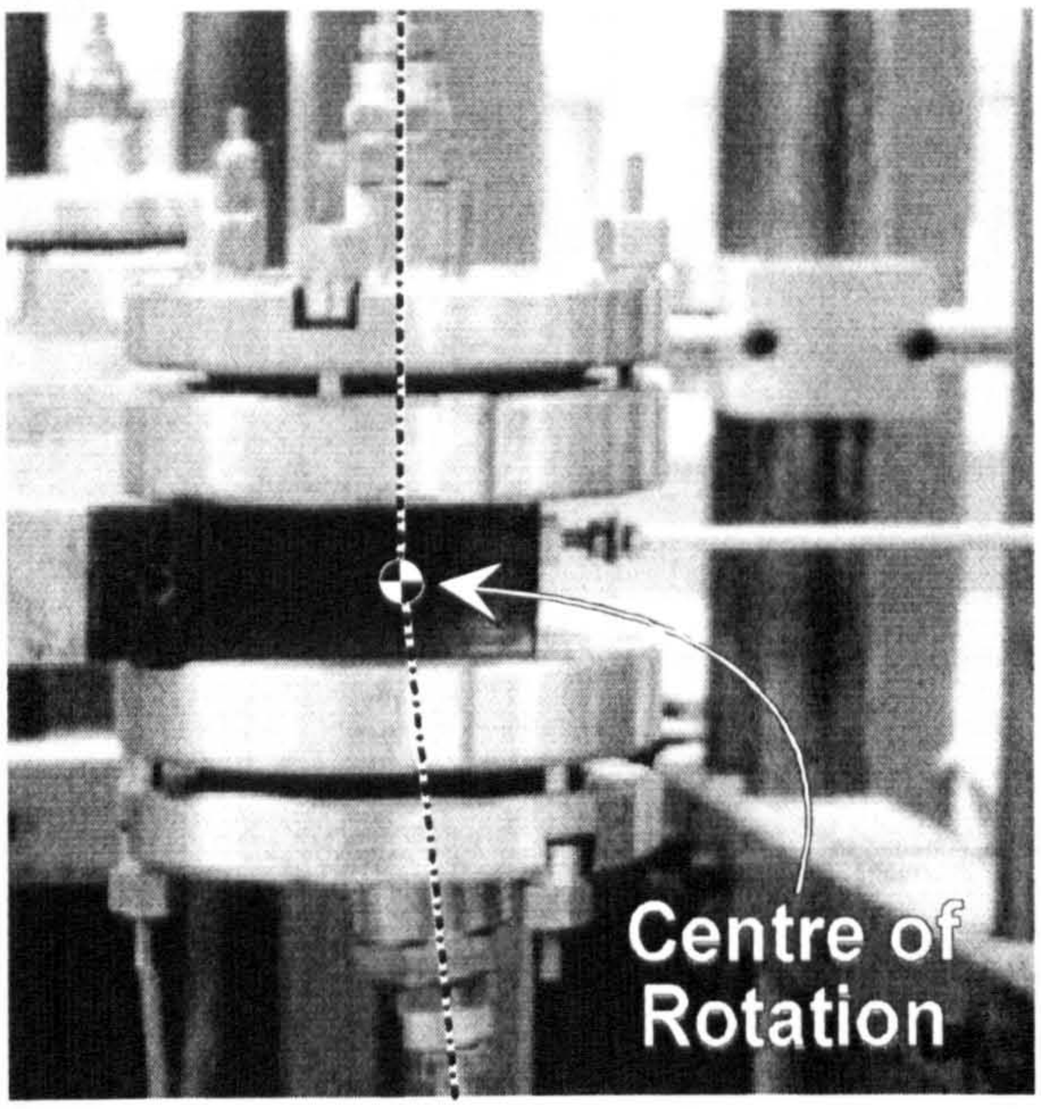

a) Centre of rotation for a typical hinge unit; column yielding configuration shown.

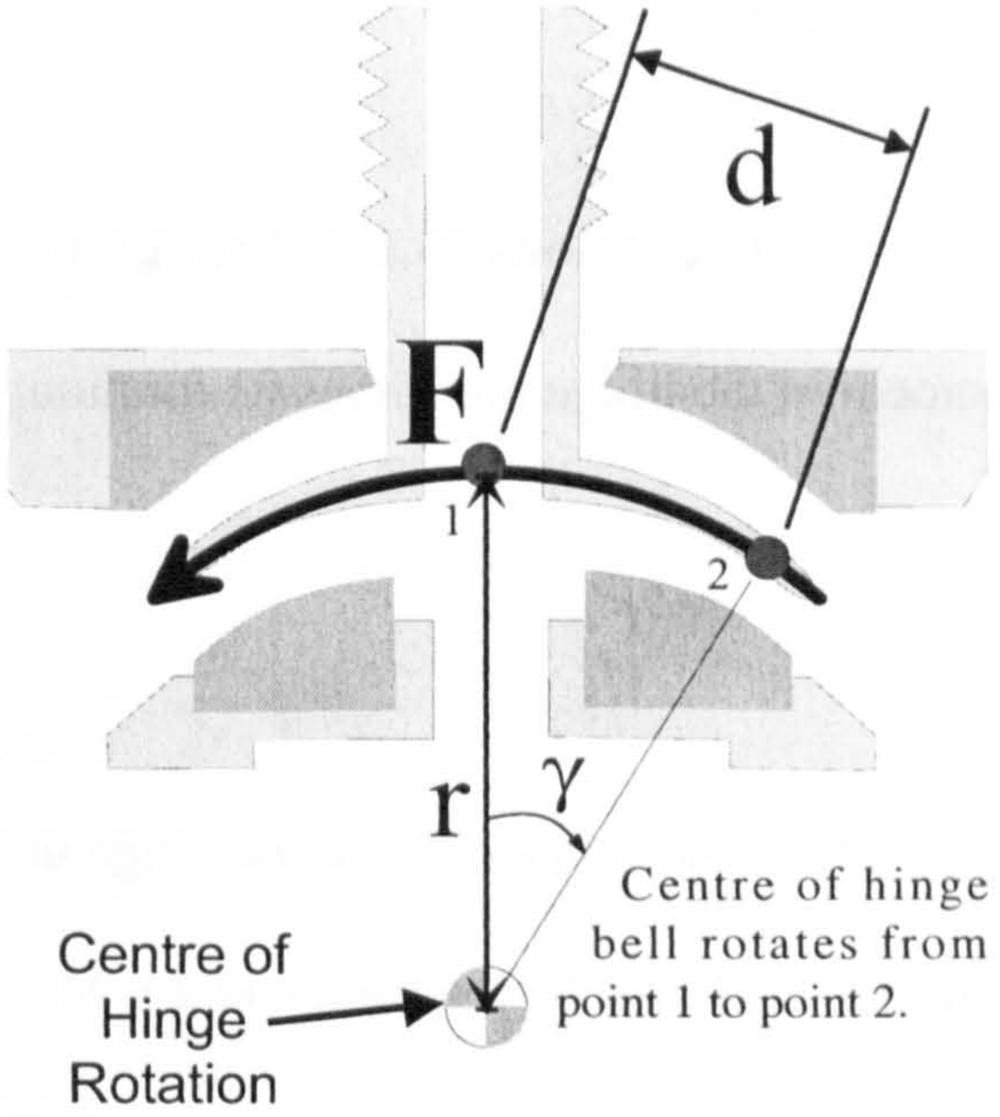

b) Cross-section of a typical hinge unit, with friction force components.

Figure 6.9: Centre of rotation and friction force components for a typical hinge unit.

Figure 6.9 shows the cross-section of a typical hinge unit. As a point on the hinge bell surface moves from point 1 to point 2, as shown, a friction force, F, is generated. This friction force is in the direction opposite the motion of the hinge rotation, and as a result absorbs a quantity of energy, E_c. This is termed *Coulomb* damping, and the energy absorbed is defined as:

$$E_c = Fd \tag{6.11}$$

where, d is the distance a point along the friction surface is moved. For the small angles of rotation experienced in the hinge units, d can also be defined as:

$$d = r\gamma \tag{6.12}$$

where, γ is the rotation of the hinge unit. The "yielding" moment in the hinge unit is the product of the friction force, F, and the distance of this force from the centre of hinge rotation, r:

$$M = Fr \tag{6.13}$$

Combining equations (6.11) through (6.13) result in the absorbed energy being the moment in the hinge unit times its rotation:

$$E_c = M\gamma \tag{6.14}$$

Hence, the absorbed energy in the hinge units is similar to that for hysteretic damping, but in terms of Moment–Rotation, and not Moment–Curvature.

The total absorbed energy of the first storey as a function of time for hinge configuration CC is shown in Figure 6.10. Because of its strength deficiency, the hinges on the centre column rotate often throughout the time-history, resulting in a greater energy absorption than the exterior columns. The energy absorbed by the left or right columns is the combined contribution of both exterior columns. The main quantity of interest in Figure 6.10 is the total absorbed energy for each column at the end of the time-history, as this can be related to a damage demand on the columns.

Figures 6.11 and 6.12 show the total absorbed energy by the hinge units in the first storey for hinge configurations CB and CC, respectively. With symmetric strength configuration (hinge CB), the energy absorbed by the right side of the first storey increases as the centre of mass is moved toward that side. The left side of the model isn't affected significantly by a change in the centre of mass. Reducing the strength of the left side of the columns (Figure 6.12), more energy is absorbed at lower forcing intensities.

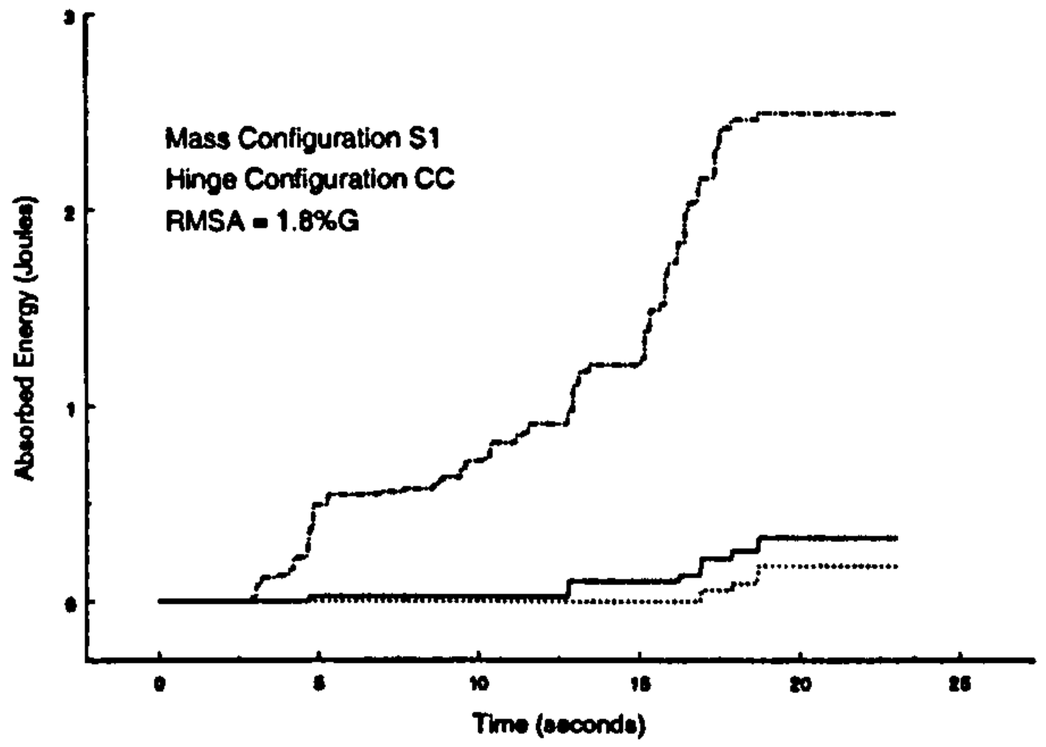

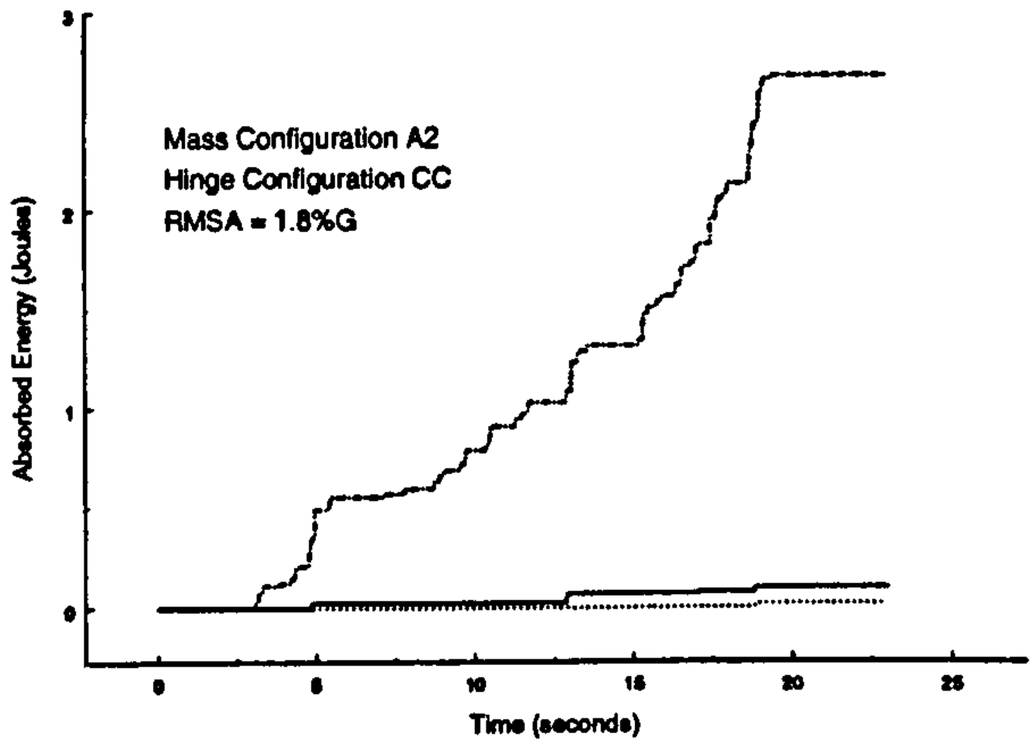

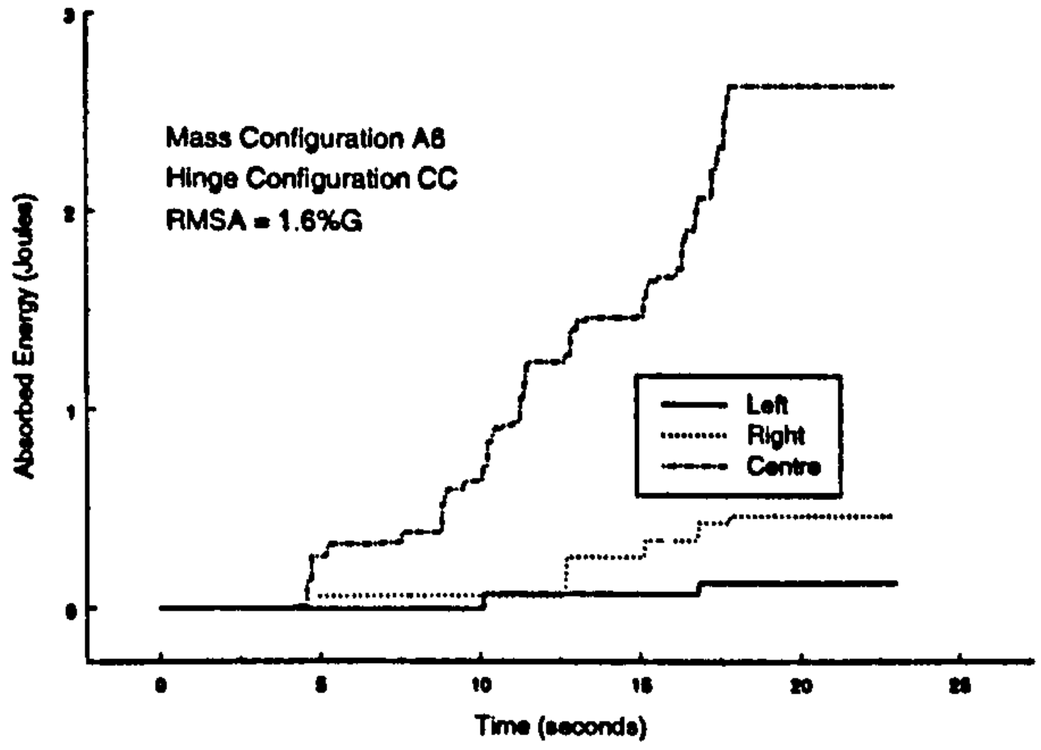

Figure 6.10: Absorbed energy verses time for three models at high forcing intensity.

6.5 CONCLUSION

The hinge units are intended to simulate experimentally the member plasticity in non-destructive shake table testing. To this extent, the hinge units performed remarkably well, as over 500 multi-storey tests[1] of varying intensity were performed over a total of 3 weeks. The design of the hinge units can also simulate hysteresis[2] in the hinge units by means of Coulomb damping. Unfortunately, the means of instrumenting the building

1. A total of 260 beam yielding tests, and 264 column yielding tests. These numbers exclude the elastic, single-storey uniaxial, single-storey biaxial, and damping tests.
2. The simulated hysteresis loops generated by the hinge units are perfectly rectangular (i.e. 90° between the elastic and plastic slopes), since they are based on hinge rotation and not member curvature

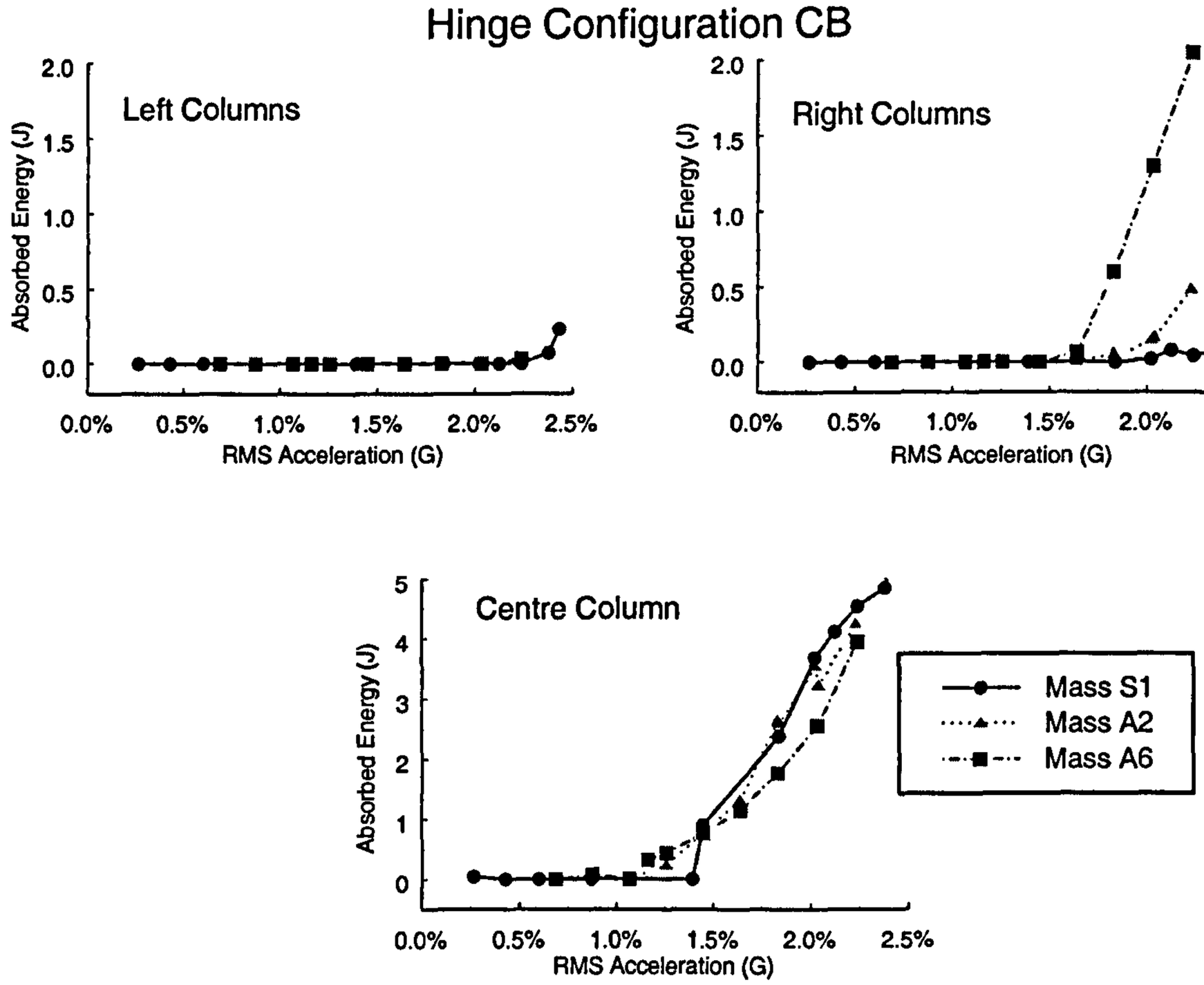

Figure 6.11: Total absorbed energy for hinge configuration CB.

model were based on a prior research grant (GR/E/83641) which was concerned with the elastic modes and displacements of the floors. As a result, the full benefit of the hinge units could not be fully explored.

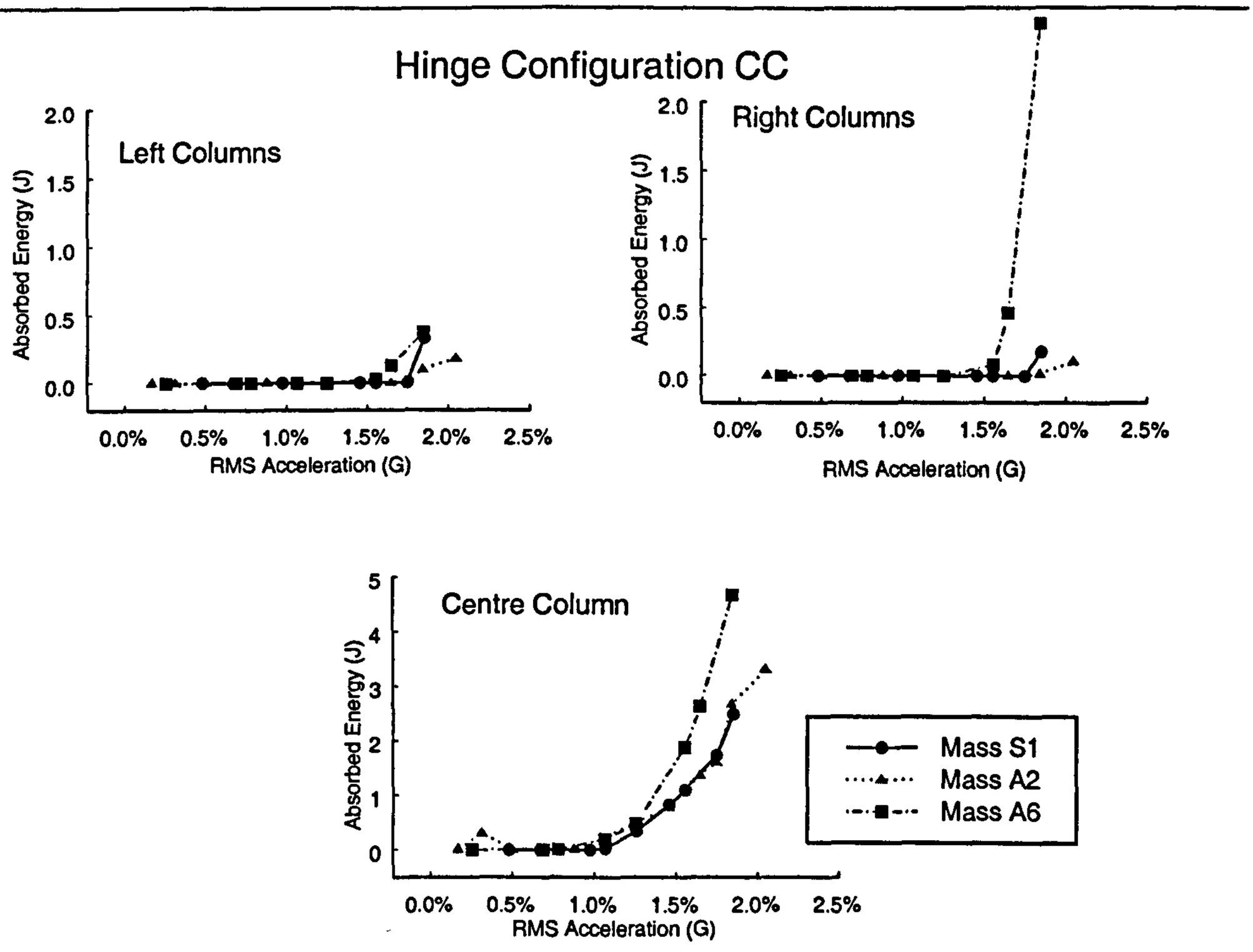

Figure 6.12: Total absorbed energy for hinge configuration CC.

CHAPTER 7

ANALYTICAL STUDY

In addition to the experimental study discussed in Chapter 5, an analytical study including both elastic and inelastic response was performed on some of the four storey model configurations. As mentioned in Chapter 3, the experimental model can be easily rendered as an analytical model with minimal assumptions, as this was one of the design goals of the experimental model. In previous analytical studies, the degrees of freedom in an analytical model have been kept to a minimum, with only the rotation and translation of each floor being considered. Also, the structural members in previous studies have dealt mainly with shear walls contributing to the only inelastic behaviour. In this study, the analytical model

tries to match the behaviour of the experimental model. A difference between this and many other analytical models is that five column members in each storey supply the structural stiffness, and that member plasticity is concentrated at specific locations in the columns (column yielding) or perimeter beams (beam yielding) of the model. As a result, the number of degrees of freedom of the computer model in this study has been increased significantly compared to previous analytical models. A commercial, general-purpose finite element program, MSC/NASTRAN (version 68.2.5), was used in performing this analytical study. Appendix B describes the numerical methodology behind the results presented in this chapter, and explains a typical input data file of a column yielding model for the MSC/NASTRAN computer program.

7.1 ANALYTICAL MODEL DESCRIPTION

Figure 7.1 illustrates a stick model representation of the two analytical model configurations. The model for the beam yielding configuration is shown in Figure 7.1a. The small boxed areas in this figure represent the zones of allowed plasticity (elastic—perfectly plastic behaviour) in the beam members. How plasticity is implemented in MSC/NASTRAN is briefly discussed in Appendix B (Section B.3 on page 245). Similarly, Figure 7.1b shows the column yielding model, with the boxed areas representing the regions of allowed plasticity in the column members.

7.1.1 Model Properties

The properties of the analytical model are essentially synonymous with those of the experimental model described in Chapter 3. The floors are perfectly rigid, and possess the same

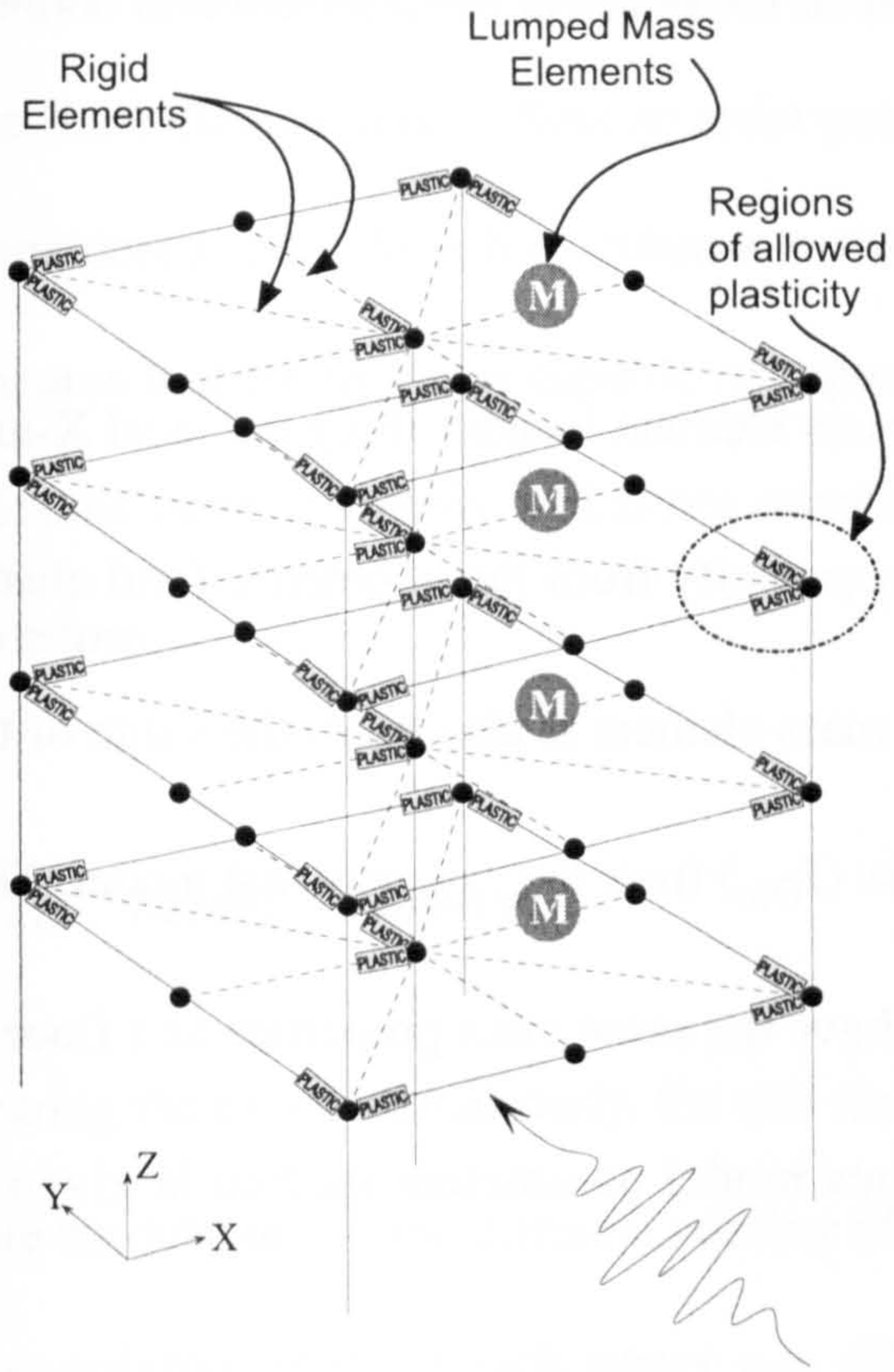

a) Beam yielding model.

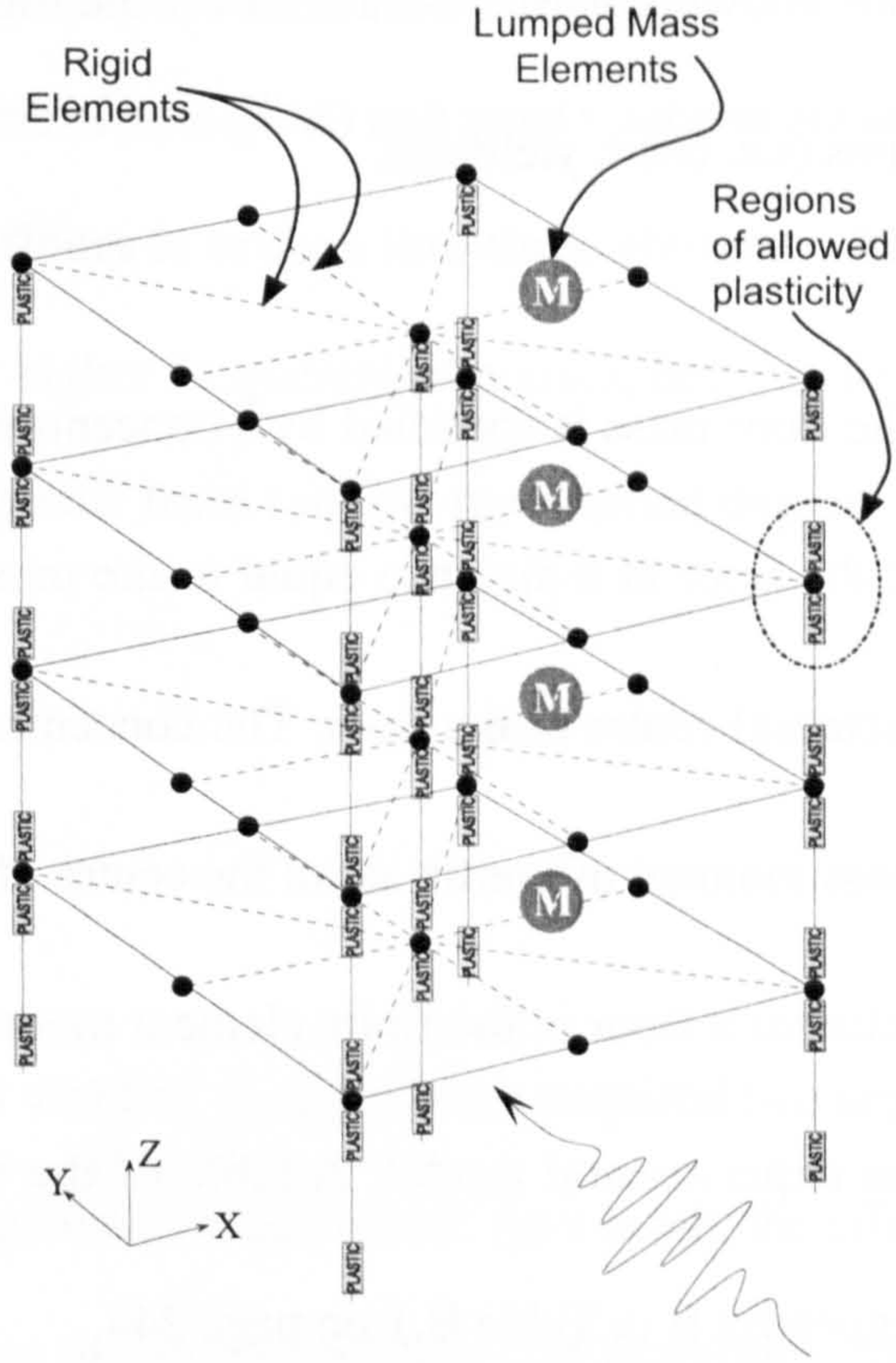

b) Column yielding model.

Figure 7.1: Schematic representation of the analytical model.

mass, mass eccentricity, and mass radius of gyration as their experimental counterparts. The floors are allowed to displace only in the X-Y plane. To enforce floor rigidity, the mid-side floor nodes, and the nodes at the floor's exterior column locations have their X-axis and Y-axis translation, as well as the rotation (Θ) about the vertical Z-axis dependent on the degrees of freedom of the centre column node of the floor. These dependencies are enforced by the use of rigid elements, with the centre column node as the independent degree of freedom, and are indicated by dashed lines in Figure 7.1. The rotations about the X-axis and Y-axis are fixed for the mid-side floor nodes, and free for all of the column nodes. Beam elements are placed around the perimeter of the floor, and restrain the nodal rotations about the X and Y-axes at the floor-column nodes. These perimeter beams are also capable of elastic–perfectly plastic behaviour at their ends which join the columns,

thus allowing plastic behaviour for the rotations of the nodes at the floor-column connections (i.e. beam yielding).

The floor mass is specified by a concentrated mass element located along the local X-axis of the floor at a distance equal to the mass eccentricity from the geometric (and elastic stiffness) centre of the floor. The concentrated mass element is also given the value of the mass moment of inertia about the centre of mass ($J_{\Theta m}$) from the experimental model. This enforces a floor in the finite element model to have the same mass properties as a floor in the experimental model. A table of the various model parameters studied is given in Appendix B in Table B.1 on page 244.

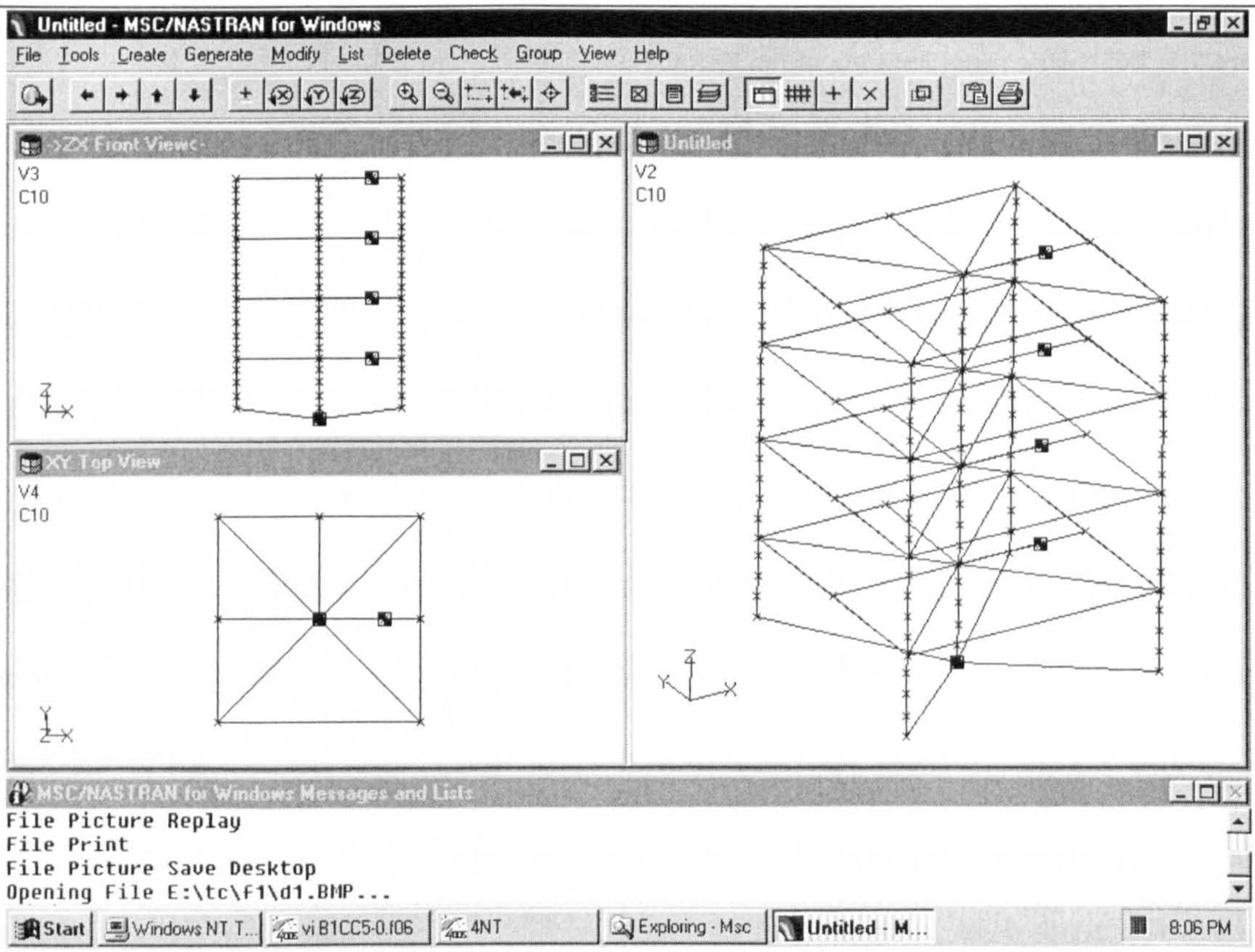

Figure 7.2: Screen plot of the analytical finite element model, showing nodes, lumped masses, members, and rigid elements.

The column masses, and their individual torsional stiffnesses are inherently formulated in the finite element model. Second order geometric effects (P–Δ) and large rotations are also considered. Each length of column between floors is broken into three elements. This ensures that the model is capable of capturing higher frequency responses, better distributes the column masses, and is not excessively stiff from too few represented degrees of freedom.

7.1.2 Model Geometry

During the experimental study, the two distinct yielding configurations required two separate models, due to the different number of hinge units on each floor. As a result, the effective column length in each storey was different in the two yielding configurations. This variation can be alleviated in the analytical model, enabling the use of a single geometric configuration. Since the column yielding experimental model has a uniform storey height distribution, this storey height was also used for the analytical model.

The inter-storey height is 343mm for both the column yielding experimental model and the analytical model. However, the effective column lengths for the experimental model are less than this value due to the physical constraints of the hinge units, as discussed in Section 4.3 on page 98. This is implemented in the analytical model with rigid elements (slaved to the floor's column nodes) placed above and below the floor at each column. The lengths of each of these rigid elements for the exterior columns are assumed equal. Likewise, the rigid element lengths for the interior column are all identical. A parametric study was performed to find both the interior and exterior rigid element lengths that minimized

the error between analytical and experimental models, in terms of the uncoupled Y-axis translational frequency and the Θ-axis rotational frequency.

7.1.3 Elastic Damping

Damping in the analytical model is defined in terms of *Rayleigh* damping. Rayleigh damping defines the damping matrix, $[C]$, as being proportional to both the stiffness, $[K]$, and mass, $[M]$, matrices:

$$[C] = \alpha_1[M] + \alpha_2[K] \tag{7.1}$$

where, α_1 and α_2 are the mass and stiffness parameters that define the shape of the Rayleigh damping curve. Equation (7.1) can be normalized by the mass matrix, which results in:

$$\alpha_1 + \alpha_2\omega_{1,2}^2 = \frac{C}{M} = 2\omega_{1,2}\xi_{1,2} \tag{7.2}$$

where ω_1 and ω_2 are the two frequencies at which Rayleigh Damping is defined, and ξ_1 and ξ_2 are their associated damping values.

Solving equation (7.2) for α_1 and α_2, in terms of the two target frequencies ω_1 and ω_2 (in radians/second) and a constant ratio of critical damping at both target frequencies, $\xi = \xi_1 = \xi_2$, results in:

$$\begin{aligned} \alpha_2 &= \frac{2\xi(\omega_2 - \omega_1)}{\omega_2^2 - \omega_1^2} \\ \alpha_1 &= 2\xi\omega_1 - \alpha_2\omega_1^2 \end{aligned} \tag{7.3}$$

The relationship between ξ and ω is found by rearranging equation (7.2), and solving for the elastic damping ratio, ξ:

$$\xi = \frac{\alpha_1 + \alpha_2 \omega^2}{2\omega} = \frac{\alpha_1 + \alpha_2 (2\pi f)^2}{4\pi f} \tag{7.4}$$

where f is the modal frequency in cycles per second ($\omega = 2\pi f$).

Figure 7.3 shows a scatter plot of the modal frequencies of the experimental models superimposed on the Rayleigh damping relationship between ξ and f, for 1.5% damping at both 1.0Hertz and 5.0Hertz. This range was selected since it encompasses the first two modal

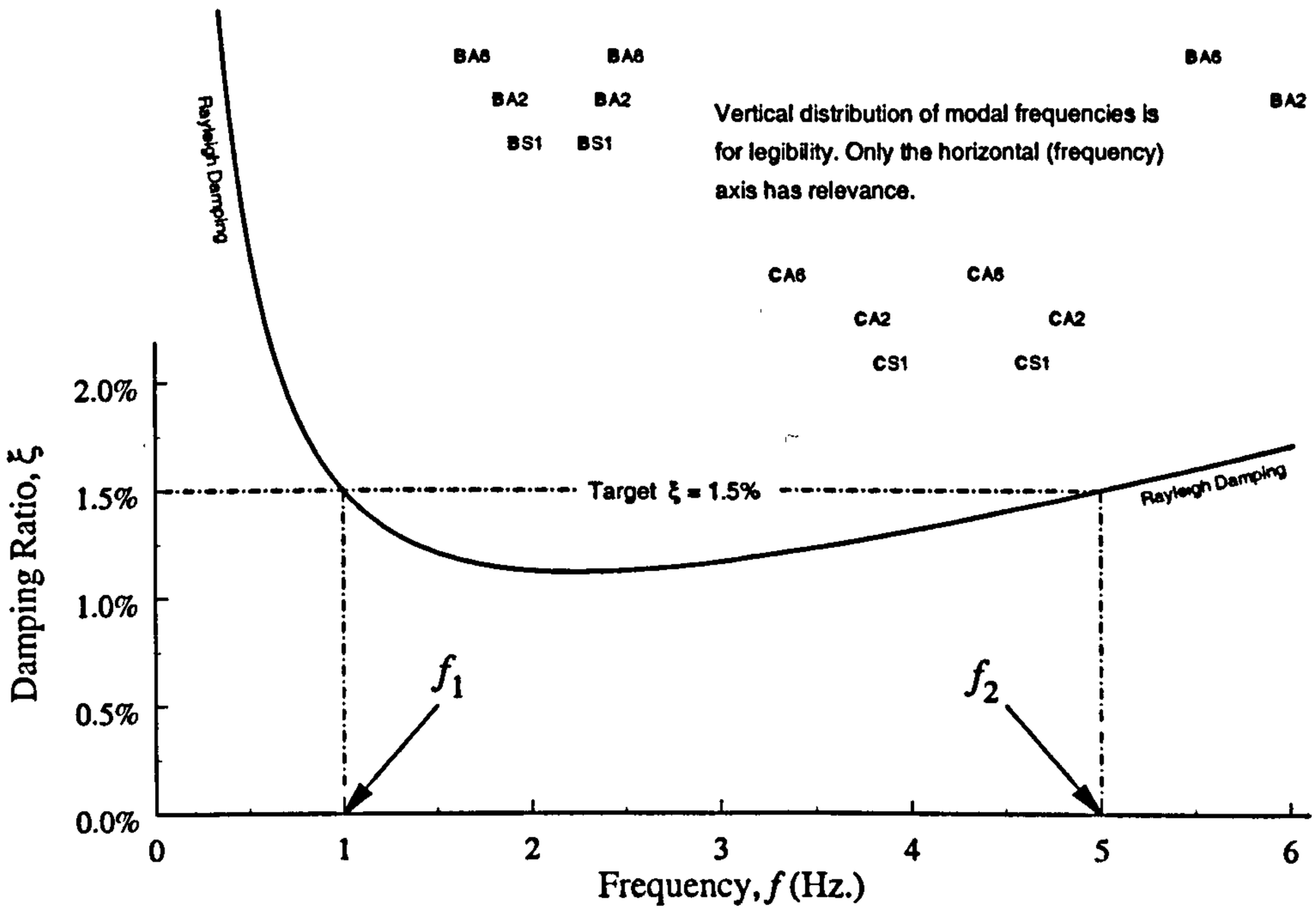

Figure 7.3: Damping versus response frequency for the specified Rayleigh damping. The symbols B*xx* (beam yielding) and C*xx* (column yielding) represent the modal frequencies for model *xx*.

frequencies for both the beam yielding and column yielding experimental models. In this range, the viscous damping varies between 1% and 1.5%—values similar to those of the experimental models. The modes with frequencies greater than 5.0Hertz have a damping ratio greater than 1.5%. This does not significantly alter the response of the computer

model since the mass participation of the first two modes in each of the three mass configurations contributes to well over 90% of the total elastic response.

7.2 ELASTIC RESPONSE

This section describes the elastic response of the analytical models, and offers a comparison to the elastic characteristics of the experimental models. The same analytical model was used for both the linear and non-linear response. The MSC/NASTRAN elastic solution sequences, which neglects material and geometric non-linearities, were used to generate the displacement responses in this section.

7.2.1 Elastic Mode Shapes and Frequencies

The elastic frequencies and mode shapes of the analytical model are intended to closely match those of the column yielding experimental model, as recorded directly by the shake table's spectral analyser. The storey heights of the column yielding experimental model and the analytical model are identical (343mm). The effective column lengths[1] were adjusted for both the internal and external columns to provide a good match in frequencies between the analytical and experimental models. The matching process was also biased toward a near unity ratio of the fundamental uncoupled rotation to translation frequency ratio, Ω:

$$\Omega = \frac{\omega_\Theta}{\omega_y} = \frac{4.0}{3.9} = 1.03 \tag{7.5}$$

1. The effective column length in the analytical model is the length of column not considered as rigid. This is analogous to the length of column between the hinge clamping collets in the experimental model.

Table 7.1 offers a comparison between the analytical and experimental elastic frequencies. The translational analytical frequencies offer a closer match to the experimental frequencies, with differences of less than 8%. The analytical rotational frequencies differ from their experimental counterparts by up to 15%. This is a result of the effective column lengths for the exterior columns being slightly less in practice than that for the analytical model. The rotational stiffness of the analytical model is slightly lower than that of the experimental model. This results in a ratio of rotational to translational frequency, Ω, being closer to unity than the experimental model, while still being within 15% of the experimental rotational frequencies.

Table 7.1: Comparison of analytical and experimental (column yielding configuration) frequencies

Mode #		Modal Frequencies (cycles per second)								
Anal.	Exp.	Mass Configuration S1			Mass Configuration A2			Mass Configuration A6		
		Exp.	Anal.	%diff	Exp.	Anal.	%diff	Exp.	Anal.	%diff
1	1	3.90	3.90	0%	3.80	3.77	0.8%	3.35	3.34	0.3%
2		*X*[a]	3.90	—	*X*	3.90	—	*X*	3.90	—
3	2	4.65	4.00	15.0%	4.83	4.17	14.7%	4.40	4.42	-0.5%
4	3	10.83	11.14	-2.8%	10.70	10.77	-0.7%	10.33	9.57	7.6%
5	—	*X*	11.14	—	*X*	11.14	—	*X*	11.14	—
6	4	13.30	11.41	15.3%	13.50	11.90	12.6%	N/A[b]	12.60	—
7	—	—	16.86	—		16.27	—	—	14.47	—

a. *X* indicates X-axis uncoupled modes, which were not recorded during the experimental tests.
b. The 6th mode for mass configuration A6 corresponds to the 4th experimental mode, which was not measured.

Figures 7.4 through 7.6 show the analytical model's modal deformations of each of the three mass configurations. Unlike the mode shapes presented in Chapter 3 (Figure 3.8 on

page 64 and Figure 3.9 on page 65) which are based on 8×8 stiffness and mass matrices, these mode shapes are taken directly from the analytical finite element model. Since the mass is always symmetric about the X-axis, the X-axis modes are uncoupled for all mass configurations, meaning they have the same frequency and mode shape for all mass configurations.

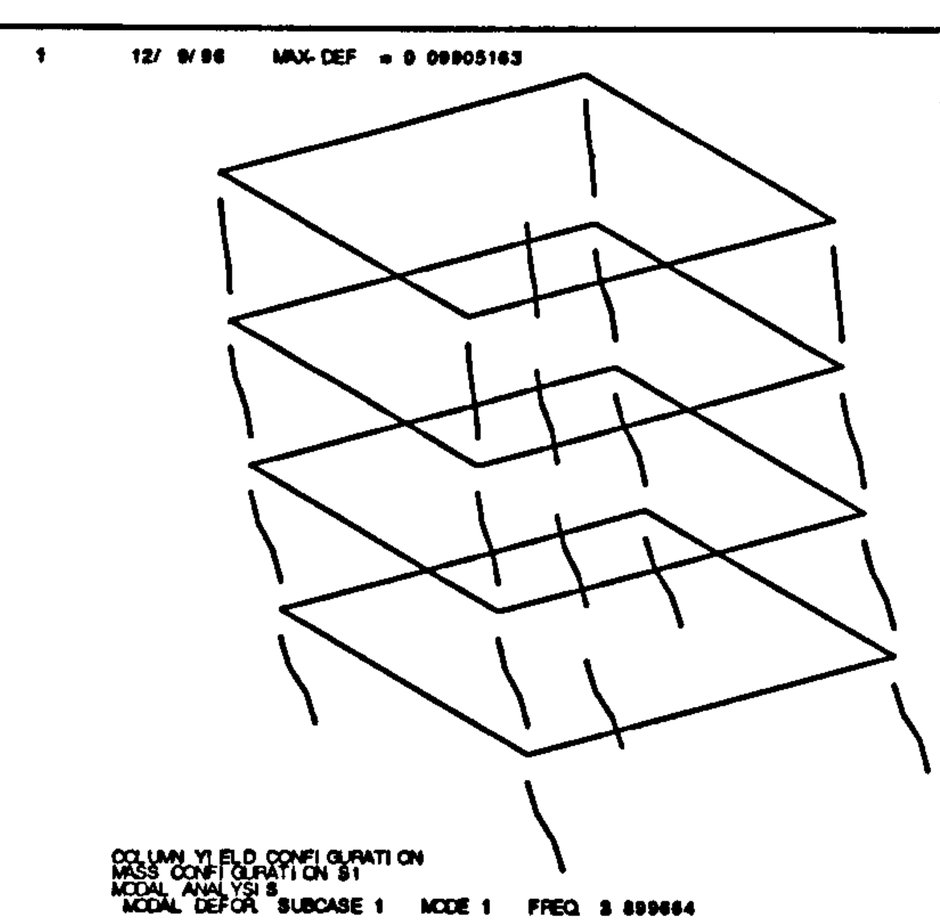

Mode 1: Primary Y-axis Translation

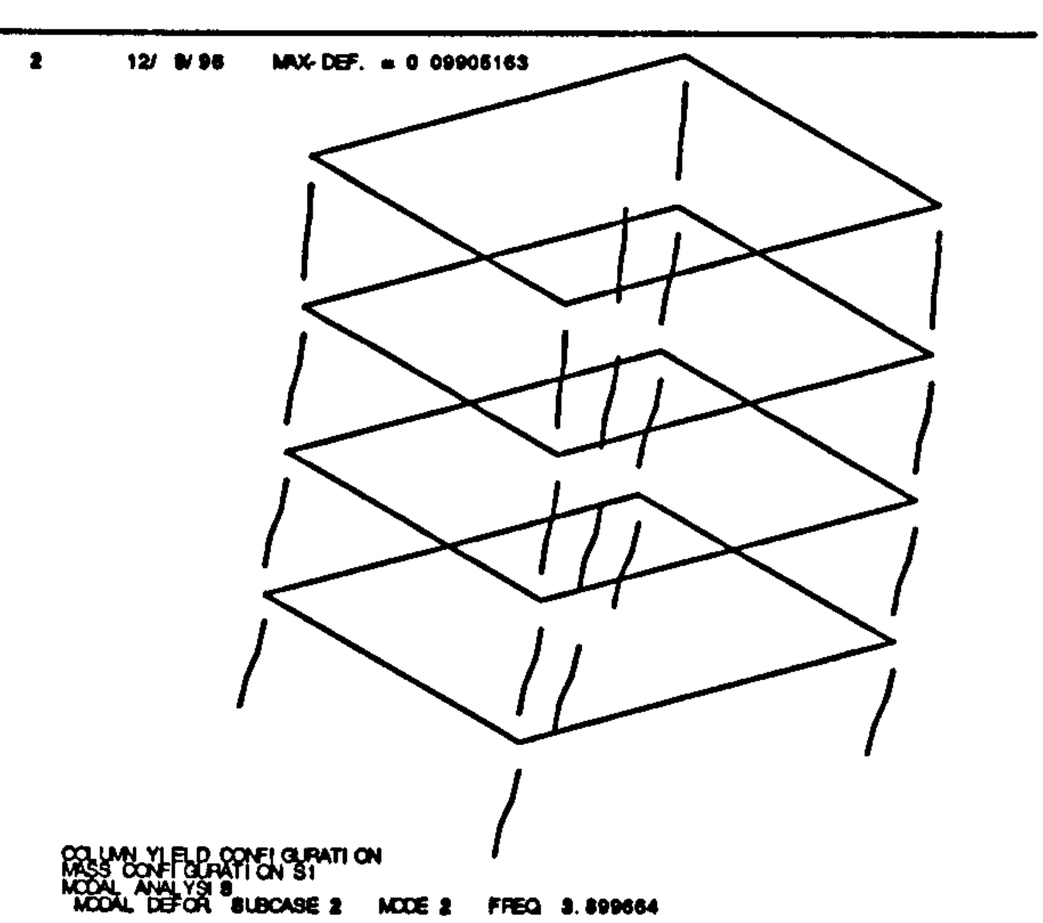

Mode 2: Primary X-axis Translation

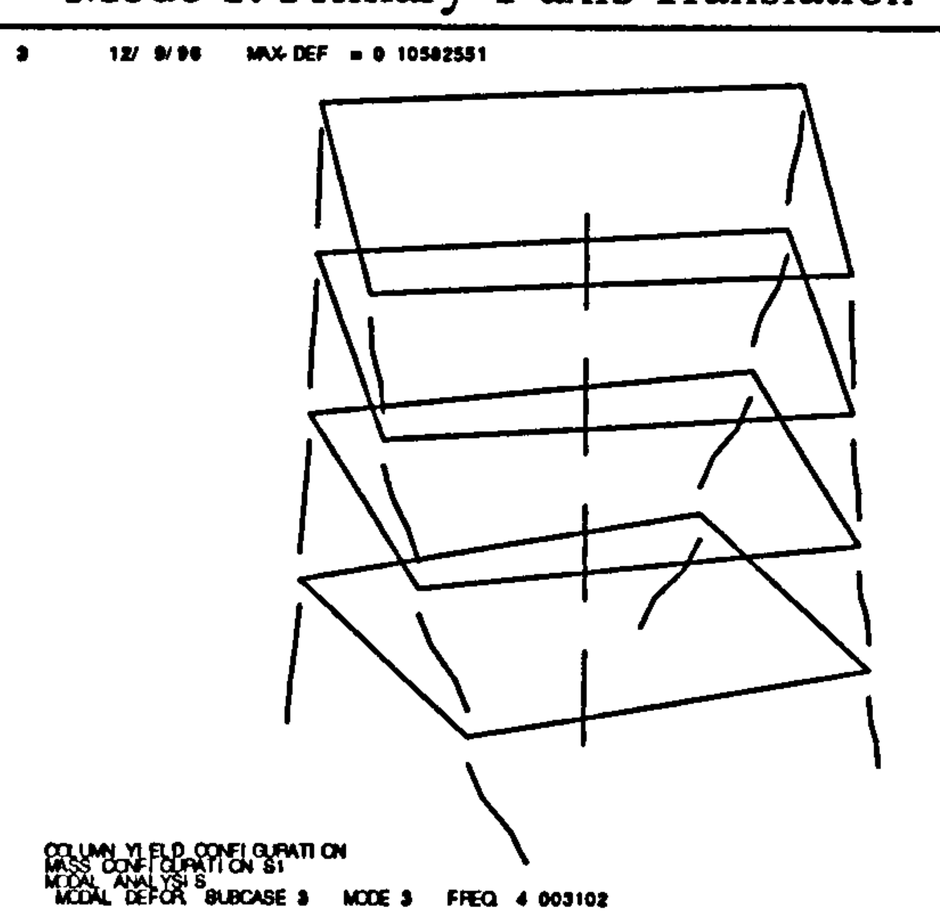

Mode 3: Primary Z-axis Rotation

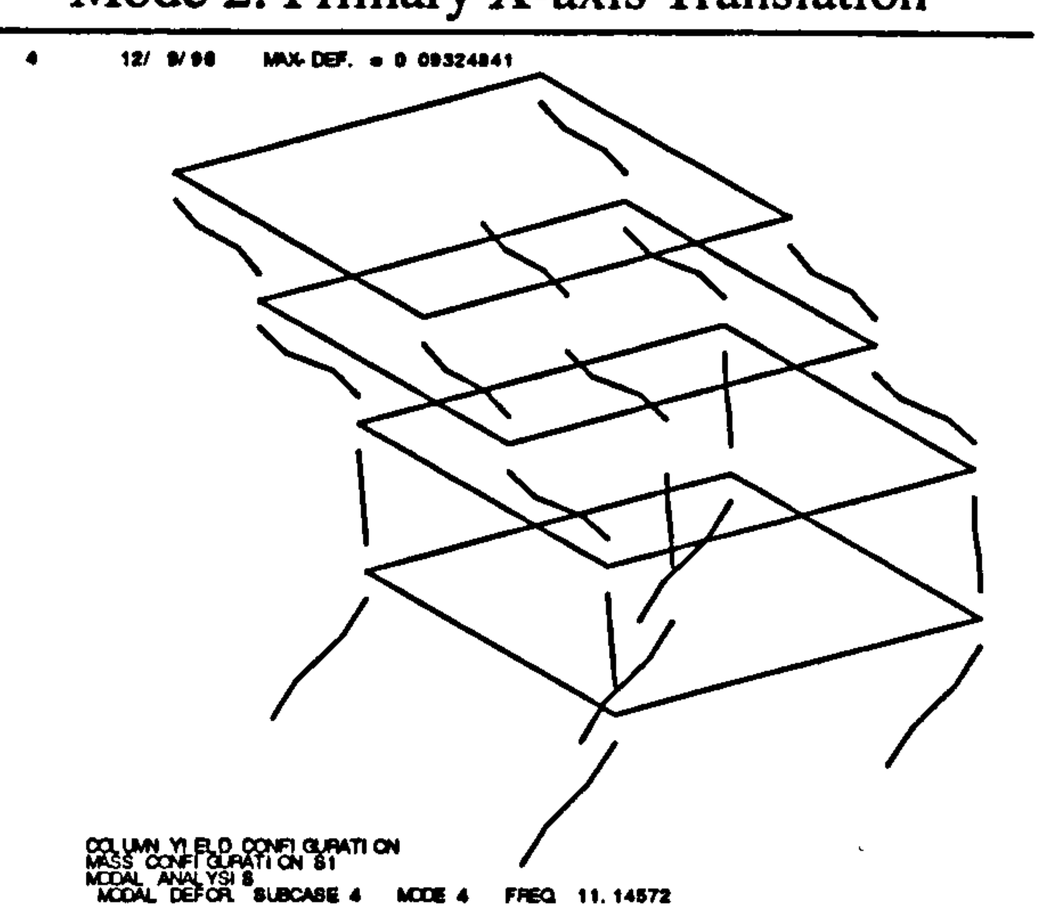

Mode 4: Secondary X-axis Translation

Figure 7.4: Mode shapes of the column yielding analytical model for mass configuration S1.

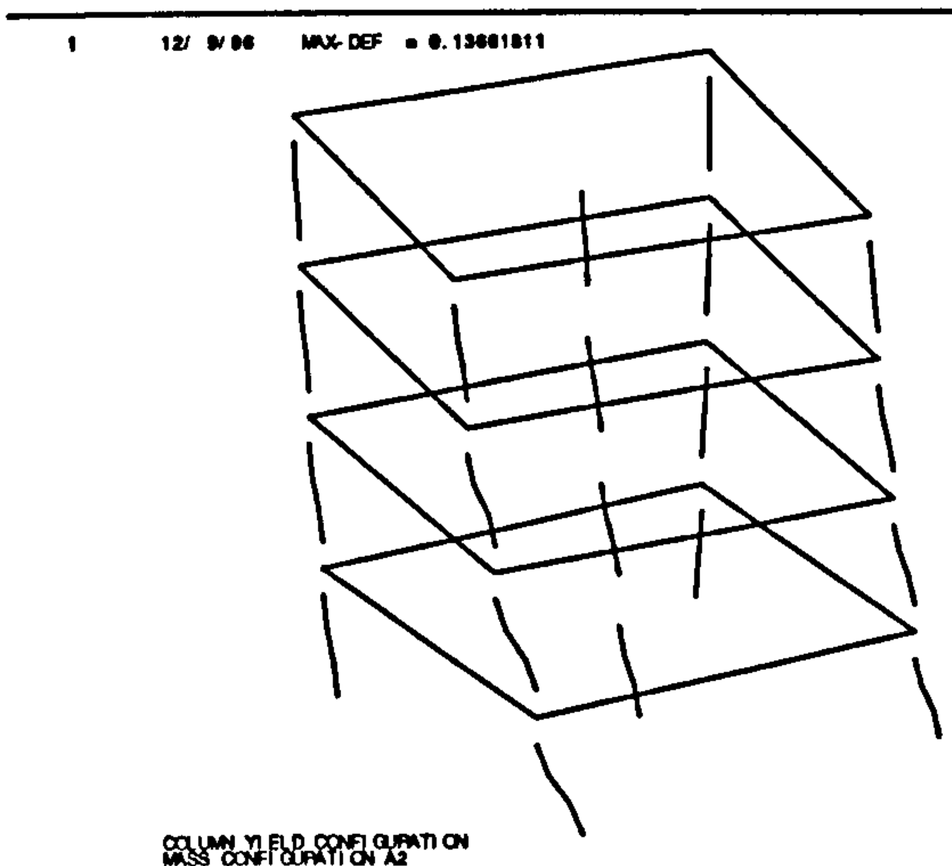

Mode 1: Coupled Mode

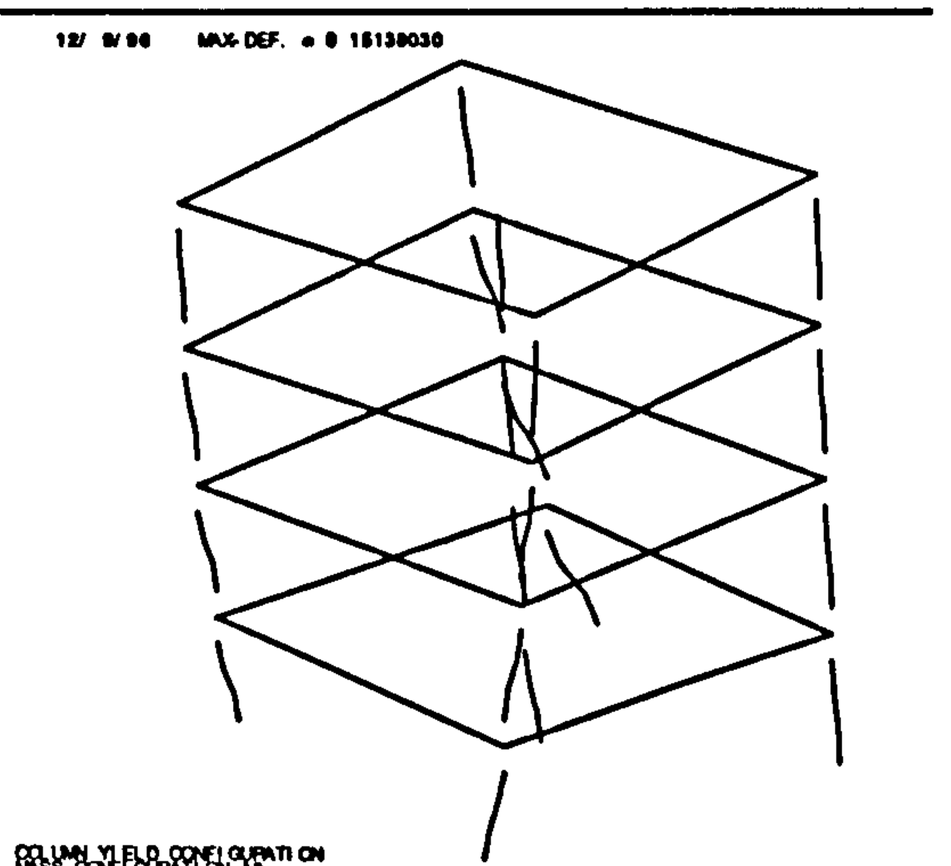

Mode 3: Coupled Mode

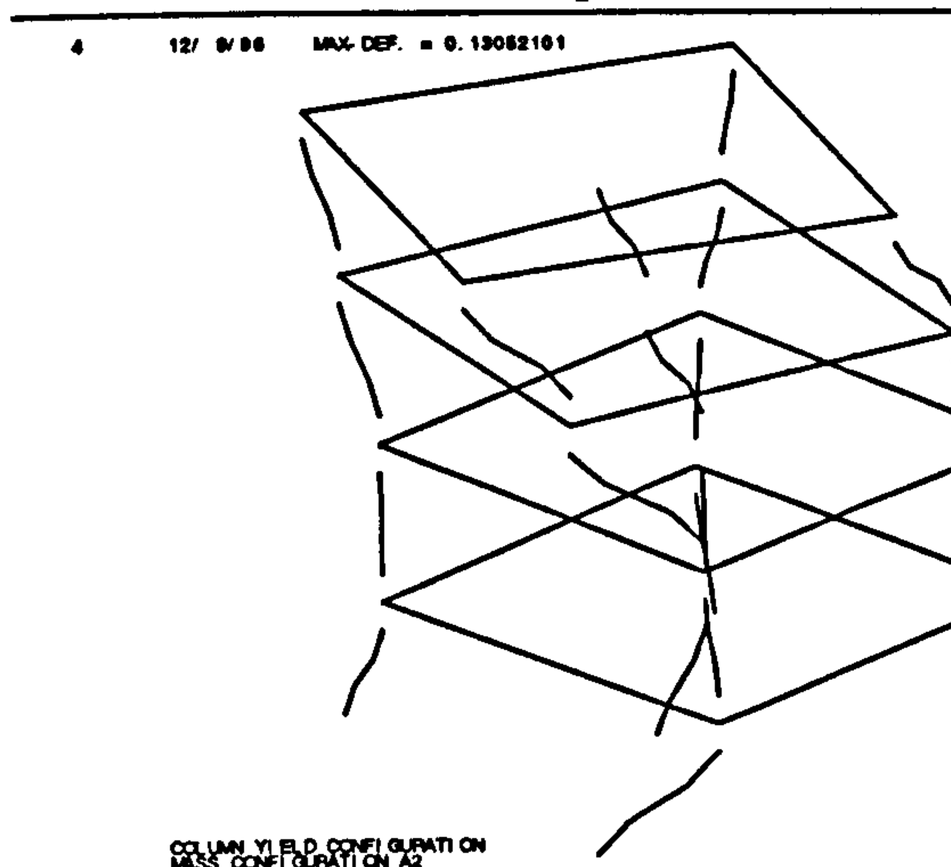

Mode 4: Coupled Mode

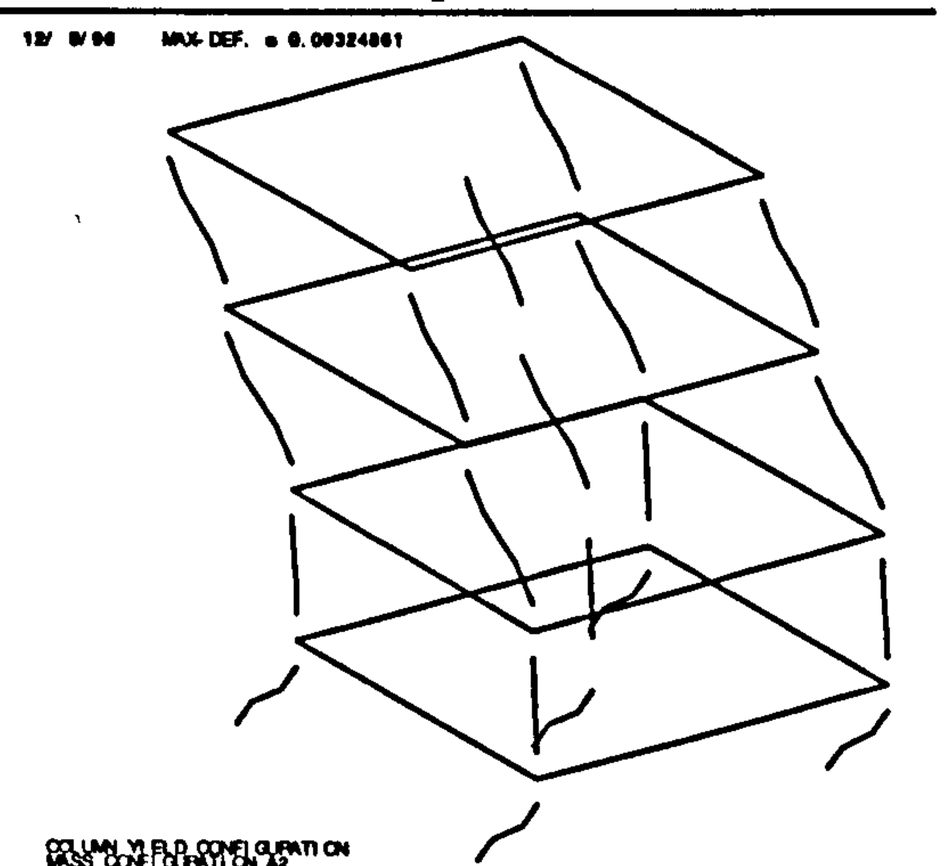

Mode 5: Secondary X-axis Translation

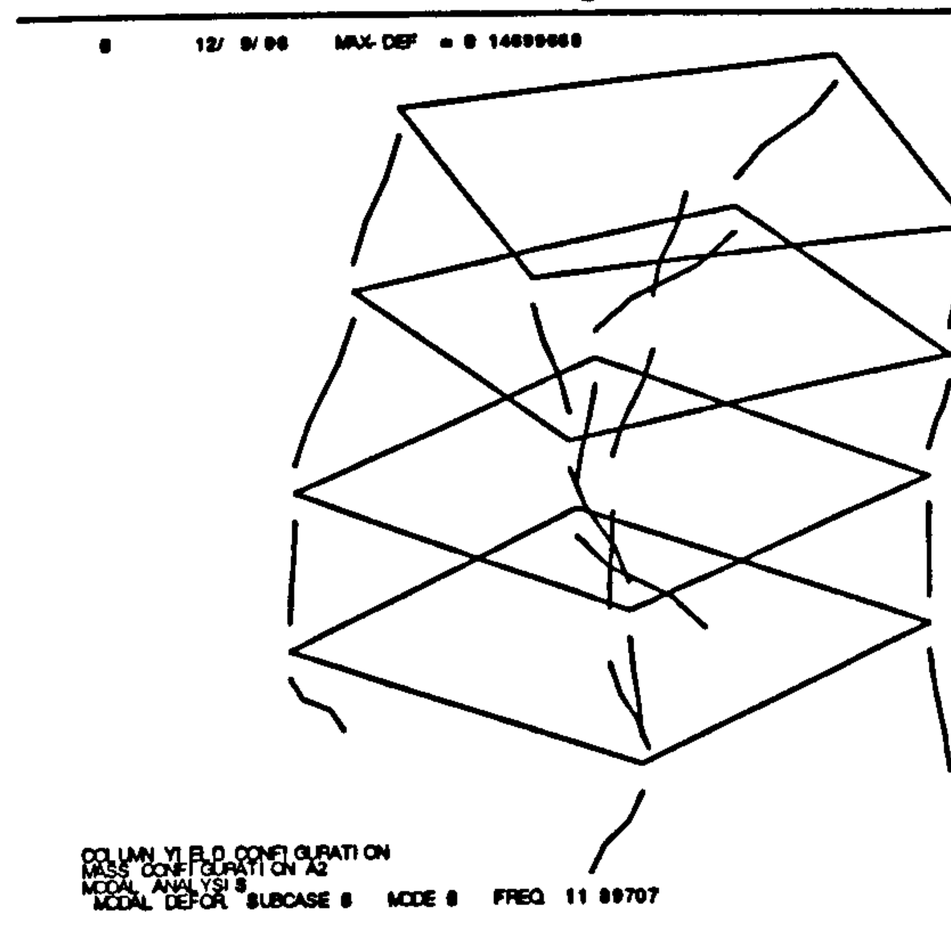

Mode 6: Coupled Mode

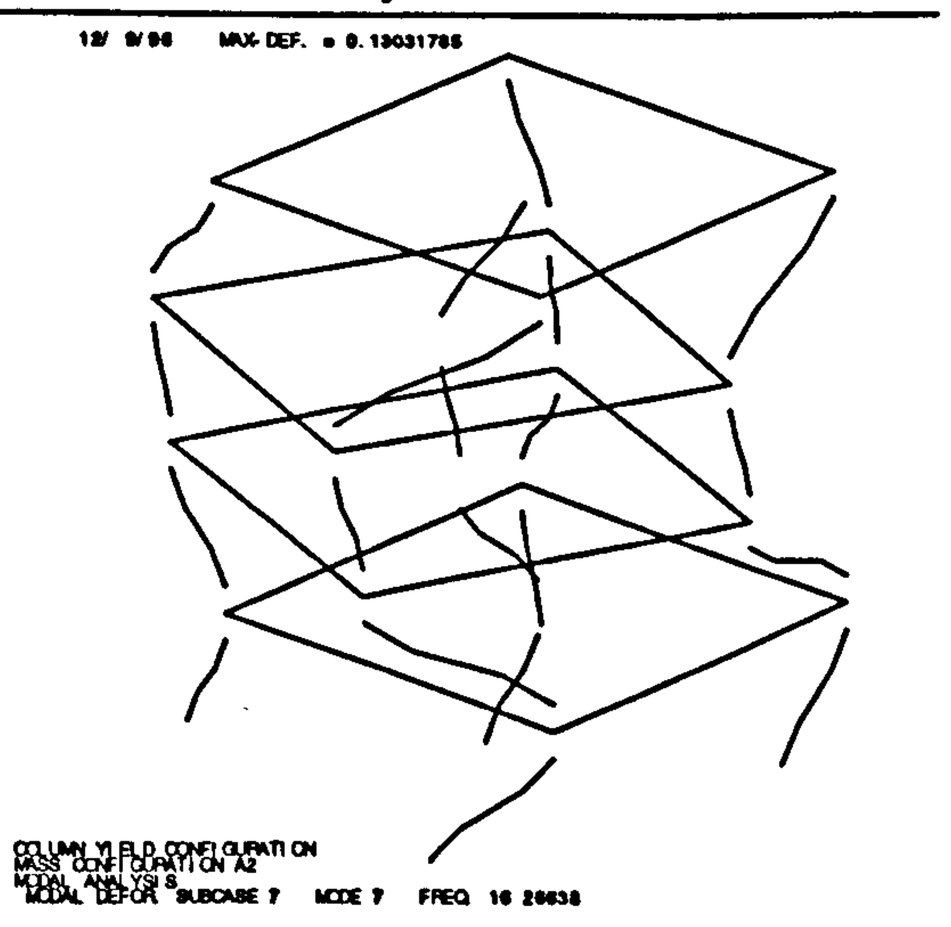

Mode 7: Coupled Mode

Figure 7.5: Mode shapes of the column yielding analytical model for mass configuration A2.

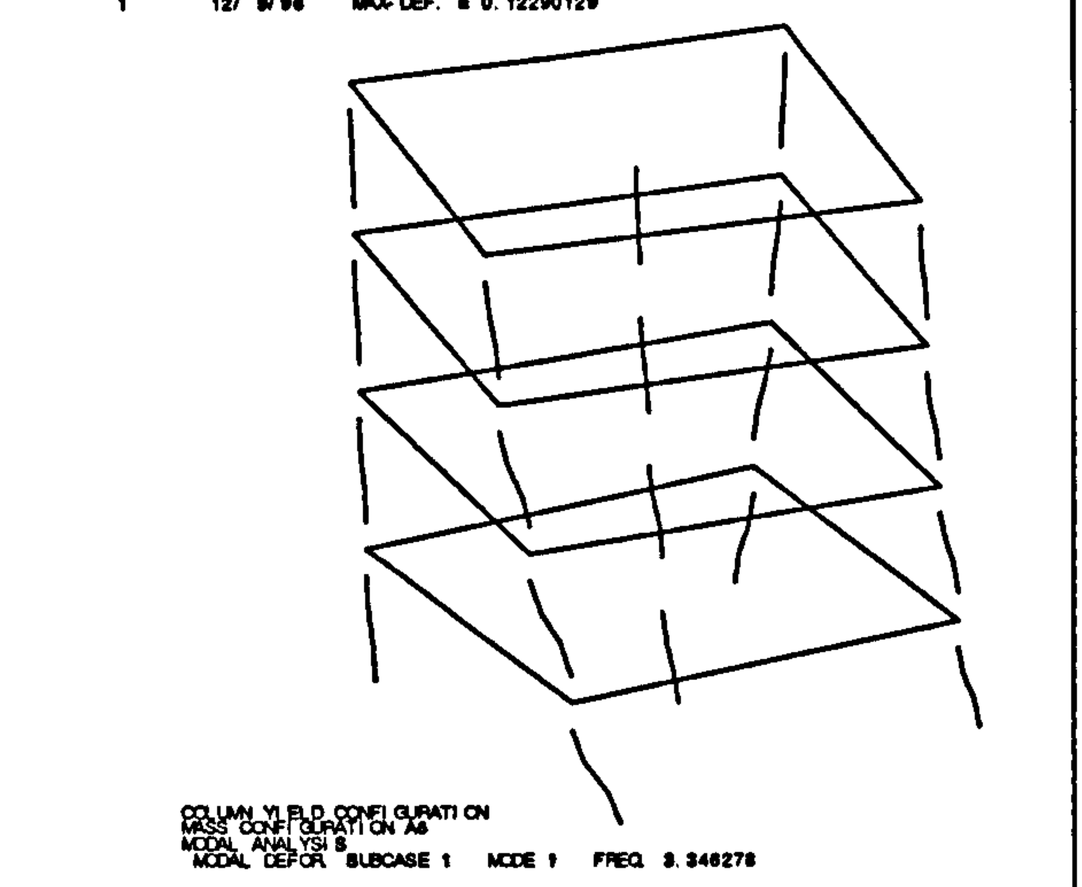

Mode 1: Coupled Mode

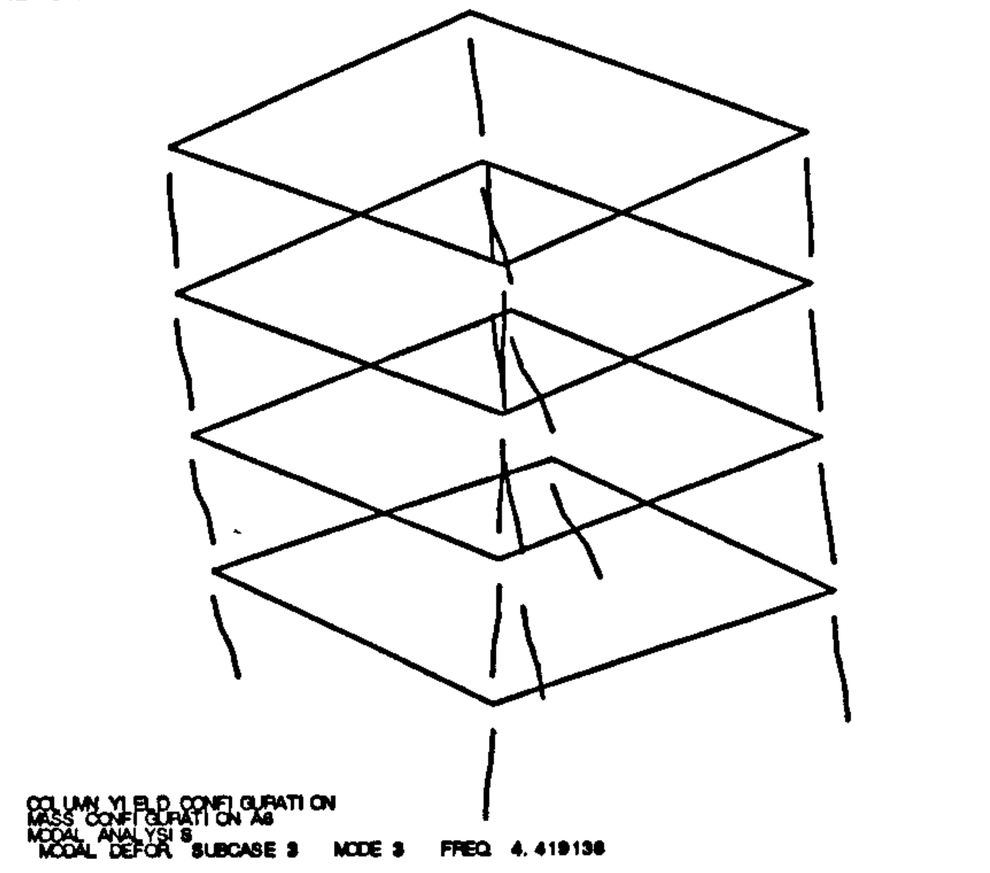

Mode 3: Coupled Mode

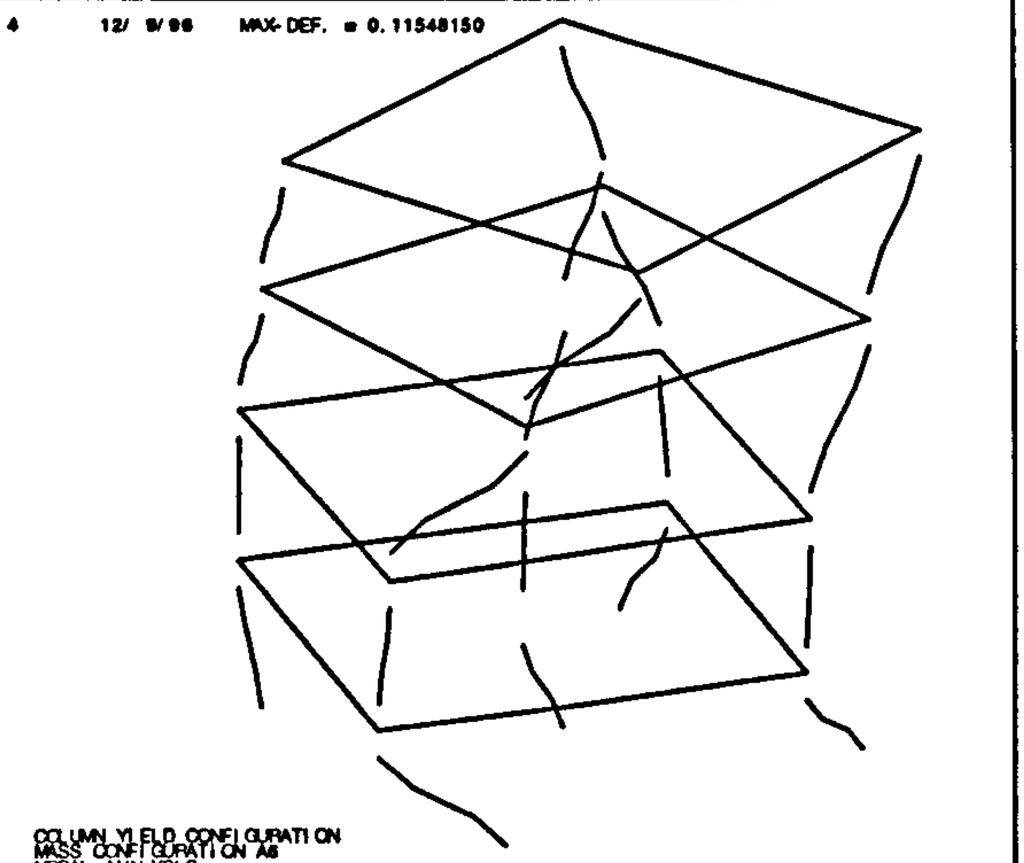

Mode 4: Coupled Mode

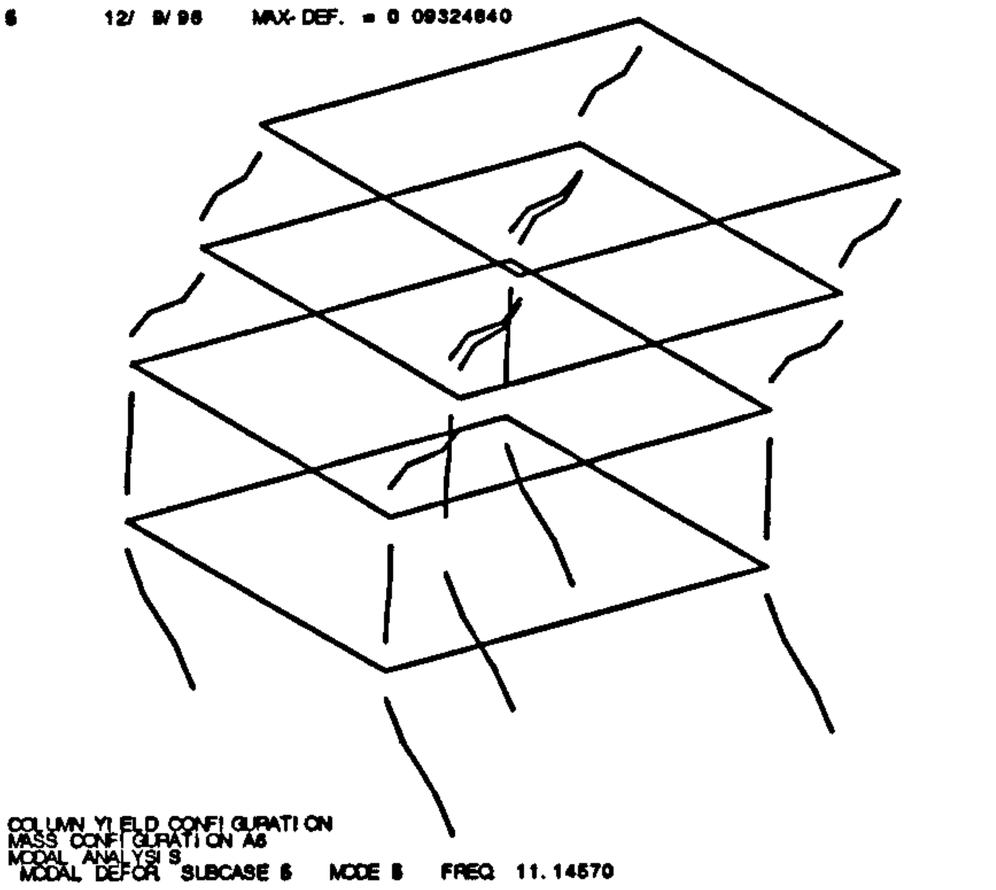

Mode 5: Secondary X-axis Translation

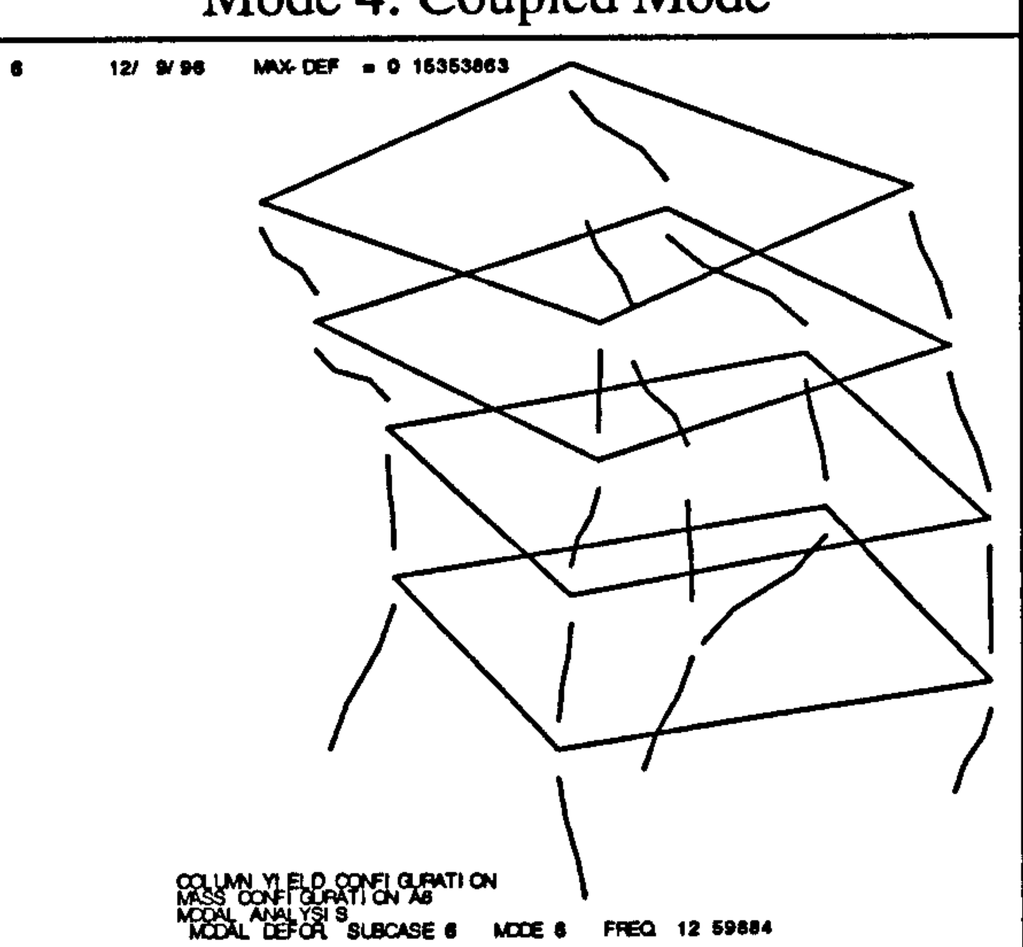

Mode 6: Coupled Mode

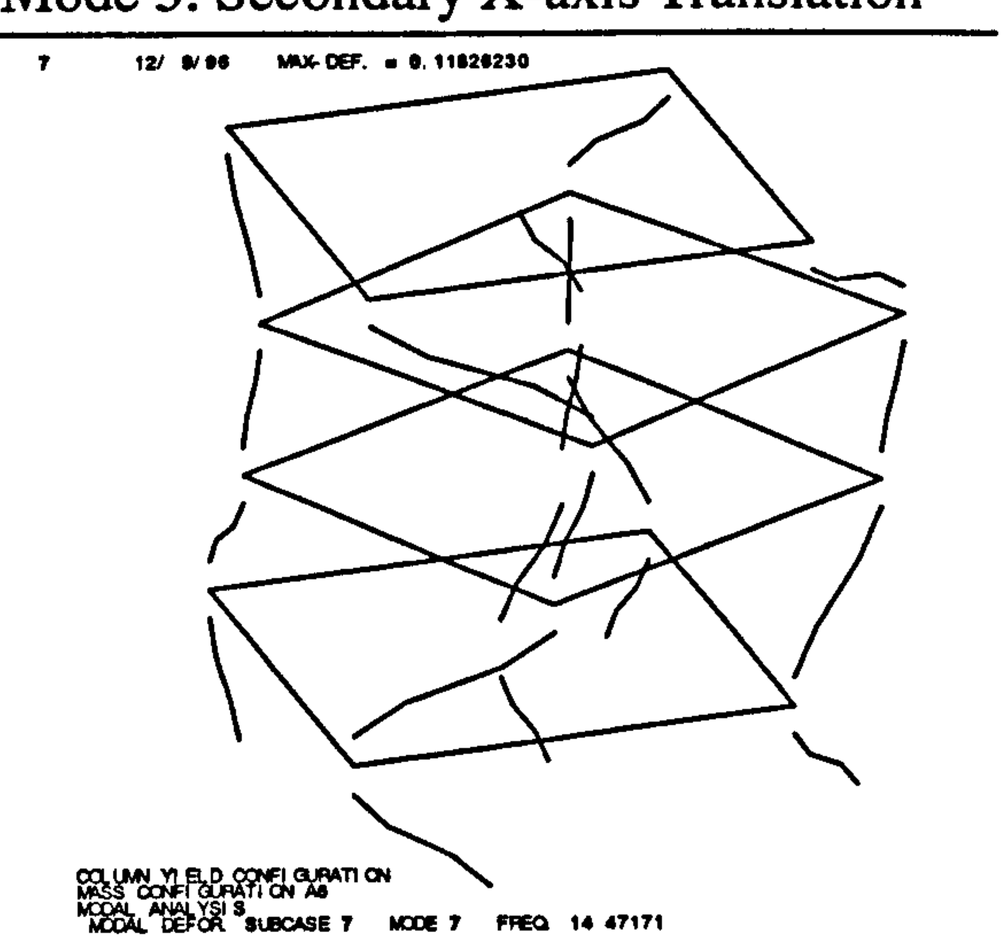

Mode 7: Coupled Mode

Figure 7.6: Mode shapes of the column yielding analytical model for mass configuration A6.

7.2.2 Modal Interaction Diagrams

In a similar manner to Figure 3.10 on page 67, Figure 7.7 illustrates the degree of modal coupling for the three studied mass configurations of the finite element model. The numbered lines in this Figure represent the mode number. As with the experimental model, the first and third modes of mass configuration S1 are pure translation, and the second and fourth modes are pure rotation. However, unlike the experimental model, the first four coupled modes are all rotational dominated. This means the elastic response of the analytical model has a slightly greater torsional component for the mass asymmetric configurations than those for the experimental model. This is probably a result of the reduced torsional frequencies of the analytical model.

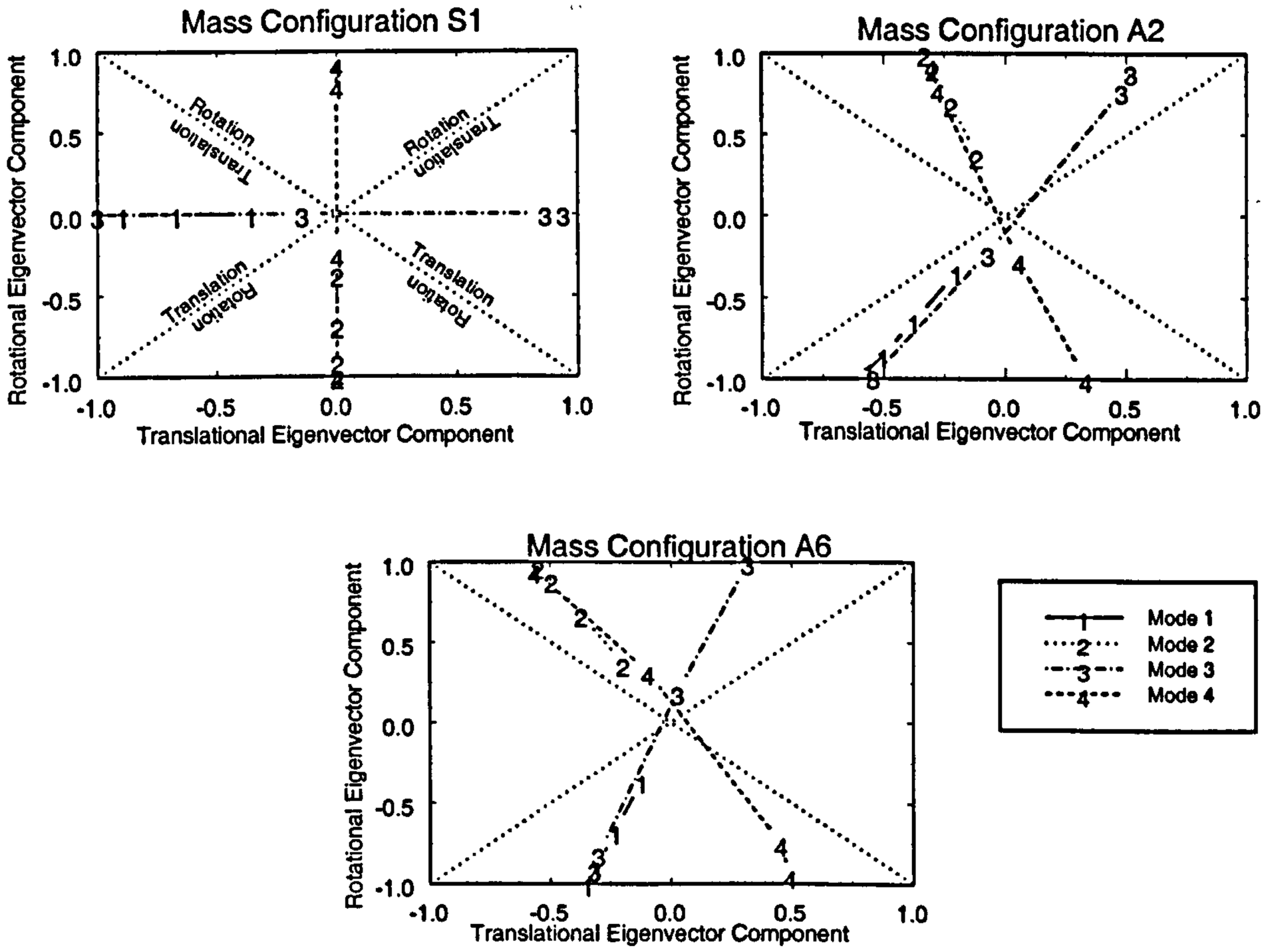

Figure 7.7: Modal component diagram for the analytical finite element model.

7.2.3 Power Spectral Densities

As previously described in Section 5.3.3 on page 132, and Section 5.9.1 on page 152, the power spectral density (PSD) is an average quantity indicating the energy content of a degree of freedom over various frequencies as a result of the applied ground motion. In other words, the PSDs shown in this section indicate the frequencies contributing to the overall response energy of the selected degree of freedom. Normally, the contribution of each mode to a response is estimated by the mass participation factor of that mode. This method is good for determining the localized modes in a structural model, but doesn't take into consideration the applied excitation.

7.2.3.1 Total Floor Displacements

Figures 7.8[1] through 7.10 show the PSDs for the total[2] floor displacements of the three mass configurations. For frequencies up to 9 Hertz, the upper floors in the translational response (for all mass configurations) contain more energy than do the lower floors, suggesting a behaviour that is primarily in the fundamental mode. For both translation and rotation of the floors, the response is primarily in the first two modes. The energy contributions from each of the first two modes is nearly equal. Above 9 Hertz, the lower floors start to contribute more to the overall spectral response. However, in this range the contribution is over a 30dB drop from that of the first two modes, indicating that the overall elastic response is primarily from the first two modes.

1. The rotation PSD in Figure 7.8 is shown for completeness, and shows a peak energy of -210dB due to computational noise.
2. Displacements measured relative to the ground motion.

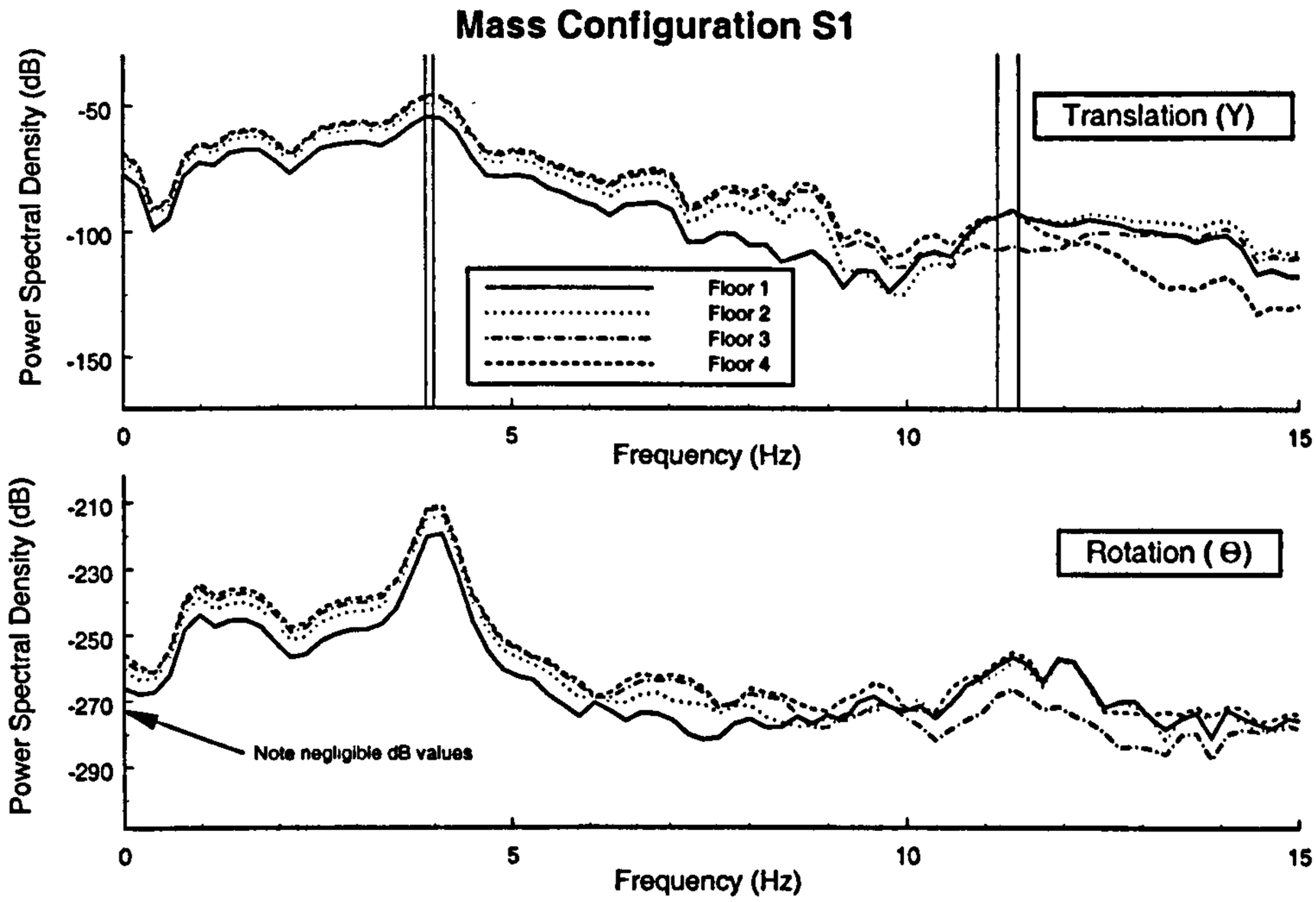

Figure 7.8: Power spectral density of the total floor displacement for mass configuration S1.

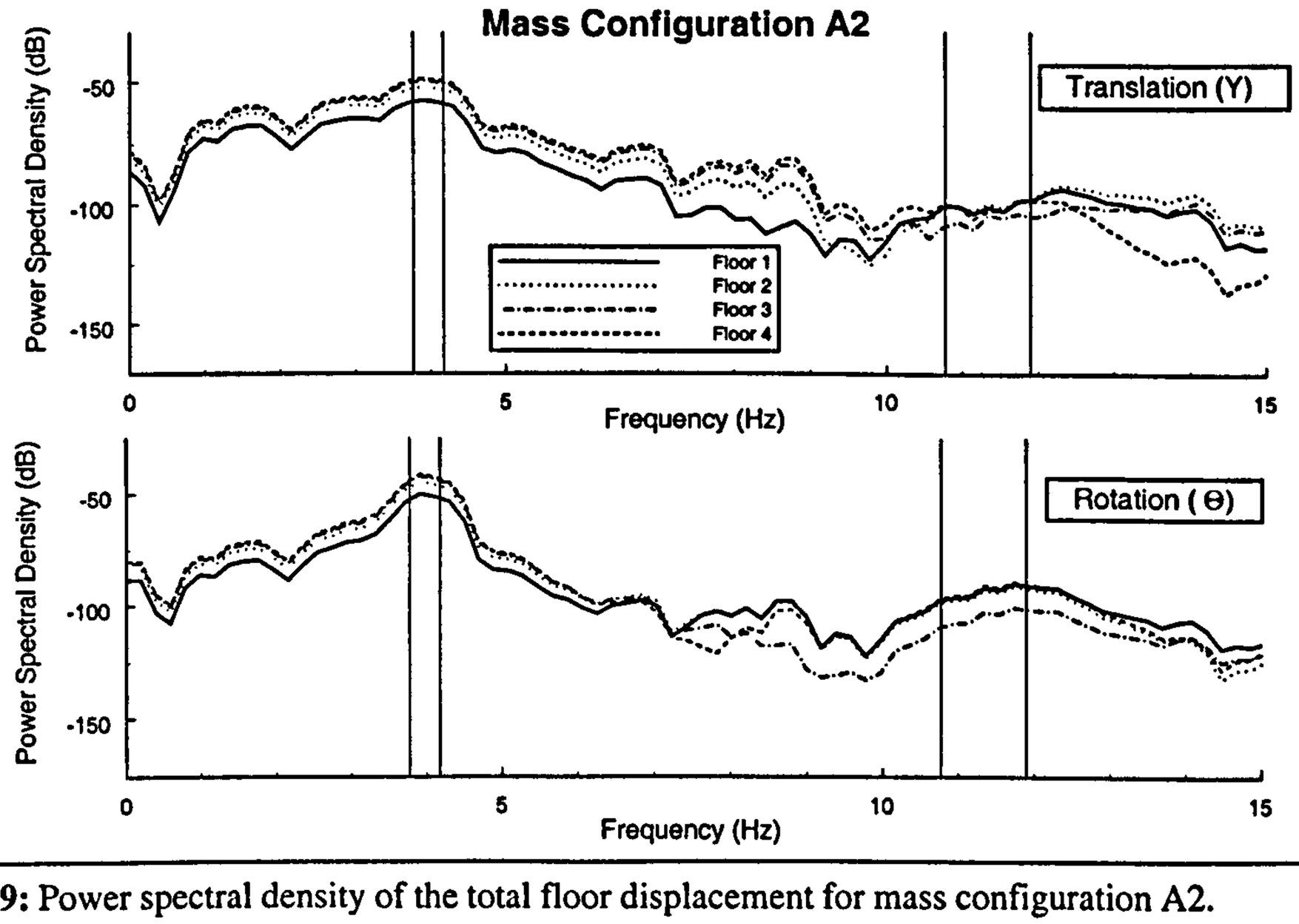

Figure 7.9: Power spectral density of the total floor displacement for mass configuration A2.

7.2.3.2 Storey displacements

Figures 7.11 through 7.13 show the PSDs from the storey displacements (i.e. relative displacement between floors). For frequencies up to 6 Hertz, the lower floors in all mass configurations contribute most of the energy in the first two modes of response. This is a

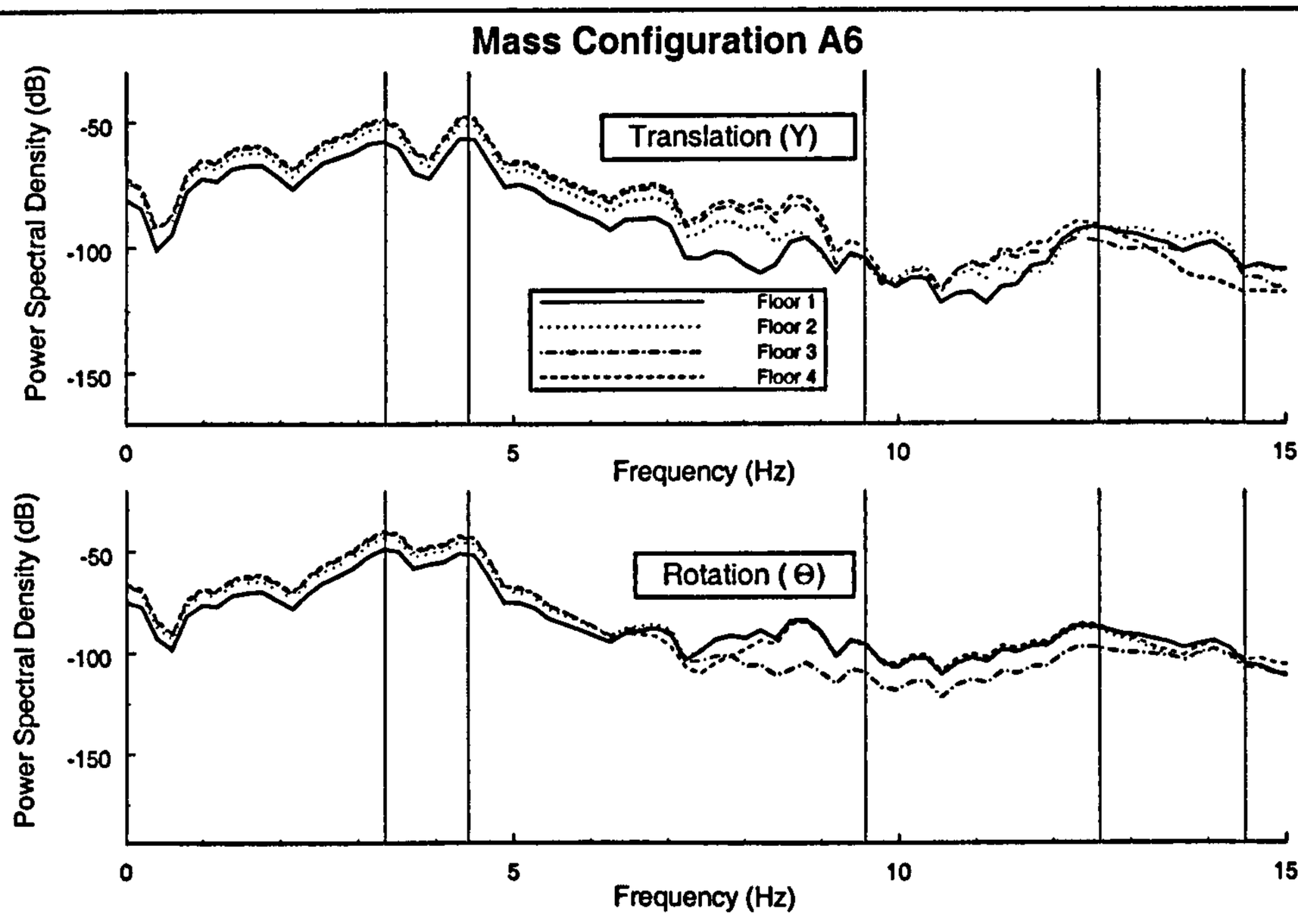

Figure 7.10: Power spectral density of the total floor displacement for mass configuration A6.

result of the larger dynamic floor mass in the lower stories, which have the same stiffness as the upper stories. Above 6 Hertz, the response energy contribution is fairly similar

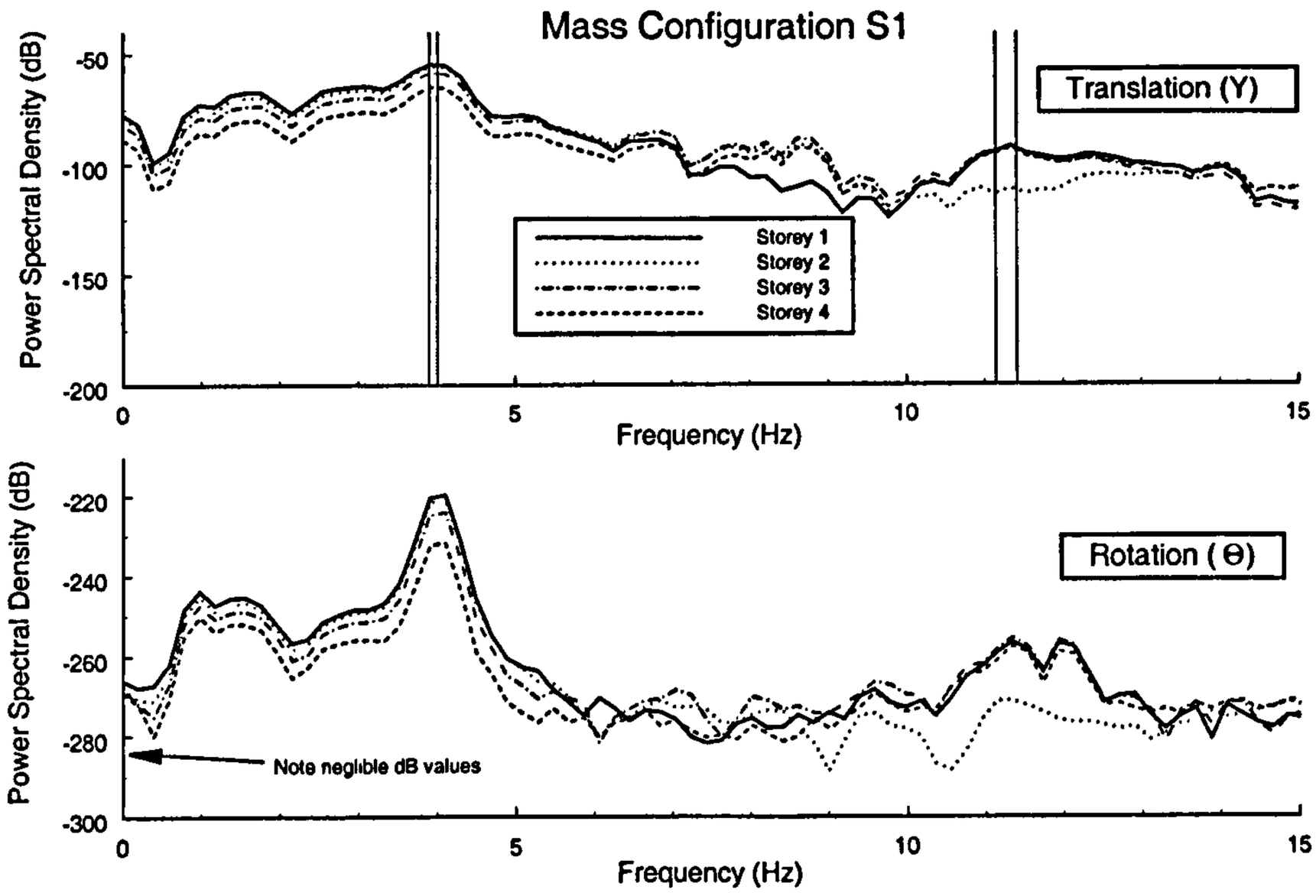

Figure 7.11: Power spectral density of the storey displacements for mass configuration S1.

between the stories, except for the second storey PSD which generally contributes the

least to the storey's response. This is due to the low relative displacement between the first and second stories in the higher modes of all mass configurations (see Figures 7.4 through 7.6).

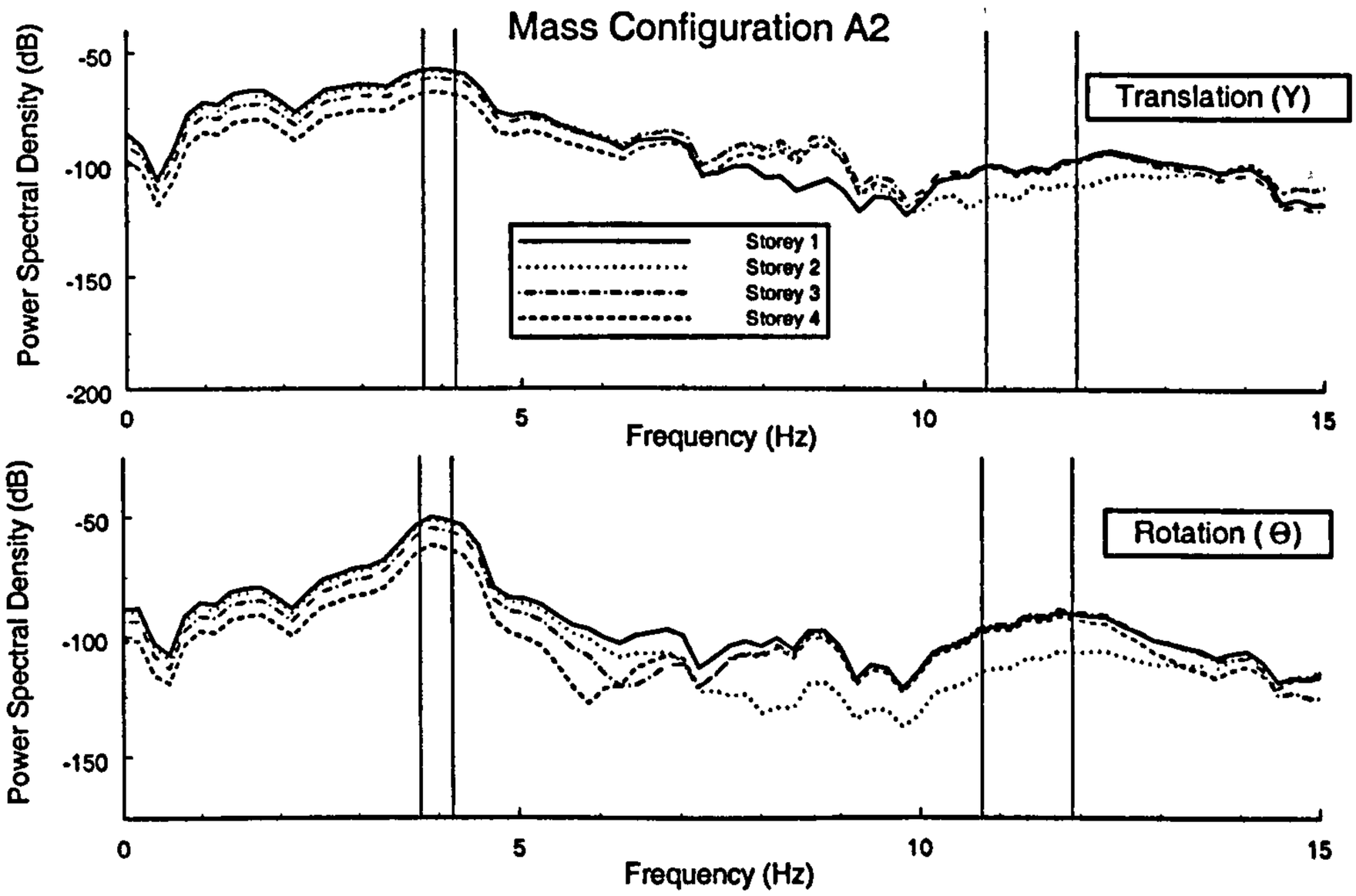

Figure 7.12: Power spectral density of the storey displacements for mass configuration A2.

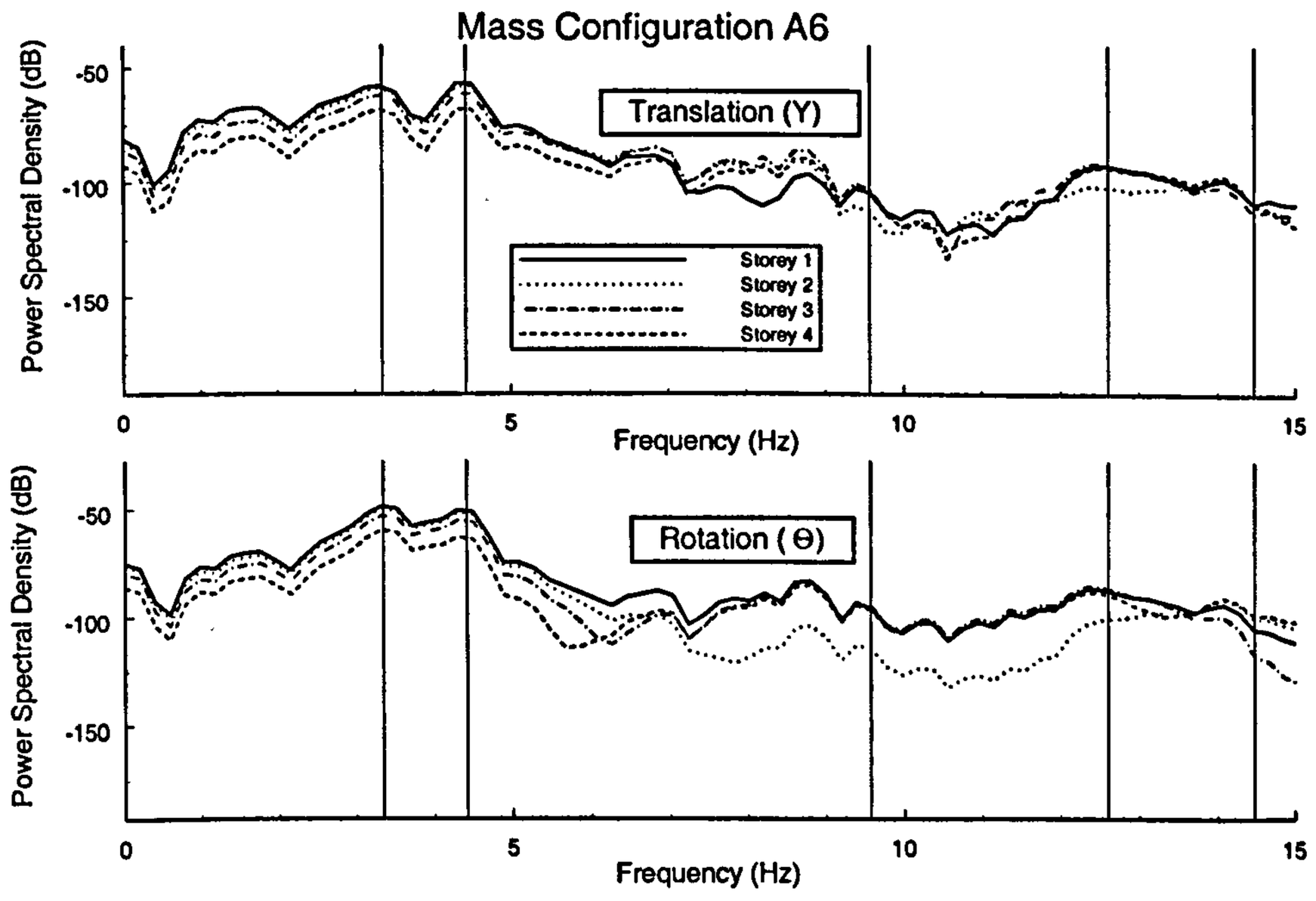

Figure 7.13: Power spectral density of the storey displacements for mass configuration A6.

As shown from the PSDs of the storey displacement, most of the elastic response energy for all mass configurations is concentrated in the first two stories of the building model. As with the relative floor displacement PSD plots, the storey displacement response energy is concentrated within the range of the first two modes.

7.2.4 Elastic Time-History Analysis

In addition to the frequency domain analyses, elastic time-histories for all mass configurations were performed on both the beam yielding and column yielding models. The resulting model displacement and force values are not presented in this section, but are used as benchmark values for evaluating the results of the following section.

7.3 NON-LINEAR ANALYSIS

The elastic analysis described in the previous section is intended to provide an overview of the elastic response of the computer model. For this section, the non-linear capabilities of the model were enabled allowing the columns or perimeter beams to yield at predetermined member moment levels. In addition to the three mass configurations in the linear analysis, the non-linear analyses have a hinge configuration as an added parameter. These hinge configurations dictate the horizontal and vertical distribution of yielding moment in each column or perimeter beam of the model. In order to simplify the number of possible permutations, only two hinge configurations were studied in this Chapter. The hinge configurations are similar to those of the column yielding experimental model: CB and CC. For the beam yielding analytical model, the same hinge configurations as the column yielding model are used, only their locations are in the perimeter beams. Table 7.2 summa-

rizes the two hinge configurations for a typical floor. There is constant vertical strength distribution in both of the two hinge configurations.

Table 7.2: Analytical model hinge unit configurations

Column/ Perimeter Beam	Yielding Moment (N-m)		Column or Perimeter Beam Definition
	Hinge BB/CB	Hinge BC/CC	
L1	13.3	9.6	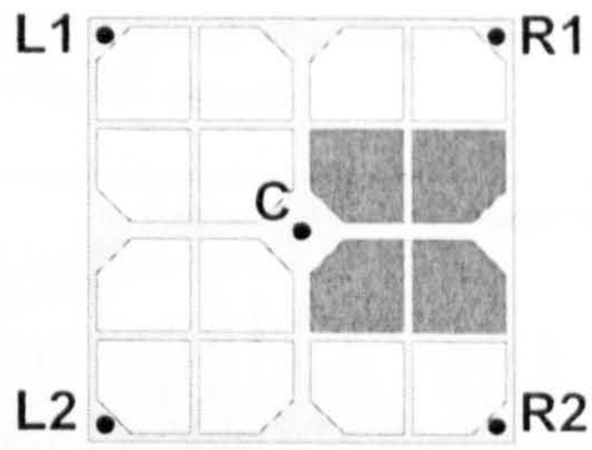
L2	13.3	9.6	
C	13.3	13.3	
R1	13.3	13.3	
R2	13.3	13.3	

Hinge configurations BB and BC denote beam yielding. Hinge configurations CB and CC denote column yielding.

Appendix D expands the analytical study to include hinge configurations that are code compatible with the Uniform Building Code for the three studied mass configurations.

7.3.1 Time-History Analysis

Time-history displacement traces are a common means of quantifying the dynamic response of a degree of freedom in a structure. Figure 7.14 shows the displacement traces (translational and rotational) of a column yielding model with Hinge Configuration CC, and base excitation intensity (RMSA[1]) of 7.7% g. The dotted lines represent the linear response, whereas the solid lines are the non-linear response. Displaying more than two time-histories for comparison purposes on a single plot can become confusing. The number of time-history plots necessary to fully describe the dynamic response of all four floors, with all three mass configurations, and both hinge configurations is inundating.

1. Root Mean Squared Acceleration (RMSA) is defined in Section 5.6.3 on page 138.

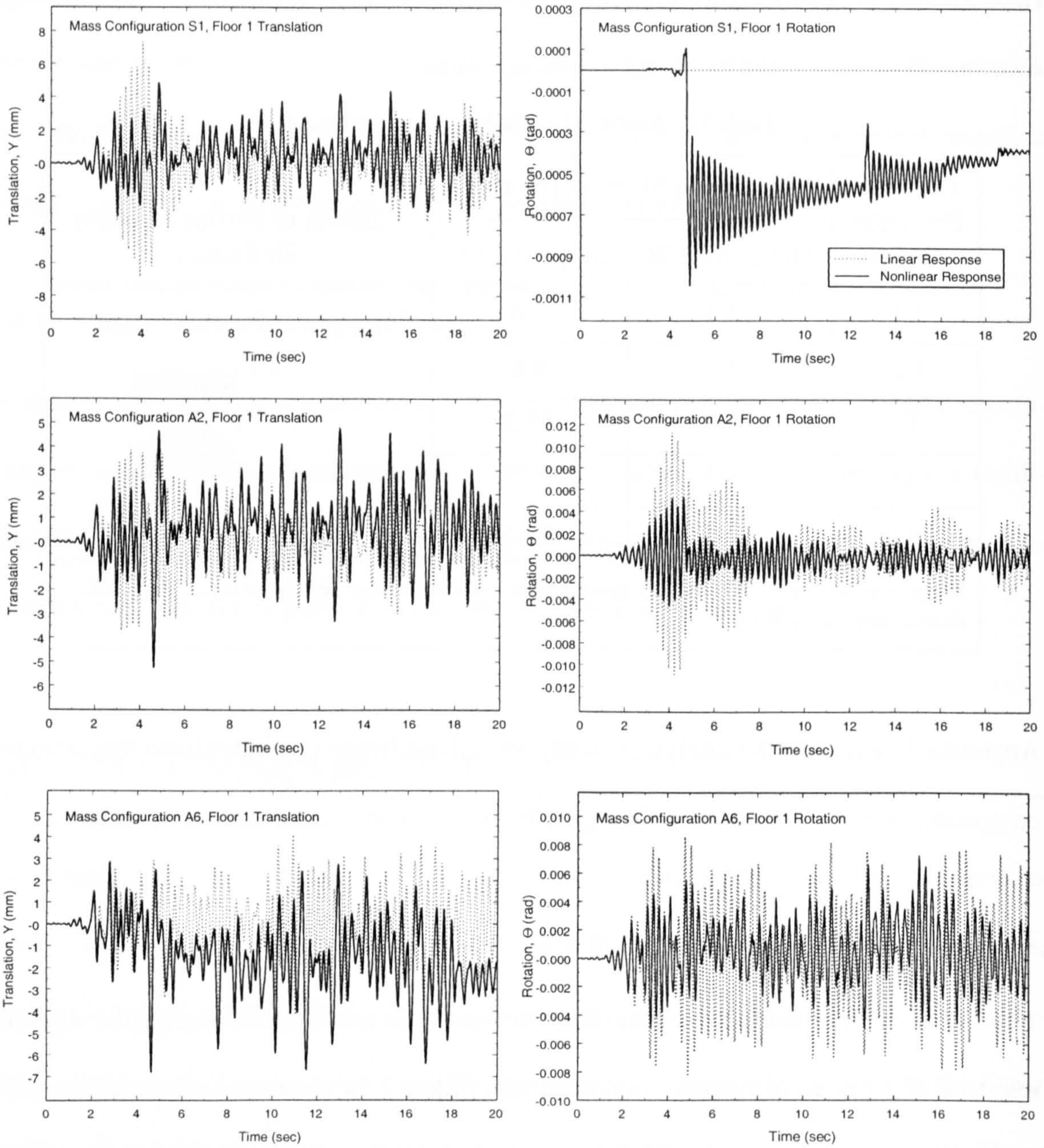

Figure 7.14: Comparison of first floor linear and non-linear time-histories for a typical column yielding model with hinge configuration CC, and an RMSA of 7.7% g

Also, it is more difficult to display response trends between the different model configurations and forcing intensities. For these reasons, emphasis is placed on the peak displacements demanded from the time-histories.

7.3.2 Peak Displacements

For the models being studied, the direction of the peak displacements is not a concern, since a reversed forcing would result in the same magnitude of response. Therefore, the displacement demand is the absolute value of the peak displacement. Figure 7.15 shows

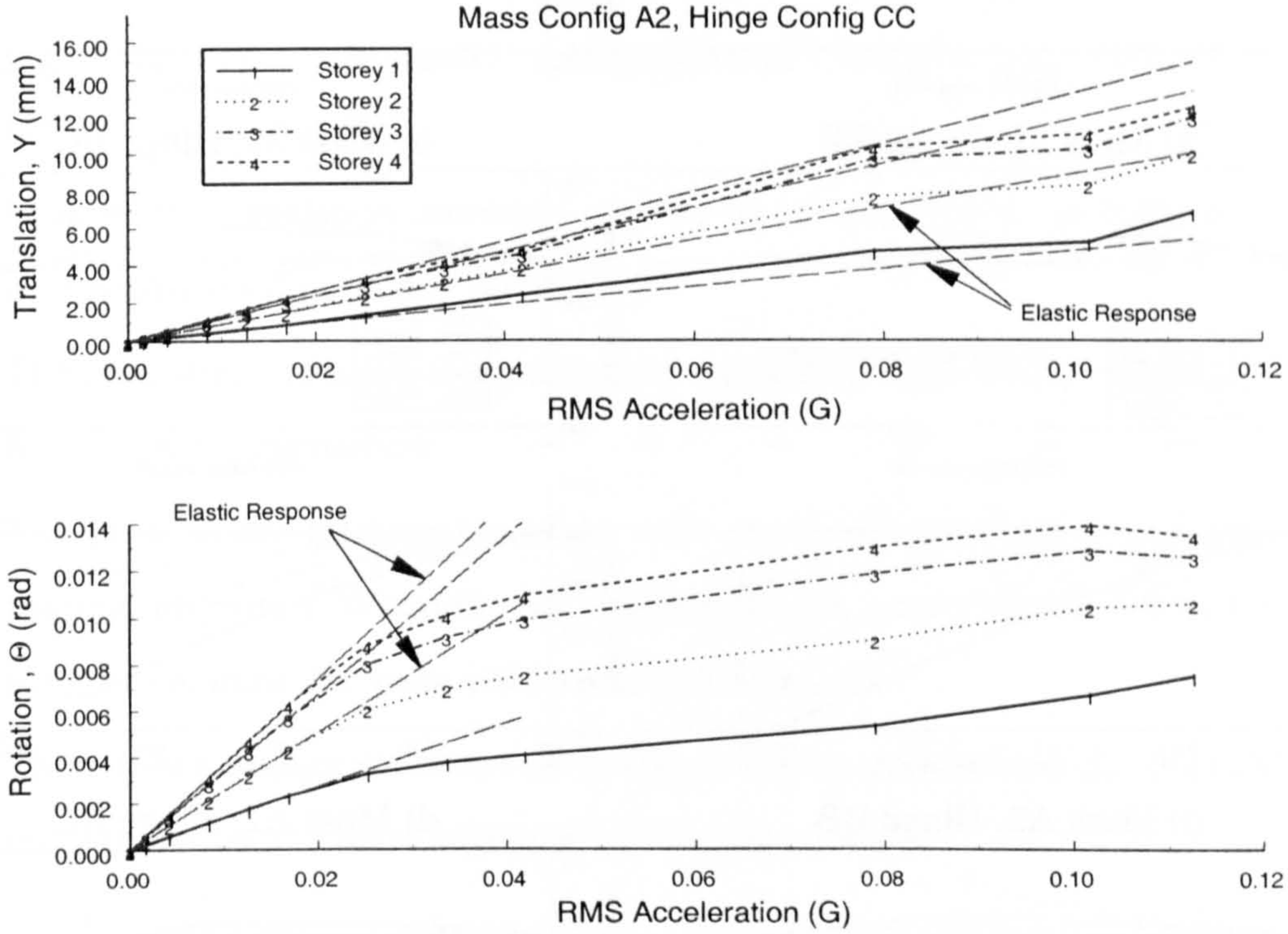

Figure 7.15: Displacement demand for a column yielding model with mass configuration A2, and hinge configuration CC.

the displacement demand of all four floors of one of the model configurations. Another way of presenting the peak displacement demand is to plot the difference between the inelastic and elastic peak displacements at the same forcing intensity:

$$\begin{aligned} Y_{\Delta} &= Y_{inelastic} - Y_{elastic} \\ \Theta_{\Delta} &= \Theta_{inelastic} - \Theta_{elastic} \end{aligned} \tag{7.6}$$

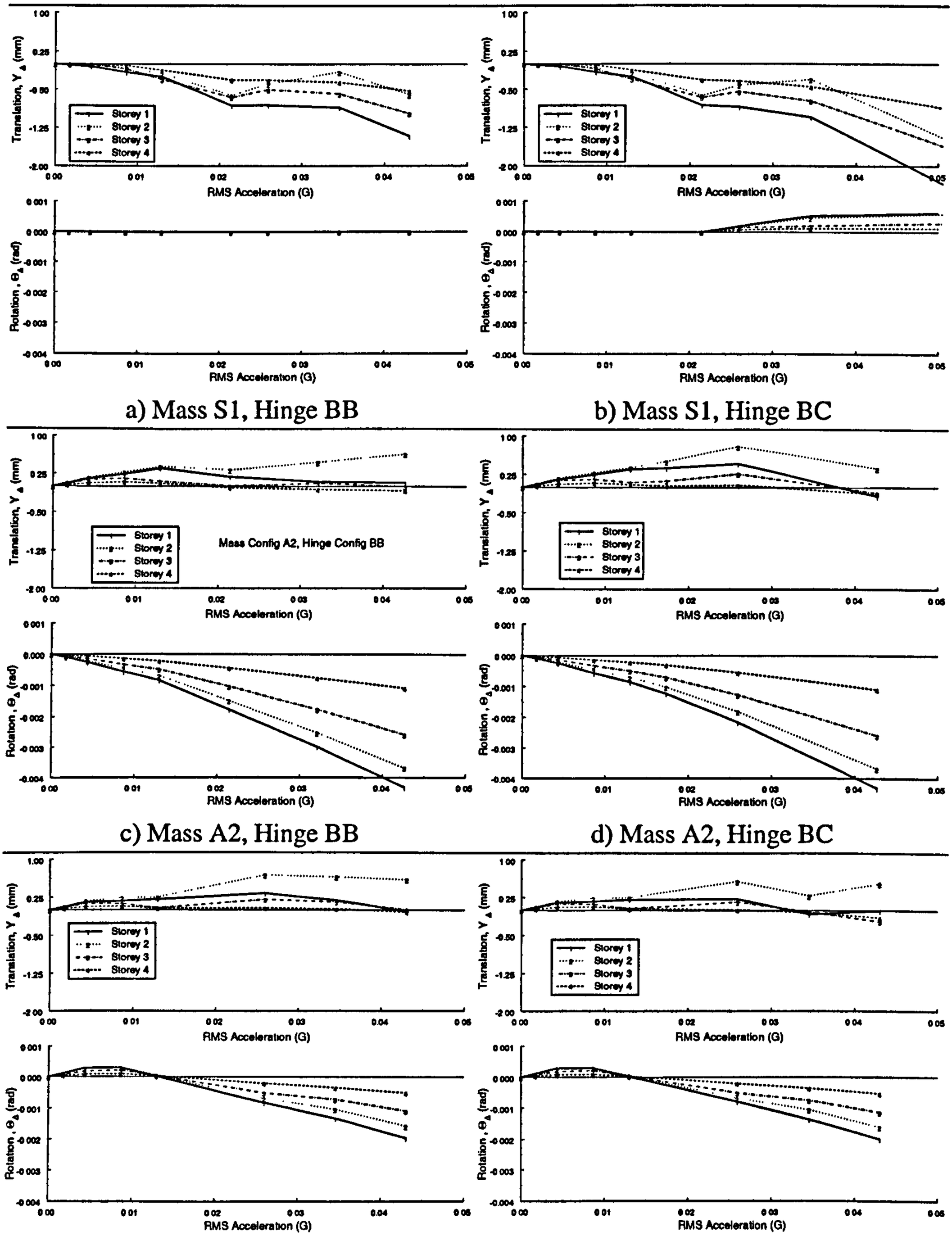

Figure 7.16: Difference between the inelastic and elastic displacement demand for all four stories of the beam yielding model.

Values of Y_Δ or Θ_Δ less then zero indicate a reduction in the peak total response due to inelastic behaviour. Figure 7.16 shows this relationship for the beam yielding model. The following points can be observed as a result of the beam yielding inelastic response:

- Peak storey translation is reduced in all four stories with the symmetric mass configuration S1.
- Peak storey rotation increases at the onset of exterior perimeter beam yielding for that symmetric mass configuration S1 and strength asymmetric hinge configuration BC.
- Peak storey translation increases slightly in all four floors for both mass asymmetric configurations A2 and A6.
- The peak storey rotation is significantly reduced in mass configuration A2, for all forcing intensities.
- The peak storey rotation increases with mass configuration A6 for low forcing intensities. When the forcing intensity is increased and yields the exterior columns, the peak storey rotation decreases.
- There is not a major influence on the peak displacements from the strength eccentricity for the mass asymmetric configurations.

Figure 7.17 shows the non-linear component of the peak displacement demand for hinge configurations CB and CC of the column yielding models. The following points can be observed as a result of the column yielding inelastic response:

- Peak storey translation is reduced for all four stories with the symmetric mass configuration S1.
- Peak storey translation increases for the first storey in mass configuration A2. This "soft" storey effect reduces the peak storey translation for the other three stories.
- The peak storey rotation is significantly reduced in mass configuration A2, for all forcing intensities.

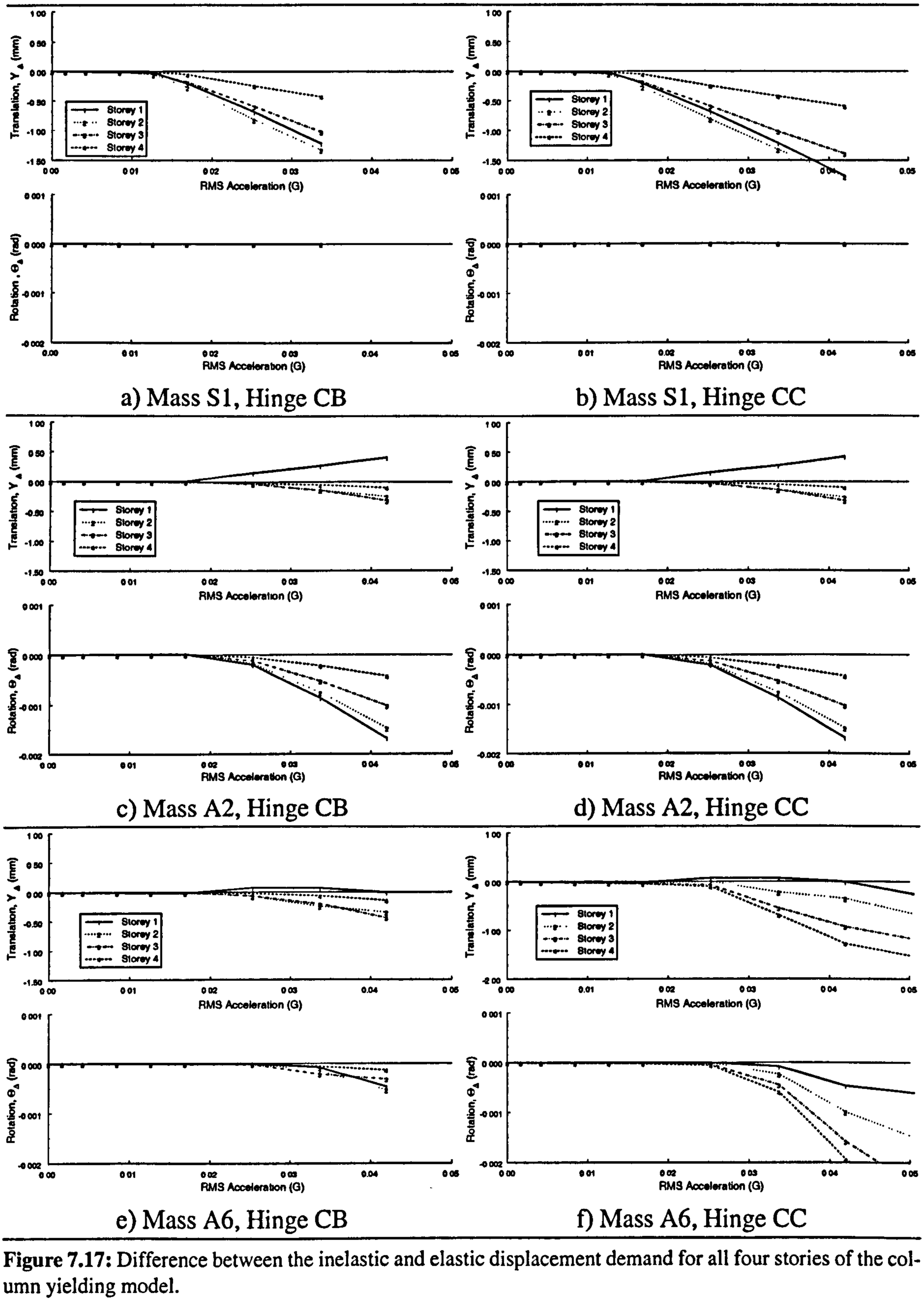

Figure 7.17: Difference between the inelastic and elastic displacement demand for all four stories of the column yielding model.

- The peak storey rotation increases with mass configuration A6 for low forcing intensities. When the forcing intensity is increased and yields the exterior columns, the peak storey rotation decreases.

7.4 HYSTERETIC ENERGY ABSORPTION

In this study, the absorbed hysteretic energy is used as a qualitative value for comparison between the various model configurations. It quantifies the amount of response energy absorbed by the structure due to its inelastic behaviour. This absorption is also termed the *hysteretic damping*, since the energy absorption acts to reduce the response of the structure to the applied ground motion (Section 6.4 on page 178). The means of computing the absorbed hysteretic energy for the analytical model is more direct than with the experimental model, since data recovery on member stresses and strains can be obtained directly from the finite element program. From the yielding members, strains can be correlated to curvature, and stresses can be integrated to obtain the moments in a member. The hysteretic energy absorbed by each member is the net area enclosed by the moment versus curvature plot of that member. The amount of hysteretic energy absorbed can be related to the damage potential of a structure. The higher the absorption demand, the higher the potential damage.

The length of the non-linear element which provides plasticity in the building model is fairly small (10mm). This small length provides a better comparison to the experimental model, where plasticity is concentrated in the hinge units. However, the resulting member curvatures are large and unrealistic due to their short member lengths. The hinge rotation,

which is the product of the member curvature and the member length (Section B.3 on page 245), provides a more meaningful description since the experimental hinge units do not have a curvature.

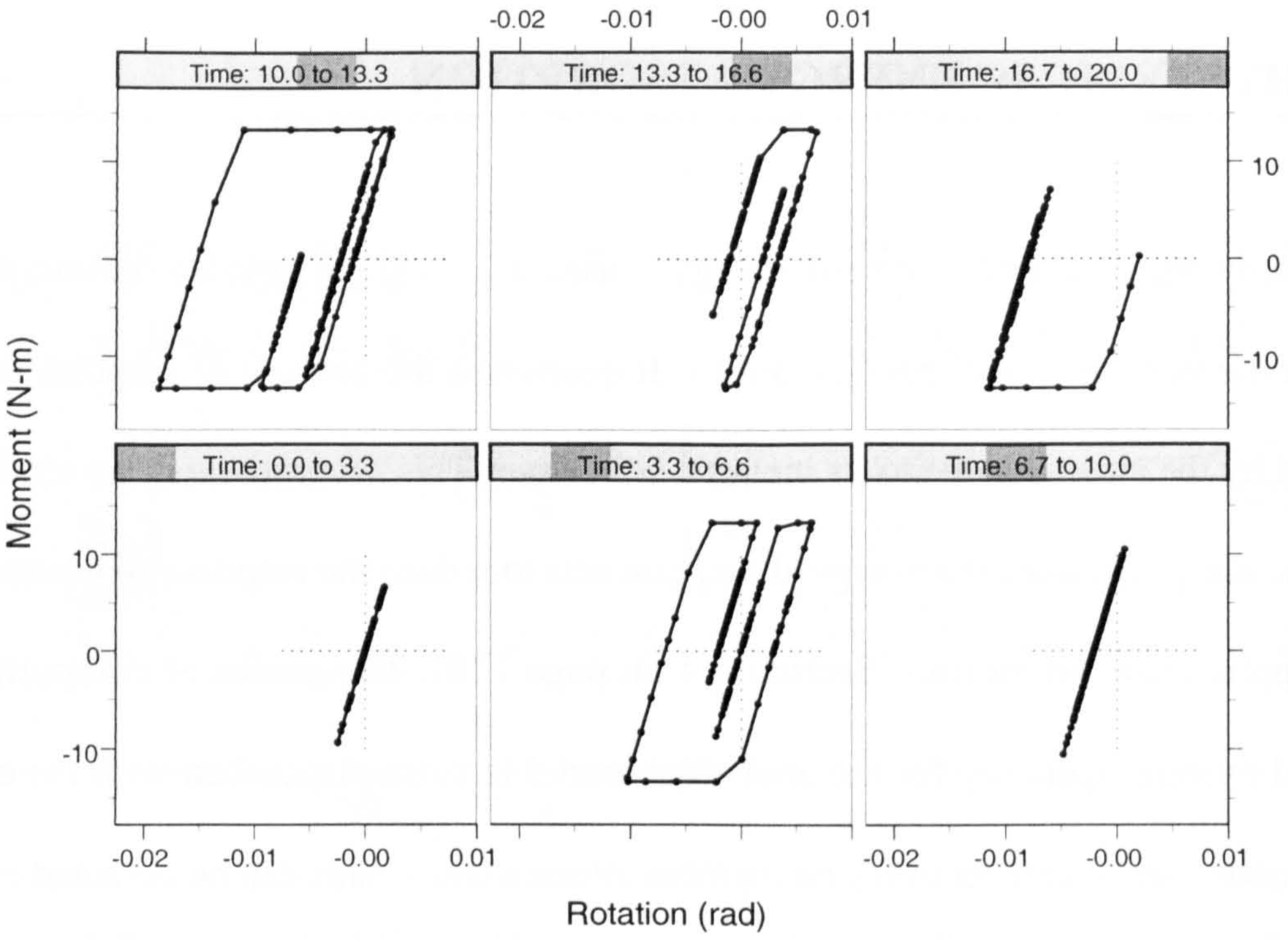

Figure 7.18: Moment versus rotation for the top of column number 2 in the first storey of a column yielding model with hinge configuration CC, mass configuration A2, and a RMSA of 7.7%g.

Figure 7.18 shows the moment versus rotation relationship for a hinge in an exterior column (left side) of a column yielding model. The energy absorption for the particular column is concentrated at three separate time intervals: 3.3 to 6.6 seconds, 10.0 to 13.3 seconds, and around 15 to 17 seconds. Each of these intervals contains only one large hysteretic loop. With the same forcing intensity and model configuration, Figure 7.19 shows the centre column with its numerous hysteresis loops in each of the time panels. This enhanced inelastic behaviour is a result of the stiff central column with the same yielding moment as the softer exterior columns. Like the experimental models, the central column

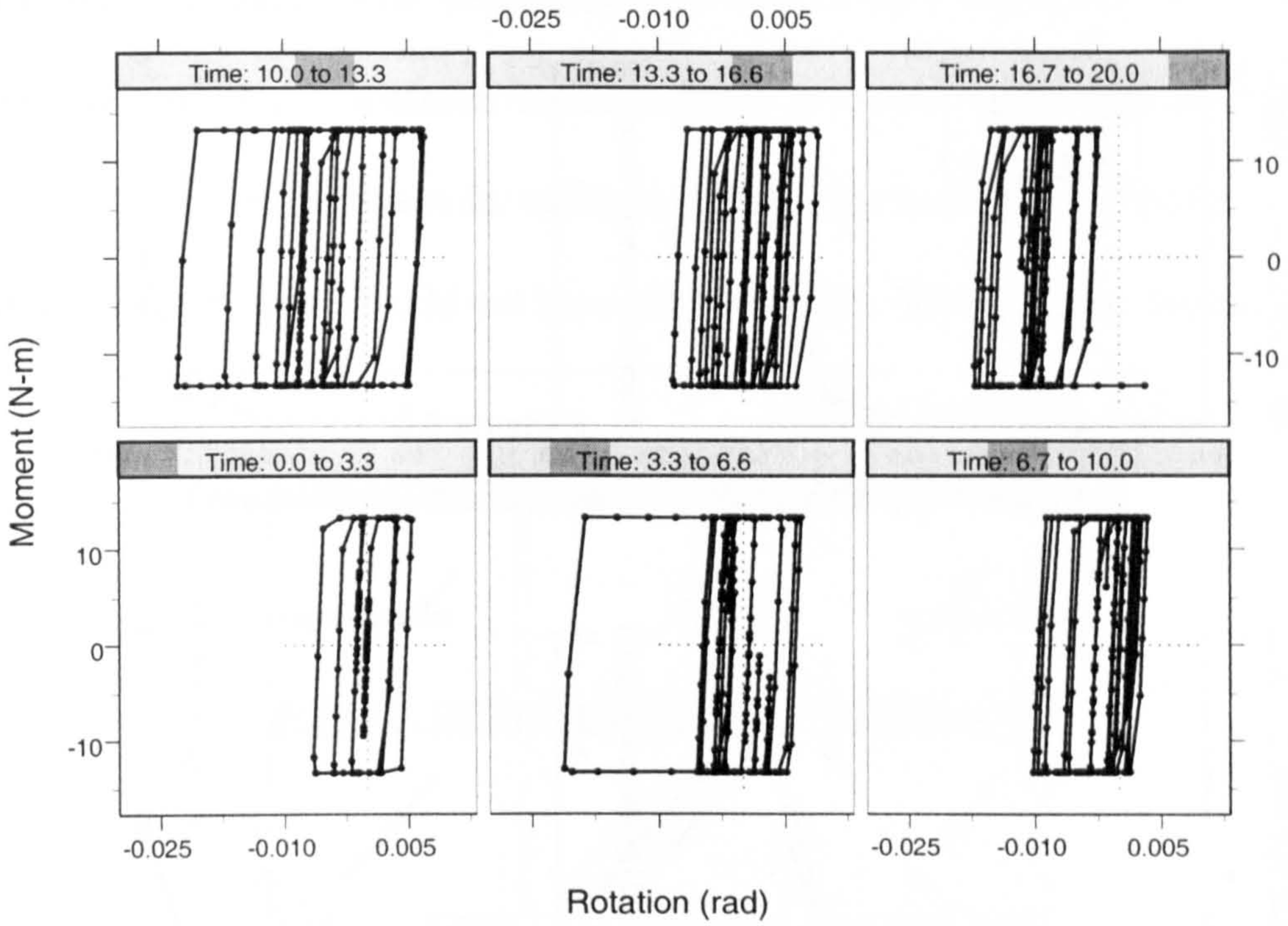

Figure 7.19: Moment versus rotation for the top of the interior column in the first storey of a column yielding model with hinge configuration CC, mass configuration A2, and a RMSA of 7.7%g.

of the analytical model yields at forcing intensities as low as 25% of that required to yield the first exterior column. This results in the central column contributing more to the hysteretic energy absorption than any other column.

Figure 7.20 totals the absorbed hysteretic energy for each side in the first storey. The first storey in the column yielding model is the only storey in which the exterior columns yield. The central column has reduced levels of inelasticity in each of the upper stories, with the fourth storey being totally elastic. The left side is the summation of columns L1 and L2, the right side is the summation of column R1 and R2. From this Figure, the following observations can be made from the energy absorption plots from the column yielding model:

- The centre column is responsible for most of the absorbed energy in a storey.

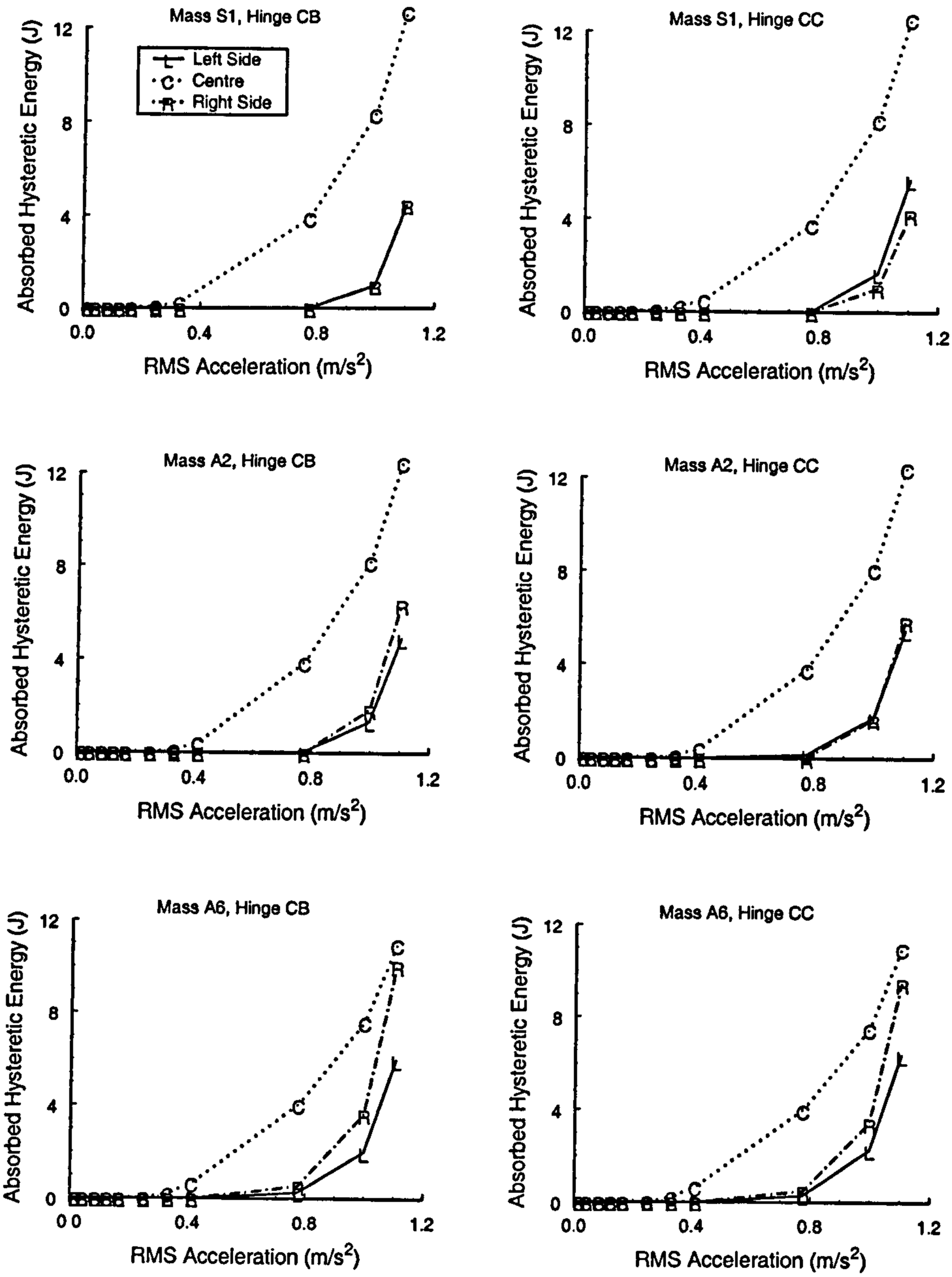

Figure 7.20: Absorbed Hysteretic Energy (in Joules) for Storey 1 of the column yielding models.

- Positioning the centre of mass toward a side of the building has the effect of increasing the hysteretic energy absorption demand on that side.

- Positioning the centre of strength toward a side of the building has the effect of reducing the hysteretic energy absorption demand on that side.

- A low net mass eccentricity[1] (e_n) results in similar energy absorption demands between the left and right sides of the building.

The hysteretic behaviour of the beam yielding configuration is different from the column yielding configuration. The elastic stiffness of the perimeter beam is much greater than that of the column members in order to better simulate the model floor rigidity. As a result, a quantitative comparison should not be made between the two yielding configurations.

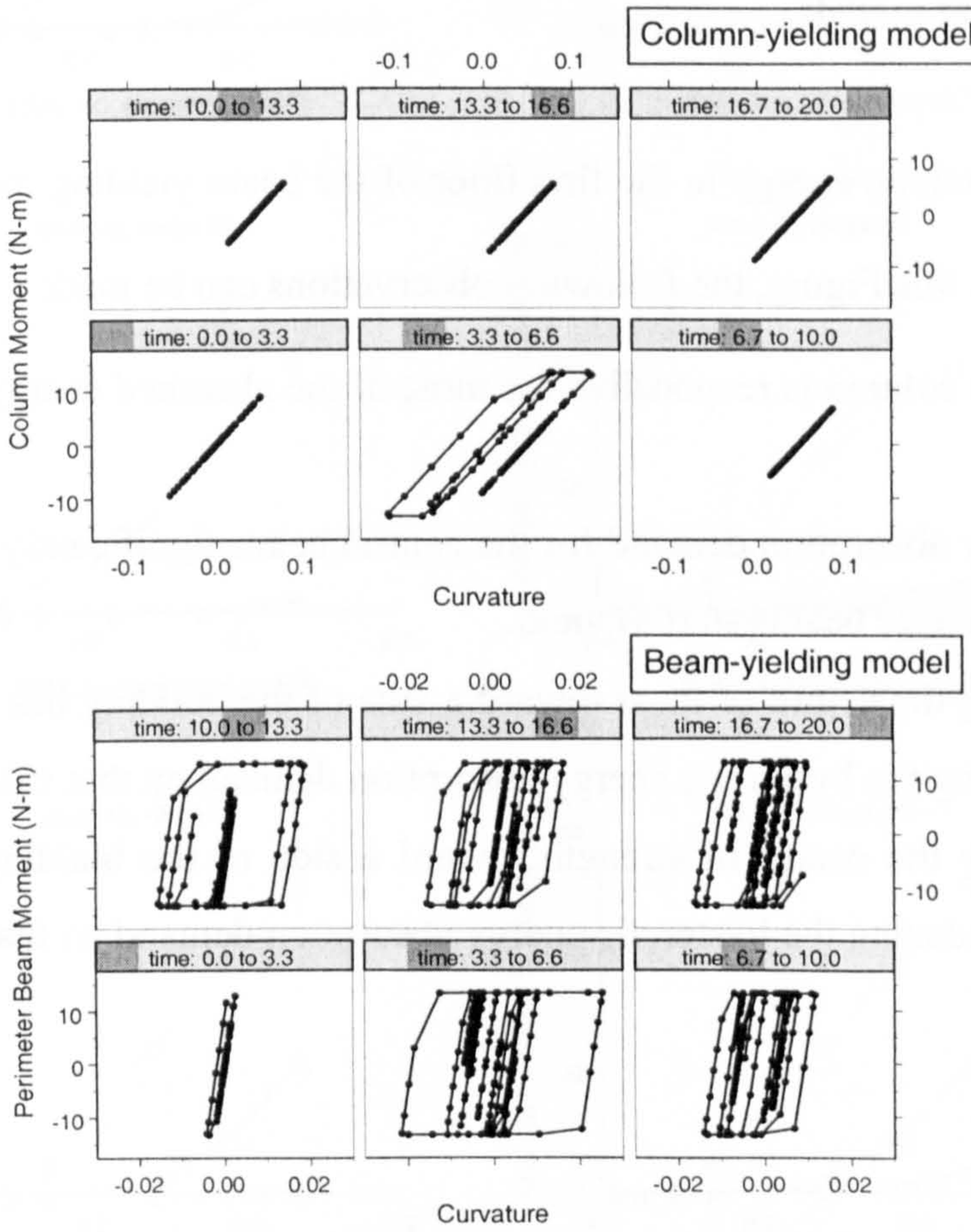

Figure 7.21: Comparison of hysteresis loops for the central column of the first storey (mass configuration S1, hinge configurations BB/CB, RMSA of 2.1% g.

Figure 7.21 shows the hysteresis plots for the same member in both the column and beam yielding model configurations. The beam yielding model has a higher energy absorption demand than that of the column yielding model with the same mass and strength distribu-

1. The net mass eccentricity is the difference between the mass and strength eccentricity, $e_n=e_m-e_s$. The net mass eccentricity is only valid for the column yielding model (see Section 4.4 on page 104).

tion. The main behavioural difference between the two yielding configurations is that the beam yielding columns can have moments higher than their yielding moment, because of member continuity. As a result, a yielding storey in the beam yielding models has a reduced stiffness, but the storey does not become perfectly plastic, as can be the case with the column yielding models.

The absorbed hysteretic energy in the first floor of the beam yielding models is shown in Figure 7.22. From this Figure, the following observations can be made:

- The centre column is responsible for most of the absorbed energy in a storey.
- The energy absorption demand for the central beam significantly increases as the perimeter beams start to yield.
- Positioning the centre of mass toward a side of the building has the effect of increasing the hysteretic energy absorption demand on that side.
- Positioning the centre of strength toward a side of the building has the effect of reducing the hysteretic energy absorption demand on that side.

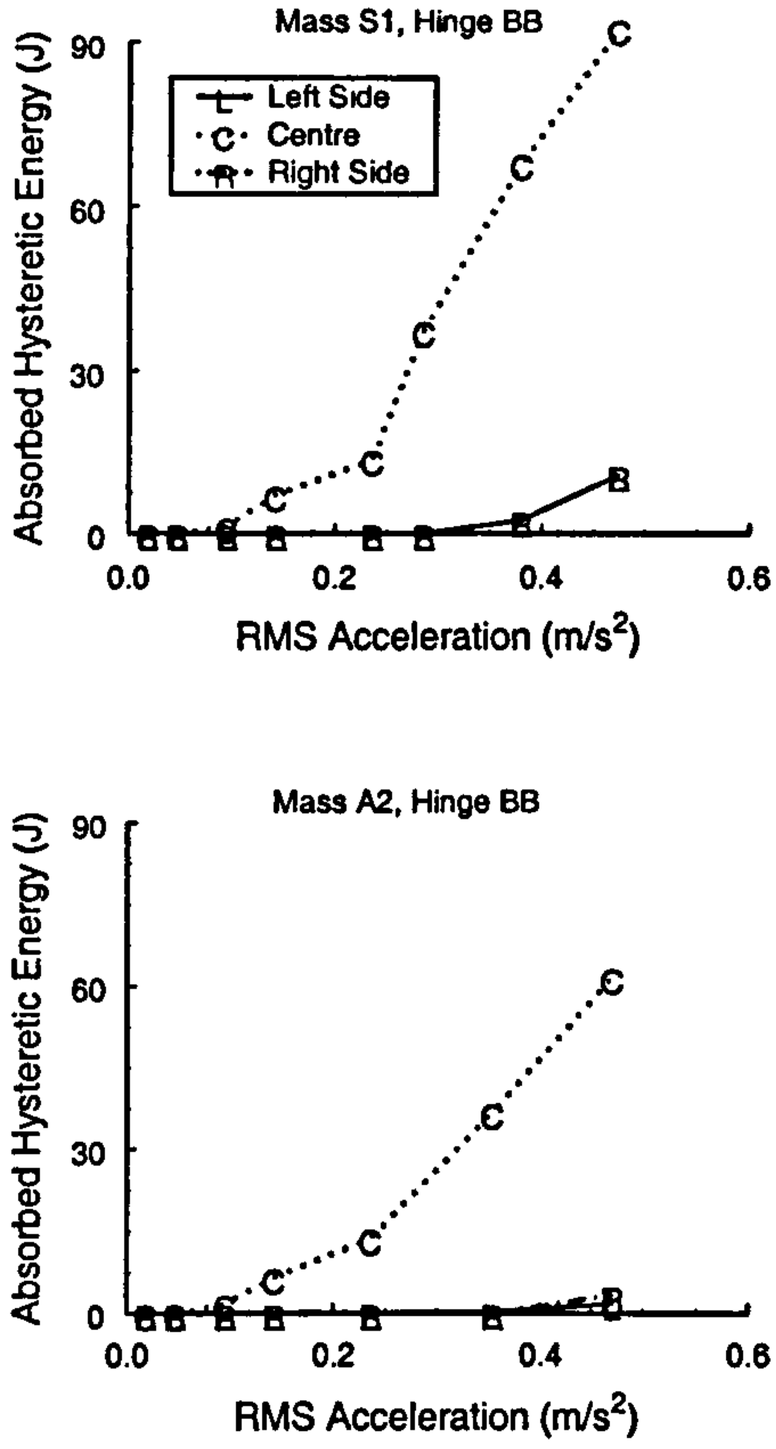

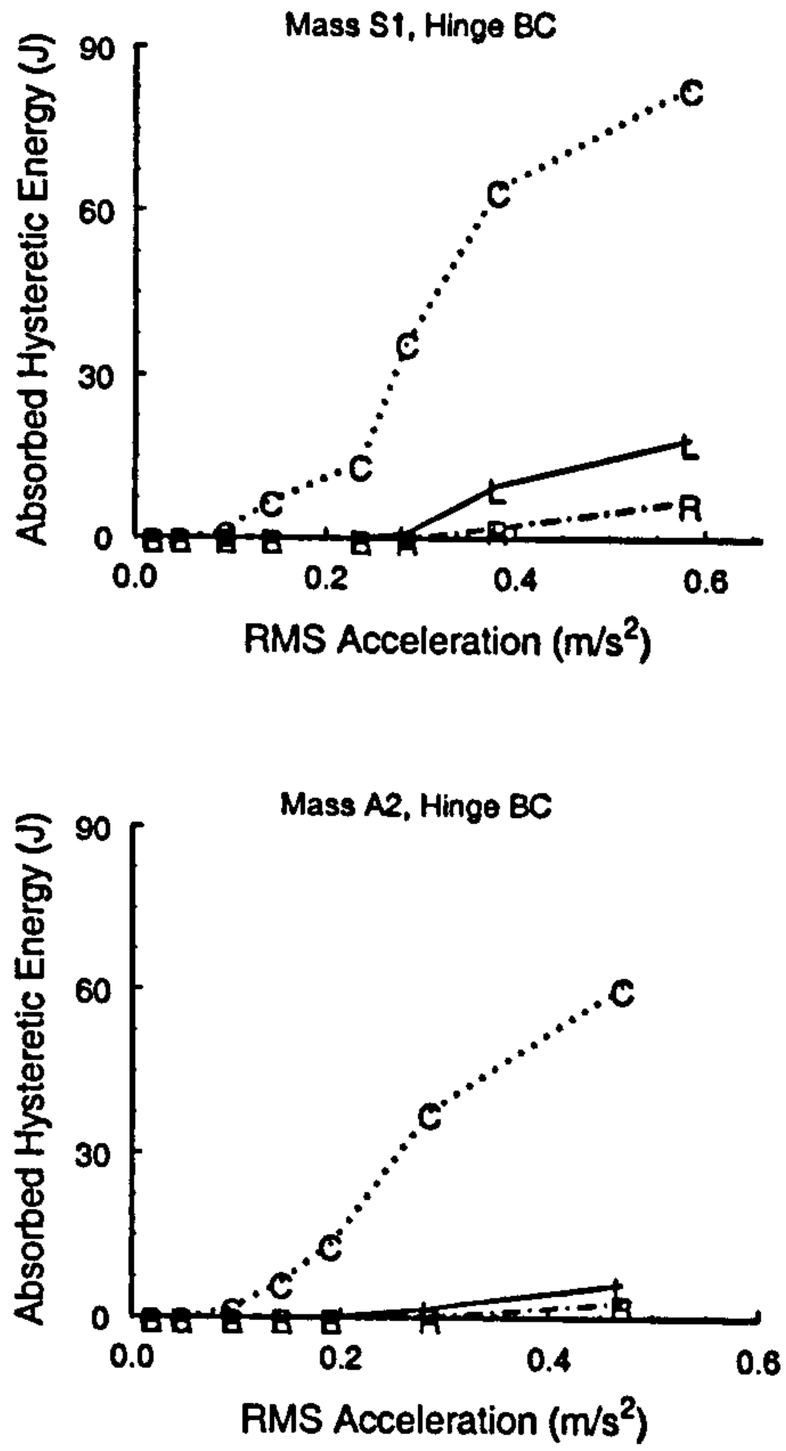

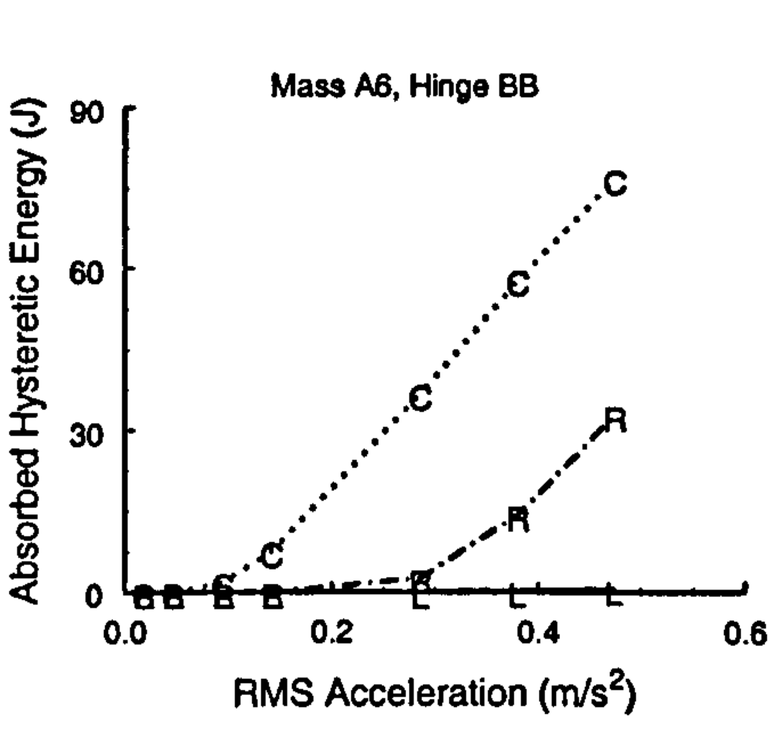

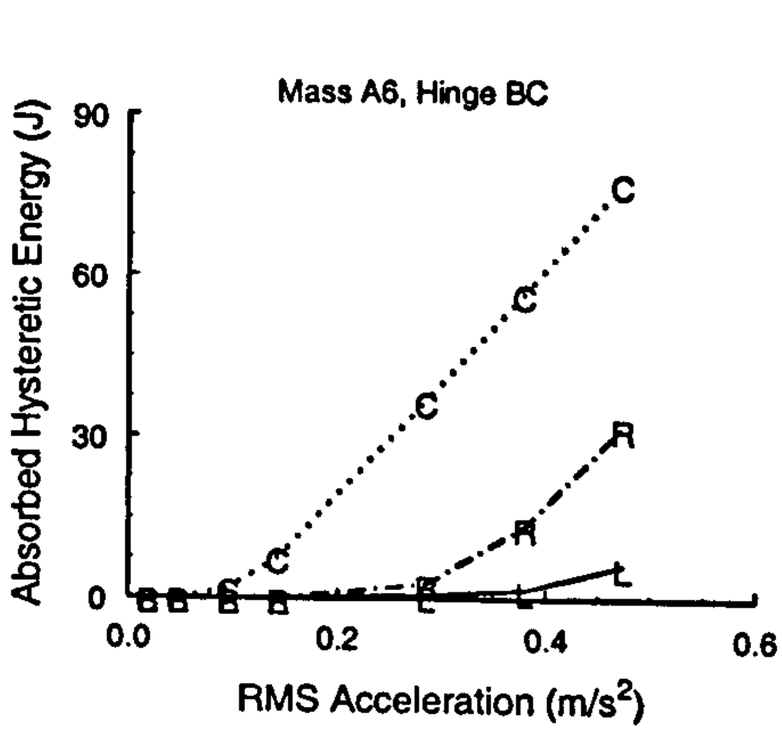

Figure 7.22: Absorbed Hysteretic Energy (in Joules) for Floor 1 of the beam yielding models.

CHAPTER 8

CONCLUSION

The principal objectives of this study were in the development and evaluation of the non-linear capabilities of the experimental model, its hinging mechanisms, and its elastic and inelastic dynamic response characteristics. Analytical models have also been developed as a comparison to the experimental model, and to predict the inelastic response of a UBC94 code compatible model. This chapter summarizes the results from the experimental model (Chapter 5), its hinging mechanisms (Chapter 6), and the analytical model (Chapter 7).

8.1 CONCLUSIONS IN RELATION TO SCOPE OF RESEARCH PROJECT

The Introduction (Chapter 1) highlighted the key objectives of this research programme.

Each of these objectives are individually addressed below:

- ***Develop and calibrate simulated hinge joint model for experimental dynamic response studies of multi-storey buildings.***

Chapter 4 (*Hinge Unit Design*), as well as a published conference paper (presented on page 313) describes the design and calibration methods for the hinge unit devices. The hinge units were calibrated both statically and dynamically. Initially, three different friction pad materials were developed for the hinge units. As a result of experimental static load testing of the hinge units, PTFE was selected as the hinge friction pad material to be used throughout this study. PTFE resulted in a low standard deviation of plastic moment between successive calibration tests for its range of moment capacity. Unfortunately, in terms of a codified strength distribution the maximum practical plastic moment for the PTFE was too small for the relatively stiff central columns. PTFE was used in all column hinges for consistency. However, a code compatible strength distribution for the studied model configuration is only possible with stainless steel as the friction pad material for the central column.

- ***Quantify the performance of the experimental hinge unit devices.***

The performance of the hinge units is presented in Chapter 6 (*Hinge Unit Performance*).

The hinge unit devices allow a great number of inelastic experimental tests to be per-

formed in a relatively short period of time. Over 520 four-storey inelastic tests (varying mass and strength eccentricity, forcing intensity, and yielding configuration) were performed over a total of three weeks. The hinge units are able to simulate hysteretic behaviour in the columns or floor beams of the experimental model through Coulomb damping. However, the energy absorption results presented in this study are based on correlating the floor displacements with the internal moments in the hinge units. This proved adequate enough to describe general behaviour, but not accurate enough to quantify the absorbed energy results. Future research should instrument with strain gauges the columns at key hinge locations. This would capture the hinge moments, which in conjunction with floor displacements (and hence associated hinge rotations) would result in quantifiable absorbed energy in each individual hinge unit.

- ***Assess the performance of the hinge units with regards to future experimental and commercial applications.***

The hinge units performed remarkably well as a means of incorporating inelastic behaviour at select locations in an experimental building model. Future research programs could benefit from their inclusion, even without moment acquisition of the hinge units. Their main experimental benefit is their repeatable ability to model plastic hinging in structural members.

Commercial applications for these hinge units are not as obvious. Although low in maintenance as an energy absorbing device, the displacements associated with plastic rotation could cause excessive damage in secondary structural or non-structural elements in a building. Therefore, their use as an energy absorption device within buildings at the floor-

column connections may not be appropriate. However, their use as an isolation system may prove to have some advantages, especially when combined with other energy absorption devices commercially available.

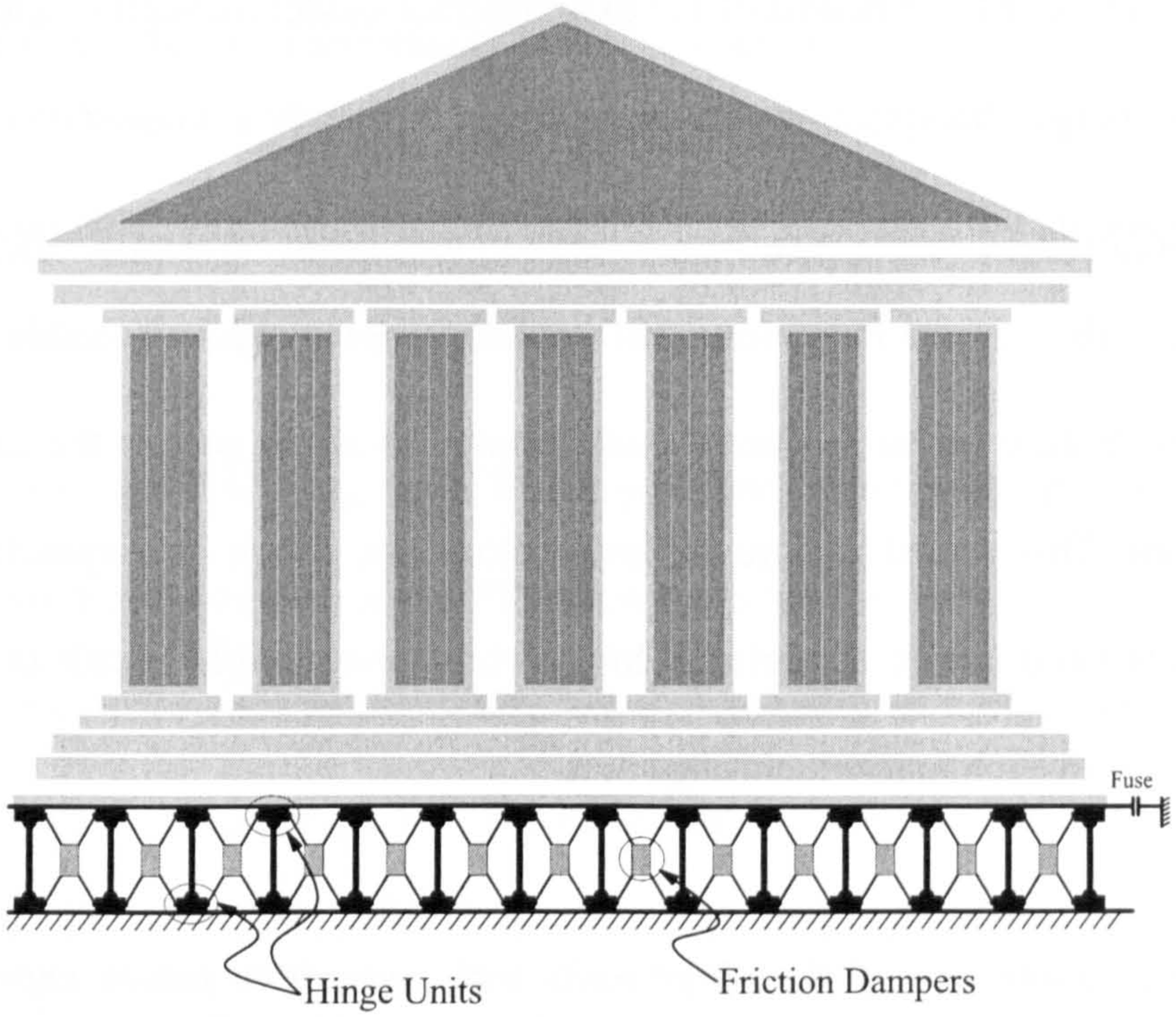

Figure 8.1: Possible commercial application for a base isolation system that utilizes the basic design of the tested hinge unit devices.

As described for both the single-storey and four-storey column yielding configurations, rotational building motions are reduced, and pure translation increased as yielding intensity in the hinge units increases. This behaviour, when combined with friction dampers (as in Figure 8.1) could prove to be an efficient isolation system provided that the building utilities are designed for the increased displacements. Fuses could easily be incorporated into the friction dampers, or at an external location as shown.

- ***Characterise the combinations of mass and strength eccentricity that give rise to significant inelastic lateral-torsional coupling in the building models.***

In general, inelastic behaviour reduced the amount of lateral-torsional interaction in the displacement response of the models. However, strength asymmetry in the mass symmetric model (S1) does introduce torsional motions upon yielding. Both the experimental and analytical models showed that during yielding, the side furthest from the centre of strength (left side) yielded first with mass configuration S1. The resulting shift in stiffness centroid from the geometric centre of the storey to a position closer to the right side of the model creates an effective mass eccentricity, thus initiating lateral-torsional interaction. For moderate forcing intensities, this behaviour normally occurred at the two ground motion impulses (near t=5s and t=13s). When the storey "snaps" back to an elastic state, the centre of stiffness coincides with the mass centre, thus no torsional forces are imposed on the model. From this point, torsional motions of the floors in the model damp down in a manner similar to free vibration decay.

- ***Highlight combinations of mass and strength eccentricities that counter-balance the adverse affects from torsional coupling.***

Other than the points addressed above, inelastic behaviour generally reduces the effects of torsional-coupling. The peak rotations of both the experimental and analytical models normally occurred during segments of the response in which the structure behaved elastically. As discussed in Chapter 5, as the forcing intensity increases, the difference between the peak floor displacements of the left and right side of the model decreases. This reduction

in side displacement ratio is most evident with mass configuration A2, where the centre of mass and strength nearly coincide.

- ***Identify changes in the dynamic amplification of torsional response due to asymmetric yielding, and how this compares to the elastic modal coupling identified in earlier studies.***

The response of the analytical models which are based on the experimental models (Chapter 7) shows a decrease in torsional response compared to that of the elastic response for the column yielding configurations. The column yielding model has a "soft-storey" effect as discussed earlier. This is not the case with the beam yielding configuration. The effective storey height for this yielding configuration increases as the hinges in the associated floor yield. This results in a more subtle period shift of the response during yielding. Translational displacements for all stories of the mass asymmetric configurations are increased over the elastic response as forcing intensity increases.

The analytical UBC94 code compatible models (Appendix D) showed that the multi-storey response in the upper storeys is different from the ground storey response when significant member inelasticity is present. This is in contrast with previous analytical studies which have assumed that the multi-storey response is an extension of single-storey response. The code compatible analytical models showed that the side closest to the centre of mass in an upper storey is more vulnerable (in terms of moment demand), even though these have a higher design strength.

- ***Identify and quantify changes to building frequencies and dynamic earthquake response, caused by plastic yield.***

The spectograms presented in Chapter 5 detailed the shift in response frequency as a result of plastic behaviour in the experimental models. Inelastic behaviour normally occurred in the first storey, as this storey is strength deficient in comparison with the upper stories in the model, as described in Appendix C.

Chapter 5 shows that the first two modes contribute most to the response of the building model. The third and fourth modes have more influence on the top two stories of the experimental model. The first floor of the column yielding configuration acts as a "soft-storey", filtering much of the input motion to the upper stories.

- ***Quantify the energy absorbing capabilities of the hinge units, and their influence on the model's response.***

Both the experimental and analytical models have the capability to absorb response energy through inelastic behaviour. Since the hinge units do not actually "yield", but rather "slip" along a friction plane, true moment-curvature type hysteretic damping is not present in the experimental hinge units. However, the experimental hinge units do experience Coulomb damping during rotation of the hinges, and this can simulate hysteretic damping (in terms of moment-rotation).

During the experimental tests, moments were not measured in the columns of the building model. The moment and rotation in a hinge unit used for the absorbed energy calculations are based on a simple Euler beam, and as a consequence did not produce reliable quantita-

tive results. However, the accuracy of the absorbed energy results are sufficient as a comparison between the different strength and mass configurations for the column yielding hinge arrangement. The beam yielding configuration was insufficiently instrumented during the experimental tests to allow reliable estimates of column moments to be made.

Chapter 6 presented a comparison of the absorbed hysteretic energy for the column yielding configuration. The centre column absorbs significantly more energy than the exterior columns. This is a result of the strength deficiency of the centre column, which "yielded" during even the low-level forcing intensities. Both the strength and mass eccentricities affected the amount of absorbed energy in the exterior column hinges. In a mass symmetric model, the side closest to the centre of strength absorbs the least amount of energy. This is a result of the reduction in hinge plastic moment at the side furthest from the centre of strength. When the centres of mass and strength nearly coincide, similar energy absorption demand is placed on the hinge units.

- ***Develop an analytical model that accurately predicts the response of the various experimental models.***

An analytical model representing the experimental model was developed, and presented in Chapter 7. The analytical model differed from the experimental model in that an actual plastic hinge length of the column was used to model member inelasticity. From this, hysteretic energy was measured in terms of moment-curvature, and not moment-rotation. Also, the moments in the plastic hinges were able to be reported, resulting in more accurate energy absorption values. The analytical model also computed all floor displacements

from the beam yielding hinge configuration. These points aside, the general behaviour of the analytical model matched closely that of the experimental models.

The symmetric mass model benefited from a reduction in peak storey translation for both the column and beam yielding model configurations. Strength eccentricity does not have a major impact on peak displacements for the mass asymmetric models A2 and A6.

- ***Determine the required design forces, and assess existing analytical and codified design procedures with regards to the analytical model.***

The main advantage of the codified analytical model over the experimental models is in the strength distribution, particularly with the centre column. Appendix A presents the Uniform Building Code (1994 edition) procedure for distributing the required storey strength amongst the individual columns. In Appendix D, an analytical model was developed that is code compatible with UBC94. The model emulates both the beam yielding and column yielding hinge arrangement, with mass configurations S1, A2, and A6. The conclusions and summary of this codified analytical model are presented at the end of Appendix D.

8.2 SUMMARY

For the class of building studied, the response results are affected by forcing intensity, storey mass eccentricity, individual member strengths, number of building floors, and location of member yielding (whether in the columns or beams of the structure). The results in this study are based on a single ground motion. An important non-linear parameter for a

spectrum compatible ground motion is the phasing of the time-history frequencies. Ground motion phasing is a parameter that was unable to be included in this study. Also, variation of the ratio of uncoupled rotation to translation frequency (Ω), an important parameter for elastic response, was not able to be considered. With all of these parameters considered, it comes to the point where the inelastic response behaviour of a specific building structure should be studied individually on a case by case basis, using its own site seismicity.

Appendicies

APPENDIX A

UNIFORM BUILDING CODE DESIGN PROCEDURES

This section details the Uniform Building Code 1994, Volume 2 (UBC94) design provisions in relation to the experimental and analytical models. Two distinct analysis procedures are offered in UBC94. These are the *static* and *dynamic* lateral-force procedure, as specified in UBC94 sections 1627.8.2 and 1627.8.3, respectively. Both of these sections are applicable to actual buildings with physical and dynamic characteristics similar to the

experimental models. These two design provisions are discussed in Sections A.3 and A.4 below.

A.1 BUILDING CLASSIFICATION

UBC94 classifies buildings as either *regular* or *irregular*, depending on the building configuration. Buildings that have significant discontinuities in either their physical configuration or their lateral force-resisting members are classified as irregular. The building models in this study do not have discontinuities in their lateral force-resisting systems, since the column arrangements are symmetric about the geometric and elastic stiffness centres of the model. These symmetries exist for all four floors.

The presence of mass eccentricity in a floor can result in a building being classified as irregular. UBC94 identifies horizontal mass eccentricity as a *plan structural irregularity.* The criteria for this torsional irregularity is when the maximum storey drift (including the accidental eccentricity, e_a) at one side of the structure is 20% greater than the average storey drift. In terms of the experimental models, this can be written as:

$$\frac{\delta_L \text{ or } \delta_R}{\Delta} > 1.2 \qquad \text{(A.1)}$$

where δ_L and δ_R are the absolute maximum floor displacements of the left and right sides, respectively. The maximum floor displacement at the centre of stiffness is indicated by Δ. Since the floor diaphragms are perfectly rigid, δ_L and δ_R for a floor can be defined as:

$$\delta_L = \Delta - \frac{b}{2}\Theta, \text{ and}$$
$$\delta_R = \Delta + \frac{b}{2}\Theta \qquad \text{(A.2)}$$

where Δ and Θ are respectively the translation and rotation at the geometric centre of the floor, and b is the distance between the two sides. Substituting equation (A.2) into equation (A.1) and simplifying, results in:

$$\left|\frac{b\Theta}{2\Delta}\right| < 0.2 \qquad \text{(A.3)}$$

Equation (A.3) is one of the criteria for classifying the model as *regular*. Otherwise, the model is identified as an *irregular* building structure. It should be noted that there are other codified guidelines for classifying a building as having plan structural irregularities. However, this is the only criteria for plan irregularities applicable to the experimental model as considered in this study.

UBC94 also indentifies buildings having *vertical structural irregularities*. These include soft-storeys (stiffness irregularity), weak-storeys (strength irregularity), vertical mass irregularity, and geometric irregularities. With certain hinge configurations, the experimental model can be classified as irregular due to discontinuities in storey capacity (weak storey). However, in determining a code compatible hinge configuration for the models, only vertical distribution of mass, stiffness, and geometry are considered. As such, the models are defined as not having vertical irregularities.

Whether a model is defined as regular or irregular affects the method of analysis used in determining the design base shear, and its distribution amongst the lateral load resisting

elements in the model. The static lateral force procedure may be used for buildings classified a *regular*. The dynamic lateral force procedure can be used for buildings classified as either *regular* or *irregular*. However, UBC94 also allows irregular buildings with less than six storeys to be analysed using the static lateral force procedure. As a result, the models in this study may have their strength distribution based on either of these two analysis methods.

Table A.1: UBC94 classification for studied building mass configurations.

		Beam Yielding Configuration	Column Yielding Configuration
Mass S1	$\frac{b\Theta}{2\Delta}$	0.14	0.13
	Classification	Regular	Regular
	A_x	1.0	1.0
Mass A2	$\frac{b\Theta}{2\Delta}$	0.27 > 0.2	0.24 > 0.2
	Classification	Irregular	Irregular
	A_x	1.12	1.06
Mass A6	$\frac{b\Theta}{2\Delta}$	0.51 > 0.2	0.47 > 0.2
	Classification	Irregular	Irregular
	A_x	1.58	1.49

Table A.1 lists the classifications for the studied experimental models. The floor displacements, Δ and Θ, are based on results from the static lateral force procedure. The parameter A_x is the torsional amplification (defined in Section A.3 below), and is only applicable to the static lateral force procedure. The static procedure classifies all but the symmetric mass configurations as irregular.

A.2 HORIZONTAL TORSIONAL MOMENTS

When floor diaphragms are rigid, as is case with the experimental models, the horizontal torsional moment is accounted for by placing the storey shear forces at possible lateral eccentricities on the floors above the storey in consideration. Each of these floors have two design eccentricities (e_1 and e_2) which are displaced from the its centre of floor mass by 5% of the building plan dimension perpendicular to the considered forcing, b. This 5% offset, defined as the accidental eccentricity, e_a, accounts for both uncertainties in construction, and the possible adverse effects of lateral-torsional coupling.

$$e_{1,2} = e_m \pm \underbrace{0.05b}_{e_a} \tag{A.4}$$

Members are designed based on the eccentricity (e_1 or e_2) which results in the most severe member force. The Uniform Building Code does not permit a reduction in member design forces due to the horizontal torsional moment. In other words, a member must be able to resist, at the very least, the horizontal shear when applied to the centre of stiffness of the stories. These two design eccentricities are depicted in Figure A.1 for a typical model floor.

A.3 STATIC LATERAL FORCE PROCEDURE

If the building structure is identified as *irregular* by violating equation (A.3), then the accidental eccentricity at each floor is also amplified by the factor A_x:

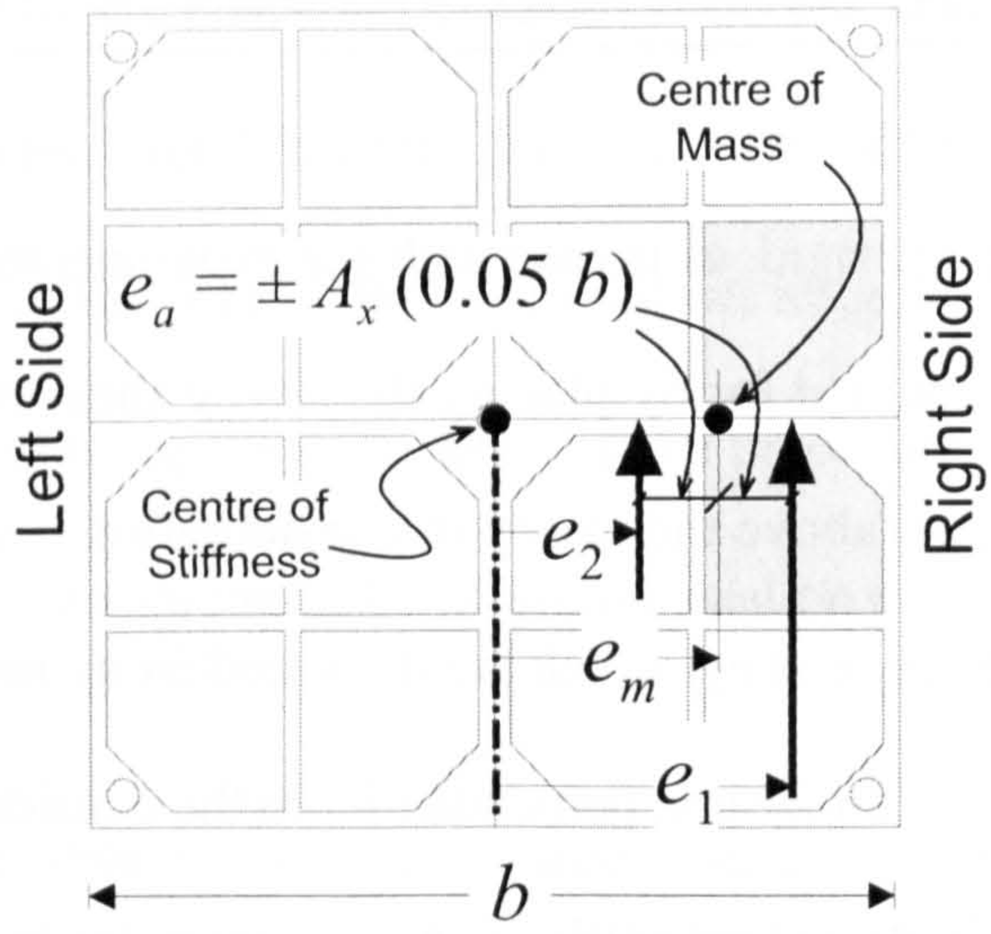

Figure A.1: Definition of design eccentricities e_1 and e_2.

$$A_x = \left(\frac{\delta_{max}}{1.2\Delta}\right)^2 \leq 3.0 \tag{A.5}$$

where δ_{max} is the maximum of the corner displacements, δ_L and δ_R, for the floor in consideration. The factor, A_x, is intended to account for increased vulnerability due to torsional effects.

The differences between the static and dynamic design procedures are mainly in the determination of the design base shear, V_b, and its vertical distribution among the floors. The Uniform Building Code specifies the design base shear for the building model as a function of the building weight, its damage capacity, importance, soil foundation, structural period, and seismic hazard:

$$V_b = \frac{ICZ}{R_w} W \tag{A.6}$$

where,

V_b The building base design shear.

Z The Seismic zone factor. Normally, this is a value between 0.075 and 0.4, and is related to the degree of seismic hazard at a particular site (0.4 corresponds to Seismic Zone 4—an area of high seismic hazard). The value can also be related to the historic peak free–field ground acceleration applicable to a region (in terms of g).

C This is a numerical coefficient in terms of the site soil condition coefficient, S, and the estimated fundamental building period, T (see equation (A.7)).

R_w This is a numerical coefficient which represents the degree of safe cyclic inelastic behaviour the structure is capable of maintaining. For an ordinary moment resisting frame, as in the experimental model, this value can be taken as 6.

W The total seismic dead load of the building, and is taken as the dead weight of the building model.

$$C \leq \begin{cases} \dfrac{1.25S}{\sqrt[3]{T^2}} & S = 1 \text{ for rock and stiff soils} \\ 2.75 \end{cases} \qquad \text{(A.7)}$$

The seismic base shear, V_b, is distributed vertically at each storey as a design force (F_x), which is proportioned by the weight of each storey (w_x), and its corresponding height above the base (h_x):

$$F_x = V_b \frac{(w_x h_x)}{\sum_{i=1}^{4} h_i w_i} + F_t \qquad \text{(A.8)}$$

and

$$F_t = \begin{cases} 0.07TV_b \leq 0.25V_b & \text{if } T > 0.7 \text{seconds} \\ 0 & \text{otherwise} \end{cases} \qquad \text{(A.9)}$$

The storey design shear at any level is the sum of the horizontal design forces at and above that level. In the above two equations, F_t is a concentrated load which is added to the top

storey design shear. This results in more demanding design storey shears, especially at higher periods where spectral accelerations normally diminish. The addition of this concentrated load is assumed zero. This is not a very significant assumption, as the experimental models, as well as most actual four–storey buildings have fundamental periods less than 0.7 seconds. In addition, it should be noted that the experimental model is not a scaled model, and as such, the application of F_t is probably not applicable.

Table A.2: Static vertical seismic design shear distribution.

Floor	Beam Yield Configuration		Column Yield Configuration	
	Storey Shear Force	Design Shear Force	Storey Shear Force	Design Shear Force
1	$0.08V_b$	V_b	$0.11V_b$	V_b
2	$0.20V_b$	$0.92V_b$	$0.22V_b$	$0.89V_b$
3	$0.30V_b$	$0.72V_b$	$0.33V_b$	$0.67V_b$
4	$0.42V_b$	$0.42V_b$	$0.34V_b$	$0.34V_b$

Table A.2 lists both the storey shear and the applied design shear forces in both model yielding configurations. Table A.3 lists the two design eccentricities for each mass configuration. For brevity, the accidental eccentricity tabulated is based on the average storey amplification, A_x, which is similar for each storey.

A.4 DYNAMIC LATERAL FORCE PROCEDURE

With this type of analysis method, the applied forcing can be either through a response spectrum, or a time–history base (ground) motion. In this study, the applied forcing is defined by the UBC94 design response spectra, as specified in equation (A.6). UBC94

Table A.3: Initial Design eccentricities

Mass Config.	Beam yielding configuration				Column yielding configuration‡			
	e_m (mm)	e_a† (mm)	e_1 (mm)	e_2 (mm)	e_m (mm)	e_a† (mm)	e_1 (mm)	e_2 (mm)
S1	0.0	50.0	–50.0	50.0	0.0	50.0	–50.0	50.0
A2	47.7	56.1	–8.4	103.8	37.6	53.0	–15.4	90.6
A6	143.0	82.0	61.0	225.0	112.7	73.2	39.5	185.9

† $e_a = A_x 5\% b$.
‡ For the first three floors only. The fourth floor has the eccentricities of the beam yield configuration.

requires that at least 90% of the participating structural mass be included in the analysis, and that these modes be combined with accepted methods that account for the modal interaction. Both the SRSS and CQC modal combination rules are acceptable methods. The CQC method has been found to produce more accurate results than SRSS for modal combinations of typical buildings [GUPTA, 1991]. However, SRSS is more widely used in practice as it too is an accepted method, easier to implement, and the resulting response is not too conservative. As with the static analysis procedure described in the previous section, the mass eccentricity of each floor must also account for the accidental eccentricity, e_a. However, the accidental eccentricity is not amplified by A_x, as the dynamic procedure implicitly accounts for the torsional amplification.

The mode shapes and their corresponding frequencies are based on the calibrated analytical results (see Section 3.3.2 on page 58). All eight modes from the mass (equation (3.6)) and stiffness (equation (3.8)) matrices are combined using the SRSS method of modal superposition, which defines the combined response value, R, as:

$$R = \sqrt{\sum_{i=1}^{N} R_i^2} \tag{A.10}$$

where, R_i is the response (or member forces) from mode i. UBC94 does not allow the total base shear calculated by this method to be less than 90% of that from equation (A.6) in the static procedure for regular buildings. This increases to 100% of the static shear for irregular buildings. For consistency, the dynamic base shears were all scaled to equal that for the static method. Therefore, the dynamic method only distributes the base shear vertically among the floors.

A.5 COMPARISON OF LATERAL FORCE PROCEDURES

The effect of mass eccentricity on the total strength distribution in the building models is to increase the strength of the exterior columns. The centre columns are unaffected by the design eccentricities, as they are positioned at the centre of elastic stiffness, where floor rotations do not increase their translational displacement demand (individual column torsional displacement demand has not been considered in this study). The ratio of increased strength demand to that of a symmetric structure with e_a=0 is the *Strength Amplification* of that column:

$$\text{Strength Amplification} = \frac{F_y\big|_{e_d = e}}{F_y\big|_{e_d = 0}} \tag{A.11}$$

where, e_d is the design eccentricity and e is either e_1 or e_2 from equation (A.4), and possibly amplified by equation (A.5). F_y is the member strength evaluated at an eccentricity of

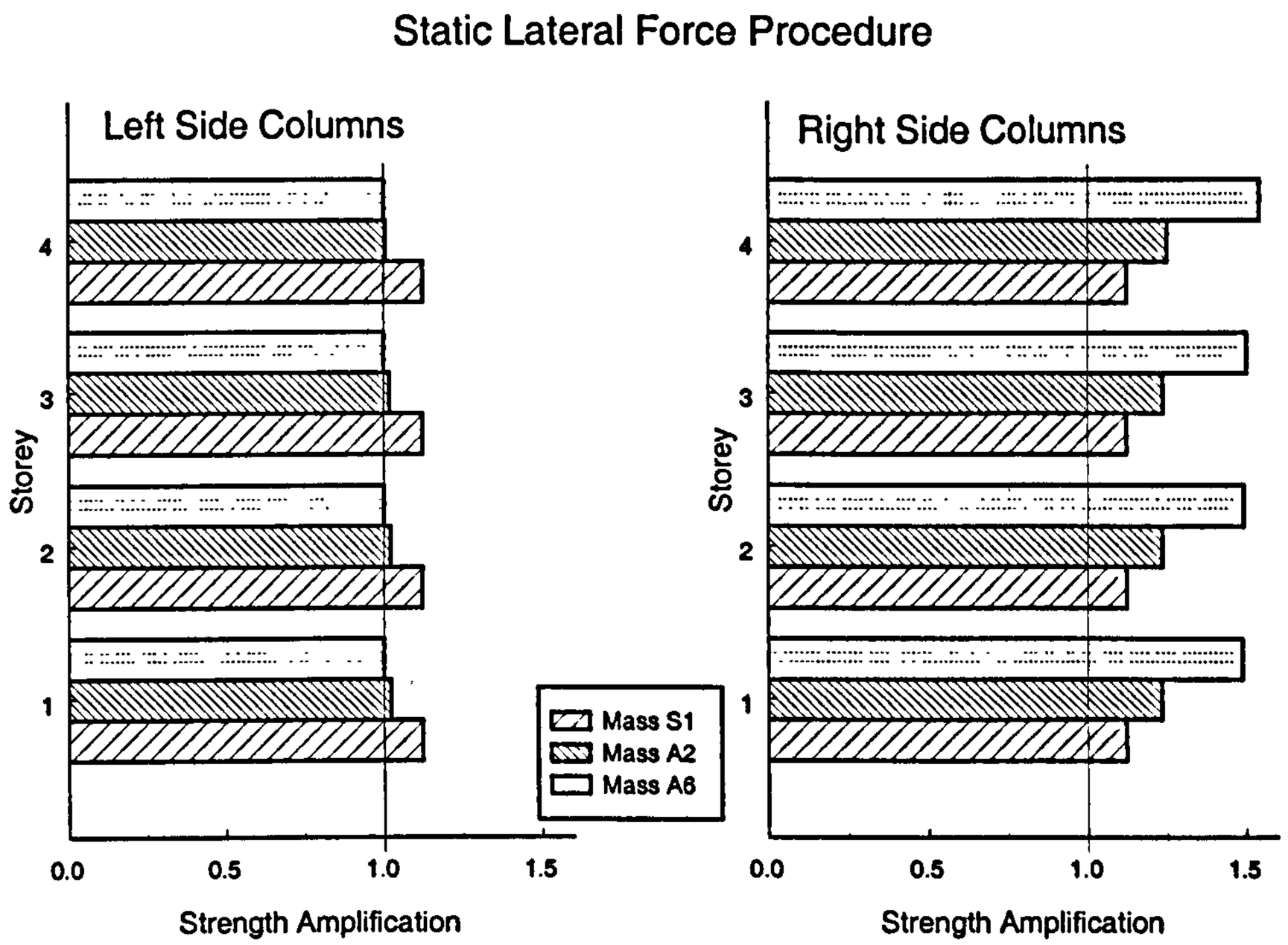

Figure A.2: Strength amplification of the left and right columns from the static lateral force procedure.

e_d with either the static or dynamic lateral force procedure. Figures A.2 and A.3 show the strength amplifications as determined by the static and dynamic lateral force procedures, respectively. The static procedure (Figure A.2) results in larger strength amplifications of the right side columns for mass configuration A6. This is a result of the amplification factor (A_x), which magnifies the applied moments at each floor. For this particular model, the 150% amplification of the accidental eccentricity is somewhat conservative when compared to the dynamic procedure. Conversely, the dynamic procedure produces greater exterior column strength demands for the symmetric mass configuration S1. Mass configuration S1 is identified as a regular structure with the static procedure, and as such its accidental eccentricity is not amplified. This results in its lower strength demands for the exterior columns.

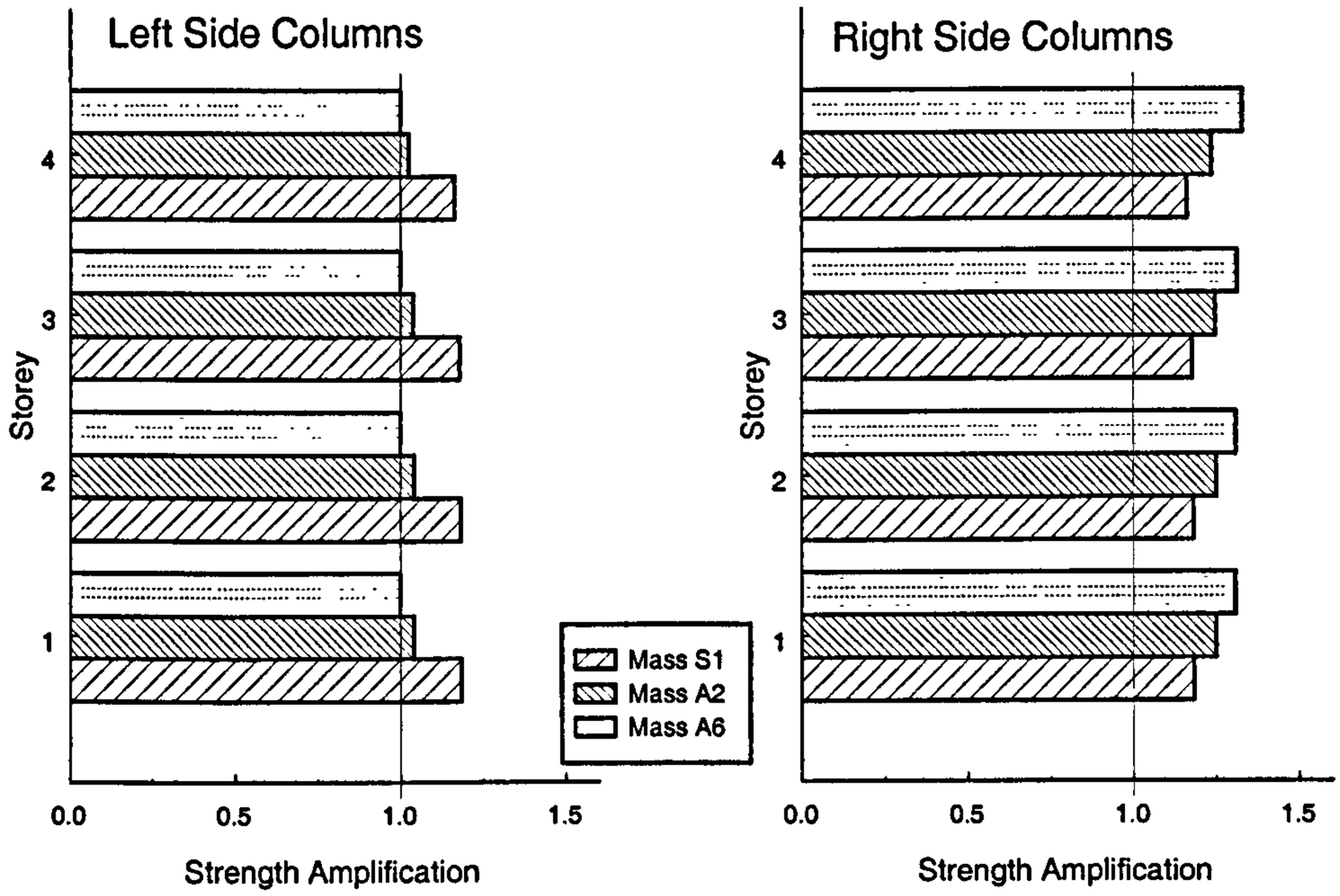

Figure A.3: Strength amplification of the left and right columns from the dynamic lateral force procedure.

Figure A.4 shows the ratio of strength amplification of the dynamic to static lateral force procedure for the exterior columns. This figure shows that the static strength amplification is reduced with respect to the dynamic strength amplification as mass eccentricity increases. This is also evident in the fourth storey, where the higher relative mass eccentricity of the fourth floor, due to its lower overall mass, influences the fourth storey in terms of a lower dynamic to static strength amplification ratio. Additionally, the left side exterior columns have a higher static to dynamic strength amplification ratio than the right side columns for a particular mass eccentricity with the difference between the two sides increasing with increasing mass eccentricity. The dynamic to static strength amplification ratio for the left side columns of mass configuration A6 is unity due to the UBC code requirement that member strength reductions due to lateral-torsional interaction are not allowed.

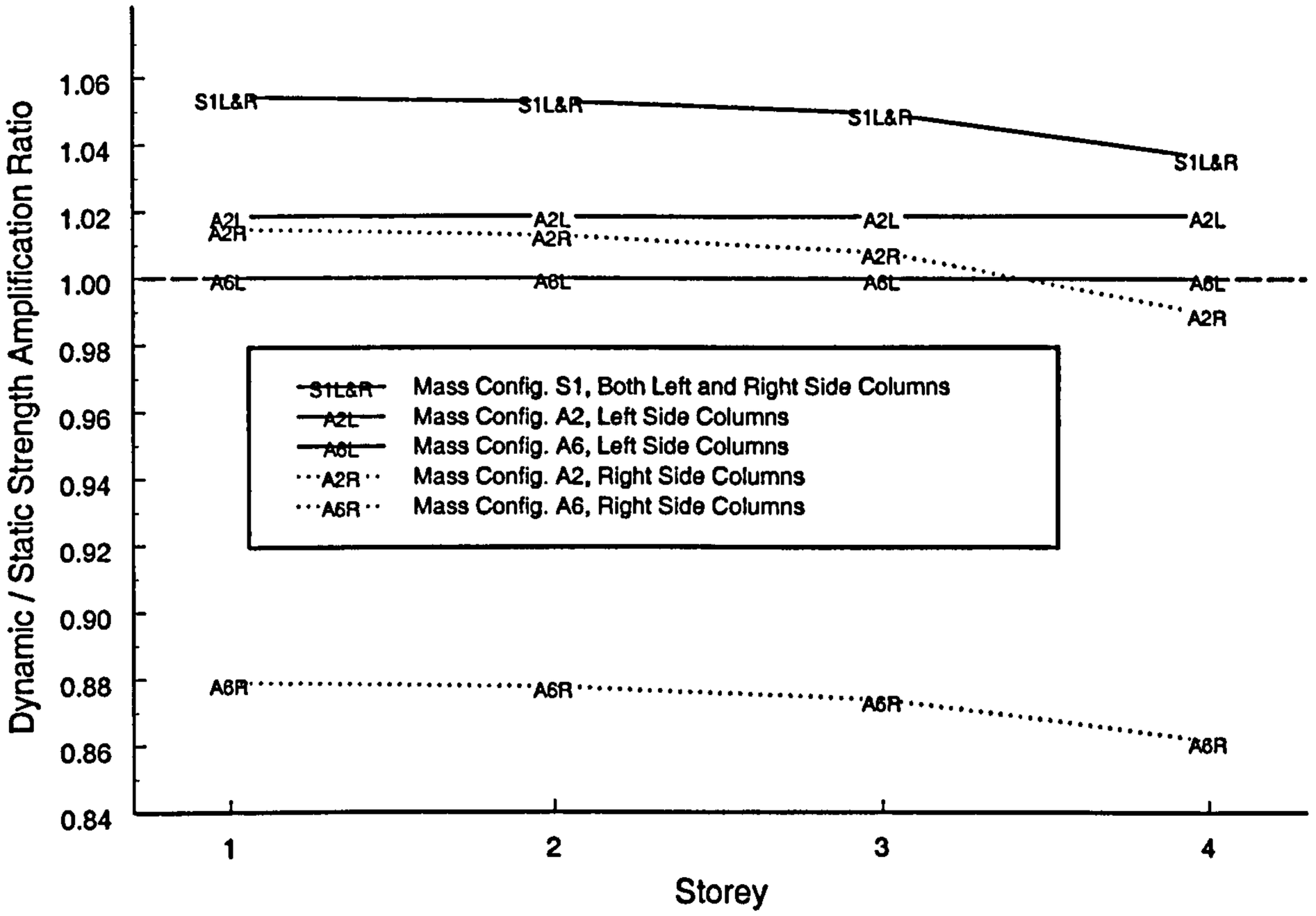

Figure A.4: Strength amplification comparison from the static and dynamic lateral force procedures.

ALL MISSING PAGES ARE BLANK

IN

ORIGINAL

APPENDIX B

ANALYTICAL MODEL

This section describes the analytical model used in this study, and the post-processing required to obtain the responses presented. Some emphasis is also placed on describing some of the peculiarities of the FEA modelling program, as well as a typical input data file to the FEA program.

B.1 STUDIED PARAMETER RANGES

The analytical model is based on the material properties and intended behaviour of the experimental model, as described in Chapter 7 (Section 7.1 on page 186). The range of mass and strength eccentricities was not expanded upon. Rather, the range of forcing intensity was increased from that of the experimental models. Table B.1 below lists the ranges of parameters studied.

Table B.1: Parameter ranges studied with the analytical models.

	Beam yielding models		Column yielding models	
	Experimental Compatible	UBC Code Compatible	Experimental Compatible	UBC Code Compatible
Forcing Intensity (RMSA)	0.17% g to 17% g	0.17% g to 3.3% g	0.17% g to 17% g	0.17% g to 3.3% g
Mass Eccentricity	S1, A2, A6	S1, A2, A6	S1, A2, A6	S1, A2, A6
Hinge Configuration	BB, BC, BD	UBC	CB, CC, CD	UBC

B.2 FORCING TIME HISTORIES

The forcing time histories are based on those recorded from the shake table surface during the experimental column yielding tests. A single base acceleration record was used for all of the analytical motions. The recorded table accelerations for the column yielding tests are superior to the beam yielding tests, which have a low signal to noise ratio in their recorded accelerations. This is a result of the low gain levels on both the A/D converter and the signal conditioner for the accelerometer (inclinometer) channel during the beam yielding tests. The column yielding acceleration record used for the analytical models was selected from a recorded table motion above a 1.5V gain that had the lowest deviation

from a trend line through the *RMS Acceleration* vs. *Voltage Gain* relationship (Figure 5.13 on page 137). This corresponded to the acceleration record from test C2CCI1. This record was uniformly scaled to the desired forcing intensity for each analytical test. The table accelerations for all analytical tests were based on this record.

B.3 ELEMENT PLASTICITY IN MSC/NASTRAN

B.3.1 Plastic Hinge Rotation

The inelastic implementation of a one-dimensional element (such as a beam, bar or rod) in MSC/NASTRAN is handled differently to that for two-dimensional (shell, plate) and three-dimensional (solid, brick) elements. Inelasticity in the one-dimensional column members is handled by a series of nonlinear, axial stress only rods. In this study, the typical arrangement of eight nonlinear rods is shown in Figure B.1. Each rod is located a distance $\sqrt{2}r$ from the centroid of the section. The parameter, r, is the radius of gyration of the section, and is defined as:

$$r = \sqrt{\frac{I}{A_o}} = \frac{R}{2} \tag{B.1}$$

The sum of the area of all inelastic rods is equal to the gross area of the column cross-section, A_0. The inelastic behaviour is governed by the stress in any of these eight rods. Since the rods are inelastic for axial deformations only, tension, compression, and bending stresses may be inelastic, but torsional stresses remain elastic.

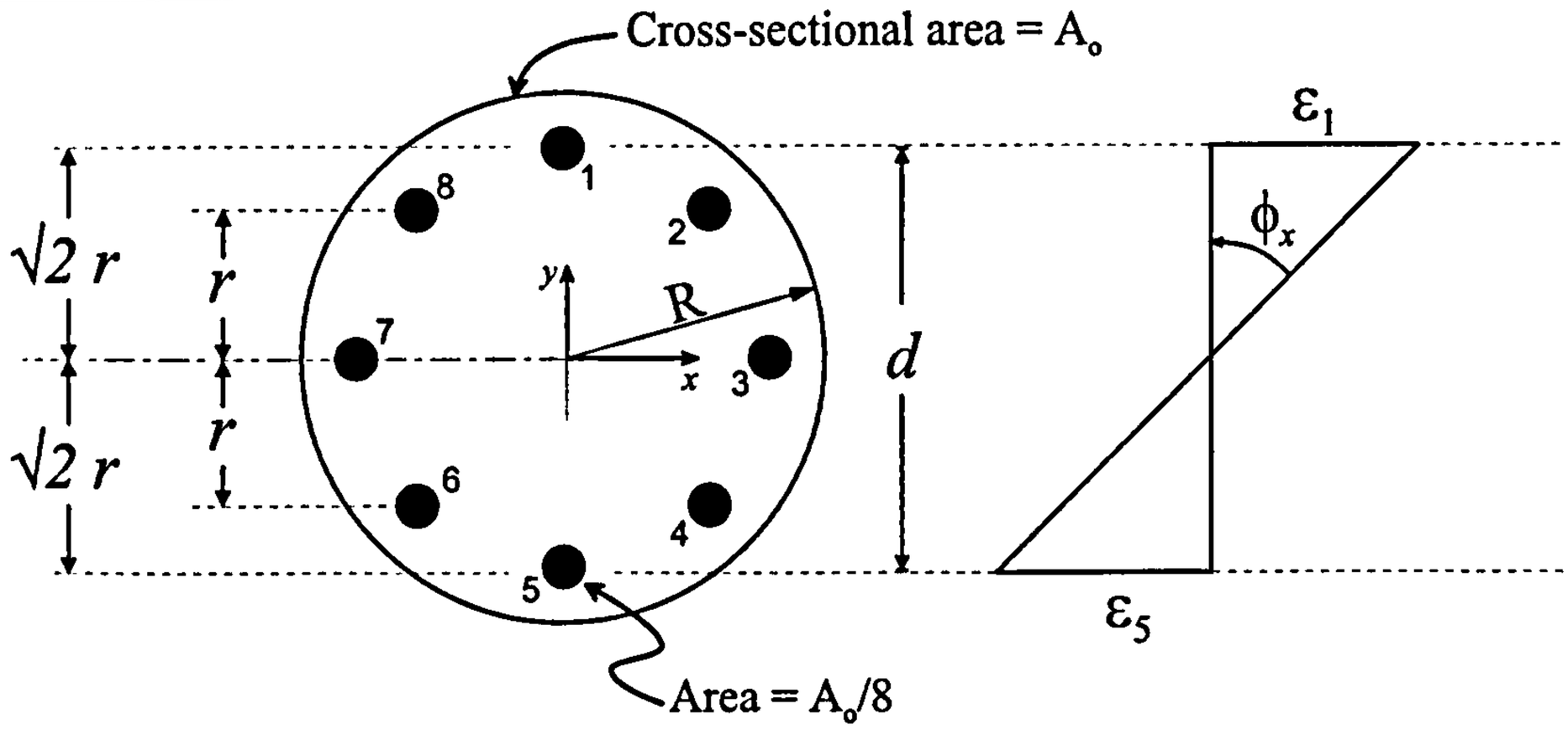

Figure B.1: Inelastic "rod" distribution in a 1-dimensional beam element.

The results from MSC/NASTRAN are reported in terms of stresses and strains for each of the eight inelastic rods in the one-dimensional member. Quantities that are more useful in this study are the moment, rotation, and curvature. Strain is linear across the cross-section of the one-dimensional member. Therefore, the curvature of the member, ϕ, as shown in Figure B.1 is:

$$\phi_x = \frac{\varepsilon_1 - \varepsilon_5}{d} = \frac{\varepsilon_1 - \varepsilon_5}{2\sqrt{2}r} \quad \text{and}$$
$$\phi_y = \frac{\varepsilon_7 - \varepsilon_3}{d} = \frac{\varepsilon_7 - \varepsilon_3}{2\sqrt{2}r} \tag{B.2}$$

where, ε_i is the strain in rod *i* (compression is *-ve*, tension is *+ve*). Curvature about the *x*-axis is ϕ_x, and curvature about the *y*-axis is ϕ_y.

The rotation of the yielding portion of the member, or hinge rotation, θ, is defined as:

$$\theta_x = l_p \phi_x \quad \text{and}$$
$$\theta_y = l_p \phi_y \tag{B.3}$$

where l_p is the length of the hinge region. In MSC/NASTRAN, this is hard-coded into the program as 1/8 of the member length. As discussed in Chapter 7, the hinge length, l_p, in the hinge unit is zero, and as such, curvature is undefined in the hinge units. In the analytical model, the length of l_p is 9mm. This length is small enough to provide a good comparison with the experimental hinge units, and large enough to ensure numerical stability[1] (convergence) during higher forcing itensities.

The moments in the hinges are computed by integrating the stresses across the cross-section of the inelastic member:

$$M_x = \frac{A_0}{8}\sum_{i=1}^{8}\sigma_i y_i \quad \text{and}$$
$$M_y = \frac{A_0}{8}\sum_{i=1}^{8}\sigma_i x_i \tag{B.4}$$

where, σ_i is the stress in rod i, and x_i and y_i are the distance to that rod along the local x or y axes of the member, respectively. The moments, rotations, and curvatures used in this study are in terms of total magnitude:

$$M = \sqrt{M_x^2 + M_y^2}$$
$$\theta = \sqrt{\theta_x^2 + \theta_y^2} \tag{B.5}$$
$$\phi = \sqrt{\phi_x^2 + \phi_y^2}$$

The fact that two rows of yielding rods (at a distance r and $\sqrt{2}r$ from member centroid along a principal axis) are present, results in a tri-linear moment-curvature behaviour, as

1. A small plastic hinge length results in large curvatures for the inelastic element. This can lead to larger strain increments per timestep which may result in convergence problems.

shown in Figure B.2. However, as the length of the plastic hinge is small, the length of the transition curve from elastic to perfectly plastic is also small.

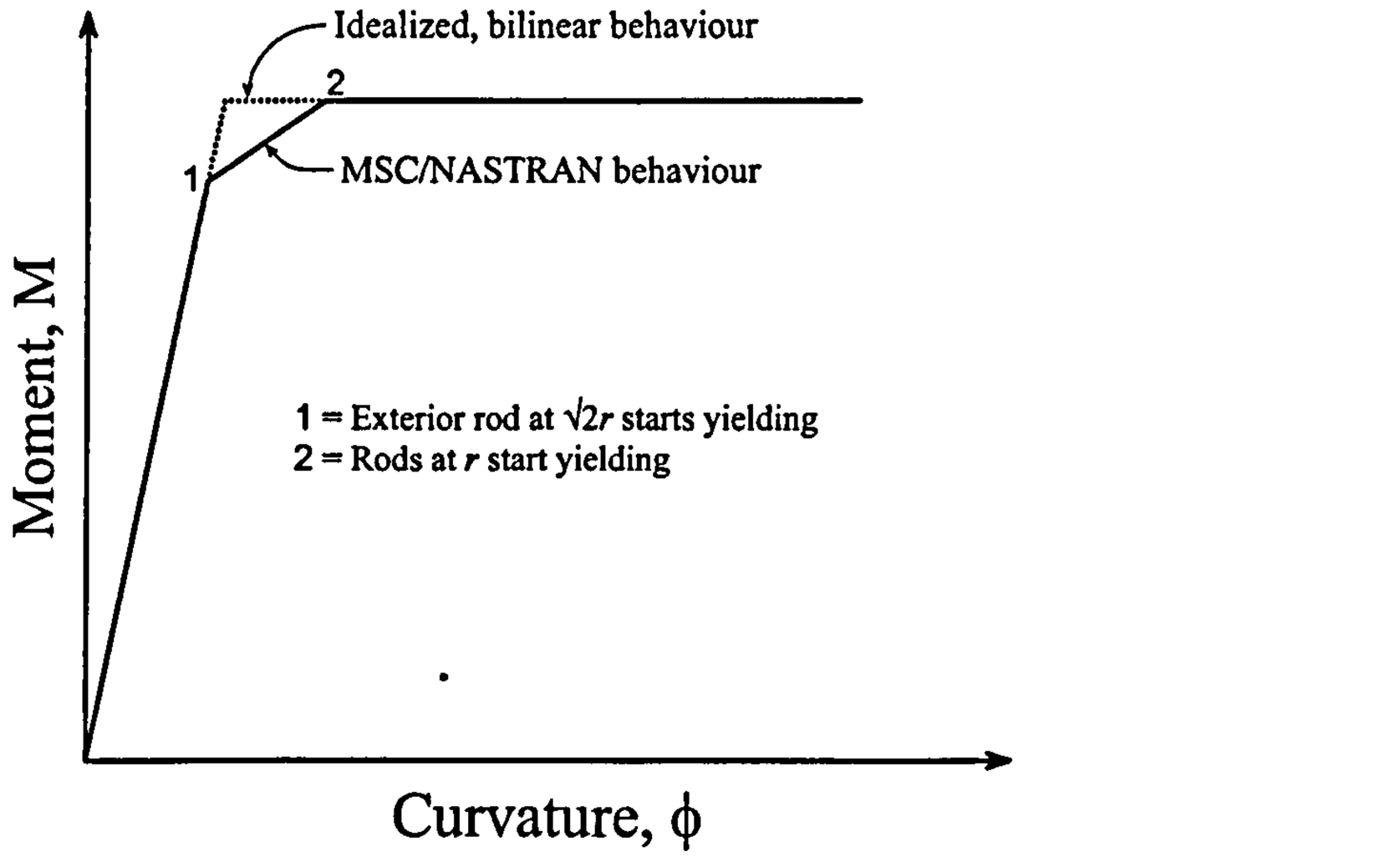

Figure B.2: Comparison of idealized bilinear behaviour, and the tri-linear MSC/NASTRAN M-ϕ behaviour.

B.4 ELASTIC DAMPING

Damping in MSC/NASTRAN is handled in terms of *structural damping* (proportional to stiffness), which can be specified for each member, or the entire structure. The formulation for the damping matrix in MSC/NASTRAN is given by:

$$\left[B_{dd}\right] = \left[B_{dd}^{1}\right] + \left[B_{dd}^{2}\right] + \frac{G}{\omega_3}\left[K_{dd}^{1}\right] + \frac{1}{\omega_4}\left[K_{dd}^{4}\right] \tag{B.6}$$

In the above equation, $\left[B_{dd}^{1}\right]$ and $\left[B_{dd}^{2}\right]$ represent the global and element structural damping matrices, respectively. The material damping matrix, $\left[K_{dd}^{4}\right]$, encompasses all the elements with an associated structural damping coefficient, and ω_4 specifies the frequency at which this level of damping occurs. None of the above forms of elastic damping are desired for the building model. From the experimental model, elastic damping measurements are

1.5%± of critical, for the first four modes. MSC/NASTRAN provides a means of specifying a uniform structural damping $\frac{G}{\omega_3}\left[K^1_{dd}\right]$, where G is the uniform damping coefficient (2ξ), and ω_3 is the frequency at which ξ is defined. Unfortunately, this form of damping becomes excessive for the third and fourth modes. Fortunately, MSC/NASTRAN allows solution sequences to be altered by the end user with the DMAP[1] programming language. This allows modifications in the logic control, such as the computation of the dynamic damping matrix, $\left[B_{dd}\right]$. Modifying equation (B.6) to incorporate Rayleigh damping, and to neglect structural damping[2] results in:

$$\left[B_{dd}\right] = \left[B^1_{dd}\right] + \alpha_1\left[M^1_{dd}\right] + \alpha_2\left[K^1_{dd}\right] \tag{B.7}$$

where α_1 and α_2 are the mass and stiffness coefficients, as determined in Chapter 7. The matrix $\left[M^1_{dd}\right]$ is the global mass matrix. The addition of the last two terms in equation (B.7) incorporate Rayleigh damping into the global damping matrix. This Rayleigh damping DMAP modification is shown at the top of the typical model input file on page 250.

B.5 TYPICAL MSC/NASTRAN INPUT FILE

The following pages show a typical MSC/NASTRAN input file for one of the column yielding model configurations.

1. Direct Matrix Abstraction Procedure (DMAP).
2. Structural damping is damping proportional to stiffness. Including the structural damping is not appropriate since Rayleigh damping is proportional to both mass and stiffness.

*MSC/NASTRAN data file: **c2cc1-0.dat***
Mass Configuration A2, Hinge Configuration CC
Forcing intensity = 1.0 x C2CCI

```
$*************************************************************
$ NONLINEAR TORSIONAL COUPLING OF A 4-STOREY BUILDING FRAME
$ UNITS: Metres, Kilograms, Seconds
$
$ ==================== NASTRAN PARAMETER SECTION
$ No machine specific parameters required
$ ========================== FILE CONTROL SECTION
$ No file or database control required
$ ==================== EXECUTIVE CONTROL SECTION
SOL, 129            $Nonlinear transient solution sequence
TIME, 9999          $Park job after 9999 minutes
$**********
$ Alter SOL 129 control sequence to incorporate Rayleigh Damping
$ ---------- RAYLEIGH DAMPING DMAP
COMPILE NLTRAN, SOUIN=MSCSOU, NOLIST, NOREF $recompile NLTRAN
ALTER 224 $ Insert these lines after line 224
TYPE PARM,,CS,Y,ALPHA1=(0.,0.),ALPHA2=(0.,0.) $ define Alpha parameters
ADD5 MDD0,KRDD,BRDD,,/TEMP/ALPHA1/ALPHA2 $ Add M & K to damp matrix
EQUIVX TEMP/BRDD/ALWAYS $ Set Alpha1 * M + Alpha2 * K to Damping (BRDD)
CEND
$
$ ======================== CASE CONTROL SECTION
TITLE=Column Yield Configuration
SUBTITLE=Mass Configuration A2
SET 1 = 5000
SET 2 = 5000, 105, 205, 305, 405
SET 3 =  110, 116, 120, 126, 130, 136, 140, 146,210, 216, 220, 226, 230, 236, 240, 246,
         ,310, 316, 320, 326, 330, 336, 340, 346,410, 416, 420, 426, 430, 436, 440, 446,
         ,510, 516, 520, 526, 530, 536, 540, 546
ACCELERATION(PUNCH) = 1
DISPLACEMENT(PUNCH) = 2
STRESS(PUNCH) = 3
SUBCASE 10
TSTEPNL=10
DLOAD = 10
LABEL=ELASTIC DIRECT TRANSIENT ANALYSIS
$
$ ============================ BULK DATA SECTION
BEGIN BULK
$ ----------DAMPING PARAMETERS (1.5% @ 1 & 5 Hz.)
PARAM, ALPHA1, 0.158142 $MASS COEFF
PARAM, ALPHA2, 7.6884-4 $STIFFNESS COEFF
$ ----------LARGE DISPLACEMENTS
PARAM, LGDISP, 1
$
TSTEPNL10       5120    3.906-3 5       AUTO            30
                1.-8    1.-10
$----MATERIAL PROPS.----
$ FLOOR BEAMS
MAT1    1       1.+12           .33
$COLUMNS  (Elastic: 3000 interior, 2000 exterior)
MAT1    2000    1.+11           .30
MAT1    3000    1.+11           .30
$
$----ECCENTRIC MASSES----
CONM2   1       51              47.1
                                                9.09
CONM2   2       52              47.1
                                                9.09
CONM2   3       53              47.1
                                                9.09
CONM2   4       54              37.1
                                                5.84
$
GRID    51              0.0376  0.0     .343
GRID    52              0.0376  0.0     .686
GRID    53              0.0376  0.0     1.029
GRID    54              0.0477  0.0     1.372
$
$----LOADING----
DLOAD   10      1.0     1.0+10  100
$ Use table 99 as enforced displacement
TLOAD1  100     90              1       99
```

```
$ Scale motion set 90 at grid 5000 (axis 2)
DAREA  90        5000     2        9.8067
$ Read Table 99 from file (taken from experimental model c2cci)
INCLUDE'e:\tc\dmotion.tbl'
$
$----MODEL GEOM.----
$  CENTRE COLUMN NODES
GRID     5                0.0      0.0      0.0633          13456
GRID     35               0.0      0.0      0.1354
GRID     65               0.0      0.0      0.2076
GRID     105              0.0      0.0      .343
GRID     135              0.0      0.0      0.4784
GRID     165              0.0      0.0      0.5506
GRID     205              0.0      0.0      .686
GRID     235              0.0      0.0      0.8214
GRID     265              0.0      0.0      0.8936
GRID     305              0.0      0.0      1.029
GRID     335              0.0      0.0      1.1644
GRID     365              0.0      0.0      1.2366
GRID     405              0.0      0.0      1.372
$
$  COLUMN 1 (FIRST QUADRANT)
GRID     1                0.463    0.463    0.0633          13456
GRID     31               0.463    0.463    0.1354
GRID     61               0.463    0.463    0.2076
GRID     101              0.463    0.463    .343
GRID     131              0.463    0.463    0.4784
GRID     161              0.463    0.463    0.5506
GRID     201              0.463    0.463    .686
GRID     231              0.463    0.463    0.8214
GRID     261              0.463    0.463    0.8936
GRID     301              0.463    0.463    1.029
GRID     331              0.463    0.463    1.1644
GRID     361              0.463    0.463    1.2366
GRID     401              0.463    0.463    1.372
$
$  COLUMN 2 (SECOND QUADRANT)
GRID     2                -0.463   0.463    0.0633          13456
GRID     32               -0.463   0.463    0.1354
GRID     62               -0.463   0.463    0.2076
GRID     102              -0.463   0.463    .343
GRID     132              -0.463   0.463    0.4784
GRID     162              -0.463   0.463    0.5506
GRID     202              -0.463   0.463    .686
GRID     232              -0.463   0.463    0.8214
GRID     262              -0.463   0.463    0.8936
GRID     302              -0.463   0.463    1.029
GRID     332              -0.463   0.463    1.1644
GRID     362              -0.463   0.463    1.2366
GRID     402              -0.463   0.463    1.372
$
$  COLUMN 3 (THIRD QUADRANT)
GRID     3                -0.463   -0.463   0.0633          13456
GRID     33               -0.463   -0.463   0.1354
GRID     63               -0.463   -0.463   0.2076
GRID     103              -0.463   -0.463   .343
GRID     133              -0.463   -0.463   0.4784
GRID     163              -0.463   -0.463   0.5506
GRID     203              -0.463   -0.463   .686
GRID     233              -0.463   -0.463   0.8214
GRID     263              -0.463   -0.463   0.8936
GRID     303              -0.463   -0.463   1.029
GRID     333              -0.463   -0.463   1.1644
GRID     363              -0.463   -0.463   1.2366
GRID     403              -0.463   -0.463   1.372
$
$  COLUMN 4 (FOURTH QUADRANT)
GRID     4                0.463    -0.463   0.0633          13456
GRID     34               0.463    -0.463   0.1354
GRID     64               0.463    -0.463   0.2076
GRID     104              0.463    -0.463   .343
GRID     134              0.463    -0.463   0.4784
GRID     164              0.463    -0.463   0.5506
GRID     204              0.463    -0.463   .686
GRID     234              0.463    -0.463   0.8214
GRID     264              0.463    -0.463   0.8936
GRID     304              0.463    -0.463   1.029
GRID     334              0.463    -0.463   1.1644
```

```
GRID    364             0.463   -0.463  1.2366
GRID    404             0.463   -0.463  1.372
$
$ LINKS BELOW FLOORS
GRID    91              0.463   0.463   0.2797
GRID    92              -0.463  0.463   0.2797
GRID    93              -0.463  -0.463  0.2797
GRID    94              0.463   -0.463  0.2797
GRID    95              0.0     0.0     0.2797
$
GRID    191             0.463   0.463   0.6227
GRID    192             -0.463  0.463   0.6227
GRID    193             -0.463  -0.463  0.6227
GRID    194             0.463   -0.463  0.6227
GRID    195             0.0     0.0     0.6227
$
GRID    291             0.463   0.463   0.9657
GRID    292             -0.463  0.463   0.9657
GRID    293             -0.463  -0.463  0.9657
GRID    294             0.463   -0.463  0.9657
GRID    295             0.0     0.0     0.9657
$
GRID    391             0.463   0.463   1.3087
GRID    392             -0.463  0.463   1.3087
GRID    393             -0.463  -0.463  1.3087
GRID    394             0.463   -0.463  1.3087
GRID    395             0.0     0.0     1.3087
$
$ LINKS ABOVE FLOORS
GRID    111             0.463   0.463   0.4063
GRID    112             -0.463  0.463   0.4063
GRID    113             -0.463  -0.463  0.4063
GRID    114             0.463   -0.463  0.4063
GRID    115             0.0     0.0     0.4063
$
GRID    211             0.463   0.463   0.7493
GRID    212             -0.463  0.463   0.7493
GRID    213             -0.463  -0.463  0.7493
GRID    214             0.463   -0.463  0.7493
GRID    215             0.0     0.0     0.7493
$
GRID    311             0.463   0.463   1.0923
GRID    312             -0.463  0.463   1.0923
GRID    313             -0.463  -0.463  1.0923
GRID    314             0.463   -0.463  1.0923
GRID    315             0.0     0.0     1.0923
$
$ MID-SIDE NODES TO SUPPORT FLOOR BEAMS AND RBES
$FIRST FLOOR
GRID    106             0.463   0.000   .343
GRID    107             0.000   0.463   .343
GRID    108             -0.463  0.000   .343
GRID    109             0.000   -0.463  .343
$SECOND FLOOR
GRID    206             0.463   0.000   .686
GRID    207             0.000   0.463   .686
GRID    208             -0.463  0.000   .686
GRID    209             0.000   -0.463  .686
$THIRD FLOOR
GRID    306             0.463   0.000   1.029
GRID    307             0.000   0.463   1.029
GRID    308             -0.463  0.000   1.029
GRID    309             0.000   -0.463  1.029
$FOURTH FLOOR
GRID    406             0.463   0.000   1.372
GRID    407             0.000   0.463   1.372
GRID    408             -0.463  0.000   1.372
GRID    409             0.000   -0.463  1.372
$
$ FLOOR BEAMS
PBEAM   1       1       0.0025  5.208-7 5.208-7
$FIRST FLOOR
CBEAM   11      1       106     101     0.0     0.0     1.0
CBEAM   12      1       107     101     0.0     0.0     1.0
CBEAM   13      1       107     102     0.0     0.0     1.0
CBEAM   14      1       108     102     0.0     0.0     1.0
CBEAM   15      1       108     103     0.0     0.0     1.0
CBEAM   16      1       109     103     0.0     0.0     1.0
```

```
CBEAM 17        1       109     104     0.0     0.0     1.0
CBEAM 18        1       106     104     0.0     0.0     1.0
$SECOND FLOOR
CBEAM 21        1       206     201     0.0     0.0     1.0
CBEAM 22        1       207     201     0.0     0.0     1.0
CBEAM 23        1       207     202     0.0     0.0     1.0
CBEAM 24        1       208     202     0.0     0.0     1.0
CBEAM 25        1       208     203     0.0     0.0     1.0
CBEAM 26        1       209     203     0.0     0.0     1.0
CBEAM 27        1       209     204     0.0     0.0     1.0
CBEAM 28        1       206     204     0.0     0.0     1.0
$THIRD FLOOR
CBEAM 31        1       306     301     0.0     0.0     1.0
CBEAM 32        1       307     301     0.0     0.0     1.0
CBEAM 33        1       307     302     0.0     0.0     1.0
CBEAM 34        1       308     302     0.0     0.0     1.0
CBEAM 35        1       308     303     0.0     0.0     1.0
CBEAM 36        1       309     303     0.0     0.0     1.0
CBEAM 37        1       309     304     0.0     0.0     1.0
CBEAM 38        1       306     304     0.0     0.0     1.0
$FOURTH FLOOR
CBEAM 41        1       406     401     0.0     0.0     1.0
CBEAM 42        1       407     401     0.0     0.0     1.0
CBEAM 43        1       407     402     0.0     0.0     1.0
CBEAM 44        1       408     402     0.0     0.0     1.0
CBEAM 45        1       408     403     0.0     0.0     1.0
CBEAM 46        1       409     403     0.0     0.0     1.0
CBEAM 47        1       409     404     0.0     0.0     1.0
CBEAM 48        1       406     404     0.0     0.0     1.0
$
$COLUMNS
PBEAM 1001      2000    5.027-5 2.01-10 2.01-10         4.02-10
PBEAM 1005      3000    1.131-4 1.018-9 1.018-9         2.036-9
$ COLUMN 1
CBEAM 110       110     1       31      1.0
PBEAM 110       110     5.027-5 2.01-10 2.01-10
        0.      0.00171 0.00171 0.      -0.00171 0.     0.      -0.00171
MAT1    110     1.+11           .30
MATS1   110             plastic 0.0     1       2       1.550+8
```

```
CBEAM 113       1001    31      61      1.0
CBEAM 116       116     61      91      1.0
PBEAM 116       116     5.027-5 2.01-10 2.01-10
        0.      0.00171 0.00171 0.      -0.00171 0.     0.      -0.00171
MAT1    116     1.+11           .30
MATS1   116             plastic 0.0     1       2       1.550+8
CBEAM 120       120     111     131     1.0
PBEAM 120       120     5.027-5 2.01-10 2.01-10
        0.      0.00171 0.00171 0.      -0.00171 0.     0.      -0.00171
MAT1    120     1.+11           .30
MATS1   120             plastic 0.0     1       2       1.550+8
CBEAM 123       1001    131     161     1.0
CBEAM 126       126     161     191     1.0
PBEAM 126       126     5.027-5 2.01-10 2.01-10
        0.      0.00171 0.00171 0.      -0.00171 0.     0.      -0.00171
MAT1    126     1.+11           .30
MATS1   126             plastic 0.0     1       2       1.550+8
CBEAM 130       130     211     231     1.0
PBEAM 130       130     5.027-5 2.01-10 2.01-10
        0.      0.00171 0.00171 0.      -0.00171 0.     0.      -0.00171
MAT1    130     1.+11           .30
MATS1   130             plastic 0.0     1       2       1.550+8
CBEAM 133       1001    231     261     1.0
CBEAM 136       136     261     291     1.0
PBEAM 136       136     5.027-5 2.01-10 2.01-10
        0.      0.00171 0.00171 0.      -0.00171 0.     0.      -0.00171
MAT1    136     1.+11           .30
MATS1   136             plastic 0.0     1       2       1.550+8
CBEAM 140       140     311     331     1.0
PBEAM 140       140     5.027-5 2.01-10 2.01-10
        0.      0.00171 0.00171 0.      -0.00171 0.     0.      -0.00171
MAT1    140     1.+11           .30
MATS1   140             plastic 0.0     1       2       1.550+8
CBEAM 143       1001    331     361     1.0
CBEAM 146       146     361     391     1.0
PBEAM 146       146     5.027-5 2.01-10 2.01-10
        0.      0.00171 0.00171 0.      -0.00171 0.     0.      -0.00171
MAT1    146     1.+11           .30
MATS1   146             plastic 0.0     1       2       1.550+8
```

```
$ COLUMN 2
CBEAM   210     210     2       32      1.0
PBEAM   210     210     5.027-5 2.01-10 2.01-10
        0.      0.00171 0.00171 0.      -0.00171 0.      0.      -0.00171
MAT1    210     1.+11           .30
MATS1   210             plastic 0.0     1       2       1.154+8
CBEAM   213     1001    32      62      1.0
CBEAM   216     216     62      92      1.0
PBEAM   216     216     5.027-5 2.01-10 2.01-10
        0.      0.00171 0.00171 0.      -0.00171 0.      0.      -0.00171
MAT1    216     1.+11           .30
MATS1   216             plastic 0.0     1       2       1.154+8
CBEAM   220     220     112     132     1.0
PBEAM   220     220     5.027-5 2.01-10 2.01-10
        0.      0.00171 0.00171 0.      -0.00171 0.      0.      -0.00171
MAT1    220     1.+11           .30
MATS1   220             plastic 0.0     1       2       1.154+8
CBEAM   223     1001    132     162     1.0
CBEAM   226     226     162     192     1.0
PBEAM   226     226     5.027-5 2.01-10 2.01-10
        0.      0.00171 0.00171 0.      -0.00171 0.      0.      -0.00171
MAT1    226     1.+11           .30
MATS1   226             plastic 0.0     1       2       1.154+8
CBEAM   230     230     212     232     1.0
PBEAM   230     230     5.027-5 2.01-10 2.01-10
        0.      0.00171 0.00171 0.      -0.00171 0.      0.      -0.00171
MAT1    230     1.+11           .30
MATS1   230             plastic 0.0     1       2       1.154+8
CBEAM   233     1001    232     262     1.0
CBEAM   236     236     262     292     1.0
PBEAM   236     236     5.027-5 2.01-10 2.01-10
        0.      0.00171 0.00171 0.      -0.00171 0.      0.      -0.00171
MAT1    236     1.+11           .30
MATS1   236             plastic 0.0     1       2       1.154+8
CBEAM   240     240     312     332     1.0
PBEAM   240     240     5.027-5 2.01-10 2.01-10
        0.      0.00171 0.00171 0.      -0.00171 0.      0.      -0.00171
MAT1    240     1.+11           .30
MATS1   240             plastic 0.0     1       2       1.154+8
CBEAM   243     1001    332     362     1.0
CBEAM   246     246     362     392     1.0
PBEAM   246     246     5.027-5 2.01-10 2.01-10
        0.      0.00171 0.00171 0.      -0.00171 0.      0.      -0.00171
MAT1    246     1.+11           .30
MATS1   246             plastic 0.0     1       2       1.154+8
$ COLUMN 3
CBEAM   310     310     3       33      1.0
PBEAM   310     310     5.027-5 2.01-10 2.01-10
        0.      0.00171 0.00171 0.      -0.00171 0.      0.      -0.00171
MAT1    310     1.+11           .30
MATS1   310             plastic 0.0     1       2       1.154+8
CBEAM   313     1001    33      63      1.0
CBEAM   316     316     63      93      1.0
PBEAM   316     316     5.027-5 2.01-10 2.01-10
        0.      0.00171 0.00171 0.      -0.00171 0.      0.      -0.00171
MAT1    316     1.+11           .30
MATS1   316             plastic 0.0     1       2       1.154+8
CBEAM   320     320     113     133     1.0
PBEAM   320     320     5.027-5 2.01-10 2.01-10
        0.      0.00171 0.00171 0.      -0.00171 0.      0.      -0.00171
MAT1    320     1.+11           .30
MATS1   320             plastic 0.0     1       2       1.154+8
CBEAM   323     1001    133     163     1.0
CBEAM   326     326     163     193     1.0
PBEAM   326     326     5.027-5 2.01-10 2.01-10
        0.      0.00171 0.00171 0.      -0.00171 0.      0.      -0.00171
MAT1    326     1.+11           .30
MATS1   326             plastic 0.0     1       2       1.154+8
CBEAM   330     330     213     233     1.0
PBEAM   330     330     5.027-5 2.01-10 2.01-10
        0.      0.00171 0.00171 0.      -0.00171 0.      0.      -0.00171
MAT1    330     1.+11           .30
MATS1   330             plastic 0.0     1       2       1.154+8
CBEAM   333     1001    233     263     1.0
CBEAM   336     336     263     293     1.0
PBEAM   336     336     5.027-5 2.01-10 2.01-10
        0.      0.00171 0.00171 0.      -0.00171 0.      0.      -0.00171
MAT1    336     1.+11           .30
```

```
MATS1  336             plastic  0.0      1        2        1.154+8
CBEAM  340    340      313      333      1.0
PBEAM  340    340      5.027-5  2.01-10  2.01-10
       0.     0.00171  0.00171  0.       -0.00171 0.       0.       -0.00171
MAT1   340    1.+11             .30
MATS1  340             plastic  0.0      1        2        1.154+8
CBEAM  343    1001     333      363      1.0
CBEAM  346    346      363      393      1.0
PBEAM  346    346      5.027-5  2.01-10  2.01-10
       0.     0.00171  0.00171  0.       -0.00171 0.       0.       -0.00171
MAT1   346    1.+11             .30
MATS1  346             plastic  0.0      1        2        1.154+8
$ COLUMN 4
CBEAM  410    410      4        34       1.0
PBEAM  410    410      5.027-5  2.01-10  2.01-10
       0.     0.00171  0.00171  0.       -0.00171 0.       0.       -0.00171
MAT1   410    1.+11             .30
MATS1  410             plastic  0.0      1        2        1.550+8
CBEAM  413    1001      34       64      1.0
CBEAM  416    416      64       94       1.0
PBEAM  416    416      5.027-5  2.01-10  2.01-10
       0.     0.00171  0.00171  0.       -0.00171 0.       0.       -0.00171
MAT1   416    1.+11             .30
MATS1  416             plastic  0.0      1        2        1.550+8
CBEAM  420    420      114      134      1.0
PBEAM  420    420      5.027-5  2.01-10  2.01-10
       0.     0.00171  0.00171  0.       -0.00171 0.       0.       -0.00171
MAT1   420    1.+11             .30
MATS1  420             plastic  0.0      1        2        1.550+8
CBEAM  423    1001     134      164      1.0
CBEAM  426    426      164      194      1.0
PBEAM  426    426      5.027-5  2.01-10  2.01-10
       0.     0.00171  0.00171  0.       -0.00171 0.       0.       -0.00171
MAT1   426    1.+11             .30
MATS1  426             plastic  0.0      1        2        1.550+8
CBEAM  430    430      214      234      1.0
PBEAM  430    430      5.027-5  2.01-10  2.01-10
       0.     0.00171  0.00171  0.       -0.00171 0.       0.       -0.00171
MAT1   430    1.+11             .30
MATS1  430             plastic  0.0      1        2        1.550+8
CBEAM  433    1001     234      264      1.0
CBEAM  436    436      264      294      1.0
PBEAM  436    436      5.027-5  2.01-10  2.01-10
       0.     0.00171  0.00171  0.       -0.00171 0.       0.       -0.00171
MAT1   436    1.+11             .30
MATS1  436             plastic  0.0      1        2        1.550+8
CBEAM  440    440      314      334      1.0
PBEAM  440    440      5.027-5  2.01-10  2.01-10
       0.     0.00171  0.00171  0.       -0.00171 0.       0.       -0.00171
MAT1   440    1.+11             .30
MATS1  440             plastic  0.0      1        2        1.550+8
CBEAM  443    1001     334      364      1.0
CBEAM  446    446      364      394      1.0
PBEAM  446    446      5.027-5  2.01-10  2.01-10
       0.     0.00171  0.00171  0.       -0.00171 0.       0.       -0.00171
MAT1   446    1.+11             .30
MATS1  446             plastic  0.0      1        2        1.550+8
$ COLUMN 5
CBEAM  510    510      5        35       1.0
PBEAM  510    510      1.131-4  1.018-9  1.018-9
       0.     0.00256  0.00256  0.       -0.00256 0.       0.       -0.00256
MAT1   510    1.+11             .30
MATS1  510             plastic  0.0      1        2        4.592+7
CBEAM  513    1005      35       65      1.0
CBEAM  516    516      65       95       1.0
PBEAM  516    516      1.131-4  1.018-9  1.018-9
       0.     0.00256  0.00256  0.       -0.00256 0.       0.       -0.00256
MAT1   516    1.+11             .30
MATS1  516             plastic  0.0      1        2        4.592+7
CBEAM  520    520      115      135      1.0
PBEAM  520    520      1.131-4  1.018-9  1.018-9
       0.     0.00256  0.00256  0.       -0.00256 0.       0.       -0.00256
MAT1   520    1.+11             .30
MATS1  520             plastic  0.0      1        2        4.592+7
CBEAM  523    1005     135      165      1.0
CBEAM  526    526      165      195      1.0
PBEAM  526    526      1.131-4  1.018-9  1.018-9
       0.     0.00256  0.00256  0.       -0.00256 0.       0.       -0.00256
```

```
MAT1    526     1.+11           .30
MATS1   526             plastic 0.0     1       2       4.592+7
CBEAM   530     530     215     235     1.0
PBEAM   530     530     1.131-4 1.018-9 1.018-9
        0.      0.00256 0.00256 0.      -0.00256 0.     0.      -0.00256
MAT1    530     1.+11           .30
MATS1   530             plastic 0.0     1       2       4.592+7
CBEAM   533     1005    235     265     1.0
CBEAM   536     536     265     295     1.0
PBEAM   536     536     1.131-4 1.018-9 1.018-9
        0.      0.00256 0.00256 0.      -0.00256 0.     0.      -0.00256
MAT1    536     1.+11           .30
MATS1   536             plastic 0.0     1       2       4.592+7
CBEAM   540     540     315     335     1.0
PBEAM   540     540     1.131-4 1.018-9 1.018-9
        0.      0.00256 0.00256 0.      -0.00256 0.     0.      -0.00256
MAT1    540     1.+11           .30
MATS1   540             plastic 0.0     1       2       4.592+7
CBEAM   543     1005    335     365     1.0
CBEAM   546     546     365     395     1.0
PBEAM   546     546     1.131-4 1.018-9 1.018-9
        0.      0.00256 0.00256 0.      -0.00256 0.     0.      -0.00256
MAT1    546     1.+11           .30
MATS1   546             plastic 0.0     1       2       4.592+7
$
$ RIGID ELEMENTS BETWEEN CENTRE COLUMN AND MID FLOOR BEAM
NODES
RBE2    910     105     123456  106     107     108     109     51
RBE2    920     205     123456  206     207     208     209     52
RBE2    930     305     123456  306     307     308     309     53
RBE2    940     405     123456  406     407     408     409     54
$ RIGID ELEMENTS BETWEEN CENTRE COLUMN AND FLOOR CORNERS
RBE2    915     105     36      101     102     103     104
RBE2    925     205     36      201     202     203     204
RBE2    935     305     36      301     302     303     304
RBE2    945     405     36      401     402     403     404
$
$ RIGID LINKS FOR PHYSICAL HINGE LENGTH
RBE2    811     101     123456  91      111
RBE2    812     102     123456  92      112
RBE2    813     103     123456  93      113
RBE2    814     104     123456  94      114
RBE2    815     105     123456  95      115
$
RBE2    821     201     123456  191     211
RBE2    822     202     123456  192     212
RBE2    823     203     123456  193     213
RBE2    824     204     123456  194     214
RBE2    825     205     123456  195     215
$
RBE2    831     301     123456  291     311
RBE2    832     302     123456  292     312
RBE2    833     303     123456  293     313
RBE2    834     304     123456  294     314
RBE2    835     305     123456  295     315
$
RBE2    841     401     123456  391
RBE2    842     402     123456  392
RBE2    843     403     123456  393
RBE2    844     404     123456  394
RBE2    845     405     123456  395
$
$ LARGE SPRINGS FOR ENFORCED MOTION
CONM2   10000   5000            1.+10
GRID    5000            0.0     0.0     0.0             13456
RBE2    950     5000    2       1       2       3       4       5
$
ENDDATA
```

APPENDIX C

ANALYTICAL MODEL MODIFICATIONS

This Appendix details the procedure used for modifying the strength distribution of the analytical models presented in Chapter 7 to that of a 1994 Uniform Building Code (UBC94) compatible design. A series of analytical models were developed that have a yielding moment (strength) distribution, in both horizontal and vertical directions, compatible with UBC94. The model modifications required to achieve code compatibility for both the analytical and experimental models are presented in this Appendix. The results

from an analytical model with these modifications are presented in Appendix D, *"Code Compatible Analytical Model"* .

Appendix A details the 1994 Uniform Building Code design procedure. The *Static Lateral Force Procedure* (Section A.3 on page 233) from Appendix A was used to perform both the vertical and horizontal strength distributions amongst the hinge units.

C.1 DESIGN SHEAR SCALING

One of the studied parameters in both the experimental and analytical responses is the increase in inelasticity caused by an increase in base excitation magnitude. In order for a comparison on the degree of inelastic behaviour to be made between the experimental/analytical models and the code-compatible analytical model, the elastic base shear capacity of the analytical model is equated to that of the column yielding experimental models. The column yielding models have a distinct shear capacity, above which a plastic failure mechanism is formed in the storey. The beam yielding configurations are indeterminate, resulting in a redistribution of the column moments once a hinge "yields". Therefore, column shear capacity is based on the maximum elastic shear in the column yielding configuration. The base shear capacity, V_{bi}, of column i, in a column yielding hinge configuration is:

$$V_{bi} = \frac{2M_{pi}}{L_i} \tag{C.1}$$

where M_{pi} is the plastic moment of the hinge units at the top and bottom of column i.

Throughout the experimental and analytical studies, the top and bottom hinge unit capaci-

ties for a column in any storey are identical. The parameter L_i is the length of column i, which is the distance from centre line to centre line of the floors, since the centre of hinge rotation coincides with the floor centre line. Table C.1 lists the yielding moments and resulting column shear capacity of the first storey in the experimental column yielding models.

Table C.1: Column moments and shear capacities for hinge configurations CB and CC.

Column Number	Column Length	Hinge Configuration CB		Hinge Configuration CC	
		M_p	V_b	M_p	V_b
1	0.343 m	13.3 N·m	77.6 N	13.3 N·m	77.6 N
2	0.343 m	13.3 N·m	77.6 N	9.9 N·m	57.7 N
3	0.343 m	13.3 N·m	77.6 N	9.9 N·m	57.7 N
4	0.343 m	13.3 N·m	77.6 N	13.3 N·m	77.6 N
5	0.343 m	13.3 N·m	77.6 N	13.3 N·m	77.6 N
		Total:	387.8 N	Total:	348.1 N

The total base shear is the sum of the first storey column shear capacities (387.1N and 348.1N for hinge configurations CB and CC, respectively). As stated earlier, strength eccentricity is introduced into a storey by lowering the plastic moments in the hinge units. As a result, lower base shear capacities are associated with higher strength eccentricities.

C.2 UBC94 VERTICAL STRENGTH DISTRIBUTION

UBC94 vertically distributes the base shear, V_b, to the individual floors based on their total height and weight, as in equations (A.8) and (A.9) from Appendix A. The design shear for a storey is then the sum of all the floor design forces above that storey. Table C.2 summa-

rizes the results from the aforementioned Appendix A equations, and lists the percentage of the base shear that is applied to each floor as its design force.

Table C.2: Vertical Shear Distribution.

Floor, i	Floor Height h_i	Floor Weight w_i	$h_i \times w_i$	Contribution to Base Shear $\frac{h_i w_i}{\sum_j h_j w_j}$
4	1.372m	37.1kg	50.9kg·m	34.43%
3	1.029m	47.1kg	48.5kg·m	32.78%
2	0.686m	47.1kg	32.3kg·m	21.86%
1	0.343m	47.1kg	16.2kg·m	10.93%
	Total:	178.4kg	147.8kg·m	100%

The percentages from Table C.2 are applied to the base shears from the two column yielding hinge configurations. The resulting floor design forces and storey shears are listed in Table C.3

Table C.3: Design floor force and storey shear.

Floor or Storey	Contribution to Base Shear	Hinge Configuration CB		Hinge Configuration CC	
		Floor Design Force	Storey Shear	Floor Design Force	Storey Shear
4	34.43%	133.5 N	133.5 N	119.9 N	119.9 N
3	32.78%	127.1 N	260.6 N	114.1 N	234.0 N
2	21.86%	84.8 N	345.4 N	76.1 N	310.1 N
1	10.93%	42.4 N	387.8 N	38.0 N	348.1 N
	Total:	$V_b = 387.8$ N		Total:	$V_b = 348.1$ N

C.3 UBC94 HORIZONTAL STRENGTH DISTRIBUTION

The design floor forces from Table C.3 are applied at a distance from the centre of stiffness known as the design eccentricity (e_1 and e_2). These are described in Appendix A (equations (A.4) and (A.5)), and summarized by equation (C.2):

$$e_{1,2} = e_m \pm \underbrace{0.05b}_{e_a} A_x \tag{C.2}$$

The parameter e_m is the mass eccentricity, e_a is the accidental eccentricity (5% of the floor dimension parallel to the mass eccentricity), and A_x is the accidental eccentricity amplification applied to irregular buildings.

The maximum column force resulting from either of these two eccentricities is taken as the required strength of that column. However, UBC94 stipulates that no column force can be reduced as a result of considering the lateral-torsion interaction. Table C.4 summarizes the design forces computed for the analytical code-compatible model in terms of base shear percentage. The actual base shear can be linked to the experimental models for comparison purposes, but the strength distribution is independent of the base shear magnitude.

Figure C.1 graphically depicts Table C.4. Increasing the mass eccentricity is accompanied by an increased share of strength demand on the right side columns. The left side columns have a slight reduction in strength demand as a result of an increasing mass eccentricity. The strength demand for the central column is identical for all mass configurations, since its location coincides with the centre of stiffness (rotation).

Table C.4: Design column forces from the UBC94 Static Lateral Force Procedure.

Mass Configuration	Floor / Storey	Design Eccentricities		Left Side[a], A		Centre, C		Right Side[a], B	
		e_1 (mm)	e_2 (mm)	Percent[b] of V_b	Controlling Eccentricity	Percent of V_b	Controlling Eccentricity	Percent of V_b	Controlling Eccentricity
S1	1	50	-50	25.9%	e_2	55.9%	$e_{1,2}$	25.9%	e_1
	2			23.1%	e_2	49.8%	$e_{1,2}$	23.1%	e_1
	3			17.4%	e_2	37.5%	$e_{1,2}$	17.4%	e_1
	4[c]	50	-50	8.9%	e_2	19.2%	$e_{1,2}$	8.9%	e_1
A2	1	99	-12	23.0%	e_2	55.9%	$e_{1,2}$	29.6%	e_1
	2			20.5%	e_2	49.8%	$e_{1,2}$	26.4%	e_1
	3			15.5%	e_2	37.5%	$e_{1,2}$	19.9%	e_1
	4[c]	112	-2.3	7.7%	e_2	19.2%	$e_{1,2}$	10.5%	e_1
A6	1	202	60	*22.1%*	0	55.9%	$e_{1,2}$	37.5%	e_1
	2			*19.7%*	0	49.8%	$e_{1,2}$	33.4%	e_1
	3			*14.8%*	0	37.5%	$e_{1,2}$	25.2%	e_1
	4[c]	246	80	*7.6%*	0	19.2%	$e_{1,2}$	14.1%	e_1

a. Individual column forces are half the indicated value, since two exterior columns are present per side.
b. Left side column forces for mass configuration A6 are based on zero eccentricity, since both e_1 and e_2 result in a reduction of column forces, which is not allowed in UBC94.
c. The design eccentricities for the fourth floor are different since the fourth floor is lighter (due to five fewer hinge units) than the other three floors.

Incorporating the greater column force resulting from the two design eccentricities increases the overall shear capacity of the building model. This can be seen by summing the column shear demand for the first storey in any of the three mass configurations in Table C.4—the result is always above V_b. The increase in base shear demand as a result of the horizontal strength distribution is termed the *over-strength ratio*, and is defined as:

$$OS = \frac{V_b'}{V_b} \tag{C.3}$$

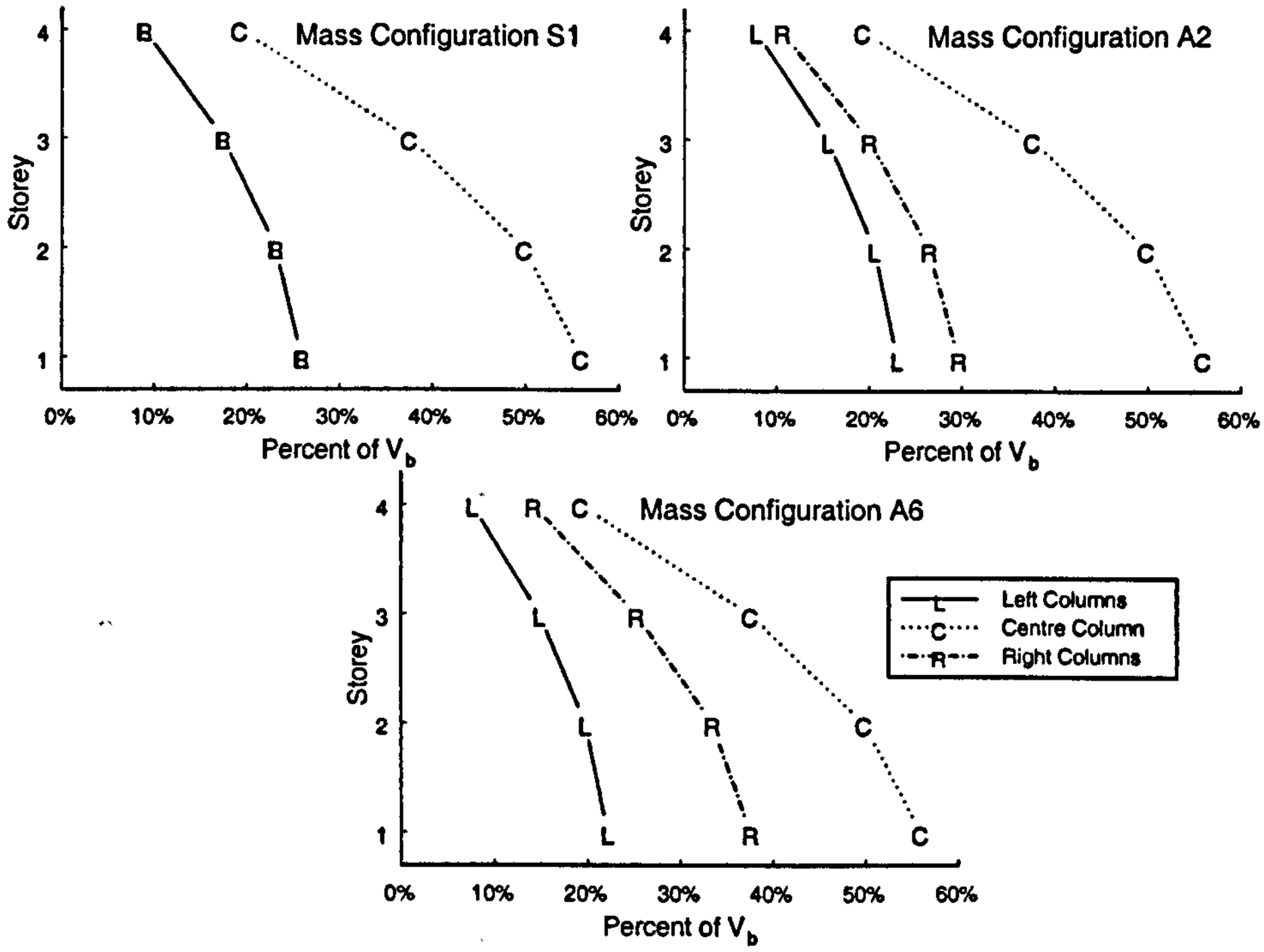

Figure C.1: Target design column shear forces (normalized by V_b).

where $V_b^{'}$ is the increased base shear demand as a result of incorporating the two design eccentricities. Figure C.2 plots the over-strength ratio for each storey of the two hinge configurations. As to be expected, a higher torsional component (mass eccentricity)

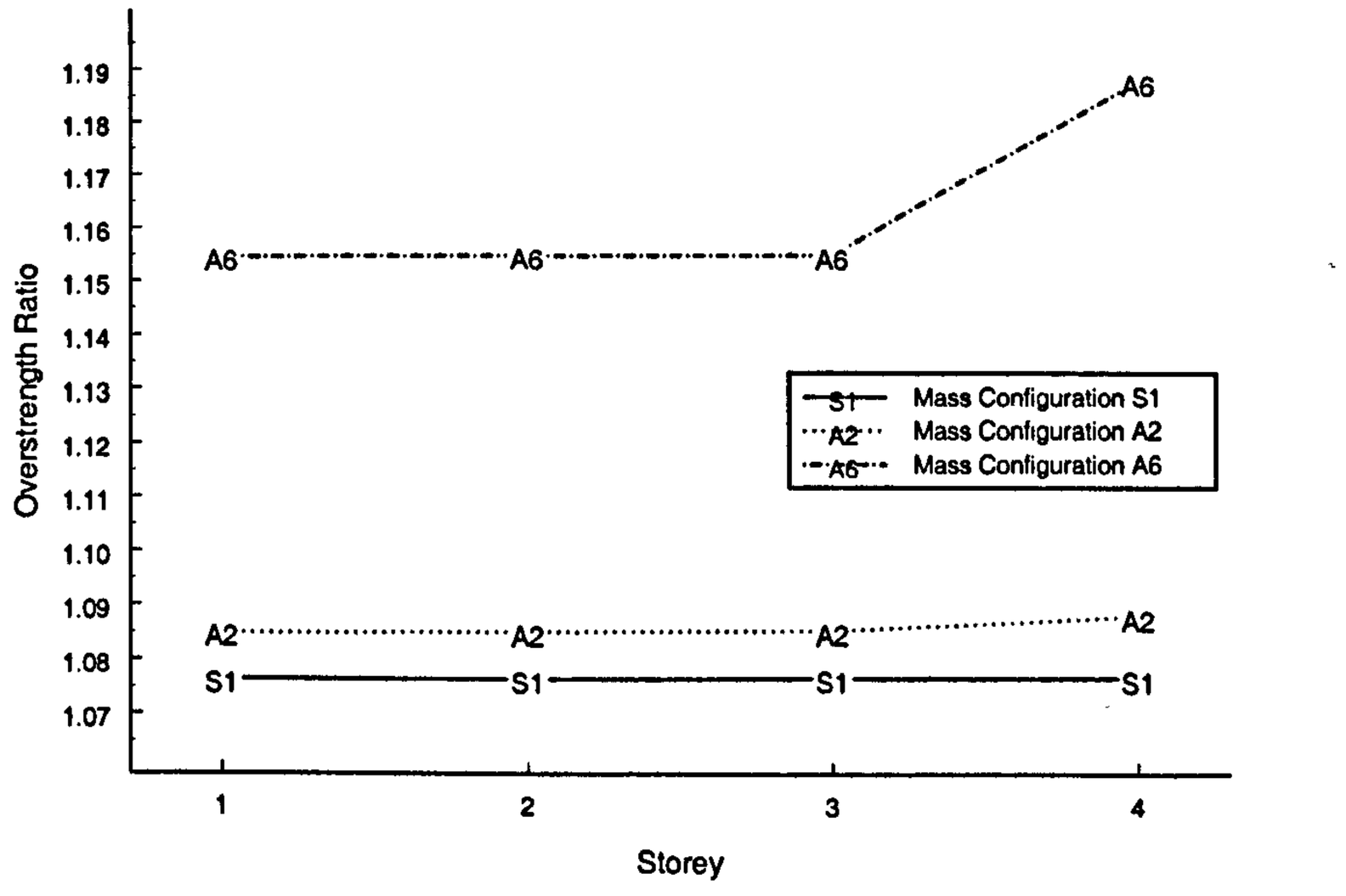

Figure C.2: Total over-strength ratio for each floor of the three studied mass configurations.

results in a higher over-strength ratio. The increase in over-strength for the fourth storey is due to the lighter weight of the fourth floor (five fewer hinge units), which results in a higher mass eccentricity for mass configurations A2 and A6.

C.4 ANALYTICAL MODEL MODIFICATIONS

The previous section determined the codified shear force demand for each column in the analytical model. Enforcing a demand to capacity ratio of unity (i.e. no over-design), the column strength capacities can be set equal to the column strength demands. Although this fact may seem trivial, designs are normally based on stiffness. As a result, there is usually some degree of over-design in strength.

Table C.5 list the codified shear capacities based on a base shear of 387.8N (from hinge configuration CB). The resulting plastic moment capacities are also indicated, and are determined by rearranging equation (C.1):

$$M_{pi} = \frac{V_{bi} L_i}{2} \tag{C.4}$$

For a code compatible model based on a base shear of 348.1N (hinge configuration CC), the moments in Table C.5 can be scaled by $\frac{348.1\text{N}}{387.8\text{N}} = 89.76\%$.

C.5 EXPERIMENTAL MODEL MODIFICATIONS

The experimental model does not have as accurate control over the hinge yielding moments as does the analytical model. The yielding moments in the hinge units are con-

Table C.5: Codified moment and column shear capacities (based on V_b=387.8N).

Mass Configuration	Storey	Left Side Columns[a]		Centre Column		Right Side Columns[a]	
		M_p (N·m)	Shear Capacity (N)	M_p (N·m)	Shear Capacity (N)	M_p (N·m)	Shear Capacity (N)
S1	4	3.0	17.3	12.8	74.6	3.0	17.3
	3	5.8	33.7	25.0	145.6	5.8	33.7
	2	7.7	44.7	33.1	193.0	7.7	44.7
	1	8.6	50.2	37.2	216.6	8.6	50.2
A2	4	2.5	14.9	12.8	74.6	3.5	20.5
	3	5.1	30.0	25.0	145.6	6.6	38.6
	2	6.8	39.8	33.1	193.0	8.8	51.1
	1	7.7	44.6	37.2	216.6	9.8	57.4
A6	4	2.5	14.7	12.8	74.6	4.7	27.3
	3	4.9	28.7	25.0	145.6	8.4	48.9
	2	6.5	38.1	33.1	193.0	11.1	64.8
	1	7.3	42.8	37.2	216.6	12.5	72.8

a. Values indicated are for a single column

trolled by the number of turns of a series of clamping nuts around the perimeter of the hinge unit (Figure 4.1 on page 83). During the experimental studies, the number of turns of the clamping nuts were performed in ½ turn increments. For greater accuracy on a possible future experimental model, the clamping nut increments could be recorded in ¼ turn increments. With this level of accuracy stated, Table C.6 lists the experimental hinge configuration for a UBC94 code compatible model. The central column hinges require a higher moment capacity than that obtainable through PTFE as the friction pad material. Therefore, stainless steel is here assumed to be used for the friction pad material of the central column hinges for the first three floors. The design base shear also has to be

Table C.6: Experimental moment and column shear capacitys based on the hinge units.

Mass Configuration	Storey	Left Side Columns		Centre Column		Right Side Columns	
		# Turns[a] (material)	Shear Capacity[b] (N)	# Turns[a] (material)	Shear Capacity[b] (N)	# Turns[a] (material)	Shear Capacity[b] (N)
S1	4	1/3 (PTFE)	38.8 (3%)	1-1/2 (PTFE)	67.9 (1%)	1/3 (PTFE)	38.8 (3%)
	3	3/4 (PTFE)	58.2 (0%)	1-1/3 (SS)	114.8 (-4%)	3/4 (PTFE)	58.2 (0%)
	2	1 (PTFE)	77.6 (0%)	1-3/4 (SS)	160.7 (-2%)	1 (PTFE)	77.6 (0%)
	1	1 (PTFE)	77.6 (-3%)	2 (SS)	183.7 (-2%)	1 (PTFE)	77.6 (-3%)
A2	4	1/3 (PTFE)	19.4 (-2%)	1-1/2 (PTFE)	67.9 (1%)	1/2 (PTFE)	38.8 (0%)
	3	2/3 (PTFE)	58.2 (1%)	1-1/3 (SS)	114.8 (-4%)	3/4 (PTFE)	58.2 (-4%)
	2	1 (PTFE)	58.2 (-4%)	1-3/4 (SS)	160.7 (-2%)	1 (PTFE)	77.6 (-5%)
	1	1 (PTFE)	77.6 (-1%)	2 (SS)	183.7 (-2%)	1-1/4 (PTFE)	96.9 (-3%)
A6	4	1/3 (PTFE)	19.4 (-2%)	1-1/2 (PTFE)	67.9 (1%)	1/2 (PTFE)	38.8 (-4%)
	3	2/3 (PTFE)	58.2 (1%)	1-1/3 (SS)	114.8 (-4%)	1 (PTFE)	77.6 (-5%)
	2	3/4 (PTFE)	58.2 (-4%)	1-3/4 (SS)	160.7 (-2%)	1-1/3 (PTFE)	116.3 (-3%)
	1	1 (PTFE)	77.6 (-2%)	2 (SS)	183.7 (-2%)	1-1/2 (PTFE)	116.3 (-7%)

(PTFE) - PTFE (Polytetrafluoroethylene) hinge pad material; (SS) - Stainless Steel hinge pad material.

a. *# Turns* indicates the number of turns for the hinge clamping nut with the hinge pad material specified.
b. The value in parenthesis is the difference from the target theoretical storey shear contribution.

reduced to 328.8N to accommodate the maximum allowable moment in the stainless steel hinge units (31.5N·m @ 2 turns). Figure C.3 plots both the target analytical, and obtainable experimental column shear capacities for the three mass configurations.

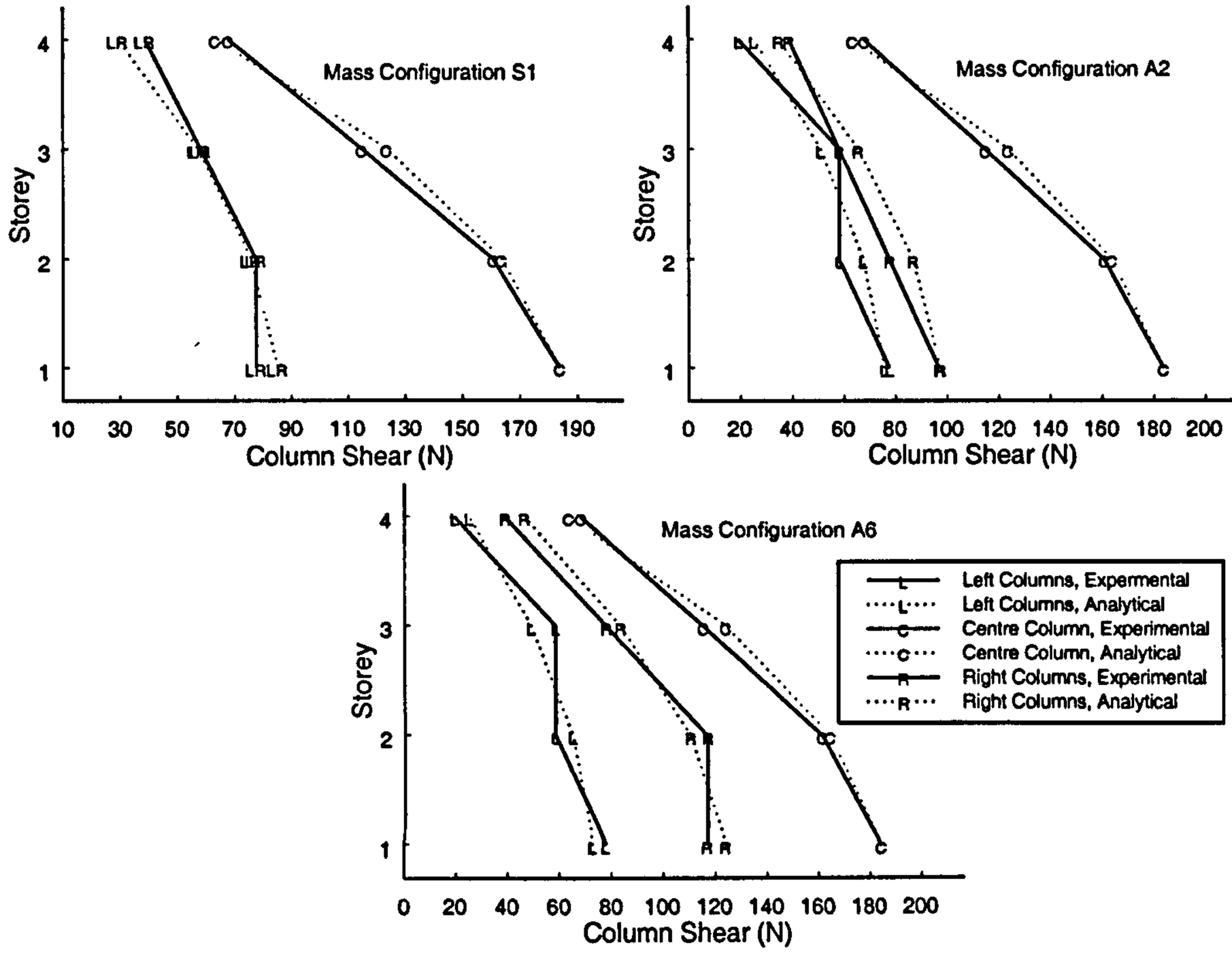

Figure C.3: Comparison between experimental and analytical codified design column shears (V_b=328.8N).

ALL MISSING PAGES ARE BLANK

IN

ORIGINAL

APPENDIX D

CODE COMPATIBLE ANALYTICAL MODEL

The modifications to the analytical model presented in Appendix C detail the strength distribution requirements for a UBC94 code compatible model. Some of the results from these modifications are presented in this Appendix for the column yielding models. The elastic characteristics of the modified analytical model are the same as those of the models presented in Chapter 7, as the modifications apply solely to the yielding moments in the column members. Appendix C details the method used to distribute the design storey

shear amongst the columns of the analytical model. The magnitude of these yielding moments for each of the three mass configurations are presented in Table C.5 on page 265.

D.1 RESPONSE RESULTS

The model response in this Appendix is presented in terms of moment demand to capacity (D/C) ratio, and absorbed hysteretic energy. These responses are presented for increasing forcing intensity. Since the shear strength of the code compatible models is more efficiently distributed when compared to the experimental hinge configurations, the initiation of member yielding occurs at a much higher forcing intensity. Where significant inelastic behaviour occurred at an RMSA of 8%g in the experimental models (and experimentally based analytical models), initial yielding for the code compatible analytical models occurs at forcing intensities no lower than an RMSA of 20%g. From this, the studied range of forcing intensities for these analytical models is between an RMSA of 8%g and 70%g. This increase in RMSA is due to a better strength distribution (particularly in the central columns) of the code compatible models over the experimental models.

D.1.1 Moment D/C Ratios

The moment demand to capacity (D/C) ratio is a measure of vulnerability, and indicates whether a column remains elastic, or experiences some inelastic behaviour. D/C ratios less than unity indicate elastic behaviour, and ratios greater than or equal to unity indicate some form of member inelasticity. Since the post-elastic stress-strain relationship for the columns in this study are perfectly-plastic, the moment D/C ratio is never greater than unity. Moment D/C ratios are being used less for analysis and design, as this ratio can only

measure vulnerabily of a particular member, not of the structural system. For this reason, displacement D/C ratios are a more common vulnerability measurement. However, displacement capacity is not a meaningful quantity for the experimental hinge units. Therefore, only the moment D/C ratios are presented in this study.

The moment D/C ratios for mass configuration S1 are shown in Figure D.1. This Figure

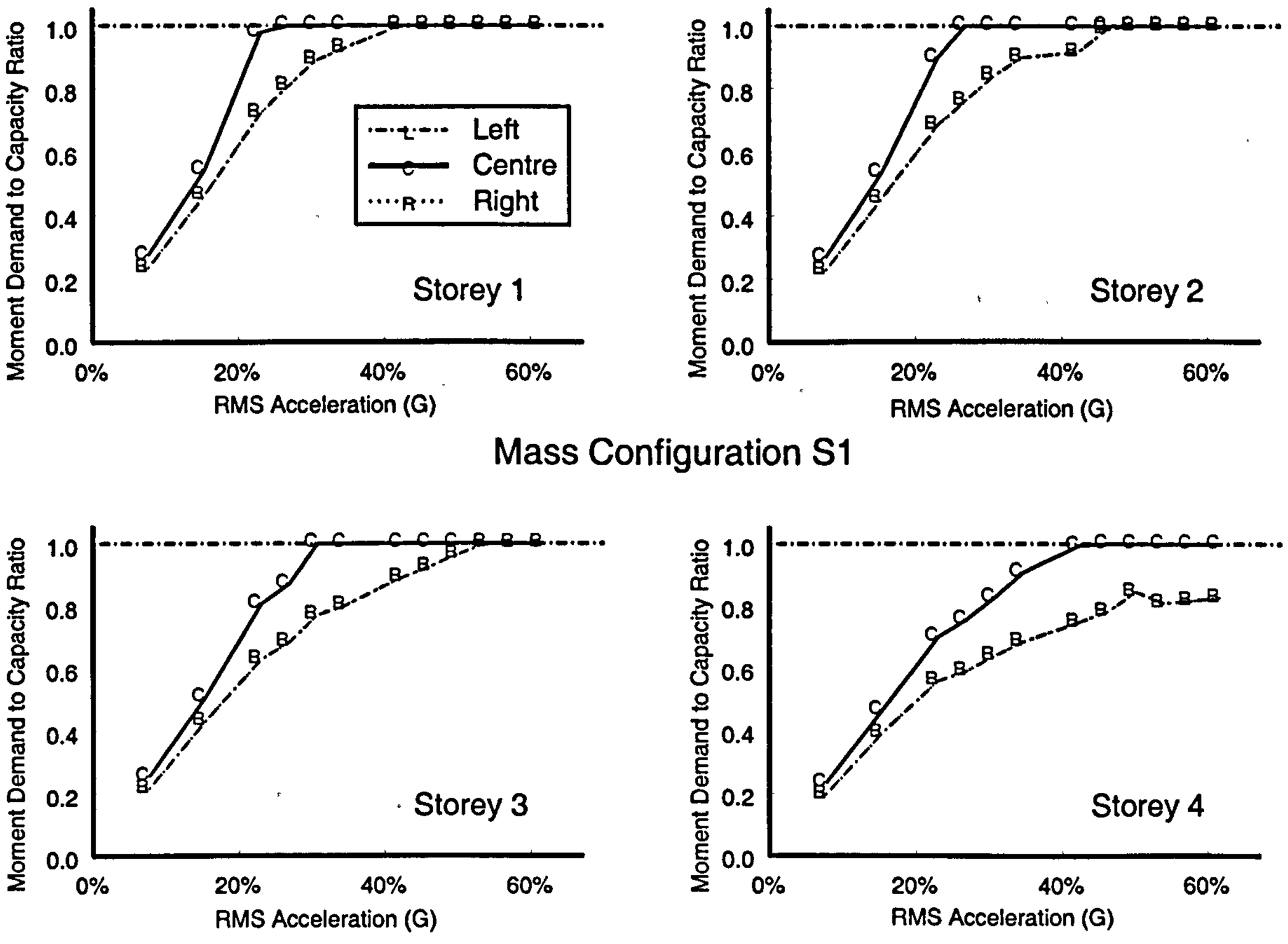

Figure D.1: Moment demand to capacity ratios for the symmetric mass (S1) column yielding models.

shows that in all four stories, the D/C ratio for the centre column is greater than either of the exterior columns. Based on its stiffness, the central column of the mass configuration S1 models, attracts over five-times the storey shear of any exterior column. However, UBC94 increases the design strength of the exterior columns as a result of the accidental

eccentricity. This over-strength (about 7.5%, as shown in Figure C.2 on page 263) results in a reduced D/C ratio from that of the central column. It is interesting to note that in Figure D.1, the D/C ratio for a completely elastic response is not linear with respect to the forcing intensity, but greater than the straight line elastic response. This is especially noticeable in the first storey at forcing intensities near an RMSA of 20% g. This is a result of the second-order geometric effects (P-Δ) from the gravity load on the displaced structure.

The exterior columns (left and right side) undergo the same response demand, as their capacities are identical in mass configuration S1. This is to be expected, as the models with mass configuration S1 are both mass and strength symmetric, resulting in no torsional response component. The D/C ratios for all columns decrease in the upper stories. Member inelasticity occurs in the central column for all four stories, decreasing in the upper stories. This is especially true once column yielding occurs in the lower stories. This is a result of the filtering, or "soft-storey" effect.

Figure D.2 shows the moment D/C ratio for mass configuration A2. As with mass configuration S1, the central column is the most vulnerable, yielding in all four stories. The central column in the first floor yields at a higher forcing intensity (RMSA) of 27%g, whereas the central column in the first floor for mass configuration S1 yields first at an RMSA of 24%g. However, the exterior columns, even with their design overstrength, are slightly more vulnerable when compared to those of mass configuration S1. The D/C ratios for the exterior columns in mass configuration A2 are similar for all but the fourth storey, where the right side columns becomes more vulnerable as the first, second, and third stories start

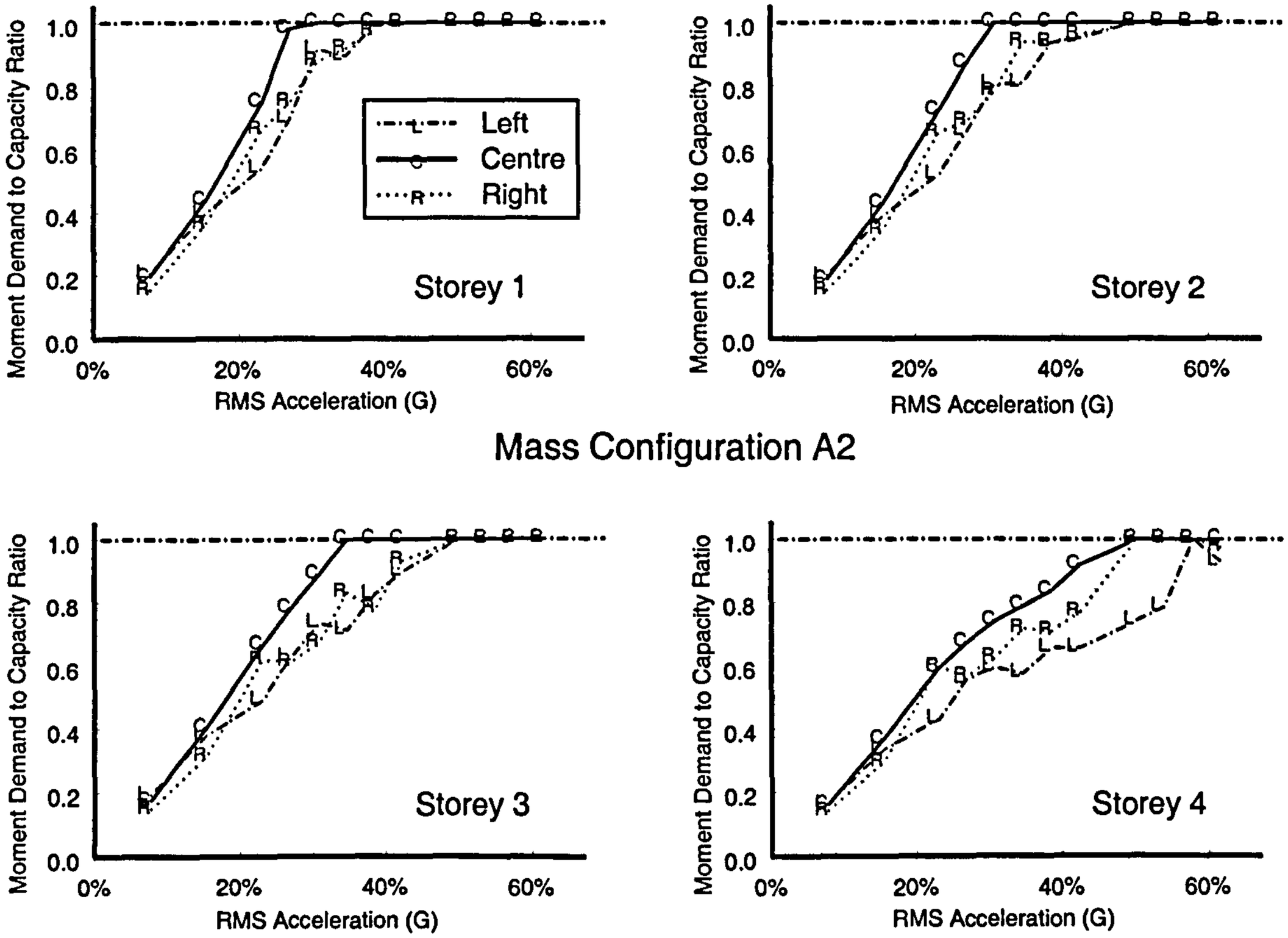

Figure D.2: Moment demand to capacity ratios for mass configuration A2.

yielding. This behaviour is exaggerated further with mass configuration A6 (Figure D.3). This figure shows that the right side columns are more vulnerable than the left side columns. This is especially true in the upper stories where the D/C ratio for the right columns are between 20% and 40% greater than those for the left side columns.

D.1.2 Absorbed Hysteretic Energy

The absorbed hysteretic energy of a yielding column is the net area enclosed by its moment verses curvature time-history. Figure D.4 show the moment verses rotation (rotation is equal to curvature times the length of column which is yielding) for a single right side column in mass configurations A2 and A6, respectively. Unlike the experimental models, the code compatible models have a better vertical strength distribution. This

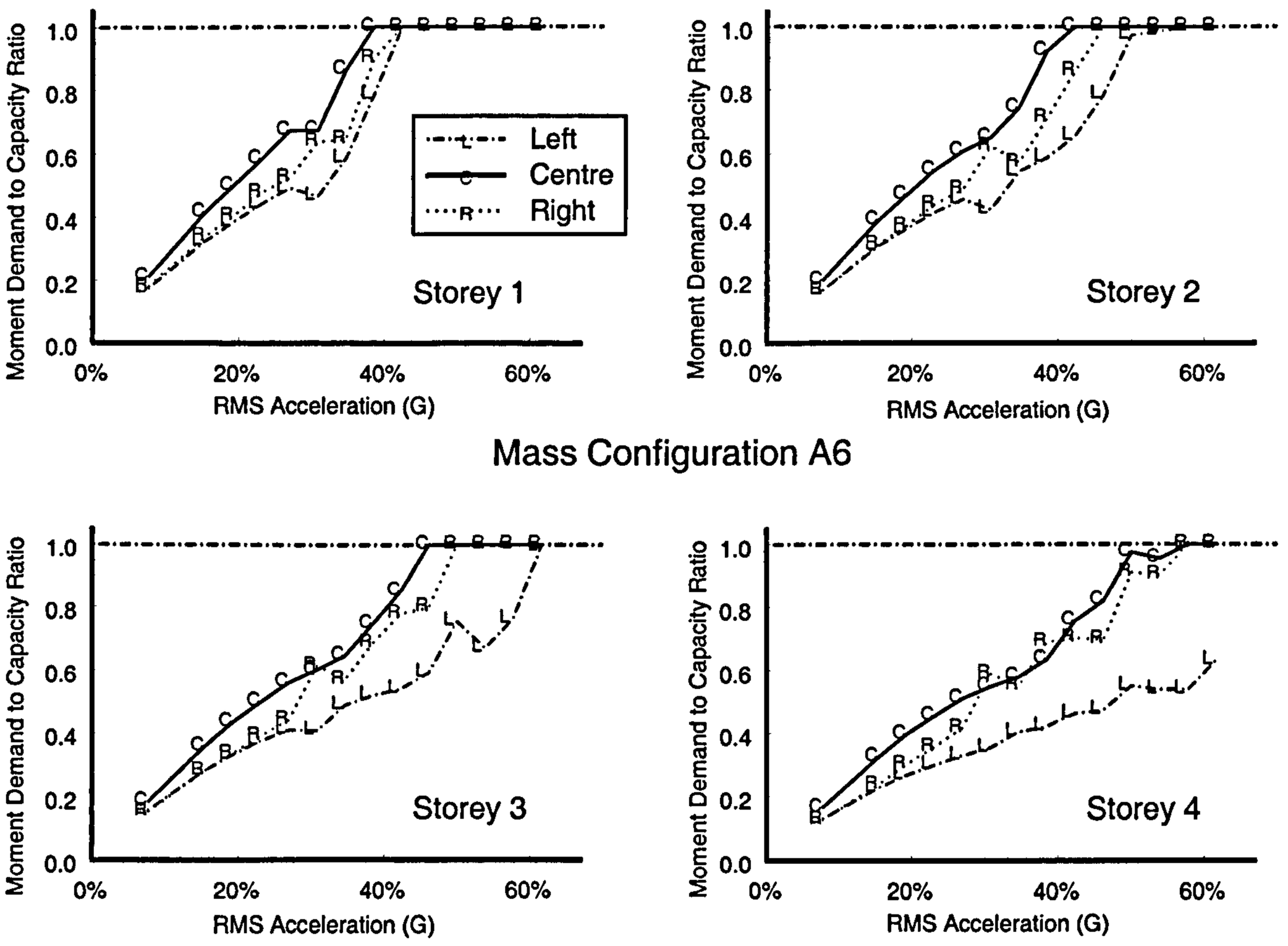

Figure D.3: Moment demand to capacity ratios for mass configuration A6.

results in member yielding amongst all four storeys, as opposed to mainly the first storey in the experimental models.

With a forcing intensity of over 50%*g* RMSA, the right column yields in the first 3 storeys in mass configuration A2, whereas with mass configuration A6, the right column in the first two storeys experiences member inelasticity. Moreover, the degree of inelastic behaviour is far greater with mass configuration A2, especially in the first storey. This is primarily attributed to the member over-strength inherent in the mass configuration A6 code compatible models (see Figure C.2 on page 263). What looks like a transitional rotational stiffness in the moment verses rotation diagrams is actually a result of the output time history sampling frequency, which was identical to that of the experimental models

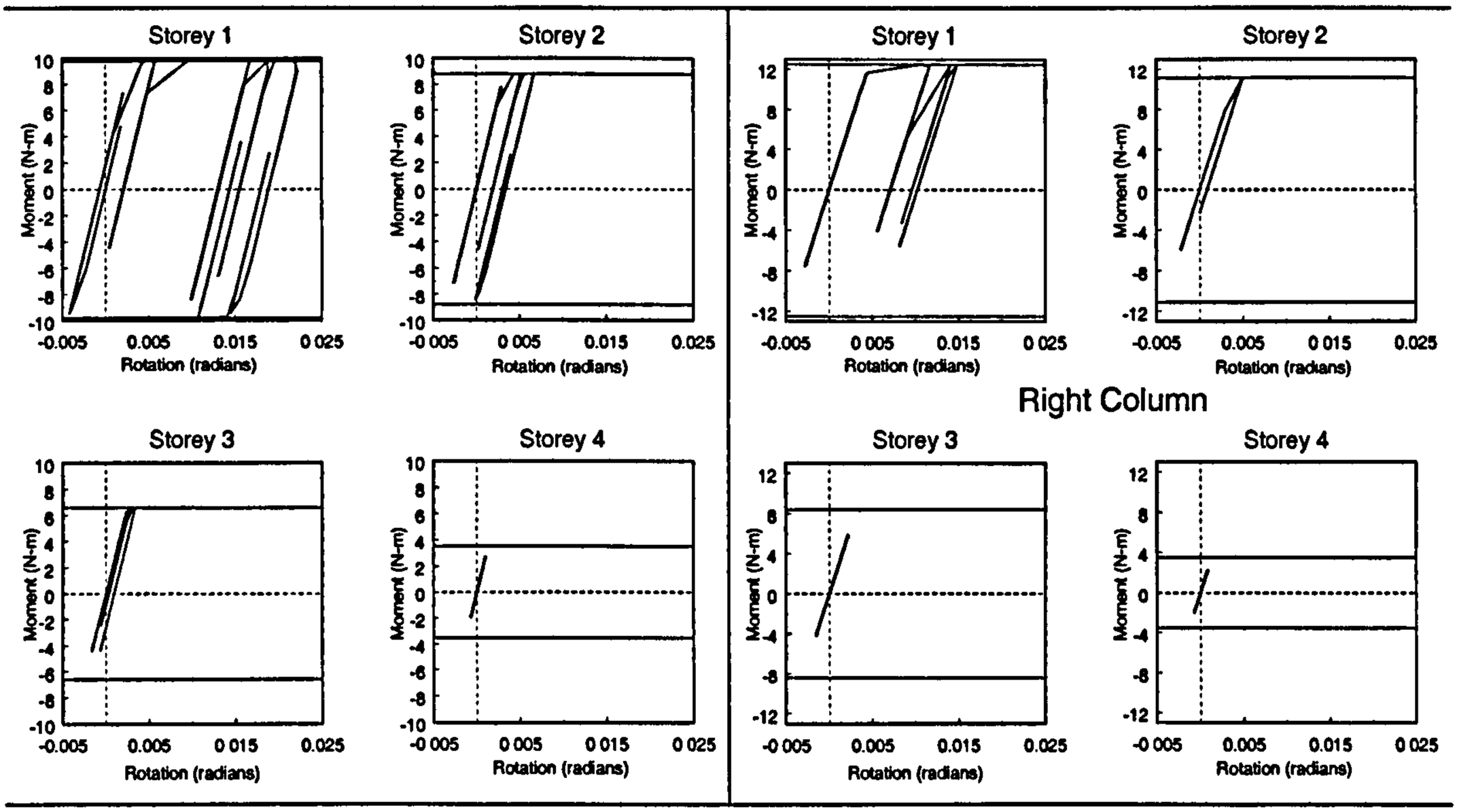

Figure D.4: Hysteresis plots for a typical right column in the mass asymmetric configurations (RMSA=54%*g*).

(128Hertz). The sampling frequency is not high enough to capture the corner points where the column initiates yielding.

Figure D.5 shows the absorbed hysteretic energy for the exterior columns in mass configuration A6. This figure shows that the first storey absorbs more energy with the right columns, and the upper storeys absorb more energy with the left columns. Additionally, the amount of energy absorbed reduces in the upper storeys. The amount of energy absorbed is exponentially related to the forcing intensity. Figure D.6 shows the absorbed energy from the exterior columns in the first storey for all three mass configurations. For the configurations studied, the higher mass asymmetry case (A6) generally absorbs less energy than either mass configuration S1 or A2. Figure D.7 shows the absorbed energy by the exterior columns in mass configuration A2. In this Figure, the right column clearly absorbs more energy than the left columns in the ground storey. The second storey does not show a significant difference between the absorption demand on the exterior columns.

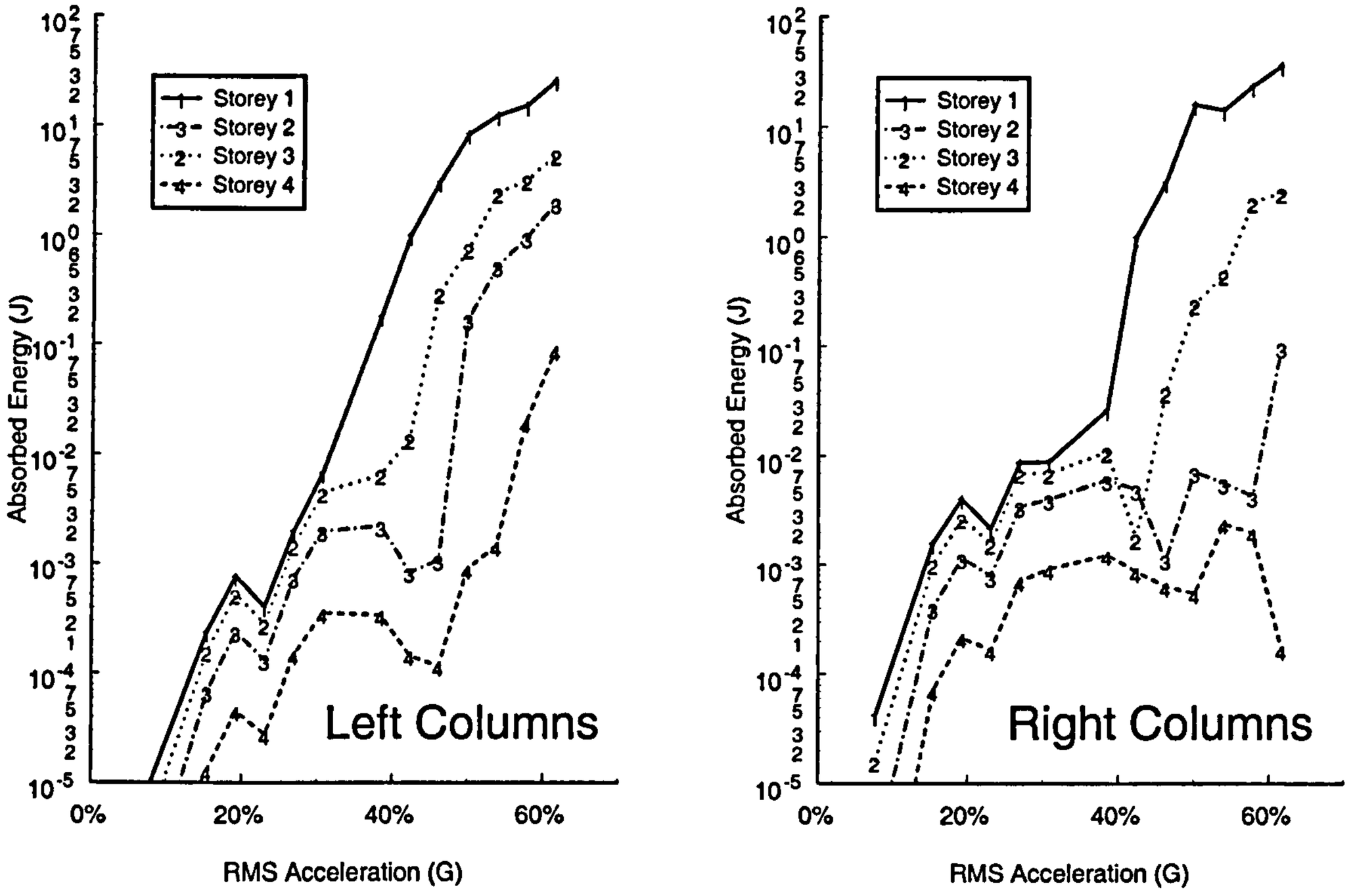

Figure D.5: Absorbed energy in the exterior columns of mass configuration A6.

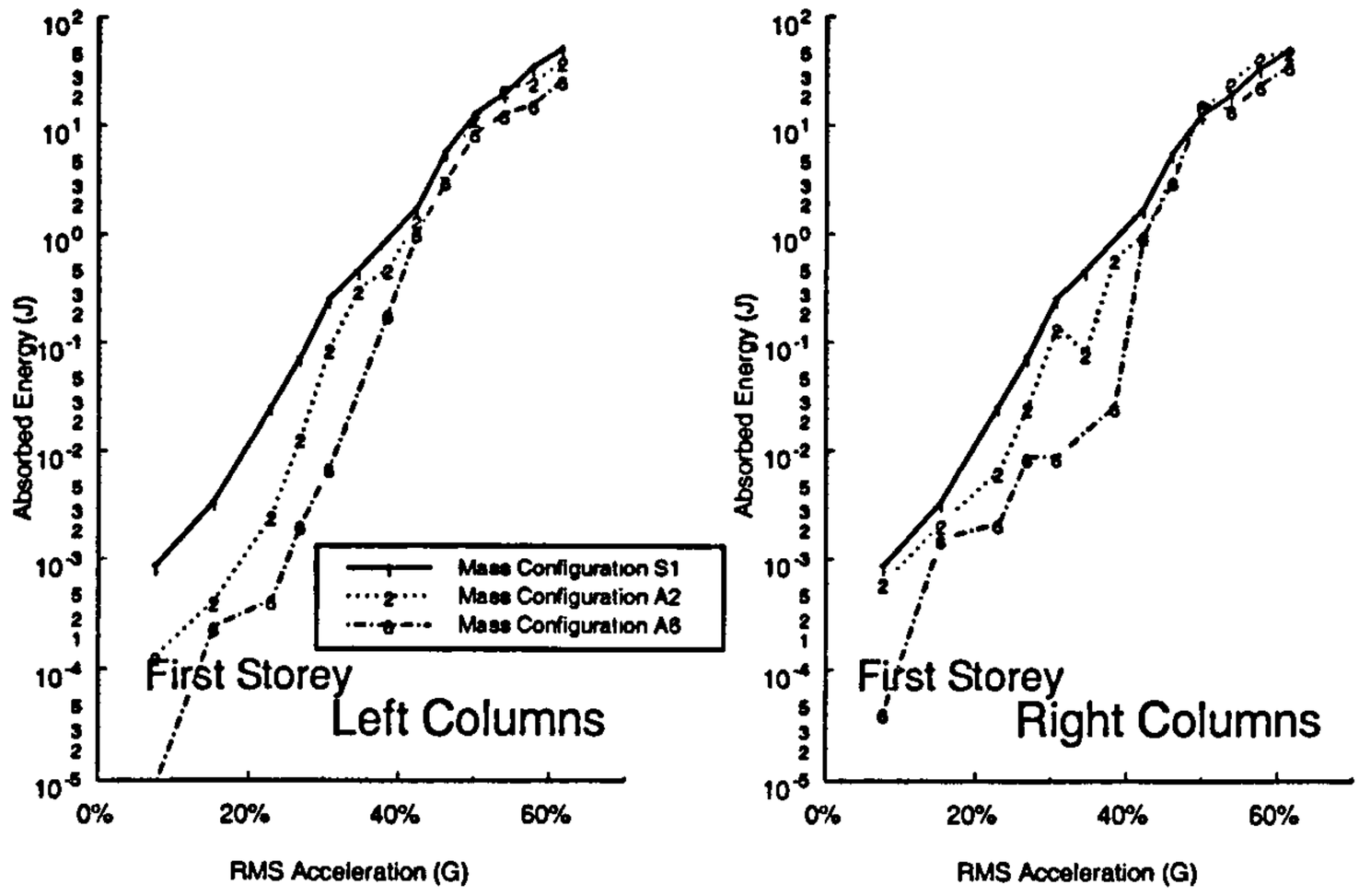

Figure D.6: Absorbed hysteretic energy in the exterior columns of the first storey for all three mass configurations.

A similar figure for mass configuration A6 is shown in Figure D.8. As with the previous Figure, this Figure shows that for the ground storey, the right column absorbs more energy

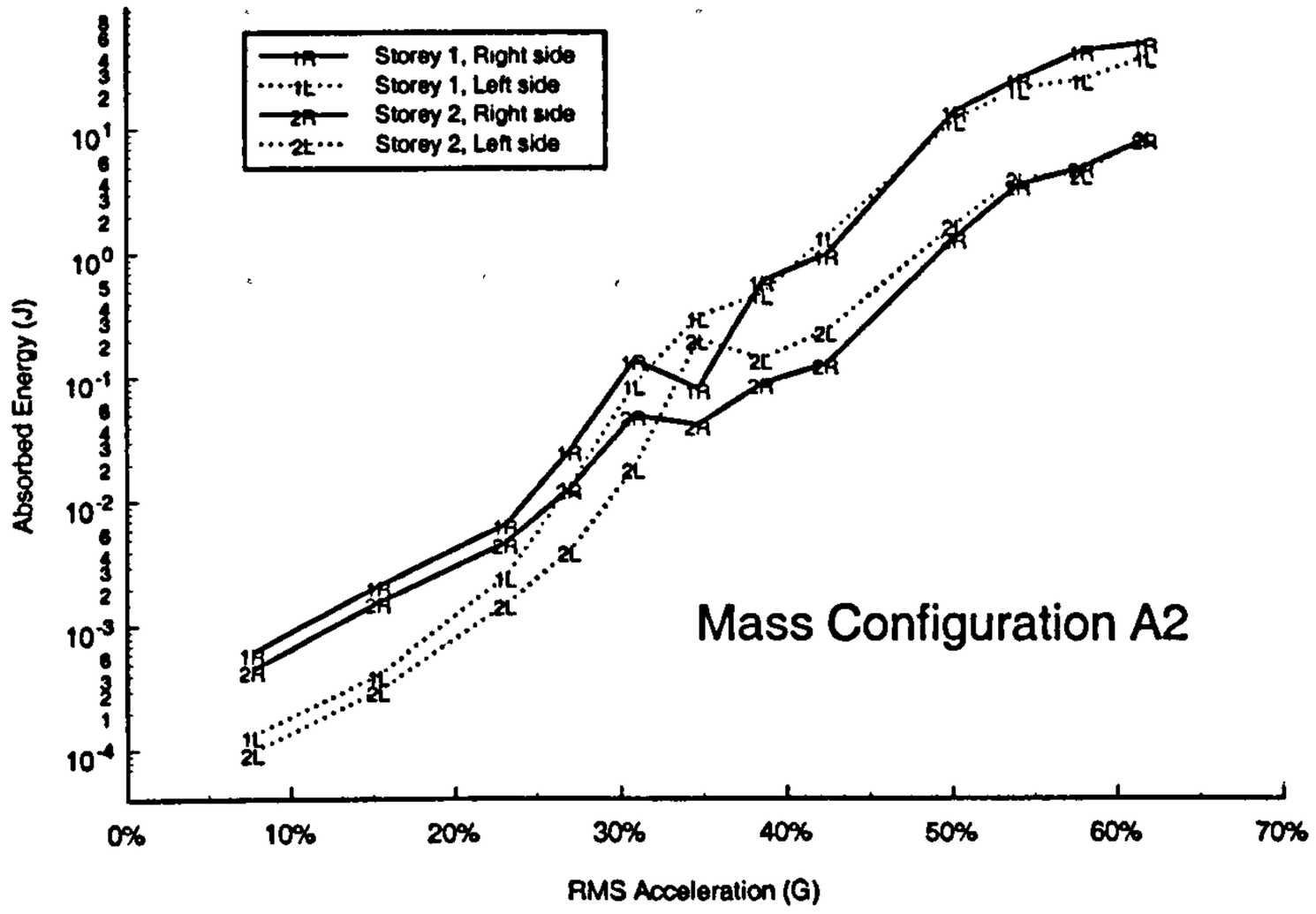

Figure D.7: Absorbed hysteretic energy by the exterior columns of the first two storeys in mass configuration A2.

than the left column. However, this is opposite in the second storey, which shows that the right column absorbs less energy than the left column.

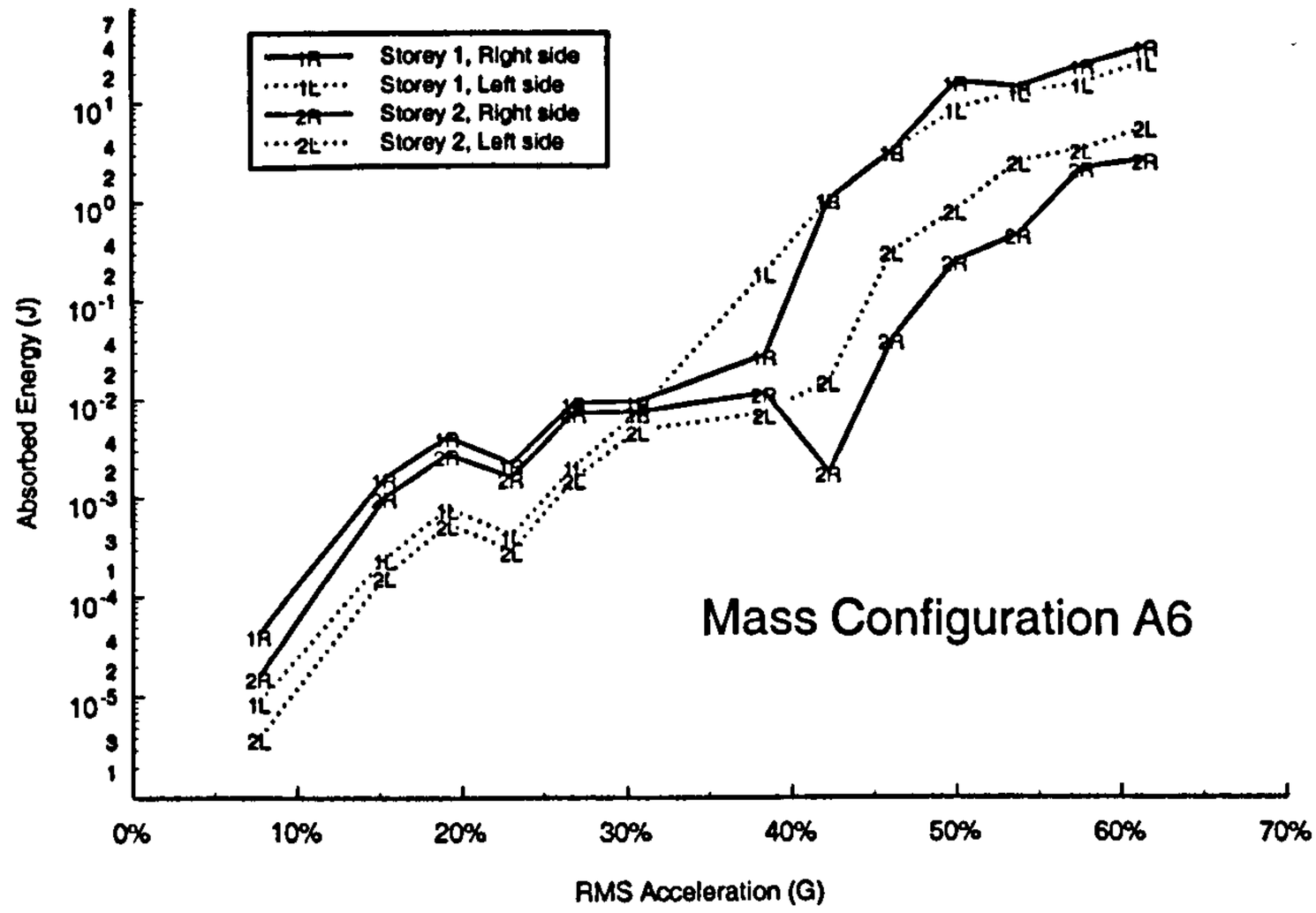

Figure D.8: Absorbed hysteretic energy by the exterior columns of the first two storeys in mass configuration A6.

D.2 CONCLUSION

The analytical models, with a strength distribution compatible with UBC94 are able to better distribute member inelastic behaviour throughout the model. Still, as with the experimental models, inelasticity is concentrated in the ground storey, and is reduced in the upper storeys. The code compatible strength distribution in the exterior columns is adequate in the first storey for all three mass configurations. However, in the upper stories the right column becomes more vulnerable, even with the design torsional amplification, A_x.

As stated earlier, the absorbed hysteretic energy is not a reliable measure of response. Although it may be related to expected building damage, it is also very sensitive to the response. However, this study does show that the ground storeys experience the most damage. Additionally, the right side columns experience more damage than the left side columns in the ground floor. For both the moment D/C ratio and energy absorption demand, the upper storey responses are influenced by any inelastic response in the ground story.

APPENDIX E

LIST OF SYMBOLS

This section briefly describes some of the variables used throughout this study.

The following is a list of the symbols used in this study:

A_x	Accidental eccentricity amplification for "irregular" buildings (see equation A.5 on page 234).
b	Plan width of structure perpendicular to forcing motion axis.
e_1, e_2	Design eccentricities from UBC, as defined in equation A.4 on page 233.

e_a	Accidental eccentricity. This is the code based eccentricity to account for uncertainties in construction and other adverse effects (from equation A.4 on page 233).
e_m	Mass eccentricity (see equation 3.2 on page 45). The mass eccentricity for floor 1 is indicated by e_{m1}
e'_m	The mass eccentricity, e_m, normalized by the building floor dimension parallel to the axis of mass eccentricity (see equation 3.4 on page 48).
e^*_m	The mass eccentricity, e_m, normalized by the mass radius of gyration, r_m, (see equation 3.5 on page 49).
e_n	Net eccentricity. This is the difference between the mass and strength eccentricity for a floor, and is defined in equation 5.6 on page 150.
e_s	Strength eccentricity as defined in equation 4.7 on page 98. The strength eccentricity for floor 1 is termed e_{s1}.
F_x	Storey design shear force (see equation A.8 on page 235).
F_y	Shear force in a column member that produces the "yielding" moment M_y. This is also the "yield" strength of a column.
g	Acceleration due to gravity.
G	Uniform damping coefficient (2ξ) at a specified response frequency. Used to compute elastic viscous damping in direct transient solution sequences (page 248).
I_5, I_{95}	These values indicate 5% and 95% of the total Arias intensity, respectively (page 133).
$J_{\Theta m}$	Polar mass moment of inertia about the centre of mass (see equation 3.3 on page 46). The value of $J_{\Theta m}$ for floor 1 is indicated by $J_{\Theta m1}$.
$J_{\Theta s}$	Polar mass moment of inertia about the centre of stiffness (see equation 3.7 on page 58). $J_{\Theta s1}$ indicates the value of $J_{\Theta s}$ for floor 1.
K_y	This is the translational stiffness along the y axis. Similarly, K_x is the translational stiffness along the x axis. Defined by equation 3.9 on page 59, the

total translational stiffness for storey 1 is indicated by K_{y1}. Translational stiffnesses of the individual column members are indicated by k_y.

K_Θ — This is the rotational stiffness about the vertical axis. As with K_y, the value of K_Θ is defined for each storey, with the rotational floor stiffness for storey 1 indicated by $K_{\Theta 1}$ (see equation 3.10 on page 59).

l_p — Plastic hinge length. This is the length of a column which is undergoing plastic yield.

M — Total floor mass (see equation 3.1 on page 45). M_1 indicates the value of M for floor 1.

M_y — Yielding moment. Sometimes referred to as the plastic moment (M_p). This is the moment at which a particular hinge unit begins to slip (simulate plastic yielding). This is also the moment in a column produced by the shear force F_y.

OS — Over-strength ratio (see equation C.3 on page 262), which is defined as the actual member strength normalized by the design member strength.

S_a — Design spectral acceleration, as defined in equation 5.1 on page 126, for the code compatible spectral shape upon which the table forcing motions are based.

S_v' — Pseudo-velocity (equation 5.2 on page 126) used to generate the code-compatible forcing motions.

t_5, t_{95} — The time at which I_5 and I_{95} occur, respectively. The time difference between t_{95} and t_5 is the *significant duration.*

r_m — Mass radius of gyration taken about the centre of mass (defined in equation 3.5 on page 49).

V_b — Design base shear for entire building structure (see equation A.6 on page 234).

X, Y, Θ — These are the three principle directions of motion of the building model. X and Y represent translations along the x and y-axes, respectively. Θ is the rotation about the vertical axis. These are the absolute measured values, with Y_1 being the y-axis motions of floor 1. See Section 5.1.1 on page 117. The relative motions are indicated by δX, δY, and $\delta\Theta$,

Y_Δ, Θ_Δ	The peak displacement difference between an elastic and inelastic analytical model response (equation 7.6 on page 205).
α_1, α_2	Rayleigh damping parameters defined in equation 7.1 on page 190.
Δ_p	This is the plastic displacement associated with a plastic hinge rotation Θ_p, which occurs when both top and bottom hinge units are "yielding" (see equation 6.8 on page 172).
δ_L, δ_R	This is the peak left side and right side displacements used by UBC in determining the classification of the building (regular or irregular) as in equation A.1 on page 230.
Θ_t, Θ_b	The is the rotation at the top (Θ_t) and bottom (Θ_b) of a "yielding" column in the column yielding configuration models (see equation 6.7 on page 172).
Θ_p	This is the plastic rotation of a yielding hinge unit (from equation 6.9 on page 172).
ϕ_x, ϕ_y	Column curvature in the plastic hinge region (within l_p).
μ_Δ	This is the displacement ductility based on the displacement at which plastic yield occurs (see equation 6.10 on page 173)
Ω	Ratio of uncoupled torsional to translational frequency (page 34, page 50).
ω	Undamped, coupled vibrational frequency. The frequency of mode 1 is indicated by ω_1.
ω_Θ	Undamped, uncoupled rotational frequency.
ω_y	Undamped, uncoupled translational frequency.
ξ	Percent of critical elastic viscous damping. See Section 3.5 on page 68.
l_e	Calibrated effective column length (see Section 4.3 on page 98).

APPENDIX F

REFERENCES

American Concrete Institute, 1973. Analysis of Structural Systems for Torsion, SP–35.

Associate Committee on the National Building Code, 1990. *National Building Code of Canada*, National Research Council of Canada, Ottawa, Ontario.

Ayre, R.S., 1943. "Experimental response of an asymmetric one-storey building model to an idealized transient ground motion", Bulletin of the Seismological Society of America, 30:91-119.

Bassett, R.H., M.R. Maheri, and A.M. Chandler, 1990. "Torsional earthquake response of frame buildings to Eurocode–8 spectrum compatible design motion", Proceedings of the 9th European Conference on Earthquake Engineering, Moscow, 5:97-106.

Bourahla, N. and Blakeborough, A., 1994. "Shake table testing of torsionally coupled knee braced frames", Fifth U.S. National Conference on Earthquake Engineering, Proceedings, Earthquake Engineering Research Inst., Oakland, California, II:773-782.

Bozorgnia, Y., and W.K. Tso, 1986. "Inelastic earthquake response of asymmetric structures", Journal of Structural Engineering, ASCE, 112:2:389–99.

Brownjohn, J.M.W., 1990. "Aquiring data using the data translation hardware and ASYST software (DASYST)", EERC Technical Instruction TI23002, Department of Civil Engineering, University of Bristol.

Chandler, A.M., and G.L. Hutchinson, 1987. "Evaluation of code torsional provisions by a time history approach", Journal of Earthquake Engineering and Structural Dynamics, 15:491–516.

Chandler, A.M., 1988(a). "Evaluation of the secondary torsional design provisions of earthquake building codes", Proceedings of the Institution of Civil Engineers, 85:2:587–607.

Chandler, A.M., R.H. Bassett, and M.R. Maheri, 1988(b). "Initial experience in dynamic torsional coupling of structural models", SECED Conference on Civil Engineering Dynamics, University of Bristol. 18pp.

Chandler, A.M., and E.A. Nichol, 1990(a). "Experimental evaluation of procedures for earthquake analysis of torsionally asymmetric buildings", European Earthquake Engineering, 4:3:43–52.

Chandler, A.M., 1990(b). "Evaluation of site-dependent spectra for earthquake-resistant design of structures in Europe and North America", Proceedings of the Institution of Civil Engineers, 90:6:605–626.

Chandler, A.M., and X.N. Duan, 1991. "Evaluation of factors influencing the inelastic seismic performance of torsionally asymmetric buildings", Earthquake Engineering & Structural Dynamics, 20:87-95.

Cheung, V.W.-T., and W.K. Tso, 1986. "Eccentricity in irregular multistorey buildings", Canadian Journal of Civil Engineering, 13:1:46-52.

Commission of the European Communites, 1993. "Eurocode No.8: Design for structures in seismic regions, Part 1, General and Building", Report EUR 12266EN, Brussels.

Correnza, J.C., and G.L. Hutchinson, 1991, "Lateral-torsional coupling in asymmetric buildings subject to seismic activity: The current understanding", Internal Report, The University of Melbourne, Department of Civil Engineering.

De la Llera, J.C., and A.K. Chopra, 1995. "Estimation of accidental torsion effects for seismic design of buildings", Journal of Structural Division, ASCE, 121:1:102–114.

De la Llera, J.C. and A.K. Chopra, 1995, "Understanding the inelastic seismic behaviour of asymmetric-plan buildings", Journal of Earthquake Engineering and Structural Dynamics, 24:549-572.

De la Llera, J.C. and A.K. Chopra, 1995, "A simplified model for analysis and design of asymmetric-plan buildings", Journal of Earthquake Engineering and Structural Dynamics, 24:573-594.

Escobar, J.A. and A.G. Ayala-Milián, 1998. "Yielding seismic response of code-designed single-storey asymmetric structures", Earthquake Engineering and Structural Dynamics, 27:525-541.

Federal Emergency Management Agency, 1988. "NEHRP Recommended Provisions for the Development of Seismic Regulations for New Buildings", National Earthquake Hazards Reduction Program, Part1-Provisions.

Federal Emergency Management Agency, 1988. "NEHRP Recommended Provisions for the Development of Seismic Regulations for New Buildings", National Earthquake Hazards Reduction Program, Part2-Commentary.

Foutch, D.A., 1978. "The vibrational characteristics of a twelve-storey steel frame building", Earthquake Engineering and Structural Dynamics, 6:265-294.

Goel, R.K., and A.K. Chopra, 1990. "Inelastic seismic response of one-story, asymmetric-plan systems", Earthquake Engineering Research Center, Report Number UCB/EERC-90/4.

Goel, R.K., and A.K. Chopra, 1993. "Seismic code analysis of buildings without locating centers of rigidity", Journal of Structural Division, ASCE, 119:10:3039–55.

Goel, R.K., 1998. "Effects of supplemental viscous damping on seismic response of asymmetric-plan systems", Earthquake Engineering and Structural Dynamics, 27:125-141.

Grigorian, M., 1993. "On the dynamic analysis of regular shear structures", Earthquake Spectra, Earthquake Engeering Research Institiute, 9:1:55–66.

Hejal, R., and A.K. Chopra, 1989. "Lateral–torsional coupling in earthquake response of frame buildings", Journal of Structural Engineering, ASCE, 115:852–67.

Humar, J.L., 1984. "Design for Seismic Torsional Forces", Canadian Journal of Civil Engineering, 11:150-163.

International Conference of Building Officials, 1988. Uniform Building Code, Whitter, CA.

International Conference of Building Officials, 1991, *Uniform Building Code*, Whitter, CA.

International Conference of Building Officials, 1994, *Uniform Building Code, Structural Engineering Design Provisions*, Vol 2., Whitter, CA.

International Conference of Building Officials, 1994, *Uniform Building Code, Analysis of revisions to the 1994 Uniform Codes*, Whitter, CA.

Ju, S.H., and M.C. Lin, 1999. "Comparison of building analyes assuming rigid or flexible floors", Journal of Structural Division, ASCE, 125:1:25-31.

Kan, C.L., and A.K. Chopra, 1977. "Effects of torsional coupling on earthquake forces in buildings", Journal of Structural Division, ASCE, 103:ST4:805–20.

Kan, C.L., and A.K. Chopra, 1979. "Linear and nonlinear equathquake response of simple torsionally coupled systems", Earthquake Engineering Research Center, Report No. UCB/EERC–79/03, University of California, Berkeley, CA.

Kan, C.L., and A.K. Chopra, 1981. "Torsional coupling and earthquake response of simple elastic and inelastic systems", Journal of Structural Division, ASCE, 107:ST8:1569–88.

Kiureghian, A.D., 1980. "A response spectrum method for random vibration", Earthquake Engineering Research Center, Report No. UCB/EERC–80/15, Univerisity of California, Berkeley, CA.

Krinitzsky, E.L., J.P. Gould, and P.H. Edinger, 1993. Fundamentals of Earthquake–Resistant Construction, New York: John Wiley & Sons.

Lin, B.C., and A.S. Papageorgiou, 1989. "Demonstration of torsional coupling caused by closely spaced periods-1984 Morgan Hill earthquake response of the Santa Clara County Building", Earthquake Spectra, 5:3:539–56.

Maheri, M.R., A.M. Chandler, and R.H. Bassett, 1991. "Coupled lateral–torsional behaviour of frame structures under earthquake loading", Journal of Earthquake Engineering and Structural Dynamics, 20:1:61-85.

Maison, B.F., C.F. Neuss, and K. Kasai, 1983. "The comparative performance of seismic response spectrum combination rules in building analysis", Earthquake Engineering and Structural Dynamics, 11:623–47.

Nagarajaiah, S., A.M. Reinhorn, and M.C. Constantinou, 1993. "Torsional coupling in sliding base–isolated structures", Journal of Structural Engineering, ASCE, 119:1:130–49.

Nagarajaiah, S., A.M. Reinhorn, and M.C. Constantinou, 1993. "Torsion in base-isolated structures with elastomeric isolation systems", Journal of Structural Division, ASCE, 119:10:2932–51.

Newmark, N.M., and W.J. Hall, 1982. Earthquake Spectra and Design, Berkeley: EERI Monograph Series, Earthquake Engineering Research Institute.

Nichol, E.A., A.M. Chandler, and R.H. Bassett, 1991. "Design and performance of model floor–column joints for simulation of inelastic structural response under earthquake loadings", International Conference on Earthquake, Blast and Impact Loadings, UMIST, Manchester, 231–40.

Paulay, T., 1997. "A review of code provisions for torsional seismic effects in buildings", Bulletin of the New Zealand National Society for Earthquake Engineering, 30:3:252-263.

Paulay, T., 1998. "Torsional mechanisms in ductile building systems", Earthquake Engineering and Structural Dynamics, 27:1101-1121

Paz, M., 1991. "Structural Dynamics, Theory and Computation", Van Nostrand Reinhold, New York, NY.

Rabiner, L.R., and R.W. Schafer, 1978. "Digital Processing of Speech Signals", Prentice-Hall, Englewood Cliffs, NJ.

Sadek, A.W., and W.K. Tso, 1988. "Strength eccentricity concept for inelastic analysis of asymmetric structures", Proceedings of 9th World Conference on Earthquake Engineering, V:91–6.

Sternik, M., and J. Gluck, 1993. "Decoupling of lateral equilibrium equations for asymmetric multistory structures", Journal of Structural Division, ASCE, 119:10:2871–82.

Tsicnias, T.G., and G.L. Hutchinson, 1981. "Evaluation of code requirements for the earthquake resistance design of torsionally coupled buildings", Proceedings of the Institution of Civil Engineers, 2:71:821-843.

Tso, W.K., and A.W. Sadek, 1985. "Inelastic seismic response of simple eccentric structures", Journal of Earthquake Engineering and Structural Dynamics, 13:255–69.

Tso, W.K., and A.W. Sadek, 1990. "Inelastic seismic response of simple eccentric structures", Journal of Earthquake Engineering and Structural Dynamics, 19:2:243–58.

Tso, W.K., and C.M. Wong, 1995. "Seismic displacements of trosionally unbalanced building", Journal of Earthquake Engineering and Structural Dynamics, 24:1371-1387.

Valmundsson, E.V. and J.M. Nau, 1997. "Seismic response of building frames with vertical structural irregularities", Journal of Structural Engineering, ASCE, 123:1:30-41.

Vanmarke, E.H., C.A. Cornell, D.A. Gasparini, and S.N. Hou, 1976. "SIMQKE - Simulation of Earthquake Ground Motions", Earthquake Engineering Research Center, University of Colifornia, Berkeley.

Wong, C.M. and W.K. Tso, 1995. "Evaluation of Seismic Torsional Provisions in Uniform Building Code", Journal of Structural Engineering, ASCI, 121:10:1436-1442.

Zayas, V.A., S.S. Low, and S.A. Mahin, 1987. "The FPS Earthquake Resisting System—Experimental Report", Earthquake Engineering Research Center, Berkeley, CA, Report No. UCB/EERC-87/01.

APPENDIX G

PUBLISHED PAPERS

Source:
European Earthquake Engineering, 1990.
Volume 4, Number 3, Pages 43-52.

Experimental Evaluation of Earthquake Analysis of Torsionally Asymmetric Buildings

A.M. Chandler and E.A. Nichol

SUMMARY - This study investigates the effectiveness of various analytical procedures used to model torsional coupling effects in the earthquake response of asymmetric frame buildings. Experimental and theoretical studies are presented, with particular focus on the rigorous time history response solution of a simplified lumped-mass model. Comparisons with response spectrum analysis indicate that the time history approach is a more reliable method of predicting the torsional coupling effect, since is accounts more accurately for the significant contributions of the second (torsionally dominated) mode to the overall structural response. This result has important implications for earthquake-resistant design procedures as recommended in current seismic building codes.

KEYWORDS: seismic response, torsion, analytical methods, shaking table.

1. Introduction

An extensive experimental test programme has been carried out using the Science and Engineering Research Council (SERC) national UK earthquake simulator facility at Bristol University to study and evaluate the phenomenon of elastic torsional coupling in asymmetric multistorey frame buildings subjected to earthquake base excitation. The experimental research has provided data on the dynamic coupling of lateral and torsional vibration modes in a series of parametrically defined cases with realistic distributions of structural stiffness and imposed masses. Complimentary analytical studies have been implemented using: (a) earthquake-resistant code design procedures based on the empirical lateral force approach, (b) simplified response spectrum analysis, and (c) time domain solutions of the dynamic equations of motion based on a simplified lumped-mass model. In each case, the results have been used to assess the effectiveness of the various theoretical approaches in determining or predicting the observed structural behaviour. Particular attention has ben given to the influence of torsional response on the peak dynamic forces affecting edge elements of the tested structures. The aim is to validate the existing analysis and design procedures listed above for a range of dynamic properties consistent with those of actual buildings.

This paper concentrates on the comparison of the observations from the experimental studies with the results obtained from both the response spectrum analysis and time domain (lumped mass) solutions. Comparisons with finite element analysis methods are currently in progress. Analytical studies based directly on earthquake-resistant code pro-

cedures for asymmetric buildings are beyond the scope of this paper, and are therefore dealt with in a separate study.

2. Ground Motion Records

The ground motion records used in this study are table generated, and based on the actual ground motion recordings from two Western US earthquakes (N-S El Centro 1940 and *N65E Parkfield 1966) and one* European earthquake (Horizontal-A Thessaloniki 1978). The table acceleration records, and their corresponding acceleration response spectra for 1.0% damping are shown in Figures 1 to 3. The input table accelerations have been appropriately scaled down from the actual earthquake records in order to ensure elastic behaviour of the model, and to limit the peak experimental floor displacements to the recording range of the transducers ($|\Delta_{peak}| \leq 10\text{mm}$).

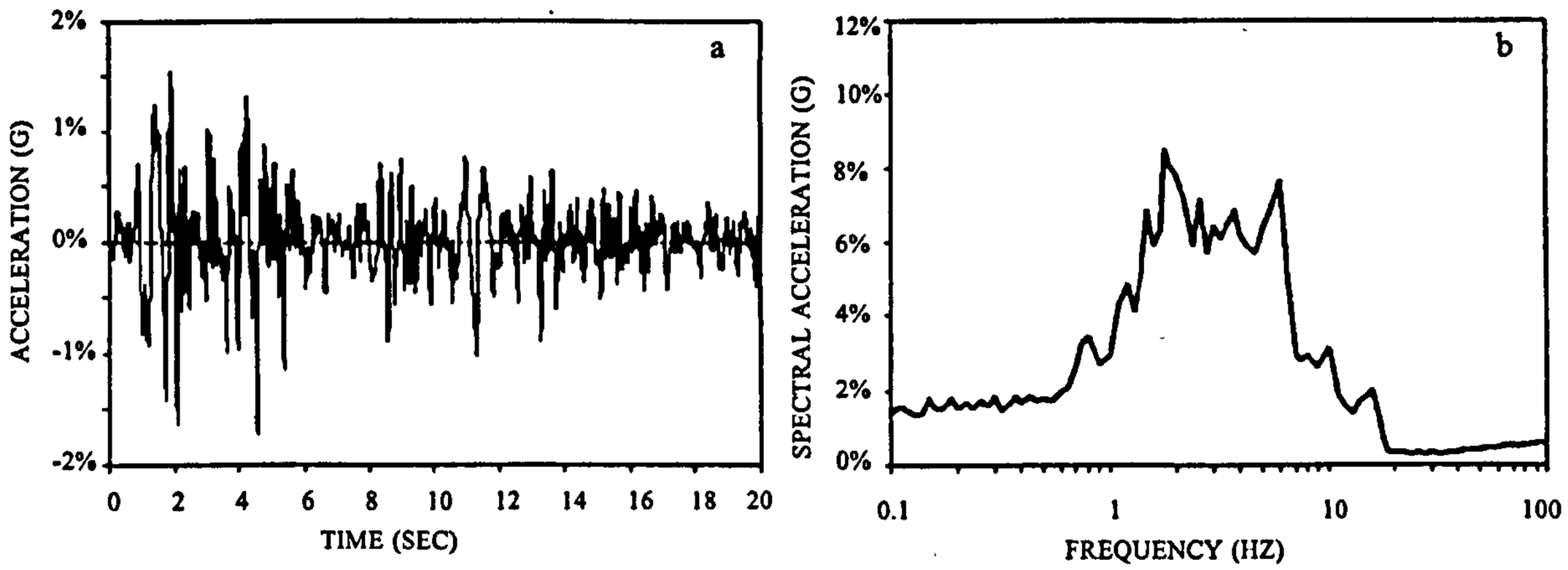

Figure 1: El Centro 1940 N-S; (a) table acceleration record and (b) corresponding 1% damped acceleration spectrum.

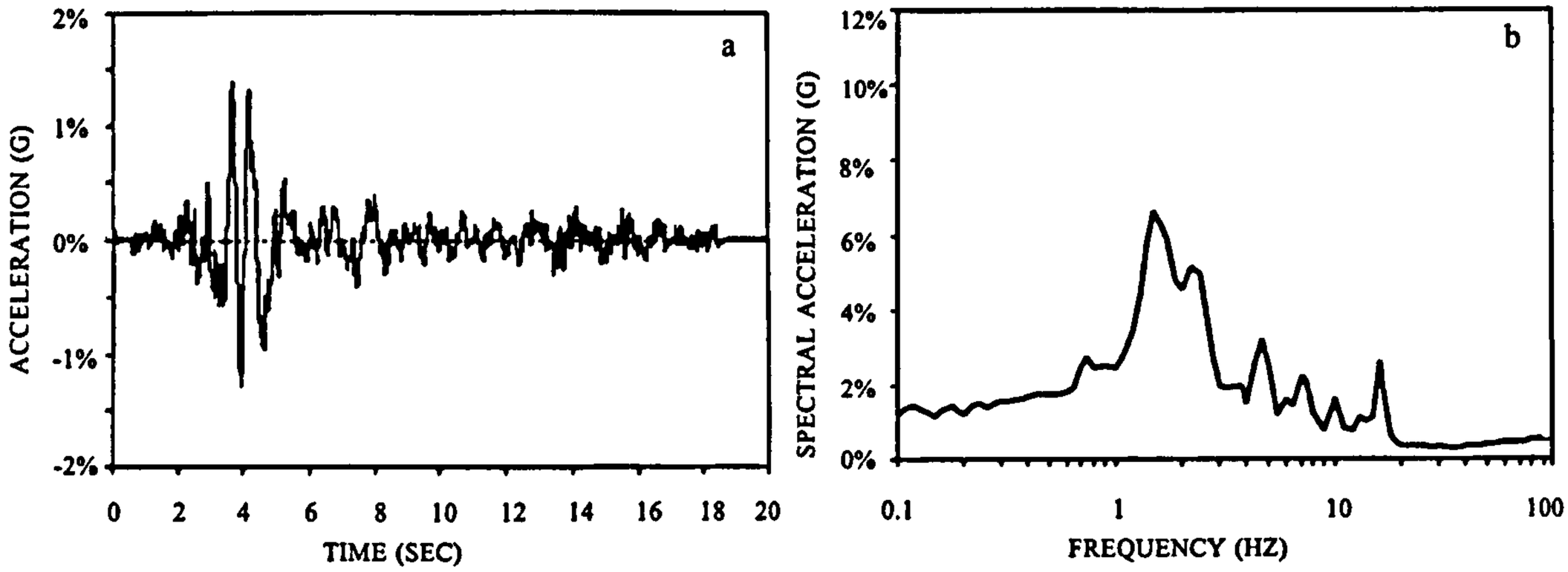

Figure 2: Parkfield 1966 N65E; (a) table acceleration record and (b) corresponding 1% damped acceleration spectrum.

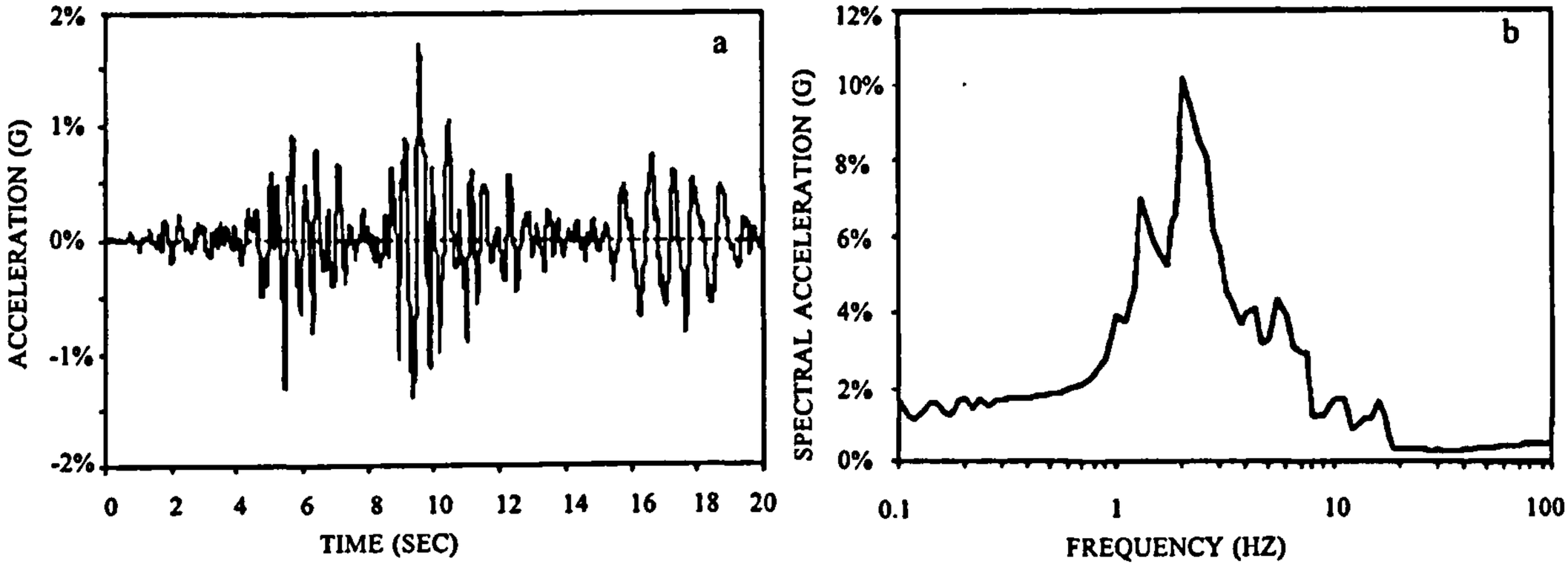

Figure 3: Thessaloniki 1978 Horizontal A; (a) table acceleration record and (b) corresponding 1% damped acceleration spectrum.

3. Description of Experimental Model

A series of experimental four-storey structural models have been tested under earthquake loadings using the SERC national UK earthquake simulator. The models are constructed of cast aluminium floors and strain-hardened brass columns. The brass columns are continuous through all floors, and are rigidly connected at the corners of each floor. Additionally, an optional column can be placed at the geometric centre of each floor (see Figure

4(a)). There are a total of 15 model configurations which are the combinations of different mass distributions, and 5 possible column arrangements [2].

The 3 possible mass arrangements consist of a symmetric mass distribution, designated S1; a low mass eccentricity ratio, A2; and a high mass eccentricity ratio, A6 (see Table 1).

Table 1: Properties of symmetric and asymmetric mass configurations.

Mass Configuration	Mass Eccentricity ratio $e^* = e_m/L$	Floor Mass (kg)	Mass Radius of Gyration, r_m (mm)	Polar Moment of Inertia, J_Θ $(kg \bullet m)^2$
S1	0%	27.1	317	2.72
A2	7%	27.1	309	2.59
A6	20%	27.1	357	3.45

The mass eccentricity ratio is defined in this study as the mass eccentricity (distance between the centre of mass and centre of stiffness) normalized by the floor dimension perpendicular to the applied ground motion. Altering the mass eccentricity is accomplished by rearranging a series of lead plates that are fitted into each cast aluminium floor (see Figure 4). During each test, the properties listed in Table 1 are identical for each floor.

The five variations of column configuration, designated CC1 to CC5, represent reasonable values of ratios for uncoupled torsional to translational frequencies, Ω, in real buildings ($0.9 \leq \Omega \leq 2.0$), see Table 2). This range encompasses the value of unity for Ω, which pre-

Table 2: Uncoupled torsional/lateral frequency ratio for various column configurations.

Column Configuration	Frequency Ratio $\Omega = \omega_\Theta/\omega_y$
CC1	0.89
CC2	1.17

Table 2: Uncoupled torsional/lateral frequency ratio for various column configurations.

Column Configuration	Frequency Ratio $\Omega = \omega_\Theta/\omega_y$
CC3	1.35
CC4	1.62
CC5	2.07

vious parametric studies have concluded will generally lead to the greatest torsional coupling effects [3, 4, 5]. Buildings with frequency ratios outside the studied range behave as essentially uncoupled structures, and are not affected significantly by torsional coupling. The modal frequencies for the various model configurations are shown in Table 3. These frequencies are comparable to those found for the lower frequencies in most actual 4 storey buildings [6].

All fifteen models have ben tested using the Parkfield table acceleration record. Additionally, the El Centro and Thessaloniki ground motions were used on models with column configuration CC2, so that a comparison could be made on the behaviour of the model using ground motions with varying spectral characteristics. Column configuration CC2 was selected since Ω is close to, but still grater than the critical value of unity. This corresponds to the ambient Ω found in most real, multistorey buildings, which is normally greater than unity [7].

The experimental test monitored the displacements on both sides of all four floors. The sides have been labelled A and B (see Figure 4), in that side A is the side furthest from the centre of mass, and is the side that is usually the least vulnerable, in terms of member shear force, to the effects of torsional coupling. The floor displacments were measured

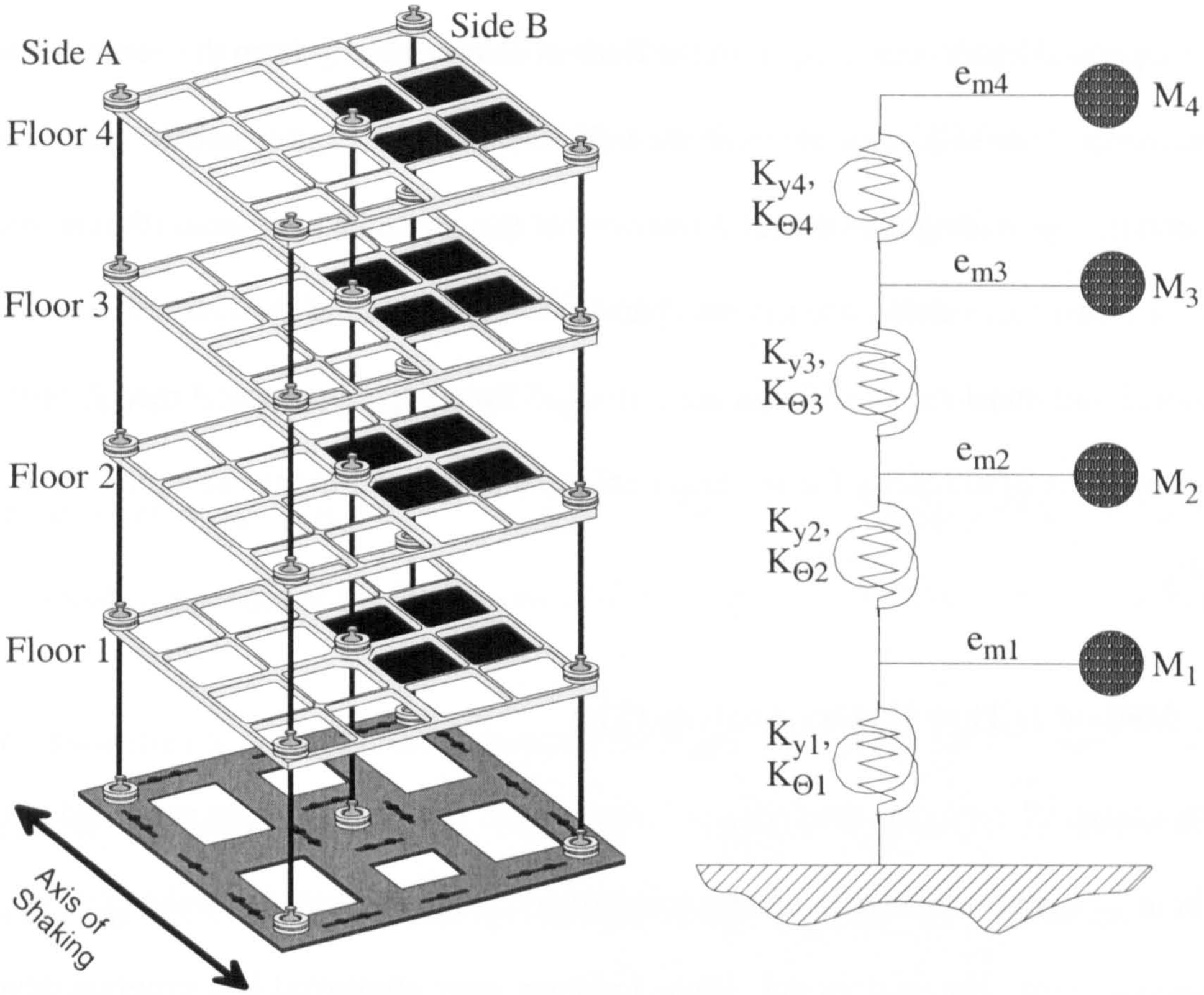

a) Experimental model. b) Analytical lumped-mass model.

Figure 4: Graphic representations of both the experimental and analytical models.

using non-contacting displacement transducers mounted on a rigid frame that was fixed to the shaking-table surface. A summary of the experimental testing procedures, and a discussion of the results in comparison with modal analysis methods have been published in a previous paper [2].

4. Methods of Analysis

A simplified lumped-mass model, as shown in Figure 4(b), has been employed as an approximation to the experimental model for a solution to both the time history integration

an modal superposition methods of analysis. The analytical model consists of four point masses separated by a distance equal to the floor mass eccentricity from the vertical structural elements. These elements combine the individual torsional and translational stiffness of the columns providing the vertical framework of the experimental model (Figure 4(a)). The point masses are confined to motions parallel to the horizontal X-Y plane. The values of torsional and translational stiffness are estimated from the experimental model, assuming the modulus of elasticity for the brass columns as the commonly accepted value of 100 GPa.

4.1. Method 1: Time History Analysis (TH)

For this analytical approach, the series of lumped-mass models have been subjected to the same base accelerations, as recorded by accelerometers mounted on the shake table of the corresponding experimental model. These loadings were employed in a program developed at University College London, to estimate the peak displacement of the floor sides A and B for all storeys. This is accomplished by using the Newmark β implicit integration scheme to evaluate the equations of motions of the model, equation (1), at time steps of 1/30 of the 4th natural coupled period of the model, thus ensuring the full contribution from the first four modes (the number of modes combined in the modal superposition method of analysis). Rayleigh damping, equation (4), is assumed appropriate for the experimental models, and is taken as 1.0% of critical for both modes 1 and 2. This is in the range of damping, in general, observed during the experimental model tests for the first few modes [2].

The lumped-mass time history analytical procedure calculates the structural displacements through a step-by-step integration of the equations of motion. Since the models studied are symmetric with respect to stiffness, the equations have been referred to the centre of stiffness, which coincides with the geometric centre of the floor plan. The dynamic response of the model can then be obtained by the solution of the following equation:

$$MU(t) + CU(t) + KU(t) = F(t) \qquad (1)$$

where, $U(t) = \left[u_1(t)\ \theta_1(t)\ \ldots\ u_4(t)\ \theta_4(t)\right]^T$, and $u_i(t)$ and $\theta_i(t)$ represent the lateral and rotational component of the displacement of the centre of stiffness of floor i, respectively.

The mass matrix M for the mass-asymmetric model con be defined in terms of the floor mass, M_i, the mass eccentricity e_i, and the mass radius of gyration, r_i, for the floor i. The local mass matrix for floor i, and the associated degrees of freedom, can be defined as:

$$M_{Li}\ddot{U}_L = \begin{bmatrix} M_i & M_i e_i \\ M_i e_i & M_i(r_i^2 + e_i^2) \end{bmatrix} \begin{bmatrix} \ddot{u}_i \\ \ddot{\theta}_i \end{bmatrix} \qquad (2)$$

Since the model is symmetric with respect to stiffness, the stiffness matrix is defined simply in terms of the translational stiffness of the column group below and above floor i ($K_y^{<-i>}$ and $K_y^{<+i>}$, respectively) and the torsional stiffness of the column group below and

above floor i ($K_\theta^{<-i>}$ and $K_\theta^{<+i>}$, respectively). The local stiffness matrix for floor i, with its associated degrees of freedom, can then be written as:

$$K_{Li}U_L = \begin{bmatrix} -K_y^{<-i>} & 0 & K_y^{<-i>} + K_y^{<+i>} & 0 & -K_y^{<+i>} & 0 \\ 0 & -K_\theta^{<-i>} & 0 & K_\theta^{<-i>} + K_\theta^{<+i>} & 0 & -K_\theta^{<+i>} \end{bmatrix} \begin{bmatrix} u_{i-1} \\ \theta_{i-1} \\ u_i \\ \theta_i \\ u_{i+1} \\ \theta_{i+1} \end{bmatrix} \quad (3)$$

The damping for the time history analysis is provided through Rayleigh damping with a constant damping ratio, ξ. The damping is defined at the first two natural circular frequencies, ω_1 and ω_2, and can be written as:

$$C = \frac{2\xi}{\omega_1 + \omega_2}(\omega_1\omega_2 M + K) \quad (4)$$

Once values for the floor rotation (in radians) and translation (in metres) are obtained, the displacments (in metres) for sides A and B of floor i are simply:

$$\begin{Bmatrix} \Delta_A \\ \Delta_B \end{Bmatrix}_i = u_i \begin{Bmatrix} 1 \\ 1 \end{Bmatrix} + \theta_i \begin{Bmatrix} -0.463 \\ 0.463 \end{Bmatrix} \quad (5)$$

4.2. Method 2: Modal Superposition (MS)

For this method of analysis, only the first four modes are assumed to contribute significantly to the overall dynamic response. This assumption has been verified in Table 3, which indicates that the first four modes contribute more than 99.5% of the total response in the analytical models. Additionally, comparing the modal contributions in all modes, the first mode has been found to account for over 80% of the total response. The exception to this is column configuration 1 (CC1), where the first mode is torsionally dominated

($\Omega < 1$). The peak acceleration for each mode is taken from the response spectrum generated from the table (base) accelerations. As with the time history calculations, the level of damping is taken as 1.0% for all modes.

The peak displacement vector for mode n, V_n, is defined in terms of the coupled mode shape vector, ϕ_n, and the maximum modal response, R_n:

$$V_n = \phi_n R_n \tag{6}$$

The maximum modal response is defined in terms of ω_n, $S_a(\omega_n, \xi)$, M_n, and L_n, which are the natural circular frequency, spectral acceleration, generalized mass, and earthquake excitation factor for mode n, respectively:

$$R_n = \frac{L_n}{M_n \omega_n^2} S_a(\omega_n, \xi) \tag{7}$$

where the earthquake excitation factor, and generalized mass for mode n are:

$$\begin{aligned} L_n &= \phi_n^T M \begin{bmatrix} 1 & 0 & \dots & 1 & 0 \end{bmatrix}^T \\ M_n &= \phi_n^T M \phi_n \end{aligned} \tag{8}$$

Having obtained the modal displacement vectors from equation (6), the peak displacements are found using the Complete Quadratic Combination (CQC) rule to combine the mode [8]. The CQC method, defined in equation (9), has been found to be particularly appropriate in analysing structures with closely spaced and/or coupled modes [9].

$$V^2 = \sum_{i=1}^{N} V_i^2 + \sum_{\substack{i=1 \\ i \neq j}}^{N} \sum_{j=1}^{N} \frac{V_i V_j}{1 + \varepsilon_{ij}^2} \qquad \text{where, } \varepsilon_{ij} = \frac{\sqrt{1-\xi^2}}{\xi}\left(\frac{\omega_i - \omega_j}{\omega_i + \omega_j}\right) \tag{9}$$

Table 3: Modal frequencies and contributions to dynamic response for the various column and mass distributions.

Mode	Mass Config. S1		Mass Config. A2		Mass Config. A6		
	Hz.	Contrib.	Hz.	Contrib.	Hz.	Contrib.	
1	2.36	0.00%	2.25	73.04%	1.70	89.76%	Column Config 1 ($\Omega = 0.89$)
2	2.65	98.73%	2.85	25.42%	3.26	8.81%	
3	6.84	0.00%	6.52	0.60%	4.94	1.13%	
4	7.71	1.10%	8.29	0.78%	7.64	0.11%	
5	10.57	0.00%	10.08	0.07%	9.44	0.06%	
6	11.98	0.14%	12.46	0.02%	9.48	0.12%	
7	13.05	0.00%	12.86	0.05%	14.71	0.02%	
8	14.84	0.03%	15.92	0.02%	18.21	0.00%	

Mode	Mass Config. S1		Mass Config. A2		Mass Config. A6		
	Hz.	Contrib.	Hz.	Contrib.	Hz.	Contrib.	
1	2.01	98.34%	1.93	82.13%	1.57	86.90%	Column Config 2 ($\Omega = 1.17$)
2	2.36	0.00%	2.52	16.71%	2.68	11.38%	
3	5.83	1.51%	5.59	0.81%	4.56	1.43%	
4	6.84	0.00%	7.30	0.16%	7.05	0.10%	
5	9.03	0.11%	8.67	0.12%	7.76	0.13%	
6	10.57	0.00%	10.72	0.04%	8.72	0.02%	
7	11.18	0.03%	11.29	0.02%	12.02	0.03%	
8	13.05	0.00%	13.95	0.01%	14.87	0.01%	

Mode	Mass Config. S1		Mass Config. A2		Mass Config. A6		
	Hz.	Contrib.	Hz.	Contrib.	Hz.	Contrib.	
1	3.17	98.66%	2.62	96.17%	2.38	93.42%	Column Config 3 ($\Omega = 1.35$)
2	4.29	0.00%	4.50	14.42%	4.52	13.86%	
3	9.22	1.17%	9.01	6.27%	7.76	1.00%	
4	12.47	0.00%	13.07	0.60%	12.04	0.08%	
5	14.31	0.12%	13.99	1.10%	13.15	0.07%	
6	17.73	0.05%	17.33	0.55%	14.91	0.02%	
7	19.32	0.00%	20.26	0.03%	20.39	0.00%	
8	23.92	0.00%	25.08	0.00%	25.55	0.00%	

Mode	Mass Config. S1		Mass Config. A2		Mass Config. A6		
	Hz.	Contrib.	Hz.	Contrib.	Hz.	Contrib.	
1	2.65	98.66%	2.62	96.17%	2.38	93.42%	Column Config 4 ($\Omega = 1.62$)
2	4.29	0.00%	4.46	2.91%	4.24	5.56%	
3	7.71	1.21%	7.61	0.81%	6.92	0.86%	
4	11.95	0.11%	11.81	0.08%	10.73	0.11%	
5	12.47	0.00%	12.94	0.01%	12.33	0.04%	
6	14.80	0.02%	14.62	0.02%	13.29	0.01%	
7	19.32	0.00%	20.05	0.00%	19.11	0.00%	
8	23.92	0.00%	24.82	0.00%	23.65	0.00%	

Mode	Mass Config. S1		Mass Config. A2		Mass Config. A6		
	Hz.	Contrib.	Hz.	Contrib.	Hz.	Contrib.	
1	3.05	97.63%	3.03	97.12%	2.88	91.73%	Column Config 5 ($\Omega = 2.07$)
2	6.31	0.00%	6.50	0.66%	5.93	3.42%	
3	8.81	2.22%	8.76	2.07%	8.32	3.72%	
4	13.56	0.10%	13.48	0.09%	12.80	0.65%	
5	16.70	0.05%	16.59	0.05%	15.77	0.28%	
6	18.21	0.00%	18.78	0.00%	17.12	0.19%	
7	28.03	0.00%	28.91	0.00%	26.36	0.00%	
8	34.51	0.00%	35.60	0.00%	32.45	0.00%	

In the above equation, V is the maximum total response, V_i and V_j are the modal responses for modes i and j in terms of the floor side displacements (Δ_A and Δ_B, as in equation (5)), and N is the number of included modes (N=4 in this study). The modal correlation coefficient, ε_{ij}, accounts for the spacing of the modes, such that as the difference between the natural frequencies ω_i and ω_j increases, the second term in equation (9) becomes negligible, thus reducing this method to that of the Square Root of Sum Squares (SRSS) method.

5. Results and Discussion

The 21 experimental test carried out in this series can be divided into two categories which highlight the influence of the column configuration, and that of the mass configuration on the results of the comparison between the analytical and experimental floor displacement. Additionally, the effect of the different ground accelerations have been observed for column configuration CC2.

5.1. Effects of Column Configuration

As discussed earlier, the column configuration controls the uncoupled frequency ratio, Ω, of the modes. Figure 5 shows the percentage variation in evaluating the peak floor displacements from the modal superposition method (MS) to those obtained from the time history analysis (TH), for the Parkfield earthquake input record. In this Figure, a positive analytical variation indicates a situation where the peak displacement calculated by the MS method is greater than that found by the TH method. The results for the low mass eccentricity models, A2, are presented in Figure 5(a) for all 5 column configurations. This figure shows that the MS method underestimates the peak displacements obtained by the

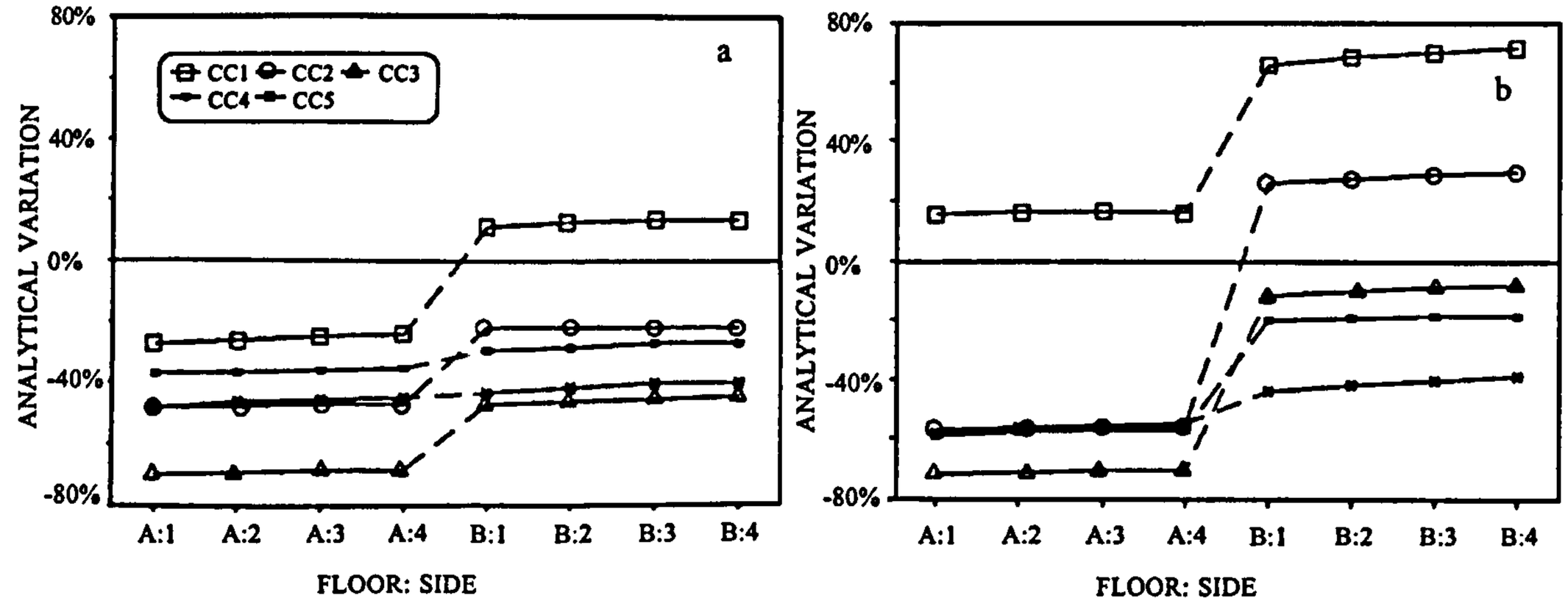

Figure 5: Comparison of analytical methods using the Parkfield ground motion. Values indicated are the modal superposition method normalized by the time history peak values. (a) Low mass eccentricity model (A2); (b) High mass eccentricity model (A6). (CC = Column Configuration)

TH method for side B to a lesser extent than for side A, thus creating the "stepping" effect between the two sides. Additionally, the differences between the two sides become less as Ω increases. The high degree of correlation between the floors for a particular side is a result of the structure responding primarily in the fundamental mode. For models with a higher mass eccentricity, Figure 5(b), the variation between results for sides A and B becomes even larger. Results for other records give consistent trends, but specific numerical variations depend on the frequency content of the ground motion record.

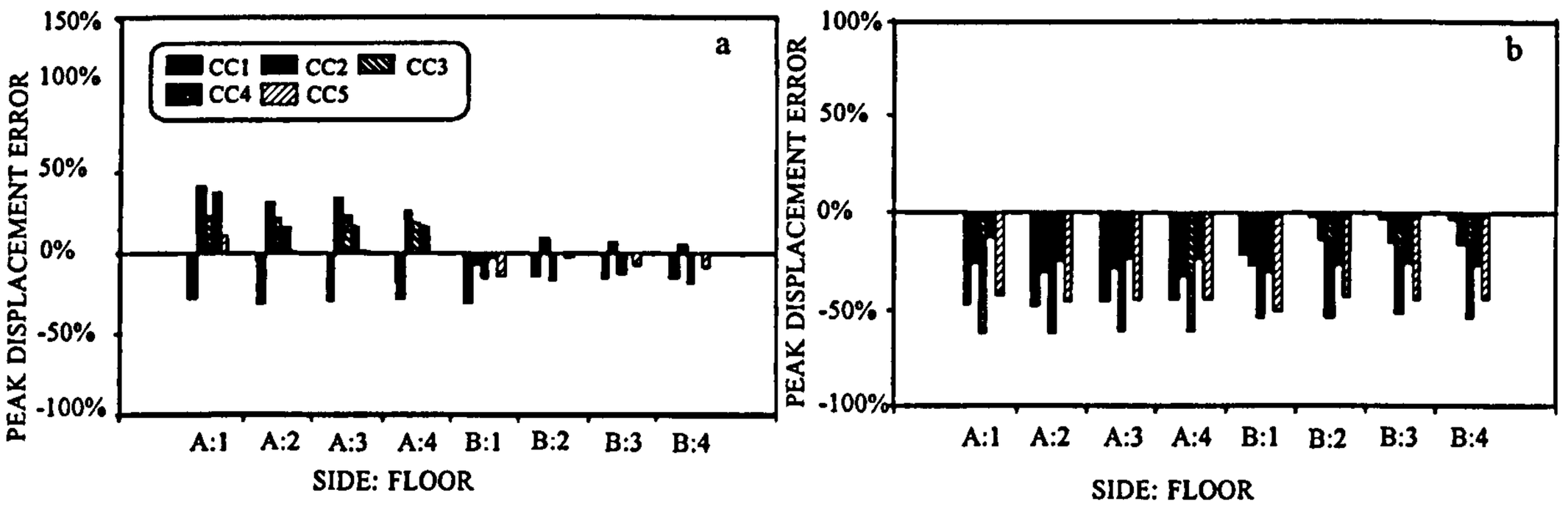

Figure 6: Comparison of analytical and experimental peak displacements for low eccentricity models (A2) using Parkfiled ground motion. Positive values indicate analytical displacements exceed experimental displacments. (a) Time history analysis method; (b) Modal superposition analysis method.

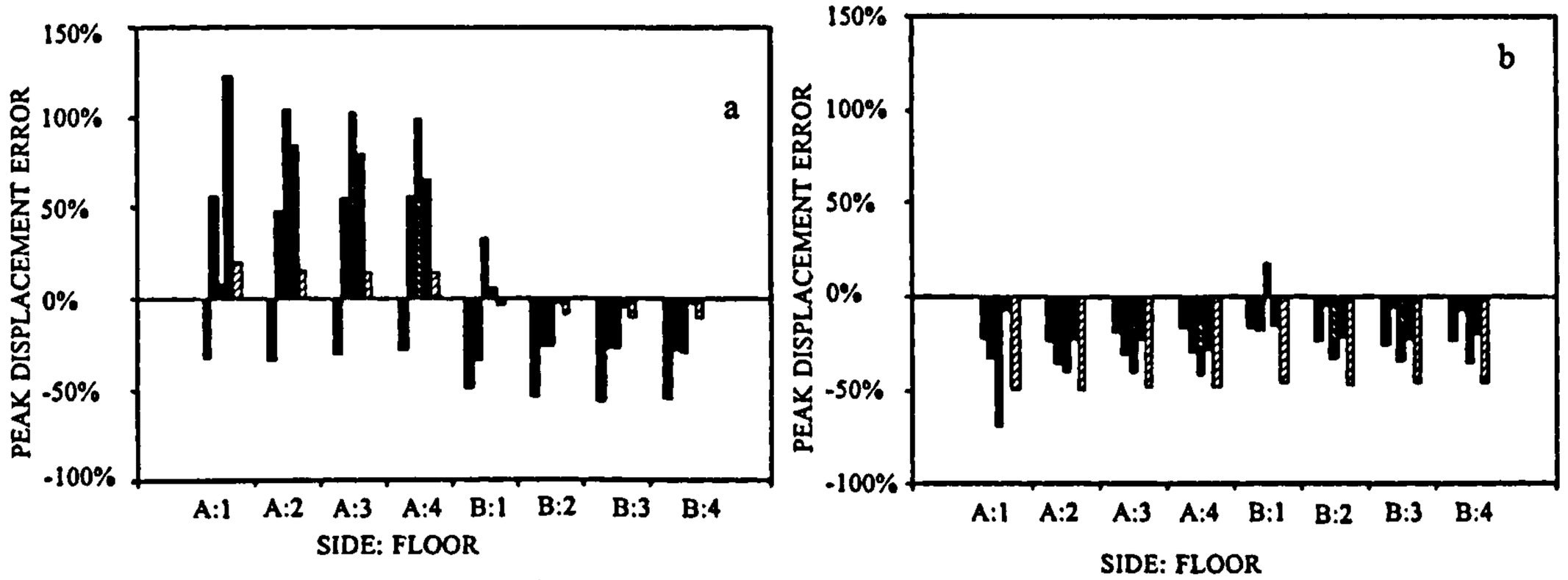

Figure 7: Comparison of analytical and experimental peak displacements for high eccentricity models (A6) using Parkfiled ground motion. Positive values indicate analytical displacments exceed experimental displacements. (a) Time history analysis method; (b) Modal superposition analysis method.

Figures 6 and 7 depict the peak displacement error for the two analytical methods, in comparison with the experimental results, for all column configurations. Hence a positive error indicates that the theoretical approach (TH or MS) overestimates the observed experimental displacement response.

For the case of the low mass eccentricity ratio, mode A2 Figure 6(a) shows that displacement errors calculated by the TH method are significantly higher for side A than for side B. Additionally, the errors on side A are larger at lower uncoupled frequency ratios, Ω (Table 2). The results using the MS method for the same model are depicted in Figure 6(b), which shows that the method underestimated, by up to 60%, the experimental response on both sides of the structures for all column configurations. This can be attributed to the characteristics of the Parkfield earthquake, and the modal combination method. Since the Parkfield ground motion contains a few fairly large cycles of acceleration about 4 seconds into the earthquake record (Figure 2(a)), the peak displacements of sides A and B occur roughly at the same time. This causes the MS method to yield non-conservative

results, since the MS (CQC) method assumes that the peak modal displacments do non occur concurrently when the modal frequencies are separated. This can also be seen in Figures 8(a), 9(a), and 10(a) for the peak side displacement of the Parkfield models. The

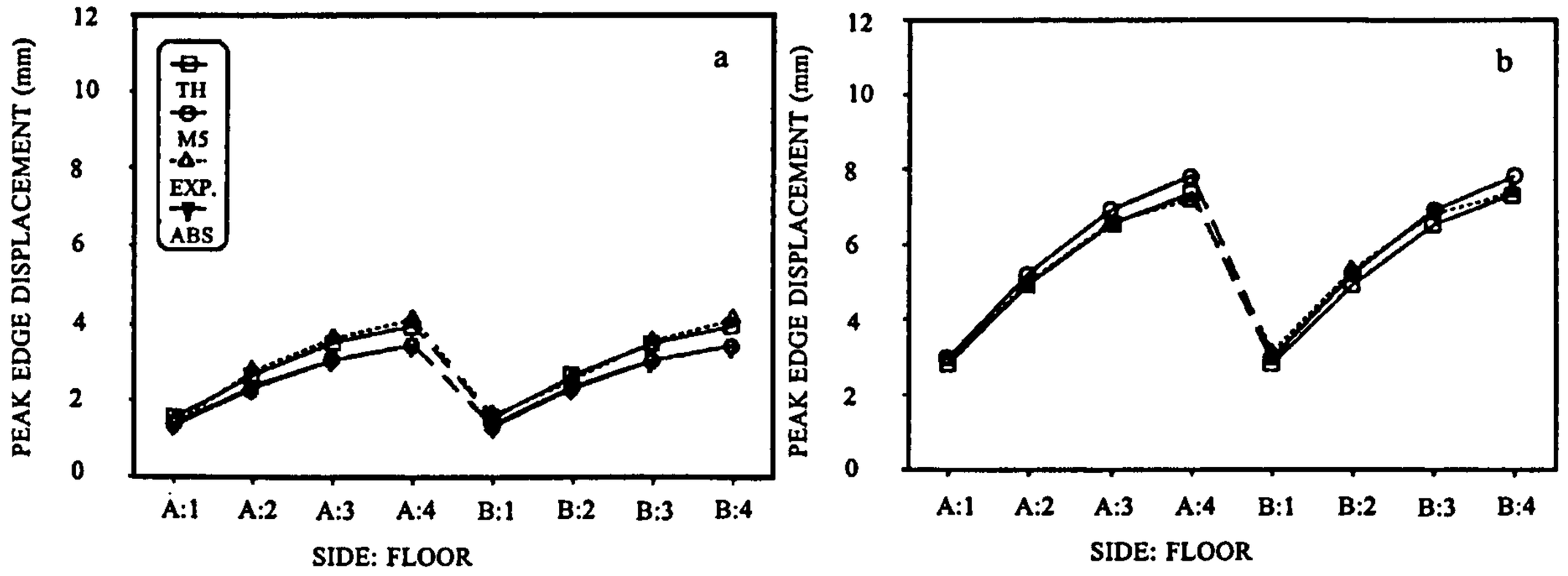

Figure 8: Peak edge displacements for the symmetric mass models, S1. (a) Parkfield; (b) Thessaloniki.

method labelled ABS in these figures is the absolute sum of the first four modal displacement vectors, and is found to achieve a better comparison with the experimental results. This also explains the net negative value of analytical variation shown in Figure 5.

Figure 8(a) indicates that as the mass eccentricity increases, so do the errors in displacement computed by the TH method. As with model A2 (Figure 6(a)), the peak displacements for model A6 are generally overestimated (except when $\Omega < 1$) on side A, and underestimated on side B. This pattern in peak displacement error between the two sides for the TH method is not unique to the Parkfield ground motion. The El Centro and Thessaloniki based ground motions yield similar results (as can be seen in Figures 9 and 10, discussed below). This suggests that the discrepancies of the TH method in predicting the side A and side B displacements arise from assumptions inherent in the lumped mass

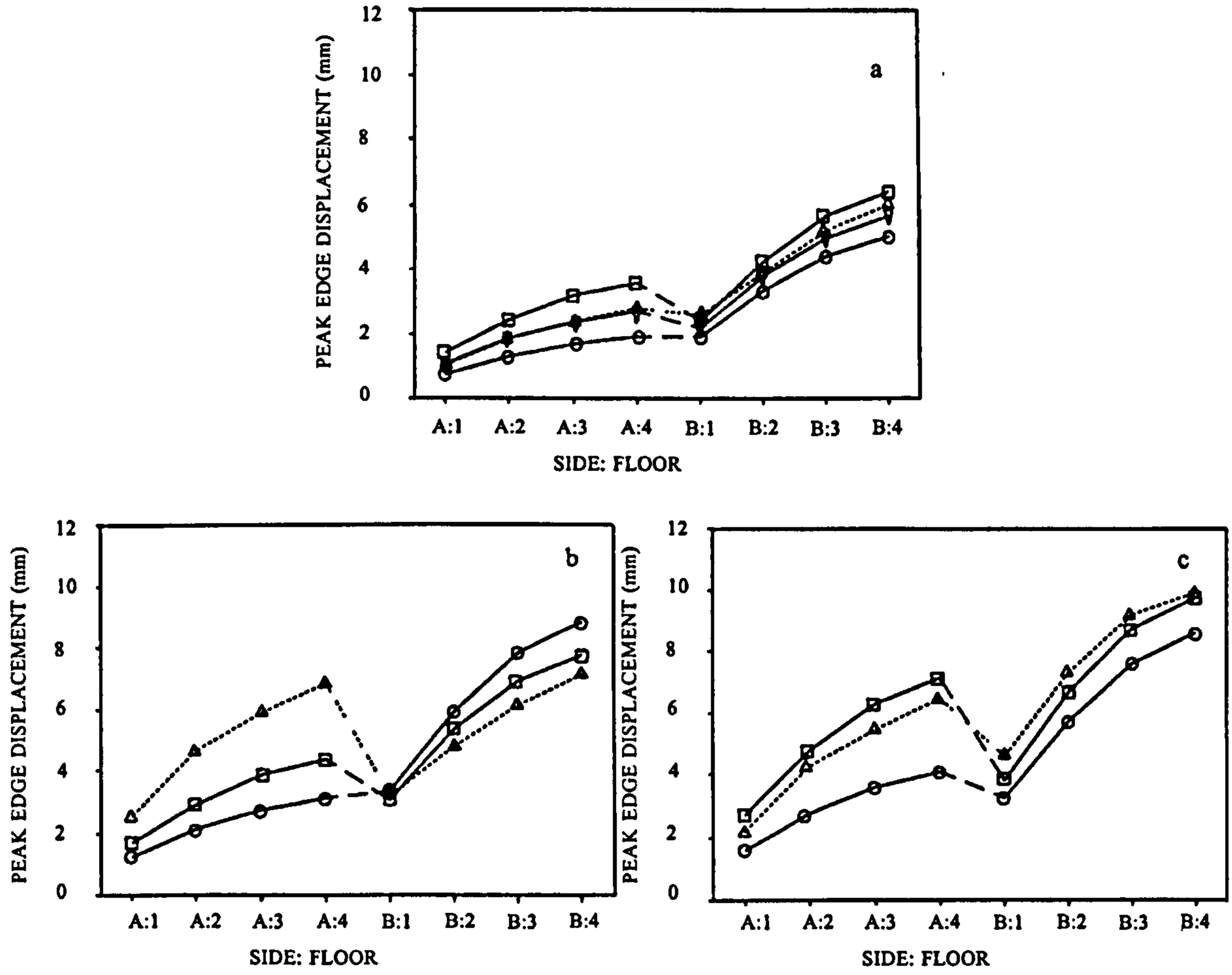

Figure 9: Peak edge displacements for the low mass eccentricity models, A2. (a) El Centro; (b) Parkfield; (c) Thessaloniki.

model, such as neglecting the torsional stiffness of the individual columns, This is less significant in column configuration CC5 due to the absence of the central column (figure 4), hence the high level of agreement between the peak displacements of the TH method and the experimental results (Figures 6 and 7). Displacements computed by the MS method again underestimate the peak response (by up to 60%), as shown in Figure 7(b). However, unlike the TH method, the displacement error is approximately the same for both sides of the structure.

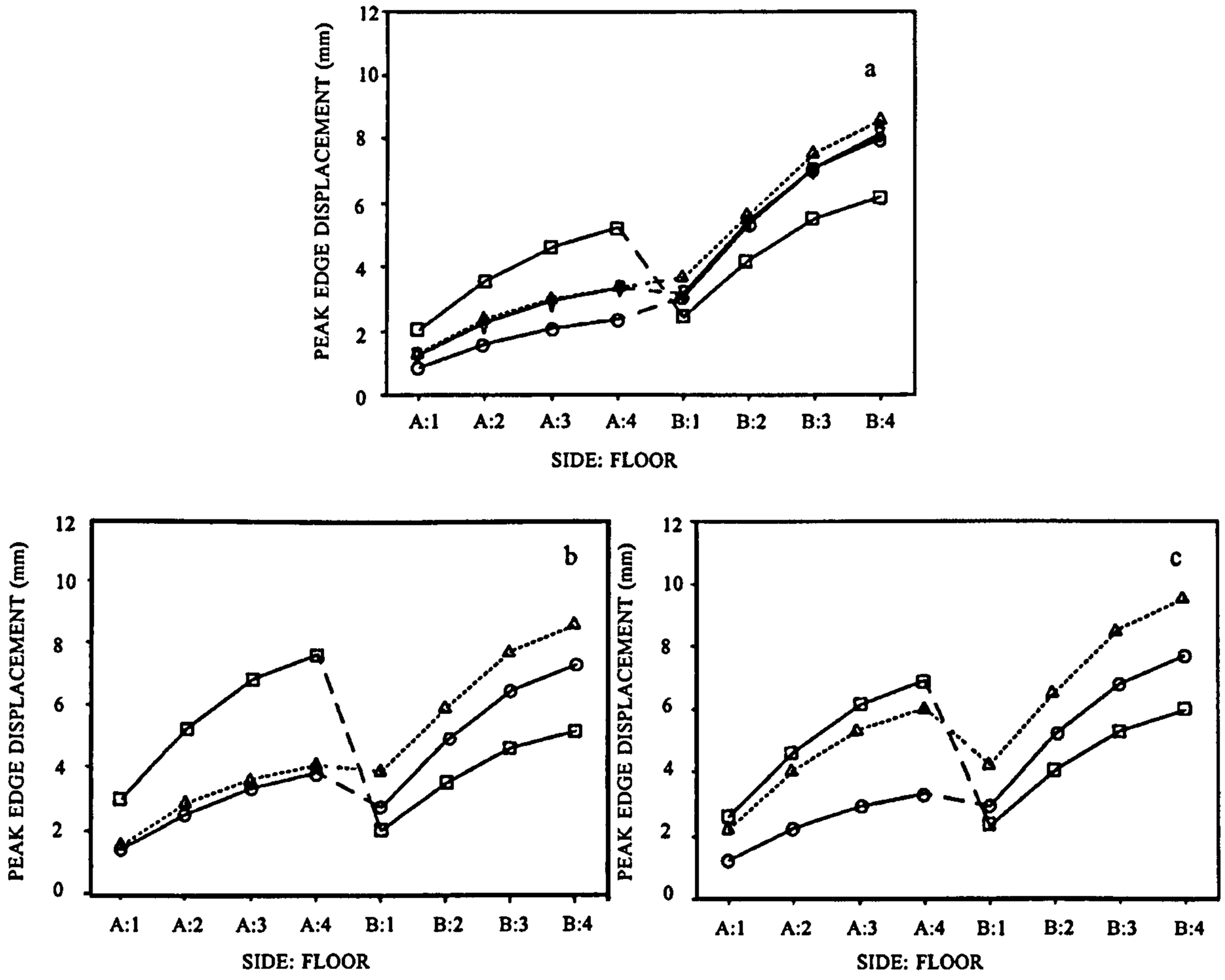

Figure 10: Peak edge displacements for the high mass eccentricity models, A6. (a) El Centro; (b) Parkfield; (c) Thessaloniki.

5.2. Effect of Mass Configuration

The different s configurations alter the structural eccentricity of the model (see Table 1). Figures 8, 9, and 10 show the peak floor displacments on side A and B of model CC2 for the two analytical methods, in comparison with the experimental results, for mass configurations S1, A2, and A6, respectively.

Figure 9 summarized the results of the symmetric mass arrangement corresponding to model configuration 2S1 (note the results for the El Centro ground motion record are not available). This mass distribution has no influence from the torsional modes of vibration

under translational base loading. Figures 8(a) and 8(b) clear show a high correlation between the experimental results and the analytical methods. The results from the TH method offer a better comparison with the experimental side displacments than does the MS method. However, the degree of correlation of the two analytical methods with the experimental results becomes poorer as mass eccentricity is introduced into the model, as can be seen in Figures 9 and 10.

Figure 10 presents the side displacements for the low mass eccentricity model 2A2. These figures correspond to the three ground motion records, and show that the MS procedure consistently underestimates the peak experimental response at side A by values between 10% and 50%, while the TH method both underestimates and overestimates the experimental values by up to 30%. The prediction of the side B displacement from the TH as method is still reasonably accurate for the case of low eccentricity, and as mentioned above, is significantly affected by the frequency content of the ground motion.

The results for the high eccentricity model, 2A6, are depicted in Figure 10. As with the low eccentricity model, the MS method of analysis underestimates the peak displacments on side A of the structure, while the TH method overestimates the peak deployment. Additionally, there is a poorer correlation between the experimental and analytical results on side B as compared to those obtained with the low eccentricity model (Figure 9). On side B, both analytical methods underestimate to varying degrees the experimental results.

6. Conclusion

From the three ground motion records used in this study, it is obvious that the frequency content and characteristics of each of these records has a significant influence on the correlation between the time-domain and modal superposition solutions. Comparing the results form all three records indicates that the modal superposition method significantly underestimates the peak displacement on the side furthest form the centre of mass (side A) for all mass asymmetric models. In contrast, time-domain solutions generally overestimate the peak displacement on this side of the building. For low mass eccentricities, time-domain solutions offer reasonable results for the more vulnerable side of the structure (side B). However, as the mass eccentricity increases, the error in the time-domain solution increases. For highly eccentric buildings, the time-domain method underestimates the side B peak displacments, and overestimates the side A peak displacments.

7. Acknowledgement

This research programme is funded by the UK Science and Engineering Research Council, whose support is gratefully acknowledged. The findings and recommendations in this paper are those of the authors and not necessarily those of the sponsor.

8. References

1. Nichol, E.A. and Chandler A.M., "Seismic Torsional Design Provisions: An Experimental Study based on Code Spectrum-Compatible Earthquake Motions", *(in preparation)*

2. Maheri M.R., Chandler A.M. and Bassett R.H., "Coupled Lateral-Torsional Behaviour of Frame Structures under Earthquake Loading", *Earthquake Engineering and Structural Dynamics*, Vol. 20, 1991.

3. Kan C.L. and Chopra A.K., "Effects of torsional coupling on earthquake forces in buildings", *J. Struct. Div Am Soc. Civ. Engrs.*, Vol. 103, No. ST4 (1977).

4. Muller F.P. and Keintzel E., "Approximate Analysis of Torsional Effects in the New German Seismic Code DIN 4149", *Proc. of the 6th European Conf. on Earthquake Eng.*, Dubrovnik, Vol. 2 (1978).

5. Tso W.K. and Dempsey K.M., "Seismic torsional provisions for dynamic eccentricity", *Earthquake Eng. Struct. Dyn.*, Vol. 8 (1980).

6. Clough R.W. and Penzien J., *Dynamics of Structures*, McGraw-Hill, New York, 1975.

7. Hart G.C., Di Julio R.M. and Lew M., "Torsional responses of high-rise buildings", *J. Struct. Div. Am. Soc. Civ. Engrs.*, Vol. 101, ST2 (1976).

8. Wilson E.L., Der Kiurghian A. and Bayo E.P., "A Replacement for the SRSS Method in Seismic Analysis", *Short Communication, Earthquake Engineering and Structural Dynamics*, Vol. 9 (1981).

9. Maison B.F., Neuss C.F. and Kasai K., "The Comparative Performance of Seismic Response Spectrum Combination Rules in Building Analysis", *Earthquake Engineering and Structural Dynamics*, Vol. 11 (1983).

ALL MISSING PAGES ARE BLANK

IN

ORIGINAL

Source:
International Conference on Earthquake, Blast,and Impact Loadings, 1991.
UMIST, Manchester, Pages 231-240.

Design and Performance of Model Floor-Column Joints for Simulation of Inelastic Structural Response under Earthquake Loading

E.A. Nichol, A.M. Chandler and R.H. Bassett

ABSTRACT - Hinged joints have been developed for use in experimental inelastic dynamic response studies of modelled buildings. These hinge simulate the formation of plastic hinges either in the column or in the beams of a building under dynamic loading. Experimental results are presented for an initial series of tests studying the inelastic behaviour of a series of single-storey building modes with varying mass asymmetry and different plastic hinge configurations.

1. Introduction

This research programme forms the second part of a study on the torsional behaviour of asymmetric buildings. The initial part of this study dealt with the elastic torsional behaviour of multi-storey mass asymmetric buildings, from which the experimental and analytical results have been presented in previous publications [1,2,3]. The current research

programme modifies the original elastic experimental model in order to accommodate inelastic structural behaviour through the use of hinges, which simulate plastic yield in the beam-column connections. From this, the effects of inelastic torsional coupling on single and multi-storey buildings can be verified experimentally, and compared to the numerous analytical studies available.

This paper describes the incorporation of hinge units in a series of single-storey building models. Details on the performance of these hinges at various yield levels and yielding distributions in buildings subjected to impulse loading and a Eurocode-8 spectrum compatible earthquake ground motion are presented herein.

2. Experimental Model

2.1. Description of Experimental Model

The building model used in this series of experiments consists of a single storey frame with 5 work-hardened brass columns, shown in Figure 1 mounted on the SERC 6-axis earthquake simulator at Bristol University. The floor, measuring approximately one metre square, incorporates a series of lead plates which can be placed in different positions within the floor frame to alter the mass eccentricity in the building. Three different mass configurations have been used in this study. These consist of one symmetric mass arrangement (S1, $e'_r = 0.0$) and two coupled asymmetric mass distributions (A2, $e'_r = 0.07$ and A6, $e'_r = 0.20$) [1]. The parameter e'_r is the stiffness eccentricity ratio, defined as the distance between the centre of stiffness or resistance (which in all models coincide with the geometric centre of the floor frame) and the centre of mass, normalized by the floor

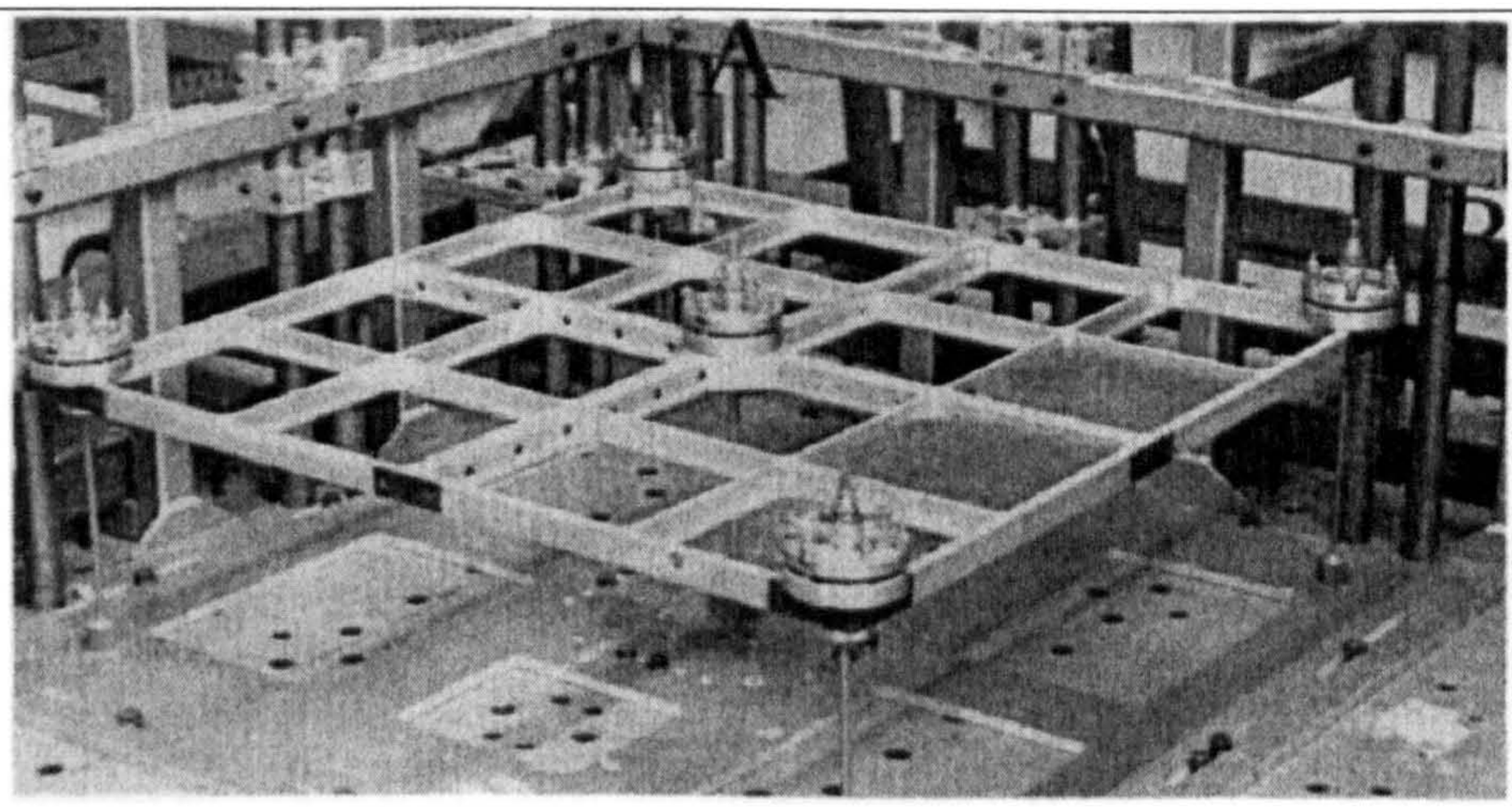

Figure 1: Single-storey experimental model, shown with mass configuration A6. The depicted hinge configuration entails floor hinges and rigid column-base connections.

dimension perpendicular to the applied loading. The mass eccentricity ratio for mass distributions A2 and A6, represent buildings with low and high asymmetry, respectively. The two asymmetric mass distributions are coupled, meaning that in the elastic range, translational ground excitations result in both translational and torsional structural behaviour. In the inelastic range, other parameters such as the strength eccentricity (distance between the centre of strength and centre of mass) and strength distribution can significantly affect the behaviour.

Displacements are measured by non-contacting transducers mounted on rigid frames adjacent to the model (Figure 1). The column diameters in the model can also b varied to produce different ratios of torsional and translational stiffness [1]. This study concentrates on a column configuration which haws a ratio of torsional to translational frequency (Ω) near unity (see Table 3), a value which will generally lead to the greatest elastic torsional coupling effects [5].

2.2. Description of Hinge Joints

The hinge joint units consist of a set of brass clamping collars with detachable friction pads on a polished brass domed hinge cap (see Figure 2). The yielding moment in the

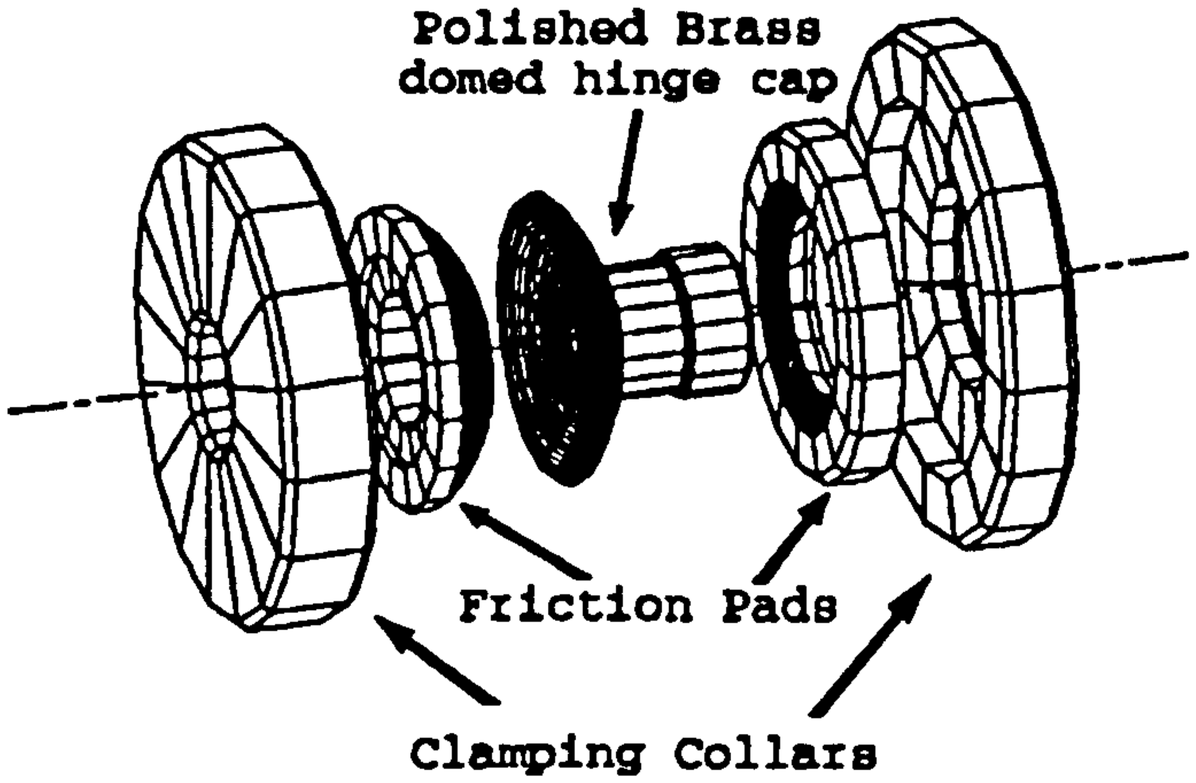

Figure 2: Exploded view of a typical hinge unit.

hinge unit can be varied through an adjustment of the clamping force and through the use of different friction pad materials. The clamping force on the friction pads can e accurately adjusted between 0.1kN and 1.3 kN. Accounting for the different friction pad materials, this variation allows hinge yield moments to be developed anywhere in the range of 1.1N·m to 30.0N·m (see Table 1). Table 2 lists the six hinge configurations used in this

Table 1: Hinge pad specifications.

Hinge pad material	M_p friction coefficient, μ_m (N·m/N)†	Minimum M_p (N·m/N)	Maximum M_p (N·m/N)
PTFE	0.011	1.1	14.1
Lignum Vitae	0.012	8.4	15.0
Stainless Steel	0.023	13.7	30.0

†Mp = $\mu_m \cdot F_c$, where M_p is the initial plastic moment and F_c is the clamping force on the hinge friction pad.

study, together with the corresponding strength eccentricity ratios. The parameters F_y and M_y are the total translational and rotational strength about the centre of strength of the single storey model, respectively.

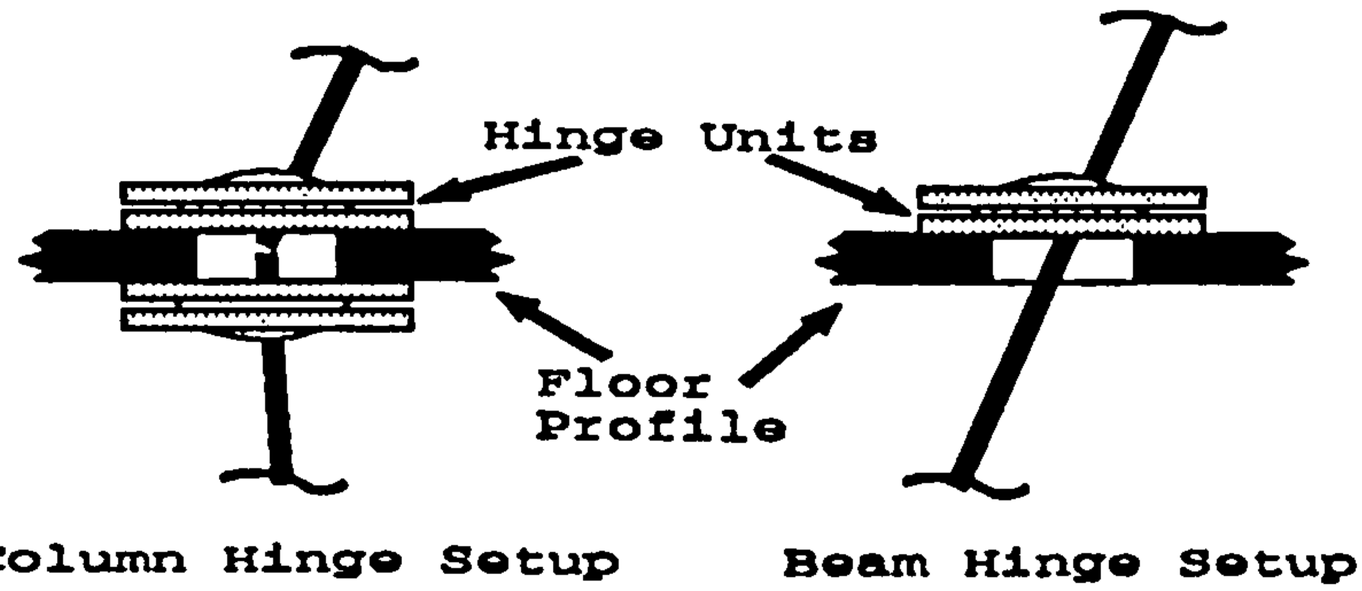

Figure 3: Hinge placement set-ups for the simulation of plastic yield in the columns or in the beams at floor level.

In studies of multi-storey buildings, the hinge units can be attached to the model at the column-floor connections in either of two set-ups (Figure 3). The column yield setup consists of a hinge unit placed on both the top and bottom of each floor, and segmented columns attached to each hinge. This allows for a discontinuity in the column curvature at each floor, thus simulating the formation of a plastic hinge located in the column at floor level. The beam yield setup places a single hinge at either the top o bottom of each floor, and employs a continuous column through the hinge unit. The resisting moment of the floor (beams) on the column is then limited to M_p (Table 1).

For the single-storey model examined in this study, emphasis has been placed on two hinge set-ups. For the impulse tests, hinges are placed at the top of each column, while the base of each column remains fixed. The earthquake tests have hinges at both the top and bottom of each column, thus allowing the possible formation of a mechanism. A photograph of the latter case is shown in Figure 5.

Table 2: Hinge configurations.

Hinge Configuration	F_y (N)	M_y (N·m)	F_y/M_y (m^{-1})	Strength eccentricity ratio, e'_s †
1	7.4	3.9	1.90	0.00
2	5.9	2.9	2.03	0.00
3	12.8	2.9	4.41	0.00
4	13.6	3.4	4.00	-0.04
5	27.5	12.5	2.20	-0.36
6	30.4	16.9	1.80	+0.17

† Negative values indicate that the location of the centre of strength is in the direction opposite the centre of mass, with respect to the geometric floor centre.

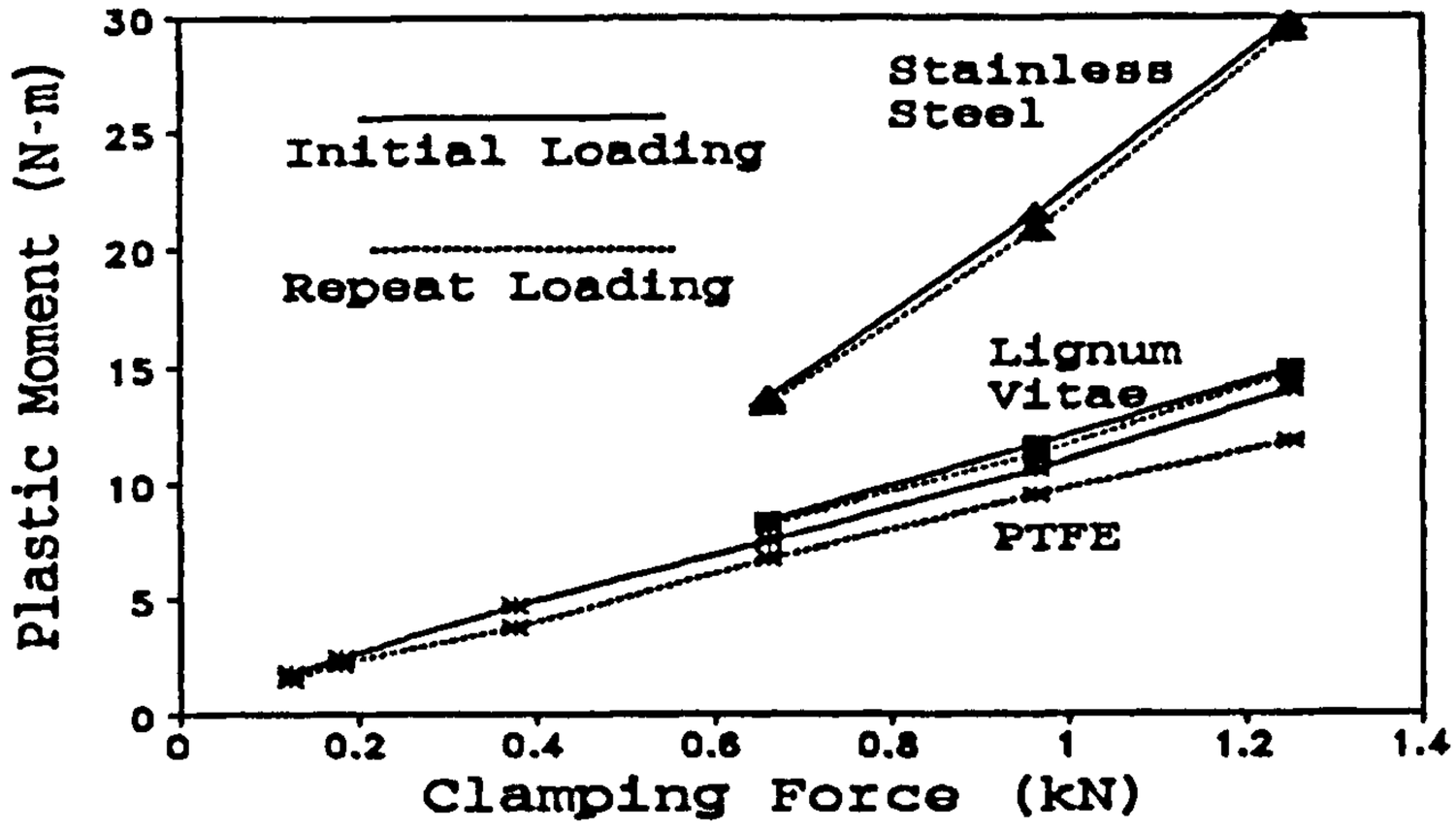

Figure 4: Mean hinge yield moment as a function of hinge clamping force for both initial and repeat loading.

2.3. Static Testing

Static tests have been performed to determine the initial yielding moment in the hinge units, and their yield capacity during repeat testing. For the initial yield tests, the clamping force in the hinge units is completely released, thus ensuring no residual shear stresses on the friction surface. The units are then re-clamped, and loaded until the onset of yielding. For the repeat yield tests, the hinge units are centred without releasing the clamping force,

then reloaded until yield. Figure 4 shows the relationship between the clamping force and

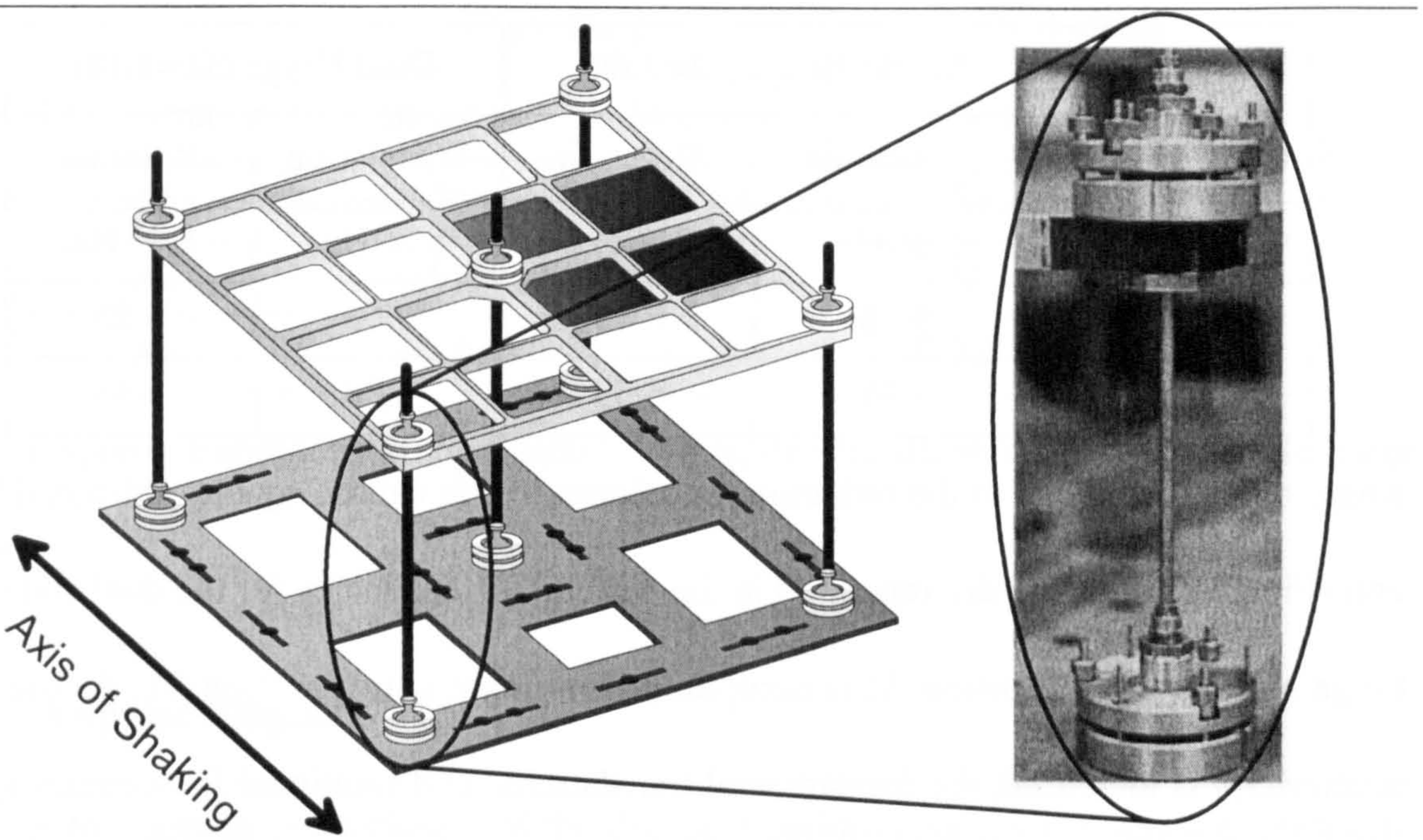

Figure 5: Single-storey dual hinge set-up.

the yield moment for both initial and repeat yielding of the hinge units for the different types of friction pad materials. The standard deviation about the mean plastic moment for PTFE (about 1%) is lower than that obtained during the static tests for either lignum vitae or stainless steel. Hence, the stainless steel and lignum vitae friction pads were not tested in the low plastic moment range, where the PTFE friction pads performed more consistently.

3. Dynamic Testing

3.1. Frequencies

The frequencies of the building models have been determined experimentally, and are listed in Table 3. The elastic stiffness of the dual hinge set-up is greater then that for the

Table 3: Elastic frequencies of vibration for the 3 mass set-ups. Single hinge indicates hinge unit at the top of each column. Dual hinge denotes hinge units at both top and bottom of every column.

Mass Configuration	Single Hinge (Ω=1.09)		Dual Hinge (Ω=1.18)	
	Translation	Rotation	Translation	Rotation
S1	5.80Hz.	6.30Hz.	6.80Hz.	8.03Hz.
A2	5.18	6.45	6.65	8.23
A6	4.75	6.53	6.08	8.35

single hinge set-up due to the reduction in column length caused by the additional hinge unit (Figure 5), thus the discrepancies in the structural frequencies for the dual and single hinge models. By definition, Ω is computed from mass configuration S1. As the mass eccentricity is increased, the fundamental translational and rotational frequencies spread apart. This in turn reduces the effects of elastic torsional coupling. However, the increase in the mass eccentricity increases the rotational displacement component in the model. The frequencies listed in Table 3 are representative values for prototype 1-2 storey buildings.

3.2. Damping

The damping ratios for the building models have been calculated by both the width of the Fourier transform resonance peak obtained from the displacement response, and through free vibration displacement decay measurements. The translational mode produced better agreement between the two methods. This is partially a result of this being the fundamental mode (Ω>1.0). The elastic damping ratios listed in Table 4 are fairly low compared with actual buildings, especially for the dual hinge set-up. When fully clamped, the hinge unites provide a higher degree of fixity than the column-base connections as is evident from the lower damping values. The influence of the low elastic damping ratios on the ine-

Table 4: Elastic damping ratios for the three mass configurations.

Mass Configuration	Single Hinge		Dual Hinge	
	Translation	Rotation	Translation	Rotation
S1	0.97%	0.47%	0.55%	0.23%
A2	0.99	0.58	0.56	0.26
A6	0.82	0.69	0.33	0.34

lastic response become negligible due to the hysteretic damping inherent in the hinge joints.

3.3. Impulse Response

In order to examine the influence of the different building parameters (mass eccentricity, strength eccentricity and distribution) on the inelastic response, a series of uniaxial impulse tests were performed. each model was loaded with two different frequencies of a modified sinusoidal acceleration impulse (Figure 6), each frequency being close to that of either its fundamental translational or rotational mode. Additionally, each impulse test was repeated through a range of peak input accelerations.

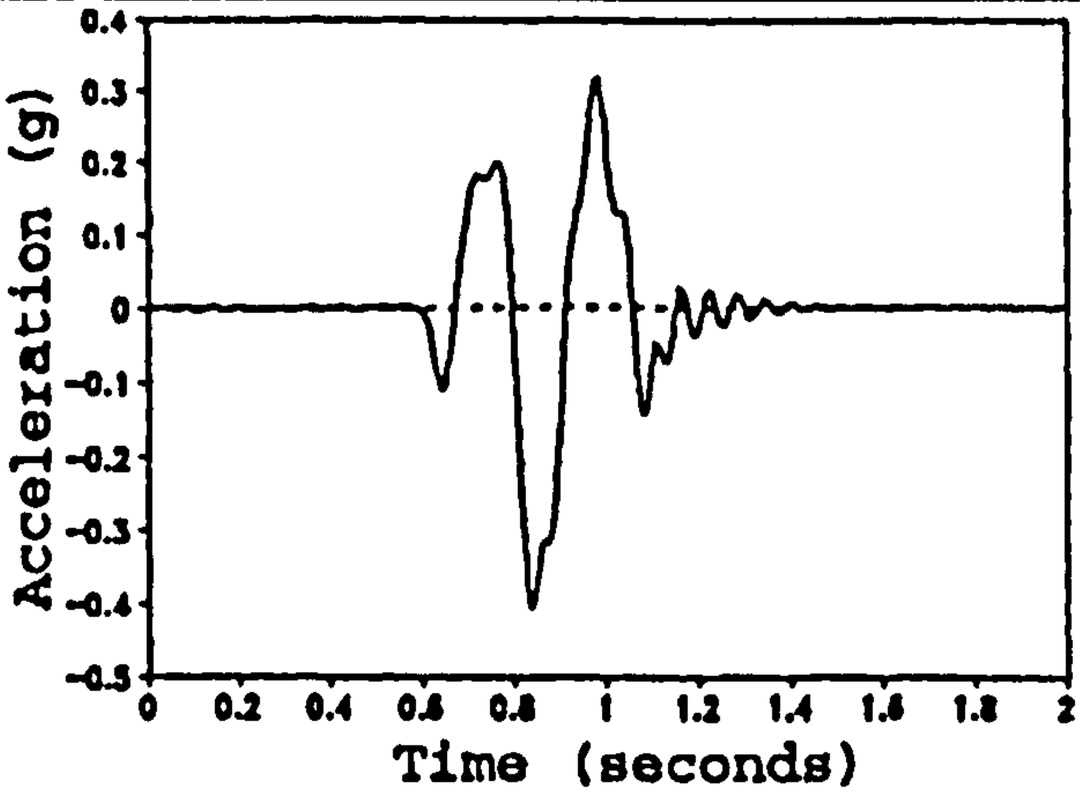

Figure 6: Acceleration time-history of typical impulse response.

3.4. Earthquake Response

In addition to the impulse tests, a simulated acceleration time-history, as specified for hard soils or rock by Eurocode 8, was used to measure the structural response. The correction factor for low damping was modified in accordance with the recommendations of reference [6]. The earthquake record has a significant duration of just over 10 seconds, with high energy content in the velocity controlled region of the response spectrum (Figure 7).

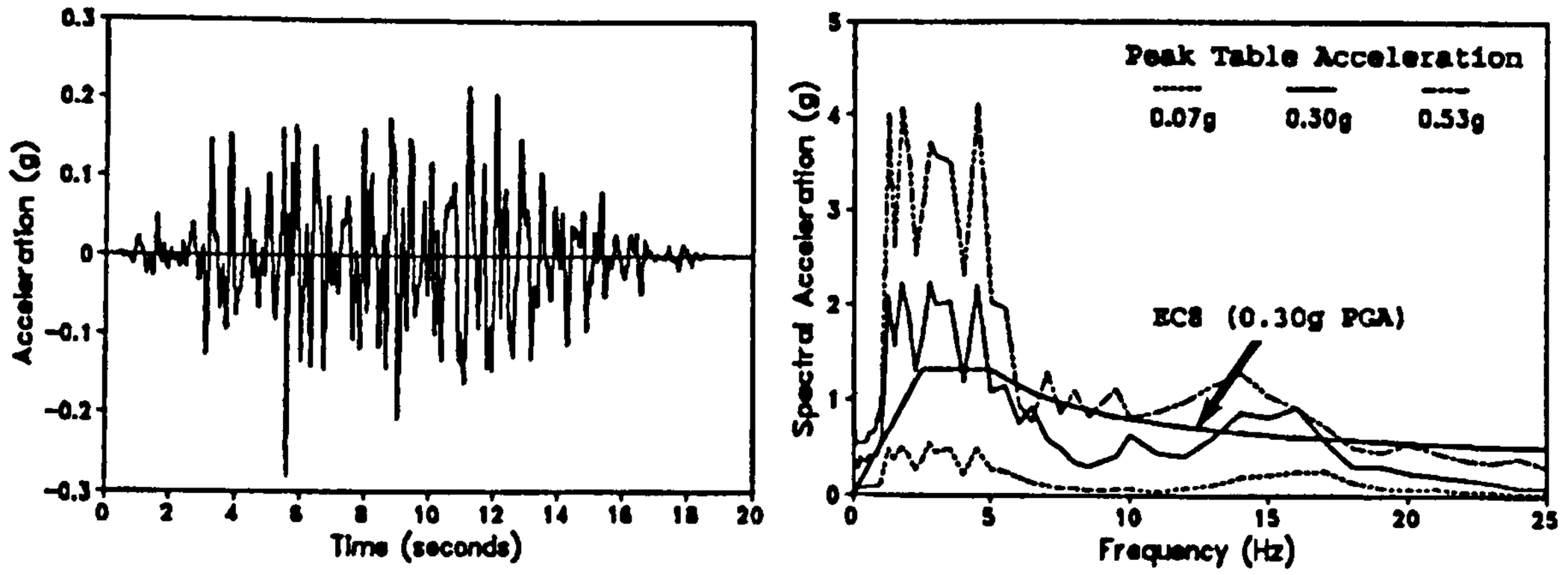

Figure 7: Eurocode 8 spectrum compatible ground acceleration (0.3g PGA, soil type A) shown with the 0.5% damped spectral acceleration response at various levels of peak ground acceleration.

This is also the range which has the most influence on the building models during inelastic behaviour, due to the reduction in frequency.

4. Analysis of Results

Figures 8 through 11 show the peak displacement response of the two sides of the model designated A and B (Figure 1, where side B is closest to the centre of mass) arising from the translational impulse applied at both the translational and rotational modal frequen-

cies. The peak displacements for each hinge configuration coincide for a particular side peak ground accelerations below 0.1g, since the structure is still behaving elastically.

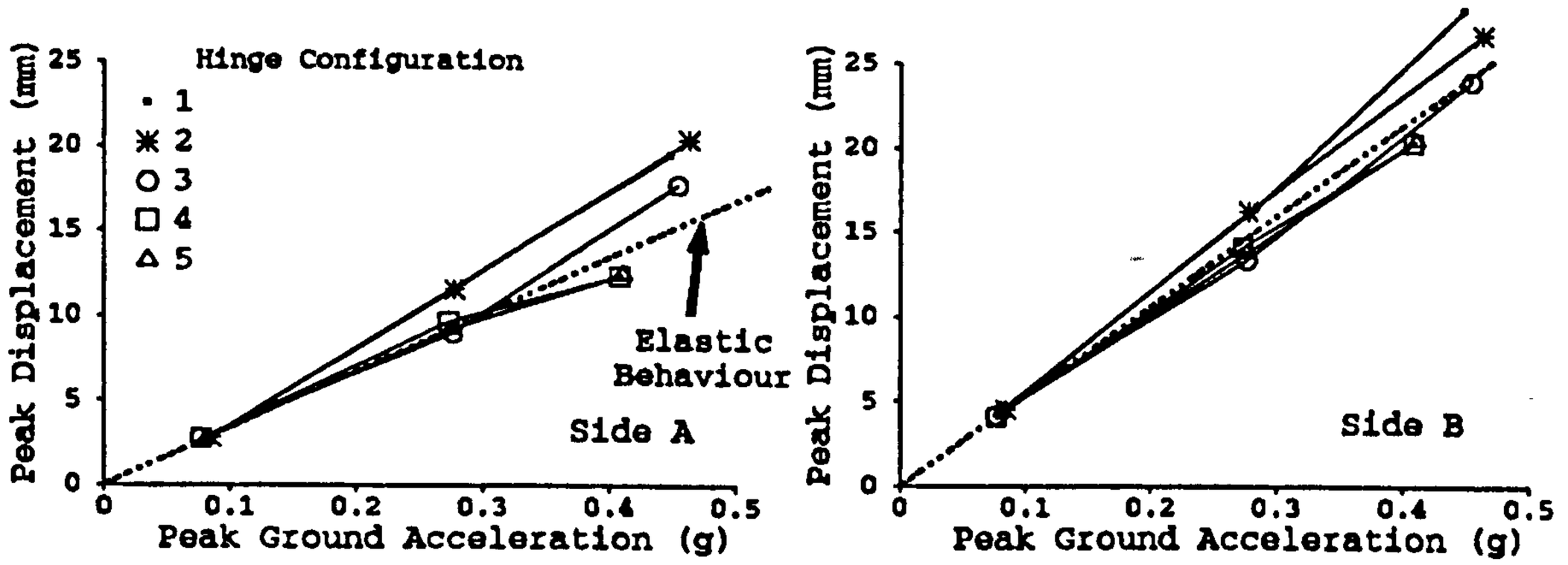

Figure 8: Peak impulse response of model A2 (low mass eccentricity) at fundamental **translational** frequency.

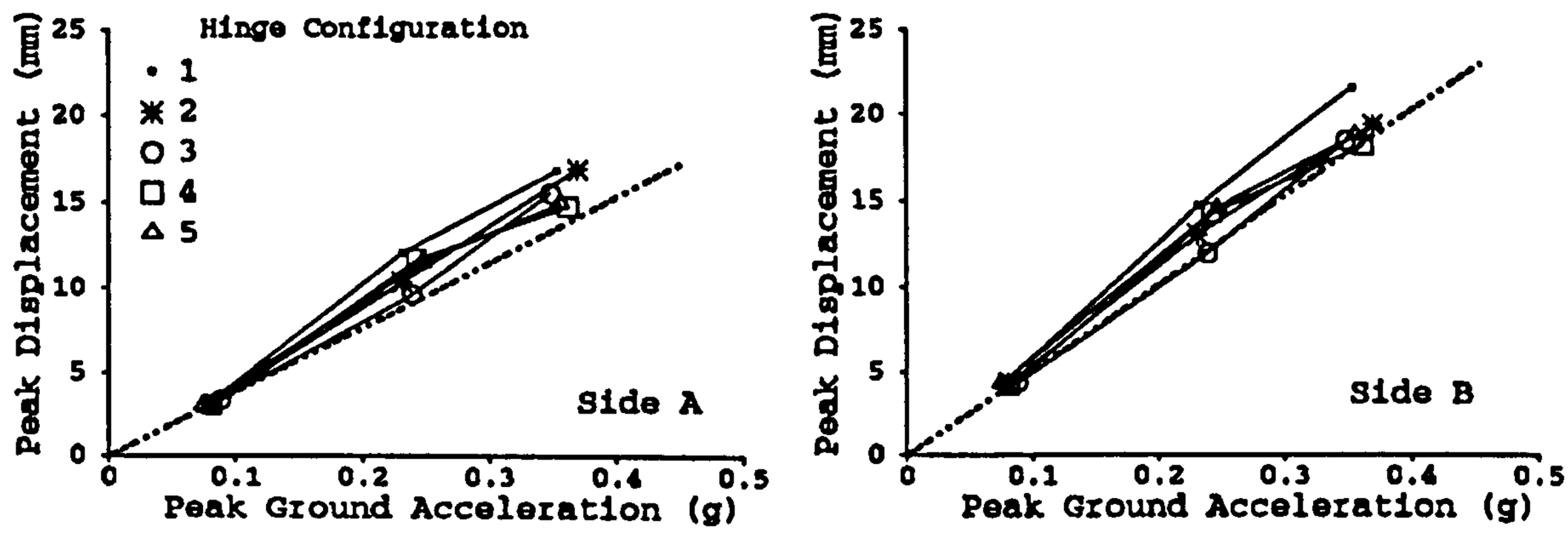

Figure 9: Peak impulse response of model A2 (low mass eccentricity) at fundamental **rotational** frequency.

Figures 8 and 9 show the peak response from the translational frequency impulses for models with low and high mass eccentricities, respectively. The peak response is always greater for side B, with the differences increasing with the mass eccentricity. For both models A2 and A6, hinge configurations 1 and 2 result in the highest displacements due to their low translational yield strength, F_y. Larger values of the moment strength, M_y (Table 2), tend to reduce the inelastic torsional behaviour of *the model.*

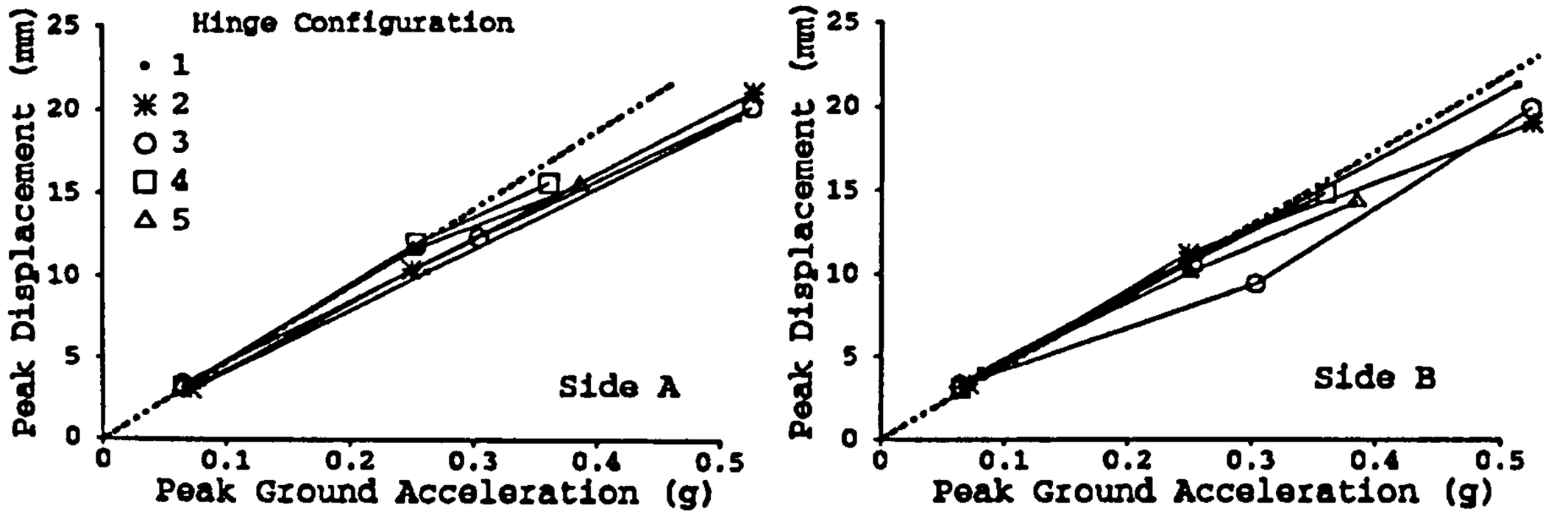

Figure 10: Peak displacements for high mass eccentricity model (A6). Translational impulse at primary rotational frequency.

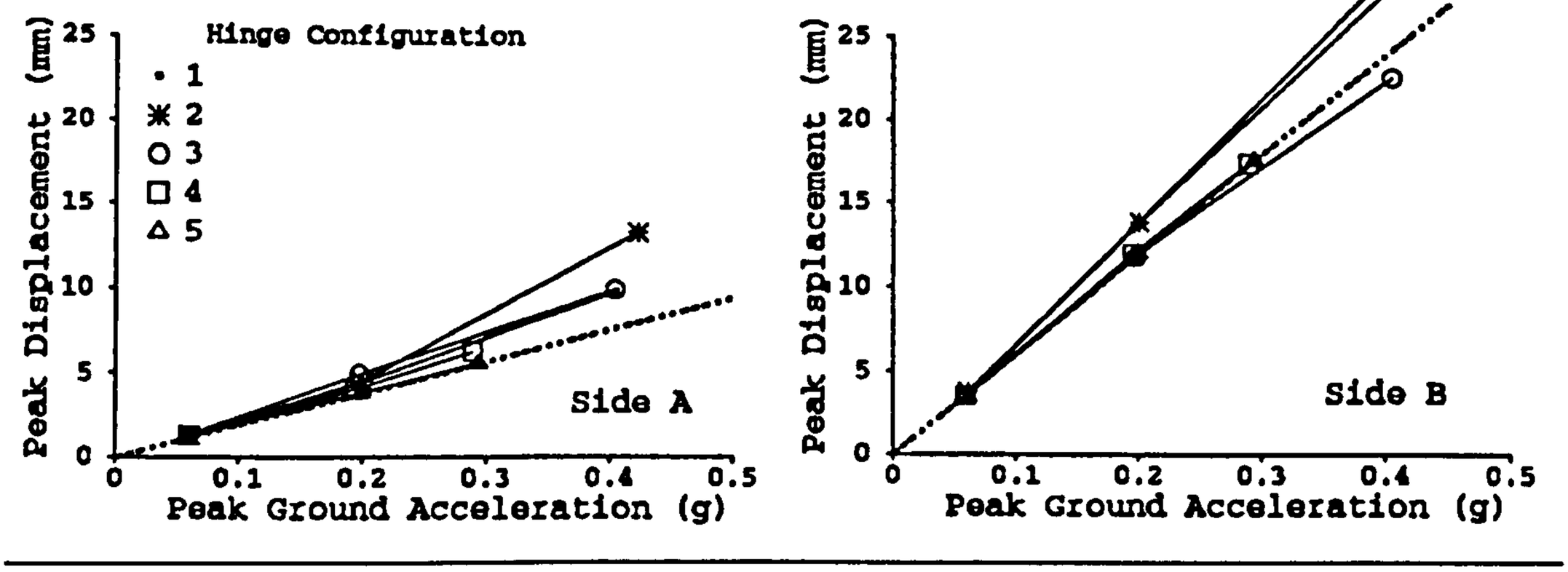

Figure 11: Peak displacement response of high mass eccentricity model (A6) at fundamental **translational** impulse frequency.

Figures 10 and 11 show the peak displacement response from the translational impulse applied at the primary rotational frequencies. the peak displacements do not vary greatly between the two sides, in contrast with the translational impulse frequency responses. However, side B is still the more vulnerable in terms of displacement, especially for the low mass eccentricity. This is the result of the modal frequency shifts due to the change in mass eccentricity. Hence, the rotational impulse frequency is much higher than from the fundamental translational frequency. This affects both the resonance response, and the influence from torsional coupling.

The earthquake input was used to determine the performance of the hinge joints under extended dynamic loading. The dual hinge set-up was used in this case (Figure 4). For brevity, only one experimental test is presented. Figure 12 shows the response of side A

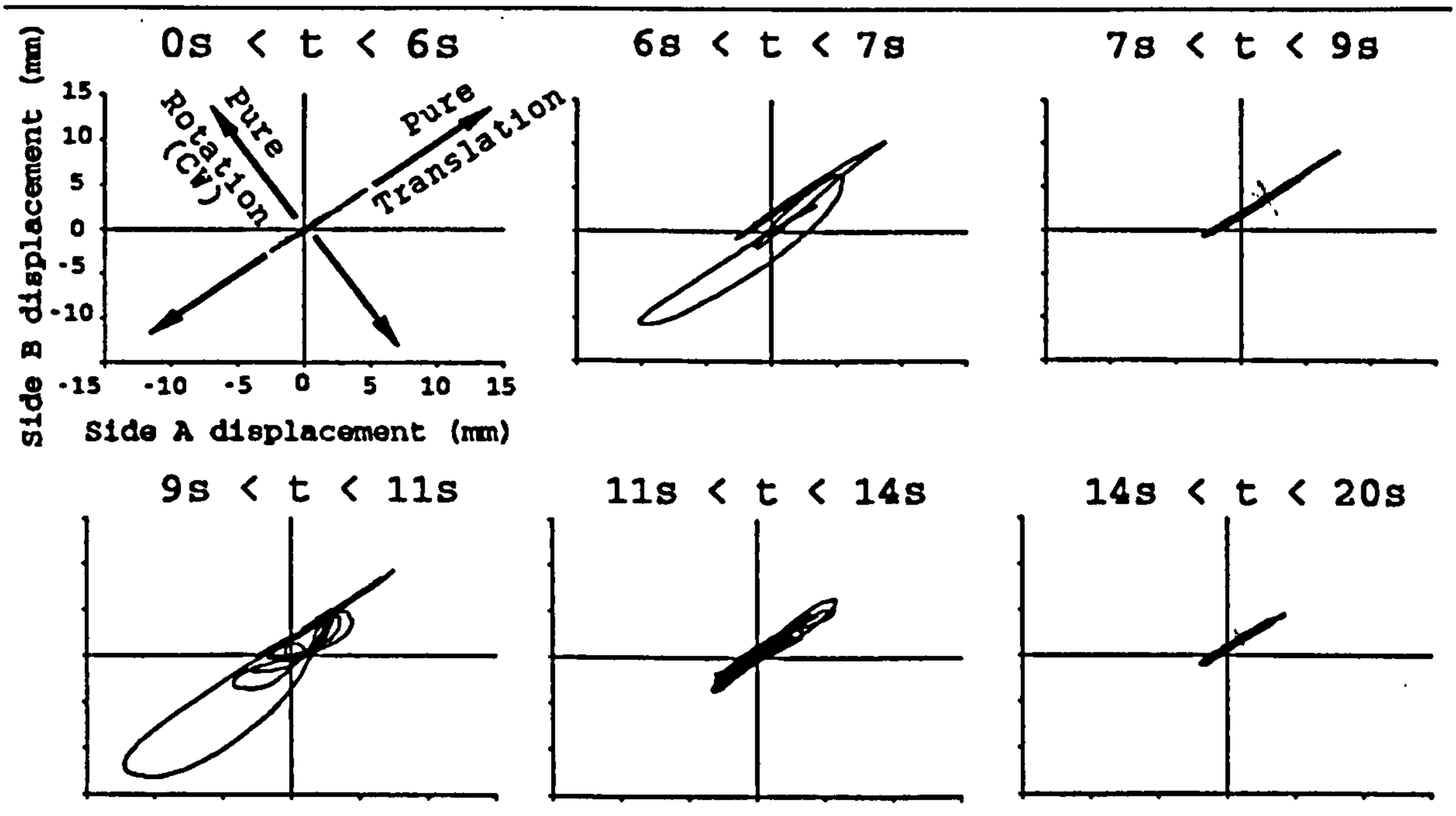

Figure 12: Plot of displacements for side B against side A for the mass symmetric (S1) strength asymmetric model (hinge configuration F, e'_s=+0.17, 0.5g PGA).

plotted against side B in a series of time-windows for the model with hinge configuration 6, and 0.5g peak ground acceleration. Because of the particular input motion, the inelastic response is concentrated in two time-windows (6s to 7s and 9s to 11s). It is shown that for the first 6 seconds, the structure behaves elastically, only in translation. Just after 6 seconds into the loading history the hinges yield, producing the first peak displacement pulse (10mm), for both sides. However, some torsional behaviour is introduced into the response from the strength eccentricity, i.e. the yield capacity on side A being less than that on side B (e'_s>0.0). The response again becomes elastic at 7 seconds with inelastic offsets of 2mm and 4mm for sides A and B, respectively. From 10 seconds into the earth-

quake record, the response again becomes inelastic leading to a final structural deformation of 1mm in translation.

5. Future Research Programme

Currently, inelastic tests are being carried out on multi-storey, variable mass asymmetric building modes. These multi-storey structures will also be modified at a later date to incorporate shear walls. The effect of the cyclic stiffness degradation that these shear walls have on the inelastic torsional behaviour, as well as the energy dissipation capacity of both the hinge units and shear walls, are to be studied.

6. Conclusions

The overall performance of the hinge joints in simulating plastic yield in the beam-column connections for the single storey experimental model are reasonable and repeatable. The results indicate that the translational yield strength and strength eccentricity are the most influential parameters in the inelastic response of the single-storey model.

7. Acknowledgement

This research programme is funded by the UK Science Engineering Research Council (Grant GR/F/60632), whose support is gratefully acknowledged. The findings and recommendations in this paper are those of the authors and not necessarily those of the sponsor.

8. References

1. Maheri, M.R., Chandler, A.M., and Bassett, R.H., 1991. "Coupled lateral-torsional behaviour of frame structures under earthquake loading", *Earthquake Engineering and Structural Dynamics*, 20:61-85.

2. Bassett, R.H., Maheri, M.R., and Chandler, A.M., 1990. "Torsional earthquake response of frame buildings to Eurocode 8 spectrum compatible design motion", *Proc. 9th Eur. Conf. Earthquake Eng.*, Moscow, 5:97-106.

3. Chandler, A.M., and Nichol, E.A., 1990. "Experimental evaluation of procedures for earthquake analysis of torsionally asymmetric buildings", *European Earthquake Engineering*, 3:*43-52.*

4. Commission of the European Communities, 1988. "Eurocode 8: Structures in seismic regions", Part 1, Brussels, Report # EUR 12266 EN.

5. Kan, C.L., and Chopra, A.K., 1977. "Elastic Earthquake Analysis of a class of Torsionally Coupled Buildings", *Journal of Structural Division*, ASCE, 103:395-412.

6. Chandler, A.M., "Evaluation of Site-Dependent Spectra for Earthquake-Resistant Design of Structures in Europe and North America", *Proc. Instn. Civ. Engrs.*, London, Part 1, (in press).